

The Effect of Laser Noise on an Optical
Orthogonal Frequency Division
Multiplexing (OFDM) System

Zuraidah Zan

Doctor of Philosophy

Monash University

July 2013

Under the Copyright Act 1968, this thesis must be used only under the normal conditions of scholarly fair dealing. In particular no results or conclusions should be extracted from it, nor should it be copied or closely paraphrased in whole or in part without the written consent of the author. Proper written acknowledgement should be made for any assistance obtained from this thesis.

I certify that I have made all reasonable efforts to secure copyright permissions for third-party content included in this thesis and have not knowingly added copyright content to my work without the owner's permission.

Thesis Declaration

I hereby declare that this thesis contains no material which has been accepted for the award of any other degree or diploma at any university or equivalent institution and that, to the best of my knowledge and belief, this thesis contains no material previously published or written by another person, except where due reference is made in the text of the thesis.

The ideas, development and writing up of the thesis were the principal responsibility of myself, the candidate, working within the Department of Electrical and Computer Systems Engineering under the supervision of Professor Arthur James Lowery (the principle supervisor) and Professor Malin Premaratne (the associate supervisor).

This thesis includes the works published in two journals and three conferences, which appear in the following chapters:

Chapter 4:

Z. Zan, & A. J. Lowery (2010). "Experimental demonstration of a flexible and stable semiconductor laser linewidth emulator." Optics Express **18**(13): 13880-13885.

Chapter 7:

Z. Zan, A. J. Lowery, & M. Premaratne (2008). Laser RIN and linewidth requirements for direct detection optical OFDM. Lasers and Electro-Optics CLEO 2008, San Jose.

Chapter 8:

Z. Zan, L. Du, & A. J. Lowery (2010). Experimental demonstration on the reduction of linewidth impact in a self-heterodyne optical OFDM system. Optical Fibre Communication Conference (OFC/NFOEC). (OSA). San Diego Convention Center: JThA8.

Chapter 9:

Schmidt, B. J. C., Z. Zan, L. Du, & A. J. Lowery (2009). 100Gbit/s transmission using single-band direct-detection optical OFDM. Optical Fibre Communication Conference (OFC/NFOEC). San Diego, CA, Optical Society of America (OSA). **postdeadline paper: PDPC3**.

Schmidt, B. J. C., Z. Zan, L. Du, & A. J. Lowery (2010). "120 Gbit/s over 500-km using single-band polarization-multiplexed self-coherent optical OFDM." Journal of Lightwave Technology **28**(4): 328-335.

I have renumbered sections of the published papers in order to generate a consistent presentation within the thesis.

Signed:.....

Date:

Acknowledgement

First and foremost, I would like to thank God: the most Gracious and the most Merciful for His guidance and spiritual comfort at every step of my journey to fulfil this thesis works and making this quest of knowledge possible.

My biggest gratitude and appreciation to my main supervisor, Prof. Arthur James Lowery for his invaluable support, guidance, encouragement, intellectual inputs and friendship for me in conducting this research to its success. I also would like to take this opportunity to express my sincerest love to my husband (and my soul); Mohd. Hanif Yaacob and my two lovely daughters; Huda and Hannan for their unconditional love, support and patience. I thank my beloved parents, Mr. Zan Dawam and Mrs. Siti Aisah Mohamad for their continuous support and encouragement.

A special thank as well to Prof. Malin Premaratne as my secondary supervisor for making my PhD program a truly fruitful experience.

I wish to thank to my colleagues Dr. Brendon James Schmidt, Dr. Liang Du, Mr. Zayid Al-Aubaidy and Mr. Mohammad Monir Morshed for their helps, good humour and providing a friendly and inspiring environment for conducting research. May the friendship lasts forever.

My thanks extended to the academic and administrative members of the Department of Electrical and Computer Systems Engineering at Monash University specifically Ms. Maria Scalzo for her helps throughout the thesis reviewing stage and Mr. Ray Cooper, Ms. Vanessa Luu and Mr Daryl Gaspero for their help in the postgraduate matters.

I thank the Ministry of Higher Education of Malaysia for awarding me the PhD scholarship and Universiti Putra Malaysia especially the staff of the Department of Computer and Communication Systems Engineering for their continuing support.

Special thank you to my parent-in-law: Mr. Yaacob Awang and Mrs. Rosnah Mahmood, and my sister and brothers for their endless encouragement, pray and support especially to Mazni Muhamad-Kadir, Salwa Hana, Shahrul Badariah, Nishrin, Fadhlina, Siti Farhana, Noor Alyani, Siti Nor Zaharah, Nor Hafizah, Noor Hidayah, Nurul Amalina, Adidah and Fatin Nadiah for their help in taking care of my daughters and providing me with the peace of mind.

My special thanks also to Mr. Asmadi Abdul Kadir and family, Mr. Nushi Mahfodz and family as well as friends and close-knitted Malaysian families of South Eastern and Melbourne for the wonderful friendship and togetherness. Representing my family, we are in debt with your support and kindness throughout our stay in Melbourne.

May peace be with you....

Contents

Thesis Declaration	i
Acknowledgment	iii
Contents	v
List of Figures	viii
List of Tables	xviii
Abstract	xxix
1. Introduction	
1.1 Research Motivation	1
1.2 Scope of the Thesis	6
1.3 Organization of the Thesis	7
1.4 List of Publications	10
1.5 References	11
2. Review of Optical Communication Systems using OFDM Modulation	
2.1 Introduction	17
2.2 OFDM for Wireless	17
2.2.1 OFDM Principles	20
2.2.2 Advantages	22
2.2.3 Limitations	24
2.3 History of Optical OFDM	26
2.4 Single-Sideband Modulation in DDO-OFDM System	32
2.4.1 Single-Drive Optical Modulator System	33
2.4.2 RF upconversion and Single Drive Optical Modulator	35
2.4.3 IQ-Modulator	37
2.4.4 Virtual Carrier with IQ-Modulator	38
2.5 Laser Noise Interaction with Fibre	39
2.6 High Speed Optical Transmission with OFDM	44
2.7 Real-Time Processing of Optical OFDM	47
2.8 Conclusions	48
2.9 References	49
3. Study of Laser Noise Characteristics	
3.1 Introduction	62
3.2 Theory of Laser Noise Characteristics	62
3.2.1 Relative Intensity Noise (RIN)	63
3.2.2 Linewidth	64
3.3 RIN Measurement	66
3.4 Laser RIN Effects with Modulating RF Tones	71
3.5 Linewidth Measurement	75
3.5.1 Delayed Self-Homodyne Technique	76
3.5.2 High Resolution Spectrophotometer	79
3.6 Conclusions	82
3.7 References	83
Declaration for Thesis Chapter 4	
4. Development of Laser Linewidth Emulator	
4.1 Introduction	87
4.2 Principle of Laser Linewidth Emulator	87

4.3	Verification of Linewidth Emulator	89
4.3.1	Simulations	89
4.3.2	Experiments	92
4.4	Application to MZI Linearity Measurement	98
4.5	Conclusions	103
4.6	References	103
5.	Laser Noise Characteristics Effects on Fibre Dispersion and Modulating RF Tones	
5.1	Introduction	105
5.2	Laser Linewidth Interaction with Fibre Dispersion and Modulating RF Tones	105
5.3	Theoretical Analysis of PM-to-IM Conversion Noise	107
5.4	Experiment of PM-to-IM Conversion Noise	111
5.5	Group Delay Effect on Modulating RF Tones	116
5.6	PM-to-IM Conversion Noise Interaction with De-correlated RF Tones	120
5.7	Conclusions	129
5.8	References	130
6.	Simulation of Linewidth and Dispersion Effects on DDO-OFDM System	
6.1	Introduction	132
6.2	Phase Modulation-to-Intensity Modulation (PM-to-IM) Conversion Noise Effects on OFDM Subcarriers	133
6.3	Effects of Laser Linewidth Interaction with Group Delay to the OFDM Subcarriers	137
6.4	Effects of PM-to-IM Conversion Noise to the System Performance without ASE Noise	148
6.5	Effects of Linewidth Interaction with Dispersion on High M-QAM OFDM Signal	154
6.6	Optical Signal-to-Noise Ratio (OSNR) Requirement with PM-to-IM Conversion Noise Limitation	158
6.7	Conclusions	166
6.8	References	168
Declaration for Thesis Chapter 7		
7.	Experimental Study of Laser Noise Effect on DDO-OFDM System	
7.1	Introduction	170
7.2	Effects of RIN and Linewidth of a Commercial DFB Laser	170
7.2.1	DDO-OFDM Transmission System using Un-shifted Optical Transmitter	171
7.2.2	DDO-OFDM Transmission System using RF-Virtual Carrier Transmitter	177
7.3	Experimental Demonstration of DDO-OFDM Transmission System using Laser Linewidth Emulator	191
7.4	Conclusions	200
7.5	References	203
Declaration for Thesis Chapter 8		
8.	Reduction of the Impact of Laser Linewidth	
8.1	Introduction	205
8.2	Theory of Reducing the Effect of Linewidth	206
8.3	Experimental Demonstration	213
8.3.1	Single Subcarrier Transmission	214
8.3.2	Multiple Subcarriers Transmission	216
8.3.3	SHO-OFDM Transmission System	217
8.4	Conclusions	225
8.5	References	226

Declaration for Thesis Chapter 9	
9. High-Speed Long Haul Transmission System using DDO-OFDM	
9.1 Introduction	228
9.2 Transmitter Design	229
9.3 Receiver Design	231
9.4 Experimental Details	232
9.5 Results and Discussions	239
9.6 Conclusions	241
9.7 References	243
10. Conclusions and Recommendations for Future Research	
10.1 Conclusions	245
10.2 Research Findings	245
10.3 Research Contributions	249
10.4 Future Works	252
10.5 References	253
Appendices	255
Appendix 1	255
Appendix 2	261
Appendix 3	266
Appendix 4	283
Appendix 5	291

List of Figures

Figure	Page
Chapter 2:	
2.2.1. Comparison between (a) conventional MCM and (b) OFDM signal spectrum.	18
2.2.2. Basic block diagram of OFDM modulation and demodulation employing filter bank.	20
2.2.3. Basic OFDM block diagram implemented using Fourier Transform	21
2.2.4. OFDM symbol with (a) OFDM waveform with a CP assignment and (b) time-frequency graph showing the delay spread occurred on the parallel data symbol after multipath fading channel.	24
2.3.1. Received electrical spectrum of a (a) SSB and (b) DSB modulation signal. (After B.J.C. Schmidt, <i>et al.</i> (2007) with permission shown in Appendix 2.1 [47].	29
2.4.1. DDO-OFDM system design employing (a) single drive-MZM with (b) and (c) represent the electrical and optical spectra without bandgap and (d) with bandgap.	33
2.4.2. DDO-OFDM system design with (a) RF signal upconversion and single-drive MZM with data assignment and electrical and optical spectra using (b) half of the subcarriers and (c) all of the subcarriers.	35
2.4.3. DDO-OFDM design setup employing (a) IQ-modulator with data assignments and optical and electrical spectra utilizing (b) $\frac{N}{4}$ subcarriers and (c) half of the subcarriers with DC.	37
2.4.4. DDO-OFDM system design using (a) virtual carrier and IQ-modulator with (b) data assignment and electrical and optical spectra utilizing all of the subcarriers.	38
2.5.1. PSDs of a laser modulated with a subcarrier transmitted with a back-to-back and 1.1 km fibre. (After G.J. Meslener (1994) [161] with permission shown in Appendix 2.2).	40
2.5.2. RF spectra of a laser (a) without modulation (b) modulated with 84 subcarriers and (c) transmitted over 560 m dispersion-shifted fibre. (After G.J. Meslener (1994) [161] with permission shown in Appendix 2.2).	41
2.5.3. Noise power spectral density (PSD) of a 300-MHz linewidth laser after fibre dispersions of (a) 5000 ps/nm (b) 10000 ps/nm (c) 15000 ps/nm and (d) 20000 ps/nm. (After S. Yamamoto and N. Edagawa (1990) [165] with permission shown in Appendix 2.3).	42
2.5.4. Noise pedestal reduction with phase decorrelation corresponding to the time delay, τ_d relative to the τ_c . (After L.E. Richter (1986) [166] with permission shown in Appendix 2.4).with (b) data assignment and electrical and optical spectra utilizing all of the subcarriers.	43

Figure	Page
2.6.1. SSB OFDM signal band after polarization multiplexing (a) single un-offset carrier and (b) two carriers with one offset of the other.	46
 Chapter 3:	
3.2.1. Theoretical laser L-I curve.	62
3.3.1. RIN measurement setup with internal equivalent circuit of the photodiode (PD) connected into the input of the DSO.	67
3.3.2. Measured L-I characteristic.	68
3.3.3. Measured spectra with high RIN resonance for I_b of 16 mA and 20 mA using Tektronix 72004 20-GHz 50-GS/s DSO.	69
3.3.4. (a) Peak RIN and peak resonance frequency vs laser's biasing current, I_b and (b) RIN vs. $10\log_{10}(P_{out}^3)$.	70
3.4.1. Investigation of carrier's RIN modulated with an RF tone: (a) carrier's RIN resonance, (b) modulated RF-tone with RIN resonance and (c) translated RIN from both carrier and tone.	72
3.4.2. Simulation setup of laser source with RIN modulation with RF tones using serrodyne modulation.	72
3.4.3. Simulated RF spectra of an unmodulated laser with RIN resonance and three RF tones at 5, 7 and 10 GHz.	73
3.4.4. Simulated spectra upon photodetection of an unmodulated laser and laser modulated with multiple RF tones.	74
3.4.5. Detected electrical spectra with 0-dB and 10-dB difference of carrier-to-tone power.	75
3.5.1. Delayed self-homodyne linewidth measurement setup of inverse laser's output power.	77
3.5.2. Plotted received RF spectra for I_b of 15-, 30- and 60-mA using data recorded with Agilent DSO.	79
3.5.3. Agilent high-resolution spectrometer consists of HRS units of coherent receiver and the lightwave mainframes and its graphical user interface (GUI).	80
3.5.4. Lorentzian curve plot to measure linewidth using HRS for I_b of 35 and 60 mA.	80
3.5.5. Measured linewidth using HRS and self-homodyne technique as a function of inverse I_b relative to I_{Th} .	81
3.5.6. Measured linewidth using HRS and self-homodyne technique as a function of inverse laser's output power.	82
 Chapter 4:	
4.2.1. Phase modulation using a LiNbO ₃ phase modulator showing the need for a reset.	88

Figure	Page
4.2.2. Phase modulation using a complex modulator showing how the phase can be driven indefinitely around the complex plane by combining the outputs of the nested upper (I) and lower (Q) modulators.	88
4.3.1. Simulation setup using self-homodyne coherent receiver with 90 ⁰ optical hybrid producing the inphase and quadrature components, which formed a circle in a complex-plane.	90
4.3.2. Simulated instantaneous phase of the received signal for laser linewidth emulator of 10-, 20- and 100-MHz showing phase random-walk within a time window.	91
4.3.3. Frequency noise, $d\theta_n(t)/dt$, and histograms with Gaussian fit showing zero-mean Gaussian distribution for the dialled up linewidth of (a) 10 MHz (b) 20-MHz and (c) 100-MHz.	91
4.3.4. Simulated laser linewidth emulator's spectra with and without electrical bandwidth limitation.	92
4.3.5. Experimental setup including the emulator and linewidth characterization.	93
4.3.6. Received I and Q waveforms of the laser linewidth emulator measurement using self-heterodyne technique.	94
4.3.7. 20 dB linewidth measurements using self-heterodyne technique for dialled linewidth of (a) 2 MHz (b) 4 MHz (c) 40 MHz and (d) 150 MHz.	95
4.3.8. HRS linewidth measurement for dialled linewidth of (a) 2MHz (b) 4MHz (c) 40 MHz and (d) 150MHz.	96
4.3.9. Experimental results for the measured linewidth vs. the dialled linewidth.	97
4.3.10. Linewidth stability comparison between the dialled linewidth laser and a commercial DFB laser.	97
4.4.1. Complex-plane (I vs. Q) when driving the modulator in its (a) linear (b) nonlinear regions and (c) RF spectra showing the increase in intensity noise for nonlinear drive.	98
4.4.2. Complex-plane of Q vs. I plots when (a) $A > B$ and (b) $A < B$ with $\phi = \frac{\pi}{2}$.	99
4.4.3. I vs. Q plots of the C-MZI's output when the RF inputs were driven with $A = B = k$ for ϕ of (a) 0 ⁰ (in phase) (b) 45 ⁰ (c) 90 ⁰ (in quadrature) and (d) 135 ⁰ .	100
4.4.4. Q vs. I plots measured using DSO when the V_c of the C-MZI was (a) 3.50V (in quadrature) and (b) 2.5V.	101
4.4.5. Q vs. I plots of back-to-back electrical measurement from the AWG's outputs into the DSO with RF amplifiers and attenuators with the signal's measured V_p of (a) 258 mV (b) 2.3 V (c) 2.45 V and (d) 2.7 V.	102
Chapter 5:	
5.2.1. Investigation of the laser phase noise interaction with dispersion using the transmission of (a) laser carrier only and (b) carrier with modulating RF tones.	106

Figure	Page
5.3.1. PM-to-IM conversion noise PSD of 5,000-, 10,000-, 15000- and 20,000 ps/nm dispersion-length products for $\Delta\nu$ of 300 MHz.	108
5.3.2. Amplitude noise of the PM-to-IM conversion noise is increased with the increase of linewidth, $\Delta\nu$.	109
5.3.3. The intensity noise power due to laser phase noise conversion into intensity across the bandwidth.	111
5.4.1. PM-to-IM conversion noise PSD measurement setup.	112
5.4.2. Measured RF spectrum showing PM-to-IM conversion noise.	113
5.4.3. Measured f_0 vs. laser's I_b after a transmission over 130- and 500-km of S-SMF.	114
5.4.4. Measured and simulated RF spectra using 8.09 MHz linewidth over 130- and 500 km.	115
5.4.5. Measured electrical spectra of DFB laser with high RIN and wider linewidth characteristics after 500- and 300 km length of fiber.	116
5.5.1. Simulation setup to show the effect of phase de-correlation between carrier and its shifted version.	117
5.5.2. High laser linewidth increases the noise pedestal amplitudes.	117
5.5.3. Spectra showing the noise pedestal is narrowing and changing into a quasi-Lorentzian shape for the respective τ_d .	118
5.5.4. Simulated spectra with (a) 1 and 2 side tones, (b) 1 and 10 side tones, (c) 5-dB and (d) 10-dB attenuation applied to each tone for the 10 side tones transmission.	119
5.6.1. Phase de-correlation effects of (a) two RF tones due to dispersion and (b) resulting phase error relative to the carrier and PM-to-IM conversion noise of the carrier.	120
5.6.2. Simulated spectra of carrier PM-to-IM conversion noise and single tone originated from 100 MHz linewidth with its f_{shift} swept across the transmission bandwidth over 500km dispersive fibre.	121
5.6.3. Experimental setup for single side tone transmission over 500 km single-mode fibre.	122
5.6.4. Measured output of a C-MZI modulated with a single side tone with 10- and 20-dB carrier-to-tone power ratio spaced at 7.5- and 12-GHz.	123
5.6.5. Measured spectrum after photodetection with side tone at 12 GHz for a back-to-back transmission.	123
5.6.6. Measured RF spectra with side tones of 7.5- and 12-GHz with carrier-to-tone power ratio of (a) 10 dB (b) 20 dB.	124
5.6.7. Simulation setup with N_k tones over 500 km SMF with zero attenuation.	125

Figure		Page
5.6.8.	Simulated RF spectra of carrier PM-to-IM and 10 side tones transmitted over 500 km dispersive fiber with side tone band is located at low and high frequency extremes of signal bandwidth.	126
5.6.9.	Simulated RF spectra of 40 side tones transmission over 500 km fiber with 0-dB, 10-dB, 15-dB and 20-dB carrier-to-side tones power ratio.	127
5.6.10.	Simulation setup to compare the PSDs obtained from the addition of the PM-to-IM conversion noise and delayed-RF tones data (A+B) with fully simulated PSDs (C).	128
5.6.11.	Simulated spectra comparing the addition of conversion noise and delayed RF tones and fully simulated spectra when both effects are present with (a) two-tones, (b) ten-tones, (c) twenty-tones over 400 km and (d) forty-tones over 625 km.	129
Chapter 6:		
6.2.1.	Simulation setup with RF virtual carrier to transmit a single OFDM subcarrier.	134
6.2.2.	A single OFDM subcarrier located at the start of the negative FFT points.	134
6.2.3.	A single OFDM SC located on the carrier's highest intensity noise and on the first null of the PM-to-IM conversion noise PSD for laser with $\Delta\nu$ of 4 MHz and transmitted over 1500 km dispersive fibre.	135
6.2.4.	Scatter plots for the subcarrier located on the (a) and (c) highest intensity noise and (b) and (d) at the first null of the carrier's PM-to-IM conversion noise PSD with $\Delta\nu$ of 20- and 100-MHz, respectively.	136
6.3.1.	Received RF spectrum of the first OFDM subcarrier at 10 GHz with (a) back-back transmission (b) 1500 km (c) 3000 km and (d) 6000 km.	138
6.3.2.	Scatter plots of the single OFDM subcarrier transmission with 4-MHz laser linewidth over (a) back-to-back (b) 1500 km (c) 3000 km and (b) 6000 km of S-SMF.	139
6.3.3.	The subcarrier location in the signal frequency band from the lowest frequency (SC1) to the highest frequency subcarrier (SC3).	140
6.3.4.	The received RF spectrum for a single OFDM subcarrier transmission over 1500 km at a different subcarrier frequency of (a) 10.04 GHz (SC1) (b) 12.51 GHz (SC2) (c) 17.49 GHz (SC3) and (d) 19.97 GHz (SC4).	141
6.3.5.	Scatter plot of a 16 QAM using a single OFDM subcarrier transmission over 1500 km with 4-MHz linewidth laser at the subcarrier index of (a) 10.04 GHz (SC1) (b) 12.51 GHz (SC2) (c) 17.49 GHz (SC3) (d) 19.97 GHz (SC4).	142
6.3.6.	Received RF spectra of a DDO-OFDM subcarriers transmission with Δf_{sc} of (a) 64 (b) 32 (c) 16 and (d) 8 zeroed subcarriers.	143
6.3.7.	16-QAM scatter plots for the transmission of the DDO-OFDM subcarriers with Δf_{sc} of (a) 64 (b) 32 (c) 16 and (d) 8 zeroed subcarriers within 2.5-GHz signal bandwidth.	145

Figure	Page
6.3.8. The received symbols are transferred into one common quadrant to plot a histogram.signal bandwidth.	146
6.3.9. Histogram plots of the inphase axis of the received symbols constellations for the Δf_{sc} of (a) 64 (b) 32 (c) 16 and (d) 8 subcarriers.	147
6.4.1. Optical spectra at C-MZI's output when (a) without frequency resolution and (b) at 0.1-nm resolution.	148
6.4.2. Received RF spectrum after photodetection.	149
6.4.3. Scatter plots of 4 QAM OFDM signal band transmitted over (a) 500 km using 8- and 15-MHz linewidth and (b) 8,000 km using 800-kHz and 1-MHz linewidth.	150
6.4.4. Q-factor versus subcarrier frequency of 10-GHz 4 QAM OFDM signal bandwidth transmitted over fibre length of 8,000 km using a laser linewidth.	151
6.4.5. Q-factor versus fibre length of 4-QAM OFDM transmissions as a function of laser linewidth.	152
6.4.6. $\log_{10}(\text{BER})$ versus laser linewidth for a transmission of 20 Gb/s with 4 QAM using 10-GHz signal bandwidth over several fibre lengths.	153
6.5.1. Scatter plots of 4-, 16- and 32-QAM with BER at around 1×10^{-3} using 5 MHz and 20 MHz laser linewidth transmitted over (a) 2000 km, (b) 400 km, (c) 200 km, (d) 500 km, (e) 100 km and (f) 50 km.	154
6.5.2. $\log_{10}(\text{BER})$ versus dispersive fibre length for (a) 4- (b) 16- and (c) 32-QAM modulated OFDM signal with 10-GHz signal bandwidth.	156
6.5.3. Fibre length versus laser linewidth taken at $\log_{10}\text{BER}$ of -3 for OFDM signal transmission using 4-, 16- and 32-QAM with 10 GHz signal bandwidth.	158
6.6.1. Simulation setup of an RF virtual carrier DDO-OFDM transmission system using a noise loading at the receiver to investigate an OSNR requirement.	159
6.6.2. Received scatter plots taken around -3 dB of $\log_{10}(\text{BER})$ for the 4-, 16-, 32- and 64-QAM modulated OFDM signals transmitted over 300 km using the linewidth and OSNR of (a) 28 MHz and 26 dB, (b) 6 MHz and 36 dB, (c) 2 MHz and 30 dB and (d) 1 MHz and 32 dB, respectively.	160
6.6.3. Q at around 1×10^{-3} BER versus subcarriers frequency for 4-, 16-, 32- and 64-QAM signal transmitted over 300 km using different linewidth at its respective OSNR.	161
6.6.4. Q taken at around 1×10^{-3} BER versus subcarrier frequency for 4-, 16-, 32- and 64-QAM OFDM signal transmitted over 300 km using 1 MHz linewidth achieved with 15-dB, 22-dB, 26-dB and 32-dB of OSNR, respectively.	162
6.6.5. $\log_{10}(\text{BER})$ versus OSNR for an OFDM signal transmitted using a variable linewidth over 300 km and modulated with (a) 4-, (b) 16-, (c) 32- and (d) 64-QAM.	163

Figure	Page
6.6.6. OSNR at 1×10^{-3} BER versus linewidth for OFDM signal using (a) 4-QAM, (b) 16-QAM, (c) 32-QAM and (d) 64-QAM transmitter over a certain dispersive-fibre length.	164
 Chapter 7:	
7.2.1. Low-rate experimental setup using a commercial DFB laser with upper half-positive FFT-points are assigned as OFDM subcarriers.	171
7.2.2. OFDM subcarrier indices with its corresponded frequency spectrum showing (a) the theory and (b) data-carrying subcarriers assignment for the experiment.	172
7.2.3. Received signal waveform plotted using Matlab with one symbol frame and the magnified signal part to find the start of the frame.	173
7.2.4. Scatter plots of the OFDM symbols modulated with 4 QAM (a) before and (b) after equalization and 32 QAM (c) before and (d) after equalization.	174
7.2.5. Energy-per-bit over noise density versus laser's output power.	175
7.2.6. Simulated signal quality, Q versus linewidth.	176
7.2.7. Experimental setup using RF-virtual carrier transmitter design.	177
7.2.8. Subcarrier indexing matrices of an i^{th} OFDM symbol with its corresponded frequency spectrum representation.	178
7.2.9. Transmitted optical spectrum with 1:1 carrier-to-subcarrier ratio to achieve an optimum system performance.	180
7.2.10. OFDM spectra with a high RIN and linewidth laser driven by 10 mA; (a) optical spectrum measured with HRS and (b) received electrical spectrum after back-to-back transmission.	180
7.2.11. Q-factor versus subcarrier frequency of back-to-back transmission using DFB laser with high RIN.	181
7.2.12. Transmit optical spectra measured with HRS (a) before and (b) after WaveShaper bandpass filter using laser I_b of 40 mA.	183
7.2.13. Received electrical spectrum of back-to-back transmission with I_b of 40 mA	184
7.2.14. Scatter plots of the received signal (a) before and (b) after signal equalization for a 4 QAM back-to-back transmission.	185
7.2.15. Q-factor versus subcarrier frequency of 4 QAM OFDM signal transmission using laser linewidth of 11.4 MHz over back-to-back, 80-, 160- 320-, 560- and 800-km of S-SMF.	186
7.2.16. Q-factor versus subcarrier frequency for laser driven by I_b of 20 mA, 30 mA and 40 mA over back-to-back, 320 km and 800 km of S-SMF.	187
7.2.17. Q-factor versus fibre length for 4 QAM OFDM transmission using laser linewidth of 11.42 MHz, 13.87 MHz and 20.94 MHz.	189

Figure	Page
7.2.18. Scatter plots of 4 QAM, 16 QAM and 32 QAM at BER of 10^{-3} transmitted using a laser linewidth of 11.42 MHz over 800 km for 4 QAM and 80 km for 16 QAM and 32 QAM.	190
7.2.19. BER versus fibre length for 4 QAM, 16 QAM and 32 QAM with a laser linewidth of 11.42 MHz driven by 40 mA I_b .	190
7.3.1. Experimental setup of a DDO-OFDM transmission system using laser linewidth emulator.	191
7.3.2. HRS linewidth measurement at 10% coupler's output of dialed linewidth of (a) 5 MHz (b) 8 MHz (c) 10 MHz and (d) 15 MHz.	193
7.3.3. HRS spectrum measurement of the OFDM signal at the transmitter's output with dialed $\Delta\nu$ of 10MHz.	194
7.3.4. C-MZI2 output signal with C-MZI1's DC leakage when (a) the OFDM signal was off and (b) the OFDM signal was on.	195
7.3.5. Signal waveform with its FFT spectrum representation when the signal was detected after the PD for (a) back-to-back and (b) 720km transmission, with dialled linewidth of 20MHz.	196
7.3.6. Received scatter plots for a DDO-OFDM transmission over (a) back-to-back (b) 240 km (c) 400 km and (d) 720 km length of fiber with dialed linewidth of 20 MHz.	197
7.3.7. Q vs. OFDM subcarrier index for every 80 km fiber length from a back-to-back to 720 km transmission using a dialed linewidth of 20 MHz.	198
7.3.8. Q vs. dialed linewidth of OFDM signal transmission for every 80 km of fibre span.	199
Chapter 8:	
8.2.1. Simulation setup for SHO-OFDM transmission system where the laser center frequency was shifted using the virtual carrier technique.	208
8.2.2. Simulated optical spectrum at the C-MZI's output after a pre-amplification.	209
8.2.3. Optical spectra after the subcarriers and carrier are isolated using the optical filters.	209
8.2.4. Simulated results comparing the reduction of noise pedestal around several subcarriers using a matched delay to the un-delayed spectrum.	210
8.2.5. Simulated signal quality, Q, vs. subcarrier frequency index with its respective scatter plots comparing the un-delayed and 1.12ns delay of the subcarriers signal band relative to the carrier.	211
8.2.6. Performance of 4-QAM transmission over 700-km of fibre showing (a) Q vs subcarriers frequency index comparing the response of the un-delayed with a set of τ_D and (b) the average Q vs the length of fibre delay line for linewidths of 1 MHz, 10 MHz and 20 MHz.	212

Figure	Page
8.2.7. Simulation result for higher M-QAM transmission with 10 MHz linewidth over 700 km (a) Q vs. the length of fiber delay line and (b) BER vs. delay for 16 QAM and 32 QAM.	213
8.3.1. Experimental setup for a single ten RF subcarriers transmission to show the noise pedestal power reduction when a matched delay is assigned.	214
8.3.2. Measured electrical spectrum showing the reduction of noise pedestal of a single subcarrier after 500 km with 10 MHz linewidth: (a) without a matched delay (b) 8cm delay (c) delay matched with 16 cm.	215
8.3.3. The decreased of the noise pedestal power with (a) un-matched delay (b) matched delay with 16cm.	216
8.3.4. Experimental setup of SHO-OFDM system showing the delay assigned to the signal branch after being filtered by a Waveshaper optical filter.	217
8.3.5. Measured optical spectra using HRS: (a) Linewidth measurement (b) The C-MZI's output signal.	218
8.3.6. HRS measurements of the carrier and subcarriers paths signals at the Waveshaper's outputs (a) carrier path filter response (b) measured signal at the carrier path (c) subcarrier path filter response and (d) measured signal at the subcarriers path.	219
8.3.7. OSNR measurement using an optical spectrum analyzer at the fibre's output.	220
8.3.8. Measured RF signal at the DSO after 720 km transmission with 10 MHz linewidth: (a) the carrier's phase-to-intensity noise conversion when the OFDM signal was turned off (b) the OFDM signal spectrum without any delay assignment.	221
8.3.9. The received RF spectrum after 720 km transmission when (a) similar detected power from both signal paths and (b) the power of the carrier path is higher than the subcarriers path.	222
8.3.10. Measured scatter plots comparing the length of the delay line assigned for 500 km (top) and 720 km (bottom): (a) no delay (b) 18.8 cm (c) 28.6 cm (d) no delay (e) 28.6 cm and (f) 39.6 cm.	223
8.3.11. Signal quality, Q, vs. subcarriers index starting from low to high frequency for 500 km transmission length.	224
8.3.12. Experimental results for 500 km and 720 km fibre length with combinations of delay line: (a) Q vs. delay line (b) BER vs. delay line.	225
Chapter 9:	
9.2.1. Desired output spectrum of the transmitter.	229
9.2.2. Basic transmitter setup for an optical polarization multiplexed signals.	230
9.2.3. Polarization-diversity receiver for a single polarization of a DDO-OFDM system.	232

Figure		Page
9.4.1.	Experimental setup for the demonstration of 120 Gb/s transmission with DDO-OFDM system.	233
9.4.2.	AWGs synchronization setup using 20 GS/s interleave mode.	234
9.4.3.	OFDM signal band from an electrical back-to-back of the AWG to the DSO (a) without pre-emphasis and (b) with pre-emphasis.	235
9.4.4.	Measured electrical spectrum at the output of a coherent receiver of an OFDM signal band (a) before and (b) after optical pre-emphasis.	236
9.5.1.	Received optical spectrum measured with Agilent HRS.	240
9.5.2.	Electrical SNR/bit (E_b/N_0) measured for the 120 Gb/s transmission experiment with 500 km SSMF for OSNR of 25.8 dB (0.1 nm) with BER of 8.2×10^{-4} .	240
9.5.3.	Received and equalized constellations of 4-QAM and 16-QAM after 500 km.	241

List of Tables

Table		Page
	Chapter 2:	
2.7.1.	Summary of optical OFDM experimental demonstrations using several types of system design. (After A.J. Lowery and L.B. Du (2011) [91] with permission shown in Appendix 2.5).	48
	Chapter 4:	
4.3.1.	Linewidth, $\Delta\nu$ relation of Heterodyne technique [9].	95
	Chapter 6:	
6.6.1.	Summary of the linewidth-range with its respective OSNR to achieve 1×10^{-3} of BER for 4 QAM, 16 QAM, 32 QAM and 64 QAM.	165
	Chapter 9:	
9.4.1.	Transmission system experimental details.	234
9.4.2.	Approximate power map of the system.	238

Monash University

Abstract

THE EFFECT OF LASER NOISE ON AN OPTICAL OFDM SYSTEM

by Zuraidah Zan

Supervisory: Professor Arthur James Lowery

Co-supervisor: Professor Malin Premaratne

Department of Electrical and Computer Systems Engineering

In recent years, researchers and network equipment manufacturers have focused on the development of a 100 Gb/s optical transmission systems to cater the ever increasing demands for bandwidth. To cater the demands, optical orthogonal frequency division multiplexing (O-OFDM) has been proposed. O-OFDM has been shown as a promising technique to increase spectral efficiency with its ability to compensate for chromatic and polarisation mode dispersion. There are two forms of receiver used for long haul O-OFDM links: coherent-OFDM (CO-OFDM) and direct detection O-OFDM (DDO-OFDM). The CO-OFDM system is known to be limited by the laser's phase noise, where the system requires a narrow linewidth laser at both transmitter and receiver, where these lasers phase must track one-another. In the DDO-OFDM system, an optical carrier is transmitted along with the subcarriers so both originate from the same laser, and both experience the same degradations along the fibre. Thus, the linewidth, or equivalently phase-noise, requirements are far less stringent than for CO-OFDM systems. However, given that laser phase noise will be converted to intensity noise (PM-to-IM conversion noise) along a dispersive fibre, there will be some effect on performance in a DDO-OFDM system. The question is whether this is significant, given that the fibre dispersion is not optically compensated as in conventional lightwave systems.

In this thesis, laser phase noise effect upon detection in a DDO-OFDM system is shown to impose broad noise pedestal around a subcarrier for higher frequency subcarriers when there is a high accumulated dispersion. The noise pedestal can introduce inter-subcarrier-interference between the adjacent subcarriers. This is different in a CO-OFDM system, where the phase noise is independent of the subcarriers' frequency and common to all subcarriers. This thesis focuses on the

DDO-OFDM system using external modulation at the transmitter. A transmission system was developed to study the effects of the laser relative intensity noise (RIN) and phase noise over a long-haul transmission, and to show the importance of the laser's characteristics. Experimental measurements on a commercial fixed-wavelength distributed feedback (DFB) laser investigated its RIN, linewidth and light vs. current (L-I) characteristics. The effect of external modulation of this laser was investigated. With the externally-modulated transmitter, the laser chirp is ignored. The linewidth measurement was done using self-homodyne technique and validated using a high-resolution spectrophotometer. The measurements showed interdependency between the linewidth and RIN, which agreed with theory. A laser linewidth emulator was developed and demonstrated experimentally. This was done by phase modulating a semiconductor's laser output to broaden its linewidth. With this laser, the linewidth can be made independent from the other laser's noise characteristics. Simulations and experiments were performed to study the interaction of linewidth and fibre dispersion. The interaction produces noise conversion from phase modulation to intensity modulation, where the noise PSD was obtained. An analytical equation of the PM-to-IM's upper-bound was derived and plotted on the noise PSD's amplitude. When the laser was modulated with RF tones, a noise pedestal around each of the tones was obtained. The peak power of the noise is shown to increase with the increased of the tone's frequency. This is due to the phase walk-off of the high frequency subcarrier from the carrier is larger than the low frequency subcarrier. The peak also increases when a wider linewidth was used. This noise was shown to cause phase rotations of the received symbols and reduces the Q performance of the DDO-OFDM system. To reduce the effect of the linewidth in the DDO-OFDM system, an experiment using a simple delay line to match the delay experienced by the subcarrier was performed. The result shows improvement of the subcarriers' Q performance. Finally, this thesis also presented the performance of the DDO-OFDM system in transmitting high-speed data of 120 Gbit/s. This experiment involved several important device improvements in order to achieve a good quality and wide RF-signal bandwidth. In this transmission, a variant of the DDO-OFDM system employing self-coherent polarization-diversity receiver design was developed.

Chapter 1

INTRODUCTION

1.1 Research Motivation

Recent statistics of worldwide Internet users from the year of 2000 until 31st December 2011 reported the growth of 528.1% of the users around the globe [1]. This increment is due to a diversity of Internet applications involving video, audio and data transmissions for example YouTube, IPTV, video conference, IPphone, skype, online gaming, and emails. In June 2008, CiscoTM reported that a video transmission itself begin to dominate the growth of Internet traffic between 2007 and 2012 [2]. The predicted growth needs to be catered with technology advancements in order to find a solution to carry 100-G Ethernet [3].

In optical communication systems, the invention of erbium-doped fibre amplifier (EDFA) has supported wavelength division multiplexing (WDM) and permitted long-haul transmission distances [4]. This optical long-haul WDM system was realized with a deployment of transoceanic fibre cable systems carrying 10 Gb/s NRZ per channel with overall maximum capacity of multiple-terabits per second [5-12]. The transmission of 10 Gb/s per channel, however, can no longer meet the ever increasing bandwidth demand hence, researchers and network developers are now migrating from 10 Gb/s to 40 Gb/s and currently looking for 100 Gb/s per wavelength channel [5, 9, 11-32]. The migration involves advances in technology to confront the system design challenges for example: achieving high spectral efficiency, managing fibre dispersion and nonlinearities, suppressing the noise due to optical amplification using signal regeneration and developing forward error correction (FEC) methods [4, 6, 33]. In the WDM transmission system, the requirement of channel spacing of at least twice the bit rate, to prevent from inter-channel interference, limits the system's obtainable spectral efficiency. Also, the high-speed transmission of NRZ signals for example at 40 Gb/s will be impaired by the chromatic dispersion. This is because of the narrow pulses spreading due to the dispersion, which causes the detrimental effect of inter-symbol interference (ISI). This has led to the employment of other modulation formats aimed for not only to increase the spectral efficiency, but also to

provide some degree of tolerance to the fibre impairments [14, 18, 19, 22, 23, 27, 28, 34-38]. Among these modulation formats is orthogonal frequency division multiplexing (OFDM); a technique which was originally developed for wireless communication systems [39-44].

OFDM in wireless communication systems was first proposed and patented by R.W. Chang (1966) to combat channel fading [39-41]. This technique is similar to a conventional multiple-carrier modulation (MCM) technique, where multiple frequency carriers (or subcarriers) are used to carry a data stream from a single channel [39-42, 45, 46]. The advantage of the OFDM technique is that it provides a better spectral efficiency than the conventional techniques. An example of the conventional MCM technique is frequency division multiplexing (FDM), where multiple frequency subcarriers were also used to carry the data stream and are frequency-multiplexed before transmission. The subcarriers, however, need to be frequency spaced apart from the adjacent subcarriers. This is to prevent interference during the channel transmission and crosstalk upon reception, but comes at the expense of inefficient bandwidth utilization [41-43, 45, 47]. This is where Chang's technique became a winner, where overlapping subcarriers were used without incurring any interference and so were crosstalk-free. The secret lies on the use of mathematically orthogonal subcarriers, obtained by the convolution of Dirac pulses at the subcarrier's frequency with a spectrum of a sinc function ($\text{sinc}(\pi/T)$) [42-47]. However, this technique remained unfeasible for several years due to complexity and requirement for a large number of RF devices, such as banks of filters to shape and match the spectrum at the transmitter and receiver, as well as local oscillators (LOs) and mixers to perform modulation and demodulation [42-44, 46, 47]. In 1971, this technique was made more feasible with the employment of the fast Fourier transform (FFT), as proposed by S.B. Weinstein and P.M Ebert [45, 46]. With this technique, N orthogonal subcarriers can be easily generated and filtered at the transmitter and receiver, respectively, by using the FFT. This eliminated the requirement for filters, LOs and mixers, which subsequently reduced the system design complexity and implementation cost. With the FFT, along with the advances in digital signal processing (DSP) and maturity in electronic devices, this technique had made its come-back in 1990s, where practical implementations of this technique were developed [44, 47]. This involved the development of various standards, for example:

European digital audio broadcast (DAB), digital video broadcast (DVB), high-speed digital subscriber lines (HDSL, ADSL, VDSL), wireless LANs (HIPERLAN/2, IEEE 802.11a, IEEE 802.16, MMAC), and fixed broadband wireless access (802.11g) [42-47].

The advantages of the OFDM technique in the wireless communication systems can be summarized as follows [42-44]:

- **Increased Spectral Efficiency**

Spectral efficiency of a wireless system can be increased with the use of the overlapping orthogonal subcarriers provided by the OFDM technique. Moreover, the overlapped subcarriers will not interfere with the adjacent subcarriers.

- **Immune to multipath fading**

The fading effect will be spread over many bits, which are carried by various subcarriers. Therefore, only several bits will be affected instead of several adjacent bits completely being destroyed as a single-carrier system. The affected bits can be corrected using error correction codes at the receiver.

- **Increased tolerance to frequency-selective fading**

The effect of frequency-selective fading is reduced and in a system analysis, it is considered to be constant over each of the subcarriers due to the use of narrow-spectrum and large number of subcarriers.

- **Eliminates inter-symbol interference (ISI)**

Inter-symbol interference can be eliminated using guard time assigned in every OFDM symbol or also known as a cyclic prefix (CP) extension. The length of the CP is made to be larger or equal to the expected delay introduced by the multipath delay spread.

- **Reduced complexity and cost of the system implementation**

With the employment of the FFT, the complexity of a wireless OFDM system design can be reduced. The generation of the orthogonal subcarriers and the modulation can be easily done with an inverse-FFT (iFFT) and its reception and demodulation using a forward-FFT (FFT). This has eliminated the requirement of banks of filters, local oscillators (LOs) and mixers.

The aforementioned OFDM advantages along with the works reported to combat fibre dispersion electronically have drawn lots of attention from the research community in optical communication systems [25, 48-53]. In an optical

communication system, two major types of OFDM have been proposed: coherent optical OFDM (CO-OFDM) and direct detection optical OFDM (DDO-OFDM). The CO-OFDM system was proposed by W. Shieh and C. Athaudage (2006) [54-56] and S.L. Jansen (2007) [57-60], which employed coherent detection receiver. The CO-OFDM was shown to achieve high spectral efficiency with 7-dB lower OSNR required at the receiver, compared with the DDO-OFDM system [61]. However, this is at the expense of system design complexity and high implementation cost due to the coherent receiver.

The DDO-OFDM system employed a simple incoherent single-photodetection optical receiver. The system demonstrations were first done by A.J. Lowery and J. Armstrong (2005 & 2006) [38, 62-64] and later on by I.B. Djordjevic and B. Vasic (2006) [31, 65]. The system was predicted to have 0.5 dB better OSNR requirement than the NRZ [38, 66] and can provide at least 2.9 bit/s/Hz spectral efficiency as compared to 0.4 bit/s/Hz for the high speed return-to-zero on-off keying RZ-OOK [65]. The simple and low-cost design of this system has made it attractive for practical system implementations for passive optical networks [67, 68]. Early work on the DDO-OFDM dealt with the issues of bipolar signal transmission of the OFDM into a unipolar optical communication environment over a short reach multi-mode fibre (MMF) [62-64, 69-72]. To deal with this issue, J.M. Tang et al. (2006) proposed a high DC-bias added to the signal to up-shift the waveform to a high average power [69, 71, 73]. This however resulted in an inefficient power consumption since the bias does not carrying any data and also risen an issue on eye-safety due to the high-optical power. A better solution to this power inefficiency was proposed by J. Armstrong and A.J. Lowery (2006) which eliminated the requirement of the high DC bias [62-64, 74]. In their technique, signal clipping was performed so that the overall signal's power is reduced when the negative signal excursions are raised to a mean level, by clipping. This technique is known as asymmetrically-clipped optical OFDM (ACO-OFDM) [62-64, 74]. Transmission over a long-haul single-mode fibre (SMF) was also reported with the demonstration of an efficient electronic chromatic dispersion compensation technique transmitting 12- and 20-Gb/s over 400- and 320-km, respectively [38, 75-77]. The OFDM technique has also being incorporated in WDM systems as reported in [66, 78]. The chromatic dispersion effects can be reduced by setting the length of the CP at the transmitter to be greater or equal to the

total delay introduced by the dispersive fibre. This helps prevent interference from adjacent symbols (ISI). The chromatic dispersion can then be compensated for by the receiver's equaliser. In conjunction with the OFDM modulation technique, compensation schemes to mitigate fibre nonlinearity effects can also be developed and applied at the transmitter or receiver [37, 79-82]. In addition, the system's spectral efficiency can also be increased with the use of various subcarriers carrying high-level modulation (M-QAM). The same advantages of high spectral efficiency and efficient chromatic dispersion compensation are also provided by the CO-OFDM transmission system [54-56, 83-85]. Indeed the CO-OFDM at least doubles its spectral efficiency over the DDO-OFDM.

Despite the advantages provided by OFDM modulation, optical OFDM is also affected by phase noise of the laser due to the use of long symbols. In CO-OFDM systems, the laser phase noise has been shown to be a prominent limiting factor of the system performance, [55, 57, 86, 87]. This is because the OFDM signal is transmitted through the dispersive fibre without a carrier. At the receiver, another LO with random phase will be used to track the signal band; hence, phase noise compensation techniques need to be developed in order to match the phase between the received signal and the receiver's LO [55, 57, 86-88]. The first successful technique was proposed by S.L. Jansen (2007) to compensate the LO phase noise using pilot tone located in the middle of the signal band and transmitted along with the signal [57]. At the receiver, the phase information held by this RF tone is used to compensate for the phase noise at the receiver's equaliser. This involves DSP calculations at the receiver end.

In DDO-OFDM transmission system, the system performance is less affected by the laser phase noise than CO-OFDM. This is because the reference carrier is transmitted together with the subcarrier producing strong phase correlation between the carrier and the subcarrier band. However, the phase noise of the laser can be converted into intensity noise by the chromatic dispersion [89-92]. This noise conversion will later enhance the detected intensity noise upon the photodetection and hence, degrades the system's signal-to-noise ratio (SNR). In a practical semiconductor laser, the phase noise is represented by its linewidth characteristic. The linewidth of a laser is inter-dependent with the other laser's noise characteristics for example the relative intensity noise (RIN). The inter-dependency of these two

noises can be demonstrated by varying the biasing current to drive the laser, which also affects its output power [4, 93]. The linewidth is inversely proportional to the laser's output power, $P (\propto P^{-1})$ while the RIN is inversely proportional to the cubed of P , ($\propto P^{-3}$). When the output power is increased to high levels, the RIN decreases slowly, approaching the P^{-1} dependence [94, 95]. This is the typical way to vary both the linewidth and the RIN of the semiconductor laser source. With this interdependency, it is hard to investigate the effects of the laser noise to the system's performance experimentally. Hence, a laser source that can vary its linewidth with a low RIN (high output power) is desirable for test and measurement purposes.

1.2 Scope of the Thesis

This thesis explores the following objectives:

- To verify and investigate the laser's noise characteristics of a commercial laser, which will then be used in experimental demonstrations.
- To study the transmitter and receiver designs used in the adaptation of the OFDM technique in an optical transmission system using direct detection receiver. This includes the design topologies in the early development and the advanced topologies of the system to transmit a high data rate.
- To propose, design and demonstrate a stable dialled-up linewidth laser where the linewidth can be varied independently with the laser's other characteristics. This laser will then be used in the DDO-OFDM transmission demonstration.
- To develop an optical modulator linearity test using an oscilloscope plotting the inphase (I) and quadrature (Q) signal components using the scope's X-Y display.
- To investigate the effects of laser's RIN to the externally modulated RF tones, which can be used to resemble the RIN effect on a single and multiple OFDM subcarriers.
- To investigate the effect of laser's linewidth interaction with chromatic dispersion in fibre using unmodulated laser and externally modulated RF tones using simulation and verified with experimental demonstration.
- To investigate the effects of the laser linewidth with chromatic dispersion demonstrating the phase modulation-to-intensity modulation (PM-to-IM)

noise conversion to the QAM modulated data in the DDO-OFDM transmission system. This will be done using both simulations and experiments.

- To develop and demonstrate a simple technique to reduce the impact of the laser noise to the DDO-OFDM system performance.
- To develop a DDO-OFDM system using commercial off-the-shelf devices for a high speed data transmission. This will involve the synchronization of the fast digital-to-analog (DACs) to obtain wider electrical signal bandwidth, devices improvement using pre-emphasis schemes, virtual carrier transmitter design and the use of polarization division multiplexing (polMux) for a dual-polarization data transmission.
- To demonstrate the potential of the DDO-OFDM system in transmitting high-data rate of 100 Gbit/s using a variant of DD receiver; the self-heterodyne optical (SHO) receiver.

Note that the study is focused on the OFDM modulation technique using a direct detection receiver design; hence, the coherent detection technique is outside the scope of this thesis.

1.3 Organization of the Thesis

This thesis is organized as follows:

- **Chapter 2:** Chapter 2 provides the history and overview of OFDM modulation techniques in wireless communication systems. The fundamentals of OFDM are explained using a block diagram for the OFDM modulation and demodulation processes. Advantages and limitations of this technique in the wireless systems are highlighted and further explained. The adaptation of this technique into a direct detection optical system is then discussed by reviewing the history of optical OFDM systems. This includes the provision of electronic dispersion compensation (EDC) in the optical transmission system and the early adoption issue of the OFDM into the system. This includes the adaptation of a bipolar nature of the OFDM signal into a unipolar environment of an optical system. A method to overcome a PAPR limitation in OFDM is also presented. DSB and SSB modulation in the optical OFDM system is also explained. Several transmission systems design

to produce SSB modulation using direct detection receiver are also presented and explained in detail by reviewing the previous works. This includes the transmitter topologies employing single-drive and dual-drive optical modulators. Reviews on an optical transmission system performance due to a laser source's noise are also presented. This includes relative intensity noise (RIN) effect on a modulated subcarrier and the interaction of laser's phase noise or linewidth with fibre dispersion. This chapter also explains the system design topologies in order to achieve a high-speed data transmission using optical OFDM systems. Finally, demonstrations of real-time transmissions of the system are also explained along with the summary of experimental demonstrations, which has been reported in the field.

- **Chapter 3:** In Chapter 3, theory of laser's characteristics is explained, which include the theory of a laser's light vs. current (L-I) curve characteristics, RIN and linewidth. Measurements of a commercial laser's characteristics are also demonstrated. Methods involved in the measurements are also explained. An extended investigation of the RIN noise translation when the laser is modulated with RF tones is also presented. This was done using simulation, where the RIN was set to be independent with the other laser's noise characteristics.
- **Chapter 4:** Chapter 4 presents the development of a laser linewidth emulator starting with the principle of this laser development. Simulations are used to verify this laser's phase noise generated digitally in terms of its statistical properties. An experimental demonstration of this laser is presented, where a tunable laser source was set at a fixed wavelength with a narrow linewidth is phase modulated with a digitally generated phase noise to widen its linewidth.
- **Chapter 5:** Chapter 5 presents the effect of laser noise when the laser is unmodulated and externally modulated with RF tones and propagated across a dispersive fibre. RIN and linewidth are investigated independently using VPItransmissionMaker simulations. Measurement of the inter-dependent effect of the RIN and linewidth are also shown using experiment. In this chapter, the derivation of a converted phase noise into intensity noise upper

bound is also presented and evaluated using MATLAB. A group delay effect on the modulated RF tones is also analysed and presented.

- **Chapter 6:** Chapter 6 presents the simulations of laser linewidth or phase noise effects to a DDO-OFDM transmission system. The study is performed by investigating the effect of the noise on a single OFDM subcarrier. The noise effect as a function of subcarrier frequency is also presented. A scatter plot investigation showing phase rotations occurred at the high frequency subcarrier are also shown. Also presented is the effect of the noise with dispersion when multiple subcarriers are used for the transmission. Finally, a full system using 1022 subcarriers from the total of 1024 is shown, where the PM-to-IM conversion noise are varied by varying the linewidth and fibre length. The effect of this conversion noise for higher M-QAM size than 4 QAM is also investigated. Finally, the OSNR requirement of a system with the conversion noise limitation is investigated and presented.
- **Chapter 7:** Chapter 7 demonstrates the effects of a PM-to-IM conversion noise and group delay to the DDO-OFDM system experimentally. In the first demonstration, a commercial DFB laser is used using two types of transmitter designs: low data rate setup using un-shifted laser's centre frequency and an RF *virtual carrier* setup. The first setup represents the common experimental setup where a laser source is used to drive a complex modulator. The system's carrier is represented by the original laser's centre frequency. With this setup, only one-quarter of the total subcarriers can be used for data carrying. In the second setup, the laser's centre frequency is suppressed by biasing the complex modulator around the null and the carrier is then supplied by an RF frequency synthesizer. This RF virtual carrier can be shifted to any frequency within the signal bandwidth. The setup can provide higher RF signal bandwidth than the first setup, where all FFT points can be used as the OFDM data subcarriers. This chapter will also demonstrate the application of a laser linewidth emulator in the DDO-OFDM system using the RF virtual transmitter design.
- **Chapter 8:** Chapter 8 demonstrates a technique to reduce the impact of laser linewidth to a DDO-OFDM system using simulation and experiment. In this chapter, a variant of the DDO-OFDM system: self-heterodyne O-OFDM

(SHO-OFDM) is developed. Simulations to show the reduction of the linewidth impact when a delay is used is presented. An experimental work of this is later shown in the chapter to validate the simulation results. In the experimental work, three experiments are demonstrated: a transmission of single subcarrier, multiple subcarriers and a full SHO-OFDM transmission system. The single and multiple subcarriers transmission are conducted in order to investigate the interaction of the linewidth with the group delay, where a noise pedestal is induced around each of the subcarriers upon photodetection. For the multiple subcarriers transmission, the subcarriers are spaced apart in order to observe the noise floor around the subcarriers. With these transmissions, a clear reduction of the noise floor can be observed at the received electrical spectrum when the delay is assigned. In the full SHO-OFDM transmission system, the noise reduction with the delay assignment is shown by the analysing the system's Q-factor and BER.

- **Chapter 9:** Chapter 9 demonstrates 120 Gb/s data rate transmission using DDO-OFDM over a long-haul fibre. A system design theory to achieve 100 GbE transmission is explained by presenting the techniques employed at the transmitter and receiver design. RF and optical device improvements technique are also presented in order to achieve a good quality and wide bandwidth RF signal. Details of the experiment are also explained including the transmitter and receiver design for a dual-polarization signal transmission. In this experiment, a new variant of a DD receiver setup used are also presented.
- **Chapter 10: Conclusions:** In this chapter, research findings based on the objectives along with the research contributions are summarized. Also presented is some recommended future works in the field.

1.4 Publications

This thesis reports the work carried out in the following publications:

- Z. Zan, A. J. Lowery, & M. Premaratne (2008). Laser RIN and linewidth requirements for direct detection optical OFDM. Lasers and Electro-Optics CLEO 2008, San Jose.
- Schmidt, B. J. C., Z. Zan, L. Du, & A. J. Lowery (2009). 100Gbit/s transmission using single-band direct-detection optical OFDM. Optical Fibre Communication

Conference (OFC/NFOEC). San Diego, CA, Optical Society of America (OSA).
postdeadline paper: PDPC3.

- Z. Zan, L. Du, & A. J. Lowery (2010). Experimental demonstration on the reduction of linewidth impact in a self-heterodyne optical OFDM system. Optical Fibre Communication Conference (OFC/NFOEC). (OSA). San Diego Convention Center: JThA8.
- Z. Zan, & A. J. Lowery (2010). "Experimental demonstration of a flexible and stable semiconductor laser linewidth emulator." Opt. Express **18**(13): 13880-13885.
- Schmidt, B. J. C., Z. Zan, L. Du, & A. J. Lowery (2010). "120 Gbit/s over 500-km using single-band polarization-multiplexed self-coherent optical OFDM." Journal of Lightwave Technology **28**(4): 328-335.

1.5 References

1. Miniwatts Marketing Group. *Internet usage statistics; the internet big picture: world internet users and population stats*. 2011. 31 December 2011; Available from: www.internetworldstats.com/stats.htm.
2. Methodology, C.V.N.I.-F.a. *Approaching the zettabyte era*. 2008 16 June 2008; white paper. Available from: http://cisco.biz/en/US/solutions/collateral/ns341/ns525/ns537/ns705/ns827/white_paper_c11-481374_ns827_Networking_Solutions_White_Paper.html.
3. Rowe, M. *OFC/NFOEC 2010: Bandwidth demand pushes optical communications*. 2010 [cited 2010 23-26 March 2010]; Available from: http://www.tmworld.com/article/454138-OFC_NFOEC_2010_Bandwidth_demand_pushes_optical_communications.php.
4. Kazovsky, L., S. Benedetto, and A. Willner, *Optical fiber communication systems*. 1st ed. 1996, Norwood: Artech House, Inc. 690.
5. Bergano, N.S. *The capabilities of the undersea telecommunications industry*. in *Optical Fiber Communication (OFC), collocated National Fiber Optic Engineers Conference, 2010 Conference on (OFC/NFOEC)*. 2010.
6. Bergano, N.S., *Wavelength division multiplexing in long-haul transoceanic transmission systems*. *Lightwave Technology, Journal of*, 2005. **23**(12): p. 4125-4139.
7. Bergano, N.S. and C.R. Davidson, *Wavelength division multiplexing in long-haul transmission systems*. *Lightwave Technology, Journal of*, 1996. **14**(6): p. 1299-1308.
8. Cooperson, D., T. Unter, and G. Wellbrock, *Tutorial Session: The need for speed: 40 G to 100 G: Evolution or Revolution?*, in *Optical Fiber Communication Conference and Exposition (OFC)*. 2008: San Diego.
9. Robinson, N., *From 10 G to 40 G to 100 G to?*, in *Plenary Sessions on MarketWatch of Optical Fiber Communication Conference and Exposition (OFC) & National Fiber Optic Engineers Conference (NFOEC)*. 2008: San Diego.
10. Melle, S., et al., *Bandwidth virtualization enables long-haul WDM transport of 40 Gb/s and 100 Gb/s services*. *Communications Magazine, IEEE*, 2008. **46**(2): p. S22-S29.

11. Mamyshev, P. *40-Gb/s transmission over systems built for 10-Gb/s*. in *Lasers and Electro-Optics, 2006 and 2006 Quantum Electronics and Laser Science Conference. CLEO/QELS 2006. Conference on*. 2006.
12. Charlet, G. and S. Bigo. *Upgrade of 10Gb/s network to 40Gb/s, challenges and enabling technologies*. in *Optical Communications, 2006. ECOC 2006. European Conference on*. 2006.
13. Hsing-Yu, C., et al., *A 40-Gb/s OFDM PON System Based on 10-GHz EAM and 10-GHz Direct-Detection PIN*. *Photonics Technology Letters, IEEE*, 2012. **24**(1): p. 85-87.
14. Spyropoulou, M., et al., *40 Gb/s NRZ Wavelength Conversion Using a Differentially-Biased SOA-MZI: Theory and Experiment*. *Lightwave Technology, Journal of*, 2011. **29**(10): p. 1489-1499.
15. Dayou, Q., et al. *40-Gb/s MIMO-OFDM-PON using polarization multiplexing and direct-detection*. in *Optical Fiber Communication-includes post deadline papers, 2009. OFC 2009. Conference on*. 2009.
16. Tan, A. and E. Pincemin, *Performance Comparison of Duobinary Formats for 40-Gb/s and Mixed 10/40-Gb/s Long-Haul WDM Transmission on SSMF and LEAF Fibers*. *Lightwave Technology, Journal of*, 2009. **27**(4): p. 396-408.
17. Bornholdt, C., et al. *40 Gbit/s directly modulated passive feedback DFB laser for transmission over 320 km single mode fibre*. in *Optical Communication, 2008. ECOC 2008. 34th European Conference on*. 2008.
18. Contestabile, G., et al. *40 Gb/s WDM NRZ-DPSK All-Optical Clock Recovery and Data Demodulation based on a Periodic Bragg Filter*. in *Optical Fiber communication/National Fiber Optic Engineers Conference, 2008. OFC/NFOEC 2008. Conference on*. 2008.
19. Yonghoon, K., et al., *Comparison of Transmission Performance of 40-Gb/s Optical Duobinary and DCS-RZ Signals Using 10- and 40-Gb/s LiNbO₃ Mach-Zehnder Modulators*. *Lightwave Technology, Journal of*, 2007. **25**(1): p. 318-324.
20. Tan, A. and E. Pincemin. *Performance Comparison of Duobinary and DQPSK Modulation Formats for Mixed 10/40-Gb/s WDM Transmission on SMF and LEAF Fibers*. in *Lasers and Electro-Optics, 2007. CLEO 2007. Conference on*. 2007.
21. Cai, J.-X., et al., *Transmission of 40-Gb/s WDM signals over transoceanic distance using conventional NZ-DSF with receiver dispersion slope compensation*. *Lightwave Technology, Journal of*, 2006. **24**(1): p. 191-200.
22. Fonseca, D., et al. *40 Gb/s OSSB NRZ transmitter for high capacity systems*. in *ECOC 2005*. Glasgow UK.
23. Zhu, B., et al., *High spectral density long-haul 40-Gb/s transmission using CSRZ-DPSK format*. *Lightwave Technology, Journal of*, 2004. **22**(1): p. 208-214.
24. DeSalvo, R., et al., *Advanced components and sub-system solutions for 40 Gb/s transmission*. *Lightwave Technology, Journal of*, 2002. **20**(12): p. 2154-2181.
25. Killey, R.I., et al., *Investigation of nonlinear distortion in 40-Gb/s transmission with higher order mode fiber dispersion compensators*. *Lightwave Technology, Journal of*, 2002. **20**(12): p. 2282-2289.
26. Pan, Z., et al., *Tunable chromatic dispersion compensation in 40-Gb/s systems using nonlinearly chirped fiber Bragg gratings*. *Lightwave Technology, Journal of*, 2002. **20**(12): p. 2239-2246.
27. Hayee, M.I. and A.E. Willner, *NRZ versus RZ in 10-40-Gb/s dispersion-managed WDM transmission systems*. *Photonics Technology Letters, IEEE*, 1999. **11**(8): p. 991-993.
28. Breuer, D., K. Obermann, and K. Petermann, *Comparison of N x 40 Gb/s and 4 x 10 Gb/s WDM transmission over standard single-mode fiber at 1.55 μ m*. *Photonics Technology Letters, IEEE*, 1998. **10**(12): p. 1793-1795.

29. Schmidt, B.J.C., et al., *100Gbit/s transmission using single-band direct-detection optical OFDM*, in *Optical Fiber Communication Conference (OFC/NFOEC)*. 2009, Optical Society of America (OSA): San Diego, CA. p. PDPC3.
30. Jansen, S.L., et al., *121.9-Gb/s PDM-OFDM Transmission With 2-b/s/Hz Spectral Efficiency Over 1000 km of SSMF*. *Lightwave Technology, Journal of*, 2009. **27**(3): p. 177-188.
31. Djordjevic, I.B. and B. Vasic, *100-gb/s transmission using orthogonal frequency-division multiplexing*. *Photonics Technology Letters, IEEE*, 2006. **18**(15): p. 1576-1578.
32. Duelk, M. *Next-generation 100 G Ethernet*. in *Optical Communication, 2005. ECOC 2005. 31st European Conference on*. 2005.
33. Agrawal, G.P., *Lightwave technology: telecommunication systems*. Vol. 2. 2005, Hoboken, New Jersey: John Wiley & Sons. 463.
34. Kuo, B.P.P., et al., *Transmission of 640-Gb/s RZ-OOK Channel Over 100-km SSMF by Wavelength-Transparent Conjugation*. *Lightwave Technology, Journal of*, 2011. **29**(4): p. 516-523.
35. Jansen, S.L., et al., *Coherent optical 25.8-Gb/s OFDM transmission over 4160-km SSMF*. *Journal of Lightwave Technology*, 2008. **26**(1): p. 6-15.
36. Li, X., R. Mardling, and J. Armstrong. *Channel capacity of IM/DD optical communication systems and of ACO-OFDM*. in *IEEE International Conference on Communications*. 2007.
37. Lowery, A.J., *Fiber Nonlinearity Mitigation in Optical Links That Use OFDM for Dispersion Compensation*. *Photonics Technology Letters, IEEE*, 2007. **19**(19): p. 1556-1558.
38. Lowery, A.J. and J. Armstrong, *Orthogonal frequency division multiplexing for dispersion compensation of long-haul optical systems*. *Optics Express*, 2006. **14**: p. 2079-2084.
39. Chang, R.W., *Synthesis of band-limited orthogonal signals for multichannel data transmission*. *Bell Systems Technical Journal*, 1966. **45**: p. 1775-1796.
40. Chang, R.W. and R.A. Gibby, *A theoretical study of performance of an orthogonal multiplexing data transmission scheme*. *IEEE Transactions of Communication Technology*, 1968. **COM-16**(4): p. 529-540.
41. Chang, R.W., *Orthogonal frequency multiplex data transmission system*, in *US Patent*, U. patent, Editor. 1970: United State of America. p. 10.
42. Hanzo, L. and T. Keller, *OFDM and MC-CDMA A Primer*. 2006: John Wiley & Sons Ltd. 411.
43. S.Bahai, a.R., B.R. Saltzberg, and M. Ergen, *Multi-carrier digital communications: theory and applications of OFDM*. 2nd ed. 2004: Springer.
44. Nee, R.V. and R. Prasad, *OFDM for wireless multimedia communications*. 2000, Boston: Artech House 260.
45. Weinstein, S.B. and P.M. Ebert, *Data transmission by frequency division multiplexing using discrete Fourier transform*. *IEEE Transactions of Communication Technology*, 1971. **19**: p. 628-634.
46. Weinstein, S.B., *The history of orthogonal frequency-division multiplexing [History of Communications]*. *Communications Magazine, IEEE*, 2009. **47**(11): p. 26-35.
47. Prasad, R., *OFDM for Wireless Communications Systems*. 2004, Artech House.
48. Watts, P.M., et al., *Performance of single-mode fiber links using electronic feed-forward and decision feedback equalizers*. *Photonics Technology Letters, IEEE*, 2005. **17**(10): p. 2206-2208.

49. Killey, R.I., et al., *Electronic dispersion compensation by signal predistortion using digital Processing and a dual-drive Mach-Zehnder Modulator*. Photonics Technology Letters, IEEE, 2005. **17**(3): p. 714-716.
50. Killey, R.I., et al., *Electronic dispersion compensation by signal predistortion*, in *Optical Fiber Communication Conference*. 2006: Anaheim, CA. p. OWB3.
51. McGhan, D., et al. *5120 km RZ-DPSK transmission over G652 fiber at 10 Gb/s with no optical dispersion compensation*. in *Optical Fiber Communication Conference, 2005. Technical Digest. OFC/NFOEC*. 2005.
52. McNicol, J., et al. *Electrical domain compensation of optical dispersion [optical fibre communication applications]*. in *Optical Fiber Communication Conference, 2005. Technical Digest. OFC/NFOEC*. 2005.
53. McGhan, D., et al. *Electronic dispersion compensation*. in *Optical Fiber Communication Conference, 2006 and the 2006 National Fiber Optic Engineers Conference. OFC 2006*. 2006.
54. Shieh, W., X. Yi, and Y. Tang, *Transmission experiment of multi-gigabit coherent optical OFDM systems over 1000km SSMF fibre*. ELECTRONICS LETTERS, 2007. **43**(3): p. 183-184.
55. Shieh, W. and C. Athaudage, *Coherent optical orthogonal frequency division multiplexing*. Electronic Letters, 2006. **42**: p. 587-588.
56. Shieh, W. and R.S. Tucker, *Polarisation mode dispersion mitigation in coherent optical orthogonal frequency division multiplexed systems*. Electronic Letters, 2006. **42**(17): p. 2.
57. Jansen, S.L., et al. *20-Gb/s OFDM transmission over 4160-km SSMF enabled by RF-pilot tone phase noise compensation*. in *Optical Fiber Communication Conference*. 2007. Anaheim, CA.
58. Jansen, S.L., I. Morita, and H. Tanaka. *10-Gb/s OFDM with conventional DFB lasers*. in *33rd European Conference and Exhibition on Optical Communication 2007*. Berlin, Germany: VDE VERLAG GMBH.
59. Jansen, S.L., I. Morita, and H. Tanaka, *16x52.5-Gb/s, 50-GHz spaced, POLMUX-CO-OFDM transmission over 4,160 km of SSMF enabled by MIMO processing*. Optical Communication - Post-Deadline Papers (published 2008), 2007 33rd European Conference and Exhibition of, 2007: p. 1-2.
60. Jansen, S.L., I. Morita, and H. Tanaka, *Experimental demonstration of 23.6 Gb/s OFDM with a colorless transmitter*, in *optoelectronics and communications conference (OECC)*. 2007. p. PD1-5.
61. Lowery, A.J., *Amplified-spontaneous noise limit of optical OFDM lightwave systems*. Optics Express, 2008. **16**(2): p. 860-865.
62. Armstrong, J., et al. *Performance of Asymmetrically Clipped Optical OFDM in AWGN for an intensity modulated direct detection system*. in *IEEE Globecom*. 2006: IEEE Communications Society.
63. Armstrong, J. and A.J. Lowery, *Power efficient optical OFDM*. ELECTRONICS LETTERS, 2006. **42**(6): p. 370-372.
64. Lowery, A.J. and J. Armstrong, *10 Gbit/s multimode fiber link using power efficient orthogonal-frequency-division multiplexing*. OPTICS EXPRESS, 2005. **13**(25): p. 10003-10009.
65. Djordjevic, I.B. and B. Vasic, *Orthogonal frequency division multiplexing for high-speed optical transmission*. Opt. Express, 2006. **14**(9): p. 3767-3775.
66. Lowery, A.J., L. Du, and J. Armstrong. *Orthogonal Frequency Division Multiplexing for Adaptive Dispersion Compensation in Long Haul WDM Systems*. in *Optical Fiber*

- Communication Conference, 2006 and the 2006 National Fiber Optic Engineers Conference. OFC 2006. 2006.*
67. Cvijetic, N. *OFDM in Optical Access Networks*. 2011: Optical Society of America.
 68. Cvijetic, N., et al., *Terabit Optical Access Networks Based on WDM-OFDMA-PON*. *Lightwave Technology, Journal of*, 2012. **30**(4): p. 493-503.
 69. Tang, J.M., P.M. Lane, and K.A. Shore, *High-speed transmission of adaptively modulated optical OFDM signals over multimode fibers using directly Modulated DFBs*. *Lightwave Technology, Journal of*, 2006. **24**(1): p. 429-441.
 70. Tang, J.M. and K.A. Shore, *Maximizing the Transmission Performance of Adaptively Modulated Optical OFDM Signals in Multimode-Fiber Links by Optimizing Analog-to-Digital Converters*. *Lightwave Technology, Journal of*, 2007. **25**(3): p. 787-798.
 71. Jolley, N.E., et al. *Generation and propagation of a 1550 nm 10 Gbit/s optical orthogonal frequency division multiplexed signal over 1000m of multimode fibre using a directly modulated DFB*. in *Optical Fiber Communication Conference, 2005. Technical Digest. OFC/NFOEC. 2005.*
 72. Hugues-Salas, E., et al., *Directly Modulated VCSEL-Based Real-Time 11.25-Gb/s Optical OFDM Transmission Over 2000-m Legacy MMFs*. *Photonics Journal, IEEE*, 2012. **4**(1): p. 143-154.
 73. Tang, J.M. and K.A. Shore, *30-Gb/s signal transmission over 40-km directly modulated DFB-laser-based single-mode-fiber links without optical amplification and dispersion compensation*. *Journal of Lightwave Technology*, 2006. **24**(6): p. 2318-2327.
 74. Panta, K.R. and J. Armstrong, *Effects of clipping on the error performance of OFDM in frequency selective fading channels*. *Wireless Communications, IEEE Transactions on*, 2004. **3**(2): p. 668-671.
 75. Schmidt, B.J.C., A.J. Lowery, and J. Armstrong, *Experimental demonstrations of electronic dispersion compensation for long-haul transmission using direct-detection optical OFDM*. *Journal of Lightwave Technology*, 2008. **26**(1): p. 196-203.
 76. Schmidt, B.J.C., A.J. Lowery, and J. Armstrong. *Experimental demonstrations of 20 Gbits/s direct-detection optical OFDM and 12Gbits/s with a colorless transmitter*. in *Optical Fiber Communication Conference. 2007. Anaheim, CA.*
 77. Lowery, A.J. and J. Armstrong. *Orthogonal-Frequency-Division Multiplexing for Optical Dispersion Compensation*. in *Optical Fiber Communication and the National Fiber Optic Engineers Conference. 2007. Anaheim, USA.*
 78. Lowery, A.J., L. Du, and J. Armstrong, *Performance of optical OFDM in ultra long-haul WDM lightwave systems*. *Journal of Lightwave Technology*, 2007. **25**: p. 131 – 138.
 79. Du, L. and A.J. Lowery. *Compensating XPM for 100 Gbit/s coherent channels with 10 Gbit/s direct-detection NRZ neighbors*. in *Optical Fiber Communication (OFC), collocated National Fiber Optic Engineers Conference, 2010 Conference on (OFC/NFOEC). 2010.*
 80. Du, L. and A.J. Lowery, *Fiber nonlinearity precompensation for long-haul links using direct-detection optical OFDM*. *Optics Express*, 2008. **16**(9): p. 6209-6215.
 81. Lowery, A.J., *Fiber nonlinearity mitigation in optical links that use OFDM for dispersion compensation*. *IEEE Photon. Technol. Lett*, 2007. **18**19: p. 1556-1558.
 82. Lowery, A.J., *Fiber nonlinearity pre- And post-compensation for long-haul optical links using OFDM*. *Optics Express*, 2007. **15**(20): p. 12965-12970.
 83. Qi, Y., et al., *Experimental Demonstration and Numerical Simulation of 107-Gb/s High Spectral Efficiency Coherent Optical OFDM*. *Lightwave Technology, Journal of*, 2009. **27**(3): p. 168-176.

84. Ma, Y., W. Shieh, and Y. Qi. *Bandwidth-Efficient 21.4 Gb/s Coherent Optical 2x2 MIMO OFDM Transmission*. in *Optical Fiber communication/National Fiber Optic Engineers Conference, 2008. OFC/NFOEC 2008. Conference on*. 2008.
85. Shieh, W., et al., *Theoretical and experimental study on PMD supported transmission using polarization diversity in coherent optical OFDM systems*. OPTICS EXPRESS, 2007. **15**(16): p. 9936-9947.
86. Yi, X., W. Shieh, and Y. Tang, *Phase estimation for coherent optical OFDM*. PHOTONICS TECHNOLOGY LETTERS, 2007. **19**(12): p. 919-921.
87. Yi, X., W. Shieh, and Y. Ma. *Phase noise on coherent optical OFDM systems with 16-QAM beyond 10Gb/s*. in *33rd European Conference and Exhibition on Optical Communication 2007*. Berlin, Germany: VDE VERLAG GMBH.
88. Xingwen, Y., S. William, and M. Yiran, *Phase Noise Effects on High Spectral Efficiency Coherent Optical OFDM Transmission*. Lightwave Technology, Journal of, 2008. **26**(10): p. 1309-1316.
89. Yamamoto, S., et al., *Analysis of laser phase noise to intensity noise conversion by chromatic dispersion in intensity modulation and direct detection optical fiber transmission*. Journal of Lightwave Technology, 1990. **8**: p. 1716-1722
90. Edagawa, N., et al., *12300 ps/nm, 2.4 Gb/s nonregenerative optical fiber transmission experiment and effect of transmitter phase noise*. Photonics Technology Letters, IEEE, 1990. **2**(4): p. 274-276.
91. Marshall, W.K., B. Crosignani, and A. Yariv, *Laser phase noise to intensity noise conversion by lowest-order group velocity dispersion in optical fiber: exact theory*. Optics Express, 2000. **23**(3): p. 165-167.
92. Marshall, W.K. and A. Yariv, *Spectrum of the intensity of modulated noise light after propagation in dispersive fiber*. PHOTONICS TECHNOLOGY LETTERS, 2000. **12**(3): p. 302-304.
93. Derickson, D., ed. *Fiber Optic Test and Measurement*. 1998, Prentice Hall: New Jersey.
94. Elsässer, W. and E.O. Göbel, *Spectral linewidth of gain- and index-guided InGaAsP semiconductor lasers*. Applied Physics Letters, 1984. **45**(4): p. 353-355.
95. Agrawal, G.P. and N.K. Dutta, *Semiconductor Lasers*. 2nd ed. 1993, New York: International Thomson Publishing.

Chapter 2

REVIEW OF OPTICAL COMMUNICATION SYSTEMS USING OFDM MODULATION

2.1 Introduction

In this chapter, the adaptation of an orthogonal frequency division multiplexing (OFDM) technique to direct detection (DD) optical communication systems is addressed. The principle of the OFDM technique for wireless communication system will be first reviewed in Section 2.2. System design, advantages and limitations of the technique in the wireless communication system will be explained. This is followed by the history of the technique in optical communication systems, presented in Section 2.3. The section will cover the history of the optical OFDM system development, starting from the early works until the recent implementation on real-time transmissions. Two major system designs; the DDO-OFDM and CO-OFDM systems are explained for long-haul transmission, with the focus of the thesis is on the DDO-OFDM system. In Section 2.4, the system designs for a single-sideband (SSB) modulation employed in the DDO-OFDM are discussed in detail. Section 2.5 presents the interaction of laser noise with fibre dispersion, which can affect the system performance. This is based on previous work reported for subcarrier multiplexing (SCM) and linewidth measurement techniques. Section 2.6 explains the background of high-speed transmission using optical OFDM and the concept of polarization multiplexing. Finally, Section 2.7 reviews real-time transmissions and summarises experimental demonstrations of optical OFDM systems using different design techniques. This is followed by conclusions in Section 2.8 and finally, references in Section 2.9.

2.2 OFDM for Wireless

Long before R.W. Chang (1966) proposed the concept of OFDM for wireless [1], frequency division multiplexing (FDM) was proposed by M. Schwartz (1910) for the US army [2]. This was implemented using non-overlapping low-frequency subcarriers to avoid ICI effects. This inefficient use of signal bandwidth was

overcome by Chang using overlapping subcarriers with no inter-symbol interference (ISI) and inter-carrier interference (ICI) upon signal reception. The technique was first developed to combat channel fading in wireless communication system [1, 3, 4]. Similar to FDM, this technique is also a type of a multi-carrier modulation (MCM) scheme, because various subcarriers are used to carry data stream from a single channel [1, 3, 4]. With the MCM technique, the data stream is divided into parallel data streams and each is modulated with either PSK or QAM.

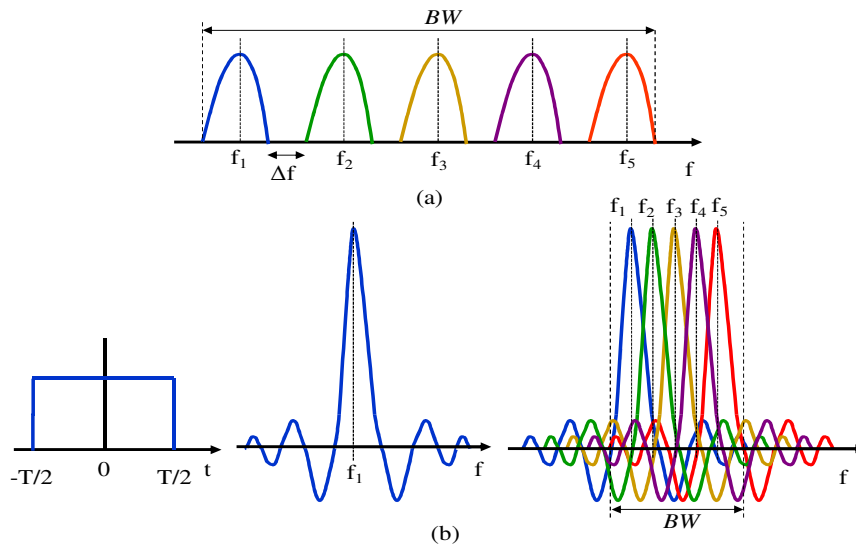


Fig. 2.2.1. Comparison between (a) conventional MCM and (b) OFDM signal spectrum.

Fig. 2.2.1 illustrates the comparison between conventional MCM applied in the FDM technique and an OFDM signal spectrum. In conventional MCM technique, a signal bandwidth, BW is divided into N frequencies to accommodate N non-overlapping subcarriers. Each subcarrier carrying different data symbol and is frequency spaced (Δf) apart from the adjacent subcarrier. This is to prevent interference and the subcarriers are then frequency-multiplexed for transmission. The use of a wide Δf prevents crosstalk at the expense of inefficient bandwidth utilization. To increase the bandwidth utilization, Chang (1966) proposed overlapping the subcarriers with a frequency spacing between the subcarriers equal to the signalling rate carried by single subcarrier [5-7]. In his system, all of the subcarriers were modulated with the same data rate, where one data symbol is carried by many subcarriers. In order to deal with the crosstalk from the overlapped subcarriers, orthogonality between the subcarriers is required. Fig. 2.2.1 (b) illustrates the OFDM signal spectrum. The orthogonality is achieved by the convolution of Dirac functions

at the subcarrier frequencies with the spectrum of a *sinc* function ($\text{sinc}(\pi fT)$). This spectrum is the Fourier transform of a square pulse, where it is one for a symbol period T and zero elsewhere. With the orthogonal property, each of the subcarriers can be filtered at the receiver without any crosstalk from the adjacent subcarriers. From the figure, a significantly narrower bandwidth is required to transmit the same number of subcarriers compared with the conventional MCM. The PSK- or the QAM-modulated data stream using M -size modulation can also increase the spectral efficiency when using larger M . The increase of the spectral efficiency using Chang's technique was also supported by B.R. Saltzberg (1967), which was published a year after [8].

Despite the high-spectral efficiency of Chang's technique, its implementation involved a complex design with large number of components required to generate and shape the subcarriers. This used banks of filters and modulators and demodulators that consisted of local oscillators (LOs) and mixers [1, 4]. This also leads to a high power consumption and increases the implementation cost. An equally complex method was also proposed by Saltzberg using a time delay assigned to inphase (I) and quadrature (Q) components of the subcarriers, before they were frequency multiplexed for transmission. This was known as offset quadrature amplitude modulation (OQAM) and is used to reduce fluctuations in power in a QAM-modulated waveform. An analytical study of crosstalk between the adjacent subcarriers was presented in [3]. Despite the elegance of this technique, it has only been used in high-frequency military systems in 1960s such as KINEPLEX, ANDEFT and KATHRYN due to its design complexity, high power consumption and implementation cost [8]. The technique remained unfeasible for commercial systems until S.B. Weinstein and P.M. Ebert (1971) proposed the use of a discrete Fourier transform (DFT) to generate and demultiplex the OFDM signals [9].

Because of advances in electronic circuits and advanced digital signal processing (DSP) for the implementation of fast Fourier transform (FFT), OFDM had made its comeback in 1990s, where it has become part of several standards such as European digital audio broadcast (DAB), digital video broadcast (DVB), high-speed digital subscriber lines (HDSL, ADSL, VDSL), wireless LANs (HIPERLAN/2, IEEE 802.11a, IEEE 802.16, MMAC), and fixed broadband wireless access (802.11g) [5-8]. OFDM has also been recently selected as a high performance local area network's

(HIPERLAN) transmission technique, as well as becoming part of the IEEE 802.11 wireless local area network (WLAN) standard.

2.2.1 OFDM Principles

Fig. 2.2.2 shows the block diagram of OFDM modulation and demodulation as proposed by Chang [10]. Banks of filters and modulators (and demodulators) with mixers and LOs are required at the transmitter (and receiver).

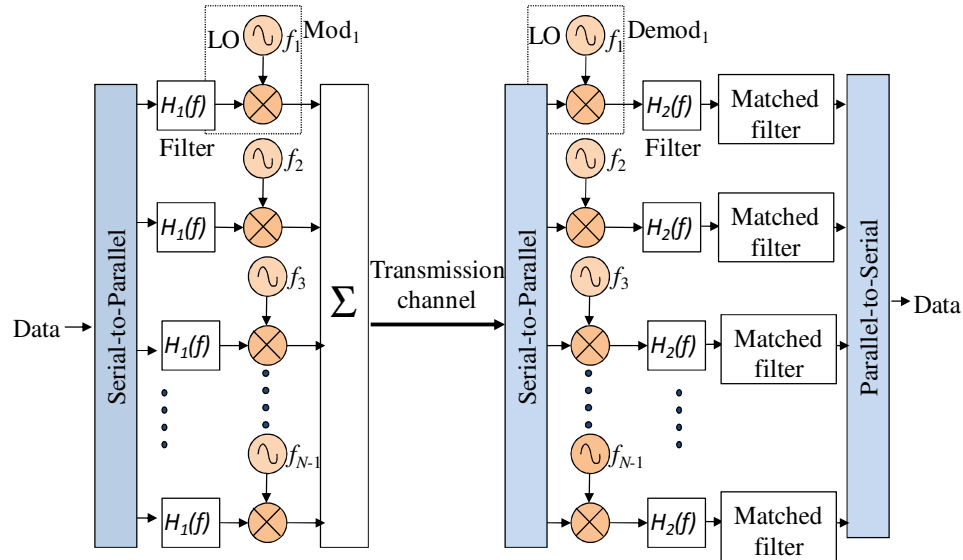


Fig. 2.2.2. Basic block diagram of OFDM modulation and demodulation employing filter bank.

At the transmitter, shaping filters with identical bandpass responses, $H_1(f)$ are applied at each subcarrier branch before each of the sub-data streams are modulated with subcarrier frequency from f_1 to f_N , for N OFDM subcarriers with equal spacing. At the receiver, the signal is demodulated by performing down-conversion using sets of demodulators, consisting of mixers and LOs before going through a baseband low-pass filter, $H_2(f)$, at each subcarrier branch. Matched filters are placed to extract the intended subcarrier spectrum. The original data stream is assembled by a parallel-to-serial conversion.

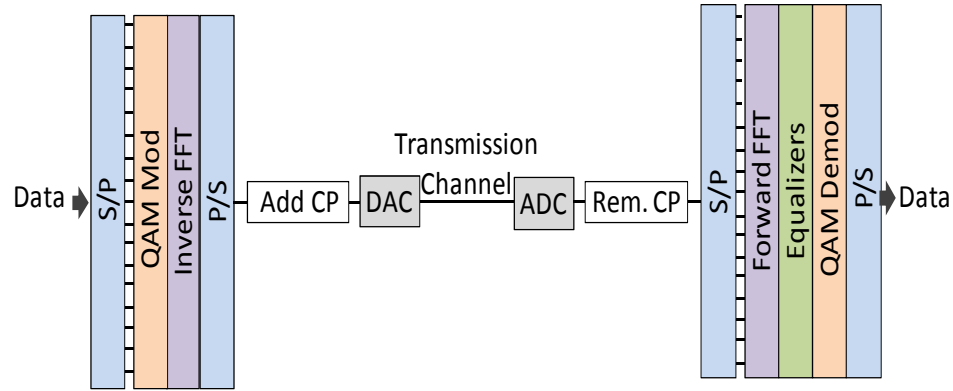


Fig. 2.2.3. Basic OFDM block diagram implemented using Fourier transforms.

Figure 2.2.3 shows the basic block diagram of the OFDM system implemented using Fourier transforms. A serial data stream is converted into lower-rate sub-streams. Each is modulated using amplitude and phase modulation, for example quadrature amplitude modulation (QAM). The resulting data symbols are carried by N -parallel subcarriers ($f_1, f_2, f_3, \dots, f_N$) [10]. These subcarriers can be easily generated using an inverse FFT (iFFT) [9, 11]. The orthogonal subcarriers can be overlapped with the adjacent subcarriers without incurring any ICI upon reception. A mathematical representation of a lower rate sub-stream modulated with the subcarrier signal can be written as

$$x_n(t) = b_n(t)e^{j2\pi f_n t}, \quad 0 \leq t \leq T_s \quad (2.2.1)$$

for one OFDM symbol, where $b_n(t)$ is a complex data at the n^{th} subcarrier and T_s is the OFDM symbol duration [3]. After the iFFT, time domain waveforms of the OFDM symbols are converted into serial and a cyclic prefix (CP) is added into the waveform. This is done by copying some part at the end part of the symbol waveform to the start of the waveform (or vice versa). The CP or guard time interval is applied to deal with the multipath delay spread that can induce ISI [8]. The CP waveform extension will be discussed in detail in the following section. After the CP assignment, the signal is converted to an analogue signal using a digital-to-analog converter (DAC). After the transmission over a multipath or dispersive channel, the CP will be first removed from the received signal after the analogue-to-digital (ADC) converter. To remove the CP, time synchronization is performed to find the start of the symbol waveform. The CP is then discarded according to the assigned CP length and the location of the CP at the transmitter. After the CP removal, the signal is converted into N -parallel signals using serial-to-parallel (S/P) converter. These N -

parallel signals are fed into a forward FFT (f-FFT), where the outputs correspond to the N -OFDM subcarriers in the form of frequency spectrum. Equalisers are then required to overcome linear amplitude and phase distortions due to the dispersive transmission channel. A simple one-tap frequency domain equaliser can be used as opposed to multiple-tap equalisers required by a single-carrier modulation system. This is due to the narrow subcarriers employed in OFDM, where each of the subcarriers experiences a flat fading. The recovered subcarriers are then QAM-demodulated and serial-converted to obtain the sequence of transmitted data.

2.2.2 Advantages

In this section, the details of how the advantages are achieved with OFDM in wireless communication systems are presented.

- **Simple System Design**

The use of inverse and forward FFT for OFDM modulation and demodulation has provided a significant advantage to the OFDM design in terms of system complexity and implementation cost. The reduction of system complexity can be seen by comparing Fig. 2.2.2 and Fig. 2.2.3 where neither banks of filters nor LOs are required to generate the OFDM subcarriers: FFTs algorithm can be easily performed using DSP [10, 11].

- **Increased Spectral Efficiency**

The spectral efficiency of the OFDM technique is provided by overlapping the orthogonal subcarriers to the adjacent subcarriers without imposing the ICI. The spectrum of the overlapped OFDM subcarriers has been shown in Fig. 2.2.1. The figure shows that more OFDM subcarriers can be assigned within a given transmission bandwidth compared to the traditional FDM. This increases the transmission rate per unit bandwidth. The ICI upon reception can be prevented even though the subcarrier spectrum is overlapped by using orthogonal subcarriers. The orthogonal subcarriers ensure the demultiplexing of each of the subcarrier will be crosstalk-free upon the reception. This is because each of the subcarriers has an integer number of cycles with exactly one cycle difference between the adjacent subcarriers in the symbol interval.

- **Flexible and Adaptive Subcarrier Modulation**

Another advantage of OFDM modulation is its flexible and adaptive properties. For example, the subcarriers can be modulated with different modulation formats for instance; higher signal quality subcarriers can be modulated to carry higher numbers of bits per symbol [5].

- **Immunity to Multipath Fading**

Multipath fading immunity is provided by the use of a CP in the transmit data symbol to eliminate ISI. Two types of CP were proposed: silent CP in [10] (a guard interval) and CP taken with the length of quarter of the start or the end of the symbol waveform in [12]. The effective CP length is taken from the maximum expected time delay spread experienced across the transmission channel [12]. The silent CP uses no signal assigned within the CP length [10]. This, however, can destroy the orthogonality of the subcarriers due to the dispersive channel. The energy of a subcarrier can be spread into the adjacent subcarrier caused by an energy leakage of a subcarrier to the adjacent subcarriers due to the dispersive channel, which can cause the ICI. Also, after a multipath or dispersive channel transmission, symbols carried by the subcarriers will arrive at the receiver after different time delays. The symbol waveform of a higher-delay subcarrier will spread into the neighbouring symbol and enter the symbol's FFT window. This will cause the ISI. To avoid this, the CP or guard interval is used where its duration is taken as the amount of the time-delay introduced by the channel. This allows some time slip between the CPs of the adjacent symbol intervals and the waveform remains periodic within its FFT-window.

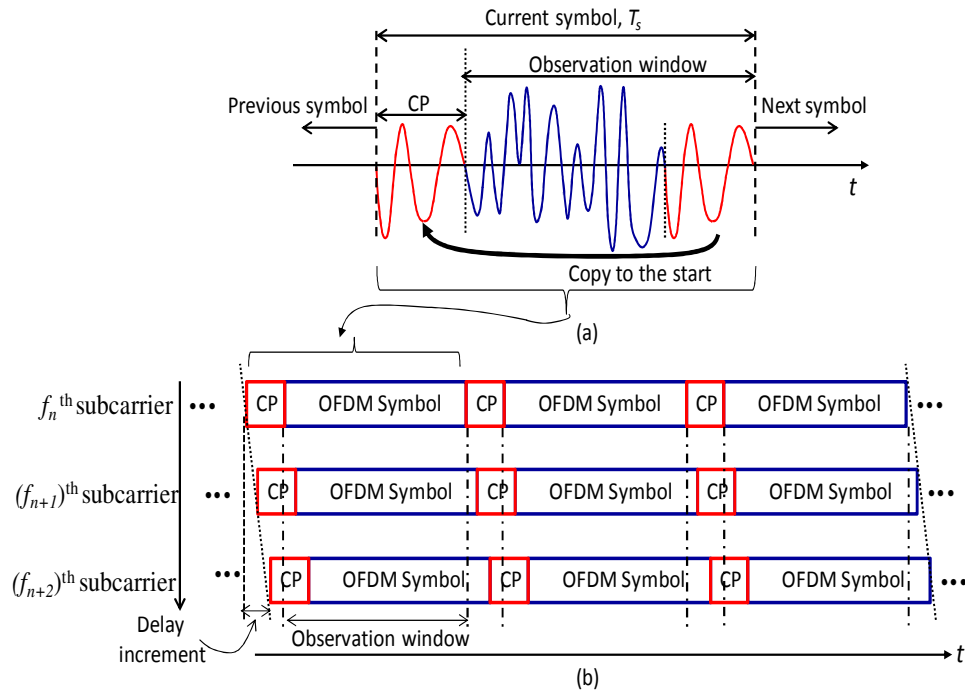


Fig. 2.2.4. OFDM symbol with (a) OFDM waveform with a CP assignment and (b) time-frequency graph showing the delay spread occurred on the parallel data symbol after multipath fading channel.

Fig. 2.2.4 shows (a) the OFDM waveform with the CP taken from the end of the symbol and placed at the beginning of the symbol and (b) time-frequency graph showing the delay spread occurred after a multipath fading channel. Fig. 2.2.4 (b) shows that the bottom signal blocks experiencing more delay spread as compared to the top blocks. The delay spread for these waveforms are illustrated to be less than the CP length. Within the observation window after the signal is received, parts of the OFDM symbol that fall outside the window can be recovered from the CP. When the delay spread occurs, the CP will ensure a periodic signal wave is achieved without any discontinuities or phase jumps within the observation window where every subcarrier is periodic within the observation window [6]. With the CP, the ICI can be prevented and hence the orthogonality is preserved between the subcarriers. However, there is some trade-off where the CP will cause a constant capacity loss since no additional data is transmitted within the CP periods.

2.2.3 Limitations

Despite all the advantageous of the OFDM technique, there are some limitations that need to be considered in designing the system.

- **PAPR**

When the modulated N -subcarriers are combined using the parallel-to-serial conversion, the signals are all added together to form an OFDM signal. However, the addition of the N signals with similar phases can produce a high peak amplitude. This is because, in theory, the N subcarriers will add constructively, which produces much higher peak amplitude than the average power [5].

Given a block of N symbols, consisting of complex data $\mathbf{X} = \{X_n, n = 0, 1, \dots, N-1\}$, where each symbol is modulated with n subcarriers, where $n = 0, 1, \dots, N-1$, the complex transmitted OFDM signals of N number of subcarriers can be written as [13-15]:

$$x(t) = \frac{1}{\sqrt{N}} \sum_{n=0}^{N-1} X_n e^{j2\pi n \Delta f t}, 0 \leq t \leq NT \quad (2.2.2)$$

with T is the period of a symbol block and NT is the total block period. The N subcarriers are orthogonal with the subcarrier spacing, Δf , denoted as $1/(T)$. The PAPR of the signal can be defined as [13-15]

$$PAPR = \max_{0 \leq t \leq NT} \frac{|s(t)|^2}{\frac{1}{NT} \cdot E[|s(t)|^2]} \quad (2.2.3)$$

where $E[\cdot]$ is a time averaging. The PAPR can become higher than the N times the average power when a higher multi-level signal for example higher M -QAM is used [13-15]. PAPR will cause power inefficiency at the transmitter because high supply voltages will be needed to accommodate the infrequent high peak amplitude of the signal waveform to prevent the signal from being clipped. Clipping will result an in-band and out-band distortions tones [13, 14, 16]. To reduce this effect, many techniques have been developed for example using a simple peak amplitude-clipping, forward error correction (FEC) and data scrambling [13, 14, 16]. The PAPR reduction technique is important since PAPR can overthrow the advantageous and implementation practicality of this technique in wireless communication systems [5-7, 13, 14, 16-20].

- **Phase Noise and Frequency Offset Sensitive**

Another limitation is the sensitivity to carrier phase noise and frequency offsets. Practically, the LO used for the carrier will has a phase that randomly varies in time, where the time derivatives of it will result in a varying frequency. Thus, the

frequency of the receiver's LO will not be ideally equal to the received LO. The phase noise of the LO at the transmitter will be superimposed on the modulating signal, where the free-running LO at the receiver will also has its own random phase that varies its frequency. This can cause limitations during the down-conversion process at the receiver where phase tracking, for example phase-locked loop (PLL) will be required.

In wireless OFDM, two types of phase noise effects have been reported by researchers [5, 21-27]. The first one is the common phase error, where the same phase variation is superimposed on every subcarrier. The Common Phase Error (CPE) can be easily removed using the PLL and a balanced receiver [5-8]. The second effect, which is more harmful, is the frequency offset of the subcarriers' frequencies [23, 24]. This can happen if the linewidth of the master oscillator is wider than the subcarrier's spacing. Since the OFDM subcarriers' orthogonality is achieved by having integer number of cycles differences between the subcarriers within the FFT interval [23, 24], the frequency offset can destroy the orthogonality of the subcarriers because the number of cycles within the interval is no longer an integer number. This will induce ICI and degrade the BER performance [5, 23-27]. To overcome the limitations, many frequency offset estimation and compensation techniques have been developed [26-33].

- **IQ Imbalance**

An IQ imbalance of the signal components can also introduce SNR penalty to the system performance [22-28]. The IQ imbalance occurs to the imperfections of the practical electronics devices for signal down-conversion to baseband. For example, practical LO, mixers and filters that are used to perform this operation can induce amplitude and phase imbalance between the I and Q ports. This can happen due to an imperfect 90° phase shift of the LO and a mismatched in the mixers branches and the filters used [34]. This will cause the ICI due to the imperfect image rejection [34-37].

2.3 History of Optical OFDM

The transmission of multiple carriers generated electrically has been implemented in optical communication systems before the adoption of OFDM technique. It is known as subcarrier multiplexing (SCM) [38], where each of the subcarrier is used to carry a

data signal. Another technique is optical frequency division multiplexing proposed in [39, 40], where it has narrower channel spacing (10 GHz) compared to a WDM system. However, these two techniques do not employ the orthogonality property to its subcarriers unlike the OFDM technique. The adoption of the OFDM technique into an optical communication system was first done in radio over fibre (RoF) to assist wireless networks [38] before it was applied for optical landline transmission.

OFDM signal transmission in an optical landline system was first inspired by electronic dispersion compensation (EDC) techniques [41-47]. In EDC, two compensation techniques were developed, where the fibre dispersion can either be pre- or post-compensated for using electronic DSP [48-54]. These techniques provide a low-cost design since the requirement of optical dispersion compensated fibre (DCF) can be eliminated. The early development of the EDC technique was done using a complex conjugate of the dispersion transfer function, proposed in 1999 by M. Sieben, et al. [55]. The EDC developments with DSP were also proposed using feed-forward, decision feedback and maximum-likelihood sequence estimation (MLSE) [42, 56, 57]. The latter demonstrated a transmission of 10.7 Gb/s over 3840 km of fibre [56].

The optical OFDM system to electrically compensate for the fibre dispersion was first proposed by two groups in 2006: A.J. Lowery and J. Armstrong [48, 49] and W. Shieh and C. Athaudage [53]. The first group proposed a direct-detection technique for the OFDM signal transmission which then followed by the later group with coherent-detection. I.B. Djordjevic and B. Vasic (2006) also presented their work on direct-detection optical OFDM system. These groups showed successful dispersion compensation technique by using the OFDM signal transmission. The EDC is achieved by using the CP extension in the OFDM symbol with similar CP assignment as in Fig. 2.2.3. An early proposal on the OFDM technique implemented in an optical communication system can be traced back in 1996, proposed by Q. Pan and R.J. Green [58, 59]. The system was known as a lightwave hybrid AM/OFDM system, which employed SCM channels to carry the OFDM signals. In 2006, J.M Tang, et al. proposed the adoption of the OFDM technique using similar optical modulation as employed in the RoF system [60, 61]. A high DC-bias was added to the signal to up-shift the waveform to a high average power [50, 60-64]. This technique is used to address the implementation issue of adapting a bipolar OFDM signals into a unipolar

power environment of intensity modulation (IM). However, this imposed other implementation problems such as eye-safety and inefficient use of the optical power since the bias is not carrying any data and subsequently reduces the system performance [60-65].

A solution to this power inefficiency was then proposed by J. Armstrong and A.J. Lowery (2006) without the requirement of the high DC bias. This was done by clipping any part of the signal that is below the average level, known as asymmetrically-clipped optical OFDM (ACO-OFDM) [62, 66]. In these works, the clipped OFDM signal's voltage was used to drive a laser using intensity modulation and direct detection (IM/DD) system design. Two versions of the ACO-OFDM system were proposed. The first [64] was done using the odd-subcarriers to carry the data while the even-subcarriers are used to accommodate the mixing of subcarriers \times subcarriers and to avoid the clipping noise [62, 66]. Another method to accommodate this mixing term is by having a frequency guardband with the same width as the OFDM signal band [62, 64]. Among the early coding techniques presented in the optical OFDM IM/DD system design was the quadrature phase shift keying (QPSK), QAM and pulse-amplitude modulation (PAM) [63, 64]. The IM/DD system was initially demonstrated using double sideband (DSB) signal modulation transmitted over multimode fibre (MMF) without any optical amplification and DCF, which aimed for a very short reach (VSR) transmission and to upgrade the data rate of an existing passive optical network (PON) [61, 64, 67]. With the OFDM technique, the effect of modal dispersion was shown to be compensated successfully [60, 61, 68].

In long haul optical transmission systems, chromatic dispersion in a single mode fibre (SMF) becomes a major limitation that needs to be overcome instead of the multipath or modal dispersion in MMF. To compensate for the CD, further advancement in the optical OFDM transmission system design is required [48]. A.J. Lowery and J. Armstrong (2006) were the first to suggest direct detection optical OFDM (DDO-OFDM) system and demonstrated this by simulating 10 Gb/s OFDM signal transmission over 4000 km standard-SMF without any DCF [48, 49]. In this work, they proposed an important finding of the incorporation of SSB or vestigial sideband (VSB) modulation to provide an efficient bandwidth utilization and support the EDC without the requirement of feedback path [48] and carrier suppression at the transmitter which increases receiver sensitivity. The work reported a sensitivity 1.8-

dB better than non-return-to-zero (NRZ) signal transmission [55]. The system also presented frequency shifting of the optical carrier to provide frequency bandgap to place the subcarrier \times subcarrier inter-modulation distortions (IMD) upon square-law detection so that it will not interfere with the signal band [49].

The first experimental demonstration of long-haul DDO OFDM system was done by B.J.C. Schmidt, A.J. Lowery and J. Armstrong (2007), transmitting 12 Gb/s over 400 km and 20-Gb/s over 320-km SMF [69]. Two methods to generate the SSB signal modulation technique were presented. The first was done using a Hilbert transform and a complex Mach-Zehnder modulator (MZM) and the second was using a single-drive MZM with a fibre Bragg grating (FBG) filter. A detailed explanation of the system design will be presented in the later section. Extended experiments were reported by Schmidt et al. demonstrating three transmitter designs to transmit 10-, 12- and 20-Gb/s over 320- to 400-km using commercially available components [70]. In these works, the EDC was performed at the receiver. This is possible because the phase distortions induced by the chromatic dispersion are preserved since the optical modulator is driven at its linear in-field region so the subcarriers map 1:1 between the optical and the electrical domains.

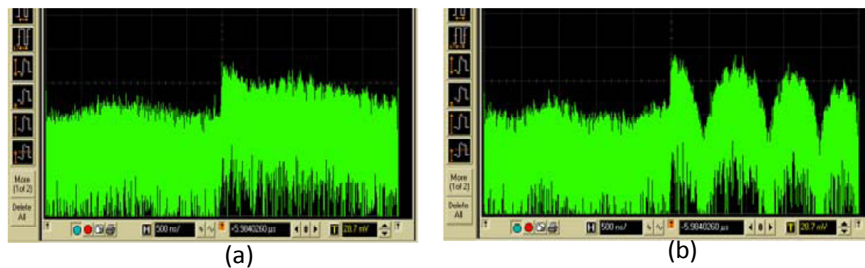


Fig. 2.3.1. Received electrical spectrum of a (a) SSB and (b) DSB modulation signal. (After B.J.C. Schmidt, et al. with permission shown in Appendix 1.1 [55].

Fig. 2.3.1 shows received electrical spectra of the (a) SSB and (b) DSB modulation signals. The use of an SSB modulation in the DDO-OFDM system for the EDC prevents the deep spectral nulls in the electrical spectra as experienced when using the DSB modulation as in Fig. 2.3.1 (b). The nulls are due to the dispersion and frequency offset between the sidebands and the carrier, where the phase of the transmitted sidebands is changed and some of the frequency components of the sideband are cancelled upon detection [70, 71]. The DSB modulation also cannot preserve the dispersion-induced phase-distortion and turn it into amplitude distortion. This is due to the sidebands back folding upon when the signal is detected [55].

Besides the power efficiency of the SSB transmission, the modulation technique also requires only one half of the optical bandwidth than that required by the DSB. The SSB also has been shown to provide much longer transmission length than the DSB [69, 70, 72-74]. Another early work of DDO-OFDM long-haul transmission was reported by D.F. Hewitt (2007) transmitting 10 Gb/s DDO-OFDM over 420 km by also using the SSB modulation with dual-drive Mach-Zehnder modulator (MZM) [75]. The system was designed without any frequency guardband where the subcarriers closest to the carrier were free from the phase delay induced by the chromatic dispersion. However, a high power carrier was used in order to suppress the subcarriers \times subcarriers noise compared with the detected signal \times carrier. The use of dual-drive MZ modulator provides a simple system design without the requirement of RF up- and down-conversion at the transmitter and receiver, respectively [48].

Other than the CD compensation [48-51, 69], Lowery (2007) was also the first to suggest fibre non-linearity compensation technique using pre- and post-compensation at the transmitter and receiver, respectively [76-78]. This allows the transmitted power per WDM wavelength can be increased to reduce the bit error rate (BER). The effects of nonlinearity interaction between the carrier and subcarriers band producing additional mixing products was also compensated by Du and Lowery (2008) using electronic pre-compensation with methods to limit the effects of the image-band [79]. Another fibre impairment that needs to be considered is polarization mode dispersion (PMD), which has been shown to be a limiting factor to the system's performance [80]. This issue was first addressed by M. Mayrock and H. Haunstein (2007) [80]. Differential group delay (DGD) induced by the PMD can cause frequency selective fading when the state-of-polarization (SOP) between the carrier and subcarriers band are misaligned [80-82]. The PMD tolerance of the DDO-OFDM system can be increased using new detection topology known as polarization diversity receiver [80-82]. Another method is by using electronic PMD compensation techniques with low-density-parity check (LDPC) coding [83].

Another long-haul optical transmission system design was also proposed just after the DDO-OFDM system using a coherent receiver known as coherent optical OFDM (CO-OFDM). The system was first proposed by Shieh and Athaudage (2006), using simulation. This showed that only 2-dB OSNR (at 12.5 GHz measurement

bandwidth) is required for 10 Gb/s transmission over 3000 km dispersive S-SMF [53]. In 2007, the first experimental demonstration of the CO-OFDM was reported by Jansen, et al., showing the reduction of phase noise effects. This was achieved by using pilot tones allocated at the middle of the subcarrier band for phase noise estimation and correction at the receiver [84]. In the CO-OFDM system, the carrier is suppressed and only the OFDM subcarrier band is transmitted. At the receiver, another optical source is required which is similar to the RF local oscillator (LO) required by the wireless OFDM system to detect the OFDM signal band [52-54, 84-94]. This is different with the DDO-OFDM system where both carrier and the subcarrier band are transmitted together along the fibre [48-51, 69, 75, 83, 95-99].

In the CO-OFDM system, the effects of the RIN and the beating noise imposed from the subcarriers \times subcarriers, subcarriers \times ASE and ASE \times ASE are cancelled with the use of balanced-detection [100, 101]. On the other hand, the laser's linewidth has been shown to be a prominent limiting factor of the CO-OFDM system performance [53, 84, 85, 88, 90, 92, 93]. The works reported using simulations and experiments showed the employment of narrow linewidth laser of 100 kHz [53, 54] and 20 kHz [52]. This is because the OFDM signal is transmitted through the dispersive fibre without the carrier and the coherent detection utilized another laser as an LO at the receiver. The phase of the received electrical signal will be different to the LO, hence, phase noise compensation techniques need to be developed in order to match the phase between the received signal and the receiver's LO [53, 85, 88, 102, 103]. With the balanced detection, the phase information of the received signal can be recovered and the interference due to the phase deviations can be successfully compensated for only if the phase deviation is insignificant over an OFDM symbol time [101]. Other compensation techniques employing pilot tones were also presented in [85, 88] along with the used of MLSE when higher M-size QAM is used [102, 103].

Besides CD compensation, the CO-OFDM system was also reported to be immune to the PMD effects when the system incorporated the polarization-diversity receiver [54]. The fibre nonlinearity compensation scheme proposed in [76, 77] can also be used for the CO-OFDM system to reduce the effect of four-wave-mixing (FWM) [104]. Recently, electronic compensation technique for cross-phase modulation (XPM) effect have been proposed by Du and Lowery (2010), presenting

4-dB signal quality improvement of 60 Gb/s transmission over 2375 km of fibre [105]. The CO-OFDM system can also provide higher spectral efficiency with 7- to 9-dB lower receiver sensitivity requirement compared to the DDO-OFDM system [100]. However, this is at the cost of the system design complexity, high implementation cost as well as the complexity in the DSP computations.

2.4 Single-Sideband Modulation in DDO-OFDM System

In general, three methods can be used to produce the SSB signal in a DDO-OFDM system design. The first is by simply using an optical filter to remove the LSB or USB as preferred by the transmitter design [69]. The second technique involved the use of Hilbert transform of a DSB signal [106] [48-51, 69, 70]. The DSB signal is added with the Hilbert transform of itself. The Hilbert transform can be easily developed using the Q output of an iFFT with its negative frequencies set to null. This can be easily done using DSP. The third method involved the DSP incorporated with the use of optical external modulator such as the MZM [48, 50, 51, 55, 107-110], optical phase modulators [55, 108, 111] or nonstandard optical modulators such as nested-MZMs [72-74, 104, 107, 110, 112-119]. In the following discussion, several transmission system design of the DDO-OFDM system employing SSB modulation will be presented.

2.4.1 Single-Drive Optical Modulator System

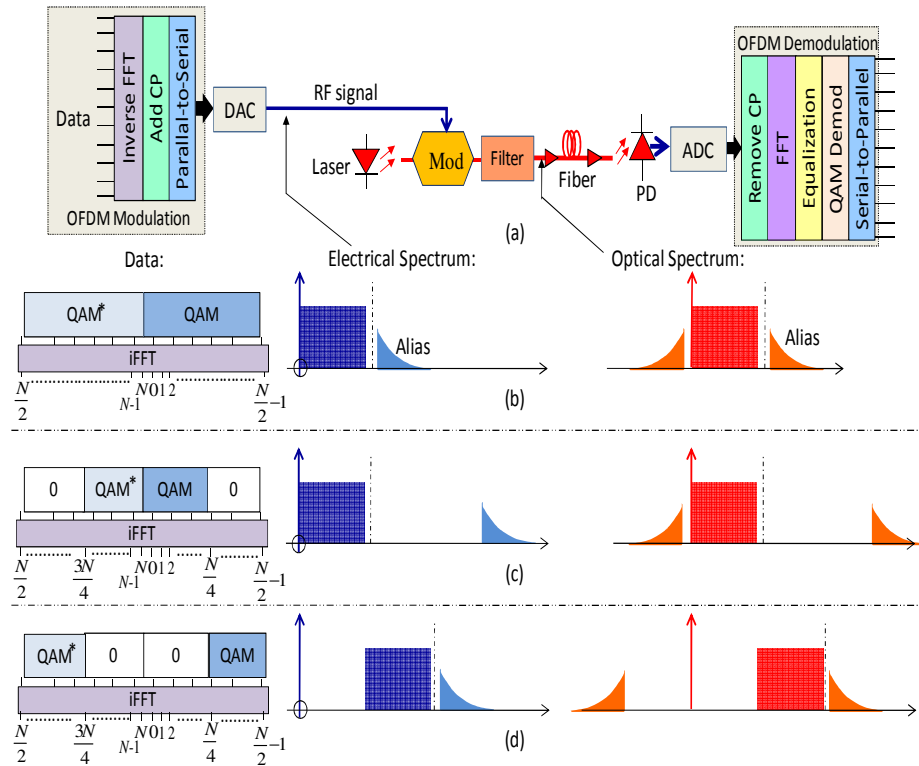


Fig. 2.4.1. DDO-OFDM system design employing (a) single drive-MZM with (b) and (c) represent the electrical and optical spectra without bandgap and (d) with bandgap.

Fig. 2.4.1 shows the transmitter design employing: (a) a standard single-drive MZM. Insets (b)-(d) represent the possible data assignments and the electrical and optical spectra. Serial data is converted into N -parallel sub-streams data and mapped with QAM before N -iFFT modulation. After the iFFT, a CP is added to each of the symbol and converted to a serial signal before loaded into a DAC. Only a single DAC is required in this system. The OFDM signal's voltage is then used to drive the standard-MZM. This outputs a DSB signal. An optical filter is used to produce the SSB signal by suppressing either the LSB or the USB of the signal, before it is propagated through an SMF fibre with EDFA after certain fibre span. The carrier can also be suppressed.

At the receiver, a simple DD receiver design using single photodiode is used to convert optical to electrical signal. The produced electrical signal consists of mixing products due to the square-law detection, where some are wanted and others not [70, 100]. The unwanted signals can appear within and outside the signal band. After the ADC, symbol synchronization is performed to find the start of the received signal. CP

removal is performed by removing part of the symbol with the length of the CP assigned at the transmitter. FFT is performed to obtain the subcarriers' frequency spectrum to demultiplex the subcarriers. Single-tap equalization is performed to correct the phase and amplitude distortions of the signal followed by QAM demodulation. The DSP part of this system is the same as the wireless OFDM technique, which has been explained in Section 2.2.1. The OFDM signal modulation and demodulation were done offline during the experimental demonstrations [34, 52, 53, 69, 70, 72-74, 84-88, 90, 92, 93, 120-128]. Real-time processing using this system design is also presented recently in [129-131].

At the input to the iFFT, a data signal can be designed to produce a real-valued signal and assigning frequency guardband [49, 62] in the signal design. This can be shown by the illustrated QAM data blocks at the iFFT in Fig. 2.4.1 (b), (c) and (d). The iFFT operation will produce a complex-valued signal carried as two real waveforms; the inphase (I) and quadrature (Q) component. In order to produce a real valued signal, data with Hermitian symmetry need to be input into the iFFT. As shown in Fig. 2.4.1 (b), this can be achieved by assigning the complex conjugate of the QAM data to the half of the subcarriers at the negative iFFT side from $\frac{N}{2}$ to $N-1$ as illustrated in the data block [70, 132]. Note that the N point in the data block will be translated as the DC point of the signal's frequency spectrum. The QAM data assignment is shown using the N -iFFT point and arranged with respect to the subcarriers frequency spectrum. An easier way to produce this real signal can be just by taking the I and discard the Q waveform. The electrical spectrum shows the signal band close to the DC with the aliasing component folded outside the signal band. The real signal is used to drive the MZM which generates a DSB signal. The MZM is biased at quadrature point or close to the null-point of the MZM's transfer function [80, 133, 134]. A filter is required for this transmitter configuration to filter out the LSB and achieved the optical spectrum as shown. Fig. 2.4.1 (c) electrical and optical spectra shows that the aliasing or "image" frequency components can be placed further away from the signal band. This is achieved by zeroing the IFFT points of $\frac{N}{4}$ - to- $\frac{N}{2} - 1$ and $\frac{N}{2}$ -to- $\frac{3N}{4}$, as shown in the data block. The $\frac{N}{4}$ of QAM data and its $\frac{N}{4}$ conjugate are assigned around the DC at the first quarter of positive- and second quarter of the negative-iFFT points, respectively. Fig. 2.4.1 (d) shows a bandgap or

frequency-guardband can also be assigned by zeroing the IFFT points from 0 -to- $\frac{N}{4}$ and $\frac{3N}{4}$ -to- N [70, 80, 133, 134]. This is to accommodate the unwanted subcarriers \times subcarriers beatings that fall near the DC after the square-law detection [100]. Note that the data assignments of (c) and (d) have a half the spectral efficiency compared with (b), due to the requirement of the frequency this frequency guardband. Thus, the DD receiver will require more signal bandwidth compared with the coherent receiver design which does not require any frequency guardband since the subcarrier \times subcarrier mixing is cancelled out by the balance photodiodes [53, 89].

2.4.2 RF upconversion and Single-Drive Optical Modulator

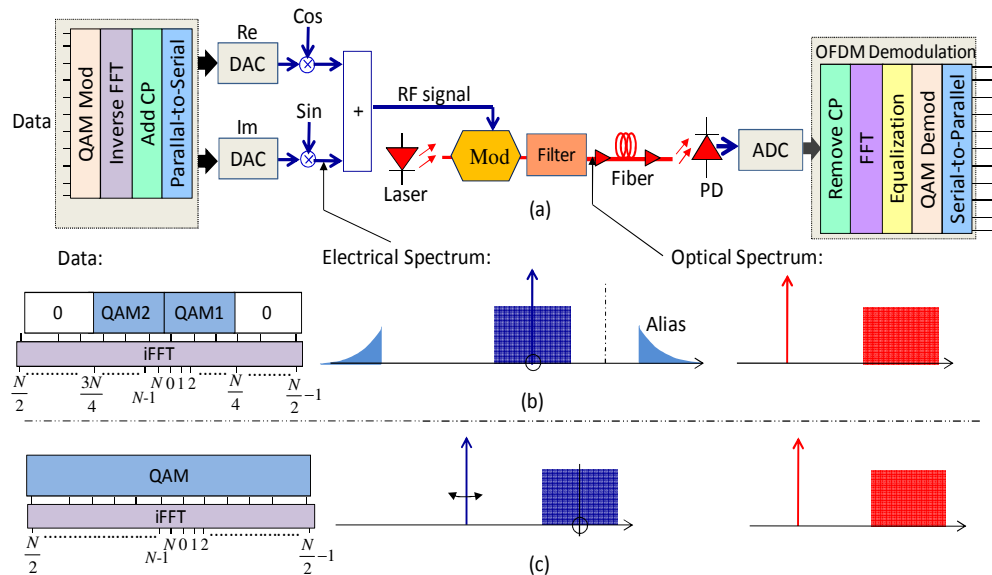


Fig. 2.4.2 DDO-OFDM system design with (a) RF signal upconversion and single-drive MZM with data assignment and electrical and optical spectra using (b) half of the subcarriers and (c) all of the subcarriers.

Fig. 2.4.2 illustrates (a) transmitter design employing electrical RF signal upconversion and a single-drive MZM with (b) and (c) illustrates the data assignments and the spectra. The OFDM modulation part is the same with the conventional OFDM for wireless as explained. Fig. 2.4.2 (a) shows that two DACs are required at the transmitter each for the inphase (I) and quadrature (Q) components of the OFDM signal. After the DACs, the I and Q signal components are mixed with cosine and sine waveforms, respectively and added together to shift the signal band to an intermediate frequency (IF). This can be done by modulating the signal with an RF local oscillator (LO) using IQ mixers [48, 49, 62, 70, 97, 98, 114, 135, 136]. The

resulting signal voltage is then used to drive the MZM and an optical DSB signal is produced. An optical filter is used to obtain the SSB signal before the fibre transmission. A DD receiver with single photodiode is used and the electrical signal is converted to digital by the ADC to perform the DSP. At the receiver DSP, the RF down-conversion is first done, followed by removing the CP. Note that, instead of using the DSP to perform the down-conversion, mixing the received signal after the DAC with cosine and sine waveforms of the same RF frequency as the transmitter to produce the original transmitted I and Q can also be done. The OFDM demodulation is the same as in the previous section.

Fig. 2.4.2 (b) shows a signal design with zero-padding added at the upper and lower half of the positive and negative frequency bands, respectively. The zero insertion is used to upsample the waveform and interpolates the waveform so that the aliasing is shifted away from the signal band, hence relaxing the requirements on the low pass filter after the DAC [49, 62, 98, 137]. This is shown at the iFFT input signal block. The data input is set around the DC (point N), at 1 to $\frac{N}{4}$ for QAM1 and at $\frac{3N}{4}$ to $N-1$ for QAM2 where 0 is set to zero. The optical carrier is suppressed and RF carrier from the RF LO is used. The RF LO can be set away from the signal band to produce the frequency bandgap [97, 121]. The flexibility of the RF LO to be set at any frequency closer or away from the signal band has also allows larger OFDM signal bandwidth. This is done by using nearly all of the iFFT points at both negative and positive frequencies to be used as the subcarriers. This is shown in the illustrated iFFT input block in Fig. 2.4.2 (c). To boost the received electrical signal power and achieve an optimum BER, the optical carrier needs to be suppressed relative to the SSB signal band. This was first demonstrated by Lowery and Armstrong (2006) [48, 49]. The suppressed carrier was then being used in all of the transmission with the SSB modulation where the optimum BER is achieved using the carrier-to-subcarrier power ratio of 1:1 [48, 49, 70, 75, 94, 97, 129, 138, 139].

2.4.3 IQ-Modulator

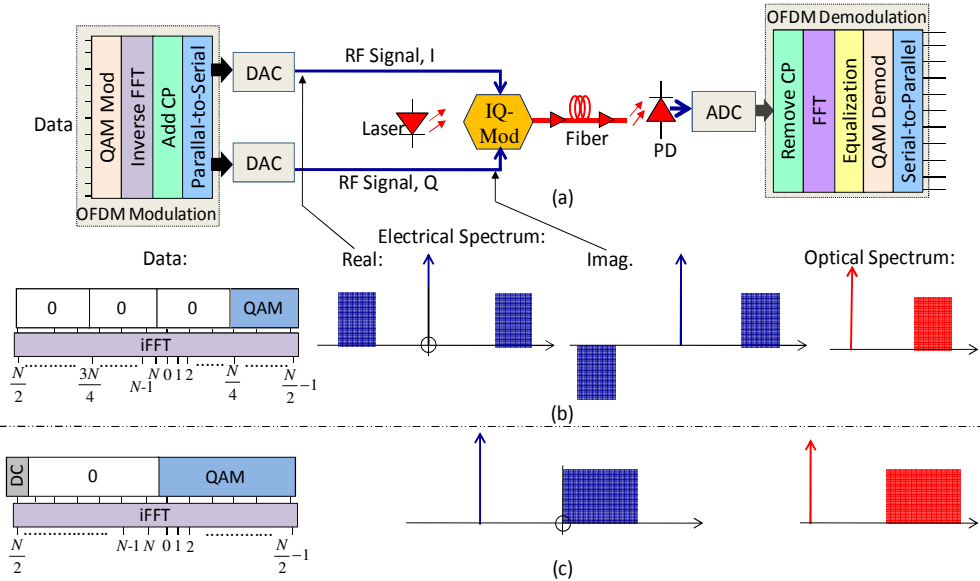


Fig. 2.4.3. DDO-OFDM design setup employing (a) IQ-modulator with data assignments and optical and electrical spectra utilizing (b) $\frac{N}{4}$ subcarriers and (c) half of the subcarriers with DC.

Fig. 2.4.3 illustrates the system design using (a) IQ modulator with the data assignments and electrical and optical spectra using (a) $\frac{N}{4}$ subcarriers and (c) half of the subcarriers with DC carrier assigned at the negative frequency end [69, 104]. I and Q components of the OFDM signal are generated at the OFDM modulation and loaded into two DACs. The voltage of the I and Q signal waveforms are used to drive the optical IQ-modulator. With this modulator, optical filter to produce SSB signal is eliminated. The implementation of this transmitter was demonstrated by Schmidt, et al. (2007) using a tuneable laser source (colourless transmitter) transmitting 12 Gb/s [140-142]. The optical SSB is generated by using the RF signal with Hilbert transform of itself to drive the IQ-modulator's RF inputs [69]. With this modulator, direct mapping of the electrical signal to the optical domain can be achieved and produced straight forward frequency translation from the optical to the electrical spectrum. This is done by operating the modulator at its linear-field region by biasing near the null power of the MZM transfer function [69, 72, 74, 76, 79, 115-117, 120, 143-149]. The modulator biasing can also be used to achieve the 1:1 carrier-to-subcarrier suppression ratio. The signal is then transmitted over the fibre and detected using a DD receiver. The same OFDM demodulation as mentioned in the previous section is performed to the received signal.

With the optical IQ modulator, input data into the FFT can be made as shown in Fig. 2.4.3 (b) and (c). Fig. 2.4.3 (b) presents zero insertion from 0 - to $-\frac{N}{4}$ IFFT points are used for the frequency band-gap. With this data configuration, only one quarter of the FFT points are used as the OFDM subcarriers. The electrical spectra illustrates the LSB signal spectrum is cancelled out when the OFDM signal with the Hilbert transform of itself are used to drive the IQ-Mod. Another technique suggested to increase the spectral efficiency was suggested by W.R. Peng et al. [146-148] the virtual SSB OFDM technique. In this technique, a DC carrier representing an RF tone is allocated at the most negative frequency and all other subcarriers are used for the data transmission without any bandgap. The subcarrier \times subcarrier mixings were cancelled by using a complex iterative calculation. As opposed to Peng's technique, Fig. 2.4.3 (c) illustrates the use of zero padding in the negative-frequency subcarriers ($\frac{N}{2} + 1$ to N) to obtain the band-gap, where the DC is set at $\frac{N}{2}$. This technique has a doubled spectral efficiency (with bangap) compared to Fig. 2.4.3 (b).

2.4.4 Virtual Carrier with IQ-Modulator

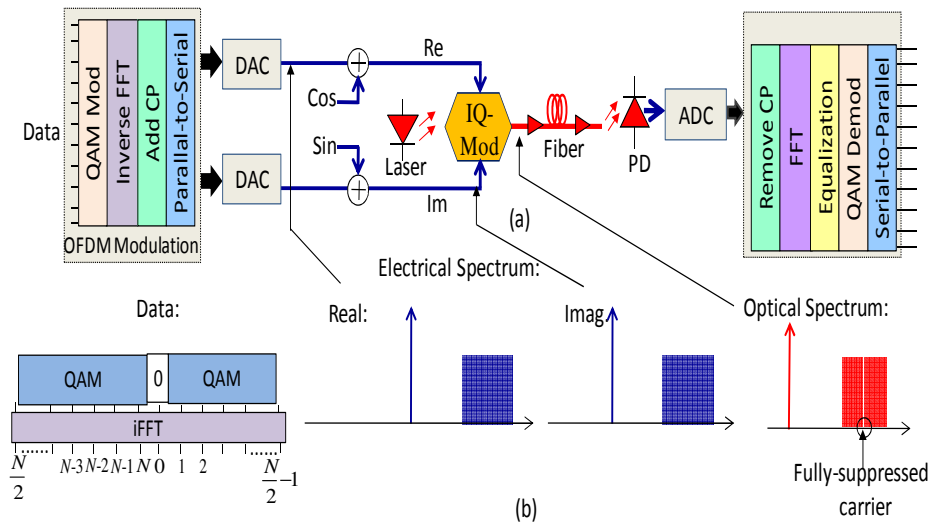


Fig. 2.4.4. DDO-OFDM system design using (a) virtual carrier and IQ-modulator with (b) data assignment and electrical and optical spectra utilizing all of the subcarriers.

Fig. 2.4.4 illustrates a system design employing (a) RF virtual carrier and IQ-modulator where (b) all of the subcarriers are used for data except the DC iFFT point. This was first suggested by Lowery & Armstrong (2006) [48] and Schmidt et al. demonstrated a flexible carrier allocation to reduce or increase the bandgap [73]. With this technique, a high sample rate ($f_{sample} = \text{signal bandwidth}$) is required by the

transmitter as in Fig. 2.4.3. Compared to the Virtual SSB OFDM, the RF tone is supplied externally by a frequency synthesizer. The RF signal is split with one of it being 90° shifted (*Sin*) from the other and added to the I signal. The IQ-modulator is biased to achieve a fully suppressed carrier. After the IQ-modulator, the laser frequency can be shifted to any frequency required for example to add, increase or reduce the band-gap by tuning the RF synthesizer [72, 74, 116]. At the receiver, the signal down-conversion can be performed either electrically using RF mixers after the photodetector or it can be digitally performed in DSP by the signal multiplication with the same RF signal's frequency.

Fig. 2.4.4 (b) shows the data input configuration where all of the subcarriers can be used for data except at 0 and Nyquist frequencies around $\frac{N}{2} - 1$ and $\frac{N}{2}$ and provide a better spectral efficiency compared to the previous techniques. The virtual carrier can also be generated optically as demonstrated by A. Ali, et al. using a single-drive modulator, which is also biased near the intensity null [150]. This was done by operating the modulator at the intensity null and adding optical biasing rather than the electrical biasing. With the virtual carrier technique, signal distortion due to the MZM nonlinearity can be reduced. However, the spectral efficiency is lower by half than the one in Fig. 2.4.3 (c). This is because the assignment of complex conjugates to half of the subcarriers.

The transmitter designs discussed above show the flexibility in the DSP OFDM signal generation. With this flexibility, the external modulator transmitter is able to achieve a desired spectral efficiency with the available equipment. These transmitter designs have been demonstrated for the high-speed data transmission of more than 100 Gb/s per channel and also being implemented for real-time transmission [72, 130, 139, 151-158]. As the employment of a band-gap reduces the spectral efficiency, a technique to reduce the bandgap was carried out using DSP by incorporating Turbo codes [159].

2.5 Laser Noise Interaction with Fibre

The performance of the transmitter design employing direct modulation of a laser and IM was shown to be limited by the nonlinearity of the laser's operating condition such as frequency chirping [60, 61, 138]. The frequency chirping is introduced to the laser field, and varies with the driving current and the other parameters such as

coupling coefficient, photon lifetime, nonlinear gain coefficient, linewidth enhancement factor. The effect of the frequency chirping was, however, reduced when a carrier-suppressed SSB signal was used [138]. The laser's nonlinearity is not important if an external modulator is employed as the laser runs continuous wave [101].

In a direct detection system, the RIN and the beat noise of the detected photocurrent cannot be cancelled out due to the employment of a single photodetector [101]. In previous work, the RIN was shown to reduce the electrical SNR and increase the BER floor of a subcarrier multiplexing (SCM) transmission system [160-164]. The idea of the SCM systems with the DDO is quite similar to the DDO-OFDM system where both transmit data using multiple subcarriers. In the SCM system, two types of RIN were analysed; the RIN originating from the laser source and the RIN due to a dispersive fibre or known as converted-RIN. Even though the laser-originated RIN usually occurs at a low frequency, the noise can be translated to a high frequency due to the mixing with the modulation signal [160-162]. This will contribute to the total noise at the high frequency and reduce the SNR.

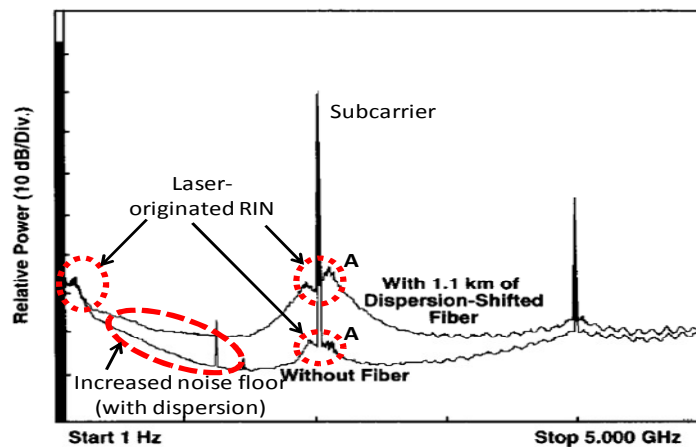


Fig. 2.5.1. PSDs of a laser modulated with a subcarrier transmitted with a back-to-back and 1.1 km fibre. (After G.J. Meslener (1994) [161] with permission shown in Appendix 1.2).

Fig. 2.5.1 shows the PSDs of a laser with a poor sidemode suppression modulated with a 2 GHz subcarrier and transmitted over back-to-back and a 1.1 km of dispersive fibre [161]. These PSDs show the intensity noise near DC with a rapid decrease at around 90 MHz and slow increase towards the resonance at above 5 GHz. A replica of a quasi-symmetrical intensity noise is also added around the subcarrier

marked with 'A'. The RF spectrum after the fibre shows a significant increment of the noise floor which will limit the system's SNR.

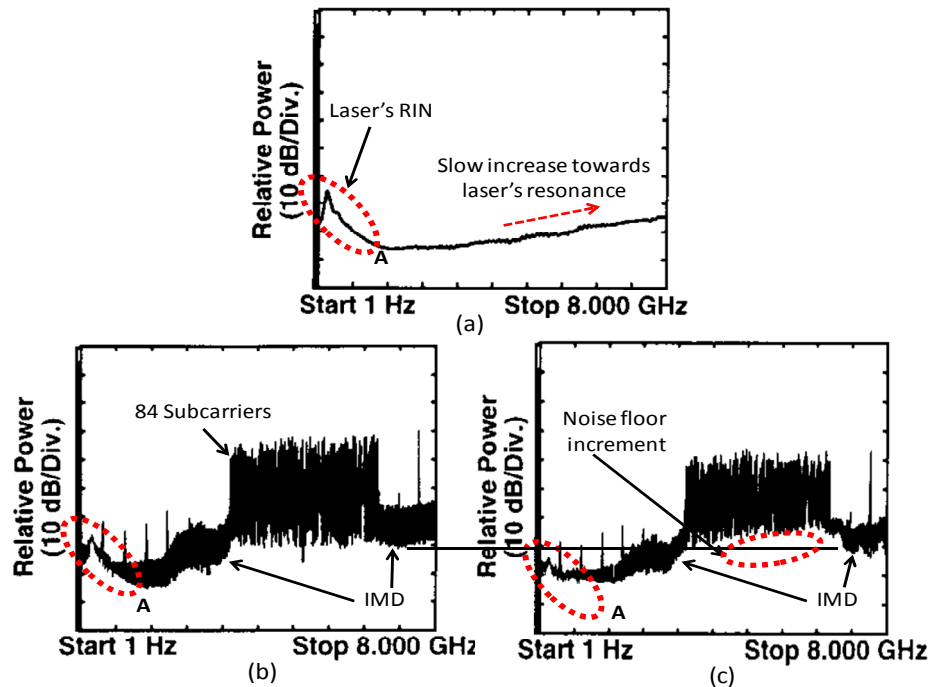


Fig. 2.5.2. RF spectra of a laser (a) without modulation (b) modulated with 84 subcarriers and (c) transmitted over 560 m dispersion-shifted fibre. (After G.J. Meslener (1994) [161] with permission shown in Appendix 1.2).

Fig. 2.5.2 shows the RF spectra of a laser (a) without modulation, (b) modulated with 84 subcarriers and (c) modulated with 84 subcarriers and transmitted over a relatively short DSF of 560 m [161]. Fig. 2.5.2 (a) shows the intensity noise near the DC (marked with A), which rapidly decreases at around 150 MHz and slowly increases towards the resonance. This can be the RIN resonance for a long-cavity (EC) laser. When this laser was modulated with subcarriers, the noise near the DC was unchanged. This is shown as in Fig. 2.5.2 (b). The noise floor under the subcarriers is due to the subcarrier \times subcarrier beat noise and also the frequency-translated low-frequency intensity noise [161]. The noise outside the subcarriers band is from the second and third-order IMD. Even though this study highlighted only the effects of the RIN with and without dispersion, the influence of the laser linewidth due to the inter-dependency of the laser noise characteristics can also affect the received spectrum's noise floor. The concept of this SCM technique is similar to the DD transmission of the OFDM subcarriers that are placed away from DC. Hence, this

study showed that the RIN can also induce some limitation to the OFDM transmission with the DD receiver.

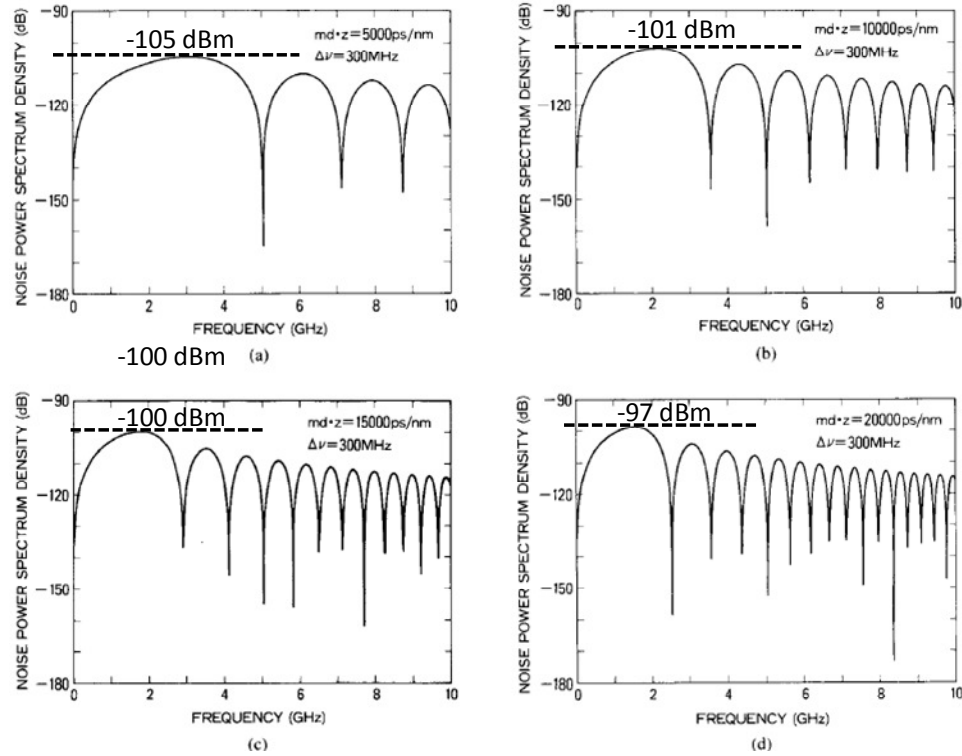


Fig. 2.5.3. Noise power spectral density (PSD) of a 300-MHz linewidth laser after fibre dispersions of (a) 5000 ps/nm (b) 10000 ps/nm (c) 15000 ps/nm and (d) 20000 ps/nm. (After S. Yamamoto and N. Edagawa (1990) [165] with permission shown in Appendix 1.3).

The second type of the RIN known as the converted-RIN is due to phase modulation-to-intensity modulation (PM-to-IM) conversion, due to the interaction between the laser linewidth and the chromatic dispersion. This was demonstrated by S. Yamamoto and N. Edagawa (1990) with the noise power spectral density (PSD) shown as in Fig. 2.5.3 [165]. The figure shows the calculated effects of a 300-MHz linewidth laser propagated through a fibre with the chromatic dispersion where the results matched the reported experimental results. With increased dispersion, the overall intensity noise is increased as shown by the increased PSD amplitude. The noise PSD can be given by [165]

$$N(f) = \frac{1}{2} \delta I(f)^2$$

$$\approx \frac{1}{2} \left[\sum_{n=0}^{\infty} 4J_n \left(\frac{1}{f} \sqrt{\frac{2\Delta\nu}{\pi}} \right) J_{n+1} \left(\frac{1}{f} \sqrt{\frac{2\Delta\nu}{\pi}} \right) \right]$$

$$\cdot \sin \left\{ \frac{1}{2} (2n+1) (2\pi f)^2 \beta'' z \right\} \quad (2.5.1)$$

where $J_n(x)$ is a Bessel function of a first kind, β'' is a second-order propagation constant and z is a fibre length. Also, the lobe amplitudes are higher near the DC and slowly reduce towards high frequencies. Frequency-selective noise power nulls were also produced where the first null can be allocated at $f_0 = \sqrt{1/2\pi\beta''z}$ [165].

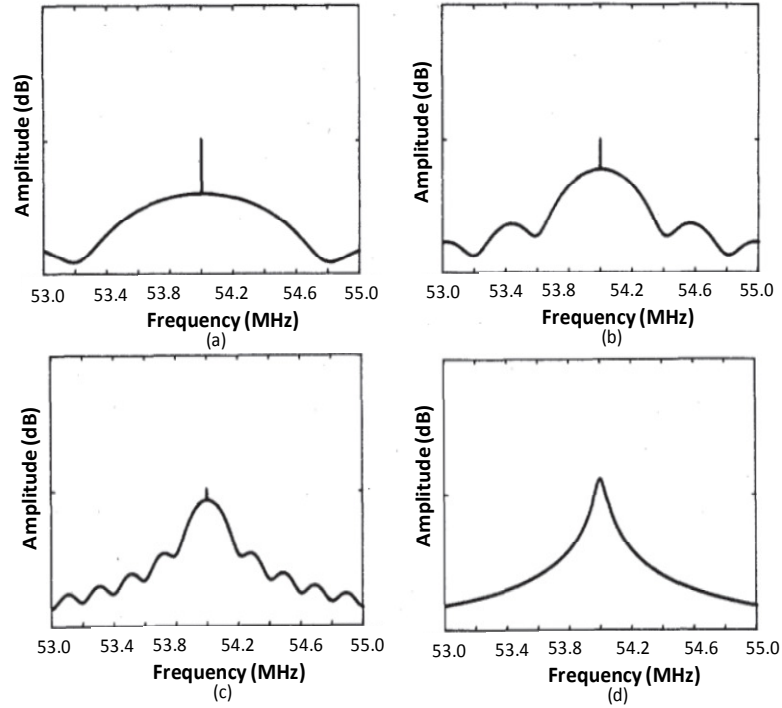


Fig. 2.5.4. Noise pedestal reduction with phase decorrelation corresponding to the time delay, τ_d relative to the τ_c . (After L.E. Richter (1986) [166] with permission shown in Appendix 1.4).

In addition to the PM-to-IM conversion noise that produced high intensity noise near the DC, another effect of the interaction of dispersion with laser linewidth was shown by L.E. Richter (1986) in his self-heterodyne high-resolution linewidth measurement demonstration [166]. In this work, the shifted laser carrier frequency detected after a recombination with the delayed version of itself showed a delta-function noise pedestal underneath the carrier. This is shown as in Fig. 2.5.4. The figure shows the noise pedestal of the detected laser carrier is reduced to a modified Lorentzian pedestal when the time delay, τ_d , relative to the coherence time, τ_c . When τ_d is increased further, the phases of the carrier with the delayed version of itself become completely decorrelated and the power spectrum will become strictly

Lorentzian [166-168]. This noise pedestal can be a concern in the transmission of multiple subcarriers allocated away from the carrier over a dispersive fibre. Each of the subcarrier would be imposed with this noise pedestal and would increase the overall noise floor. Thus the investigation of the linewidth effects to the DDO-OFDM system performance is required.

2.6 High Speed Optical Transmission with OFDM

The potential of DDO-OFDM system for transmitting high-speed data has been identified during the early works on the system development. This was done by Djorjdevic and Vasic (2006), who proposed transmitting 100 Gb/s over 1200 km of dispersive fibre with the used of DCF [97]. The system reported the employment of LDPC coding technique, where the spectral efficiency of at least 2.9 bits/s/Hz can be achieved. During the early years of the system development, only small number of reports have been published on experimental demonstrations of the DDO-OFDM system transmitting signal of more than 10 Gb/s per wavelength. In the CO-OFDM system, 20 Gb/s transmission over 4160-km of fibre was demonstrated in 2007 by Jansen et al. with the success of compensating a prominent limiting factor in coherent receiver; the phase noise effects of the LO using RF-pilot tones [84]. In the same year, transmission of 16×52.5 Gb/s over 4160-km SMF was also reported by the same author with the application of polarization multiplexing technique (PolMux) and multiple-input multiple-output (MIMO) [90]. Another group reported the transmission of 10.59 Gb/s and 15.89 Gb/s with 16- and 64-QAM by also employing the phase noise compensation technique [85, 88].

High-speed transmission with the CO-OFDM system can be easily achieved with the fact that this system has higher spectral efficiency and required 7-9 dB lower receiver sensitivity compared with the DDO-OFDM system [48, 49, 100, 104, 169]. This is because no frequency gap is required since the coherent receiver will cancel out the mixing between the subcarriers \times subcarriers and new stronger carrier (LO) is added at the receiver without the limitation of link loss providing the system with high received power [100, 104]. Despite these benefits, the real implementation of this system will require large number of devices that induced high design complexity and cost as well as large computations in DSP, which make the DDO-OFDM system a winner in this view point.

For the DDO-OFDM system, several techniques of system performance optimization have been developed to achieve the transmission of more than 10 Gb/s per wavelength over a long-haul fibre [48-51, 69, 70, 73, 76, 77, 79, 116, 118, 120, 135, 143-147, 149, 156, 169-175]. These techniques include transmitter and receiver design optimization [49-51, 69, 70, 73, 116, 119, 120, 169, 176, 177], spectral efficiency improvement [73, 146, 169, 176], multiplexing techniques applications [49, 51, 149, 171, 178], fibre impairment compensation techniques [49, 50, 76-79, 119, 143] and error-correction coding [83, 99]. Transmissions using wavelength division multiplexing (WDM) have been shown in [49, 51, 156, 170]. Receiver sensitivity optimizations using carrier-suppression [48, 49, 51, 169] and appropriate optical modulator biasing [111, 150, 169, 179] have also been presented theoretically and experimentally.

The techniques developed to increase the spectral efficiency can be classified into two categories: the optimization of the bandwidth utilization using DSP and the application of electrical and optical devices. As shown in the previous sections, spectral efficiency can be increased by using many iFFT points for data transmission [146, 147]. Other than this, a higher number of M -QAM levels can be adaptively assigned to each of the subcarrier relative to the channel response [61, 180, 181]. Several works were also done to reduce or eliminate the guard band required by the DDO-OFDM systems in order to optimize the spectral efficiency. M. Schuster, et al. suggested SSB with data modulation onto the envelope or the signal power to eliminate the guard band [157, 173-175, 182]. A virtual SSB transmission employing tuneable guard band and without guard bands was also presented in 2008 by W.R. Peng, et al. [145]. The trade off of these techniques is the complex DSP calculations at both transmitter and receiver to deal with the inter-modulation distortion products [183]. The second category implemented to increase the spectral efficiency is by employing the RF devices for example the addition of the RF virtual carrier after the DACs [49, 73, 144, 146].

Multiplexing techniques were also employed to increase the transmission rate for example the WDM [49, 51, 156, 170, 184-191], the subcarrier multiplexing (SCM) [84, 192] and the polMux techniques [93, 122, 123, 184, 189, 193]. Several works incorporating WDM have been presented with the highest transmission rate reported to the date is 24 Tb/s with 1.3 Tb/s per channel [189]. This is referred as a polMux-

CO-OFDM superchannel system and some works are also reported with the demonstration of a reconfigurable add-drop multiplexer (ROADM) [139, 188-191, 194, 195]. The polMux technique was initially demonstrated in the CO-OFDM system [84, 90], which then extended into the DDO-OFDM system.

The application of the polMux in the DDO-OFDM system was initially doubted due to the PMD and polarization dependent loss (PDL) effects [82, 90]. This is because the PMD will cause the state-of-polarization (SOP) to vary with frequency and results in a signal fading due to the misalignment between the carrier and the signal band and the PDL can cause the orthogonality loss between the X- and Y-polarizations. However, these effects were shown to be minimal in the OSNR penalties for the DDO-OFDM system with the incorporation of a polarization diversity receiver [81, 119, 171].

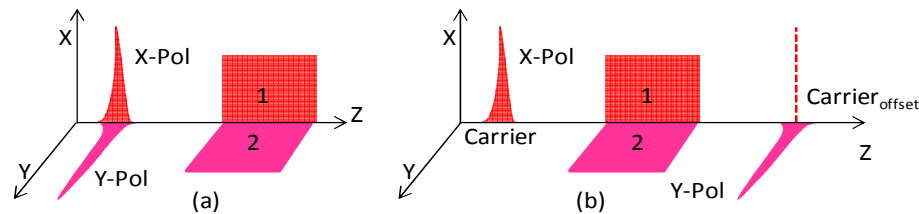


Fig. 2.6.1. SSB OFDM signal band after polarization multiplexing (a) single un-offset carrier and (b) two carriers with one offset of the other.

Fig. 2.6.1 illustrates the resulting PolMuxed signal showing two types of spectrum with (a) single un-offset carrier and (b) two carriers with one is offset to the other. The illustrations show that each X- and Y-polarization carrier is carrying different signal bands of 1 and 2, respectively. This figure theoretically shows how the transmission rate can be increased, where both carrier and signal bands on both polarizations are overlapped in frequency, which doubles the spectral efficiency. The polarization multiplexing of the two signals can be done using a polarization beam splitter or combiner [81, 82, 90, 149, 171, 196]. With the employment of the PolMux technique, transmission of 22.4 Gb/s over 1000 km SMF has been reported with the DDO-OFDM system and 40 Gb/s demonstrated for PON application over 20-km SMF [153, 196]. With the incorporation of the polarization diversity receiver, transmission rates of 100 Gb/s and beyond have been demonstrated using PolMux in DDO-OFDM system [72, 74, 81, 82, 119, 139, 151-153, 178, 197, 198]. Recent work also incorporated multiple-signal band multiplexing, where the signal bands are modulated onto an electro-optically generated comb of frequencies [192, 199]. With

this technique, transmission of 117 Gb/s over 1200 km of SMF has been demonstrated in 2011 by Peng, et al. [198].

2.7 Real-Time Processing of Optical OFDM

Real-time processing of optical OFDM signals have been demonstrated where the DDO-OFDM's transceiver design is developed using field-programmable-gate-array (FPGA) [200-202]. The real-time transmissions with IM/DD were also presented demonstrating 3 Gb/s 16-QAM modulated over 75 km SMF [155], 5.25 Gb/s using 128-QAM over 25 km SMF [154, 203], 6.56 Gb/s over 25 km SMF [204], 11.25 Gb/s over 25 km using clock recovery synchronization [205] and using a directly modulated VCSEL. The optical OFDM system with nonlinearity compensation techniques done electronically for XPM and FWM have also been demonstrated using Volterra electrical equaliser model for 16 QAM 100 Gb/s over 800 km of fibre [206, 207]. Also, many of the system designs presented in Section 2.4 [129-131] were employed for real-time transmission demonstrating high-speed data transmission of more than 100 Gb/s per channel [72, 130, 139, 151-158]. These works show the feasibility of the DDO-OFDM system to be employed as a real and practical commercial high-speed transmission system. However, the real-time experimental demonstration is limited by the electronics speed, for example the DAC and ADC. Higher sample rates than the current few tens of GSample/s of data converters is required in order to provide the high-speed data transmission [104, 208-210].

Table 2.7.1: Summary of optical OFDM experimental demonstrations using several types of system design. (After A.J. Lowery and L.B. Du (2011) [104] with permission shown in Appendix 1.5).

Author	Publication	Paper	Year	Format	Rate (GHz)	Ub-bands	λ_s	Intra-chan SE	Intra-chan SE	Distance (km)	PolMux?	Real time/offline
Jansen	OFC	pdp15	2007	CO	20	2	1	1.56	-	4160	No	Offline
Schmidt	OFC	9dpl8	2007	DDO	20	1	1	2	-	320	No	Offline
Jansen	OFC	pdp2	2008	CO	121.9	4	10	5.35	2.44	1000	Yes	Offline
Yang	OFC	pdp7	2008	CO	107	5	1	3.34	-	1000	Yes	Offline
Yamada	OFC	pdp5	2008	NoGI	88.8	2	50	3	1.78	800	Yes	Offline
Masuda	OFC	pdpb5	2009	NoGI	111	2	135	2.78	2.22	6248	Yes	Offline
Takahashi	OFC	pdpb7	2009	CO	65.1	1	8	9.72	7	240	Yes	Offline
Ma	OFC	pdpc1	2009	CO	1080	36	1	3.37	-	600	Yes	Offline
Dischler	OFC	pdpc2	2009	CO	1200	50	1	3.33	-	400	Yes	Offline
Schmidt	OFC	pdpc3	2009	DDO	100	1	1	3.57	-	500	Yes	Offline
Qian	OFC	pdpd5	2009	DDO	108	2	1	-	-	20	Yes	Offline
Yang	OFC	pdpc5	2009	CO	3.6	15 × 3.6	15	1.2	-	-	Yes	Real time
Giddings	Opt. Exp.	vol 17	2009	IM	3	1	1	-	-	0.5	No	Real time
Buchali	ECOC	pd2.1	2009	CO	12.1	9 × 12.1	9	1.6	-	12.1	No	Real time T_x
Benlachte	ECOC	pd2.4	2009	DDO	8.36	1	1	1.045	-	1600	No	Real time T_x
Chandrasef	ECOC	pd2.6	2009	NoGI	1200	24	1	3.7	-	7200	Yes	Offline
Giddings	Opt. Exp.	vol 18	2010	IM	11.25	1	1	-	-	25	No	Real time
Hillerkuss	OFC	pdpc1	2010	All opt	10,800	75	1	5.76	-	-	No	No DSP
Dischler	OFC	pdpd2	2010	CO	253	15	3	2.81	2.53	764	Yes	Offline, field trial
Qian	OFC	pdpd9	2010	IM	41.25	1	2	-	-	20	No	Real time
Takiguchi	ECOC	pd1.4	2010	All opt	100	10	1	1	-	-	No	No DSP
Peng	ECOC	pd2.5	2010	DDO	213.7	9	1	2.67	-	720	No	Offline
Liu	ECOC	pd2.6	2010	CO	606	10	1	7.76	-	1600	Yes	Offline
Brahim	ECOC	pd3.4	2010	fast	14.348	1	1	1	-	-	No	Offline

The summary of the experimental demonstrations of the optical OFDM system using several types of system design can be shown in Table 2.6.1. With this table, the histories of both CO- and DDO-OFDM long-haul transmission systems along with the achieved data speed are presented. Also summarised in the table is the design with no-guard-interval (NoGI) OFDM signal band by multiplexing multiple optical signal bands using polMux with a coherent detection, which transmitted multiple Tb/s data rate [184, 186, 211]. After the early works using offline processing, the first real-time experimental demonstration was presented in 2009 using the CO system [203]. However, the real-time signal processing demonstrations showed significantly lower data rates as compared to the demonstrations done with the offline signal processing. This is due to the limitation of the current the electronic devices speed particularly the speed of the DACs and ADCs. Furthermore, a large quantity of FPGAs will be required to do a parallel processing when high rate data is involved [104, 212].

2.8 Conclusions

The OFDM technique has been shown to be beneficial to the wireless communication system with the provisioning of the immunity to the multipath-fading that eliminates the ICI and ISI. This technique has been explained using the fundamental building blocks of the OFDM design presenting the modulation and demodulation processes. The design can be adapted into the optical transmitter and receiver design using DSP.

The advantages of the OFDM adaptation for optical communication systems have been explained, and include the immunity to the linear distortion caused by the CD and PMD realized with the use of the CP assigned, according to the delay introduced by the total dispersion. The preliminary issue on the adaptation of the bipolar signal of the OFDM into a unipolar environment of the optical communication system was also discussed. For long-haul transmission system, two types of optical OFDM system design were reported: direct-detection and coherent receivers. The performances and differences between these two receiver designs were discussed by reviewing previously reported work. Since the thesis is focusing on DDO-OFDM system, more detail explanations on the system design with SSB modulation were given. The effects of the laser noise characteristics due to the chromatic dispersion in fibre were explained by discussing the effects reported for SCM with NRZ. High-speed data transmission using the DDO-OFDM system employing polarization division multiplexing or PolMux was also reviewed. Finally, recent real-time transmissions of the optical OFDM system were discussed with the summary of experimental demonstrations done with offline and real-time DSP using several different system designs.

2.9 References

1. Chang, R.W., *Synthesis of band-limited orthogonal signals for multichannel data transmission*. Bell Systems Technical Journal, 1966. **45**: p. 1775-1796.
2. Schwartz, M., *The origins of carrier multiplexing: Major George Owen Squier and AT&T*. Communications Magazine, IEEE, 2008. **46**(5): p. 20-24.
3. Chang, R.W., *Orthogonal frequency multiplex data transmission system*, in *US Patent*, U. patent, Editor. 1970: United State of America. p. 10.
4. Chang, R.W. and R.A. Gibby, *A theoretical study of performance of an orthogonal multiplexing data transmission scheme*. IEEE Transactions of Communication Technology, 1968. **COM-16**(4): p. 529-540.
5. Nee, R.V. and R. Prasad, *OFDM for wireless multimedia communications*. 2000, Boston: Artech House 260.
6. Hanzo, L. and T. Keller, *OFDM and MC-CDMA A Primer*. 2006: John Wiley & Sons Ltd. 411.
7. S.Bahai, a.R., B.R. Saltzberg, and M. Ergen, *Multi-carrier digital communications: theory and applications of OFDM*. 2nd ed. 2004: SPringer.
8. Prasad, R., *OFDM for Wireless Communications Systems*. 2004, Artech House.
9. Saltzberg, B.R., *Performance of an efficient parallel data transmission system*. IEEE Transactions of Communication Technology, 1967. **15**: p. 805-811.
10. Weinstein, S.B. and P.M. Ebert, *Data transmission by frequency division multiplexing using discrete Fourier transform*. IEEE Transactions of Communication Technology, 1971. **19**: p. 628-634.

11. Weinstein, S.B., *The history of orthogonal frequency-division multiplexing [History of Communications]*. Communications Magazine, IEEE, 2009. **47**(11): p. 26-35.
12. Peled, A. and A. Ruiz. *Frequency domain data transmission using reduced computational complexity algorithms*. in *Acoustics, Speech, and Signal Processing, IEEE International Conference on ICASSP '80*. 1980.
13. Han S.H., and Lee J.H., *An overview of peak-to-average power ratio reduction techniques for multicarrier transmission*. Wireless Communications, IEEE, 2005. **12**(2): p. 56-65.
14. Ochiai, H. and H. Imai, *On the distribution of the peak-to-average power ratio in OFDM signals*. Communications, IEEE Transactions on, 2001. **49**(2): p. 282-289.
15. Ochiai, H. and H. Imai, *Performance of the deliberate clipping with adaptive symbol selection for strictly band-limited OFDM systems*. Selected Areas in Communications, IEEE Journal on, 2000. **18**(11): p. 2270-2277.
16. Ochiai, H. and H. Imai, *Performance analysis of deliberately clipped OFDM signals*. Communications, IEEE Transactions on, 2002. **50**(1): p. 89-101.
17. Armstrong, J., *Peak-to-average power reduction for OFDM by repeated clipping and frequency domain filtering*. ELECTRONICS LETTERS, 2002. **38**(5): p. 246-247.
18. Tao, J., Y. Yang, and S. Yong-Hua, *Exponential companding technique for PAPR reduction in OFDM systems*. Broadcasting, IEEE Transactions on, 2005. **51**(2): p. 244-248.
19. Tarokh, V. and H. Jafarkhani, *On the computation and reduction of the peak-to-average power ratio in multicarrier communications*. Communications, IEEE Transactions on, 2000. **48**(1): p. 37-44.
20. Van Eetvelt, P., G. Wade, and M. Tomlinson, *Peak to average power reduction for OFDM schemes by selective scrambling*. ELECTRONICS LETTERS, 1996. **32**(21): p. 1963-1964.
21. Wu, S. and B.-N. Yeheskel, *OFDM systems in the presence of phase noise: consequences and solutions*. Communications, IEEE Transactions on, 2004. **52**(11): p. 1988-1996.
22. Shentu, J., K. Panta, and J. Armstrong, *Effects of phase noise on performance of OFDM systems using an ICI cancellation scheme*. Broadcasting, IEEE Transactions on, 2003. **49**(2): p. 221-224.
23. Armada, A.G., *Understanding the effects of phase noise in orthogonal frequency division multiplexing (OFDM)*. Broadcasting, IEEE Transactions on, 2001. **47**(2): p. 153-159.
24. Armada, A.G. and M. Calvo, *Phase noise and sub-carrier spacing effects on the performance of an OFDM communication system*. Communications Letters, IEEE, 1998. **2**(1): p. 11-13.
25. Tomba, L., *On the effect of Wiener phase noise in OFDM systems*. Communications, IEEE Transactions on, 1998. **46**(5): p. 580-583.
26. Nikookar, H. and R. Prasad. *On the sensitivity of multicarrier transmission over multipath channels to phase noise and frequency offset*. in *IEEE International Symposium on Personal, Indoor and Mobile Radio Communications, PIMRC*. 1996.
27. Pollet, T., M. Van Bladel, and M. Moeneclaey, *BER sensitivity of OFDM systems to carrier frequency offset and Wiener phase noise*. Communications, IEEE Transactions on, 1995. **43**(234): p. 191-193.
28. Biao, C. and W. Hao, *Blind estimation of OFDM carrier frequency offset via oversampling*. Signal Processing, IEEE Transactions on, 2004. **52**(7): p. 2047-2057.
29. Lin, D.D., et al., *Joint estimation of channel response, frequency offset, and phase noise in OFDM*. Signal Processing, IEEE Transactions on, 2006. **54**(9): p. 3542-3554.

30. Yan, F., W.P. Zhu, and M.O. Ahmad, *Carrier frequency offset estimation and I/Q imbalance compensation for OFDM systems*. Eurasip Journal on Advances in Signal Processing, 2007.
31. Moose, P.H., *A technique for orthogonal frequency division multiplexing frequency offset correction*. Communications, IEEE Transactions on, 1994. **42**(10): p. 2908-2914.
32. Schmidl, T.M. and D.C. Cox, *Robust frequency and timing synchronization for OFDM*. Communications, IEEE Transactions on, 1997. **45**(12): p. 1613-1621.
33. van de Beek, J.J., M. Sandell, and P.O. Borjesson, *ML estimation of time and frequency offset in OFDM systems*. Signal Processing, IEEE Transactions on, 1997. **45**(7): p. 1800-1805.
34. Al Amin, A., et al. *Effect of hybrid IQ imbalance compensation in 27.3-Gbit/s direct-detection OFDM transmission*. in *Optical Fiber Communication - includes post deadline papers, 2009. OFC 2009. Conference on*. 2009.
35. Xinying, L., et al. *Study of IQ imbalance effect in direct-detection optical OFDM systems*. in *Communications and Photonics Conference and Exhibition (ACP), 2009 Asia*. 2009.
36. Peng, W.-R., et al. *Experimental demonstration of compensating the I/Q imbalance and bias deviation of the Mach-Zehnder modulator for an RF-tone assisted optical OFDM system*. in *Optical Communication, 2008. ECOC 2008. 34th European Conference on*. 2008.
37. Tarighat, A., R. Bagheri, and A.H. Sayed, *Compensation schemes and performance analysis of IQ imbalances in OFDM receivers*. Signal Processing, IEEE Transactions on, 2005. **53**(8): p. 3257-3268.
38. Hui, R., et al., *Subcarrier multiplexing for high-speed optical transmission*. Lightwave Technology, Journal of, 2002. **20**(3): p. 417-427.
39. Toba, H., K. Inoue, and K. Nosu, *A Conceptual Design on Optical Frequency-Division-Multiplexing Distribution Systems with Optical Tunable Filters*. Selected Areas in Communications, IEEE Journal on, 1986. **4**(9): p. 1458-1467.
40. Toba, H. and K. Nosu, *Optical frequency-division multiplexing systems - review of key technologies and applications*. IEEE Transactions on Communications, 1992. **E75B**(4): p. 243-255.
41. Killey, R.I., et al., *Investigation of nonlinear distortion in 40-Gb/s transmission with higher order mode fiber dispersion compensators*. Lightwave Technology, Journal of, 2002. **20**(12): p. 2282-2289.
42. Watts, P.M., et al., *Performance of single-mode fiber links using electronic feed-forward and decision feedback equalizers*. Photonics Technology Letters, IEEE, 2005. **17**(10): p. 2206-2208.
43. Killey, R.I., et al., *Electronic dispersion compensation by signal predistortion using digital Processing and a dual-drive Mach-Zehnder Modulator*. Photonics Technology Letters, IEEE, 2005. **17**(3): p. 714-716.
44. Killey, R.I., et al., *Electronic dispersion compensation by signal predistortion*, in *Optical Fiber Communication Conference*. 2006: Anaheim, CA. p. OWB3.
45. McGhan, D., et al. *5120 km RZ-DPSK transmission over G652 fiber at 10 Gb/s with no optical dispersion compensation*. in *Optical Fiber Communication Conference, 2005. Technical Digest. OFC/NFOEC*. 2005.
46. McNicol, J., et al. *Electrical domain compensation of optical dispersion [optical fibre communication applications]*. in *Optical Fiber Communication Conference, 2005. Technical Digest. OFC/NFOEC*. 2005.

47. McGhan, D., et al. *Electronic dispersion compensation*. in *Optical Fiber Communication Conference, 2006 and the 2006 National Fiber Optic Engineers Conference. OFC 2006*. 2006.
48. Lowery, A.J. and J. Armstrong, *Orthogonal frequency division multiplexing for dispersion compensation of long-haul optical systems*. *Optics Express*, 2006. **14**: p. 2079-2084.
49. Lowery, A.J., L. Du, and J. Armstrong. *Orthogonal Frequency Division Multiplexing for Adaptive Dispersion Compensation in Long Haul WDM Systems*. in *Optical Fiber Communication Conference, 2006 and the 2006 National Fiber Optic Engineers Conference. OFC 2006*. 2006.
50. Lowery, A.J. and J. Armstrong. *Orthogonal-Frequency-Division Multiplexing for Optical Dispersion Compensation*. in *Optical Fiber Communication and the National Fiber Optic Engineers Conference*. 2007. Anaheim, USA.
51. Lowery, A.J., L. Du, and J. Armstrong, *Performance of optical OFDM in ultra long-haul WDM lightwave systems*. *Journal of Lightwave Technology*, 2007. **25**: p. 131 – 138.
52. Shieh, W., X. Yi, and Y. Tang, *Transmission experiment of multi-gigabit coherent optical OFDM systems over 1000km SSMF fibre*. *ELECTRONICS LETTERS*, 2007. **43**(3): p. 183-184.
53. Shieh, W. and C. Athaudage, *Coherent optical orthogonal frequency division multiplexing*. *Electronic Letters*, 2006. **42**: p. 587-588.
54. Shieh, W. and R.S. Tucker, *Polarisation mode dispersion mitigation in coherent optical orthogonal frequency division multiplexed systems*. *Electronic Letters*, 2006. **42**(17): p. 2.
55. Sieben, M., J. Conradi, and D.E. Dodds, *Optical single sideband transmission at 10 Gb/s using only electrical dispersion compensation*. *Journal of Lightwave Technology*, 1999. **17**(10): p. 1742-1749.
56. Färbert, A., et al. *Performance of a 10.7 Gb/s receiver with digital equaliser using maximum likelihood sequence estimation*. in *European conference of optical communications*. 2004, Postdeadline. Stockholm, Sweden.
57. Elbers, J.P., et al. *Measurement of the dispersion tolerance of optical duobinary with an MLSE-receiver at 10.7 Gb/s*. in *Optical Fiber Communication Conference, 2005. Technical Digest. OFC/NFOEC*. 2005.
58. Qi, P. and R.J. Green, *Bit-error-rate performance of lightwave hybrid AM/OFDM systems with comparison with AM/QAM systems in the presence of clipping impulse noise*. *Photonics Technology Letters, IEEE*, 1996. **8**(2): p. 278-280.
59. Green, R.J. and Q. Pan, *Clipping noise effects on the performance of digital baseband signal in lightwave hybrid digital and analogue transmission systems*. *IEE Proceedings: Optoelectronics*, 1998. **145**(6): p. 335-338.
60. Tang, J.M. and K.A. Shore, *30-Gb/s signal transmission over 40-km directly modulated DFB-laser-based single-mode-fiber links without optical amplification and dispersion compensation*. *Journal of Lightwave Technology*, 2006. **24**(6): p. 2318-2327.
61. Tang, J.M., P.M. Lane, and K.A. Shore, *High-speed transmission of adaptively modulated optical OFDM signals over multimode fibers using directly Modulated DFBs*. *Lightwave Technology, Journal of*, 2006. **24**(1): p. 429-441.
62. Lowery, A.J. and J. Armstrong, *10 Gbit/s multimode fiber link using power efficient orthogonal-frequency-division multiplexing*. *OPTICS EXPRESS*, 2005. **13**(25): p. 10003-10009.

63. Armstrong, J. and A.J. Lowery, *Power efficient optical OFDM*. ELECTRONICS LETTERS, 2006. **42**(6): p. 370-372.
64. Armstrong, J., et al. *Performance of Asymmetrically Clipped Optical OFDM in AWGN for an intensity modulated direct detection system*. in *IEEE Globecom*. 2006: IEEE Communications Society.
65. Saleh, A.A.M., *Fundamental limit on number of channels in subcarrier-multiplexed lightwave CATV*. Electronic Letters, 1989. **25**: p. 776-777.
66. Panta, K.R. and J. Armstrong, *Effects of clipping on the error performance of OFDM in frequency selective fading channels*. Wireless Communications, IEEE Transactions on, 2004. **3**(2): p. 668-671.
67. Lee, S.C.J., et al., *PAM-DMT for Intensity-Modulated and Direct-Detection Optical Communication Systems*. Photonics Technology Letters, IEEE, 2009. **21**(23): p. 1749-1751.
68. Giacomidis, E., et al., *Adaptive-Modulation-Enabled WDM Impairment Reduction in Multichannel Optical OFDM Transmission Systems for Next-Generation PONs*. Photonics Journal, IEEE, 2010. **2**(2): p. 130-140.
69. Schmidt, B.J.C., A.J. Lowery, and J. Armstrong. *Experimental demonstrations of 20 Gbits/s direct-detection optical OFDM and 12Gbits/s with a colorless transmitter*. in *Optical Fiber Communication Conference*. 2007. Anaheim, CA.
70. Schmidt, B.J.C., A.J. Lowery, and J. Armstrong, *Experimental demonstrations of electronic dispersion compensation for long-haul transmission using direct-detection optical OFDM*. Journal of Lightwave Technology, 2008. **26**(1): p. 196-203.
71. Gliese, U., S. Norskov, and T.N. Nielsen, *Chromatic dispersion in fiber-optic microwave and millimeter-wave links*. Microwave Theory and Techniques, IEEE Transactions on, 1996. **44**(10): p. 1716-1724.
72. Schmidt, B.J.C., et al., *100Gbit/s transmission using single-band direct-detection optical OFDM*, in *Optical Fiber Communication Conference (OFC/NFOEC)*. 2009, Optical Society of America (OSA): San Diego, CA. p. PDPC3.
73. Schmidt, B., A.J. Lowery, and L.Du. *Low sample rate transmitter for direct-detection optical OFDM*. in *Optical Fiber Communication - includes post deadline papers, 2009. OFC 2009. Conference on*. 2009.
74. Schmidt, B.J.C., et al., *120 Gbit/s over 500-km using single-band polarization-multiplexed self-coherent optical OFDM*. Journal of Lightwave Technology, 2010. **28**(4): p. 328-335.
75. Hewitt, D.F. *Orthogonal Frequency Division Multiplexing using Baseband Optical Single Sideband for Simpler Adaptive Dispersion Compensation*. in *Optical Fiber Communication and the National Fiber Optic Engineers Conference, 2007. OFC/NFOEC 2007. Conference on*. 2007.
76. Lowery, A.J., *Fiber nonlinearity mitigation in optical links that use OFDM for dispersion compensation*. IEEE Photon. Technol. Lett, 2007. **18**19: p. 1556-1558.
77. Lowery, A.J., *Fiber nonlinearity pre- And post-compensation for long-haul optical links using OFDM*. Optics Express, 2007. **15**(20): p. 12965-12970.
78. Lowery, A.J., S. Wang, and M. Premaratne, *Calculation of power limit due to fiber nonlinearity in optical OFDM systems*. Optics Express, 2007. **15**(20): p. 13282-13287.
79. Du, L. and A.J. Lowery, *Fiber nonlinearity precompensation for long-haul links using direct-detection optical OFDM*. Optics Express, 2008. **16**(9): p. 6209-6215.
80. Mayrock, M. and H. Haunstein, *PMD Tolerant Direct-Detection Optical OFDM System*. Optical Communication (ECOC), 2007 33rd European Conference and Exhibition of, 2007: p. 1-2.

81. Xie, C. *PMD Insensitive Direct-Detection Optical OFDM Systems Using Self-Polarization Diversity*. in *Optical Fiber communication/National Fiber Optic Engineers Conference, 2008. OFC/NFOEC 2008. Conference on*. 2008.
82. Zinan, W. and X. Chongjin. *PMD and PDL tolerance of polarization division multiplexed signals with direct detection*. in *Optical Communication, 2008. ECOC 2008. 34th European Conference on*. 2008.
83. Djordjevic, I.B., *PMD compensation in fiber-optic communication systems with direct detection using LDPC-coded OFDM*. *Opt. Express*, 2007. **15**(7): p. 3692-3701.
84. Jansen, S.L., et al. *20-Gb/s OFDM transmission over 4160-km SSMF enabled by RF-pilot tone phase noise compensation*. in *Optical Fiber Communication Conference*. 2007. Anaheim, CA.
85. Yi, X., W. Shieh, and Y. Ma. *Phase noise on coherent optical OFDM systems with 16-QAM beyond 10Gb/s*. in *33rd European Conference and Exhibition on Optical Communication 2007*. Berlin, Germany: VDE VERLAG GMBH.
86. Tang, Y., K.-P. Ho, and W. Shieh. *Optimal design for coherent optical OFDM transmitter employing pre-distortion*. in *33rd European Conference and Exhibition on Optical Communication 2007*. Berlin, Germany: VDE VERLAG GMBH.
87. Shieh, W., et al., *Theoretical and experimental study on PMD supported transmission using polarization diversity in coherent optical OFDM systems*. *OPTICS EXPRESS*, 2007. **15**(16): p. 9936-9947.
88. Yi, X., W. Shieh, and Y. Tang, *Phase estimation for coherent optical OFDM*. *PHOTONICS TECHNOLOGY LETTERS*, 2007. **19**(12): p. 919-921.
89. Shieh, W., H. Bao, and Y. Tang, *Coherent optical OFDM: Theory and design*. *Optics Express*, 2008. **16**(2): p. 841-859.
90. Jansen, S.L., I. Morita, and H. Tanaka, *16x52.5-Gb/s, 50-GHz spaced, POLMUX-CO-OFDM transmission over 4,160 km of SSMF enabled by MIMO processing*. *Optical Communication - Post-Deadline Papers (published 2008), 2007 33rd European Conference and Exhibition of*, 2007: p. 1-2.
91. Jansen, S.L., et al. *20-Gb/s OFDM Transmission over 4,160-km SSMF Enabled by RF-Pilot Tone Phase Noise Compensation*. 2007: Optical Society of America.
92. Jansen, S.L., et al., *Coherent optical 25.8-Gb/s OFDM transmission over 4160-km SSMF*. *Journal of Lightwave Technology*, 2008. **26**(1): p. 6-15.
93. Jansen, S.L., I. Morita, and H. Tanaka. *10x121.9 Gb/s PDM-OFDM Transmission with 2-b/s/Hz spectral efficiency over 1,000 km SSMF*. in *Optical Fiber Communication Conference and Exposition National Fiber Optic Engineers Conference*. 2008. San Diego
94. Jansen, S.L., et al. *Optical OFDM - A Candidate for Future Long-Haul Optical Transmission Systems*. in *Optical Fiber communication/National Fiber Optic Engineers Conference, 2008. OFC/NFOEC 2008. Conference on*. 2008.
95. Hewitt, D.F. and E. Skafidas. *Performance and Applications of Gigabit OFDM over Optical Fibre Systems in Metro and Access Networks*. in *Optical Communications, 2006. ECOC 2006. European Conference on*. 2006.
96. Hewitt, D., T. An Vu, and C. Chang-Joon. *10 Gb/s Long-Reach Optical Access with Multi-Mode Fiber Distribution Using Baseband Single-Sideband OFDM*. in *Optical Fiber communication/National Fiber Optic Engineers Conference, 2008. OFC/NFOEC 2008. Conference on*. 2008.
97. Djordjevic, I.B. and B. Vasic, *100-gb/s transmission using orthogonal frequency-division multiplexing*. *Photonics Technology Letters, IEEE*, 2006. **18**(15): p. 1576-1578.

98. Djordjevic, I.B. and B. Vasic, *Orthogonal frequency division multiplexing for high-speed optical transmission*. Opt. Express, 2006. **14**(9): p. 3767-3775.
99. Djordjevic, I.B., B. Vasic, and M.A. Neifeld, *LDPC-Coded OFDM for Optical Communication Systems with Direct Detection*. Selected Topics in Quantum Electronics, IEEE Journal of, 2007. **13**(5): p. 1446-1454.
100. Lowery, A.J., *Amplified-spontaneous noise limit of optical OFDM lightwave systems*. Optics Express, 2008. **16**(2): p. 860-865.
101. Kazovsky, L., S. Benedetto, and A. Willner, *Optical fiber communication systems*. 1st ed. 1996, Norwood: Artech House, Inc. 690.
102. Xingwen, Y., S. William, and M. Yiran, *Phase Noise Effects on High Spectral Efficiency Coherent Optical OFDM Transmission*. Lightwave Technology, Journal of, 2008. **26**(10): p. 1309-1316.
103. Shieh, W.W., *Maximum-likelihood phase and channel estimation for coherent optical OFDM*. IEEE photonics technology letters, 2008. **20**(8): p. 605-607.
104. Lowery, A.J. and L. Du, *Optical orthogonal division multiplexing for long haul optical communications: A review of the first five years*. Optical Fiber Technology, 2011. **17**(5): p. 421-438.
105. Du, L. and A.J. Lowery, *Practical XPM Compensation Method for Coherent Optical OFDM Systems*. Photonics Technology Letters, IEEE, 2010. **22**(5): p. 320-322.
106. Hahn, S., *Hilbert Transforms in Signal Processing*. 1996, Boston MA: Artech House.
107. Fonseca, D., et al. *Single sideband demonstration using a four phase-modulators structure*. in *2004 IEEE/LEOS - Workshop on Advanced Modulation Formats*. 2004.
108. Loayssa, A., et al., *Design and performance of the bidirectional optical single-sideband modulator*. Journal of Lightwave Technology, 2003. **21**(4): p. 1071-1082.
109. Fonseca, D., A.V.T. Cartaxo, and P. Monteiro, *Modelling and experimental validation of an x-cut four phase modulators structure*. IEE Proceedings: Optoelectronics, 2006. **153**(4): p. 145-151.
110. Fonseca, D., A.V.T. Cartaxo, and P. Monteiro, *Optical single-sideband transmitter for various electrical signaling formats*. Journal of Lightwave Technology, 2006. **24**(5): p. 2059-2069.
111. Fonseca, D., et al. *40 Gb/s OSSB NRZ transmitter for high capacity systems*. in *ECOC 2005*. Glasgow UK.
112. Higuma, K., et al. *X-cut LiNbO3 optical SSB modulators*. in *Pacific Rim Conference on Lasers and Electro-Optics, CLEO - Technical Digest*. 2001.
113. Takano, K., N. Sakamoto, and K. Nakagawa. *Waveform degradation by SPM in carrier-suppressed optical SSB transmission with NRZ and RZ formats*. in *IEEE/LEOS Advance Modulation Formats Workshop*. 2004. San Francisco, CA.
114. Randel, S., et al. *Myths and Truths about Optical OFDM*. in *IEEE/LEOS Summer Topical Meetings, 2007 Digest of the*. 2007.
115. Yi, H., E. Viterbo, and A.J. Lowery. *Improving the sensitivity of direct-detection optical OFDM systems by pairing of the optical subcarriers*. in *Optical Communication (ECOC), 2011 37th European Conference and Exhibition on*. 2011.
116. Zan, Z., L. Du, and A.J. Lowery, *Experimental demonstration on the reduction of linewidth impact in a self-heterodyne optical OFDM system*, in *Optical Fiber Communication Conference (OFC/NFOEC)*, O.S.o.A. (OSA), Editor. 2010: San Diego Convention Center. p. JThA8.
117. Zan, Z. and A.J. Lowery, *Experimental demonstration of a flexible and stable semiconductor laser linewidth emulator*. Opt. Express, 2010. **18**(13): p. 13880-13885.

118. Du, L. and A.J. Lowery. *Compensating XPM for 100 Gbit/s coherent channels with 10 Gbit/s direct-detection NRZ neighbors*. in *Optical Fiber Communication (OFC), collocated National Fiber Optic Engineers Conference, 2010 Conference on (OFC/NFOEC)*. 2010.
119. Schmidt, B.J.C., A.J. Lowery, and J. Armstrong, *Impact of PMD in Single-Receiver and Polarization-Diverse Direct-Detection Optical OFDM*. *Lightwave Technology, Journal of*, 2009. **27**(14): p. 2792-2799.
120. Zan, Z., A.J. Lowery, and M. Premaratne. *Laser RIN and linewidth requirements for direct detection optical OFDM*. in *Lasers and Electro-Optics CLEO 2008*. 2008. San Jose.
121. Schmidt, B.J.C., A.J. Lowery, and J. Armstrong, *Experimental Demonstrations of Electronic Dispersion Compensation for Long-Haul Transmission Using Direct-Detection Optical OFDM*. *Lightwave Technology, Journal of*, 2008. **26**(1): p. 196-203.
122. Jansen, S.L., et al., *121.9-Gb/s PDM-OFDM Transmission With 2-b/s/Hz Spectral Efficiency Over 1000 km of SSMF*. *Lightwave Technology, Journal of*, 2009. **27**(3): p. 177-188.
123. Jansen, S.L., et al., *132.2-Gb/s PDM-8QAM-OFDM Transmission at 4-b/s/Hz Spectral Efficiency*. *Photonics Technology Letters, IEEE*, 2009. **21**(12): p. 802-804.
124. Jansen, S.L., et al., *Coherent Optical 25.8-Gb/s OFDM Transmission Over 4160-km SSMF*. *Lightwave Technology, Journal of*, 2008. **26**(1): p. 6-15.
125. Jansen, S.L., I. Morita, and H. Tanaka. *10-Gb/s OFDM with conventional DFB lasers*. in *33rd European Conference and Exhibition on Optical Communication 2007*. Berlin, Germany: VDE VERLAG GMBH.
126. Gangxiang, S., et al., *Experimental Demonstration of CO-OFDM Optical Network with Heterogeneous ROADM Nodes and Variable Channel Bit-Rates*. *Communications Letters, IEEE*, 2011. **15**(8): p. 890-892.
127. Yang, Q., Y. Ma, and W. Shieh. *107 Gb/s coherent optical OFDM reception using orthogonal band multiplexing*. in *optical fiber communication conference and exposition national fiber optic engineers conference*. 2008. San Diego.
128. Ma, Y., W. Shieh, and Y. Qi. *Bandwidth-Efficient 21.4 Gb/s Coherent Optical 2x2 MIMO OFDM Transmission*. in *Optical Fiber communication/National Fiber Optic Engineers Conference, 2008. OFC/NFOEC 2008. Conference on*. 2008.
129. Rosenkranz, W., A. Ali, and J. Leibrich. *Orthogonal frequency division multiplexing (OFDM) in optical communications with direct detection for metro networks*. in *Transparent Optical Networks, 2009. ICTON '09. 11th International Conference on*. 2009.
130. Chao, T., et al. *200Gs/s real-time optical-sampling-based orthogonal frequency division multiplexing system*. in *Optical Fiber Communication (OFC), collocated National Fiber Optic Engineers Conference, 2010 Conference on (OFC/NFOEC)*. 2010.
131. Giddings, R.P., et al., *Experimental Demonstration of Real-Time Optical OFDM Transmission at 7.5 Gb/s Over 25-km SSMF Using a 1-GHz RSOA*. *Photonics Technology Letters, IEEE*, 2010. **22**(11): p. 745-747.
132. Lee, S.C.J., et al. *24-Gb/s transmission over 730 m of multimode fiber by direct modulation of an 850-nm VCSEL using discrete multi-tone modulation*. in *Optical Fiber Communication and the National Fiber Optic Engineers Conference, 2007. OFC/NFOEC 2007. Conference on*. 2007.
133. Ali, v., J. Leibrich, and W. Rosenkranz, *Impact of Nonlinearities on Optical OFDM with Direct Detection*. *Optical Communication (ECOC), 2007 33rd European Conference and Exhibition of*, 2007: p. 1-2.

134. Ali, A., J. Leibrich, and W. Rosenkranz. *Spectral Efficiency and Receiver Sensitivity in Direct Detection Optical-OFDM*. in *Optical Fiber Communication - includes post deadline papers, 2009. OFC 2009. Conference on*. 2009.
135. Dischler, R. and F. Buchali. *Experimental Assessment of a Direct Detection Optical OFDM System Targeting 10Gb/s and beyond*. in *Optical Fiber communication/National Fiber Optic Engineers Conference, 2008. OFC/NFOEC 2008. Conference on*. 2008.
136. Mehedy, L., M. Bakaul, and A. Nirmalathas, *Frequency interleaving towards spectrally efficient directly detected optical OFDM for next-generation optical access networks*. *Optics Express*, 2010. **18**(22): p. 23161-23172.
137. Mehedy, L., M. Bakaul, and A. Nirmalathas. *Spectrally-efficient 100 Gb/s transmission in next-generation optical access networks employing directly detected optical-OFDM*. in *Telecommunication Networks and Applications Conference (ATNAC), 2010 Australasian*. 2010.
138. Wei, J.L., X.Q. Jin, and J.M. Tang, *The Influence of Directly Modulated DFB Lasers on the Transmission Performance of Carrier-Suppressed Single-Sideband Optical OFDM Signals Over IMDD SMF Systems*. *Lightwave Technology, Journal of*, 2009. **27**(13): p. 2412-2419.
139. Peng, W.-R., et al. *Transmission of a 213.7-Gb/s single-polarization direct-detection optical OFDM superchannel over 720-km standard single mode fiber with EDFA-only amplification*. in *Optical Communication (ECOC), 2010 36th European Conference and Exhibition on*. 2010.
140. Smith, G.H., D. Novak, and Z. Ahmed. *Novel technique for generation of optical SSB with carrier using a single MZM to overcome fiber chromatic dispersion*. in *Microwave Photonics, 1996. MWP '96. Technical Digest., 1996 International Topical Meeting on*. 1996.
141. Cizek, V., *Discrete Hilbert transform*. *Audio and Electroacoustics, IEEE Transactions on*, 1970. **18**(4): p. 340-343.
142. McNicol, J., et al. *Electrical domain compensation of optical dispersion in Optical Fiber Communication Conference, 2005. Technical Digest. OFC/NFOEC*. 2005.
143. Peng, W.R. and S. Chi, *Improving the Transmission Performance for an Externally Modulated Baseband Single Sideband OFDM Signal Using Nonlinear Post-compensation and*. *Optical Communication (ECOC), 2007 33rd European Conference and Exhibition of*, 2007: p. 1-2.
144. Peng, W.R., et al., *Theoretical and Experimental Investigations of Direct-Detected RF-Tone-Assisted Optical OFDM Systems*. *Journal of Lightwave Technology*, 2009. **27**(10): p. 1332-1339.
145. Peng, W.R., et al., *Spectrally Efficient Direct-Detected OFDM Transmission Incorporating a Tunable Frequency Gap and an Iterative Detection Techniques*. *Lightwave Technology, Journal of*, 2009. **27**(24): p. 5723-5735.
146. Peng, W.-R., et al. *Experimental Demonstration of 340 km SSMF Transmission Using a Virtual Single Sideband OFDM Signal that Employs Carrier Suppressed and Iterative Detection Techniques*. in *Optical Fiber communication/National Fiber Optic Engineers Conference, 2008. OFC/NFOEC 2008. Conference on*. 2008.
147. Peng, W.-R., et al. *Experimental demonstration of 1600 km SSMF transmission of a generalized direct detection optical virtual SSB-OFDM system*. in *Optical Communication, 2008. ECOC 2008. 34th European Conference on*. 2008.
148. Feng, K.-M., and Peng W.-R. *Enhancing spectral efficiency and receiving sensitivity in a direct-detected OFDM system*. in *Photonics Global Conference (PGC), 2010*. 2010.

149. Peng, W.-R., K.-M. Feng, and A.E. Willner. *Direct-detected polarization division multiplexed OFDM systems with self-polarization diversity*. in *IEEE Lasers and Electro-Optics Society, 2008. LEOS 2008. 21st Annual Meeting of the*. 2008.
150. Ali, A., et al. *Optical biasing in direct detection optical-OFDM for improving receiver sensitivity*. in *Optical Fiber Communication (OFC), collocated National Fiber Optic Engineers Conference, 2010 Conference on (OFC/NFOEC)*. 2010.
151. Al Amin, A., et al. *Polarization multiplexed 100 Gbps direct-detection OFDM transmission without MIMO processing*. in *Optical Communication, 2009. ECOC '09. 35th European Conference on*. 2009.
152. Al Amin, A., et al., *100-Gb/s Direct-Detection OFDM Transmission on Independent Polarization Tributaries*. *Photonics Technology Letters, IEEE*, 2010. **22**(7): p. 468-470.
153. Dayou, Q., et al. *108 Gb/s OFDMA-PON with polarization multiplexing and direct-detection*. in *Optical Fiber Communication - includes post deadline papers, 2009. OFC 2009. Conference on*. 2009.
154. Jin, X.Q., et al. *End-to-end real-time demonstration of 128-QAM-encoded optical OFDM transmission with a 5.25bit/s/Hz spectral efficiency over IMDD systems*. in *Optical Fiber Communication (OFC), collocated National Fiber Optic Engineers Conference, 2010 Conference on (OFC/NFOEC)*. 2010.
155. Jin, X.Q., et al. *Real-Time 3Gb/s 16QAM-encoded optical OFDM transmission over 75km metroCor SMFs with negative power penalties*. in *OptoElectronics and Communications Conference, 2009. OECC 2009. 14th*. 2009.
156. Dayou, Q., et al., *10Gbit/s WDM-SSB-OFDM transmission over 1000km SSMF using conventional DFB lasers and direct-detection*. *Electronics Letters*, 2008. **44**(3): p. 223-225.
157. Schuster, M., et al. *120 Gb/s OFDM Transmission with Direct Detection using Compatible Single-Sideband Modulation*. in *Optical Fiber communication/National Fiber Optic Engineers Conference, 2008. OFC/NFOEC 2008. Conference on*. 2008.
158. Peng, W.-R., et al. *Over 100-Gb/s direct-detection optical OFDM transmission*. in *Optoelectronics and Communications Conference (OECC), 2011 16th*. 2011.
159. Cao, Z., et al., *Direct-Detection Optical OFDM Transmission System Without Frequency Guard Band*. *Photonics Technology Letters, IEEE*, 2010. **22**(11): p. 736-738.
160. George, M. *Analysis of mode-partition noise for subcarrier modulated transmission systems*. 1992: Optical Society of America.
161. Meslener, G.J., *Mode-partition noise in microwave subcarrier transmission systems*. *Lightwave Technology, Journal of*, 1994. **12**(1): p. 118-126.
162. Xiaolin, L., et al., *Analysis of relative intensity noise in semiconductor lasers and its effect on subcarrier multiplexed lightwave systems*. *Lightwave Technology, Journal of*, 1994. **12**(7): p. 1159-1166.
163. Laurêncio, P., S.O. Simões, and M.C.R. Medeiros, *Impact of the Combined Effect of RIN and Intermodulation Distortion on OSSB/SCM Systems*. *J. Lightwave Technol.*, 2006. **24**(11): p. 4250-4262.
164. Morgado, J.A.P. and A.V.T. Cartaxo. *New semi-analytical method of estimating the influence of laser noise on direct detection system performance*. in *4th Pacific Rim Conference on Lasers and Electro-Optics (CLEO)*. 2001.
165. Yamamoto, S., et al., *Analysis of laser phase noise to intensity noise conversion by chromatic dispersion in intensity modulation and direct detection optical fiber transmission*. *Journal of Lightwave Technology*, 1990. **8**: p. 1716-1722

166. Richter, L.E., et al., *Linewidth determination from self-heterodyne measurements with subcoherence delay times*. Quantum electronics letters, 1986. **QE-22**(11): p. 2070-2074.
167. Van Exter, M.P., S.J.M. Kuppens, and J.P. Woerdman, *Excess phase noise in self-heterodyne detection*. Quantum Electronics, IEEE Journal of, 1992. **28**(3): p. 580-584.
168. Ludvigsen, H., M. Tossavainen, and M. Kaivola, *Laser linewidth measurements using self-homodyne detection with short delay*. Optics Communications, 1998. **155**(1): p. 180-186.
169. Lowery, A.J. *Improving Sensitivity and Spectral Efficiency in Direct-Detection Optical OFDM Systems*. in *Optical Fiber communication/National Fiber Optic Engineers Conference, 2008. OFC/NFOEC 2008. Conference on*. 2008.
170. Dayou, Q., et al. *8x11.5-Gb/s OFDM Transmission over 1000km SSMF using Conventional DFB Lasers and Direct-Detection*. in *Optical Fiber communication/National Fiber Optic Engineers Conference, 2008. OFC/NFOEC 2008. Conference on*. 2008.
171. Dayou, Q., et al. *22.4-Gb/s OFDM transmission over 1000 km SSMF using polarization multiplexing with direct detection*. in *Optical Fiber Communication - includes post deadline papers, 2009. OFC 2009. Conference on*. 2009.
172. Chun-Ting, L., et al. *Experimental demonstration of optical colorless direct-detection OFDM signals with 16- and 64-QAM formats beyond 15 Gb/s*. in *Optical Communication, 2008. ECOC 2008. 34th European Conference on*. 2008.
173. Schuster, M., et al., *Compatible Single-Sideband Modulation for Optical Transmission of OFDM-Signals Using Direct Detection*. Photonic Networks, 2008 ITG Symposium on, 2008: p. 1-5.
174. Schuster, M., et al., *Spectrally Efficient Compatible Single-Sideband Modulation for OFDM Transmission With Direct Detection*. Photonics Technology Letters, IEEE, 2008. **20**(9): p. 670-672.
175. Schuster, M., et al. *Implementation aspects of OFDM with compatible single-sideband for direct-detection*. in *OptoElectronics and Communications Conference, 2009. OECC 2009. 14th*. 2009.
176. Peng, W.-R., et al. *Experimental demonstration of 1600 km SSMF transmission of a generalized direct detection optical virtual SSB-OFDM system*. in *Optical Communication, 2008. ECOC 2008. 34th European Conference on*. 2008.
177. Peng, W.-R., K.M. Feng, and A.E. Willner. *Direct-detected polarization division multiplexed OFDM systems with self-polarization diversity*. in *IEEE Lasers and Electro-Optics Society, 2008. LEOS 2008. 21st Annual Meeting of the*. 2008.
178. Cvijetic, N., et al. *Efficient and robust MIMO DSP equalization in POLMUX OFDM transmission with direct detection*. in *Optical Communication (ECOC), 2011 37th European Conference and Exhibition on*. 2011.
179. Leibrich, J., et al., *Impact of Modulator Bias on the OSNR Requirement of Direct-Detection Optical OFDM*. Photonics Technology Letters, IEEE, 2009. **21**(15): p. 1033-1035.
180. Tang, J.M. and K.A. Shore, *Maximizing the Transmission Performance of Adaptively Modulated Optical OFDM Signals in Multimode-Fiber Links by Optimizing Analog-to-Digital Converters*. Lightwave Technology, Journal of, 2007. **25**(3): p. 787-798.
181. Tang, J.M. and K.A. Shore. *Transmission performance maximization of adaptively modulated optical OFDM signals in MMF based links using optimum analogue-to-digital converters*. in *Optical Fiber Communication and the National Fiber Optic Engineers Conference*. 2007. Anahaim, USA.

182. Schuster, M., et al., *Spectrally Efficient OFDM-Transmission with Compatible Single-Sideband Modulation for Direct Detection*. Optical Communication (ECOC), 2007 33rd European Conference and Exhibition of, 2007: p. 1-2.
183. Peng, W.-R., I. Morita, and H. Tanaka. *Enabling high capacity direct-detection optical OFDM transmissions using beat interference cancellation receiver*. in *Optical Communication (ECOC), 2010 36th European Conference and Exhibition on*. 2010.
184. Yamada, E., et al. *Novel no-guard interval PDM CO-OFDM transmission in 4.1 Tb/s (50 x 88.8-Gb/s) DWDM link over 800 km SMF including 50-GHz spaced ROADM nodes*. in *optical fiber communication conference and exposition national fiber optic engineers conference*. 2008. San Diego.
185. Melle, S., et al., *Bandwidth virtualization enables long-haul WDM transport of 40 Gb/s and 100 Gb/s services*. Communications Magazine, IEEE, 2008. **46**(2): p. S22-S29.
186. Sano, A., et al., *No-guard-interval coherent optical OFDM for 100-Gb/s long-haul WDM transmission*. Journal of Lightwave Technology, 2009. **27**(16): p. 3705-3712.
187. Tan, A. and E. Pincemin, *Performance Comparison of Duobinary Formats for 40-Gb/s and Mixed 10/40-Gb/s Long-Haul WDM Transmission on SSMF and LEAF Fibers*. Lightwave Technology, Journal of, 2009. **27**(4): p. 396-408.
188. Liu, X., et al. *7 x 224-Gb/s WDM transmission of reduced-guard-interval CO-OFDM with 16-QAM subcarrier modulation on a 50-GHz grid over 2000 km of ULAF and five ROADM passes*. in *Optical Communication (ECOC), 2010 36th European Conference and Exhibition on*. 2010.
189. Dong, Z., et al. *24Tb/s (24x1.3Tb/s) WDM transmission of terabit PDM-CO-OFDM superchannels over 2400km SMF-28*. in *Optoelectronics and Communications Conference (OECC), 2011 16th*. 2011.
190. Liu, X., et al. *3 x 485-Gb/s WDM transmission over 4800 km of ULAF and 12 x 100-GHz WSSs using CO-OFDM and single coherent detection with 80-GS/s ADCs*. in *Optical Fiber Communication Conference and Exposition (OFC/NFOEC), 2011 and the National Fiber Optic Engineers Conference*. 2011.
191. Cvijetic, N., et al., *Terabit Optical Access Networks Based on WDM-OFDMA-PON*. Lightwave Technology, Journal of, 2012. **30**(4): p. 493-503.
192. Kobayashi, T., et al., *Electro-optically multiplexed 110Gbit/s optical OFDM signal transmission over 80km SMF without dispersion compensation*. Electronics Letters, 2008. **44**(3): p. 225-226.
193. Chang, D., et al. *Analysis of OSNR margin improvement in beyond 100Gb/s PDM-DQPSK systems due to FEC*. in *Communications and Photonics Conference and Exhibition (ACP), 2009 Asia*. 2009.
194. Liu, X., et al. *1.12-Tb/s 32-QAM-OFDM superchannel with 8.6-b/s/Hz intrachannel spectral efficiency and space-division multiplexing with 60-b/s/Hz aggregate spectral efficiency*. in *Optical Communication (ECOC), 2011 37th European Conference and Exhibition on*. 2011.
195. Yuanxiang, C., et al., *Experimental Demonstration of ROADM Functionality on an Optical SCFDM Superchannel*. Photonics Technology Letters, IEEE, 2012. **24**(3): p. 215-217.
196. Dayou, Q., et al. *40-Gb/s MIMO-OFDM-PON using polarization multiplexing and direct-detection*. in *Optical Fiber Communication - includes post deadline papers, 2009. OFC 2009. Conference on*. 2009.
197. Pengyu, G., et al. *1.28 Tbit/s/channel single-polarization DQPSK transmission over 525 km using ultrafast time-domain optical fourier transformation*. in *Optical Communication (ECOC), 2010 36th European Conference and Exhibition on*. 2010.

198. Peng, W.-R., et al. *117-Gb/s optical OFDM super-channel transmission over 1200-km SSMF using direct detection and EDFA-only amplification*. in *Optical Fiber Communication Conference and Exposition (OFC/NFOEC), 2011 and the National Fiber Optic Engineers Conference*. 2011.
199. Sakamoto, T., T. Kawanishi, and M. Izutsu, *Asymptotic formalism for ultraflat optical frequency comb generation using a Mach-Zehnder modulator*. *Optics Letters*, 2008. **32**(11): p. 1515-1517.
200. Benlachtar, Y., et al., *Generation of optical OFDM signals using 21.4 GS/s real time digital signal processing*. *Opt. Express*, 2009. **17**(20): p. 17658-17668.
201. Benlachtar, Y., et al. *21.4 GS/s real-time DSP-based optical OFDM signal generation and transmission over 1600 km of uncompensated fibre*. in *Optical Communication, 2009. ECOC '09. 35th European Conference on*. 2009.
202. Killey, R.I., et al. *Recent progress on real-time DSP for direct detection optical OFDM transceivers*. in *Optical Fiber Communication Conference and Exposition (OFC/NFOEC), 2011 and the National Fiber Optic Engineers Conference*. 2011.
203. Giddings, R.P., et al. *First experimental demonstration of real-time optical OFDM transceivers*. in *Optical Communication, 2009. ECOC '09. 35th European Conference on*. 2009.
204. Jin, X.Q., et al. *First experimental demonstration of end-to-end real-time optical OFDM symbol synchronization using subtraction and Gaussian windowing in 25km SMF IMDD systems*. in *Optical Communication (ECOC), 2010 36th European Conference and Exhibition on*. 2010.
205. Giddings, R.P. and J.M. Tang. *World-first experimental demonstration of synchronous clock recovery in an 11.25Gb/s real-time end-to-end optical OFDM system using directly modulated DFBs*. in *Optical Fiber Communication Conference and Exposition (OFC/NFOEC), 2011 and the National Fiber Optic Engineers Conference*. 2011.
206. Jie, P. and C. Chi-Hao, *Nonlinear Electrical Compensation for the Coherent Optical OFDM System*. *Lightwave Technology, Journal of*, 2011. **29**(2): p. 215-221.
207. Jie, P. and C. Chi-Hao, *Nonlinear Electrical Predistortion and Equalization for the Coherent Optical Communication System*. *Lightwave Technology, Journal of*, 2011. **29**(18): p. 2785-2789.
208. Gunning, F.C.G., T. Healy, and A.D. Ellis. *298 Gbit/s coherent WDM transmission over 80 km of SMF at 1 bit/s/Hz spectral efficiency*. in *Optical Communication, 2005. ECOC 2005. 31st European Conference on*. 2005.
209. Gunning, F.C.G., et al. *Multi-banded coherent WDM transmission*. in *Optical Communication, 2005. ECOC 2005. 31st European Conference on*. 2005.
210. Gunning, F.C.G., T. Healy, and A.D. Ellis, *Dispersion tolerance of coherent WDM*. *Photonics Technology Letters, IEEE*, 2006. **18**(12): p. 1338-1340.
211. Yamada, E., et al., *1 Tbit/s (111 Gbit/s/ch X 10 ch) no-guard-interval CO-OFDM transmission over 2100 km DSF*. *ELECTRONICS LETTERS*, 2008. **44**(24): p. 1417-1418.
212. Birk, M., et al. *Field trial of a real-time, single wavelength, coherent 100 Gbit/s PM-QPSK channel upgrade of an installed 1800km link*. in *Optical Fiber Communication (OFC), collocated National Fiber Optic Engineers Conference, 2010 Conference on (OFC/NFOEC)*. 2010.

Chapter 3

STUDY OF LASER NOISE CHARACTERISTICS

3.1 Introduction

Laser source noise characterization is required to investigate the effects of the noise on a DDO-OFDM system. For example, measurement of an L-I characteristic can be used in order to select an appropriate current level to produce a required power. In this chapter, the theory of the laser noise characteristics will be first explained (Section 3.2). This section includes the theory of a laser L-I curve characteristic, relative intensity noise (RIN) and linewidth [1-11]. In Section 3.3, these characteristics will be measured. Section 3.4 presents the RIN translation when the high RIN laser is modulated with multiple RF tones. In Section 3.5, two methods to measure the laser linewidth are presented using self-homodyne technique and high-resolution spectrophotometer. Finally, Section 3.6 concludes the works and the results achieved in this chapter. Section 3.7 presents the references.

3.2 Theory of Laser Noise

Many studies have shown that laser noise can increase the BER floor of a system [6, 7, 9, 12-15]. RIN and linewidth of a laser are due to intensity and phase fluctuations in the laser cavity. The fluctuations are related with a current supplied to drive the laser source, where the laser's output power is increased with the increase of the biasing current. This can be explained using the L-I curve [16].

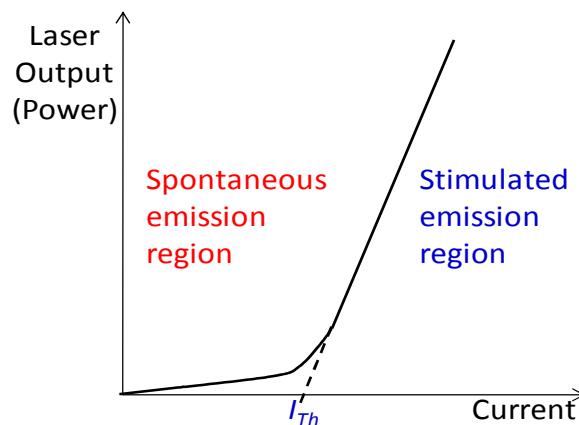


Fig. 3.2.1. Theoretical laser L-I curve.

Fig. 3.2.1 shows the variation of output power with current, for a typical semiconductor laser. The laser needs to be driven more than the threshold current to radiate coherent light. At the vicinity of the threshold current, I_{Th} , the emission has a wide linewidth and a high RIN [16]. The RIN and linewidth are reduced with increasing current, as is the laser's output power [17].

3.2.1 Relative Intensity Noise (RIN)

RIN results from the intensity fluctuations of a steady-state laser oscillation field due to spontaneous emission into the field and the response of the electron and photon populations in the laser cavity [18]. When a laser has a high RIN, a high frequency resonance peak occurs at several giga-hertz of the detected laser's spectrum. The increase of the laser's RIN relates to the P_{out} of the laser. As illustrated in Fig. 3.2.1, P_{out} increases with the increase of the drive current above I_{Th} . With this increment, the RIN resonance peak decreases in magnitude and shifts in frequency. Theoretically, the RIN is proportional to P_{out}^{-3} .

The RIN at a steady-state can be defined as the ratio between the mean-square of the noise PSD in a 1-Hz bandwidth and the square of the average optical signal power [18, 19]:

$$\text{RIN}(\omega) = \frac{\overline{|\Delta P(\omega)|^2}}{\overline{P}^2} \quad (3.2.1)$$

and can also be defined in terms of photocurrent:

$$\text{RIN}(\omega) = \frac{i_n^2(\omega)}{I_{DC}^2} \quad (3.2.2)$$

where $i_n^2(\omega)$ is the measured noise current PSD in amps^2/Hz and I_{dc} is the average dc photocurrent. RIN is usually expressed in dB/Hz and can be defined by taking the log of eq. 3.2.2:

$$\text{RIN}(\omega) = 10 \log_{10} \left(\frac{i_n^2(\omega)}{I_{DC}^2} \right) \quad (3.2.3)$$

The RIN will be converted directly into an electrical noise by the photodetector. This can be a limiting factor to the SNR performance of an optical system since it cannot be improved upon by increasing the received signal power. The SNR can be achieved from the ratio of the detected rms RF power to the noise power resulting [16, 20]

$$\text{SNR} = \frac{P_{RF}}{P_{RIN}} = \frac{\left(\frac{m^2 \cdot P_{opt}^2 \cdot r^2}{2} \right) Z_L}{RIN \cdot P_{opt}^2 \cdot r^2 \cdot B \cdot Z_L} = \frac{m^2}{2B \cdot RIN} \quad (3.2.4)$$

Where m is the optical modulation index of the transmitter modulation for example, amplitude modulation (AM), P_{opt} is the optical power input to the photodetector, r is the photodetector responsivity, B is the signal bandwidth and Z_L is the load impedance of the photodetection circuit.

3.2.2 Linewidth

Phase noise of a semiconductor laser originates from the phase variations due to spontaneous emission adding to the optical field. The laser spectrum was found to be a Lorentzian shape by Fleming and Mooradian (1981) [21]. Similar to RIN, the laser linewidth also changes with the laser's P_{out} . A laser will have a wide linewidth when it is biased around the vicinity of the I_{Th} of the L-I curve. Increasing the P_{out} reduces the linewidth of the laser. Theoretically, the linewidth is reduced such that linewidth $\propto P_{out}^{-1}$ [22].

The linewidth, $\Delta\nu$ of a laser can be derived by considering an optical field undergoing the phase fluctuations with stabilized amplitude. This can be written as

$$E_s(t) = E_o \exp j[\omega_o t + \phi(t)] \quad (3.2.5)$$

where E_o gives the amplitude, the ω_o is the average angular optical carrier frequency ($2\pi f_o$) and $\phi(t)$ represents the random phase fluctuations of the laser. Given the autocorrelation function of the optical field is

$$R_E(\tau) = \langle E^*(t)E(t+\tau) \rangle = \langle \exp[j\Delta\phi(t,\tau)] \rangle \exp(j\omega_o\tau) \quad (3.2.6)$$

where the $\Delta\phi(t,\tau)$ represents the random phase changes between times t and $t + \tau$ and can be written as

$$\Delta\phi(t,\tau) = \phi(t+\tau) - \phi(t) \quad (3.2.7)$$

This random phase changes is often assumed as a zero-mean random Gaussian process with variance, σ_ϕ^2 of

$$\sigma_\phi^2 = 2\pi\Delta\nu T \quad (3.2.8)$$

where T is the period of $|(t + \tau) - t|$. Using the relation of [23];

$$\langle \exp[\pm j\Delta\phi(t, \tau)] \rangle = \exp\left[-\frac{1}{2}\langle \Delta\phi^2(\tau) \rangle\right] \quad (3.2.9)$$

the autocorrelation of Eq. (3.2.5) can be written as

$$R_{E_s}(\tau) = P_s \exp(j\omega_o\tau) \exp\left[-\frac{1}{2}\langle \Delta\phi^2(\tau) \rangle\right] \quad (3.2.10)$$

The laser phase noise is often described as a Wiener Lévy process and the Lorentzian spectrum can be found by taking a Fourier transform with respect to τ of Eq. 3.2.10 resulting [16, 18, 24];

$$G_{E_s}(f) = \frac{2P_s}{\pi\Delta\nu} \cdot \frac{1}{1 + \left[\frac{2(f - f_o)}{\Delta\nu}\right]^2} \quad (3.2.11)$$

where f_o is the laser's center frequency and $\frac{2P_s}{\pi\Delta\nu}$ is the peak power. Since $\Delta\nu$ is taken at the full-width-half-maximum (FWHM) of the spectrum, therefore the power in the bandwidth of $\Delta\nu$ is $\frac{P_s}{\pi\Delta\nu}$, taken by dividing the peak power of Eq. 3.2.11 by two. This represents the power at the half maximum of the spectrum where the width of $\Delta\nu$ is taken. In [25], an average phase change, $\langle \Delta\phi \rangle$ at time t of a laser field is given by:

$$\langle \Delta\phi \rangle = -\frac{\alpha\beta_{sp}t}{2I} \quad (3.2.12)$$

where I is the average intensity, β_{sp} is the average spontaneous emission rate and α is the ratio of the changes in the real and imaginary part of the refractive index with carrier density. The changes are due to the restoration of the laser to its steady-state intensity condition. The mean square phase change at time t is given by [25]:

$$\langle \Delta\phi^2 \rangle = \frac{\beta_{sp}}{2I} (1 + \alpha^2) t \quad (3.2.13)$$

where α also represents the linewidth enhancement factor. This parameter was mathematically derived by C.H. Henry (1982) [25], which explains the significant additional linewidth broadening measured by M.W. Fleming and A. Mooradian (1981) [21].

If the coupling of the electron and photon populations within the laser cavity is ignored, the phase ϕ is a Brownian-motion process with Gaussian probability distribution due to the spontaneous emission events. As shown in[25], full-width half-

maximum (FWHM) Lorentzian, $\Delta\nu$ can be taken as the power spectrum of the laser shown in [21]. This is done by taking the Fourier transform of the autocorrelation of the laser field complex amplitude at a given time. The width of the Lorentzian is:

$$\Delta\nu = \frac{\beta_{sp}}{4\pi I} (1 + \alpha^2) \quad (3.2.14)$$

where $(1 + \alpha^2)$ represents the rate of the linewidth increment. Linewidth can also be written as:

$$\Delta\nu = \frac{1}{\pi t_c} \quad (3.2.15)$$

where t_c is the laser's coherence time which can be related to $\langle \Delta\phi^2 \rangle$ by [25]:

$$\frac{1}{t_c} = \frac{\langle \phi(\tau)^2 \rangle}{2t} \quad (3.2.16)$$

3.3 RIN Measurement

The RIN of a laser will be added into the total intensity noise power with the other noise power such as shot and thermal noise. By characterizing the RIN of laser source used in a transmission system, the potential maximum SNR of the system could be predicted. In this section, the measurement of the RIN of a commercial distributed feedback laser (DFB) laser will be presented. The measurement was done to characterize the RIN of the laser, which will be later used as a source in optical OFDM transmitter design. In this measurement, L-I characteristic of the laser will be measured. Measurements on the RIN using wide bandwidth photodetector (PD), RF amplifier and calibrated digital sampling oscilloscope (DSO) are then presented. This characterization is important in order to identify the relation between the laser's biasing current, I_b with the RIN and linewidth in the later section.

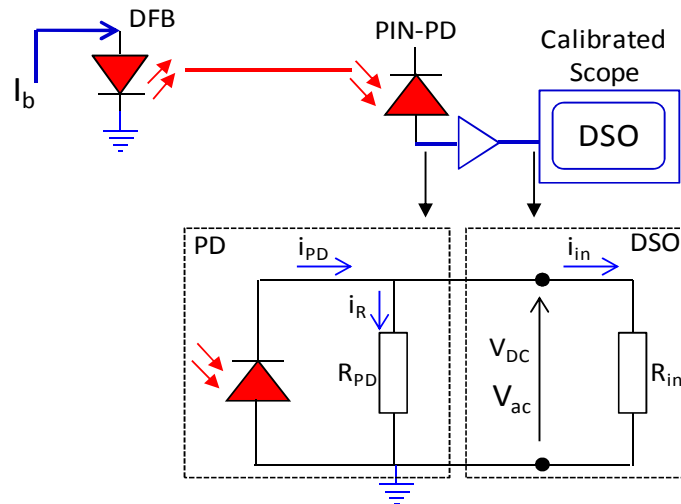


Fig. 3.3.1. RIN measurement setup with internal equivalent circuit of the photodiode (PD) connected into the input of the DSO.

Fig. 3.3.1 shows the setup to measure the RIN of the laser source where the inset represents the internal equivalent circuit of the PD, which is connected to the input of the DSO. The L-I curve for the laser source can also be plotted using this measurement setup. The laser source was an ILX Lightwave laser diode mount (LDM-4616) with a FLD5F6CX-E36 DFB laser. The driving current, I_b supplied into the DFB laser was varied in order to increase and reduce the laser's output power, P_{out} , where at the same time will also vary the RIN. The DFB laser output intensity fluctuations were detected by a DC-coupled Discovery DSC40S PIN photodiode (PD) with a bandwidth of 30 GHz. The responsivity of the PIN-PD was 0.26 A/W. The electrical output of the PIN-PD was amplified and displayed using a calibrated Agilent 81004A 10-GHz 40-GS/s digital sampling oscilloscope (DSO). A Fast-Fourier transform (FFT) was applied to the time domain signal captured at the DSO to view the noise power spectral density of the laser. The internal equivalent circuit of the PD has a termination resistor with resistance, R_{PD} of 50 Ω and the DSO internal input's load resistance, R_{in} is also 50 Ω . In this measurement, the DSO was calibrated to give the electrical power, P_{elect} into the R_{in} to be integrated over its resolution bandwidth, B_{res} in order to measure the RIN correctly.

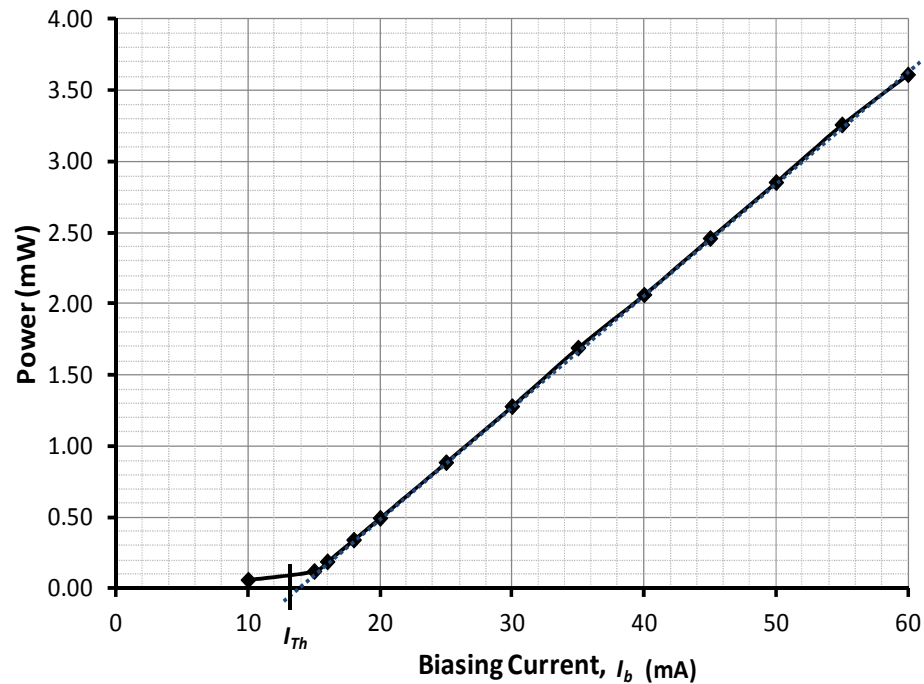


Fig. 3.3.2. Measured L-I characteristic.

Fig. 3.3.2 shows the graph of the received approximate output power of the laser versus the supplied I_b . The graph presents the L-I characteristic of the laser. The output power was calculated by taking the measured dc-voltage, V_{DC} across a 25Ω impedance due to the 50Ω termination of R_{PD} , as shown by the inset of Fig. 3.3.1 in order to find the dc-current, i_{DC} . The approximate output power is then calculated by dividing the i_{DC} with the PD's responsivity of 0.26 A/W . The V_{DC} was measured by using the mean measurement function of the DSO. From this graph, the I_{Th} of the laser is identified at around 13 mA by extending the trend-line down to the I_b axis. The graph shows that, at very low I_b (approximately 10 mA), the power emitted is due to a spontaneous emission. Once the I_b reaches I_{Th} , the output power linearly increases with I_b . Below and at the vicinity of the I_{Th} , the laser is dominated by spontaneous emission, where the intensity and phase fluctuations of the lasing field are significant. When the I_b increases beyond the I_{Th} , stimulated emission dominates where the laser's output power increases with the $(I_{Th} - I_b)$.

To characterize the RIN of the laser, the biasing current, I_b of the DFB was varied from 10 mA to 60 mA and the noise density was analysed.

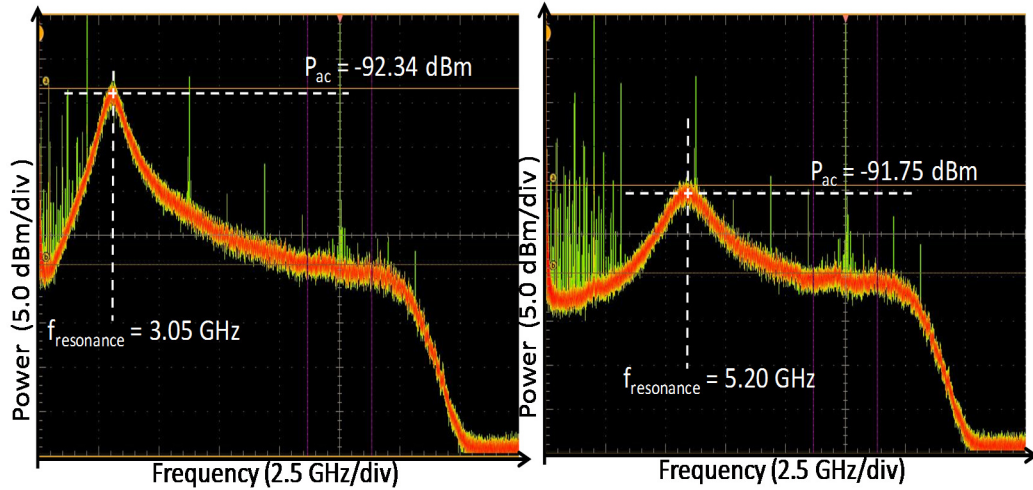


Fig 3.3.3. Measured spectra with high RIN resonance for I_b of 16 mA and 20 mA using Tektronix 72004 20-GHz 50-GS/s DSO.

Fig. 3.3.3 shows the example of a measured spectra with noticeable RIN resonances where the resonance peak ac-power, P_{ac} is increased with the increased of the I_b . The spectra were measured by using the FFT-measurement function of the DSO with maths averaging done over 50 FFTs. Some frequency components are also shown at low frequency and across the DSO bandwidth due to the instrument's noise. A high resonance peak power is shown with the supplied I_b of 16 mA, which is close to the measured value of the I_{Th} (13 mA). When I_b was increased further, the power of the resonance peak was reduced, as shown by the spectrum for I_b of 20 mA. Note that the resonance frequency, $f_{resonance}$, is also shifted to a higher frequency.

To calculate the RIN value of the DFB laser, the average V_{DC} of the signal waveform and the average P_{ac} from the measured FFT-spectrum as shown in Fig. 3.4.1 were recorded. The measured RIN was calculated by using the following equation;

$$RIN = 10 \log_{10} \left[\frac{P_{ac} \times R_{in}}{2B_{res} \cdot V_{DC}^2} \right] \quad (3.3.1)$$

with B_{res} of 610.35 kHz and the DSO measures the power developed across R_{in} of 50 Ω as shown in Fig. 3.3.1. In the calculation, Eq. (3.3.1) was simplified and taken in terms of the AC and DC photocurrents; i_{ac} and i_{DC} as follows;

$$RIN = 10 \log_{10} \left[\frac{i_{ac}^2}{B_{res} \times i_{DC}^2} \right] \quad (3.3.2)$$

Since the PD is internally terminated by 50Ω , both i_{ac} and i_{DC} across V_{ac} and V_{DC} , respectively are subjected to the impedance of 25Ω . The RIN measurement can be done by taking the ratio of the i_{ac} and i_{DC} over 1-Hz bandwidth. By applying base-10 logarithm as in Eq. 3.3.2, the unit of dB/Hz is achieved.

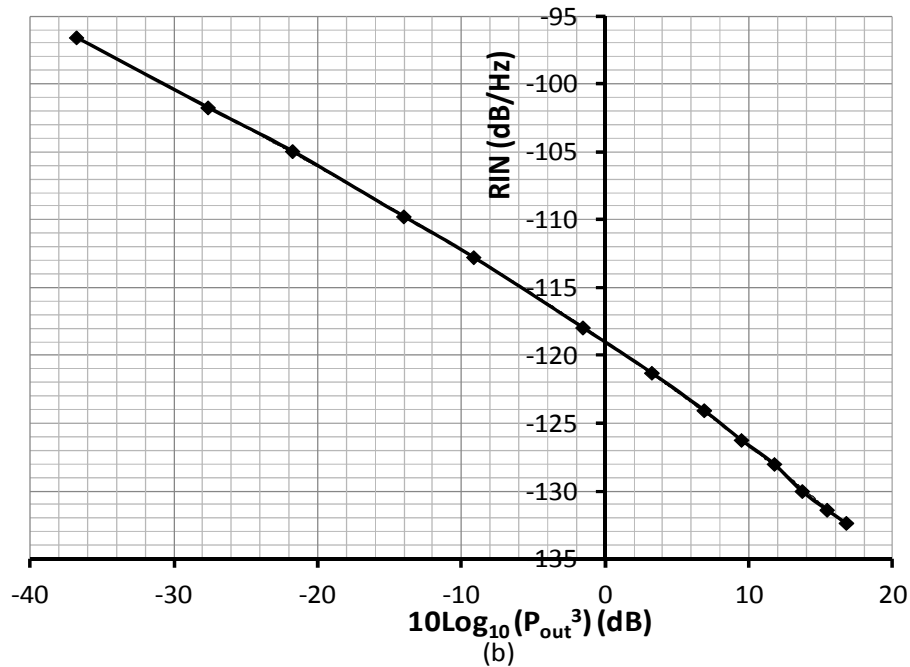
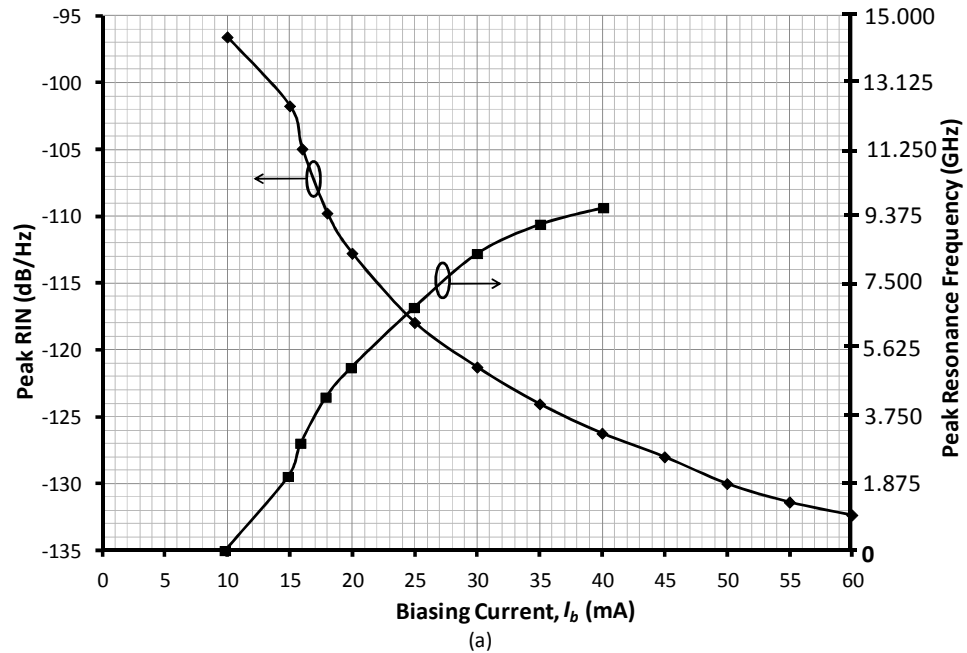


Fig. 3.3.4. (a) Peak RIN and peak resonance frequency vs laser's biasing current, I_b and (b) RIN vs. $10\log_{10}(P_{out}^3)$.

Fig. 3.3.4 shows (a) the peak RIN level and resonance frequency versus the I_b and (b) RIN versus the $10\log_{10}(P_{out}^3)$, where P_{out} is the laser's output power. From Fig. 3.3.4

(a), when the I_b was set to the lowest, a highest RIN was measured but no resonance peak was encountered. At this I_b , the measurement was dominated by a shot noise. When the I_b is at the vicinity of the I_{Th} (15 mA and 16 mA), highest RIN were achieved at approximately -101.7 dB/Hz and -104.9 dB/Hz, respectively. This is due to the high intensity fluctuations in the laser field. At these points, high RIN resonance peaked at 2.11 GHz and 3.05 GHz were observed. When the I_b is increased further, the RIN is significantly reduced and became saturated approximately around -132 dB/Hz at the I_b of 50 mA and above. This particular DFB laser has a maximum biasing current of 60 mA. When the I_b is far above the I_{Th} , a stimulated emission is dominant and the intensity fluctuation is reduced. The graph also shows that the RIN peak frequency resonances were also shifted to the high frequency with the increased of the I_b . This RIN peak could become a problem to a system using multiple subcarriers placed at the high frequency spectrum, where the RIN resonance could reduce the SNR of the subcarriers. However, the graph also shows the reduction of the RIN power with the shifted of the RIN peak frequency. From Fig. 3.3.4 (b), the graph shows that the measured RIN satisfies the theory of RIN is inversely proportional to the laser's output power cubed ($RIN \propto P_{out}^{-3}$).

3.4 Laser RIN Effects with Modulating RF Tones

In this section, extended effect of high RIN laser modulated with RF tone is shown using VPItranmissionMakerTM. The simulated spectrum with carrier and RF tones resembles a system using multiple subcarriers for data transmission such as the DDO-OFDM system. Each of the RF tones is expected to be imposed with the carrier's RIN since the tones up-shift the RIN spectrum share [5, 17, 26, 27]. In this section, the RIN effect with several modulating tones is also investigated. This study is important since the effects of RIN were reported to reduce the SNR and BER performance prior to the detection of a transmitted signal [9, 12-14, 28] and furthermore, the DDO-OFDM system uses a large number of subcarriers for data transmission [29-34]. The property of the RIN power spectrum of a commercial DFB laser has been shown experimentally as in Section 3.3, which comprises a resonance peak at several GHz when a low laser drive current, I_b was applied. This can also affect the transmission of signal using several subcarriers.

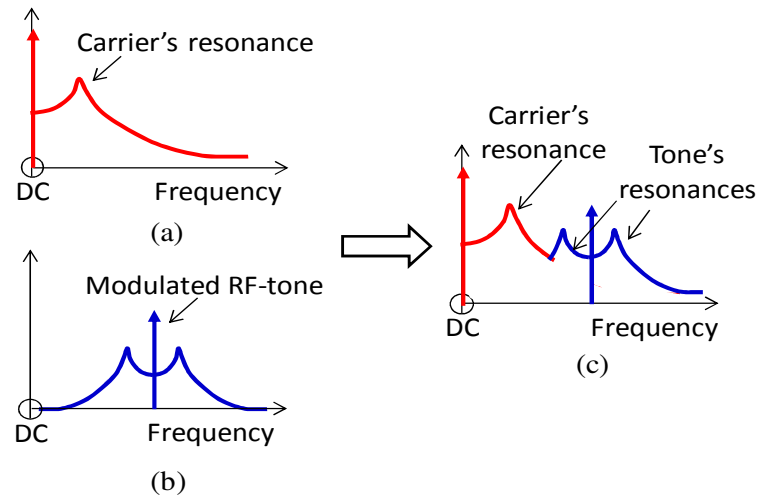


Fig. 3.4.1. Investigation of carrier's RIN modulated with an RF tone: (a) carrier's RIN resonance, (b) modulated RF-tone with RIN resonance and (c) translated RIN from both carrier and tone.

Fig. 3.4.1 illustrates the electrical spectra of: (a) carrier with its RIN resonance (b) modulated RF-tone with double-sided resonance and (c) translated RIN when an RF tone is modulated with the carrier. The resonance peak of a laser with high RIN can be seen at several giga-hertz away from the DC. When the laser is modulated with an RF-tone, the tone will be imposed with a double-sided RIN spectrum, which originates from the carrier as shown in Fig. 3.4.1 (b). The RIN translation of the carrier and tone modulation can be illustrated as Fig. 3.4.1 (c). The noise spectrum will have both the carrier's resonance and the double-sided resonance of the tone. In order to investigate this effect, VPItransmissionMaker was used to simulate the RIN and its resonance. The VPI SM_RE model was used, which solves the laser rate equations, and this includes the cancellation between intensity and phase fluctuations.

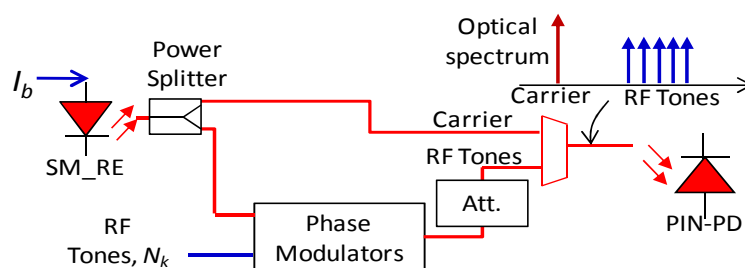


Fig. 3.4.2. Simulation setup of laser source with RIN modulation with RF tones using serrodyne modulation.

Fig. 3.4.2 shows the simulation setup using SM_RE driven with an I_b of 25 mA, which produced RIN resonant at the peak of 3.5 GHz with -110 dB/Hz. Serrodyne modulation was used to create frequency-shifted versions of the laser line. These are

called RF tones, though they could be optical subcarriers if modulated with data. In simulations, this can be implemented using phase modulators driven by linear ramps. With this setup, an optical spectrum of laser carrier with RIN resonance and side tones shown by the inset was achieved. N_k is the number of side tones, where $k = 1, 2, 3, 4, \dots, N-1, N$. In this simulation, N was set to 512. An attenuator is used after the phase modulator to reduce the total power of the side tones in order to achieve 1:1 carrier-to-side tones power ratio. The signal is detected using a PIN photodiode.

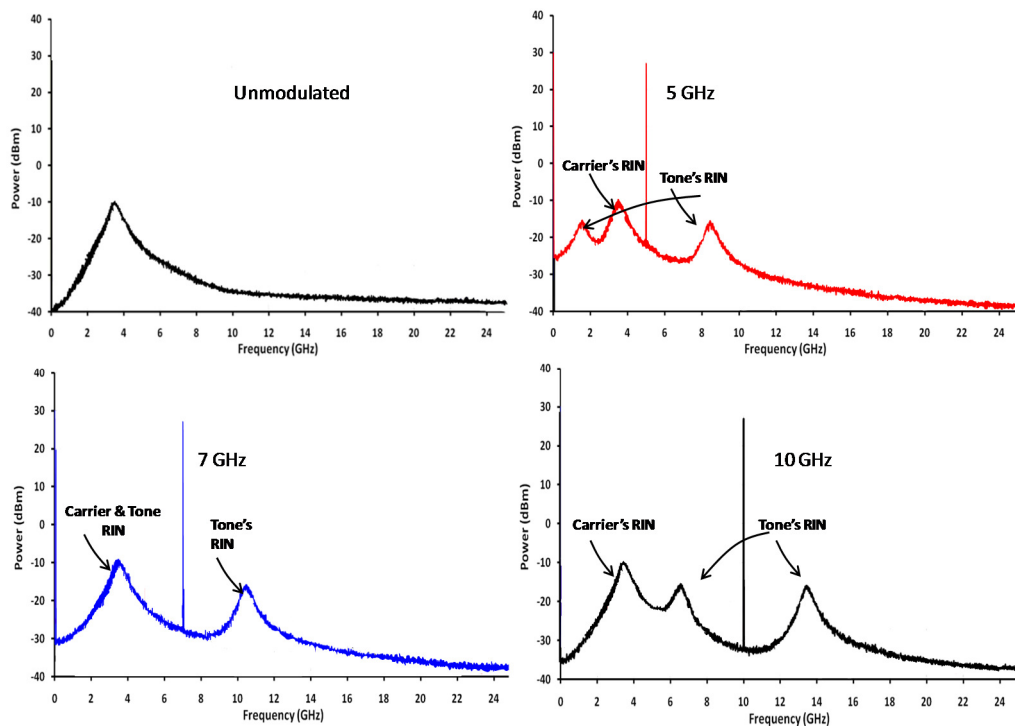


Fig. 3.4.3. Simulated RF spectra of an unmodulated laser with RIN resonance and three RF tones at 5, 7 and 10 GHz.

Fig. 3.4.3 shows the simulated spectra showing RIN resonance of an unmodulated laser and when RF tones at 5-, 7- and 10-GHz are modulated with the laser. The highest resonance peak at 3.4 GHz comes from the carrier, which can be seen in the unmodulated spectrum. This peak is also imposed into the RF tone's spectra. The spectra show that each tone translates the frequency of the RIN peak around the tone's peak. The new peaks are at ± 3.4 GHz, which is the frequency of the RIN of the unmodulated laser source.

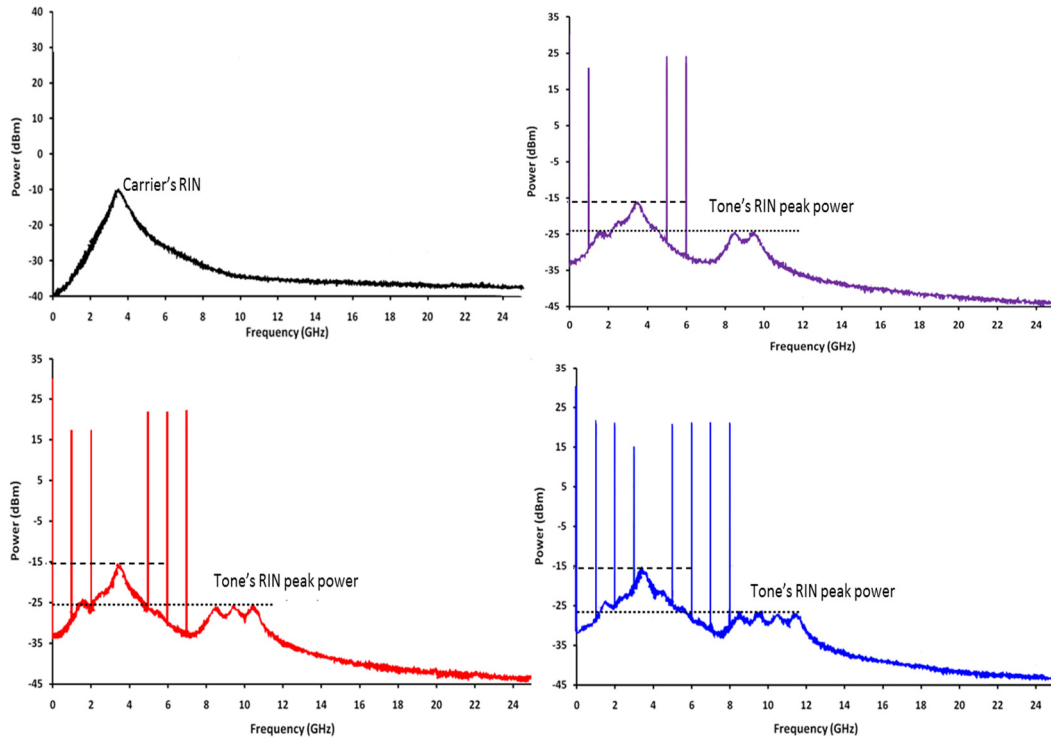


Fig. 3.4.4. Simulated spectra upon photodetection of an unmodulated laser and laser modulated with multiple RF tones.

Fig. 3.4.4 shows the simulated RF spectra when a signal of an unmodulated laser and with multiple tones is detected by the PIN PD. The same simulation setup as in Fig. 3.4.2 was used where the RF-tones power were attenuated in order to have a 1-to-1 ratio of the optical carrier to the power in all of the tones. Double-sided RIN appears but its noise level is decreased when more tones are added. This is because the power per tone is reduced when more tones are modulated hence reduces the tone's RIN peak power. The tones' RINs sum in terms of power so the total RIN increases with the number of tones over a greater bandwidth. This shown by the RIN peaks at upper-side of the tones. The carrier's RIN is shown to be independent of the number of tones where its peak remains unchanged. This carrier's RIN also contains the lower-side RIN peaks of the tones. The carrier's RIN peak can be seen at 3.4 GHz. In terms of a DDO-OFDM system, this peak resonance can be neglected since the system requires a frequency gap to allocate the subcarrier \times subcarrier mixing to [29-37]. The high RIN resonance will fall within this gap and it will not interfere with the signal band.

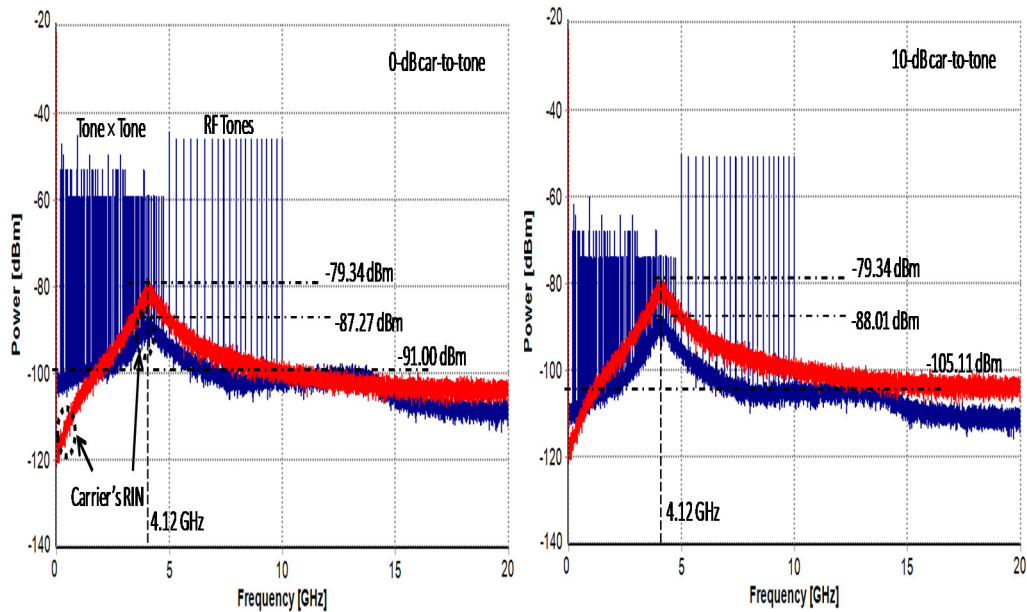


Fig. 3.4.5. Detected electrical spectra with 0-dB and 10-dB difference of carrier-to-tone power.

Fig. 3.4.5 shows the electrical spectra upon photodetection when the signal has a 1-to-1 carrier-to-tone power ratio (left) and when the tones' power is reduced by 10-dB relative to the carrier (right). The red spectrum shows the RIN of the carrier from an unmodulated laser with the resonance peak at 4.12 GHz. The tones are located within a 5-GHz signal bandwidth, where the first tone is located at 5-GHz away from the DC to accommodate for the tone \times tone mixing products. In this figure, the tones occur at the region where the power of the RIN resonance starts to reduce. The noise is higher at lower frequencies. The noise floor of the tones located at 7- to 10-GHz is flattened. If the tones are located at the frequency region with the sharp increase of the resonance, for example lower than 4.12 GHz, the higher frequency tones will have higher noise floor compared with the low frequency tones. When the tones power is reduced by 10-dB relative to the carrier, the noise floor underneath the tones is also reduced, compared to the 1-to-1 carrier-to-tone power ratio by 14 dB. This shows that noise power due to RIN is reduced with the reduction of the tones power.

3.5 Linewidth Measurement

Linewidth characterization of a laser is important in order to predict its effect to a transmission system and thus identify the system's linewidth requirement. An accurate measurement is therefore important to characterize the laser's linewidth before the laser being used at the transmitter. In this section, the linewidth

characteristic of the same Fujitsu FLD5F6CX-E36 laser diode used for the RIN measurement will be analysed and measured. To measure the linewidth, an ordinary optical spectral analyser (OSA) could not be used. This is because of the OSA's typical resolution bandwidth is 0.1 nm which is about 12.5 GHz for 1550-nm wavelength. This is too wide for linewidth measurement, where the typical linewidth of a DFB laser is in megahertz range. Several methods can be used to measure the linewidth, which include self-homodyne and self-heterodyne measurement techniques [20]. These measurement techniques utilize the concept of interference between two optical fields to produce intensity variations in order to be detected by a photodiode. With self-heterodyne technique, the laser will be frequency shifted, where the peak amplitude frequency of the captured RF spectrum is shifted away from the dc [38]. This is different with self-homodyne technique where no frequency shift is required [20].

In this experimental work, two methods were used in order to characterize the phase noise or the linewidth characteristic of the DFB laser. The first measurement was done using the delayed self-homodyne linewidth measurement technique and the second measurement was done using high-resolution spectrometer (Agilent HRS 83453B), which has hundreds of times better resolution compared with a typical OSA [39]. Measurements done with these two techniques will be first explained and the measured linewidth are then plotted in the same graph for comparison.

3.5.1 Delayed Self-Homodyne Technique

Delayed self-homodyne linewidth measurement is an efficient and low-cost technique that can provide high resolution spectrum to measure a narrow linewidth laser [20, 40-43]. With this technique, fewer optical devices are required compared with the self-heterodyne technique [38]. This is because the self-homodyne technique does not require an electro-optic modulator or phase modulator to frequency shift the laser's centre frequency of the detected RF-spectrum [20, 38].

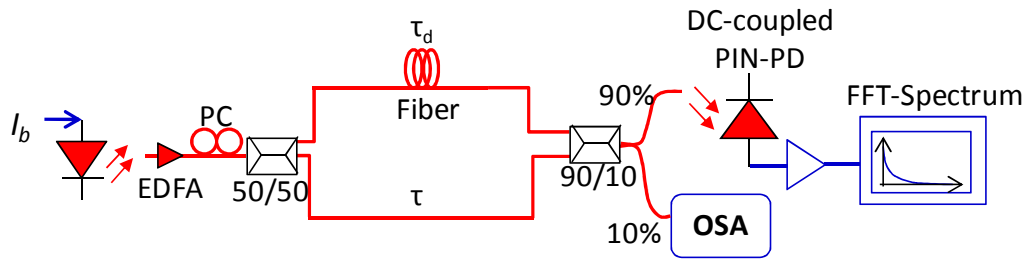


Fig. 3.5.1. Delayed self-homodyne linewidth measurement setup.

An experiment arrangement for delayed self-homodyne linewidth measurement is shown as in Fig. 3.5.1. The I_b of the laser was varied from 15 mA to 60 mA to identify the linewidth with respect to the I_b . The figure shows that the linewidth measurement setup resembles an interferometer, in which the optical signal is split into two different paths by a coupler 50/50. The first branch is connected into a delay line made from a 30-km spool of single mode fibre. This fibre spool introduced τ_d time delay with respect to the signal propagation time without any delay line: τ at the second branch assigned using a patch-cord. The two branches are then combined using a 90/10 coupler. The 90% coupler's output is detected by a DC-coupled Discovery DSC40S PIN photodiode (PD) into an Agilent 81004A 10-GHz 40 GS/s DSO, where an RF spectrum of the detected signal is obtained by applying the FFT-function of the DSO. The 10% output of the coupler is connected to an OSA to view the optical spectrum. Technically, a photodiode can only measure the intensity and not the phase component of an optical field. However, with this interferometer arrangement setup, the phase or frequency fluctuations will be converted into intensity variations, where it can be detected by the photodiode.

In this setup, the τ_d is a critical parameter where an appropriate value relative to the un-delayed signal propagation time, τ need to be identified. The assigned τ_d in the first branch will decorrelate the laser's spectrum at the delay line from the one emitted by the laser as if the signals of the two branches are originated from two different lasers. The τ_d will initiate the operation of the optical circuit setup in a way that it will operate either in a coherent or incoherent interference regime [44]. To measure the laser linewidth, the circuit needs to be operated in the incoherent interference regime in order to have the signal mixing in such a way that the signals at both paths are emitted from two independent lasers with an identical linewidth characteristic. The mixing between the decorrelated and the original laser spectra was captured on the DSO using its FFT-function upon photodetection.

To identify the required delay-line, the difference between τ_d and τ , ($\tau_d - \tau$), needs to be much greater than the laser coherence time, τ_c ($\tau_d - \tau \gg \tau_c$) [20, 44]. The laser τ_c is related to the FWHM linewidth by $\Delta\nu = 1/\pi\tau_c$ [25]. In other words, the τ_d requirement can also be accomplished by using the following condition;

$$\tau_d \geq \frac{1}{\Delta\nu} \quad (3.5.1)$$

With this condition, the required fiber delay line defined by the length of the optical fiber can be verified using the relation of;

$$L_c = \frac{c}{n} \times \frac{1}{\Delta\nu} \quad (3.5.2)$$

Where: L_c is the laser coherence length, c defines as the speed of light in vacuum taken as 3×10^8 m/s and n is the refractive index of fiber taken as 1.46, where c/n defines the velocity of light in the fibre. With this relation, the minimum requirement of the fiber length to measure a certain laser linewidth can be estimated. Also, this relation indicates that for a very narrow linewidth laser, a very long fiber length will be required.

For the delay line of 30 km, the τ_d is equivalent to 150 μ s. Using the relationship in Eq. 3.4.2, the minimum $\Delta\nu$ that could be measured by using τ_d of 150 μ s is 6.84 kHz. The mixing between the delayed and un-delayed spectrum is captured at the DSO upon the photodetection. The captured RF spectrum showed a half Lorentzian-shape curve at the dc, where the negative half of it is overlapped on the positive half. The RF spectra captured on the DSO are recorded with respect to the I_b increment.

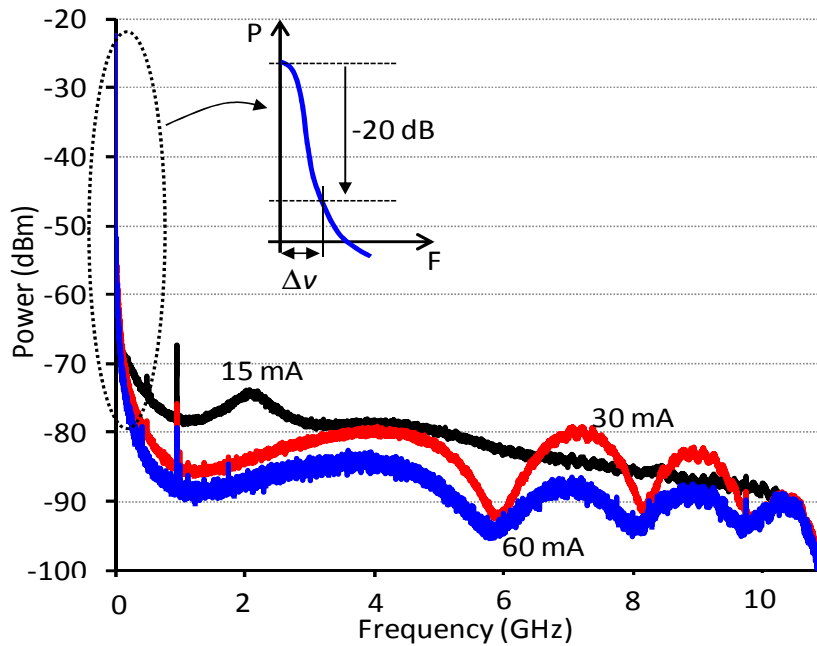


Fig. 3.5.2. Plotted received RF spectra for I_b of 15-, 30- and 60-mA using data recorded with Agilent DSO.

Fig. 3.5.2 shows the captured RF spectra for I_b of 15-, 30- and 60-mA, where these spectra were plotted using the FFT-function data recorded from the Agilent DSO. These plots show half spectrum where it is centred at the DC, which is produced by the overlapping of the spectrum's negative-half on top of its positive-half. The inset of the plot represents the measurement taken during the experiment, which was done by magnifying the captured spectrum on the scope close to dc. The measurement of the spectral width were taken at -20- and -30-dB down the peak power and a correction factor was applied to get the full-width-half-maximum (FWHM) linewidth for each I_b . During this experiment, the captured spectrum was magnified to view 0.5 million-points of memory depth in order to have a 20 kHz frequency resolution at 10-GHz sample rate to obtain the linewidth measurement. From the measured spectral width at 20- and 30-dB, the FWHM $\Delta\nu$ of the laser was achieved by using the correction factors of $\Delta\nu\sqrt{99}$ and $\Delta\nu\sqrt{999}$, respectively [20].

3.5.2 High-Resolution Spectrophotometer (HRS)

The second method used to measure the linewidth of the DFB laser was by using an Agilent 83453B high-resolution spectrometer. The device is shown as in Fig. 3.5.3 shows the HRS unit that includes an 8164B lightwave mainframe that consists of attenuator module 81571, 81634B power sensor module, 81600B tunable laser source (TLS) and Agilent multi-wavelength meter. Also included in the device are an

E9393A coherent receiver unit and a tunable laser source as the local oscillator (LO). The device basically employed heterodyne optical receiver, where the LO is swept across the wavelength to measure the optical spectrum [45].

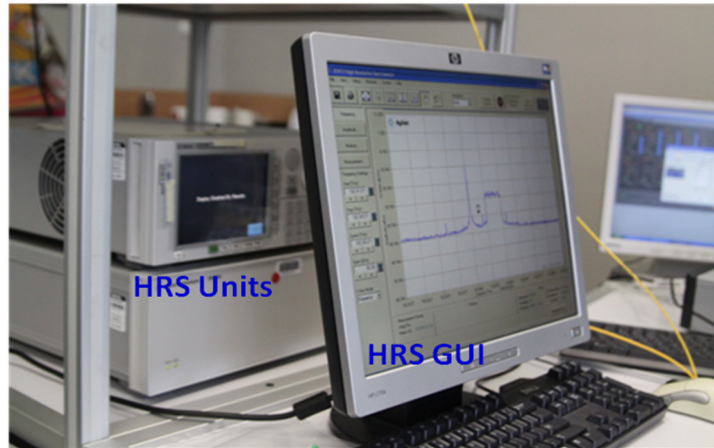


Fig. 3.5.3. Agilent high-resolution spectrometer consists of HRS units of coherent receiver and the lightwave mainframes and its graphical user interface (GUI).

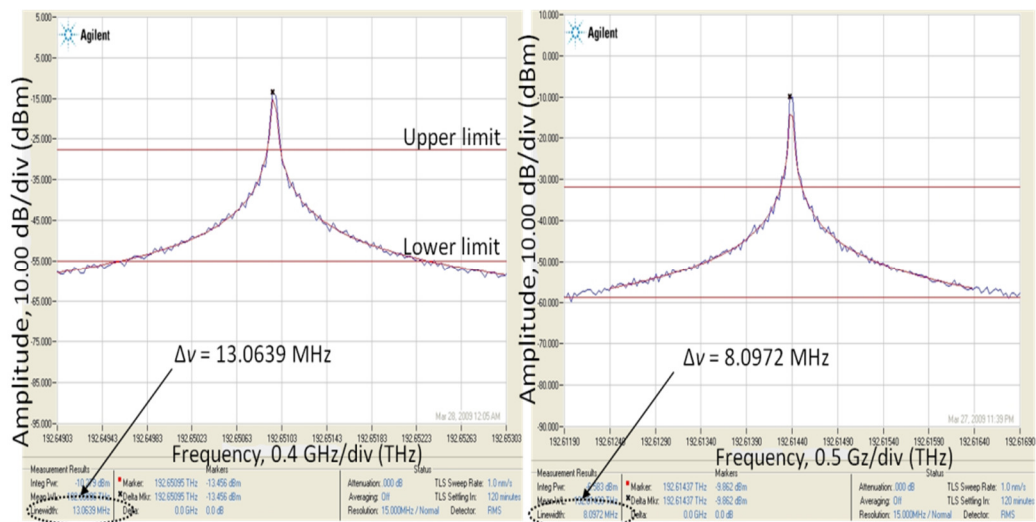


Fig. 3.5.4. Lorentzian curve plot to measure linewidth using HRS for I_b of 35 and 60 mA.

The measured linewidth using the HRS for I_b of 35 and 60 mA is shown as in Fig. 3.5.4. The HRS fits a Lorentzian curve to the measured spectral width. The measurement of the linewidth is taken by initiating an upper and lower limit where this region should only cover the traces with the best Lorentzian fit on the spectral width. The linewidth is determined by the HRS software by computing the linewidth at each data point within this initiated limit and averaged it. The measured FWHM linewidth was then recorded with respect to the I_b .

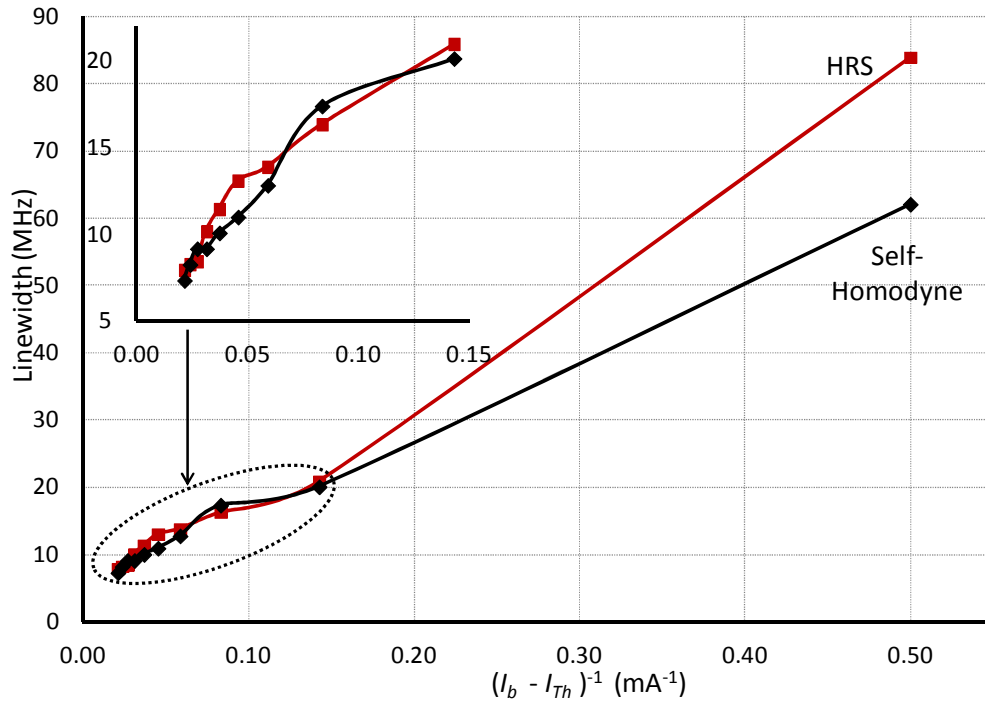


Fig. 3.5.5. Measured linewidth using HRS and self-homodyne technique as a function of inverse I_b relative to I_{Th} .

Fig. 3.5.5 shows the measured linewidth as a function of inverse I_b deviation relative to I_{Th} ($I_b - I_{Th}$) using HRS and self-homodyne technique. The measured I_{Th} of this laser is 13 mA and the I_b was varied from 15 mA to 60 mA. However, it should be noted that the value of the I_{Th} can vary with the operating temperature over time. The plot shows that the narrowest linewidth that can be provided by this DFB laser is 7.92 MHz and 7.31 MHz with the maximum allowed I_b of 60 mA measured with HRS and self-homodyne technique, respectively. As mentioned before, the critical requirement of the self-homodyne technique in order to have an accurate measurement of linewidth is to have $\tau_d - \tau$ to be much greater than τ_c . If the chosen τ_d is smaller than τ_c , the measurement resolution will be limited due to the differential-time delay induced by the delay-line of the interferometer-like circuitry [46].

The graph of Fig. 3.5.5 shows that the linewidth is directly proportional to the inverse of I_b in excess of I_{Th} . The graph also shows that when I_b is much greater than I_{Th} , much narrower linewidths can be achieved. This can be clearly seen by the inset of the magnified graphs for the I_b deviation of 0.02 to 0.14. At I_b close to I_{Th} , wide linewidth was measured where 84.01 MHz was measured with the HRS and 62.13 MHz with the self-homodyne technique. The measurement with both HRS and self-homodyne technique match well with each other except for I_b close to I_{Th} . This is

because for the low I_b , the laser emitted low output power. The low output power produced low peak amplitude power spectrum on the HRS so a limited number of points were available. This could reduce the accuracy of the linewidth measurement.

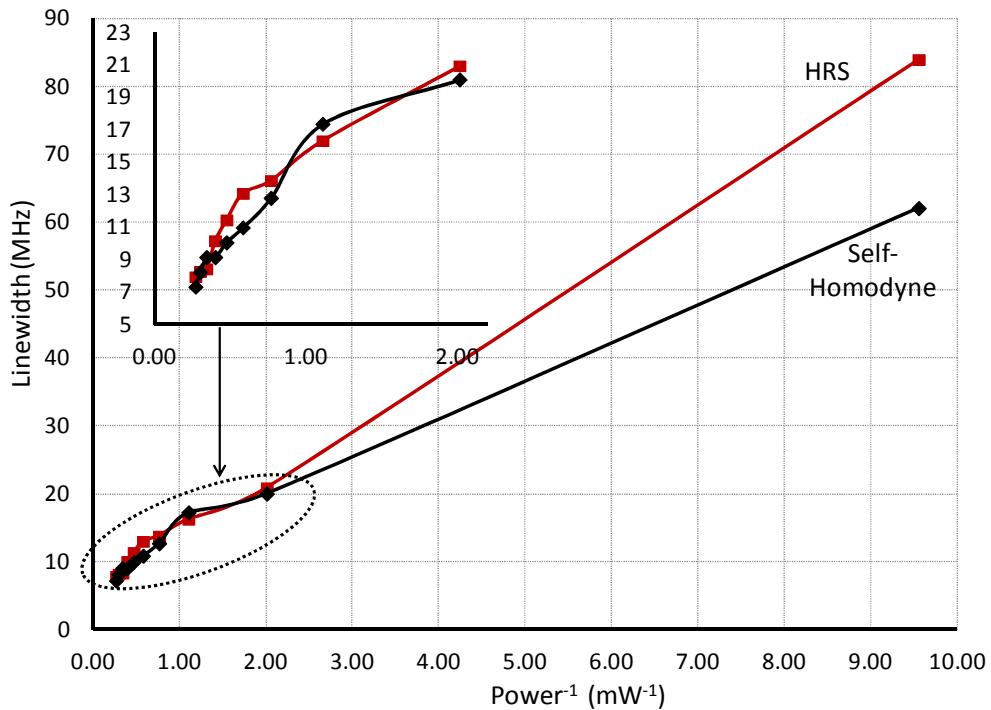


Fig. 3.5.6. Measured linewidth using HRS and self-homodyne technique as a function of inverse laser's output power.

Fig. 3.5.6 shows the measured linewidth using HRS and self-homodyne technique as a function of the inverse of laser's output power. The laser's output power was measured as presented in Section 3.3. This plots shows that the measured linewidth is directly proportional to the inverse output power, which agrees with the semiconductor laser linewidth theory [25].

3.6 Conclusions

In this chapter, the relation of laser noise characteristics the RIN and linewidth, has been explained. The L-I characteristic measurement of a DFB laser has been measured and plotted, where the I_{Th} of the laser has been obtained from the curve. This curve is important to relate the I_b with the P_{out} and subsequently with the RIN and linewidth when the laser is supplied with I_b at the vicinity of or high above the I_{Th} . For this specific DFB laser, an I_{Th} of 13 mA was obtained. Methods to measure RIN and linewidth have been presented. The measured RIN and linewidth satisfied the theory of $RIN \propto P_{out}^{-3}$ and linewidth $\propto P_{out}^{-1}$ when the I_b was increased. Critical

factors in the measurements of the RIN and linewidth have been identified. In the RIN measurement, the RF spectrum analyser (DSO) used in the setup need to be calibrated in order to have an accurate measurement. An extended investigation of RIN when the laser is externally modulated with RF tones was also presented using simulation. The results show that each of the tone was imposed with a double-sided RIN resonance. The RIN's peak frequency of the tone was taken from the tone to its peak frequency, where the frequency difference is similar to the carrier's RIN peak frequency. The RF tones were generated from the laser hence, the same RIN resonance as the carrier's RIN is imposed to each of the tone with lower RIN's peak power. This was shown in the detected electrical spectrum. The RIN's peak power is reduced when more tones were used and when the tones power is decreased. In terms of a DDO-OFDM system, the tones represent the OFDM subcarriers. The tone's RIN are summed up so the total RIN is independent of the total number of tones. The carrier's RIN can be neglected since the resonance's peak power will fall within a frequency guardband, which usually employed in the DDO-OFDM system to place the intermodulation distortion (IMD) due to subcarrier \times subcarrier mixing [30-33]. For the linewidth measurement with self-homodyne technique, a sufficient length of the delay line needs to be identified in order to produce an incoherent mixing of the light from the branches upon photodetection. Results obtained using self-homodyne technique matched well with the HRS.

3.7 References

1. Sato, K., *Intensity noise of semiconductor laser diodes in fiber optic analog video transmission*. Quantum Electronics, IEEE Journal of, 1983. **19**(9): p. 1380-1391.
2. Yamamoto, S., et al., *Analysis of laser phase noise to intensity noise conversion by chromatic dispersion in intensity modulation and direct detection optical fiber transmission*. Journal of Lightwave Technology, 1990. **8**: p. 1716-1722
3. Edagawa, N., et al., *12300 ps/nm, 2.4 Gb/s nonregenerative optical fiber transmission experiment and effect of transmitter phase noise*. Photonics Technology Letters, IEEE, 1990. **2**(4): p. 274-276.
4. Lee, Y.H., J. Woo, and H.W. Tsao, *The impact of laser phase noise on the coherent subcarrier multiplexing system*. Lightwave Technology, Journal of, 1991. **9**(3): p. 347-355.
5. Lu, X., et al., *Analysis of relative intensity noise in semiconductor lasers and its effect on subcarrier multiplexed lightwave systems*. Lightwave Technology, Journal of, 1994. **12**(7): p. 1159-1166.
6. Ribeiro, R.F.S., J.R.F.d. Rocha, and A.V.T. Cartaxo, *Influence of laser phase noise on dispersive optical fiber communication systems*. Photonics Technology Letters, 1995. **7**(12): p. 1510-1512.

7. Marshall, W.K., B. Crosignani, and A. Yariv, *Laser phase noise to intensity noise conversion by lowest-order group velocity dispersion in optical fiber: exact theory*. Optics Express, 2000. **23**(3): p. 165-167.
8. Morgado, J.A.P. and A.V.T. Cartaxo. *New semi-analytical method of estimating the influence of laser noise on direct detection system performance*. in *4th Pacific Rim Conference on Lasers and Electro-Optics (CLEO)*. 2001.
9. Morgado, J.A.P. and A.V.T. Cartaxo, *Assessment of laser noise influence on direct-detection transmission system performance*. Journal of Lightwave Technology, 2003. **21**(3): p. 759-768.
10. Savory, S. and A. Hadjifotiou, *Laser linewidth requirements for optical DQPSK systems*. Photonics Technology Letters, IEEE, 2004. **16**(3): p. 930-932.
11. Sharma, V., A. Singh, and A.K. Sharma, *Analysis of the impact of laser line width over RIN, power penalty and bit rate including higher-order dispersion in WDM systems*. Optik, 2009. **120**(15): p. 741-745.
12. Laurêncio, P.R. and M.C.R. Medeiros, *Relative Intensity Noise in Optical Single Side Band Systems with Multiple In-Line Amplifiers: Analysis and Validation*. Fiber and Integrated Optics, 2008. **27**(2): p. 78 - 88.
13. Laurêncio, P., S.O. Simões, and M.C.R. Medeiros, *Impact of the Combined Effect of RIN and Intermodulation Distortion on OSSB/SCM Systems*. J. Lightwave Technol., 2006. **24**(11): p. 4250-4262.
14. Ahmed, M. and M. Yamada, *Effect of intensity noise of semiconductor lasers on the digital modulation characteristics and the bit error rate of optical communication systems*. Journal of Applied Physics, 2008. **104**(1): p. 013104-7.
15. Ahmed, M., M. Yamada, and S.W.Z. Mahmoud, *Analysis of semiconductor laser dynamics under gigabit rate modulation*. Journal of Applied Physics, 2007. **101**(3): p. 033119-033119-9.
16. Kazovsky, L., S. Benedetto, and A. Willner, *Optical fiber communication systems*. 1st ed. 1996, Norwood: Artech House, Inc. 690.
17. Vahala, K. and A. Yariv, *Semiclassical theory of noise in semiconductor lasers--Part II*. Quantum Electronics, IEEE Journal of, 1983. **19**(6): p. 1102-1109.
18. Agrawal, G.P. and N.K. Dutta, *Semiconductor Lasers*. 2nd ed. 1993, New York: International Thomson Publishing.
19. Brilliant, A., *Digital and Analog Fiber Optic Communications for CATV and FTTx Applications*. 2008: SPIE Press.
20. Derickson, D., ed. *Fiber Optic Test and Measurement*. 1998, Prentice Hall: New Jersey.
21. Fleming, M.W. and A. Mooradian, *Fundamental line broadening of single-mode (GaAl) As diode lasers*. Applied Physics Letters, 1981. **38**: p. 511.
22. Elsässer, W. and E.O. Göbel, *Spectral linewidth of gain- and index-guided InGaAsP semiconductor lasers*. Applied Physics Letters, 1984. **45**(4): p. 353-355.
23. Carlson, A.B., P.B. Crilly, and J. Rutledge, *Communication systems: an introduction to signals and noise in electrical communication*. 4th ed: McGraw-Hill.
24. Agrawal, G.P., *Fiber-optic communication systems*. 1997, New York: John Wiley and sons. 555.
25. Henry, C.H., *Theory of the linewidth of semiconductor lasers*. IEEE Journal of Quantum Electronics, 1982. **QE-18**(2): p. 259-264.
26. Marshall, W.K. and A. Yariv, *Spectrum of the intensity of modulated noise light after propagation in dispersive fiber*. PHOTONICS TECHNOLOGY LETTERS, 2000. **12**(3): p. 302-304.

27. Meslener, G.J., *Mode-partition noise in microwave subcarrier transmission systems*. Lightwave Technology, Journal of, 1994. **12**(1): p. 118-126.
28. Zan, Z., A.J. Lowery, and M. Premaratne. *Laser RIN and linewidth requirements for direct detection optical OFDM*. in *Lasers and Electro-Optics CLEO 2008*. 2008. San Jose.
29. Lowery, A.J. and J. Armstrong, *10 Gbit/s multimode fiber link using power efficient orthogonal-frequency-division multiplexing*. OPTICS EXPRESS, 2005. **13**(25): p. 10003-10009.
30. Lowery, A.J. and J. Armstrong, *Orthogonal frequency division multiplexing for dispersion compensation of long-haul optical systems*. Optics Express, 2006. **14**: p. 2079-2084.
31. Lowery, A.J., L. Du, and J. Armstrong. *Orthogonal Frequency Division Multiplexing for Adaptive Dispersion Compensation in Long Haul WDM Systems*. in *Optical Fiber Communication Conference, 2006 and the 2006 National Fiber Optic Engineers Conference. OFC 2006*. 2006.
32. Schmidt, B.J.C., A.J. Lowery, and J. Armstrong. *Experimental demonstrations of 20 Gbits/s direct-detection optical OFDM and 12Gbits/s with a colorless transmitter*. in *Optical Fiber Communication Conference*. 2007. Anaheim, CA.
33. Lowery, A.J., L. Du, and J. Armstrong, *Performance of optical OFDM in ultra long-haul WDM lightwave systems*. Journal of Lightwave Technology, 2007. **25**: p. 131 – 138.
34. Lowery, A.J. and J. Armstrong. *Orthogonal-Frequency-Division Multiplexing for Optical Dispersion Compensation*. in *Optical Fiber Communication and the National Fiber Optic Engineers Conference*. 2007. Anaheim, USA.
35. Lowery, A.J., S. Wang, and M. Premaratne, *Calculation of power limit due to fiber nonlinearity in optical OFDM systems*. Optics Express, 2007. **15**(20): p. 13282-13287.
36. Lowery, A.J., *Amplified-spontaneous noise limit of optical OFDM lightwave systems*. Optics Express, 2008. **16**(2): p. 860-865.
37. Schmidt, B.J.C., A.J. Lowery, and J. Armstrong, *Experimental demonstrations of electronic dispersion compensation for long-haul transmission using direct-detection optical OFDM*. Journal of Lightwave Technology, 2008. **26**(1): p. 196-203.
38. Okoshi, T., K. Kikuchi, and A. Nakayama, *Novel method for high resolution measurement of laser output spectrum*. ELECTRONICS LETTERS, 1980. **16**(16): p. 630-631.
39. Agilent. *Agilent 83453B high-resolution spectrometer*.2005 [cited 2008]; Available from:
<http://www.home.agilent.com/agilent/product.jsp?cc=AU&lc=eng&nid=-536900356.536883064&pageMode=SP>.
40. Ryu, S. and S. Yamamoto, *Measurement of direct frequency modulation characteristics of DFB-LD by delayed self-homodyne technique*. ELECTRONICS LETTERS, 1986. **22**(20): p. 1052-1054.
41. Nazarathy, M., et al., *Spectral analysis of optical mixing measurements*. Lightwave Technology, Journal of, 1989. **7**(7): p. 1083-1096.
42. Ludvigsen, H., J. Kokkonen, and M. Tossavainen. *Self-Homodyne Laser Linewidth Measurements*. in *Lasers and Electro-optics Europe, 1996. CLEO/Europe., Conference on*. 1996.
43. Ludvigsen, H., M. Tossavainen, and M. Kaivola, *Laser linewidth measurements using self-homodyne detection with short delay*. Optics Communications, 1998. **155**(1): p. 180-186.

-
44. Hui, R. and M. O'Sullivan, *Fiber optic measurement techniques*. 1st ed. 2009, Burlington, MA, USA: Elsevier.
 45. Agilent Technologies, *High resolution spectrometer user's guide*. January 2005 [cited 2009; Available from: <http://cp.literature.agilent.com/litweb/pdf/83453-90001.pdf>].
 46. Richter, L.E., et al., *Linewidth determination from self-heterodyne measurements with subcoherence delay times*. Quantum electronics letters, 1986. **QE-22**(11): p. 2070-2074.

Chapter 4

DEVELOPMENT OF LASER LINEWIDTH EMULATOR

4.1 Introduction

The performance of many optical communication systems depends critically on the characteristics of a semiconductor laser at the transmitter [1-5]. In order to investigate the system's requirements on the laser characteristics, it would be useful to have an optical source whose linewidth could be "dialed up" without affecting its output power, intensity noise or modal structure. This dialed up optical source could reduce the system's development cost by eliminating the need to test a number of lasers with different characteristics. A typical way to vary the linewidth of a semiconductor laser is by using the dependence of linewidth, $\Delta\nu$, on the inverse of laser output power, $\Delta\nu = F(1/P)$ [6, 7]. However, creating a wide linewidth requires operation at very low powers and this causes a decrease in spectral purity such as the appearance of additional lasing modes and a very high RIN.

In this chapter, the technique of emulating a semiconductor laser with the dialed up linewidth is presented. Section 4.2 presents the principle of the linewidth emulator. In section 4.3, the principle of this emulator is verified using simulation. An experimental demonstration of this is also shown. The laser linewidth emulator can also be used to measure a linearity of an external optical modulator. This is shown using simulation and experiment in Section 4.4. Finally, Section 4.5 presents the conclusion and Section 4.6 is the references.

4.2 Principle of Laser Linewidth Emulator

The principle of the emulator is to phase-modulate the output of a narrow-linewidth laser to broaden its linewidth using digitally-generated phase modulation. That is, the phase, θ_n , at sample time $n \cdot \Delta T$ will be updated every time-step, ΔT . The change in phase per times step, $\theta_n - \theta_{n-1}$ is a Gaussian random variable with variance, σ^2 [8], with the value

$$\sigma^2 = 2\pi\Delta\nu\Delta T \quad (4.2.1)$$

This phase could be applied using a lithium niobate (LiNbO_3) phase modulator as illustrated in Fig. 4.2.1.

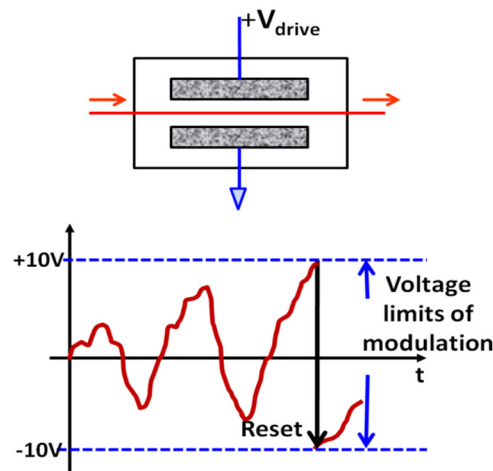


Fig. 4.2.1. Phase modulation using a LiNbO_3 phase modulator showing the need for a reset. Fig. 4.2.1 shows the LiNbO_3 phase modulator has a limited modulation range, which is set by the limits of its drive voltage. Thus the phase has to be “reset” by adding or subtracting 2π radians whenever a voltage limit is approached. This reset produces a large frequency chirp, which is undesirable.

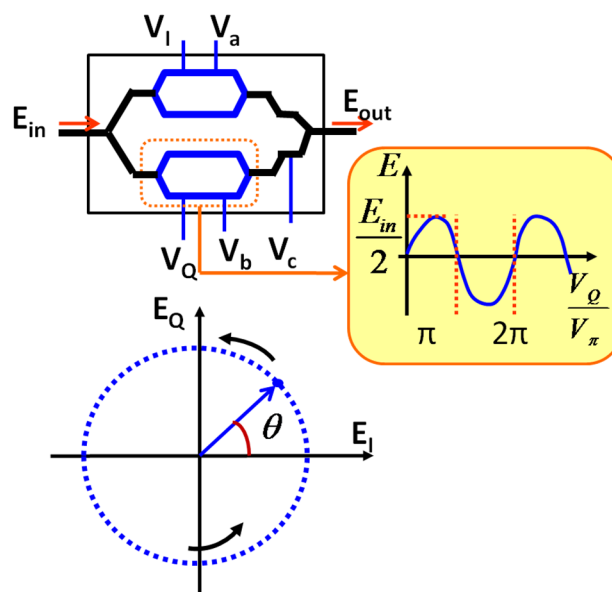


Fig. 4.2.2. Phase modulation using a complex modulator showing how the phase can be driven indefinitely around the complex plane by combining the outputs of the nested upper (I) and lower (Q) modulators.

Fig. 4.2.2 illustrates C-MZI's configuration. Instead of using the LiNbO_3 modulator, a complex optical modulator (C-MZI) based on nested Mach-Zehnder Interferometers (MZIs), can be used. With this modulator, the phase can be driven around the complex plane indefinitely, without the requirement for reset events. The

output field, E_{out} , of the C-MZI, when its upper and lower MZIs are combined in quadrature by adjusting V_c , is related to its input field, E_{in} , by

$$E_{out} = \frac{E_{in}}{2} \left[\sin\left(\frac{\pi V_I}{2 V_\pi}\right) + j \sin\left(\frac{\pi V_Q}{2 V_\pi}\right) \right] \quad (4.2.2)$$

This assumes zero excess loss and bias trimming (V_a , V_b), so that the upper and lower MZIs produce zero output for zero drive and the perfect balance of power between all modulator arms. For linear operation, V_I and V_Q should be much smaller than the voltage that is required to switch the modulators from fully on to fully off, V_π , therefore

$$E_{out} = \frac{E_{in}\pi}{4V_\pi} (V_I + jV_Q) \quad (4.2.3)$$

Thus, to obtain a phase shift θ_n

$$V_{I,n} = k \cos \theta_n \quad \text{and} \quad V_{Q,n} = k \sin \theta_n \quad (4.2.4)$$

Where k is the drive amplitude and should be far smaller than V_π to ensure that the C-MZI is operating in its linear region. The effects of varying the k to the C-MZI will be shown in Section 7.4. With the C-MZI, a frequency shift, Δf can also be imposed on the emulated laser's output by applying a continuously increasing phase shift as follows

$$V_{I,n} = k \cos(\theta_n + 2\pi\Delta f n \Delta T) \quad \text{and} \quad V_{Q,n} = k \sin(\theta_n + 2\pi\Delta f n \Delta T) \quad (4.2.5)$$

4.3 Verification of the Linewidth Emulator

In order to verify the performance of the emulator, simulations using VPItransmissionMaker version 8.5 and experimental works were conducted. In this verification, the statistical properties of the emulator's output signal are presented and the emulator measurement was done using a self-homodyne measurement technique.

4.3.1 Simulations

The simulation setup of the emulator can be shown as in Fig. 4.3.1. The green inset of the figure shows the emulator which consists of the continuous wave laser module, laserCW, X and Y polarization extractor, signal processing (SP) interface and a C-MZI. The laserCW module was used to generate the phase modulation signals, where its $\theta_n - \theta_{n-1}$ is a Gaussian random variable with σ^2 as presented in Eq. 4.2.1. A single polarization output of laserCW was isolated and the

signal was converted into the electrical signals of the I and Q components. This was done by using a VPI SP interface module and a component that converts a complex signal into I and Q signals. The I and Q signals were then converted into analog signals by the digital-to-analog converter (DAC) to drive the C-MZI. The signals were amplified using RF amplifiers with the gain denoted by k . This produced the resulting C-MZI's RF driving signals of $V_{I,n}$ and $V_{Q,n}$. These I and Q signals can be plotted onto a complex-plane which produced a unit circle.

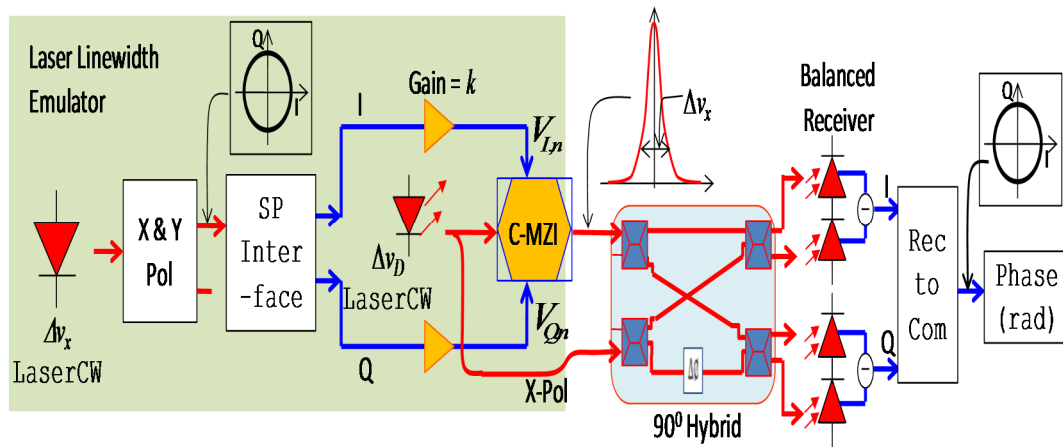


Fig. 4.3.1. Simulation setup using self-homodyne coherent receiver with 90° optical hybrid producing the inphase and quadrature components, which formed a circle in a complex-plane.

The C-MZI was then fed from a laser with a linewidth Δv_D . The minimum linewidth for this emulator is the linewidth of the laser that driven the C-MZI, which is Δv_D in this setup. The output spectrum of the C-MZI will be a laser spectrum with Δv_x linewidth shown by the inset. In this design, a self-homodyne coherent receiver was used to obtain the I and Q components of the C-MZI's output signal. This receiver contains a 90° hybrid and two balanced-receivers. With this receiver, the same laser used to drive the C-MZI was also used as the local oscillator (LO)[9]. Hence, the $V_{I,n}$ and $V_{Q,n}$ are as Eq. 4.2.4. The detected I and Q are the signal components of the emulated laser field with the dialled up Δv . The RF spectrum of either I or Q can be used to measure the linewidth where a half spectrum of the FWHM can be obtained [9].

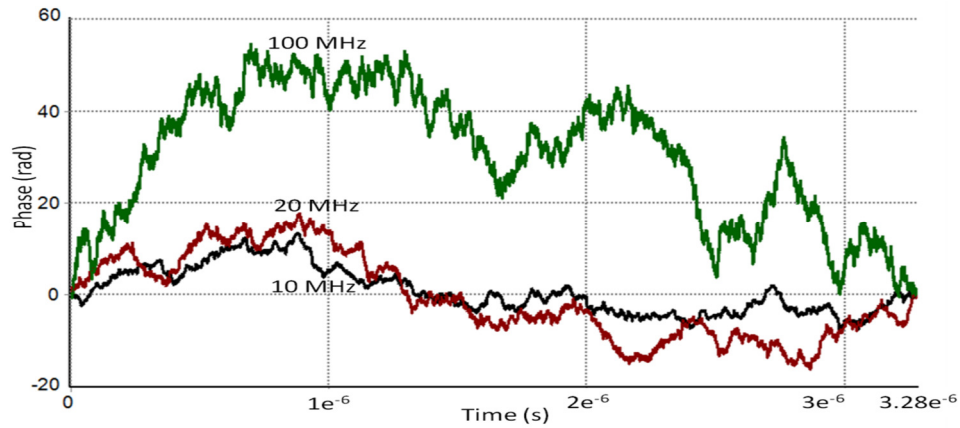


Fig. 4.3.2. Simulated instantaneous phase of the received signal for laser linewidth emulator of 10-, 20- and 100-MHz showing phase random-walk within a time window.

Fig. 4.3.2 shows the random-walk of the received signal's instantaneous phase, $\theta_n(t)$, over a time window, with the linewidth of the emulator was set to 10 MHz, 20 MHz and 100 MHz. The plots were obtained by adding $\pm 2\pi$ when the phase jumps between the consecutive times are greater than or equal to π radians. The plots show that a wider linewidth gives larger phase changes within the time window. Theoretically, the phase change in the laser field is due to the spontaneous emission of photons each with a random phase [7, 8, 10]. However, a significant contributor to the linewidth broadening is the laser cavity refractive index, n , due to the change in the carrier density that follows a spontaneous emission event. This linewidth broadening is described by the linewidth enhancement factor, $(1+\alpha^2)$ [6].

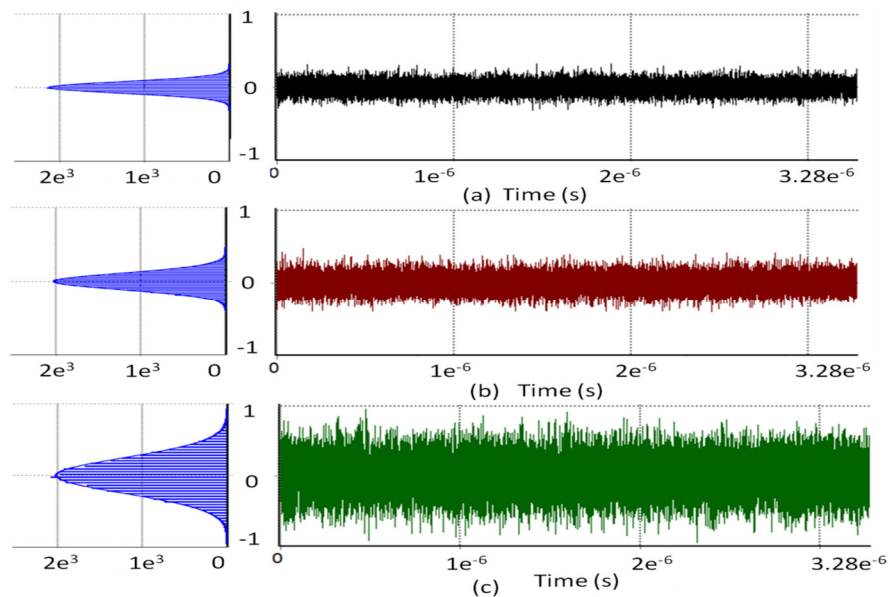


Fig. 4.3.3. Frequency noise, $d\theta_n(t)/dt$, and histograms with Gaussian fit showing zero-mean Gaussian distribution for the dialled up linewidth of (a) 10 MHz (b) 20-MHz and (c) 100-MHz.

Fig. 4.3.3 shows the frequency noise, $d\theta_n(t)/dt$, obtained by taking the time derivatives of the phase changes and its histograms with Gaussian fit for the dialled up linewidth of 10 MHz (a), 20 MHz (b) and 100 MHz (c). The plots show that the resulting linewidth of the emulator with a zero-mean Gaussian distribution, which satisfied the theory of the laser phase noise model [6, 10-13].

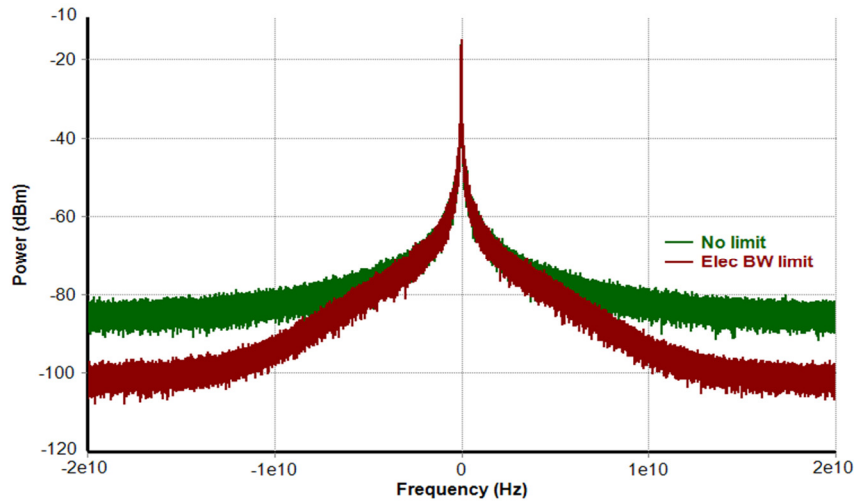


Fig. 4.3.4. Simulated laser linewidth emulator's spectra with and without electrical bandwidth limitation.

Fig. 4.3.4 shows the simulated effects of limiting the RF bandwidth of the signals at the C-MZI's RF inputs. This limitation was added to model the possible effects of the combined frequency response of the digital-to-analog converters, drive electronics and optical modulator. Without any limit to the bandwidth, the obtained spectrum is a Lorentzian shape. When 4th-order Bessel filters with 2.5 GHz limited the electrical bandwidth at the RF inputs of the C-ZMI, the higher-frequencies of the tails of the Lorentzian spectrum are reduced in power. This bandwidth limitation will change the statistics of the phase noise; for example, the variance of the frequency noise or frequency fluctuations (the time-derivative of the phase) will be reduced.

4.3.2 Experiments

Fig. 4.3.5 shows the experimental setup of the emulator and the linewidth measurement technique. The laser source used was a Photonics Tunics External Cavity Laser (ECL) tuned to 193.0 THz with a 256-kHz linewidth, $\Delta\nu_D$. The green inset shows the laser emulator which includes a Tektronix 7102 2×10GS/s arbitrary waveform generator (AWG) driving a Sumitomo T-SBXI.5-20P 40-Gbit/s complex optical modulator. The modulating signals, V_I and V_Q were generated using

VPItransmissionMaker™ using its “laserCW” model at a 10-GHz optical simulation bandwidth (10GS/s sample rate). The I and Q signals were 52.4288- μ s long and the AWG repeated them continuously. With this AWG, the V_I and V_Q will be converted to an analog drive signal for the C-MZI. Because the AWG repeats the same sequence periodically (every T_{AWG}), the optical spectrum comprises delta functions spaced at $1/T_{WG}$. However, if the primary laser source’s $\Delta\nu_D$ is significant compared to $1/T_{AWG}$; each delta function will be convolved with this $\Delta\nu_D$, causing the spectrum to be continuous. This produces some phase correlation between the successive periods. However, the correlation will reduce when $T_{AWG}\cdot\Delta\nu \gg 1$. This characteristic must be considered when using the emulator in a system or measurement where a long-scale correlation ($>T_{AWG}$) may be important.

The signals were amplified using Marki Microwave AP-0020E2P 20-GHz bandwidth RF amplifiers. The DC biases (V_a , V_b , shown in Fig. 4.2.2) were adjusted to ensure each MZI was biased at null power and V_c was adjusted so that the upper and lower MZI’s outputs are in quadrature. In the experiment, k was 1.35V and the V_π of the C-MZI was 5.6V.

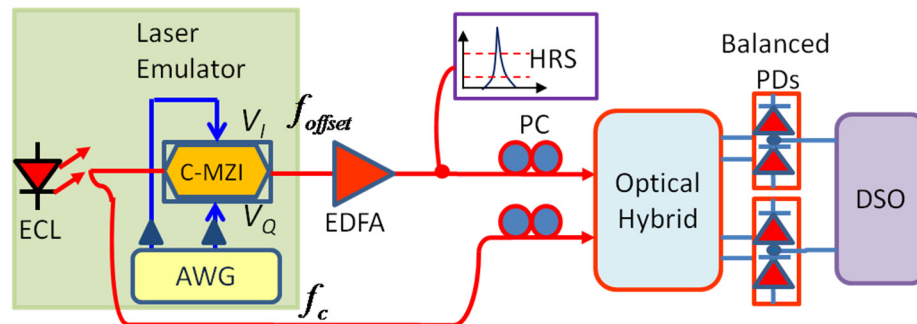


Fig. 4.3.5. Experimental setup including the emulator and linewidth characterization.

To measure the linewidth of the emulator, the output of the C-MZI was amplified to compensate the insertion loss by using a LightWave 2020 Erbium-Doped Fiber Amplifier (EDFA). Two measurement methods were used to measure the laser emulator linewidth. The first method used a self-heterodyne linewidth measurement technique [9, 14]. This is shown by the right-hand side of Fig. 4.3.5. This technique requires a frequency offset, f_{offset} . This will give a double-sided laser spectrum, centered at f_{offset} away from DC [9]. The f_{offset} of 2.5 GHz was generated by multiplying a linearly-increasing phase to the modulating signal, $e^{j\alpha t}$. This is shown by Eq. 4.2.5. The measurement is based on the interference between the two optical fields; the local oscillator (LO) field and the dialled-linewidth laser field, which has

been shifted to f_{offset} from the LO center frequency, f_c [9]. The LO for this emulator setup was taken from the ECL, after a 50/50 coupler. Also, in this setup, the RF amplifiers used at the C-MZI's inputs were DC-blocked amplifier. Hence, the center frequency of the laser linewidth emulator needs to be shifted to avoid the DC-block.

The optical devices used for this technique include: polarization controllers, a Kyria MINT 90° optical hybrid and two U²T 30-GHz balanced PDs. The balanced PDs output signals were the I and Q signal components of the emulator. These signals were pre-amplified with MiniCircuits, ZX60-14012L-st RF amplifiers before being fed into a Tektronix 72004 20-GHz 50-GSa/s digital sampling oscilloscope (DSO). The DSO bandwidth was 16 GHz (hardware mode) to exclude the DSO's DSP noise at the high frequencies. To obtain the PSD of the received waveform, a fast Fourier transform (FFT) was applied to the I waveform. The Q waveform would give an identical result. The received I and Q waveforms on the DSO can be shown as in Fig. 4.3.6.

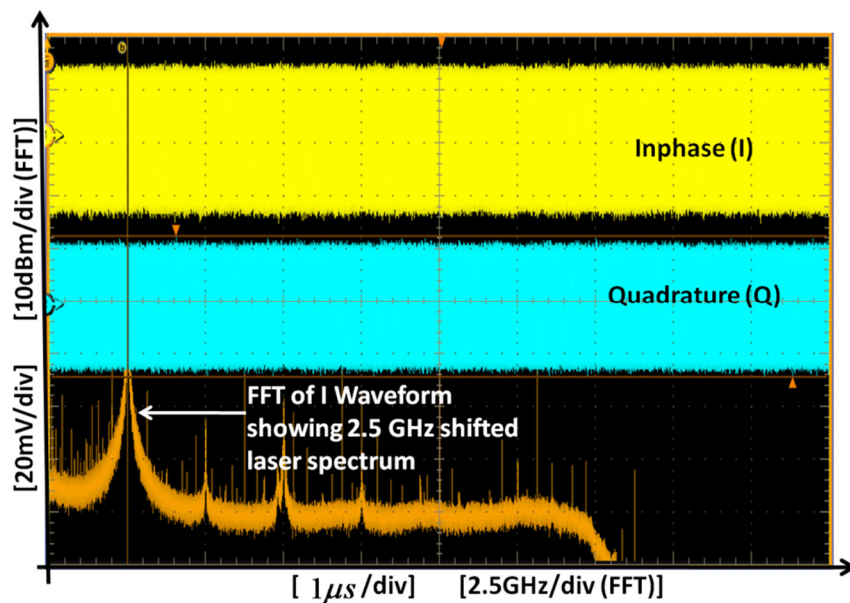


Fig. 4.3.6. Received I and Q waveforms of the laser linewidth emulator measurement using self-heterodyne technique.

As shown in Fig. 4.3.6, the FFT spectrum of the I waveform produced the Lorentzian-shaped spectrum, centered at 2.5 GHz (f_{offset}). By magnifying this spectrum, the FWHM linewidth of the emulator can be measured and calculated by referring to the heterodyne technique relation as follows [9]

Table 4.3.1. Linewidth, $\Delta\nu$ relation of Heterodyne technique [9].

Measured Full-Width Point	Corresponding Width
-3 dB	$\Delta\nu$
-10 dB	$\sqrt{9}\Delta\nu$
-20 dB	$\sqrt{99}\Delta\nu$
-30 dB	$\sqrt{999}\Delta\nu$

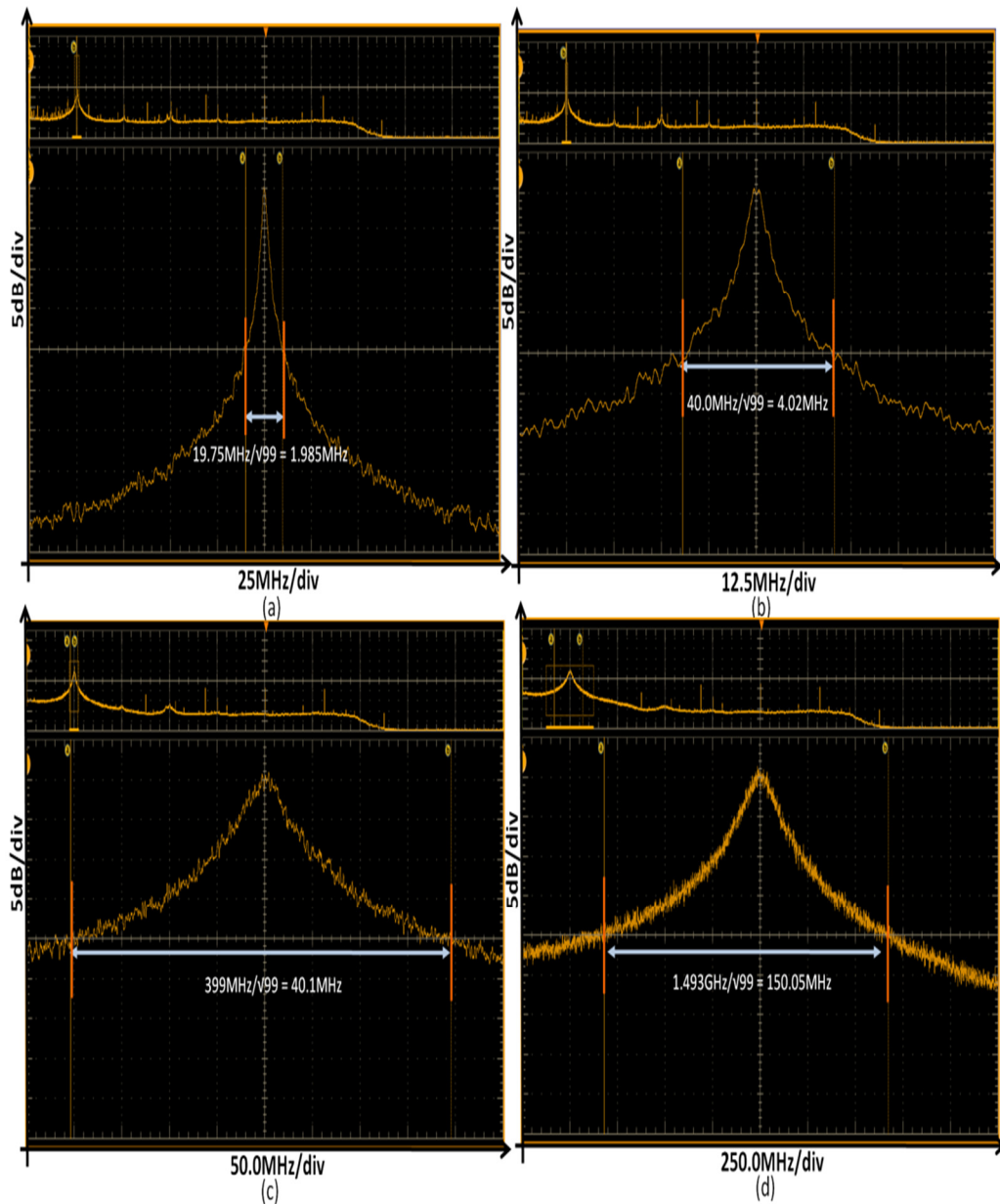


Fig. 4.3.7. 20 dB linewidth measurements using self-heterodyne technique for dialled linewidth of (a) 2 MHz (b) 4 MHz (c) 40 MHz and (d) 150 MHz.

Fig. 4.3.7 shows the measured emulor spectrum with dialled linewidth of (a) 2 MHz, (b) 4 MHz, (c) 40 MHz and (d) 150 MHz. The measured spectra show double-sided Lorentzian spectrum of the laser. The linewidth was measured by taking the

width 20-dB down from the peak power of the spectrum. The linewidth was calculated using $\sqrt{99\Delta\nu}$ relation as shown in Table 4.3.1. The spectra show that the measured linewidth are in good agreement with the dialled linewidth of the emulator. The other measured linewidth with different dialled linewidth are shown in Appendix 2.1.

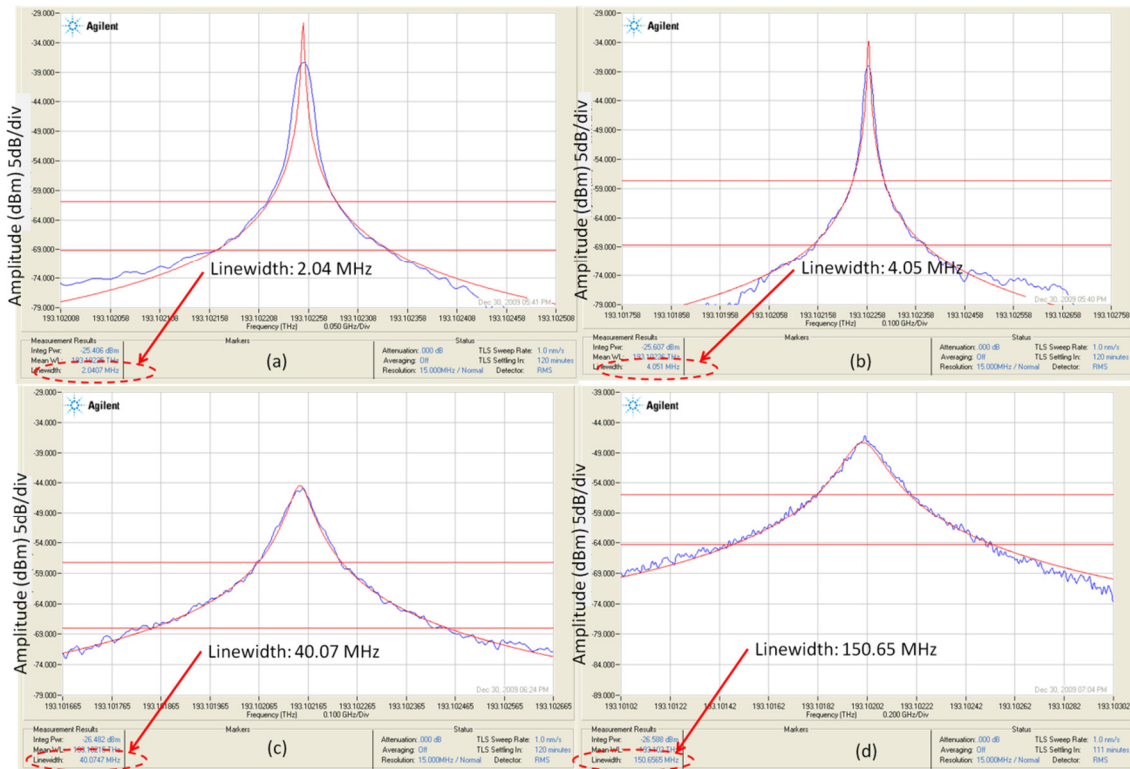


Fig. 4.3.8. HRS linewidth measurement for dialled linewidth of (a) 2MHz (b) 4MHz (c) 40 MHz and (d) 150MHz.

The other linewidth measurement method to use an Agilent High Resolution Spectrophotometer (HRS). The measurement using HRS was taken after the output of the emulator was amplified by an EDFA as shown in Fig. 4.3.5. Fig. 4.3.8 shows the measured linewidth using the HRS for the dialled linewidths of 2 MHz, 4 MHz, 40 MHz and 150 MHz. The HRS fitted a Lorentzian curve to its spectrum, giving linewidth estimations that matched with the dialled linewidth. More of the spectra obtained from the HRS linewidth measurement are shown in Appendix 2.2.

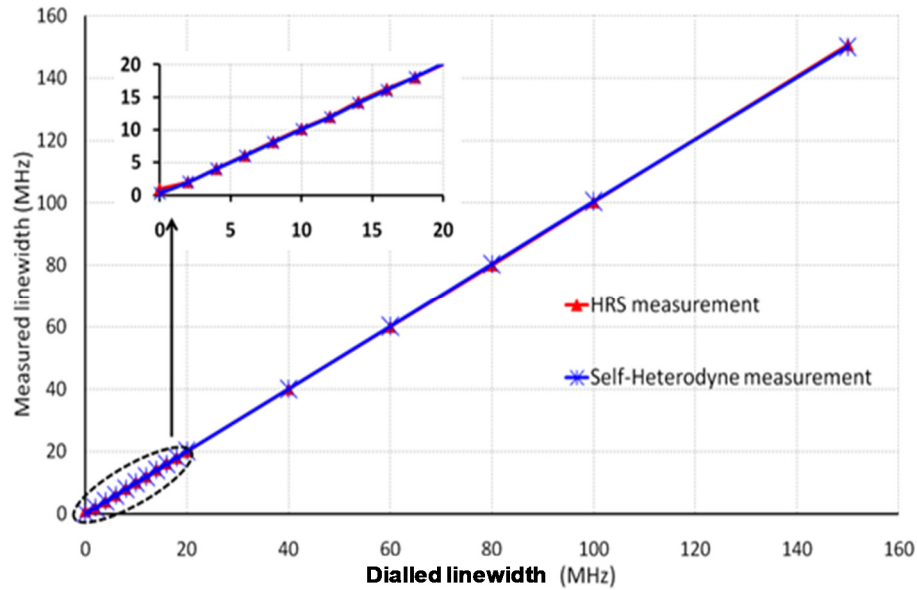


Fig. 4.3.9. Experimental results for the measured linewidth vs. the dialed linewidth.

Fig. 4.3.9 shows the linewidth from the measurement with HRS and the self-heterodyne receiver for various dialed linewidths. The two measurements show that the linewidth follows the desired dialed linewidth accurately over a wide range of linewidths.

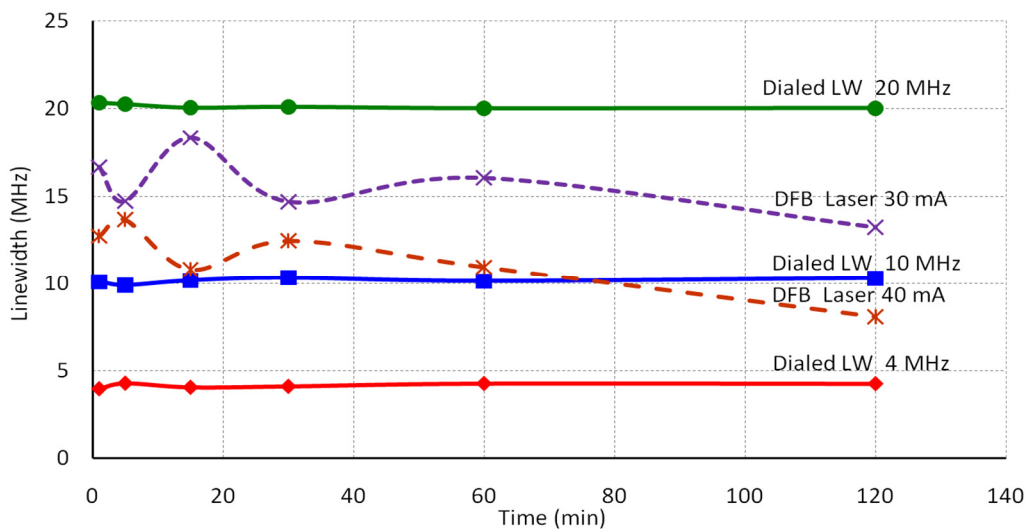


Fig. 4.3.10. Linewidth stability comparison between the dialed $\Delta\nu$ laser and a commercial DFB laser.

Fig. 4.3.10 shows the stability of the laser emulator compared with a commercial DFB laser (FLD5F6CX-E36) operated at 30 mA and 40 mA, measured over 2 hours, using the HRS. The measured linewidth of the DFB laser fluctuates by up to a factor of two, whereas the emulated linewidth laser remains stable over time because it is

generated digitally. This will provide a reliable laser linewidth and increase the accuracy in a system performance evaluation.

4.4 Application to MZI Linearity Measurement

The laser linewidth emulator setup can also be used to measure the linearity of an optical modulator and the phase difference between the inner MZIs. This linearity measurement can also explain the effects of varying k on the phase modulation of the C-MZI in the emulator setup. The theory of the C-MZI linearity measurement can be understood by referring to the Lissajous curve [15]. The simulation setup for this measurement is the same as in Fig. 4.3.1. In order to explain the C-MZI driving voltages according to the Lissajous's conditions, Eq. 7.2.4 is re-written as;

$$V_I = A \sin(\omega t) \quad \text{and} \quad V_Q = B \sin(\omega t + \phi) \quad (4.4.1)$$

where A and B are the drive amplitudes of the V_I and V_Q signals into the RF inputs of the C-MZI, ω is the frequency and ϕ is the phase difference between the top and lower MZI as shown in Fig. 4.3.1. The A and B are denoted by k in the $\Delta\nu$ emulator setup.

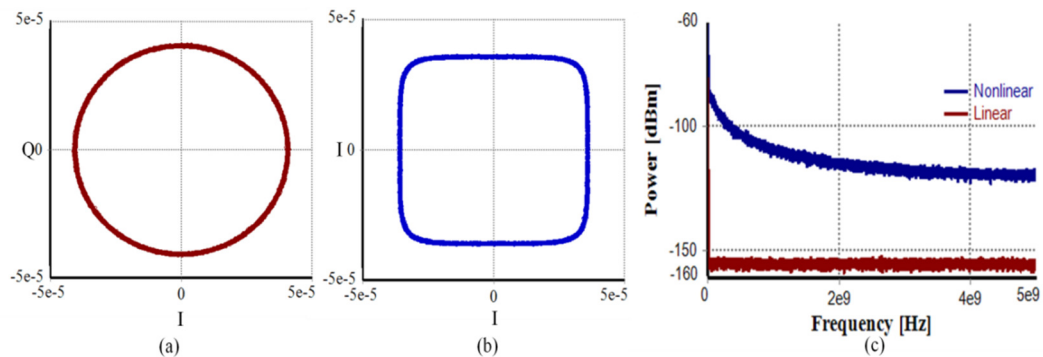


Fig. 4.4.1. Complex-plane (I vs. Q) when driving the modulator in its (a) linear (b) nonlinear regions and (c) RF spectra showing the increase in intensity noise for nonlinear drive.

Fig. 4.4.1 shows the I versus Q plots when the C-MZI was driven in its (a) linear and (b) nonlinear regions. In this simulation, A is equal to B , which denotes by k , which is the amplitude of the V_I and V_Q signals in the emulator setup and ϕ is equal to $\frac{\pi}{2}$, in order to bias the inner MZIs in quadrature. For the linear region, a low drive level was applied ($A = B = k = 0.1 \times V_\pi$); Fig. 4.4.1 (a) shows that there is only phase modulation indicated by a circle in the complex plane. This k and ϕ condition matched with the Lissajous curve theory which also produced a circle plot [15].

When the modulator is driven into its nonlinear region ($A = B = k = V_\pi$), the output amplitude depends on the phase, as indicated by the square shape shown in Fig. 4.4.1 (b). Fig. 4.4.1 (c) shows the RF spectrum of the modulator's output for linear and nonlinear drive levels. This shows that driving the modulator into the nonlinear region causes a large increase in the intensity noise of the laser linewidth emulator. This would itself affect the performance of most systems when they are tested using the emulator.

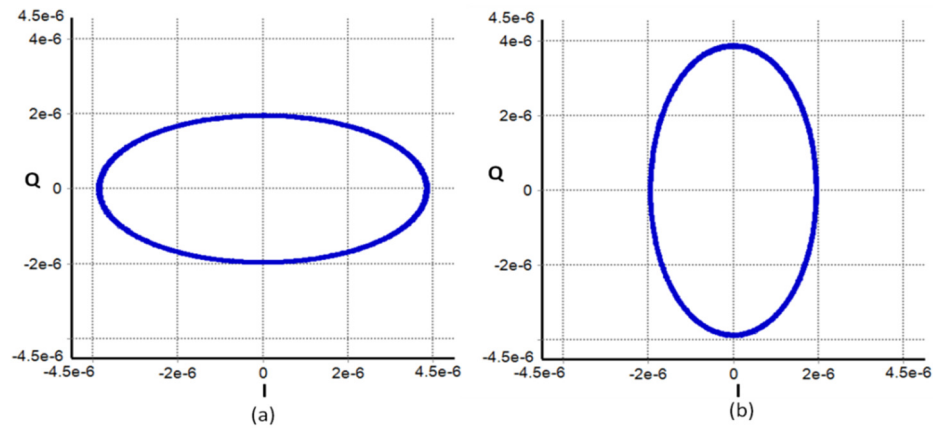


Fig. 4.4.2. Complex-plane of Q vs. I plots when (a) $A > B$ and (b) $A < B$ with $\phi = \frac{\pi}{2}$.

Fig. 4.4.2 shows the Q vs. I plots for $\phi = \frac{\pi}{2}$ with (a) A is greater than B ($A = 2B$) and (b) when A is smaller than B . This also represents that the top MZI is driven with a higher driving voltage compared to the lower MZI. With these conditions, the plot is no longer a circle but produces an ellipse shape. When the lower MZI is driven with a higher driving voltage ($A < B$) where in this simulated result, $B = 2A$, the plot will also produce an ellipse shape but with the largest diameter aligned to the Q-axis. This shows that there is some power imbalance between the top and lower MZIs, or one MZI is experiencing a higher loss than the other.

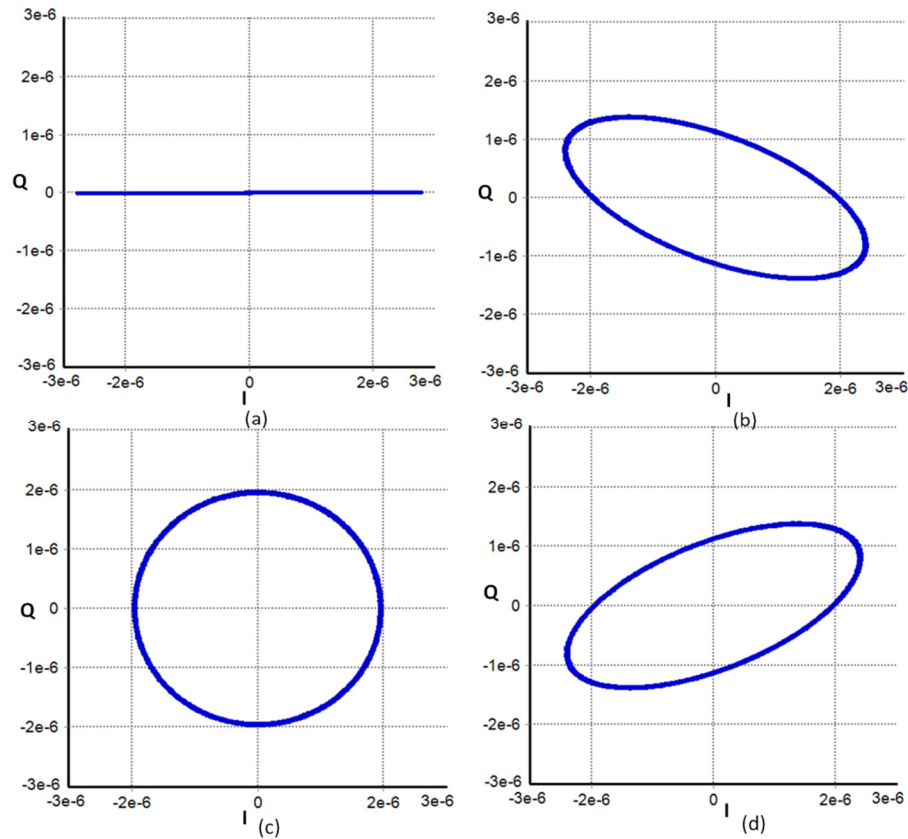


Fig. 4.4.3. I vs. Q plots of the C-MZI's output when the RF inputs were driven with $A = B = k$ for ϕ of (a) 0° (in phase) (b) 45° (c) 90° (in quadrature) and (d) 135° .

Fig. 4.4.3 shows the resulting I vs. Q plots when the ϕ between the top and lower MZIs was varied with: (a) 0° when both MZIs were in phase, (b) 45° , (c) 90° when both MZIs were in quadrature and (d) 135° . This shows that the ϕ between the inner MZIs can also be measured using this technique. The applied driving magnitudes were $A = B = k = 0.1 \times V_\pi$. These plots can be used to measure the ϕ of the C-MZI and to tune the V_c so that the inner MZIs' output signals are combined in quadrature.

The linearity measurement of the Sumitomo T-SBXI.5-20P 40-Gbit/s C-MZI can be achieved using the same linewidth emulator setup as Fig. 4.3.5. To obtain the plot in a complex-plane, the DSO ran in the X-Y mode with both of the I and Q signals detected from the balanced receiver connected to the DSO's inputs.

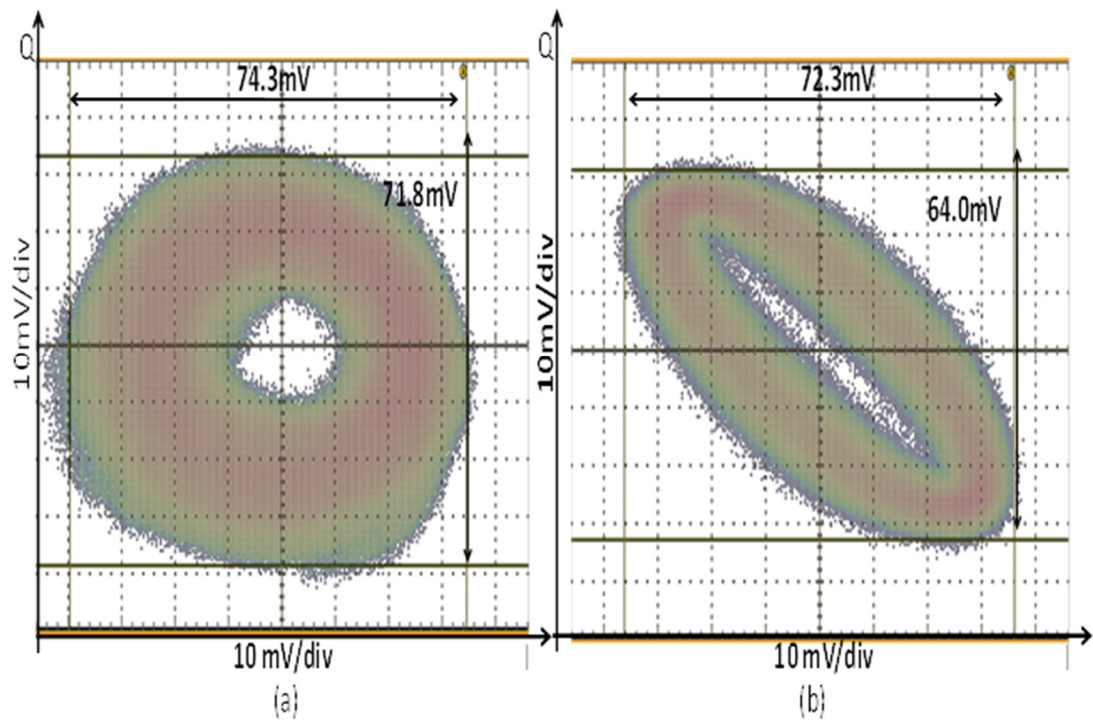


Fig. 4.4.4. Q vs. I plots measured using DSO when the V_c of the C-MZI was (a) 3.50V (in quadrature) and (b) 2.5V.

Fig. 4.4.4 shows the Q vs. I plot measured using a DSO running in X-Y mode when the V_c driving the C-MZI was (a) 3.5V and (b) 2.5V. The X and Y input signals into the DSO were the I and Q components of the C-MZI's output signal, respectively. The I and Q signals were obtained using the self-heterodyne coherent receiver with the signals' peak-to-peak voltage, V_{pp} of 522 mV. Fig. 4.4.4 (a) shows that the V_c driving the C-MZI was set to combine the inner MZIs' signals in quadrature. This is shown by the round circle plot of the signal. Fig. 4.4.4 (b) shows a tilted ellipse shape of Q vs. I. This shows that the inner MZIs were not in quadrature. With this plot, the driving V_c can be tuned in order to achieve the circle shape plot. Fig. 4.4.4 also satisfied the simulated results to measure the ϕ between the inner MZIs.

In order to measure the linearity of the C-MZI, the experimental setup requires the RF components that can amplify high peak-to-peak voltages (V_{pp}). This is to prevent power clipping due to the components from influencing the Q vs. I plot, when the V_a and V_b are increased. The V_a and V_b are increased until the C-MZI is operated in the nonlinearity part of its transfer curve. The V_{pp} limitation of the RF components can be investigated using a back-to-back electrical measurement. The back-to-back measurement also included Marki Microwave AP-0020EZP 20-GHz RF amplifiers

and the combination of attenuators to increase and decrease the power. Since the RF amplifiers used were DC-blocked, a 1-GHz frequency shift was imposed into the digital phase modulation signal.

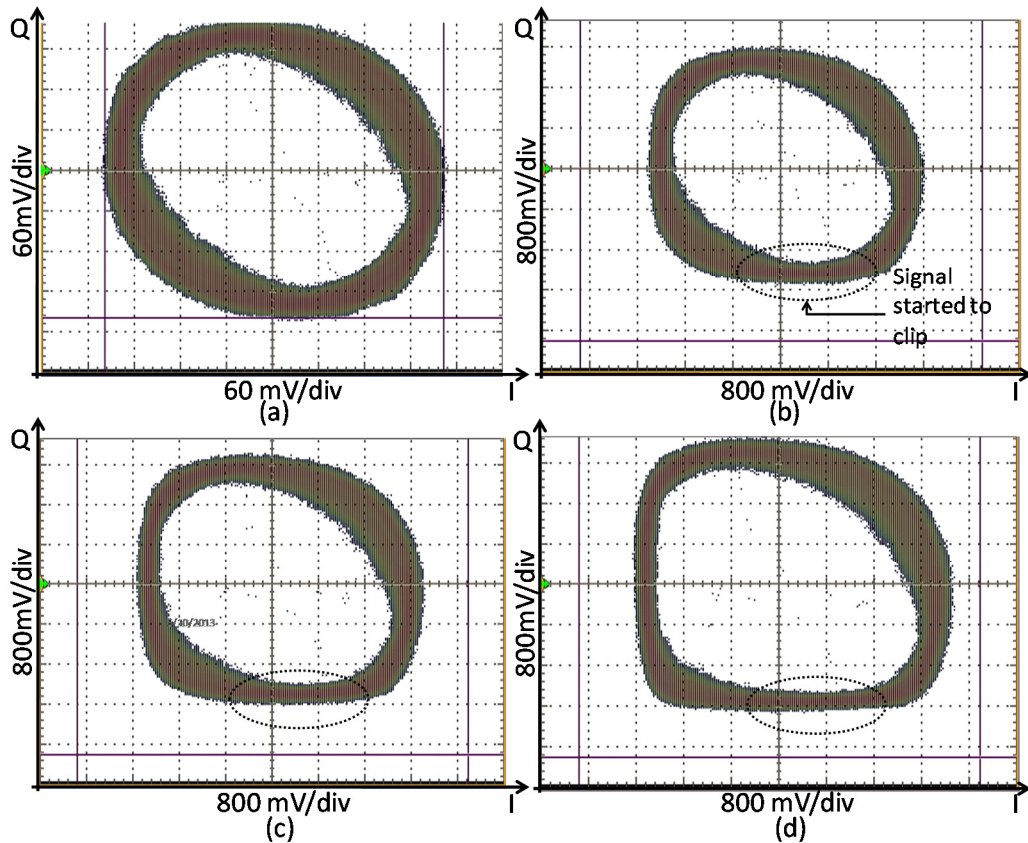


Fig. 4.4.5. Q vs. I plots of back-to-back electrical measurement from the AWG's outputs into the DSO with RF amplifiers and attenuators with the signal's measured V_p of (a) 258 mV (b) 2.3 V (c) 2.45 V and (d) 2.7 V.

Fig. 4.4.5 shows the Q vs. I plots measured for the back-to-back electrical measurement from AWG's outputs into the triggered DSO. Fig. 4.4.5 (a) shows the plot when the RF signals' peak voltage, V_p , into the DSO was 258mV. The plot shows a wide-open ellipse with small tilt. A perfect circle was not achieved due to the delay between the cable connections into the DSO that can introduce some phase shift to the plotted signal. To increase the RF signal power, the attenuators were removed to produce an increase of power. Fig. 4.4.5 (b) shows that the signal plot began to clip for the V_p of 2.3 V. The clipping on the Q vs. I plot became severe and produced a square-edge plot when the V_{pp} was increased to 2.45 V and 2.7 V shown as in Fig. 4.4.5 (c) and (d), respectively. With this RF component's limitation, an accurate C-MZI linearity measurement could not be done since the power clipping will influence

the measurements. This is because the RF limitations were much smaller than the V_π which is the half-wave voltage of the under-measurement C-MZI of 5.6 V.

4.5 Conclusions

A laser with a linewidth dial-able over a range of 256 kHz to 150 MHz was developed and demonstrated. This was done by phase modulating the laser's output signal using a complex modulator with a digitally generated phase-modulation signal. A stable dialled linewidth over several hours was achieved, since it is generated digitally. This emulator can be used in systems to investigate the effects of linewidth on the system performance. For successful operation, a source with low IN and narrow linewidth should be chosen. The complex modulator should be driven in its linear region otherwise IN will be added. The specifications of the RF components in terms of operating frequency range and power limitation should be indentified in order to consider the emulator design with frequency shifting. In the application of MZI linearity measurement, the operating power limitation of the RF components should be identified in order to have an accurate measurement of the biasing amplitude when the MZI begins to enter its nonlinear region.

4.6 References

1. Zan, Z. and A.J. Lowery, *Experimental demonstration of a flexible and stable semiconductor laser linewidth emulator*. Opt. Express, 2010. **18**(13): p. 13880-13885.
2. Morgado, J.A.P. and A.V.T. Cartaxo, *Assessment of laser noise influence on direct-detection transmission system performance*. Journal of Lightwave Technology, 2003. **21**(3): p. 759-768.
3. Marshall, W.K., B. Crosignani, and A. Yariv, *Laser phase noise to intensity noise conversion by lowest-order group velocity dispersion in optical fiber: exact theory*. Optics Express, 2000. **23**(3): p. 165-167.
4. Laurêncio, P., S.O. Simões, and M.C.R. Medeiros, *Impact of the Combined Effect of RIN and Intermodulation Distortion on OSSB/SCM Systems*. J. Lightwave Technol., 2006. **24**(11): p. 4250-4262.
5. Ahmed, M. and M. Yamada, *Effect of intensity noise of semiconductor lasers on the digital modulation characteristics and the bit error rate of optical communication systems*. Journal of Applied Physics, 2008. **104**.
6. Henry, C.H., *Theory of the linewidth of semiconductor lasers*. IEEE Journal of Quantum Electronics, 1982. **QE-18**(2): p. 259-264.
7. Fleming, M.W. and A. Mooradian, *Fundamental line broadening of single-mode (GaAl) As diode lasers*. Applied Physics Letters, 1981. **38**: p. 511.
8. Kazovsky, L., S. Benedetto, and A. Willner, *Optical fiber communication systems*. 1st ed. 1996, Norwood: Artech House, Inc. 690.

-
9. Derickson, D., ed. *Fiber Optic Test and Measurement*. 1998, Prentice Hall: New Jersey.
 10. Lax, M., *Classical Noise. V. Noise in Self-Sustained Oscillators*. *Physical Review*, 1967. **160**(2): p. 290-306.
 11. Haug, H., *Quantum-Mechanical Rate Equations for Semiconductor Lasers*. *Physical Review*, 1969. **184**(2): p. 338.
 12. McCumber, D.E., *Intensity Fluctuations in the Output of cw Laser Oscillators. I*. *Physical Review*, 1966. **141**(1): p. 306.
 13. Yamamoto, Y., *AM and FM quantum noise in semiconductor lasers--Part I: Theoretical analysis*. *Quantum Electronics, IEEE Journal of*, 1983. **19**(1): p. 34-46.
 14. Schmidt, B.J.C., et al., *120 Gbit/s over 500-km using single-band polarization-multiplexed self-coherent optical OFDM*. *Journal of Lightwave Technology*, 2010. **28**(4): p. 328-335.
 15. Maor, E., *Trigonometric delights*. 2002: Princeton University Press.

Chapter 5

INTERACTION OF LASER NOISE WITH MODULATED RF TONES AND FIBRE DISPERSION

5.1 Introduction

It is known that an O-OFDM system uses many subcarriers to transmit its data. In order to investigate the effects of laser noise on these subcarriers, studies using simple transmission of a single tone, and then several RF tones, provide a better understanding on how the laser noise affects the OFDM subcarriers. In this chapter, the effect of the laser noise when the laser is externally modulated with RF tones and fed through a dispersive fibre will be explained. Independent effects of RIN and linewidth are investigated using VPItransmissionMakerTM simulations. The interactions of interdependent RIN and linewidth is shown using experimental measurements. Section 5.2 explains the investigation hypothesis of the laser linewidth interaction with a chromatic dispersion with and without externally modulated RF tones. Section 5.3 presents the theory of the PM-to-IM conversion noise. In this section, the derivation of an intensity noise bound due to the conversion of phase noise to intensity noise is presented and evaluated using MATLAB. In Section 5.4, measurements of the laser's PM-to-IM conversion noise is performed. Section 5.5 explains the group delay effect, when the RF tones originated from a wide linewidth laser are transmitted over dispersive fibre. The interaction of the PM-to-IM conversion noise with de-correlated RF tones is presented in Section 5.6, where the effect is shown using simulations and experiments. Finally, Section 5.7 concludes this chapter and references is listed in Section 5.8.

5.2 Laser Linewidth Interaction with Fibre Dispersion and Modulating RF Tones

In direct-detection optical communication system, the laser phase noise can indirectly reduce the SNR by adding intensity noise after photodetection [1-5]. This is because the phase noise is converted into intensity noise by chromatic dispersion (CD) in fibre. As a result, the received noise is increased and degrades the receiver's sensitivity. Higher OSNR was required for a system with a dispersive fibre than without, in order to achieve a minimum BER of 1×10^{-9} as reported in [1-6]. For example, 9-dB more

OSNR was required for a transmission over 255-km of dispersive fibre with laser phase noise [3]. RIN also degrades the BER performance [7-10]. In addition to the CD, the laser linewidth limitation to system performance also depends on the signal modulation type and the order of the modulation used at the transmitter [11-13]. For example, the OSNR degradation of 16-QAM is 10-dB higher than a BPSK modulation format due to its higher number of bits per symbol [11, 14]. The phase noise degrades the performance of this system since the Euclidean distance between the symbols of this modulation format is smaller and more phase levels is used. Due to this, the system is more susceptible to the phase error since the phase distance between the symbols becomes smaller [14].

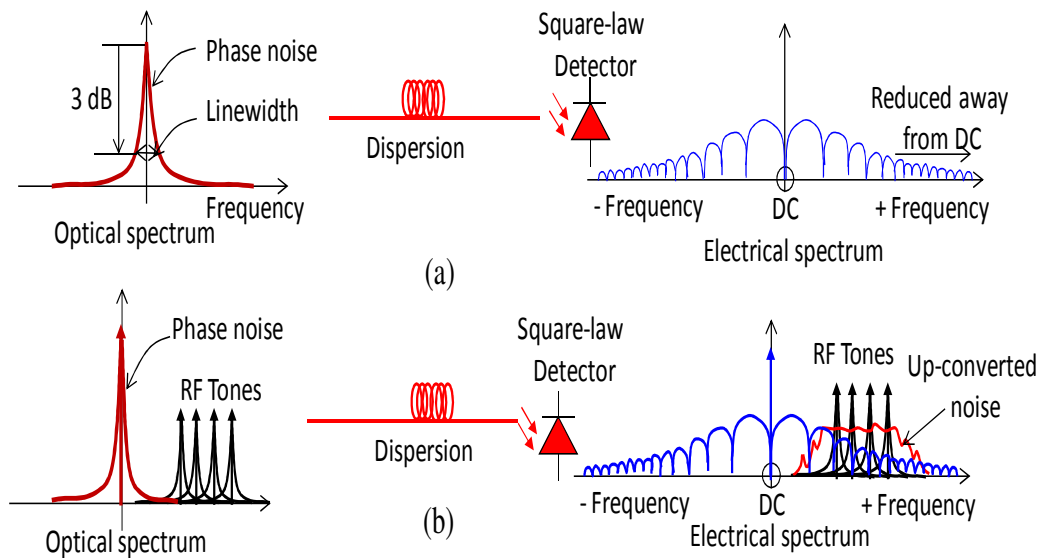


Fig. 5.2.1. Investigation of the laser phase noise interaction with dispersion using the transmission of (a) laser carrier only and (b) carrier with modulating RF tones.

Fig. 5.2.1 illustrates the investigation hypothesis for the laser phase noise interaction with CD when (a) only the laser carrier and (b) laser with modulating RF tones are transmitted over the fibre. The amount of laser phase noise can be defined by the FWHM linewidth since it is directly related to the laser phase noise [15]. The phase modulation-to-intensity modulation (PM-to-IM) conversion noise has been studied analytically by Yamamoto et al. [5], which has been explained in Chapter 2. The resulting electrical spectrum at the receiver is illustrated in Fig. 5.2.1 (a), where spectrum with sidelobes due to phase noise to intensity noise conversion in the fibre is shown. Fig. 5.2.1 (b) illustrates the hypothesis when the laser with wide linewidth is modulated with the RF tones. This is important in order to examine whether the laser's noise could increase the noise floor of the signal band, which can reduce the system's

receiver sensitivity and to determine the noise governed underneath each of the tone due this noise interaction. The figure also shows the up-converted noise tone around the RF tones, which is due to the interaction between the adjacent tones upon photodetection.

5.3 Theoretical of the PM-to-IM Conversion Noise

An analytical model of the conversion noise can be formulated by approximating the phase noise of a laser's optical to a summation of sinusoids using a Fourier series [16]. The optical field is then expanded to a Bessel function in order to represent the amplitudes of the sidebands or the harmonics and the frequency spacing of the sidebands at both positive and negative sides of the spectrum [5, 16]. This can be regarded as Bessel expansion for a frequency modulated (FM) signal. To plot the noise PSD, the analytical equation of the PM-to-IM conversion noise presented in [5] is rewritten for convenience;

$$\begin{aligned}
 N(f) &= \frac{1}{2} \delta I(f)^2 \\
 &\approx \frac{1}{2} \left[\sum_{n=0}^{\infty} 4J_n \left(\frac{1}{f} \sqrt{\frac{2\Delta\nu}{\pi}} \right) J_{n+1} \left(\frac{1}{f} \sqrt{\frac{2\Delta\nu}{\pi}} \right) \right. \\
 &\quad \left. \cdot \sin \left(\frac{1}{2} (2n+1) \ddot{\beta} (2\pi f)^2 z \right) \right]^2
 \end{aligned} \tag{5.3.1}$$

where $N(f)$ is the noise PSD after the photodetection in dBW, J_n is Bessel function of a first kind, $\Delta\nu$ is the laser linewidth, $\ddot{\beta}$ is the second derivative of the propagation constant and z is the fiber length. To plot $N(f)$, direct relation between $\ddot{\beta}$ and dispersion used

$$\ddot{\beta} = \frac{\lambda^2}{2\pi c} D \tag{5.3.2}$$

where c is 3×10^8 m/s speed of light, λ is taken as 1536 nm and D is the dispersion of the fiber taken as 16.67 ps/nm-km standard-single mode fibre (S-SMF). Substituting Eq. 5.3.2 into 5.3.1, the $N(f)$ can be written as follows;

$$N(f) = \frac{1}{2} \left[\sum_{n=0}^{\infty} 4J_n \left(\frac{1}{f} \sqrt{\frac{2\Delta\nu}{\pi}} \right) J_{n+1} \left(\frac{1}{f} \sqrt{\frac{2\Delta\nu}{\pi}} \right) \right]^2$$

$$\cdot \sin \frac{1}{2} (2n+1) (2\pi c) D \cdot z \Big]^2 \quad (5.3.3)$$

where z is in metres (m), D in s/m^2 and $\lambda=c/f$ is used during the substitution in the equation. Using this equation, $N(f)$ can be plotted as in Fig. 2.5.3 using MATLAB where maximum number of Bessel terms was 20.

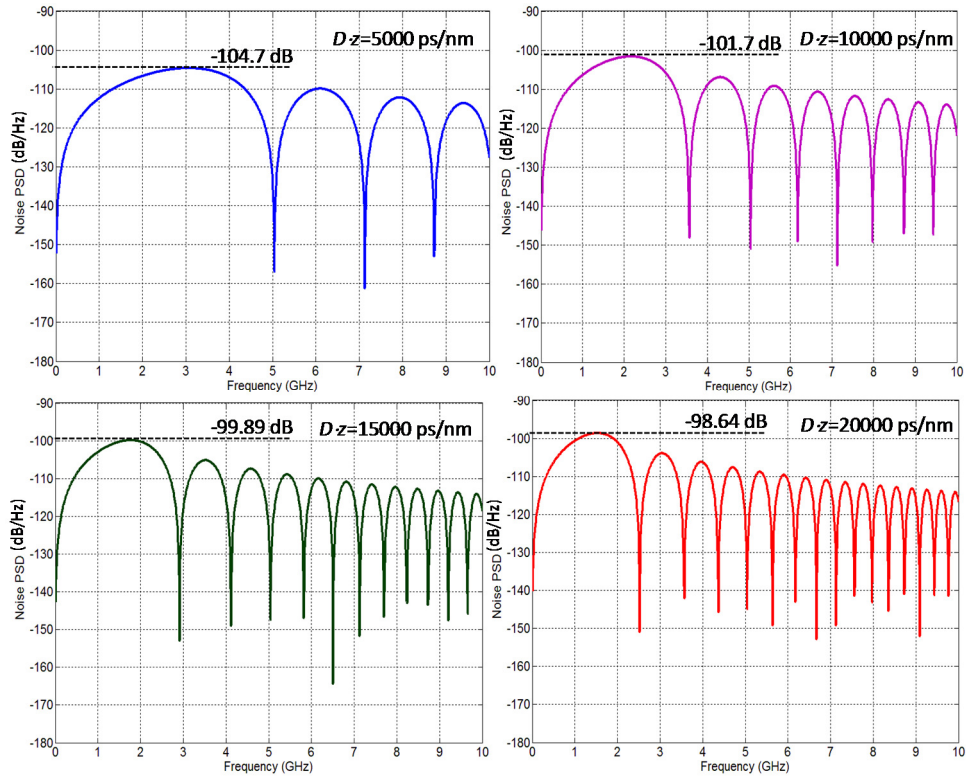


Fig 5.3.1. PM-to-IM conversion noise PSD of 5,000-, 10,000-, 15,000- and 20,000 ps/nm dispersion-length products for linewidth of 300 MHz.

Fig. 5.3.1 shows the noise power spectral density (PSD) upon the detection of an optical signal after dispersion-length products ($D \cdot z$) of 5,000, 10,000 and 20,000 ps/nm with linewidth, $\Delta\nu$ taken as 300 MHz to match the plots in Fig. 2.5.3 reported in [5]. The comparison shows that the plotted PSDs matched the PSDs in Fig 2.5.3. It shows that the noise power level is increased with longer fibres, shown by the peak power of the first side-lobe, where for a dispersion of 16.67 ps/(nm·km), $D \cdot z$ of 5,000 ps/nm is equivalent to 300 km fibre length, 10,000 ps/nm to 600 km, 15,000 ps/nm to 900 km and 20,000 ps/nm to 1200 km. The first null of the side-lobes plotted in this figure also satisfied the PSDs shown in Fig. 2.5.3, where the frequency of the first null is [5]

$$\begin{aligned}
 f_0 &= \sqrt{\frac{1}{2\pi\beta \cdot z}} \\
 &= \sqrt{\frac{c}{\lambda^2 D \cdot z}}
 \end{aligned}
 \tag{5.3.4}$$

With this equation, the calculated f_0 is 5.04 GHz for 5,000 ps/nm, 3.57 GHz for 10,000 ps/nm, 2.91 GHz for 15,000 ps/nm and 2.52 GHz for 20,000 ps/nm where λ taken as 1.536 μm at which the dispersion coefficient is calculated. Again, these f_0 values matched the plotted noise PSD of Fig. 2.5.3.

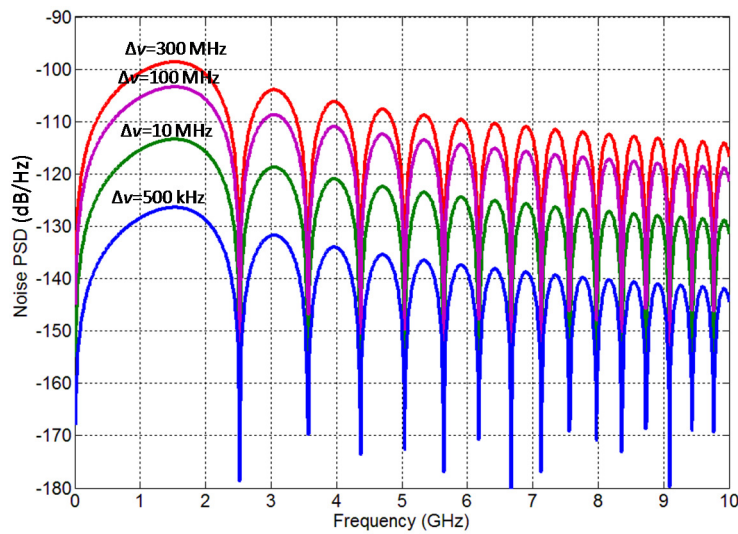


Fig. 5.3.2. Amplitude noise of the PM-to-IM conversion noise is increased with the increase of linewidth, $\Delta\nu$.

Fig. 5.3.2 shows the calculated noise PSD plots with fiber length of 1200 km ($D \cdot z$ of 20,000 ps/nm) when the linewidth was taken as 500 kHz, 10 MHz, 100 MHz and 300 MHz. The plots show that the intensity noise power level is increased when wider linewidth was used over the same dispersive fibre length. The noise power scales to 1:1 with the increase of the linewidth. These values agree with Fig. 2.5.3 in Reference [5]. A typical value of $\Delta\nu$ for a commercial distributed feedback (DFB) is around 10 MHz, compared with hundreds of kilo-hertz of an external cavity laser (ECL) [15, 17]. In order to find the noise floor of the PM-to-IM conversion noise, an upper intensity noise bound plotted at the peak amplitudes of the sidelobes in the noise PSD is obtained. This was not presented by Yamamoto in his analysis [5]. In order to obtain the upper noise bound over the bandwidth, a Bessel function of first kind of order n in the envelope is

considered to represent the sine function in Eq. 5.3.3. The envelope of Eq. 5.3.3 can be written as

$$E(f) = \frac{1}{2} \left(\sum_{n=0}^{\infty} 4J_n \left(\frac{1}{f} \sqrt{\frac{2\Delta\nu}{\pi}} \right) J_{n+1} \left(\frac{1}{f} \sqrt{\frac{2\Delta\nu}{\pi}} \right) \right)^2 \quad (5.3.5)$$

The Bessel function is defined as

$$J_n(x) = x^n \sum_{m=0}^{\infty} \frac{(-1)^m x^{2m}}{2^{2m+n} m! \Gamma(n+m+1)} \quad (5.3.6)$$

However, the Bessel function decays rapidly with n , so

$$E(f) \approx 8 \left(J_0 \left(\frac{1}{f} \sqrt{\frac{2\Delta\nu}{\pi}} \right) J_1 \left(\frac{1}{f} \sqrt{\frac{2\Delta\nu}{\pi}} \right) \right)^2 \quad (5.3.7)$$

The small argument approximation for Bessel function from [5] is as follows. This is done by taking $m = 0$ in Eq. 5.3.7.

$$J_n(x) = \frac{x^n}{2^n \Gamma(n+1)} \quad (5.3.8)$$

Where $\Gamma(\bullet)$ is the Gamma function. Using this in Eq. 5.3.6, the upper bound of the intensity noise is found.

$$\begin{aligned} E(f) &\approx 2 \left(\left(\frac{1}{f} \sqrt{\frac{2\Delta\nu}{\pi}} \right) \right)^2 \\ &\approx \frac{4\Delta\nu}{f^2 \pi} \end{aligned} \quad (5.3.9)$$

Fig. 5.3.3 of Eq. 5.3.3 and 5.3.9 confirms the accuracy in predicting the upper bound.

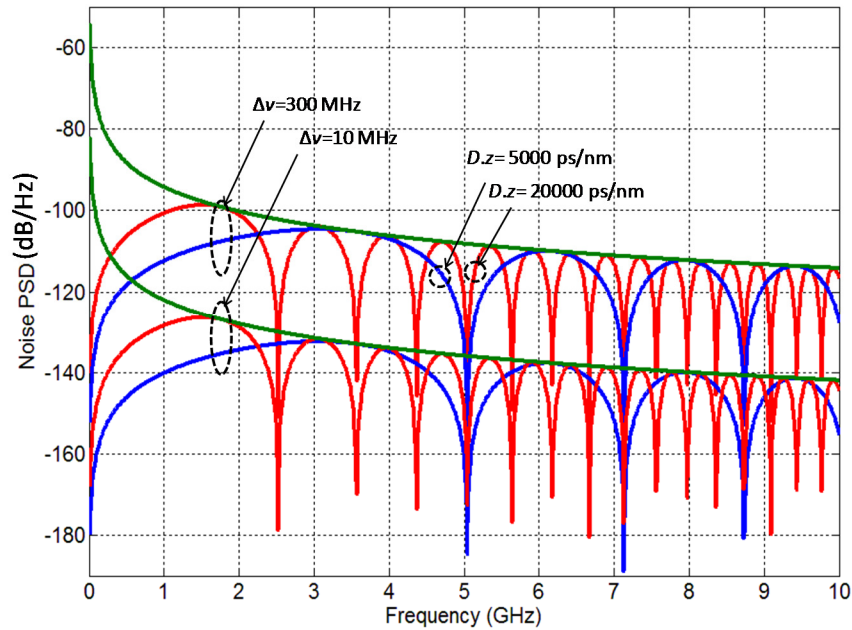


Fig. 5.3.3. The intensity noise power due to laser phase noise conversion into intensity across the bandwidth.

Fig. 5.3.3 shows the plotted boundary achieved using Eq. 5.3.9 with its respected PM-to-IM conversion noise PSDs plotted along to show the accuracy of the equation. The bound of the intensity noise power represent the upper-bound of the noise floor across the bandwidth after an optical signal is detected by a photodiode. The plots show that with the same linewidth, the bounds works for various dispersion-length products. This noise floor will be added into other intensity noise upon photodetection such as the laser's RIN, shot and thermal noise of the receiver, intensity noise due to beating of signal with amplified spontaneous emission (signal \times ASE) and ASE with itself (ASE \times ASE). Without dispersive fibre in a system, no noise conversion from phase to intensity occurred, where only the laser's RIN is presented. This is due to the interdependence between the noise characteristics of a laser. For example, phase fluctuations, which present the linewidth are also accompanied by the intensity fluctuations that represent the intensity noise. This can be illustrated using a complex field as explained by Henry (1982) [18]. A flat PSD without any sidelobes and nulls will be seen at the laser.

5.4 Experiment of PM-to-IM Conversion Noise

In this experiment, a commercial DFB laser was used to show the interaction of the linewidth with fibre dispersion, which produced the spectrum with the sidelobes of the PM-to-IM conversion noise. The linewidth of the laser was varied by tuning the

supplied biasing current, I_b . This, however, will also introduce the laser RIN due to the interdependence among the laser's characteristics as discussed in Chapter 3. Nevertheless, the RIN can be neglected if I_b is far beyond the laser's I_{Th} [15]. At this point, the PSD of the PM-to-IM conversion noise will dominate the receiver's electrical spectrum.

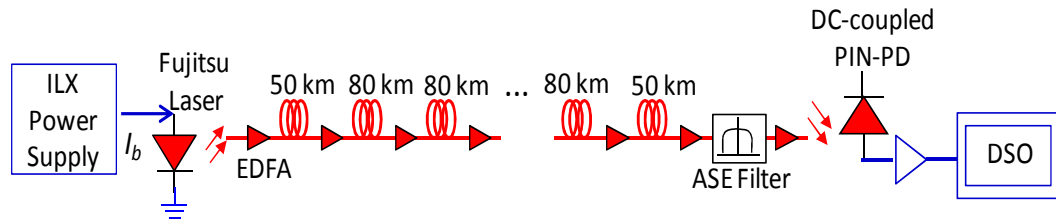


Fig. 5.4.1. PM-to-IM conversion noise PSD measurement setup.

Fig. 5.4.1 shows the PM-to-IM conversion noise measurement setup. To measure the PSD of the conversion noise, a Fujitsu DFB laser FLD5F6CX-E36, driven with a ILX LDM 4616 power supply was used. The measurement setup shows the transmission of the laser output into a 500-km system with 80-km fiber spans and 50-km spans at both start and end of fiber. A Finisar Waveshaper was set with a 3-pixel passband at a center frequency of 192.55 THz where the pixel size is 7.5 GHz giving a 22.5 GHz filter bandwidth to limit the ASE noise. The PM-to-IM conversion noise was also measured for 130 km transmission length. A wide bandwidth DC-coupled Discovery DSC40S PIN PD with a minimum bandwidth of 14 GHz was used as the receiver. The received RF spectrum was captured with a Tektronix 72004 20-GHz 50-GSa/s digital sampling oscilloscope (DSO). The DSO bandwidth was set to 16 GHz hardware.

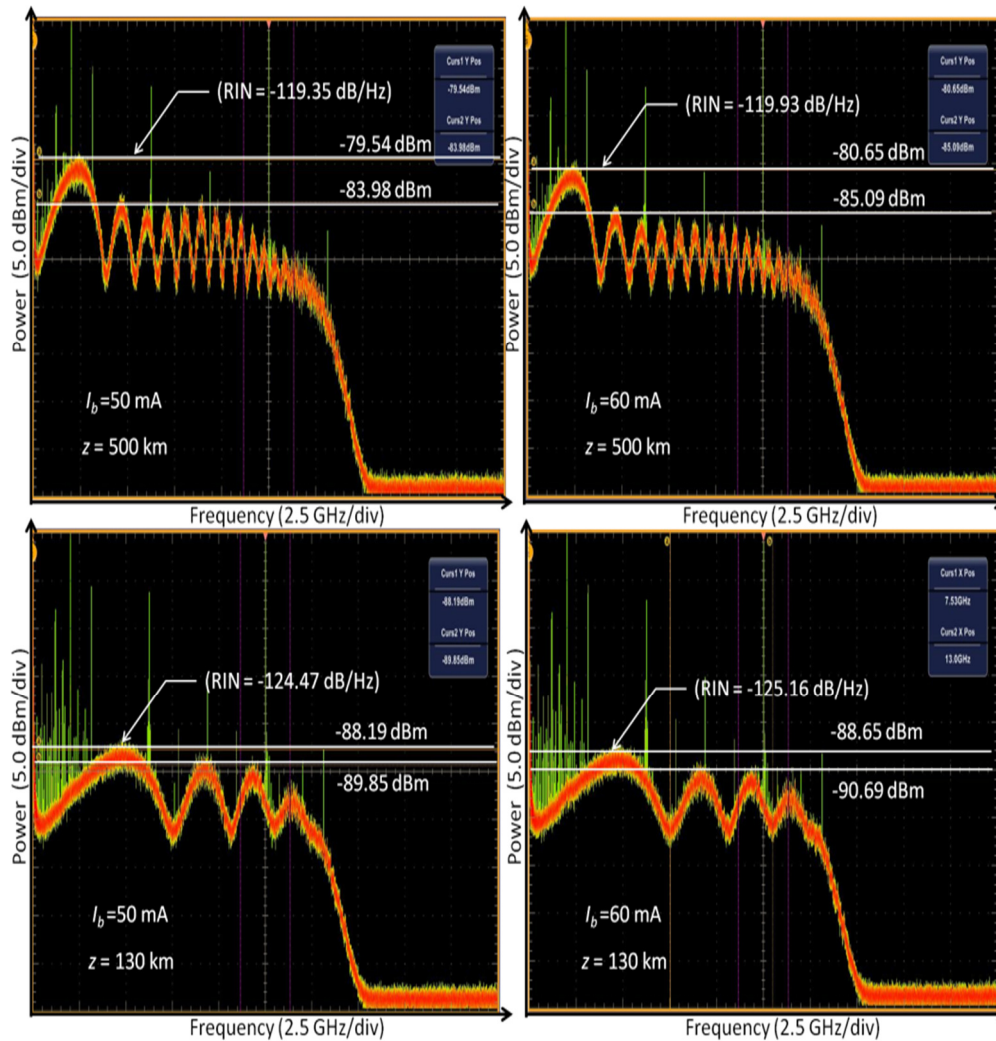


Fig. 5.4.2. Measured RF spectrum showing PM-to-IM conversion noise.

Fig. 5.4.2 shows the received RF spectrum when an optical signal was propagated over 500- and 130-km of fiber which equal to 8335- and 2167 ps/nm of $D \cdot z$. The DFB laser was driven by I_b of 50 and 60 mA. At this I_b , the linewidth measured was 10 MHz for 50 mA and 8.09 MHz for 60 mA. The measured RIN is calculated using Eq. 3.3.2 for the peak of the first sidelobe. It shows that for the increase of I_b , which also signified the decrease of linewidth of the laser, the RIN is decreased. The RIN is also decreased with reduced dispersion or a shorter fibre length. The amplitude of the PSD is increased with the increased of linewidth. For the amount of $D \cdot z$ and the laser's linewidth used, the frequency of the first null of the sidelobes, f_0 , agreed with Eq. 5.3.4. For fibre length of 500 km, f_0 recorded for I_b of 50 and 60 mA was 3.88 GHz and for fiber length of 130 km, the f_0 was 7.55 GHz I_b of 50 and 60 mA.

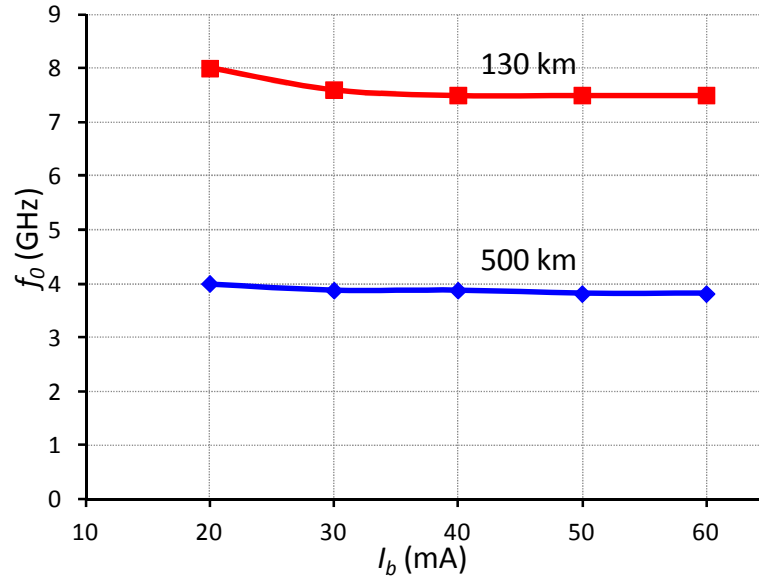


Fig. 5.4.3. Measured f_0 vs. laser's I_b after a transmission over 130- and 500-km of S-SMF.

Fig. 5.4.3 shows the first sidelobe's frequency-null, f_0 , obtained from the measured spectra of the PM-to-IM conversion noise versus laser biasing current, I_b of the laser after a transmission over 130- and 500-km of S-SMF. As expected, the plots show that with the f_0 of the PM-to-IM conversion noise remains nearly constant with the increase of the I_b . The increase of the I_b also represents the narrowing of the laser's linewidth. Hence, with the dispersion, the f_0 is not influenced by the changes of the laser linewidth. Note that, at the low I_b of 20 mA, the f_0 is slightly larger than for the high I_b . This is because the spectrum at low I_b is dominated by the RIN of the laser, where the first sidelobe lies within the laser's RIN resonance.

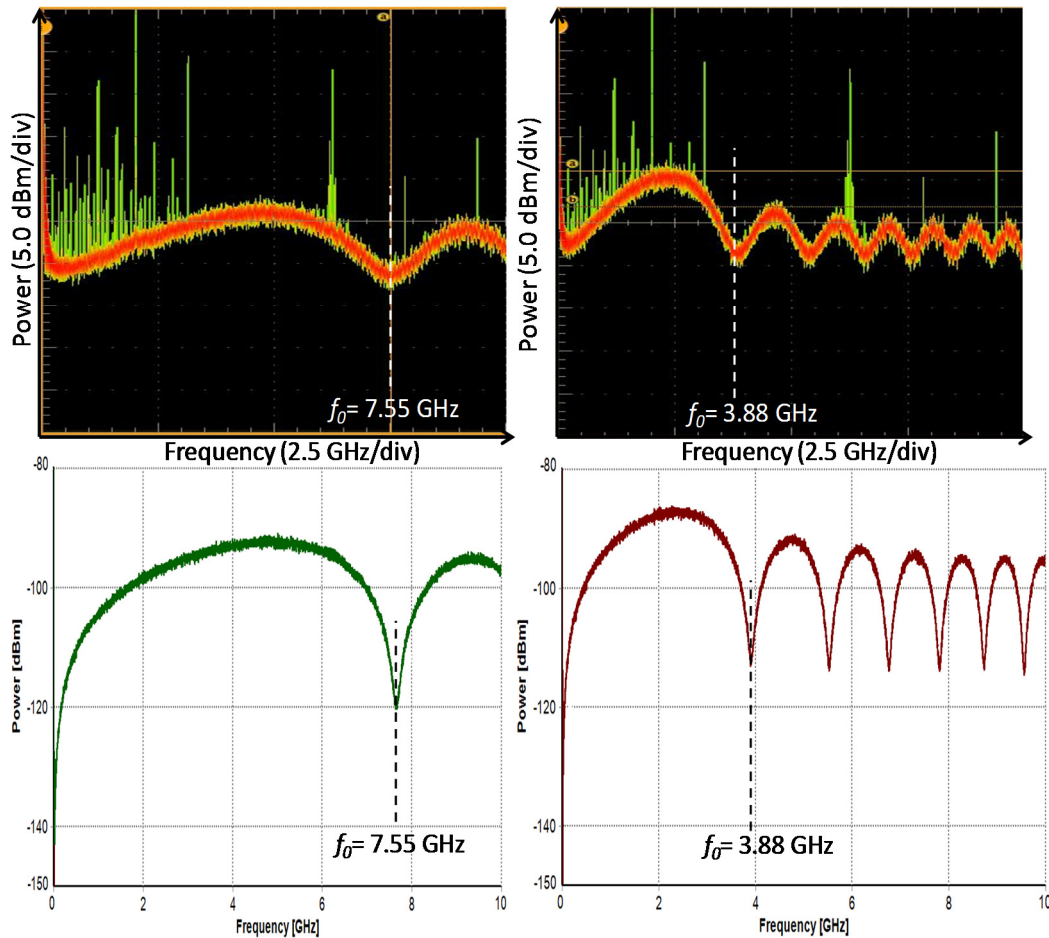


Fig. 5.4.4. Measured and simulated RF spectra using 8.09 MHz linewidth over 130- and 500 km.

Fig. 5.4.4 shows the measured and simulated RF spectra using VPItransmissionMakerTM with laser linewidth of 8.09 MHz propagated over the 130- and 500-km S-SMF. The measured spectra are obtained using I_b of 60 mA. These spectra are used to show the number of sidelobes and the f_0 frequency obtained using experiment match the simulated results, regardless the received power. The number of sidelobes and the frequency will remain unchanged for the same amount of dispersion even when the linewidth is changing. In a practical laser, its noise characteristics are interdependent of one another. Independent settings of RIN and the linewidth of the laser could not be achieved in a real experiment. For this reason, when I_b was lower than 50- and 60-mA presented in Fig. 5.4.2, the RIN of the laser can also be seen in the resulting PM-IM conversion noise PSD. When the I_b was set to 20 mA, the measured linewidth of the DFB laser was 29.15 MHz with the measured RIN characteristic of -118.51 dB/Hz. The measured results are shown as in Fig. 5.4.5.

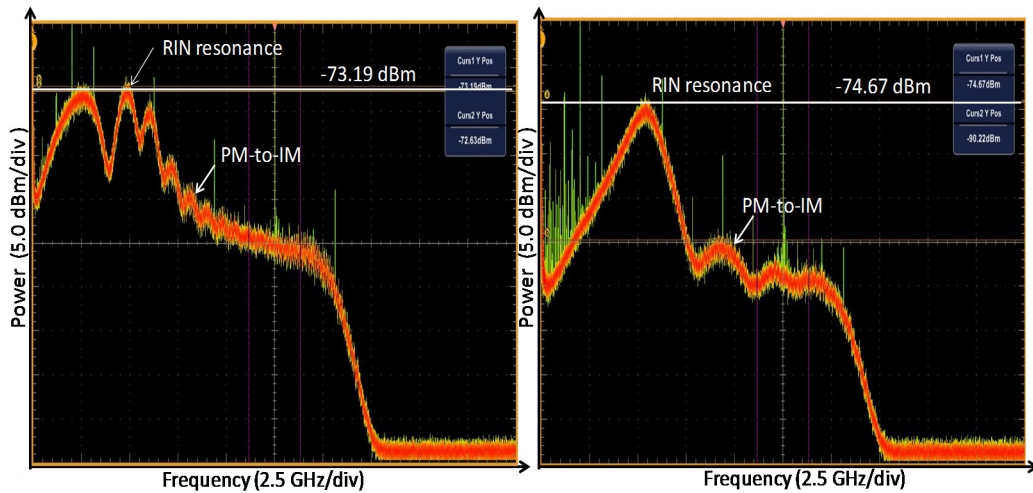


Fig. 5.4.5. Measured electrical spectra of DFB laser with high RIN and wider linewidth characteristics after 500- and 300 km length of fiber.

Fig. 5.4.5 shows the measured electrical spectra using a RIN dominated laser with 84 and 21 MHz linewidth driven with 16 and 19 mA I_b , respectively, transmitted over 500- and 300-km of S-SMF fibre. The linewidth were measured using Agilent HRS. The PSD shows that the RIN of the laser is added into the intensity noise due to the PM-IM conversion which results in a higher RIN value of -108.51 dB/Hz for 500 km and -111.25 dB/Hz for 300 km.

5.5 Group Delay Effect on Modulating RF Tones

In a transmission system where RF tones or subcarriers originate from the same laser and both are transmitted over a dispersive fibre, there is a strong phase correlation between the carrier and the RF tones. This permits the use of a direct-detection receiver design with single photodetector. However, the signal propagation over the dispersive fibre can induce group delay effect where this can de-correlate the phase of the RF tones relative to the carrier and induce some time delay upon photodetection. The effect of this phase de-correlation had been demonstrated by L.E. Richter and H.I. Maldelberg et al. through their linewidth measurement technique as presented in Section 2.5. This effect can be shown using VPITransmissionMaker™ simulation.

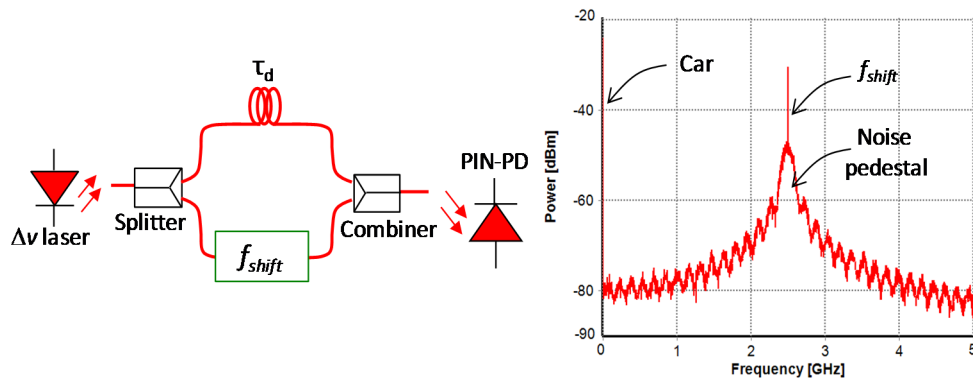


Fig. 5.5.1. Simulation setup to show the effect of phase de-correlation between carrier and its shifted version.

Fig. 5.5.1 shows the simulation setup to demonstrate the effect of phase de-correlation using a self-heterodyne linewidth measurement technique. A laser's output with linewidth, $\Delta\nu$ is split into two branches. One branch is connected to a time delay module with τ_d delay and the other into a frequency shifter module that frequency-shifted the carrier's frequency by 2.5 GHz. These two light beams are then combined and detected using a PIN-PD. The mixing between the delayed carrier and the RF tone can be seen at the received RF spectrum. It shows that the RF tone achieved from shifting the carrier to 2.5 GHz is governed by noise pedestal for the laser linewidth of 10 MHz where the τ_d was 636.62 ps.

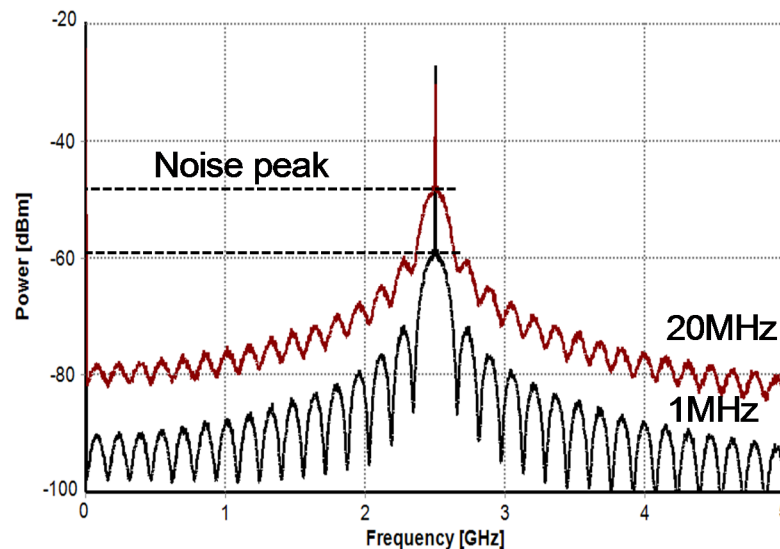


Fig. 5.5.2. High laser linewidth increases the noise pedestal amplitudes.

Fig. 5.5.2 shows the effect when linewidth is increased from 1- to 20-MHz. The power spectra show the increment of the noise pedestal power with the increased linewidth. From the view point of linewidth measurement, the shape of these spectra is

considered as a quasi-Lorentzian, which will not provide an accurate linewidth measurement due to the noise pedestal. To produce an acceptable noise pedestal or a complete Lorentzian-shaped spectrum, Richter and Maldelberg suggested that the τ_d used in the linewidth measurement setup in Fig. 5.5.1 has to be at least six times the laser's coherence time, $\tau_d \geq 6\tau_c$ where $\tau_c = 1/\pi\Delta\nu$, in order to have an accurate measurement of the spectrum [19]. For these spectra, τ_d equal to $0.02\tau_c$ was used and hence the undesirable noise pedestal is clearly shown, since the required delay is 50 times shorter than τ_c .

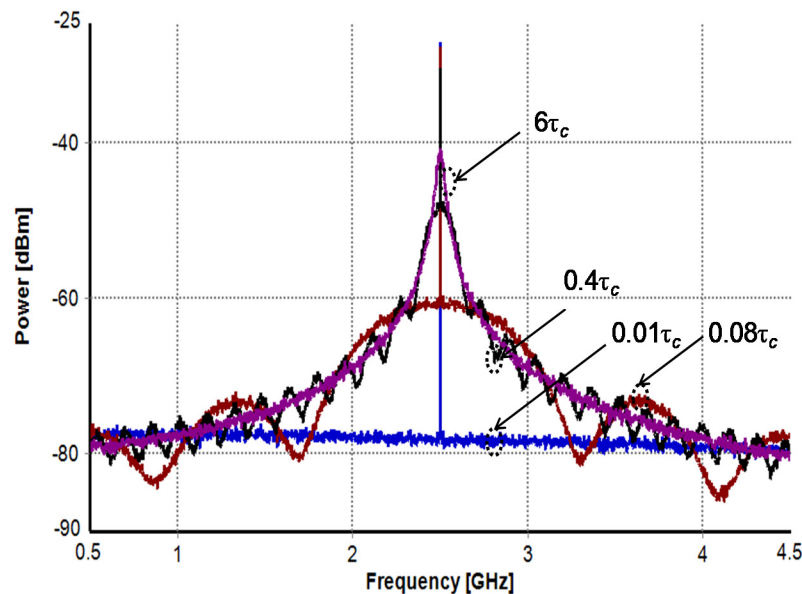


Fig. 5.5.3. Spectra showing the noise pedestal is narrowing and changing into a quasi-Lorentzian shape for the respective τ_d .

Fig. 5.5.3 shows the power spectra where the noise pedestal shape narrows and changes into a quasi-Lorentzian shape when longer τ_d is assigned. These are simulated for linewidth of 20 MHz which gives τ_c of 15.9 ns. The spectrum shows that, when a very short delay of $0.01\tau_c$ (0.159 ns) was used, the peak power of the noise pedestal governing the tone is very low, close to -80 dBm. The noise peak power increases with increased τ_d until the shape turns to a quasi-Lorentzian, where the beat signal of the delayed and un-delayed beams is quasi-Lorentzian*quasi-Lorentzian, where * is convolution. At $6\tau_c$, the noise pedestal has completely gone, which agrees with the minimum time delay, suggested in Reference [19]. This also means that the phase noise of the optical beams at the two branches in Fig. 5.5.1 is substantially de-correlated.

The effect of group delay with a single modulating RF tone presented so far shows that a noise pedestal will be induced around the tone when a wide linewidth laser is used. Also, the changes from a wide pedestal with nulls into a quasi-Lorentzian shape of the noise were also shown when the laser's phase was decorrelated using τ_d , relative to the laser's τ_c . The effect of multiple tones will now be considered.

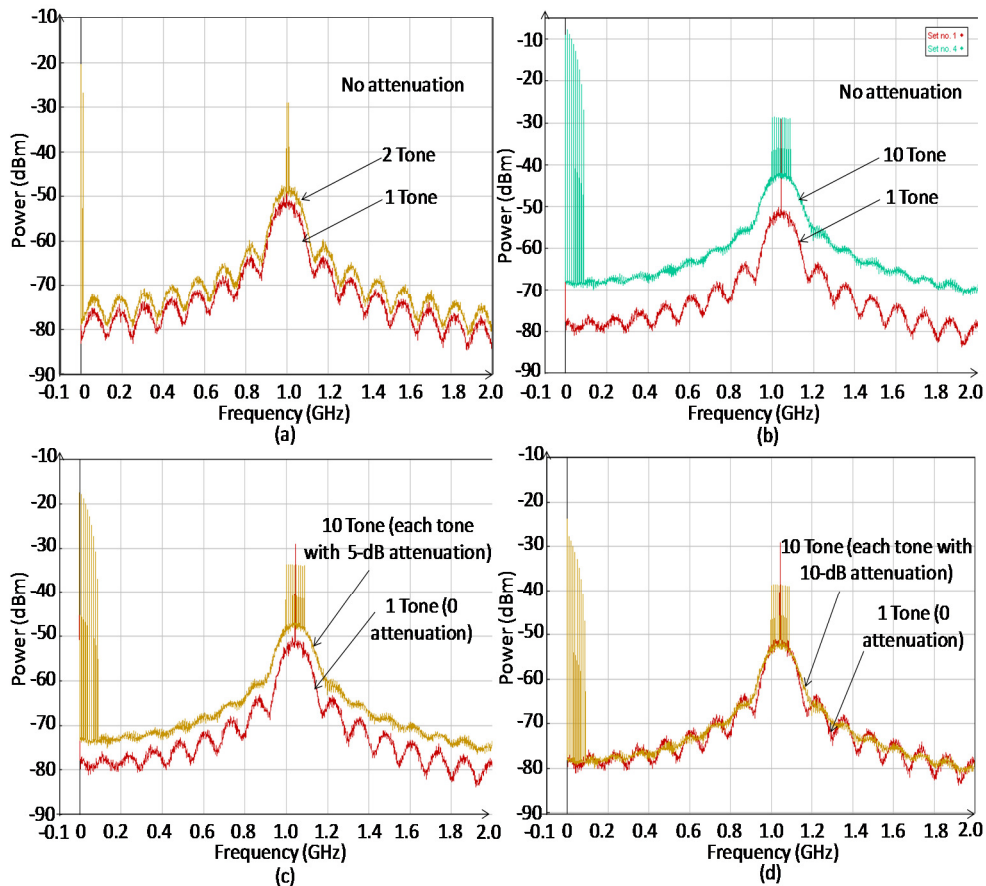


Fig. 5.5.4. Simulated spectra with (a) 1 and 2 side tones, (b) 1 and 10 side tones, (c) 5-dB and (d) 10-dB attenuation applied to each tone for the 10 side tones transmission.

Fig. 5.5.4 shows the simulation results of (a) 1 and 2 tones and (b) 1 and 10 side tones without any attenuation with and (c) 5-dB and (d) attenuation applied to each of the 10 tones where zero attenuation applied to the single tone case. The simulation setup is the same as in Fig. 5.5.1, where the tones originate from the same carrier, which was done by having 1 and 10 frequency shifter modules. These spectra show that the noise pedestal power is increased with the increase of power in the side tones. The shape of the noise pedestal governed the 10 tones are also flat and symmetrical which presents that the noise pedestal peak power is the same for the tone at lower and higher frequency. This shows that the resulting PSD is a summation of the PSDs due to each tone. Intermodulation distortion (IMD) mixing products can be seen near the dc, which

is due to the mixing of tones \times tones. The spectra show that the IMD is reduced with the reduced power of the side tones. The IMD products can be eliminated using coherent or balanced receiver design.

5.6 PM-to-IM Conversion Noise Interaction with De-correlated RF Tones

The effect of a wide linewidth laser with dispersion in fibre, which causes PM-to-IM conversion noise, has been presented in Section 5.3 and 5.4. In Section 5.5, phase de-correlation of the side-tone due to fibre group delay, causes a noise pedestal around the side-tone. In this section, the interaction of these two effects is considered. This is important for a system that uses sidebands such as DDO-OFDM transmission system over a dispersive fibre. This is because in the DDO-OFDM system, a high number of subcarriers will be employed. Apart from the detected PM-to-IM conversion noise due to the carrier with a wide linewidth, each of these subcarriers will have its own underlying noise pedestal which may contribute to the overall detected system's intensity noise. The hypotheses of these two effects on a transmission of side-tones over a dispersive fibre can be illustrated as in the following figure.

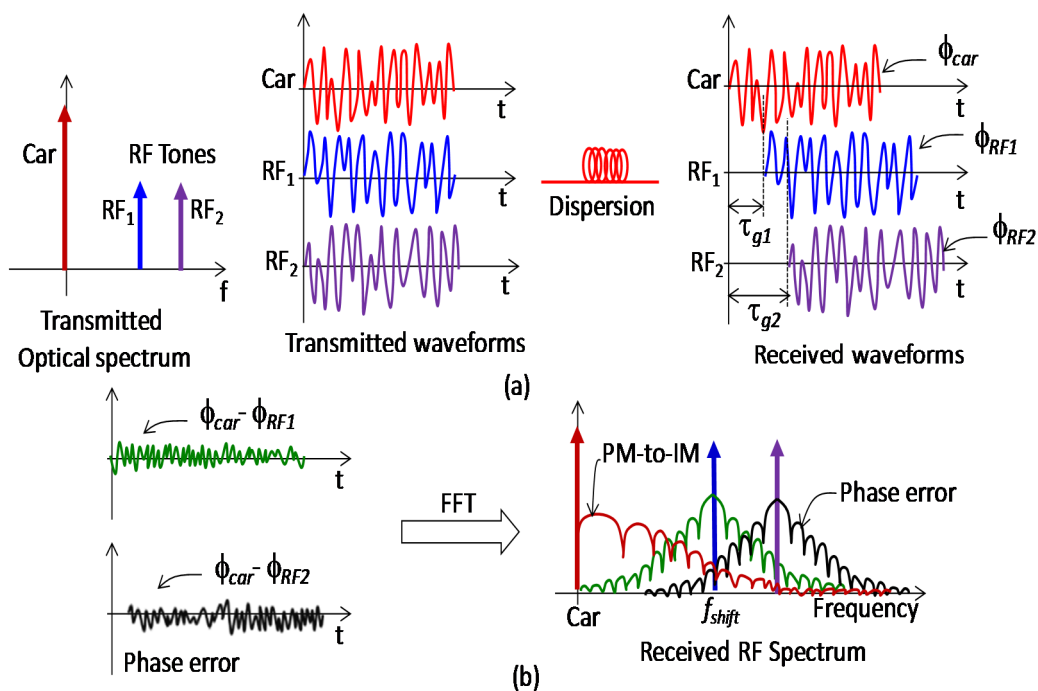


Fig. 5.6.1. Phase de-correlation effects of (a) two RF tones due to dispersion and (b) resulting phase error relative to the carrier and PM-to-IM conversion noise of the carrier.

Fig. 5.6.1 shows the illustration of (a) transmitted optical spectrum with two RF tones and its respective waveforms and the waveforms upon photodetection after signal propagation through a dispersive fibre. The received waveforms illustrate the effects

of group delay with τ_g delay relative to the carrier. This can be seen as the tones are walking away from the carrier after the dispersive fibre. Fig. 5.6.1 (b) illustrates the phase error between the carrier and RF tone waveform, where each of these phase error is transformed into the noise pedestal around a tone. The carrier's PM-to-IM is also illustrated. When two tones are transmitted together, the interaction between the noise pedestal underlying the two tones and the carrier's conversion noise needs to be investigated. To do this, simulation setup as in Fig. 5.5.1 was used with an addition of dispersive fibre with zero attenuation before the PIN PD.

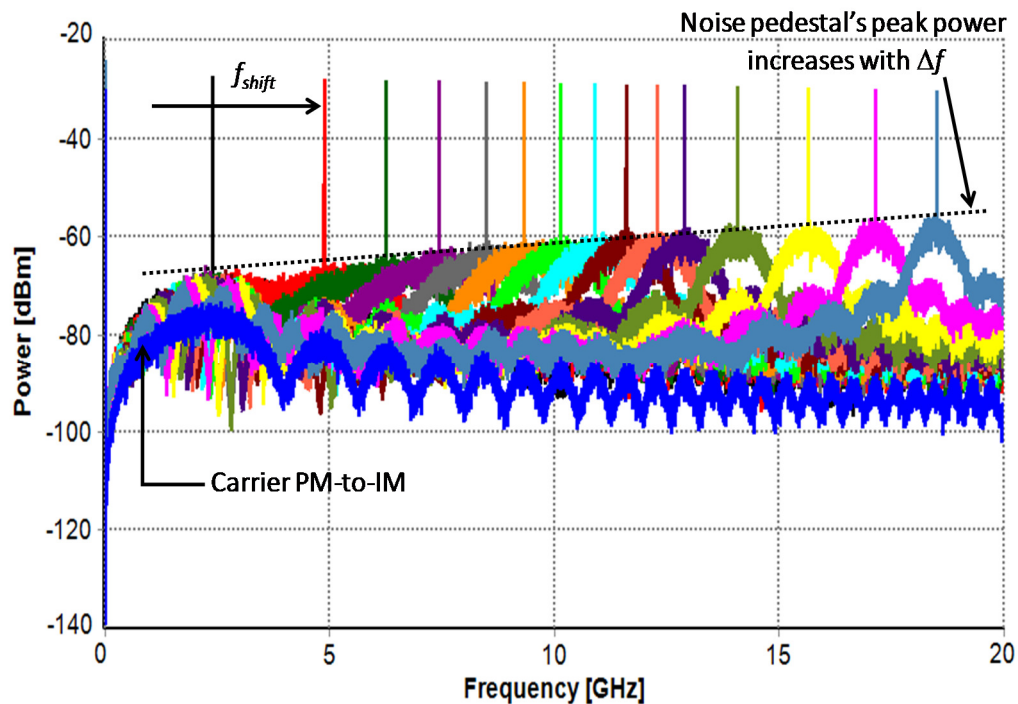


Fig. 5.6.2. Simulated spectra of carrier PM-to-IM conversion noise and single tone originated from 100 MHz linewidth with its f_{shift} swept across the transmission bandwidth over 500km dispersive fibre.

Fig. 5.6.2 shows the simulated spectra of the carrier PM-to-IM conversion noise without any RF side tone and with single side tone with its frequency is swept across the transmission bandwidth and transmitted over 500 km of dispersive fibre. This result shows that the noise pedestal peak power is increased with increasing frequency shift. This result can be explained by the hypothesis illustrated in Fig. 5.6.1, where the side tone that is assigned far from the carrier will experience longer delay relative to the carrier. This is illustrated by τ_{g2} , which has more delay relative to the carrier as compared to τ_{g1} . Due to the dispersion, each side tone will experience a different group delay relative to the carrier due to the walk-away from the carrier, causing a greater

phase decorrelation between it and the carrier. In another simulation, a narrower linewidth laser source was used. The results showed the same increase of peak noise pedestal power towards the high frequency side-tones but with a lower level overall noise power than the one achieved with wider linewidth. The RF tones in this simulation resemble the OFDM subcarriers. This shows that with a wide linewidth laser and dispersion in a system, the high frequency subcarriers will experience more SNR degradation compared to the low frequency subcarriers.

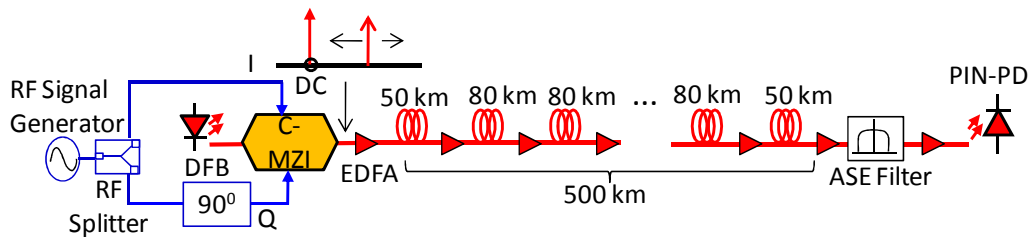


Fig. 5.6.3. Experimental setup for single side tone transmission over 500 km single-mode fibre.

The increase of the noise pedestal's peak power around a high frequency tone is also investigated experimentally as shown by the following discussion. Fig. 5.6.3 shows the experimental setup using ILX Lightwave bias supply driving a FLD5F6CX-E36 Fujitsu DFB laser modulated with single side tone by a complex optical modulator and transmitted over 500 km single mode fibre (SMF). The RF tone was generated using a Hewlett Packard 83620A synthesized sweeper. The complex modulator used was a Sumitomo T. SBX1.5-10 20 Gb/s where the inphase (I) and quadrature (Q) signal inputs were supplied by the synthesizer. The synthesizer's output was split by a splitter where 90° phase shifter was used at one of the output to produce the Q component. The DC-biases to the C-MZI were set to 2.9 V for port A, 1.45 V for port B and 4.58 V for port C to bias near the null of the transfer curve and obtained the USB tone. The DFB was tuned to 1555.75 nm with I_b of 50 mA which generated 10 MHz linewidth, as measured with an Agilent HRS. The output of the C-MZI showed the optical spectrum centred at 192.70 THz and the RF tone with a variable frequency achieved by tuning the synthesizer. The RF tone was set to 7.5 and 12 GHz.

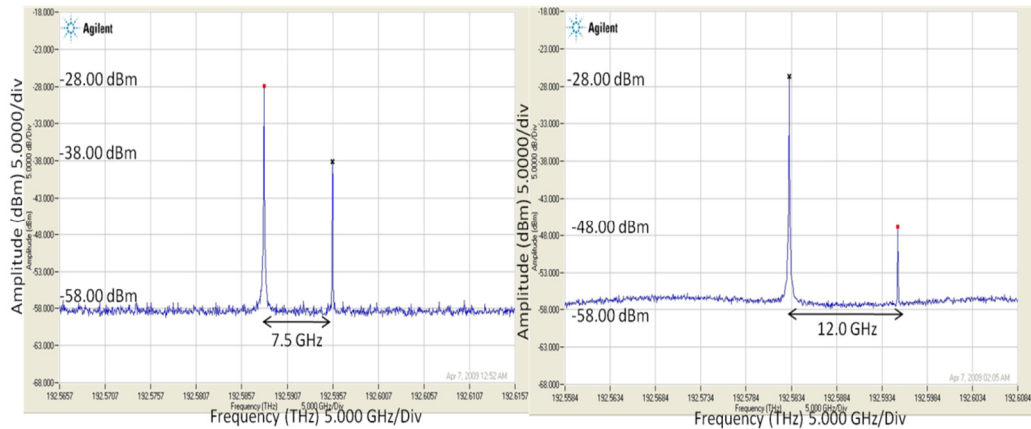


Fig. 5.6.4. Measured output of a C-MZI modulated with a single side tone with 10- and 20-dB carrier-to-tone power ratio spaced at 7.5- and 12-GHz.

Fig. 5.6.4 shows the optical spectrum after the C-MZI measured by using the HRS. The side tone power was decreased by adjusting the RF power at the synthesizer in order to get the desired carrier-to-tone power ratio. The output of the C-MZI was then amplified by a Lightwaves2020 erbium-doped fibre amplifier (EDFA) before the fiber of 50 and 80 km per span. A JDSU 1 nm bandpass filter was used to limit the effects of the ASE noise and the signal was pre-amplified before it was detected by a Discovery DSC40S PIN PD with 0.26 A/W responsivity. The RF signal was then captured by using the Tektronix 72004 20-GHz 50-GS/s DSO running at a 15 GHz (hardware) bandwidth.

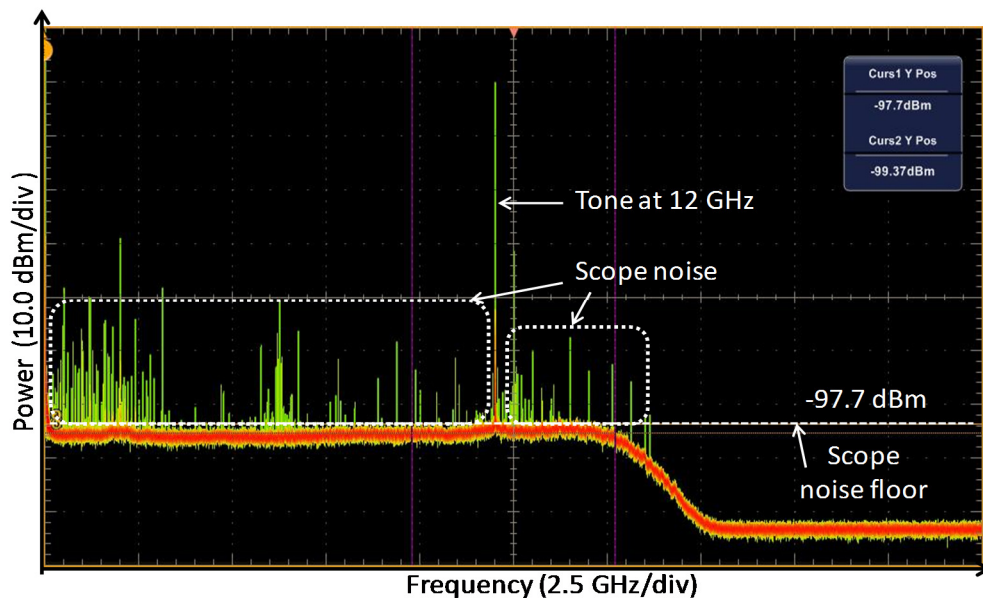


Fig. 5.6.5. Measured spectrum after photodetection with side tone at 12 GHz for a back-to-back transmission.

Fig. 5.6.5 shows the measured RF spectrum of a back-to-back transmission when FFT-function was applied to the received waveform on the DSO. The DSO was set to infinite persistence and temperature-colour grading display. The tone was located at 12 GHz by tuning the synthesizer. A flat noise floor is observed in the absence of dispersion, but with spurious tones from the oscilloscope digitisation. The other spectral components captured are due to the noise of the DSO.

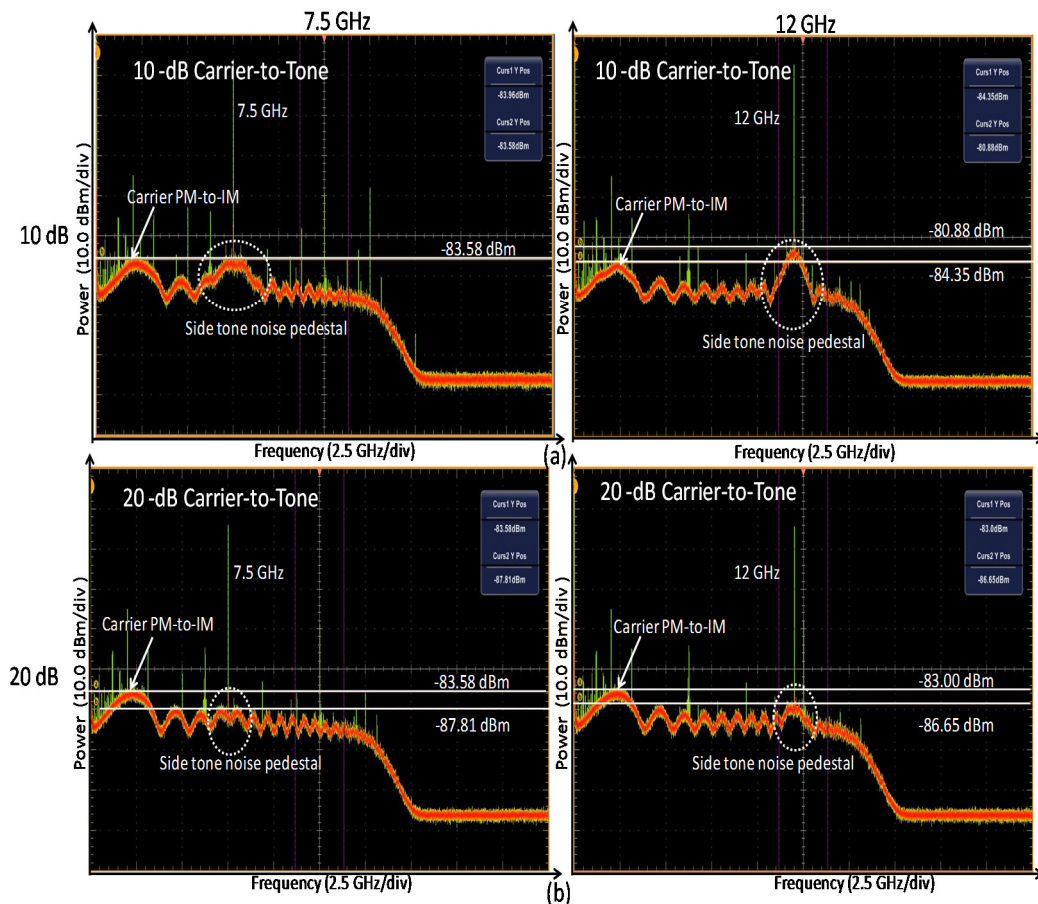


Fig. 5.6.6. Measured RF spectra with side tones of 7.5- and 12-GHz with carrier-to-tone power ratio of (a) 10 dB (b) 20 dB.

The changes of the noise pedestal around a tone with frequency shifting and the tone's power can be shown with the received electrical spectrum. Fig. 5.6.6 shows the received RF spectra when the signal was transmitted over 500-km of dispersive fiber with the side tone tuned to 7.5- and 12-GHz with the power ratio of carrier-to-tone set to (a) 10 dB and (b) 20 dB. In Fig. 5.6.6, the carrier PM-to-IM peak power near the DC is unchanged at around -83.58 dBm when a side tone was inserted. For a high power side tone with 10 dB ratio, a noise pedestal can be clearly seen around the side tone and this reduces in power when the side tone power with 20-dB less than the carrier. These

results agree with the simulated results presented in Fig. 5.5.4. In both cases, the higher frequency side tone has a higher noise pedestal peak power than the low frequency side tone, which matches the simulated results in Fig. 5.6.2.

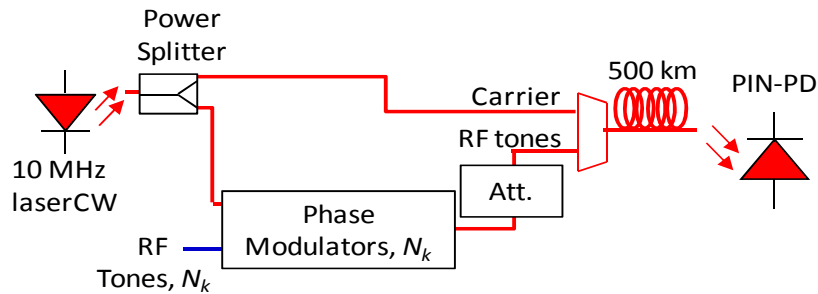


Fig. 5.6.7. Simulation setup with N_k tones over 500 km SMF with zero attenuation.

To investigate the effect of many tens of side tones which resembles the DDO-OFDM subcarriers transmission, a simulation model as in Fig. 5.6.7 is used. In this setup, the side tones are modulated by a continuous wave laser (laserCW) model with a 10-MHz linewidth. With the VPI model `laserCW`, the RIN characteristic can be disabled and the linewidth is independent with the other laser characteristics. The RF tones were generated using an ideal phase modulation. The k^{th} RF tones were generated over a total number of tones or block length of N , where $k = 1, 2, 3, 4, \dots, N$. In this simulation, N was set to 512 and 10 and 40 RF tones were transmitted to investigate the effect of PM-to-IM conversion noise.

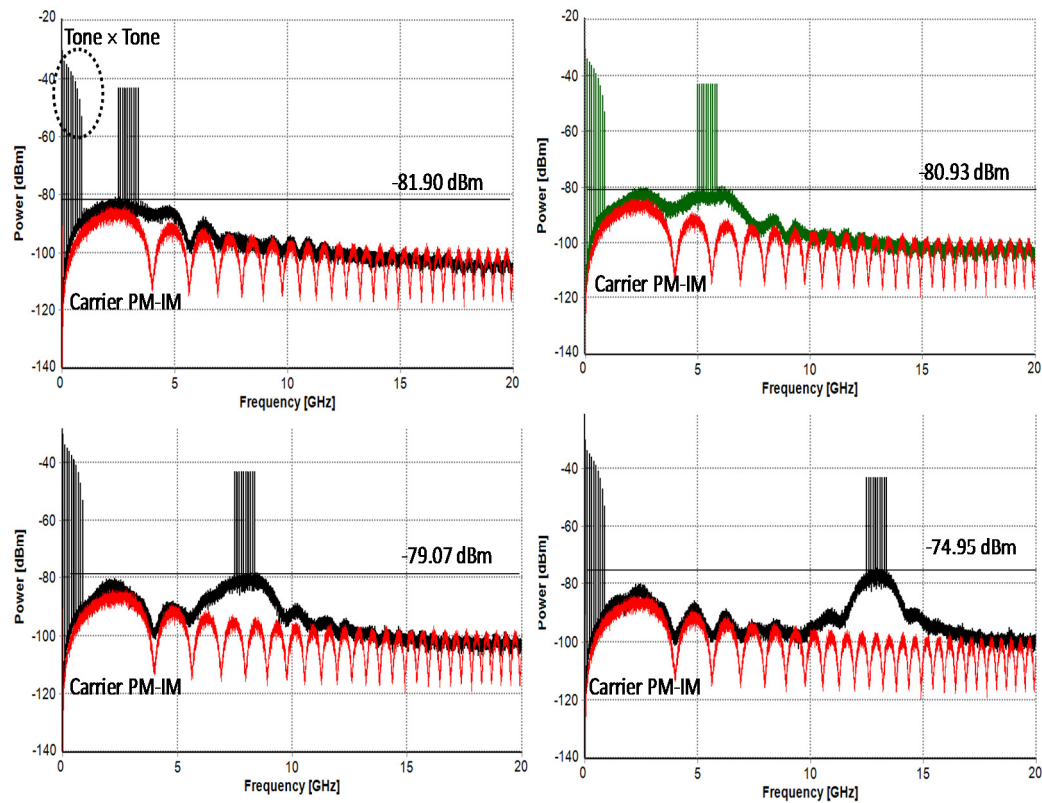


Fig. 5.6.8. Simulated RF spectra of carrier PM-to-IM and 10 side tones transmitted over 500 km dispersive fiber with side tone band is located at low and high frequency extremes of signal bandwidth.

Fig. 5.6.8 shows the simulated RF spectra when 10 side tones were transmitted over 500 km of fibre with dispersion coefficient of $16.67 \text{ ps}/(\text{nm}\cdot\text{km})$. The side tones band is shifted where the lowest frequency tone is set to 2.5-, 5-, 7.5- and 12.5-GHz. A 1-to-1 carrier-to-side tone power ratio was used. The spectral components near the DC represent the beat noise due to tone \times tone mixing. The spectra show that the carrier's PM-to-IM stays the same when the laser is modulated with the side tones. This is shown when the band is frequency shifted away from the first carrier's PM-to-IM sidelobe. When the tone band is located at 2.5 GHz, a small noise pedestal is produced, which is shown by a small increase of the carrier's PM-to-IM first sidelobes noise and its first null frequency. When the band is moved to a higher frequency, the noise pedestal around the band has an increased peak level. This is shown by the band located on 12.5 GHz, where it is dominated by a noise pedestal with 7-dB increase of the noise power level. This result shows that the noise pedestal power level underlying the band is increased when its centre frequency is increased. This agrees with the measured spectra showed in Fig. 5.6.6, where the noise pedestal around the high frequency tone is higher than the low frequency tone. The measured spectra also shown that the carrier's PM-

to-IM stays the same with the high power noise pedestal occurred around the high frequency tone. This is shown by the similar peak power level of the first PM-to-IM sidelobe with the shifted tone's frequency.

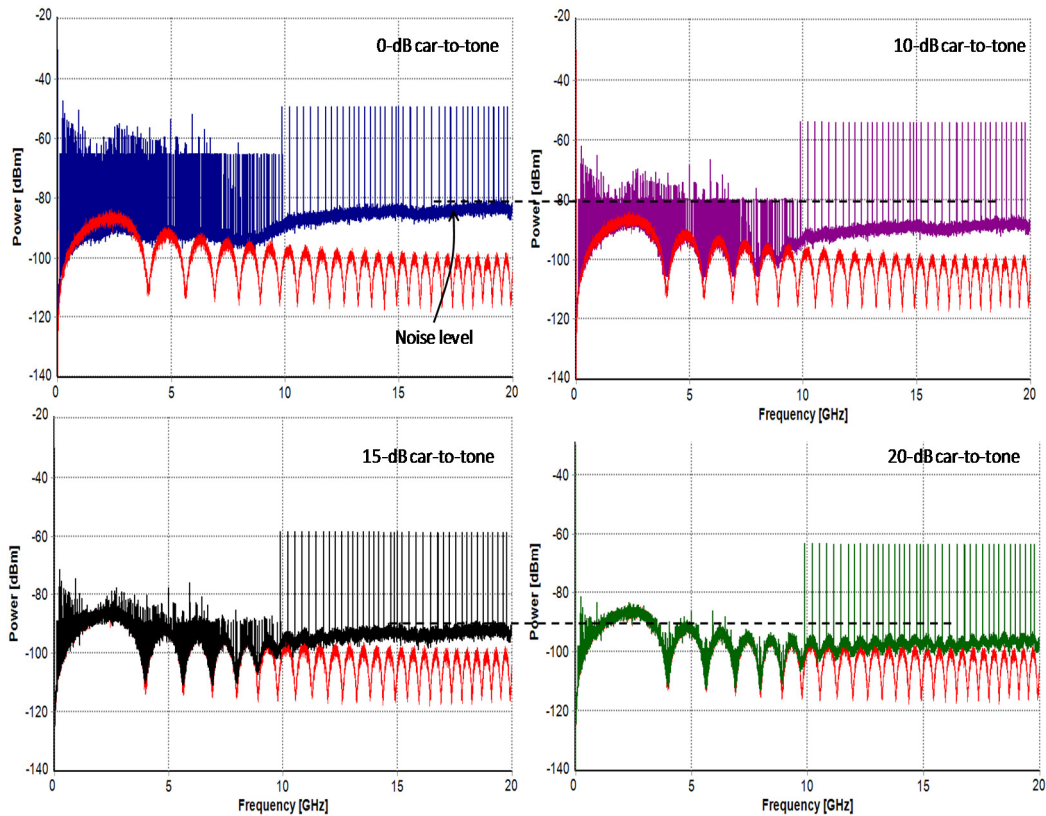


Fig. 5.6.9. Simulated RF spectra of 40 side tones transmission over 500 km fiber with 0-dB, 10-dB, 15-dB and 20-dB carrier-to-side tones power ratio.

Fig. 5.6.9 shows the transmission of 40 RF side tones over a 500 km dispersive fiber using 10 MHz linewidth. In this transmission, the carrier-to-side tones power ratio was varied for 0 dB, 10 dB, 15 dB and 20 dB. The spectra show that the overall noise floor power is decreased when the side tones power is decreased. When a 20-dB power ratio was employed, the noise floor governed by the side tones is equal to the carrier's PM-to-IM conversion noise PSD and no tone \times tone beat noise is observed. At 0-dB or 1:1 carrier-to-tones power ratio, the noise is at the highest level as compared to when the tones power is reduced relative to the carrier. This is because the tones are generated from the laser. The tones will possess the same noise characteristics as the laser, which in this case, the noise pedestal is due to the PM-to-IM conversion noise. The reduction of the tones power will also reduce the noise pedestal power. In a viewpoint of a data transmission system, these low-power tones could not be used since the tones will produce a small OSNR level at the photodetector with the presence of the other system

noise such as the ASE noise. The higher frequency tones show a higher noise level. This is because the higher frequency tones have more phase errors than the tones at the lower frequency, which is closer to the carrier or DC due to the group delay. In a DDO-OFDM transmission system, close to a 1:1 carrier-to-subcarrier power ratio is required to achieve an optimum transmission performance [20-22]. However, the results achieved here suggested that the highest frequency subcarriers will have lower performance compared to low frequency subcarriers when wide linewidth laser source is used at the transmitter design.

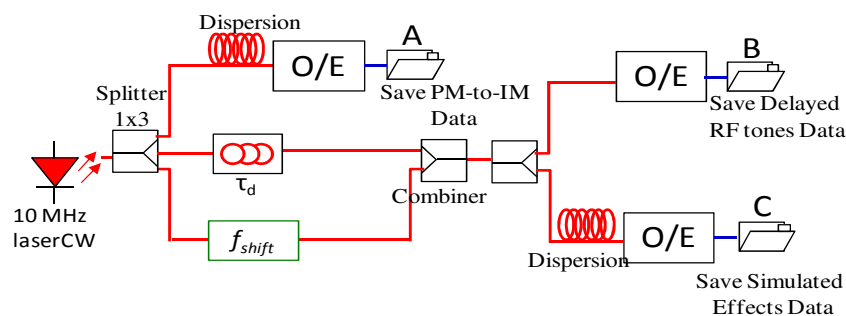


Fig. 5.6.10. Simulation setup to compare the PSDs obtained from the addition of the PM-to-IM conversion noise and delayed-RF tones data (A+B) with fully simulated PSDs (C).

To investigate the noise correlation between the carrier's PM-to-IM sidelobes and the noise pedestals around each of the shifted tones, simulation using VPItransmissionMakerTM has been conducted. Fig. 5.6.10 shows the simulation setup to show that the resulting PSDs when both conversion noise and delayed RF tones are present is similar to the summation of the spectra of each case individually. For the PM-to-IM conversion noise simulation, the laserCW module with 10-MHz linewidth is launched over a dispersive fibre and the data is saved in file A. For the delayed RF tones effect, the setup is the same as previous setup where f_{shift} generates the RF tones by frequency shifting the carrier. The result without going through a fibre is saved in B. The addition of A and B was performed in Microsoft Excel and the resulting spectrum was plotted. This spectrum is compared with the spectrum achieved by fully simulated the effects in VPItransmissionMakerTM and which saved in C.

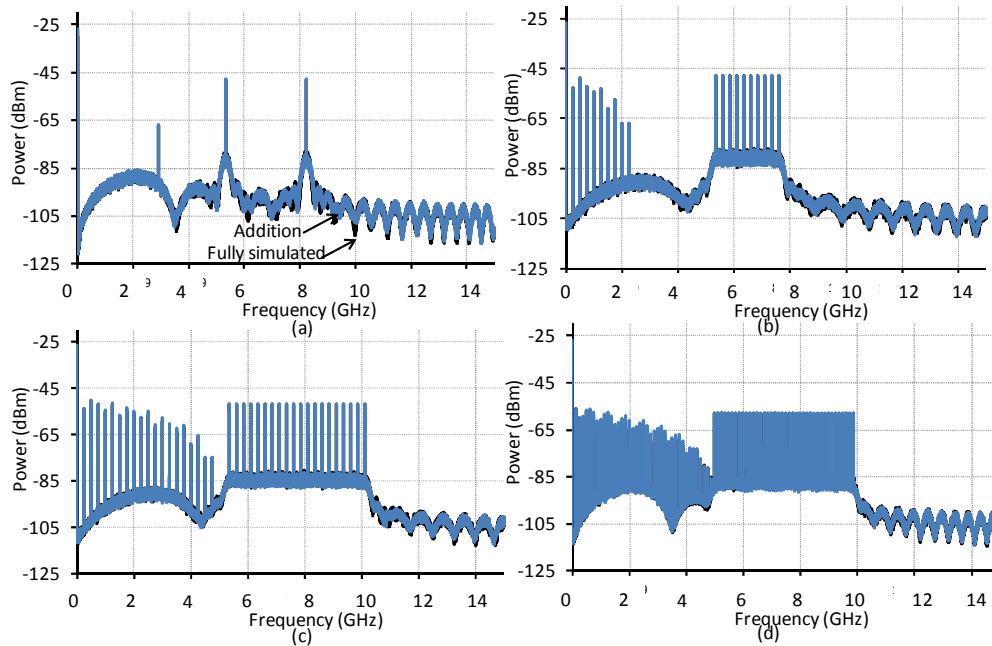


Fig. 5.6.11. Simulated spectra comparing the addition of conversion noise and delayed RF tones and fully simulated spectra when both effects are present with (a) two-tones, (b) ten-tones, (c) twenty-tones over 400 km and (d) forty-tones over 625 km.

Fig. 5.6.11 shows the simulated spectra plotted from the addition of the conversion noise and the delayed RF tones (blue) and underneath is the spectrum obtained by fully simulated both effects with (a) two-tones, (b) ten-tones, (c) twenty-tones over 400 km and (d) forty-tones over 625 km with dispersion of 16 ps/nm-km. The spectra show a straight forward relation of the conversion noise and the delayed RF tones since these effects can be calculated independently then added in the electrical power domain. This means they are substantially decorrelated. These spectra matched the spectra obtained by simulating both effects using VPItransmissionMaker™.

5.7 Conclusions

In this chapter, the effects of laser noise; RIN and phase noise or linewidth have been investigated. The interdependent effect of the laser's RIN and linewidth with fibre dispersion has been shown experimentally. The obtained electrical spectra showed that a high peak RIN resonance is induced in the carrier's PM-to-IM noise sidelobes when the laser is driven by a low biasing current to produce high RIN. The effect of laser phase noise or linewidth interaction with fibre dispersion with and without external modulated tones was also investigated. The result presented the PM-to-IM conversion noise PSD of an unmodulated laser propagating along a dispersive fibre. An experimental measurement was also done, which matches the simulated results. An

upper-bound equation of the conversion noise PSD was also derived. The group delay interaction with the wide linewidth laser externally modulated with the RF tones was also investigated using simulation and experiment. The results show a noise pedestal is imposed around each of the tones. The effect of a de-correlated RF tone due to the group delay was also presented, where the noise pedestal peak power around each tone is increased for the high frequency tones. The noise pedestal when many tones were transmitted over a dispersive fibre is also investigated. The result shows that the noise pedestal is decreased when the tone power is reduced. However, too low a tone power will result in a low OSNR when the tones are used for a data transmission. The result also shows that the PSD of the conversion noise and the delayed RF-tones can be added in electrical domain which was done using excel addition and verified using VPItransmissionMaker™ simulation.

5.8 References

1. Marshall, W.K., B. Crosignani, and A. Yariv, *Laser phase noise to intensity noise conversion by lowest-order group velocity dispersion in optical fiber: exact theory*. Optics Express, 2000. **23**(3): p. 165-167.
2. Marshall, W.K. and A. Yariv, *Spectrum of the intensity of modulated noise light after propagation in dispersive fiber*. PHOTONICS TECHNOLOGY LETTERS, 2000. **12**(3): p. 302-304.
3. Ribeiro, R.F.S., J.R.F.d. Rocha, and A.V.T. Cartaxo, *Influence of laser phase noise on dispersive optical fiber communication systems*. photonics technology letters, 1995. **7**(12): p. 1510-1512.
4. Morgado, J.A.P. and A.V.T. Cartaxo, *Dispersion supported transmission technique: comparison of performance in anomalous and normal propagation regimes*. IEE Proceedings: Optoelectronics, 2001. **148**(2): p. 107-116.
5. Yamamoto, S., et al., *Analysis of laser phase noise to intensity noise conversion by chromatic dispersion in intensity modulation and direct detection optical fiber transmission*. Journal of Lightwave Technology, 1990. **8**: p. 1716-1722
6. Wedding, B., B. Franz, and B. Junginger, *10-Gb/s optical transmission up to 253 km via standard single-mode fiber using the method of dispersion-supported transmission*. Journal of Lightwave Technology, 1994. **12**(10): p. 1720-1727.
7. Zan, Z., A.J. Lowery, and M. Premaratne. *Laser RIN and linewidth requirements for direct detection optical OFDM*. in *Lasers and Electro-Optics CLEO 2008*. 2008. San Jose.
8. Laurêncio, P., S.O. Simões, and M.C.R. Medeiros, *Impact of the Combined Effect of RIN and Intermodulation Distortion on OSSB/SCM Systems*. J. Lightwave Technol., 2006. **24**(11): p. 4250-4262.
9. Ahmed, M. and M. Yamada, *Effect of intensity noise of semiconductor lasers on the digital modulation characteristics and the bit error rate of optical communication systems*. Journal of Applied Physics, 2008. **104**(1): p. 013104-7.
10. Laurêncio, P.R. and M.C.R. Medeiros, *Relative Intensity Noise in Optical Single Side Band Systems with Multiple In-Line Amplifiers: Analysis and Validation*. Fiber and Integrated Optics, 2008. **27**(2): p. 78 - 88.

11. Fuqin, X., *Digital modulation techniques*. 2nd ed. 2006, Norwood, MA: Artech House. 1029.
12. Prasad, R., *OFDM for Wireless Communications Systems*. 2004, Artech House.
13. Hanzo, L. and T. Keller, *OFDM and MC-CDMA A Primer*. 2006: John Wiley & Sons Ltd. 411.
14. Seimetz, M., *High-order modulation for optical fiber transmission*. 2009, Berlin, Germany: Springer-Verlag Berlin Heidelberg. 251.
15. Kazovsky, L., S. Benedetto, and A. Willner, *Optical fiber communication systems*. 1st ed. 1996, Norwood: Artech House, Inc. 690.
16. Chraplyvy, A.R., et al., *Phase modulation to amplitude modulation conversion of CW laser light in optical fibres*. *Electronics Letters*, 1986. **22**(8): p. 409-411.
17. Derickson, D., ed. *Fiber Optic Test and Measurement*. 1998, Prentice Hall: New Jersey.
18. Henry, C.H., *Theory of the linewidth of semiconductor lasers*. *IEEE Journal of Quantum Electronics*, 1982. **QE-18**(2): p. 259-264.
19. Richter, L.E., et al., *Linewidth determination from self-heterodyne measurements with subcoherence delay times*. *Quantum electronics letters*, 1986. **QE-22**(11): p. 2070-2074.
20. Lowery, A.J., L. Du, and J. Armstrong. *Orthogonal Frequency Division Multiplexing for Adaptive Dispersion Compensation in Long Haul WDM Systems*. in *Optical Fiber Communication Conference, 2006 and the 2006 National Fiber Optic Engineers Conference. OFC 2006*. 2006.
21. Schmidt, B.J.C., A.J. Lowery, and J. Armstrong. *Experimental demonstrations of 20 Gbits/s direct-detection optical OFDM and 12Gbits/s with a colorless transmitter*. in *Optical Fiber Communication Conference*. 2007. Anaheim, CA.
22. Lowery, A.J., L. Du, and J. Armstrong, *Performance of optical OFDM in ultra long-haul WDM lightwave systems*. *Journal of Lightwave Technology*, 2007. **25**: p. 131 – 138.

Chapter 6

SIMULATION OF LINEWIDTH AND DISPERSION EFFECT ON DDO-OFDM SYSTEM

6.1 Introduction

In wireless OFDM systems, the phase noise of a local oscillator is an important parameter that can limit the system performance. The phase noise can cause a leakage of discrete Fourier transform (DFT) modulated subcarriers and destroy orthogonalities of the subcarriers [1-3]. Subsequently, this will cause phase rotation and interference between the subcarriers [2, 4]. These effects will increase the noise level and reduce a signal-to-noise ratio (SNR) of the received signal. The same degradation due to the phase noise is also faced by CO-OFDM system. In CO-OFDM systems, the phase noise is introduced by the laser linewidth, $\Delta\nu$, at both transmitter and receiver. The lasers used in CO-OFDM transmitters and receivers resemble the LOs in the wireless OFDM system. In CO-OFDM system, linewidth effects can be cancelled by using a similar technique used in wireless OFDM, for instance by using the pilot tone [5, 6]. This technique is applicable since the phase rotation due to the linewidth remains unchanged within the OFDM symbol period.

In DDO-OFDM transmission system, the carrier is transmitted along with the subcarriers. Both carrier and the subcarriers will experience the same degradation across the fibre and produce a strong phase correlation. Thus, the linewidth, or equivalently phase-noise requirement is far less stringent than for coherent systems [5-7], where two lasers must track one-another. With DD, the phase component of a laser field could not be directly responded by a photodetector (PD). However, given that the laser phase noise will be converted to intensity noise (IN) along a dispersive fibre, there will be some effect on performance in a DD-OFDM system. In Chapter 5, the effect of the PM-to-IM conversion noise and the time delay induced by the interaction of a laser's linewidth and dispersion has been explained. Therefore, it is essential to investigate these two effects to the transmission of the OFDM subcarriers using a DD receiver. The fundamental effects of these can be explained by investigating each of

the OFDM subcarriers across the signal bandwidth. It is also important to investigate the frequency dependence of the OFDM subcarriers with the presence of dispersion. This is crucial due to the fact that a large signal bandwidth with a high number of subcarriers is usually employed in an O-OFDM system in order to achieve a high data rates with a long-haul transmission.

In this chapter, the investigation of the effects of the laser linewidth with the chromatic dispersion to the DDO-OFDM transmission system will be presented. In Section 6.2, the effect of the PM-to-IM conversion noise on a single OFDM subcarrier is determined. This involves investigation to the received scatter plots when the subcarrier's frequency is increased. Section 6.3 presents the effect of a group delay due to the dispersion to the OFDM subcarriers. This involves the investigation using a transmission of single subcarrier placed at a fixed frequency with the increase of fibre length and when the subcarrier's frequency is varied at a fixed length. The effects of the interference between the adjacent subcarrier's noise pedestals are also investigated in this section. Section 6.4 investigates the effect of the PM-to-IM conversion noise to the DDO-OFDM system's performance without the influence of an ASE noise, followed by the effects to a large M -size QAM modulated signal in Section 6.5. Finally, the system degradation in terms of bit error rate (BER) and optical signal-to-noise-ratio (OSNR) penalty due to the linewidth with dispersion and high M -size QAM are also verified in Section 6.6 before conclusions in Section 6.7. Section 6.8 shows the references list.

6.2 Phase Modulation-to-Intensity Modulation (PM-to-IM) Conversion Noise Effects on OFDM Subcarriers

In a DDO-OFDM transmission system, the fundamental effect of the PM-to-IM conversion noise can be initially investigated by transmitting a single OFDM subcarrier. A simulation was done by setting the subcarrier frequency to be at the highest amplitude of the conversion noise PSD sidelobe (first sidelobe near the DC) and at the first null frequency, f_0 . The f_0 can be calculated using Eq. 5.3.4 for a certain length \times dispersion product as in Section 5.3. In the simulation, independent linewidth characteristic of the laser was imposed using `laserCW` module.

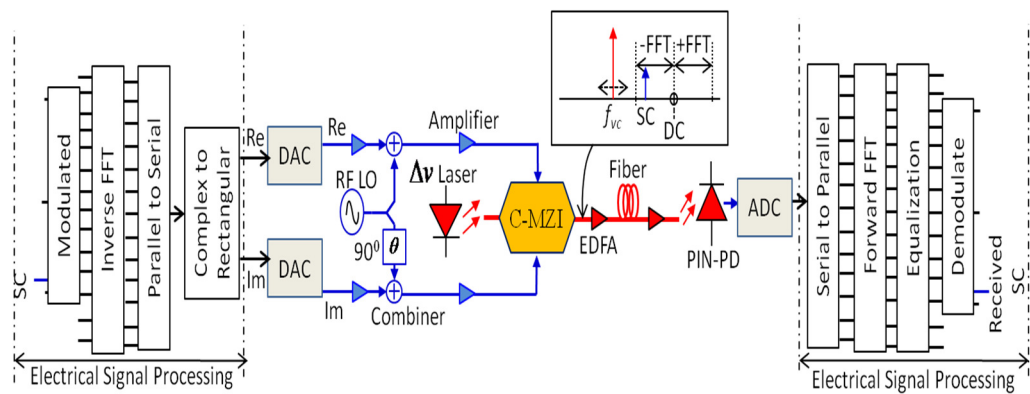


Fig. 6.2.1. Simulation setup with RF virtual carrier to transmit a single OFDM subcarrier.

Fig. 6.2.1 shows the simulation setup to transmit a single OFDM subcarrier using an RF virtual carrier technique. The RF virtual carrier technique is an efficient transmitter design, which provides flexibility to vary its power and tune the frequency of the optical carrier across the signal bandwidth [8]. The OFDM signal generation of 300 symbols was done in the electrical signal processing part using MATLAB R2007b. The transmitter MATLAB code can be found in Appendix 3.1. The FFT-size, N used was 1024. The N points can be assigned with the OFDM subcarriers, which are orthogonal to each other. In this simulation, a subcarrier was assigned at the point 514 of the FFTs, which was located on the negative FFT points.

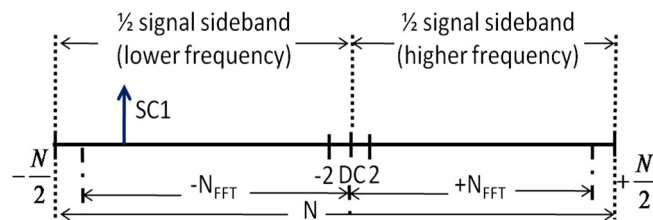


Fig. 6.2.2. A single OFDM subcarrier located at the start of the negative FFT points.

Fig. 6.2.2 shows the subcarrier assignment set at the start of the negative FFT points. The negative FFT points represent the subcarriers that can be assigned at the lower half frequency of a signal band. The subcarrier is modulated with 16 QAM data and the rest of the FFT points are assigned with zeros. To generate the OFDM subcarrier, the iFFT is applied and the transmit data is transposed into serial data of real and imaginary signal components. These electrical signals are converted into analogue signals by a digital to analogue converter (DAC). The signals are up-sampled into 80-GHz sampling frequency. The signals are then added with an RF local oscillator (LO), where the 90° phase shift is added into the imaginary (Im) signal component to suppress the RF upper

sideband [8]. The signals are connected into a complex modulator (C-MZI) and driven by a `laserCW` model with $\Delta\nu$, linewidth. The inset of Fig. 6.2.1 shows the optical spectrum representation with the single subcarrier at the negative FFT point. The optical carrier frequency is tunable by tuning the frequency of the RF LO. The signal is transmitted over 1500 km with only chromatic dispersion presented. The signal is received using PIN PD with a responsivity of 1.0. The signal is then down-converted into baseband signal by multiplying the received signal with a complex exponential signal with the frequency of the RF LO. After a serial-to-parallel data conversion, FFT is applied to convert the data from time to frequency domain. Equalization is performed by using a normalized channel estimation of the received signal with a long training symbol. The equalized data is then demodulated and the original data of the subcarrier is recovered.

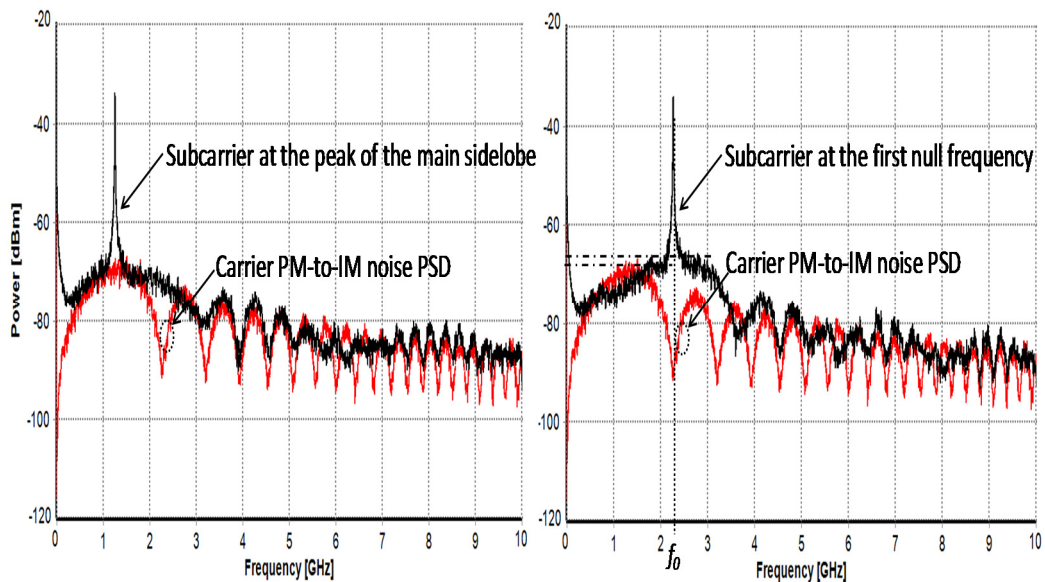


Fig. 6.2.3. A single OFDM subcarrier located on the carrier's highest intensity noise and on the first null of the PM-to-IM conversion noise PSD for a laser linewidth of 4 MHz and transmitted over 1500-km dispersive fibre.

Fig. 6.2.3 shows the received RF spectra of the single OFDM subcarrier transmission by using `laserCW` model with a linewidth of 20 MHz and 100 MHz. The red noise PSD represents the carrier's PM-to-IM conversion noise PSD after 1500 km of fibre, which is equivalent to 24000 ps/(nm·km) dispersion. The subcarrier is located on the top of the first sidelobe and at the first null, f_0 of the carrier's noise PSD. From the received RF spectra, when the subcarrier is located on the f_0 , it can be seen that the

IN floor has increased slightly with 1.3-dB higher IN around the subcarrier compared to the IN of the carrier's conversion noise PSD.

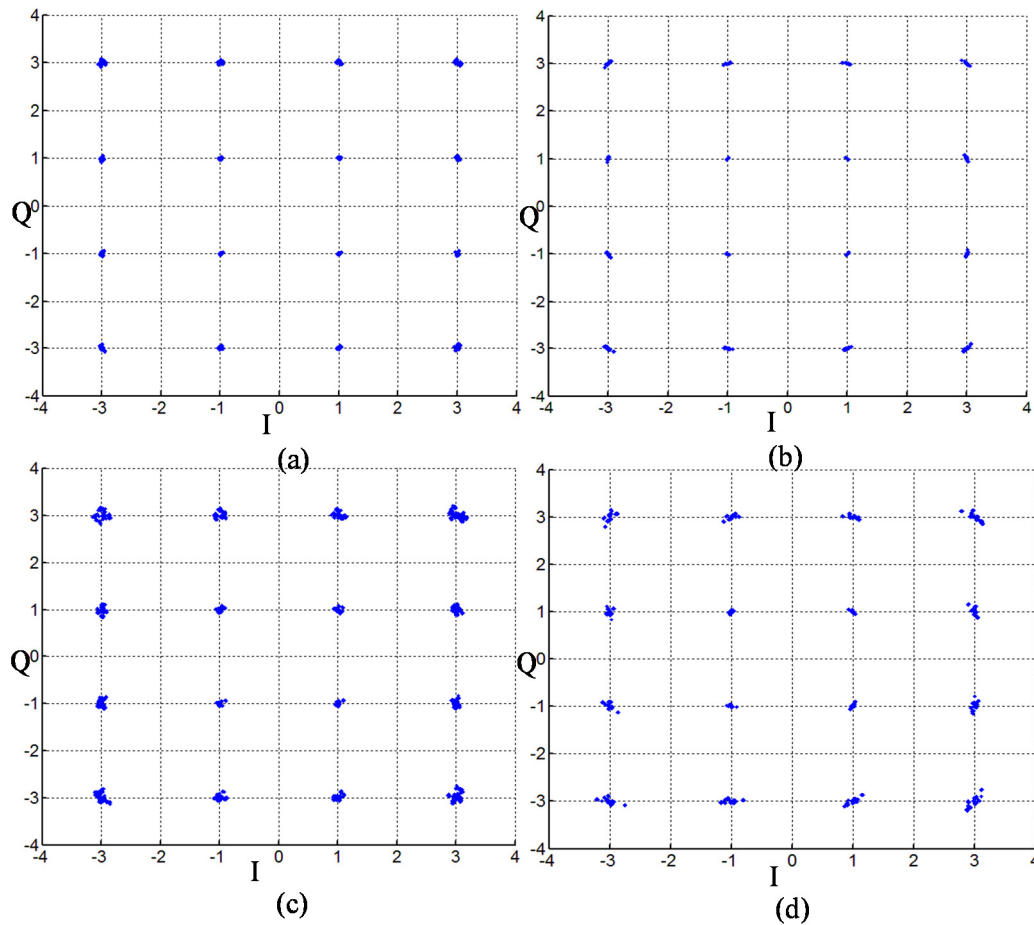


Fig. 6.2.4. Scatter plots for the subcarrier located on the (a) and (c) highest intensity noise and (b) and (d) at the first null of the carrier's PM-to-IM conversion noise PSD with a linewidth of 20 MHz and 100 MHz, respectively.

Fig. 6.2.4 shows the scatter plots when the subcarrier was transmitted over 1500 km of fibre with a linewidth of 20 MHz and 100 MHz. Fig. 6.2.4 (a) shows the plot when the subcarrier is at the peak IN of the first sidelobe and Fig. 6.2.4 (b) at the f_0 for the laser's linewidth of 20 MHz. Fig. 6.2.4 (c) and (d) shows the plot for the linewidth of 100 MHz when the subcarrier is at the peak of the first sidelobe and at the f_0 , respectively. From the plot, phase noise in the constellation can be seen when the subcarrier is located on the f_0 of the carrier's conversion noise PSD. The deviation of the phase rotation is smaller when the subcarrier is located on the top of the main sidelobe. At this location, the noise PSD gives the highest intensity noise, which produced a rounder and un-rotated scatter plot.

6.3 Effects of Laser Linewidth Interaction with Group Delay to the OFDM Subcarrier

In the DDO-OFDM transmission system, the time delay, τ_d , is imposed into each of the subcarriers by the dispersion. For example, when a subcarrier located at 12.5 GHz away from the DC is transmitted over a 500 km of fibre using 10-MHz linewidth, the amount of the delay imposed to the subcarrier can be calculated by;

$$\tau_d = D \cdot L \cdot \Delta\lambda \quad (6.3.1)$$

where L is the fibre length, D in s/m^2 and $\Delta\lambda$ is 0.1-nm wavelength resolution. The 12.5-GHz subcarrier frequency is used as a reference since $\Delta\lambda$ is 0.1 nm. After 500 km, the τ_d applied to the subcarrier is 0.8 ns. This is much smaller than the value of τ_c which is 31.83 ns calculated by using [10]

$$\tau_c = \frac{1}{\Delta\nu\pi} \quad (6.3.2)$$

Due to this, the noise pedestal as in Fig. 5.5.3 will be induced around the subcarrier at the output of the fibre. To investigate the effect of the noise pedestal, a single and a small number of OFDM subcarrier transmissions over the dispersive fibre have been done. The single subcarrier transmission will show the fundamental effects of the noise pedestal to the subcarrier with a variable linewidth, $\Delta\nu$ and D . This will also show the frequency dependence of the subcarrier across the signal bandwidth. The multiple subcarriers transmission will be used to investigate the interference effect between the adjacent subcarriers' noise pedestal. This was done by varying the subcarrier's spacing.

To investigate this effect, simulation setup of a virtual RF carrier DDO-OFDM transmission system was used. The laser model used was the `laserCW` in `VPITransmissionMaker`TM version 8.5, which models a DFB laser with an independent and variable $\Delta\nu$ characteristic. With this laser model, $\Delta\nu$ can be varied without laser's RIN and reduction in the laser's output power.

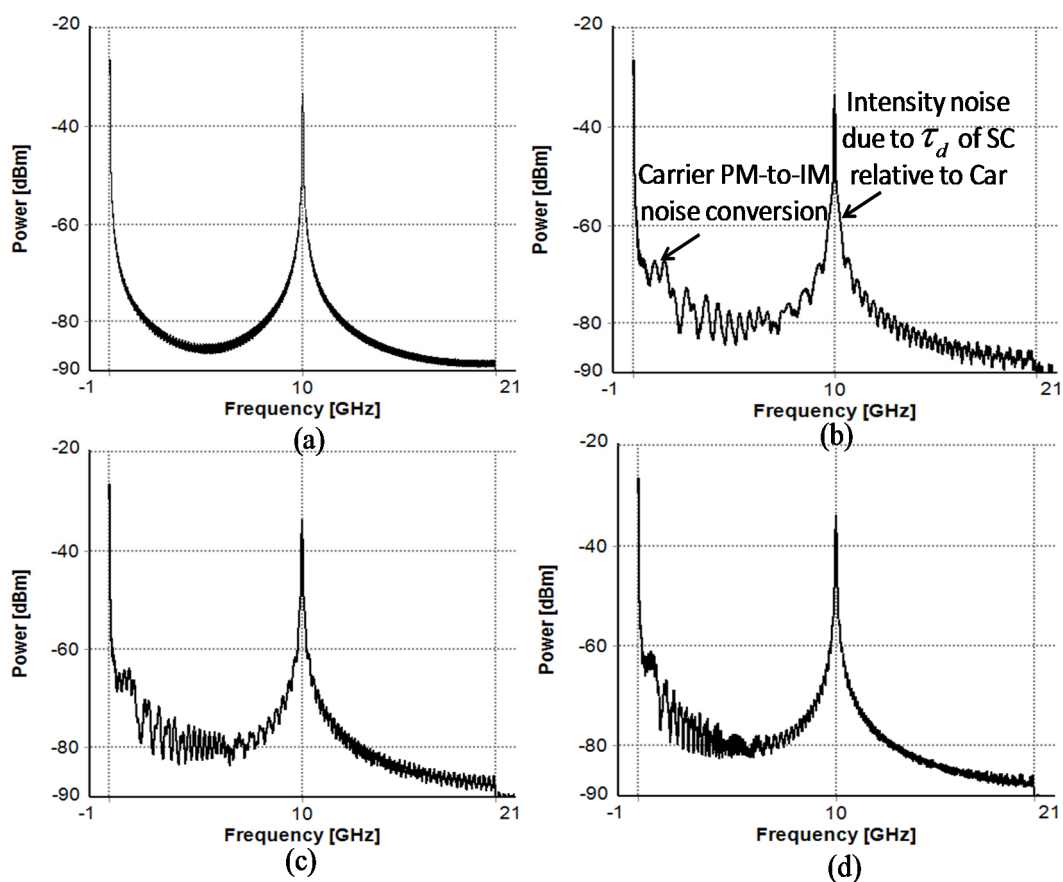


Fig. 6.3.1. Received RF spectrum of the first OFDM subcarrier at 10 GHz with (a) back-back transmission (b) 1500 km (c) 3000 km and (d) 6000 km.

Fig. 6.3.1 shows the received RF spectra for a single subcarrier located at 10 GHz with back-to-back transmission, 1500 km, 3000 km and 6000 km of z with D of 16 ps/(nm·km). In this simulation, a laser linewidth of 4-MHz was used at the transmitter. Fig. 6.3.1 (a) shows that no noise ripples appeared in RF spectrum of back-to-back transmission. As explained before, the noise pedestal around the subcarrier is appeared with the present of dispersion in the fibre, as shown in Fig.6.3.1 (b), (c) and (d).

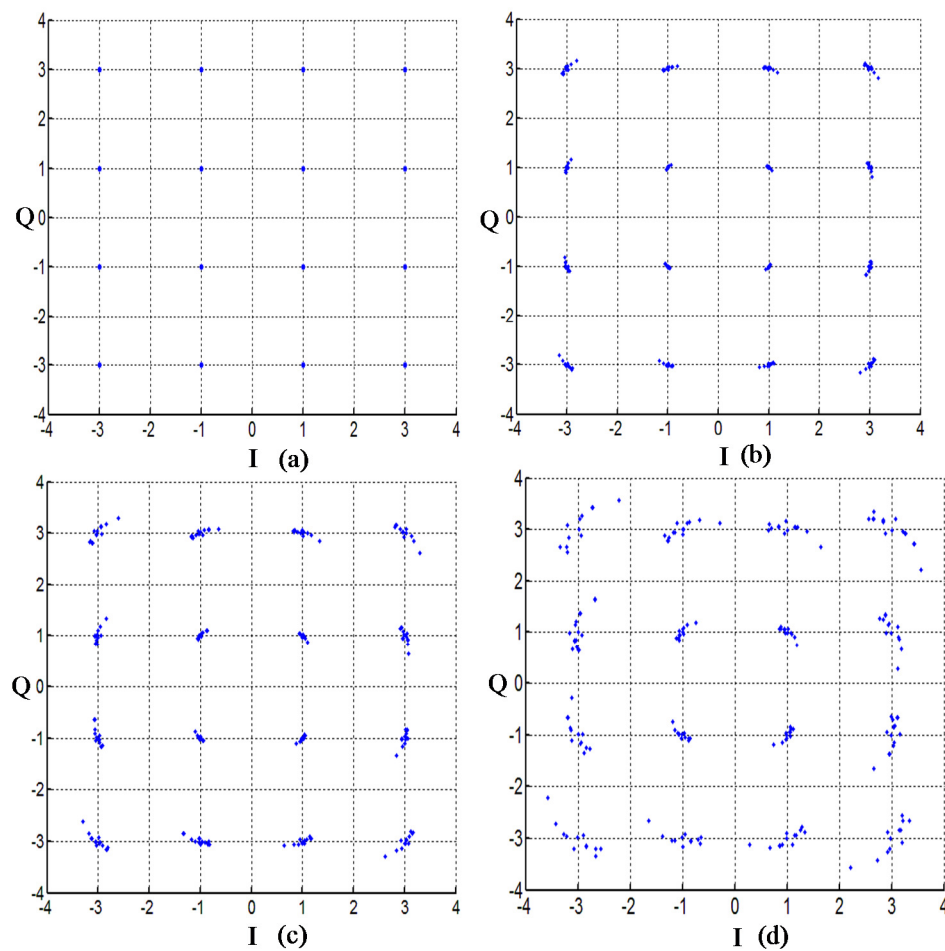


Fig. 6.3.2. Scatter plots of the single OFDM subcarrier transmission with 4-MHz laser linewidth over (a) back-to-back (b) 1500 km (c) 3000 km and (b) 6000 km of S-SMF.

Fig. 6.3.2 shows the scatter plots of the received subcarrier. The laser linewidth of 4 MHz was used at the transmitter to transmit the subcarrier over a back-to-back, 1500 km, 300 km and 6000 km of an S-SMF. A 16-QAM Gray-coded data of 300 symbols was modulated to the OFDM subcarrier. The subcarrier was set on the negative side of the FFT points. For the back-to-back (zero dispersion), the plot shows a noiseless scatter plot as in Fig. 6.3.2 (a). When the subcarrier was transmitted over the 1500 km, which is equivalent to 24000 ps/nm of $D \cdot z$, the constellation plot shows that the received symbols are phase rotated. The phase rotation of the symbols became more severe for the higher dispersion shown in Fig. 6.3.2 (c) for the 3000 km (48000 ps/nm) and (d) for 6000 km (96000 ps/nm).

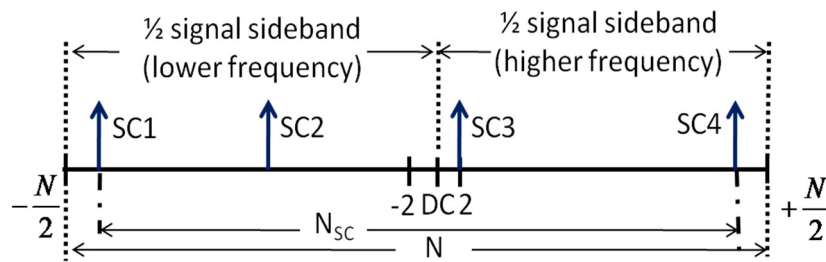


Fig. 6.3.3. The subcarrier location in the signal frequency band from the lowest frequency (SC1) to the highest frequency subcarrier (SC3).

Fig. 6.3.3 shows the subcarrier allocation across the N -FFT points for the investigation of the linewidth effect to the single subcarrier at four different frequencies. In this transmission, the single subcarrier will be transmitted over z -km. The four different frequencies of the subcarriers are represented by the SC1, SC2, SC3 and SC4, where SC1 is the lowest. The SC1 is placed at point 514, SC2 at 768, SC3 at 256 and SC4 at 510 of N equals to 1024 of the FFT-points. The transmission signal bandwidth used is 10 GHz. A frequency bandgap of 10 GHz was used to separate the start of the signal bandwidth from the carrier. This was done by setting the RF virtual frequency to 15 GHz. Therefore, SC1 is placed at 10.04 GHz, SC2 at 12.51 GHz, SC3 at 17.49 GHz and SC4 at 19.97 GHz. The bandgap is included because it is typically used in the DDO-OFDM system to place the unwanted subcarrier \times subcarrier beating noise upon a photodetection [11, 12]. The signal is transmitted over 1500 km of fibre.

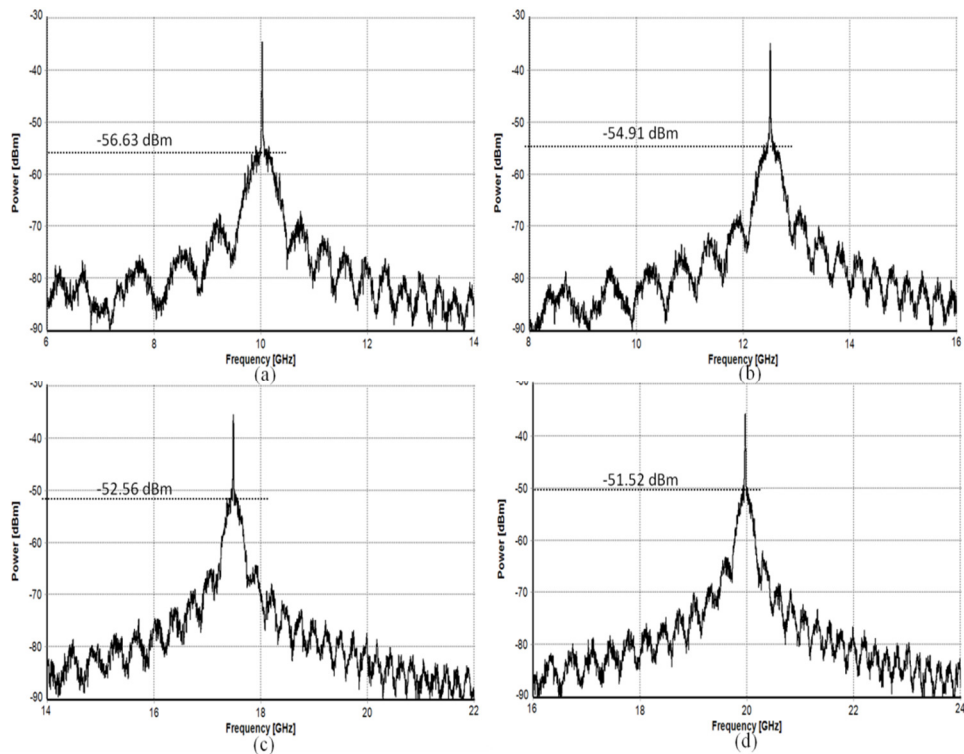


Fig. 6.3.4. The received RF spectrum for a single OFDM subcarrier transmission over 1500 km at a different subcarrier frequency of (a) 10.04 GHz (SC1) (b) 12.51 GHz (SC2) (c) 17.49 GHz (SC3) and (d) 19.97 GHz (SC4).

Fig. 6.3.4 shows the detected electrical spectrum with a noise pedestal around the subcarrier of (a) SC1 at 10.04 GHz, (b) SC2 at 12.51 GHz, (c) SC3 at 17.49 GHz and (d) SC4 at 19.97 GHz, after a transmission over 1500 km of S-SMF. The noise pedestal appeared due to the delay of the subcarrier relative to the carrier where the phase correlation is related to the $R_t = \frac{\tau_d}{\tau_c}$ [14]. As shown in Chapter 5 (externally modulated RF tones), the power of the noise pedestal around the subcarrier is increased for the high frequency subcarrier.

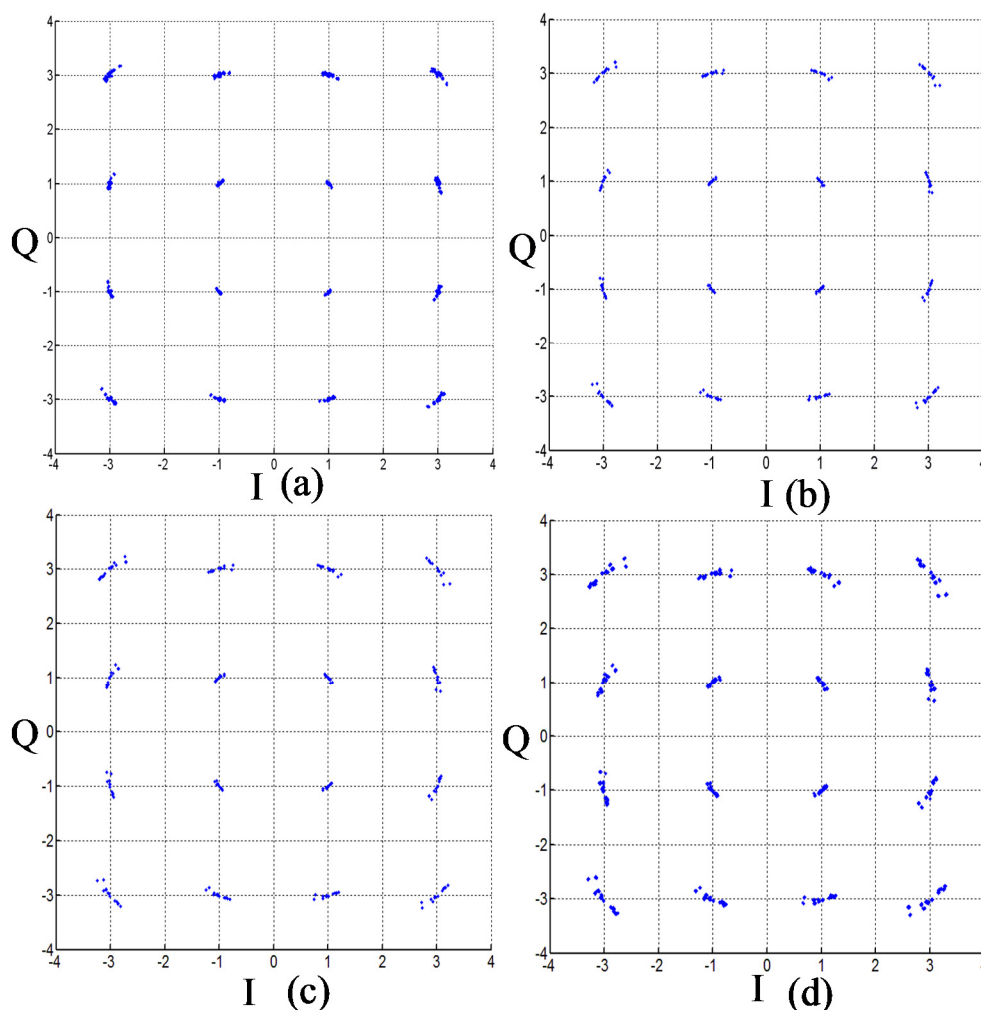


Fig. 6.3.5. Scatter plot of a 16 QAM using a single OFDM subcarrier transmission over 1500 km with 4-MHz linewidth laser at the subcarrier index of (a) 10.04 GHz (SC1) (b) 12.51 GHz (SC2) (c) 17.49 GHz (SC3) (d) 19.97 GHz (SC4).

Fig. 6.3.5 shows the received scatter plots for a single subcarrier transmitted over 1500 km with different subcarrier frequency location using 4-MHz laser linewidth. The SC1 is the lowest frequency (the first subcarrier in the subcarrier band) in the 10 GHz signal bandwidth. Even though SC1 is the first subcarrier in the band, the phase rotations of the received symbols are present. This is due to the 10-GHz bandgap separation between the first subcarrier and DC. Fig. 6.3.5 (b), (c) and (d) show that the phase noise effect becomes severe for the high frequency subcarrier, where the phase rotations are more significant. This is due to the increased of the noise pedestal's power around the high frequency subcarrier shown in Fig. 6.3.4. This is because more phase walk-off is experienced by the subcarrier at the high frequency due to the group delay effect.

Since the OFDM subcarriers spectra are orthogonal and partially overlapped in a way that it is still maintaining the orthogonality [1], it is significant to investigate the interference effects of the noise pedestal around each of the subcarriers, when they are placed adjacently. For this investigation, the same simulation setup in Fig. 6.2.1 was used with multiple OFDM subcarriers. The signal bandwidth was fixed to 2.5 GHz, which is equivalent to 256 data subcarriers (N_{sc}) from 1024 of N . The subcarrier's spacing, Δf_{sc} , was varied and achieved using zeroed FFT points in between the adjacent subcarriers. The smallest Δf_{sc} between any two subcarriers was 9.766-MHz. This was obtained when the subcarriers were placed at the consecutive FFT points.

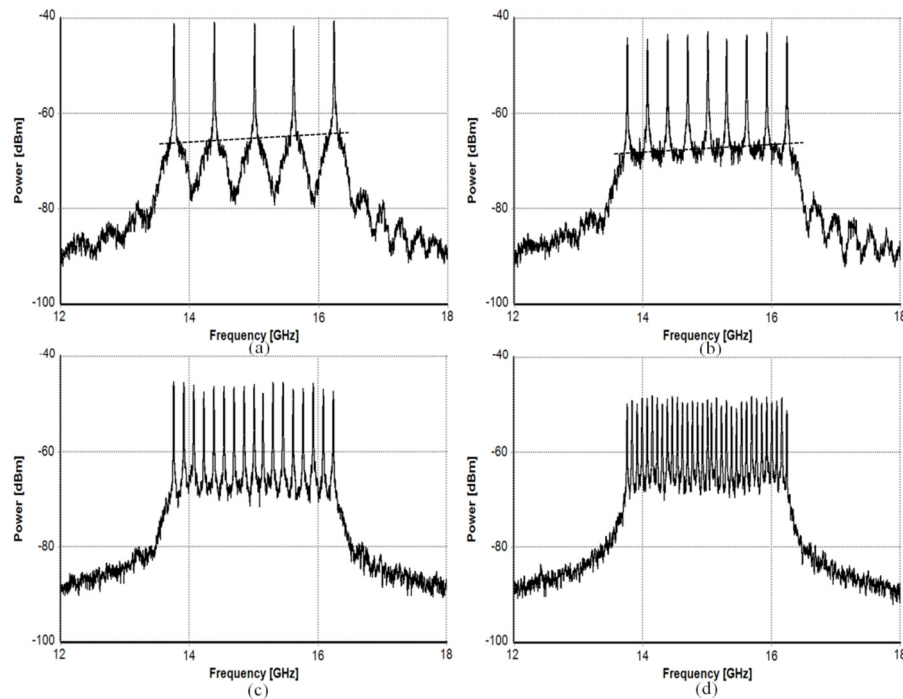


Fig. 6.3.6. Received RF spectra of a DDO-OFDM subcarriers transmission with Δf_{sc} of (a) 64 (b) 32 (c) 16 and (d) 8 zeroed subcarriers.

Fig. 6.3.6 shows the electrical spectra of multiple OFDM subcarriers transmitted using 4 MHz linewidth over 1500 km of fibre with (a) 64, (b) 32, (c) 16 and (d) 8 zeroed subcarriers to represent the subcarrier spacing, Δf_{sc} . In terms of frequency, the 64 zeroed subcarrier is equivalent to 625 MHz, 32 equivalent to 312.5 MHz, 16 equivalent to 156.25 MHz and 8 equivalent to 78.125 MHz. In the DDO-OFDM transmission with Δf_{sc} of 64, the RF spectrum shows that only the tails of the noise pedestals of each subcarriers are overlapped. This is shown as in Fig. 6.3.6 (a). The increase of the noise pedestal power around each of the subcarriers from the low to high frequency index

can be clearly seen when Δf_{sc} is large. This is shown in Fig. 6.3.6 (a) and (b). This is due to the delay of the first subcarrier is less than the delay induced to the subcarrier which is placed far from the carrier. In a DDO-OFDM system with a bandgap equals to the subcarrier bandwidth, the highest frequency index subcarriers (or the N^{th} subcarrier) has twice the delay experienced by the first subcarrier [14]. For the Δf_{sc} of 32, 16 and 8, the broad main lobes of the noise pedestals around the subcarriers are strongly overlapped and results in the interference between the subcarriers. The increase of the noise pedestal power shows in Fig. 6.3.6 with the phase rotations of the higher-frequency subcarriers in Fig. 6.3.5 show that the phase noise due to the laser linewidth upon detection in the DDO-OFDM transmission system is a function of the subcarriers' frequencies and the transmission distance. This confirms the study presented in [14]. Fig. 6.3.5 and 6.3.6 suggest that for a high accumulated dispersion, the higher-frequency subcarriers will suffer more from phase noise. This has been shown in Fig. 5.6.2, where the receiver's RF spectrum shows that the noise pedestal's peak power increases with the subcarrier frequency. The phase noise effect upon detection in the DDO-OFDM system is different from the CO-OFDM system, where in CO-OFDM system, the phase noise is independent of the subcarriers' frequency and common to all subcarriers known as common phase error (CPE) [6, 14, 25-27]. Fig. 6.3.6 also shows the broad noise pedestal around the subcarrier for higher frequency subcarriers when there is a high accumulated dispersion. This broad noise pedestal can introduce inter-subcarrier-interference (ISCI) between the adjacent subcarriers [14].

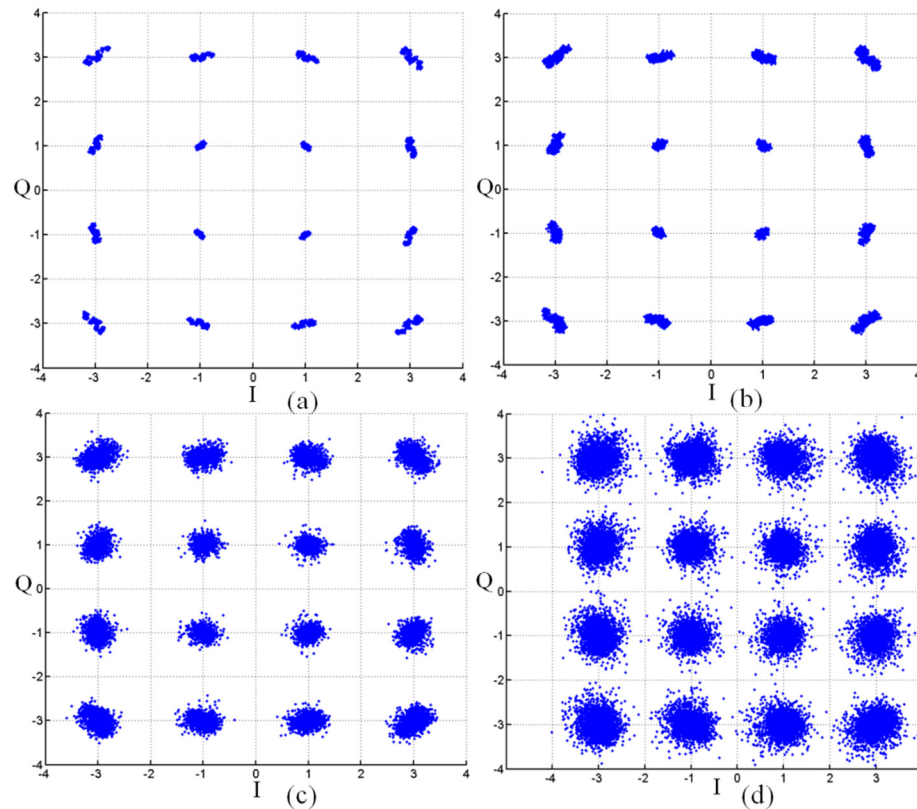


Fig. 6.3.7. 16-QAM scatter plots for the transmission of the DDO-OFDM subcarriers with Δf_{sc} of (a) 64 (b) 32 (c) 16 and (d) 8 zeroed subcarriers within 2.5-GHz signal bandwidth.

Fig. 6.3.7 shows the received scatter plots for the transmission of the DDO-OFDM subcarriers with the Δf_{sc} of 64-, 32-, 16- and 8-zeroed subcarriers. For the large Δf_{sc} of 64 and 32, the laser phase noise or the linewidth can be clearly seen affecting the received symbols with the phase rotations, as shown in Fig. 6.3.7 (a) and (b). When a smaller Δf_{sc} of 16 subcarriers was used, an ellipse shape of the phase rotated symbols constellations are shown in Fig. 6.3.7 (c). It can be seen that the outer quadrant symbols of (1,3), (3,1), (3,3), (-1,3), (-3,1), (-3,3), (-1,-3), (-3,-1), (-3,-3), (1,-3), (3,-1) and (3,-3) show a larger phase rotation compare to the inner quadrant symbols of (1,1), (-1,1), (-1,-1) and (1,-1). This shows that the linewidth of a laser will affect the outer QAM symbols more than the inner symbols. When the Δf_{sc} is smaller (8 subcarriers), the scatter plot in each symbol quadrant becomes more round, shown in Fig. 6.7.8 (d), compared to the ellipse shape of the symbol when the subcarrier separation is large. This investigation shows that, when no inter-subcarrier-interference (ISCI) denoted by the large Δf_{sc} , the linewidth of the laser has a strong influence on the received signal scatter plot. When the Δf_{sc} is smaller, the ISCI becomes more dominant compared to the phase rotation effects.

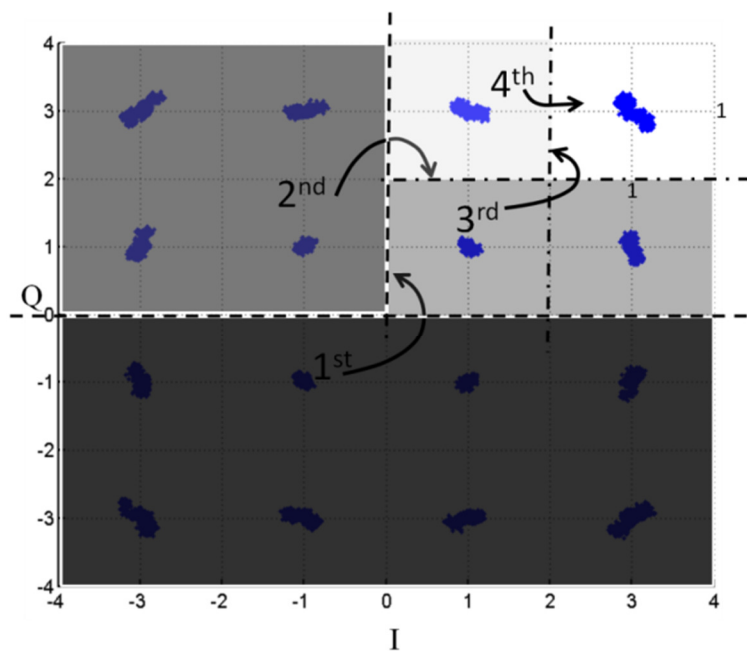


Fig. 6.3.8. The received symbols are transferred into one common quadrant to plot a histogram.

The distribution of the received symbols can be examined by plotting the histogram of them. Fig. 6.3.8 shows the method used to plot a histogram for the received symbols on a scatter plot by transferring the symbols into one common quadrant. To transfer the symbols into one common quadrant, the symbols are flipped based on the inphase (I) and quadrature (Q) axes. The steps and directions of the symbols flipping can be explained using Fig. 6.3.8. The first flip transferred all the symbols of the negative quadrature (Q) axis into the positive Q axis. The second flip transferred the symbols from the negative inphase (I) into the positive I. This results in the 4 quadrants of the symbols mapped onto (1,1), (-1,1), (-1,-1) and (1,-1). In order to get all of the symbols into one quadrant where all the symbols mapped onto the point (1,1), the same flips done in the first and second steps are repeated. When all of the symbols are transferred into one quadrant, a histogram was plotted for the I or Q axes. It was assumed that all the received symbols are mapped within the correct quadrant in the constellation plot.

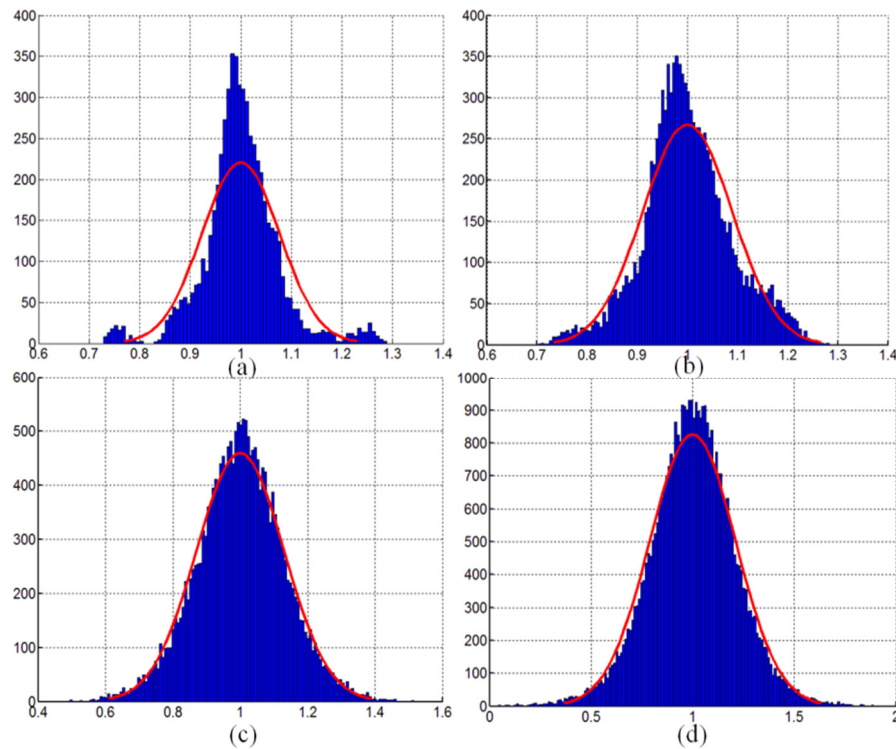


Fig. 6.3.9. Histogram plots of the inphase axis of the received symbols constellations for the Δf_{sc} of (a) 64- (b) 32- (c) 16- and (d) 8-subcarriers.

Fig. 6.3.9 shows the histogram plots of the inphase axis of the received symbols constellations shown in Fig. 6.3.8 for the Δf_{sc} of 64-, 32-, 16- and 8-zeroed subcarriers. From the histograms of Fig. 6.3.9 (a) and (b), the histograms are skewed to the left as compared to the normal distribution fit. This shows that, when phase noise induces the phase rotations of the received symbols, the distribution becomes non-Gaussian as more symbols fell near the boundary of the other symbol's quadrant, which indicates a large phase error. When smaller Δf_{sc} is applied, the noise pedestals around each of the SCs are interfering with each other, producing the more symmetric histogram, closer to the Gaussian fit. This is shown in Fig. 6.3.9 (c) and (d). The histograms suggest that, when there is only a single source of the interference that is the phase noise, the error is contributed by the phase noise itself (Fig. 6.3.9 (a) and (b)). When there are multiple sources of phase noise (coming from each of the overlapped subcarriers noise pedestal), the combined error produces more circular symbol and approximately symmetric Gaussian symbols plot (Fig. 6.3.9 (c) and (d)). A MATLAB receive code for this can be found in Appendix 3.2.

6.4 Effects of PM-to-IM Conversion Noise to the System Performance without ASE noise

Investigation on the effects of a PM-to-IM conversion noise to a DDO-OFDM system performance was done using a CWLaser module in VPItransmissionMaker version 8.5. The simulation setup used is similar to the setup in Fig. 6.2.1 using RF virtual carrier transmitter design. The number of subcarriers used to carry the data was 1022 from the total of 1024 iFFT-points with 300 OFDM symbols. The sample rate was set 10 GHz which was up-sampled to 80-GHz using 8 times oversampling. The simulations are done over 25 runs where different set of random data was used at each run. The transmit OFDM signal's real and imaginary components were generated using MATLAB and read by the simulator. The transmit code can be found in Appendix 3.3. In this simulation, the 4 QAM signal is transmitted which gives 20 Gb/s data rate. The signal is transmitted over several fibre length with variable laser linewidth in order to investigate the effects of the linewidth to the fibre dispersion. No amplified spontaneous emission (ASE) noise from the EDFA is considered. The received data was obtained in the form of text file and decoded using MATLAB to obtain average values of $\frac{E_b}{N_0}$, Q-factor and BER over the 25 runs. The receive code can be found in Appendix 3.4.

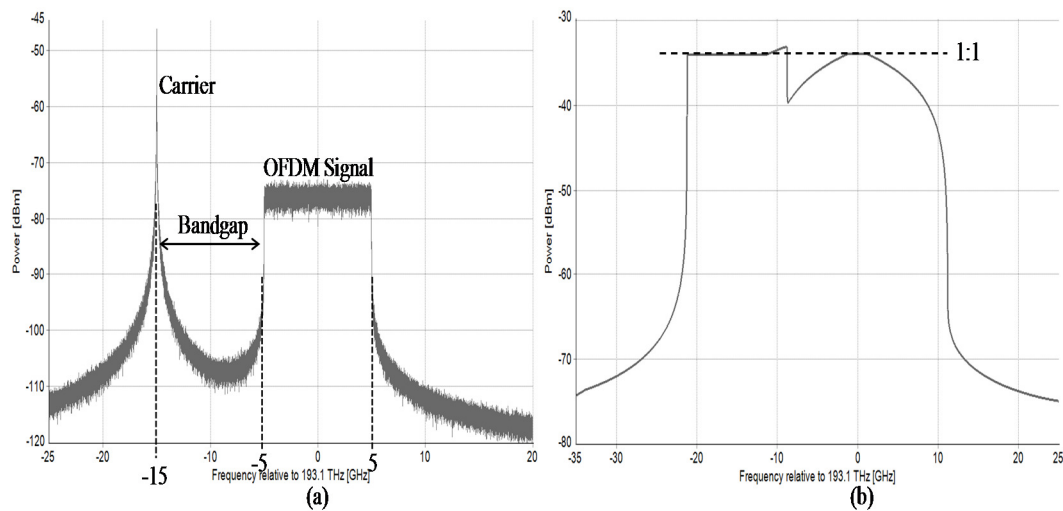


Fig. 6.4.1. Optical spectra at C-MZI's output when (a) without frequency resolution and (b) at 0.1-nm resolution.

Fig. 6.4.1 shows the optical spectra at the C-MZI output taken when (a) no frequency resolution is used and (b) with 0.1-nm resolution bandwidth. This spectrum

is taken before the transmitter pre-amplifier. Fig. 6.4.1 (a) shows the carrier and the OFDM signal band of 10-GHz from -5 GHz to +5 GHz. With the RF virtual carrier, both positive and negative FFT-points can be used for a data transmission. The carrier is tuned to 15 GHz. This gives a bandgap of 10 GHz, which separates the signal band away from the carrier. The bandgap is used to place the unwanted subcarriers \times subcarriers mixing upon photodetection [12, 15-17]. This mixing noise is also known as inter-modulation distortion (IMD). Fig. 6.4.1 (b) shows the spectrum at 0.1-nm resolution bandwidth. The carrier and signal band power is shown to be in 1-to-1 ratio in order to achieve the best system performance [12, 15-19].

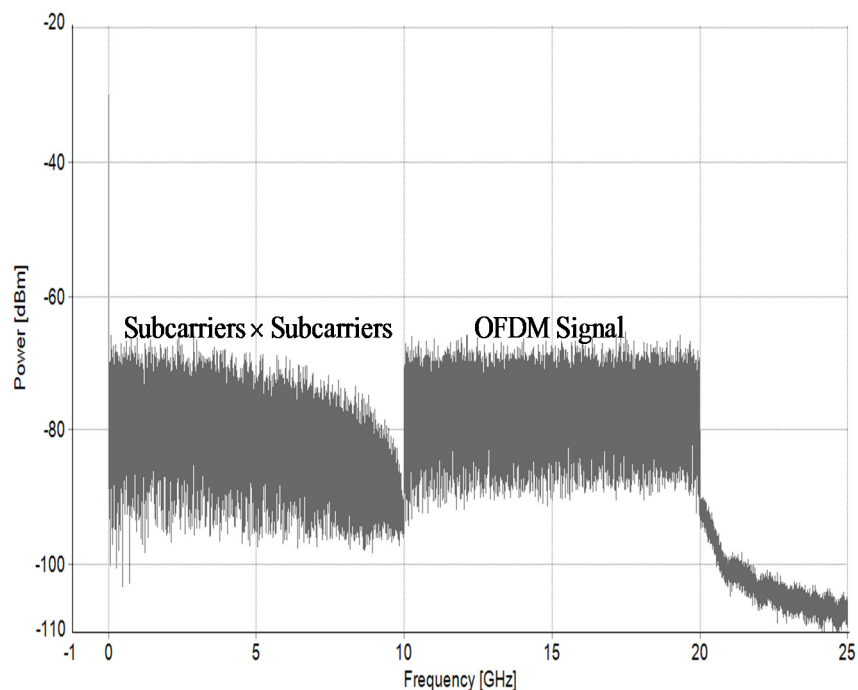


Fig. 6.4.2. Received RF spectrum after photodetection.

Fig. 6.4.2 shows the received RF spectrum obtained after a photodetection. The spectrum shows that the subcarrier \times subcarrier mixing falls within the bandgap without interfering with the OFDM signal band. The OFDM signal is shown from 10- to 20-GHz, which produced by the mixing of carrier \times subcarriers [19]. A relatively flat signal band is also shown across this signal bandwidth.

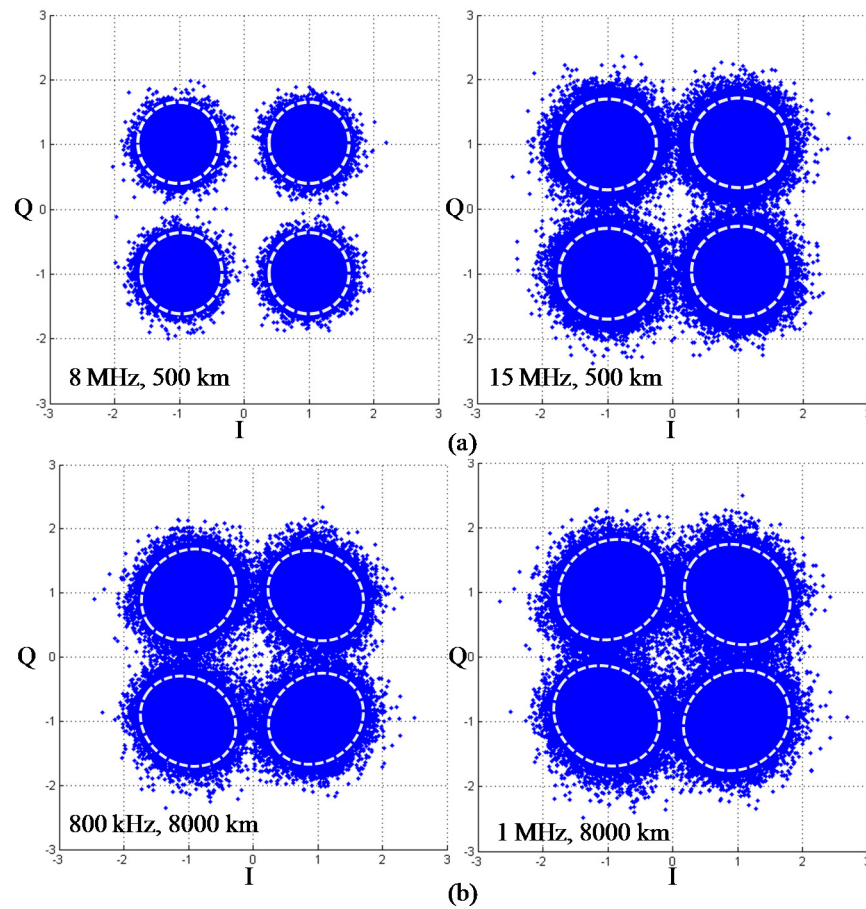


Fig. 6.4.3. Scatter plots of 4 QAM OFDM signal band transmitted over (a) 500 km using 8- and 15-MHz linewidth and (b) 8,000 km using 800-kHz and 1-MHz linewidth.

Fig. 6.4.3 shows the scatter plots of 4 QAM with 10-GHz signal bandwidth, transmitted over (a) 500 km S-SMF using wide linewidth laser of 8 MHz and 15 MHz and (b) an ultra-long haul 8,000 km using linewidth of 800 kHz and 1 MHz. The transmission is done to observe the effect of the laser's phase noise and a high dispersion to the received scatter plots. The S-SMF's dispersion coefficient was set to 16.75 ps/(nm·km) which gives the total dispersion-length product of 8,375 ps/nm and 134,000 ps/nm for 500 km and 8,000 km, respectively. As shown in Fig. 6.4.3 (a), a round scatter plot is achieved when the wide linewidth laser of both 8- and 15-MHz is used at the transmitter. The dotted-line circle is drawn on top of the symbols points as a reference. The round-shape scatter plot is also observed for the transmission over 2,000- and 4,000-km at a BER of 1×10^{-3} . As explained in Section 6.3, a phase rotation of the OFDM symbols can be imposed due to the phase error of the subcarriers relative to the carrier, which caused the noise pedestal around each of the subcarriers. The phase error can be clearly seen when the subcarriers are spaced far from each other. However,

at the ultra-long fibre transmission of 8,000 km, some phase rotations of the symbol plots can be observed as in Fig. 6.4.3 (b) using laser linewidths of 800-kHz and 1-MHz. Dotted-line ellipses are drawn on top of the plots as the reference to show the rotated symbols plot. This shows that even though the subcarriers are closely-spaced to each other in which the ISCI is dominating the system performance, the phase rotation can still be experienced by the symbol when an extremely high dispersion is imposed in the transmission. This is because at this fibre length, a large group delay effect is imposed to each of the subcarrier relative to the carrier.

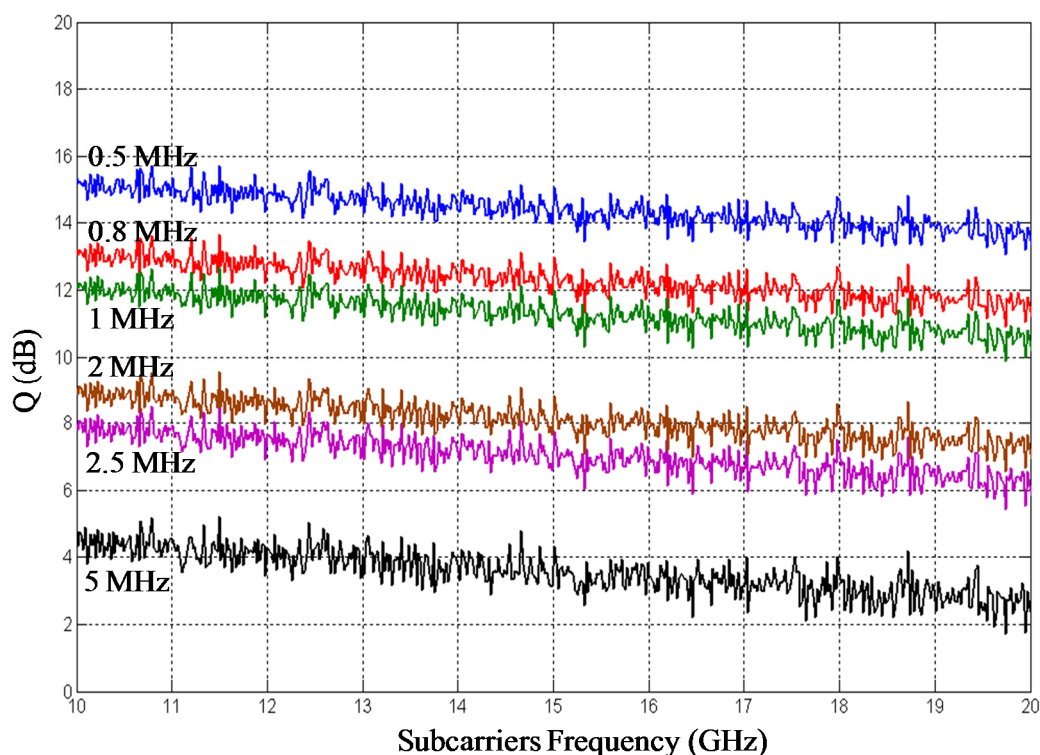


Fig. 6.4.4. Q-factor versus subcarrier frequency of 10 GHz 4 QAM OFDM signal bandwidth transmitted over fibre length of 8,000 km using a laser linewidth.

Fig. 6.4.4 shows the plots of Q-factor versus subcarrier frequency of 4 QAM OFDM signal with 10-GHz bandwidth transmitted over 8,000 km of fibre using a certain laser linewidth at the transmitter. The plots show that the Q performance is decreased by 2 dB from the low to high frequency subcarriers. This is due to the phase-walk-off of the subcarriers that are situated far from the carrier is higher than the one closer to the carrier. This results in higher phase error at the high frequency subcarriers. The plots also show that the Q is limited by the linewidth. The narrowest linewidth of 0.5 MHz gives the best Q performance across the subcarriers. Reduction of the overall Q can be seen when wider linewidth is used. At 8,000 km dispersive fibre, the Q is

reduced by the average of 2.1 dB when the linewidth is increased by 300 kHz from 0.5 MHz to 0.8 MHz. Higher decrement of 3.1 dB is shown when 1-MHz wider linewidth is used from 1 MHz to 2 MHz. With 3-MHz wider linewidth, the Q is decreased by 4.6 dB shown by the linewidth from 2 MHz to 5 MHz.

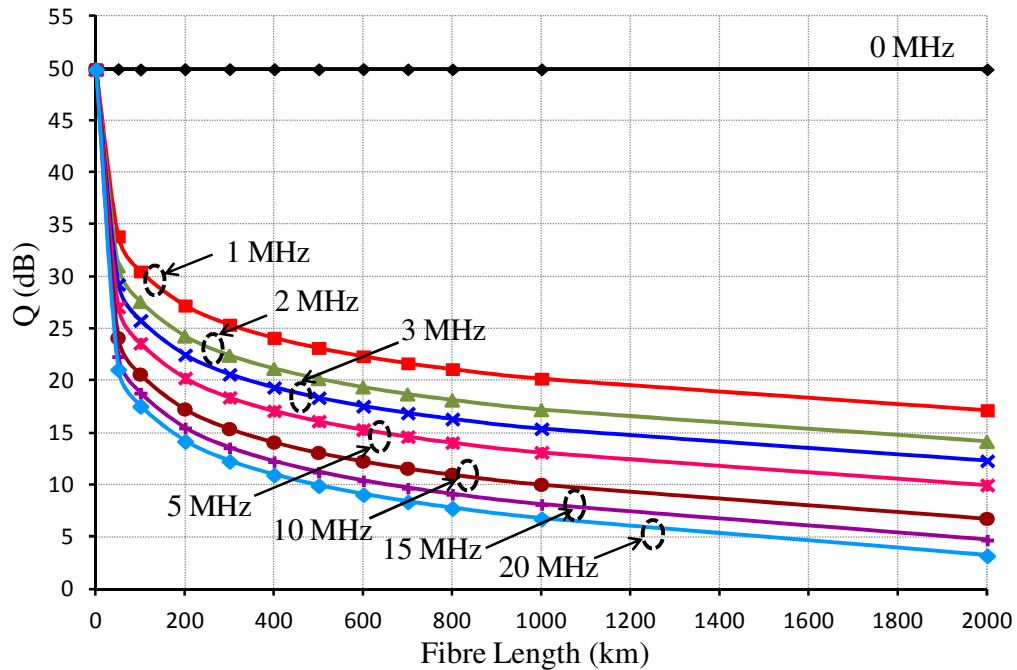


Fig. 6.4.5. Q-factor versus fibre length of 4-QAM OFDM transmissions as a function of laser linewidth.

Fig. 6.4.5 shows the Q-factor versus fibre length for 4-QAM OFDM signal transmitted using several laser linewidths. When no laser phase noise applied at the transmitter (0-MHz linewidth), the Q is constant at 50 dB across the fibre length. The Q started to decrease once the laser phase noise is applied to the transmitter with the present of dispersion. The dispersion imposed is from the fibre length varied from the shortest distance of 50 km and increased to 2,000 km. At every linewidth, the Q performance is decreased with the increase of dispersion. The plots show that the narrowest linewidth gives the best Q across the fibre lengths. When the linewidth is wider, the Q is decreased. This is shown by 3-dB Q degradation when linewidth was widened from 1 MHz to 2 MHz. When the linewidth was set to 3 MHz, the Q is reduced by 1.9 dB from the linewidth of 2 MHz. The degradation of 3 dB is also encountered when the linewidth was varied from 5 MHz to 10 MHz. This degradation is increased further when the linewidth was widened by 5 MHz stages shown by 2 dB from 10 MHz to 15 MHz and 1.3 dB from 15 MHz to 20 MHz linewidth is used. Note that, for 4

QAM DDO-OFDM transmission, 9.8-dB Q is required in order to achieve 1×10^{-3} BER [19, 20].

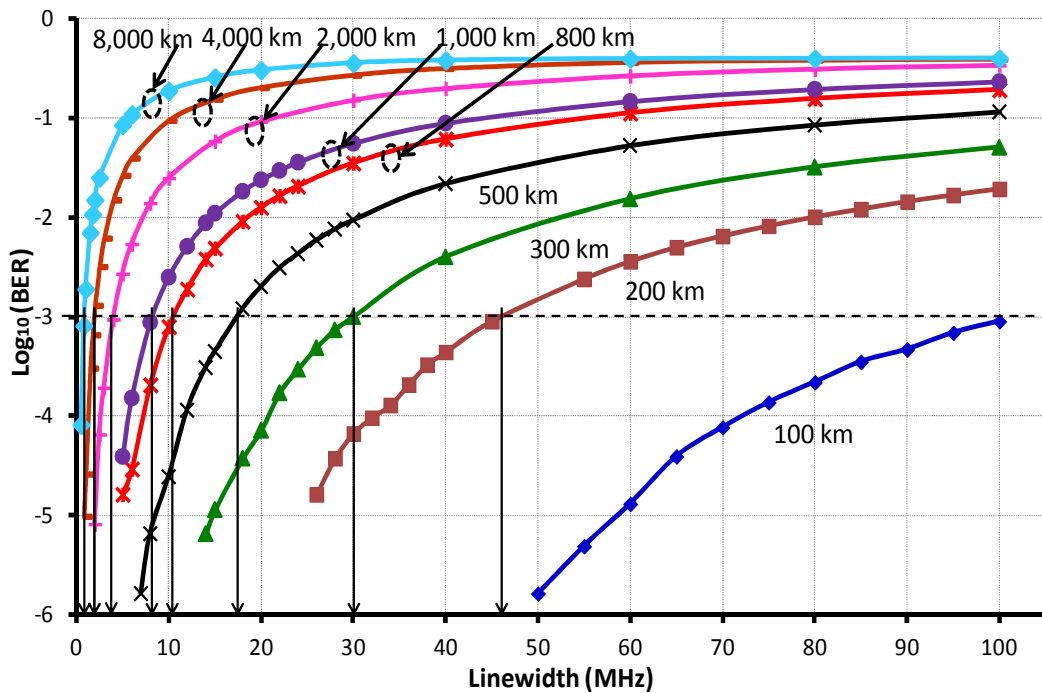


Fig. 6.4.6. $\log_{10}(\text{BER})$ versus laser linewidth for a transmission of 20 Gb/s with 4 QAM using 10-GHz signal bandwidth over several fibre lengths.

Fig. 6.4.6 shows the plots for BER versus linewidth for a transmission of 20 Gb/s with 4 QAM using a 10-GHz signal bandwidth over several dispersive fibre lengths. In this simulation, only the linewidth and the dispersion are imposed into the system without any ASE noise. From this graph, the linewidth requirement to achieve the acceptable BER of 10^{-3} at each transmission length can be identified. At a short length of 100 km, linewidth of more than 100 MHz can be used to achieve this minimum BER. At 200 km, this BER can be achieved using around 46 MHz of linewidth, 300 km using 30 MHz, 500 km using 17.4 MHz and at 800 km using 10.5 MHz. At an ultra-long haul transmission distance of 1,000 km, this minimum BER can be achieved using 8.4 MHz, 2,000 km using 4.1 MHz, and at 4,000 km using 2 MHz. This shows that without the ASE noise, an ultra-long haul transmission system can be achieved using a wider linewidth laser as compared to the coherent system which requires narrow linewidth of hundreds of kilohertz [5, 7, 21-24]. These also show that a low-cost laser with wide linewidth such as a distributed-feedback laser (DFB) can be used in the DDO-OFDM transmitter design. Finally, at 8,000 km of transmission length, linewidth at around 750 kHz is required to achieve this BER. At this length, the accumulated group delay from

fibre dispersion is large and imposed large phase error at each of the subcarrier relative to the carrier.

6.5 Effects of Linewidth Interaction with Dispersion on High M -QAM OFDM Signal

In this section, the transmissions of higher than 4 QAM M -size data transmission were done to investigate the effect of laser phase noise interaction with fibre dispersion. This can be done using the same simulation setup as in Fig. 6.2.1. In this simulation, 4, 16 and 32 QAM modulated OFDM signals are transmitted over several fibre lengths using several different linewidth lasers at the transmitter. The laser used was a `laserCW` module. A 10-GHz signal bandwidth is used which gives 20-, 40- and 50-Gb/s data rates for the 4-, 16- and 32-QAM, respectively.

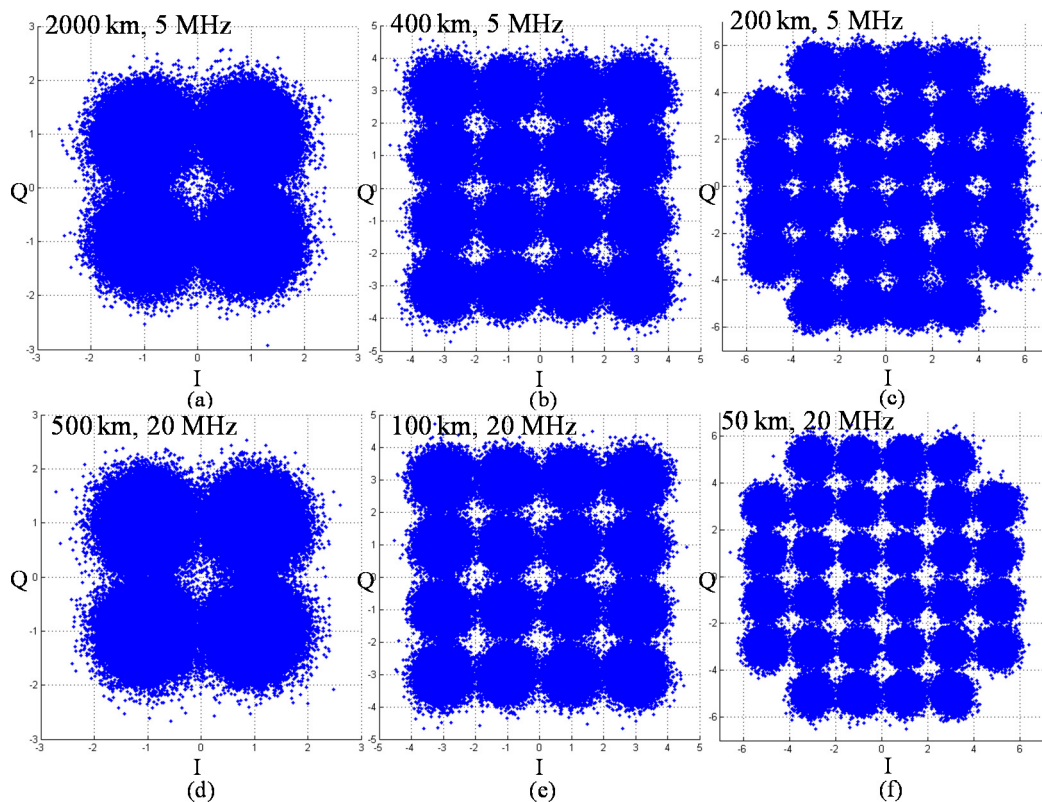
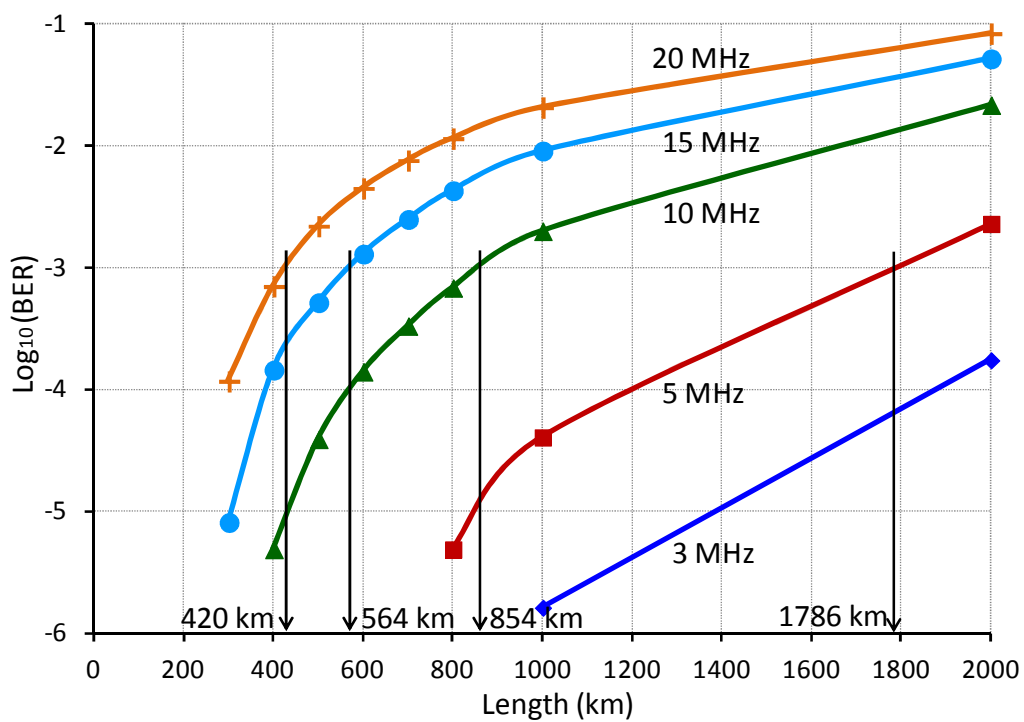


Fig. 6.5.1. Scatter plots of 4, 16 and 32 QAM with BER at around 10^{-3} using 5 MHz and 20 MHz laser linewidths transmitted over (a) 2000 km, (b) 400 km, (c) 200 km, (d) 500 km, (e) 100 km and (f) 50 km.

Fig. 6.5.1 shows the scatter plots of 4-, 16- and 32-QAM of OFDM signal transmitted using 5-MHz laser linewidth over (a) 2000 km, (b) 400 km, and 200 km of a dispersive fibre with BERs of 2.3×10^{-3} , 1.4×10^{-3} and 1.4×10^{-3} , respectively. A

wider linewidth laser of 20 MHz is used over (d) 500 km, (e) 100 km and (f) 50 km the BER of 2.2×10^{-3} , 9.4×10^{-3} and 4.7×10^{-3} , respectively. All the plots show a round-shaped of the received symbols at around it origin as compared to the scatter plots of an ultra-long haul transmission in Fig. 6.4.3. This shows that the phase noise influence to the received OFDM symbol due to the PM-to-IM conversion noise is not as significant as when an ultra-large dispersion is involved. The round-shaped received symbols will produce a Gaussian distribution when a histogram is plotted. This is similar to the histogram plotted in Fig. 6.3.10 (d) when a narrower subcarrier spacing is applied.



(a)

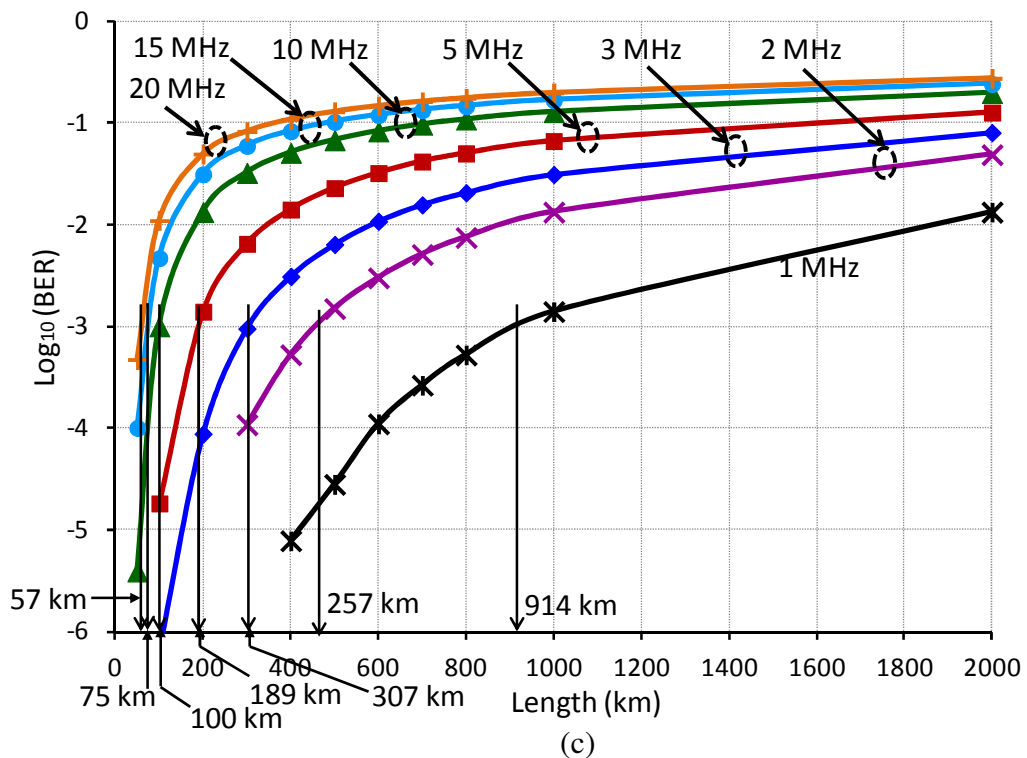
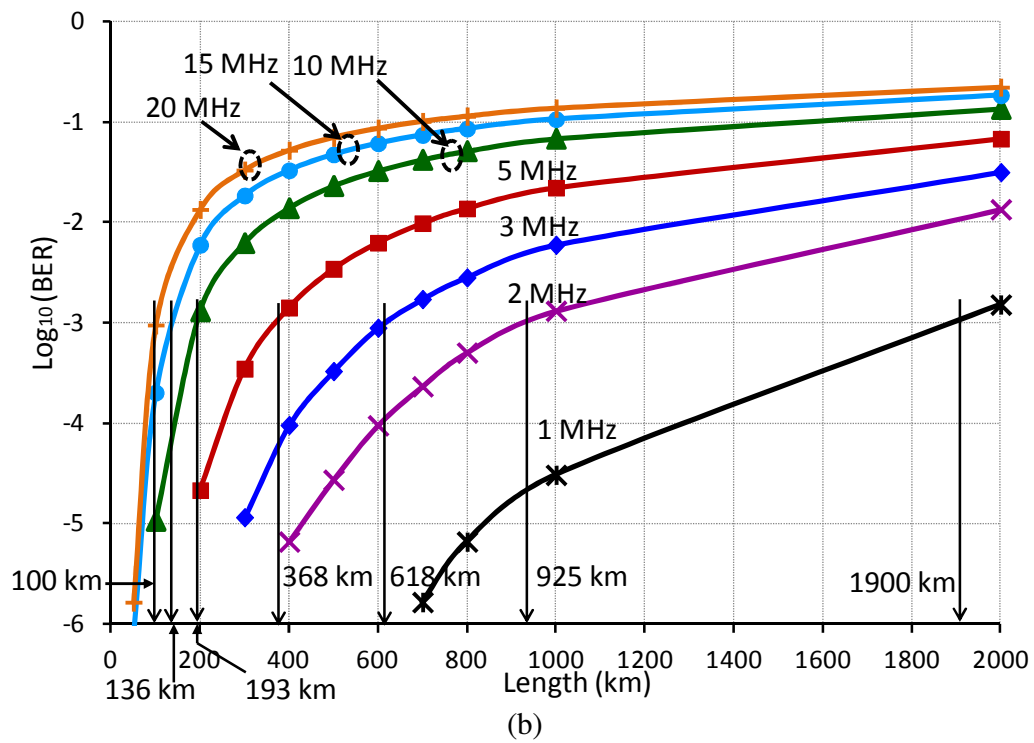


Fig. 6.5.2. BER versus dispersive fibre length for (a) 4- (b) 16- and (c) 32-QAM modulated OFDM signal with 10-GHz signal bandwidth.

Fig. 6.5.2 shows the plots of BER versus fibre length of a dispersive-fibre for an OFDM signal transmission using (a) 4-, (b) 16-, and (c) 32-QAM with 10-GHz signal

bandwidth. The transmissions were done using the same signal bandwidth in order to have a comparable effect of phase error at the highest frequency or the farthest subcarrier from the optical carrier, in which an upper sideband signal band was used. In each plot, a line is drawn to show the crossing at the minimum BER = 10^{-3} requirement for forward error correction (FEC) with its respective transmission length. In Fig. 6.5.2 (a), a small M-size using 4-QAM shows that the transmission length of more than 2000 km can be achieved using a 3-MHz laser linewidth with the absent of ASE noise. With a wider linewidth of 5 MHz, 1786 km of transmission length can be achieved. The linewidth was increased to 20 MHz where 420 km is achieved at the minimum BER. When the number per bits in a symbol is increased to 4, the maximum length at the BER = 10^{-3} is reduced significantly. This is shown by Fig. 6.5.2 (b) using 16-QAM OFDM signal transmission. Using 1 MHz, the length of 1900 km can be achieved. This length is significantly reduced when 2-MHz linewidth was used, with the approximate maximum length of 925 km. The maximum length is further reduced with the increased of linewidth. At 5 MHz, only 368 km can be achieved as compared to 1786 km when using 4 QAM. With 20-MHz, the 16-QAM signal transmission can only reach 100 km. When a higher M-size QAM was used, the limitation of the phase noise with the dispersion is increased. This can be seen from the plot in Fig. 6.5.2 (c) for a 32 QAM signal transmission. At 1-MHz linewidth, the maximum distance achieved is around 914 km as compared to 1900 km for the 16 QAM. Note that, the 32 QAM symbol has one additional bit in its symbol compared to the 16 QAM. Thus, system designers need to carefully consider the severe limitation experienced by 32 QAM data as compared to the 16 QAM since only a small increase of data rate can be achieved with the 32 QAM. When the linewidth is increased to 2 MHz, the maximum length achieved is reduced significantly to 257 km. When a wider linewidth was used, the length is gradually reduced. At 20-MHz linewidth, only a short length of 57 km can be achieved which reduced almost half of the length achieved with 16 QAM at 20 MHz. The plots present here show that the limitation of the PM-to-IM conversion noise due to the wide linewidth laser is less severe when using smaller M-size QAM constellation. These plots can be used to estimate the maximum transmission length for 4-, 16- and 32-QAM with 10-GHz signal bandwidth.

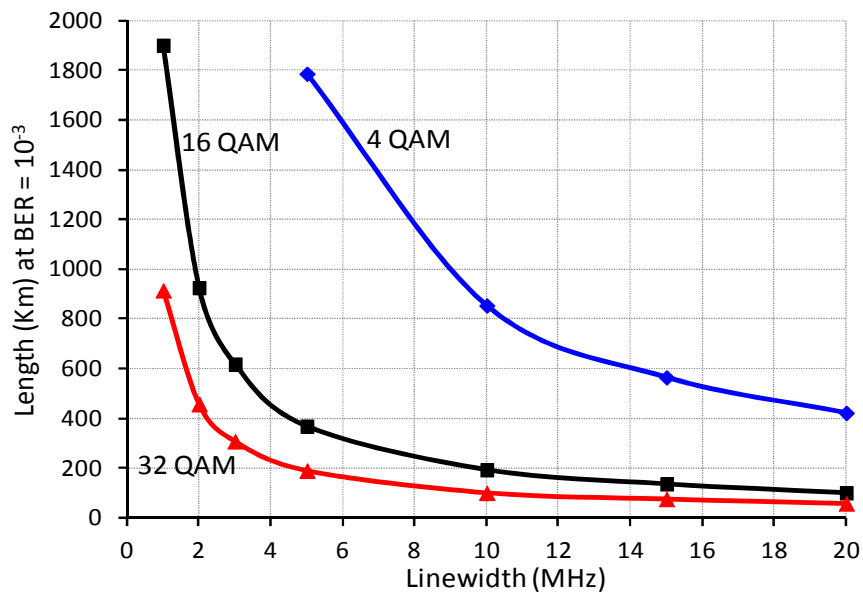


Fig. 6.5.3. Fibre length versus laser linewidth taken at $BER = 10^{-3}$ for OFDM signal transmission using 4-, 16- and 32-QAM with 10 GHz signal bandwidth.

Fig. 6.5.3 shows the fibre length versus linewidth taken at -3 dB of $\log_{10}(BER)$ for 4-, 16- and 32-QAM OFDM signal with 10-GHz signal bandwidth. The figure shows that the smaller M-size QAM can tolerate with a wider linewidth as compared to the larger M-size. A significant reduction of the maximum fibre length is shown when the linewidth used is increased from 1 MHz to 2 MHz. When the linewidth is further widened from 10 MHz to 20 MHz, the decrease of the achieved maximum lengths is small and more gradual are shown. This shows that the PM-to-IM conversion noise is already dominating the system due to the large laser phase noise.

6.6 Optical Signal-to-Noise Ratio (OSNR) Requirement with PM-to-IM Conversion Noise Limitation

In this section, the requirement of an optical signal-to-noise ratio (OSNR) of the OFDM signal with the effect of PM-to-IM conversion noise is presented. In this simulation, the OSNR requirements of the transmitted signal modulated using 4-, 16-, 32- and 64-QAM are presented. Noise power loading using a white Gaussian noise source obtained using `GWNoise` module in `VPItransmissionMaker` version 8.5 was used in order to achieve the OSNR level.

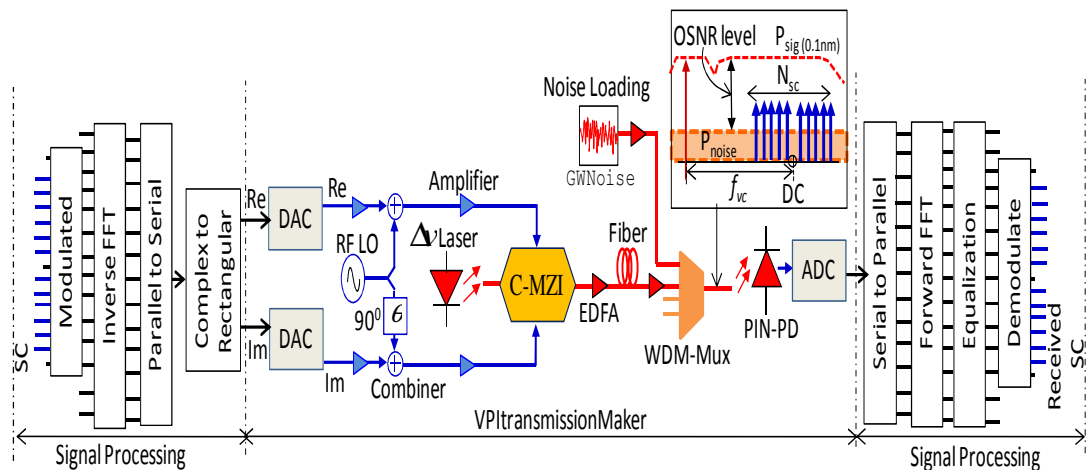


Fig. 6.6.1. Simulation setup of an RF virtual carrier DDO-OFDM transmission system using a noise loading at the receiver to investigate an OSNR requirement.

Fig. 6.6.1 shows the simulation setup of a DDO-OFDM system using a virtual carrier transmitter with a noise power loading applied at the receiver. The transmitter part of the system is similar to the setup in Fig. 6.2.1 but with all of the subcarrier used except for the one at DC, $\frac{N}{2}$ and $\frac{N}{2} + 1$, where N is the total number of subcarriers or the FFT-points. The signal processing part was done using MATLAB version R2008a and the code can be found in Appendix 3.3. The generated real (Re) and imaginary (Im) signals are then transmitted in the VPI's simulation setup. An S-SMF with dispersion of 16 ps/(nm-km) was used in the setup where the length is varied. A noise loading which introduces the noise power density into the system, with an EDFA to control the OSNR level over a 12.5-GHz resolution bandwidth or 0.1 nm is applied before a photodetector. An OSNR meter was used after the WDM multiplexing to confirm that a correct OSNR level is achieved. After the photodetector, the signal is converted into a digital signal using an ADC and processed using MATLAB. The received code can be found in Appendix 3.4 and a VPItransmissionMaker's simulation schematic can be found in Appendix 3.5. The phase noise is varied by varying the linewidth of the laser in order to investigate the OSNR requirement with the PM-to-IM conversion noise. The signal bandwidth used was 10 GHz for every M -QAM modulation with the virtual carrier frequency set to 15 GHz. The transmitted optical spectrum is similar to the spectrum in Fig. 6.4.1.

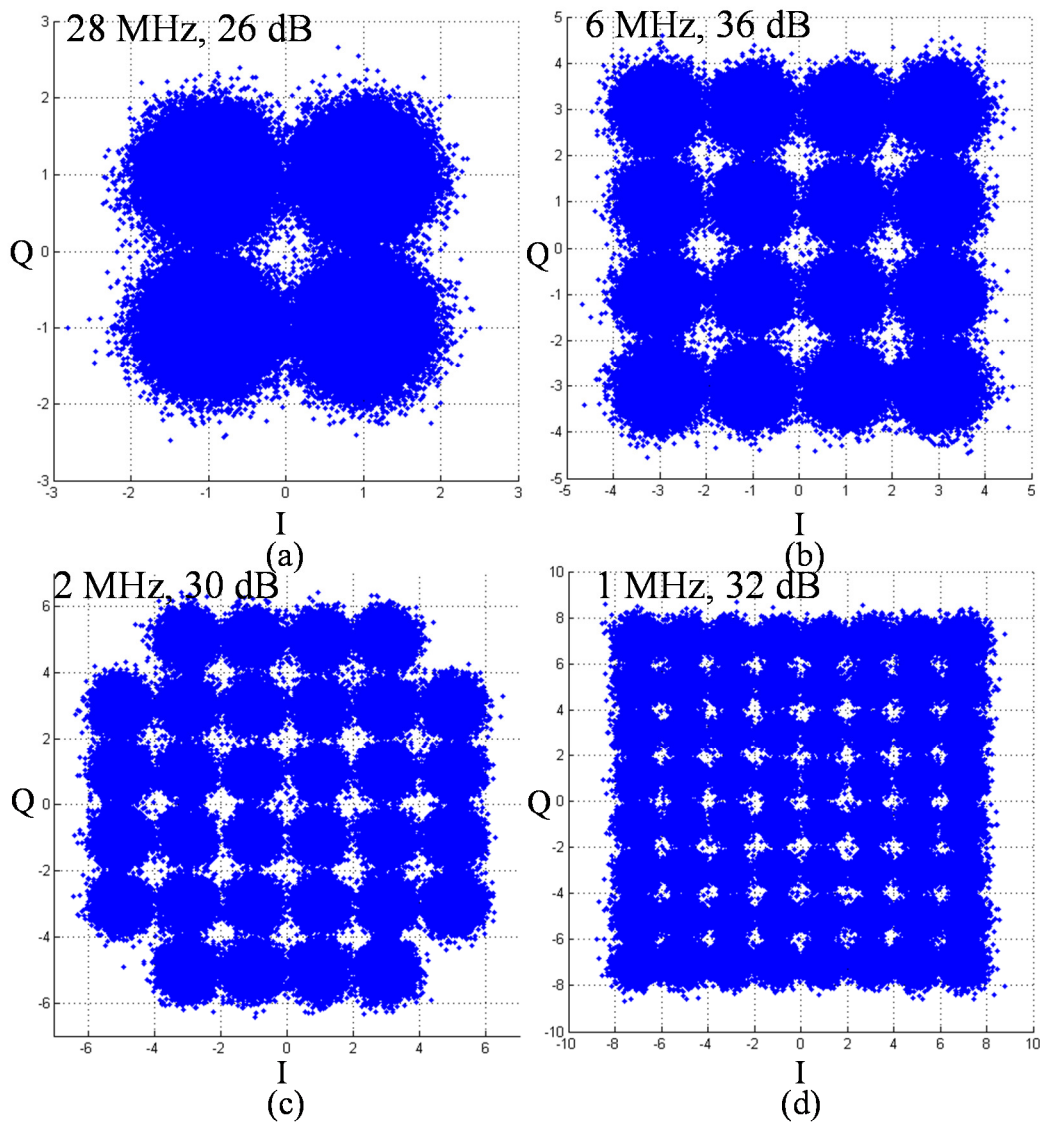


Fig. 6.6.2. Received scatter plots taken around -3 dB of $\log_{10}(\text{BER})$ for the 4-, 16-, 32- and 64-QAM modulated OFDM signals transmitted over 300 km using the linewidth and OSNR of (a) 28 MHz and 26 dB, (b) 6 MHz and 36 dB, (c) 2 MHz and 30 dB and (d) 1 MHz and 32 dB, respectively.

Fig. 6.6.2 shows the scatter plots of 4-, 16-, 32- and 64-QAM OFDM signal received after 300 km of dispersive fibre. The scatter plots taken at around $\text{BER} = 10^{-3}$ and at the widest linewidth that can be used to achieve the minimum BER requirement at 300 km length. Fig. 6.6.2 (a) shows the scatter plot for a 4 QAM using 28-MHz linewidth which requires a 26 dB of OSNR. Fig. 6.6.2 (b) shows a 16 QAM scatter plot using 6 MHz with much higher OSNR requirement of 36 dB. With a higher M -size QAM modulation, a much narrower linewidth at a high OSNR needs to be used to achieve the minimum BER requirement. The scatter plot of this can be shown in Fig.

6.6.2 (c) and (d) where 2-MHz linewidth with 30-dB OSNR and 1 MHz with 32-dB OSNR are required for 32- and 64-QAM, respectively.

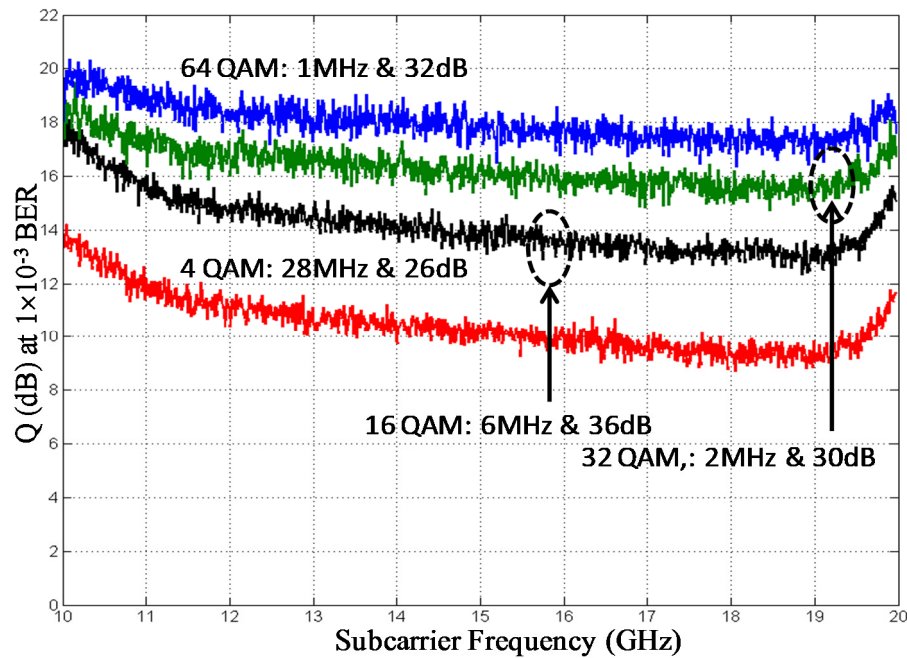


Fig. 6.6.3 Q at around 1×10^{-3} BER versus subcarriers frequency for 4-, 16-, 32- and 64-QAM signal transmitted over 300 km using different linewidth at its respective OSNR.

Fig. 6.6.3 shows a Q-factor taken at around 1×10^{-3} of the average BER versus subcarriers frequency for 4-, 16-, 32-, and 64-QAM of an OFDM signal transmitted over 300 km using the widest linewidth that can be achieved with its respective OSNR requirement. For 4 QAM, the widest linewidth that can be used with the present of the PM-to-IM conversion noise effect is at 28 MHz, achieved with 26-dB OSNR. When the M -size is increased to 16, the widest linewidth is reduced to only 6 MHz with 10-dB increased of the OSNR requirement. For 32-QAM, only 2-MHz linewidth can be used with the OSNR of 30 dB. At 64 QAM, 1-MHz linewidth can be used to achieve the minimum acceptable BER by using the OSNR of 32 dB.

The overall graphs show that the Q-performance is reduced towards the high-frequency subcarriers. This is due to the delay effects caused by the differential group delay of a dispersive fibre. The subcarriers that are far from the carrier will have larger delay as compared to the one closer to the carrier. This delay causes a phase decorrelation between the carrier and the subcarriers upon a photo-detection, which has been explained in Chapter 5. The Q-degradation from the low- to high-frequency subcarriers is higher when a wide linewidth laser is used. When using a 28-MHz

linewidth for 4 QAM transmission, about 5-dB Q-difference is shown between the low- and high-frequency subcarriers. For 16 QAM using 6 MHz, approximately 4.6-dB Q-difference is shown. This Q-difference is reduced when much narrower linewidth was used at the transmitter. This can be shown by only around 2.5-dB difference when using 2-MHz linewidth to transmit 32 QAM and about 0.5-dB difference when using a 1-MHz linewidth to transmit 64 QAM.

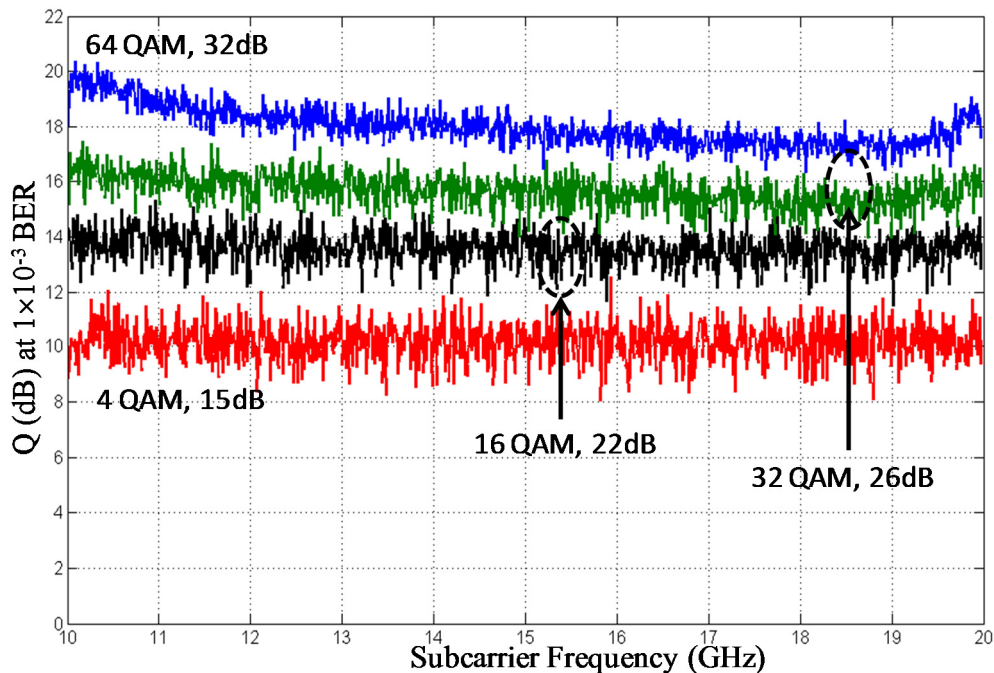


Fig. 6.6.4. Q taken at around 10^{-3} BER versus subcarrier frequency for 4-, 16-, 32- and 64-QAM OFDM signal transmitted over 300 km using 1 MHz linewidth achieved with 15 dB, 22 dB, 26 dB and 32 dB of OSNR, respectively.

Fig. 6.6.4 shows the Q taken at around 1×10^{-3} of average BER versus subcarrier frequency for 4-, 16-, 32- and 64-QAM signal transmitted over 300 km using 1-MHz laser linewidth using its respective OSNR requirement. The Q is relatively constant across the subcarrier frequency when transmitting 4-, 16- and 32-QAM. This shows that the delay effect caused by the interaction between the laser phase noise of the carrier and the subcarriers with the fibre dispersion is insignificant due to small laser phase noise which relates to the narrow linewidth of 1-MHz. However, at 64 QAM, the transmission using 1-MHz linewidth over the 300 km of dispersive fibre imposed the delay effect shown by the reduction of the Q from the low- to the high-frequency subcarriers. This shows that the high M -size QAM is susceptible to the laser phase

noise and much narrow linewidth is required in order to obtain an acceptable system performance.

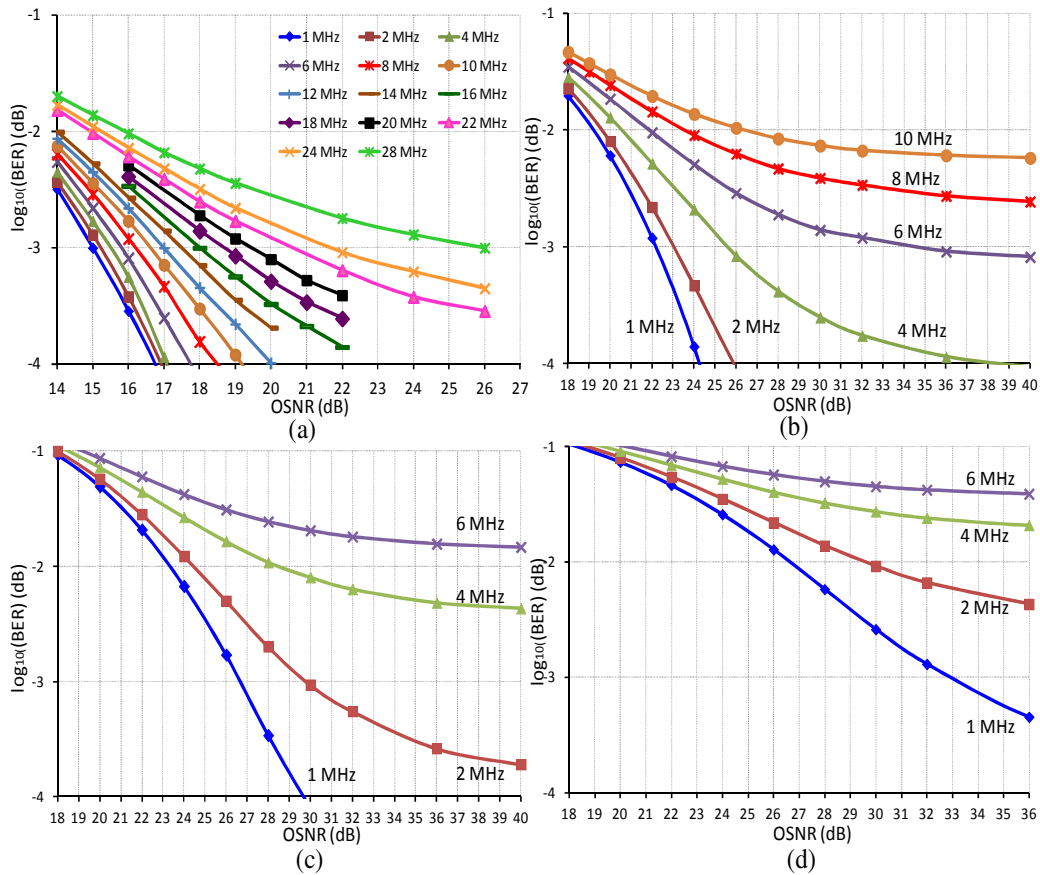


Fig. 6.6.5. BER versus OSNR for an OFDM signal transmitted using a variable linewidth over 300 km and modulated with (a) 4-, (b) 16-, (c) 32- and (d) 64-QAM.

Fig. 6.6.5 shows the plots of BER versus OSNR for an OFDM signal transmitted using a variable linewidth over 300 km dispersive fibre with (a) 4-, (b) 16-, (c) 32- and (d) 64-QAM data modulation. With these plots, the required OSNR to achieve the minimum BER requirement can be obtained at $\text{BER} = 10^{-3}$ crossing to the curves. For the 4 QAM signal transmissions, the OSNR at the range of 15- to 26-dB is required to achieve the minimum BER using the laser linewidth ranging from 1 MHz to 26 MHz. In Fig. 6.6.5 (b), the widest linewidth that can be used to transmit 16 QAM signal over 300 km is 16 MHz with a high OSNR requirement at around 34 dB. With 1-MHz linewidth, an additional of 7-dB OSNR is required to transmit 16 QAM signal as compared to 15 dB for a 4 QAM signal. For 32 QAM signal shown in Fig. 6.6.5 (c), only the linewidth of 1- and 2-MHz crossing the $\text{BER} = 10^{-3}$ line showing the OSNR requirement of 26.7 dB and 30 dB, respectively. A higher OSNR is required for 1-MHz linewidth transmitting 32 QAM as compared to 4 QAM which requires additional of

11.7-dB OSNR and the additional of 4.7 dB when compared with 16 QAM. In Fig. 6.6.5 (d), 64 QAM signal transmission shows that only 1-MHz curve crossing the $\text{BER} = 10^{-3}$ line, which shows a high OSNR requirement of 33 dB. These plots show the laser linewidth limitation in the transmission of high M -size QAM which requires high OSNR. The higher OSNR is also required when wider linewidth laser is used at the transmitter. The sensitivity plots for the other transmission length ranging from 100 km to 1000 km can be found in Appendix 3.6.

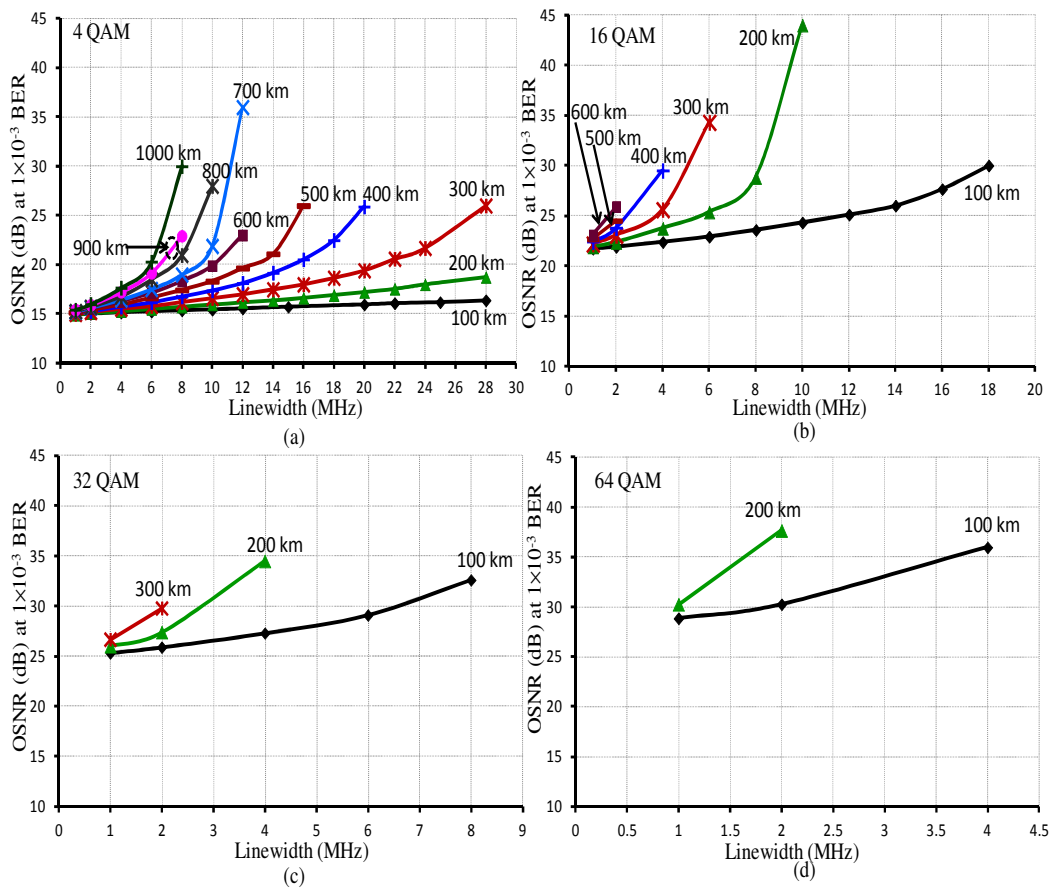


Fig. 6.6.6. OSNR at 1×10^{-3} BER versus linewidth for OFDM signal using (a) 4-QAM, (b) 16-QAM, (c) 32-QAM and (d) 64-QAM transmitter over a certain dispersive-fibre length.

Fig. 6.6.6 shows the OSNR requirement to achieve a minimum BER of 1×10^{-3} versus laser linewidth to transmit (a) 4-QAM, (b) 16-QAM, (c) 32-QAM and (d) 64-QAM over a certain dispersive-fibre length. The approximation of the OSNR values were taken at a $\text{BER} = 10^{-3}$ crossings from the sensitivity graphs shown in Fig. 6.6.5 and Appendix 3.6. The graphs show an exponential increased of the OSNR requirement for all M -size QAM at every given fibre length when wider linewidth laser was used at the transmitter. Also, a high-level OSNR is also required for the transmission of high

M-size QAM due to the increased of the number of symbols. For example, at 1-MHz linewidth, 4 QAM requires around 15-dB OSNR for all lengths to achieve the minimum BER requirement. The 16 QAM data transmission requires 7.5-dB more OSNR than the 4 QAM. For 32-QAM, a minimum of 26-dB OSNR is required which equivalent to 3.5-dB more OSNR than the 16-QAM. The 64 QAM requires a minimum of 33 dB which equals to 7-dB OSNR more than that required by the 32 QAM. Note that, for the 4 QAM transmissions through 100-to-400-km and for 16 QAM at 100-km fibre length, a wider linewidth can still be used to achieve the minimum BER at the expense of a high OSNR. Other than these, the sensitivity curve of BER vs. OSNR began to saturate and does not cross at the 10^{-3} line. This can be seen from the plots available in Appendix 3.6. These graphs can be used as a reference for power sensitivity requirement to achieve a design goal that involves the use of wide linewidth laser to reach a certain length with the available OSNR in order to transmit a certain data rate.

Table 6.6.1: Summary of the linewidth-range with its respective OSNR to achieve 1×10^{-3} of BER for 4 QAM, 16 QAM, 32 QAM and 64 QAM.

Length (km)	4 QAM		16 QAM		32 QAM		64 QAM	
	LW (MHz)	OSNR (dB)	LW (MHz)	OSNR (dB)	LW (MHz)	OSNR (dB)	LW (MHz)	OSNR (dB)
100	1 - 28	15 - 16.4	1 - 18	21.7 - 30	1 - 8	21.9 - 28.8	1 - 4	28.9 - 30.3
200	1 - 28	15 - 18.8	1 - 10	21.9 - 44	1 - 4	26 - 34.5	1 - 2	30.3 - 37.7
300	1 - 28	15 - 26	1 - 6	22.2 - 34	1 - 2	26.7 - 29.8		
400	1 - 20	15.2 - 26	1 - 4	22.4 - 29.5				
500	1 - 16	15.16 - 26	1 - 2	22.7 - 24.5				
600	1 - 12	15.3 - 23	1 - 2	23.1 - 25.9				
700	1 - 12	15.2 - 36						
800	1 - 10	15.3 - 28						
900	1 - 8	15.4 - 22.9						
1000	1 - 8	15.4 - 30						

Table 6.6.1 shows the summary of the linewidth with its respective minimum OSNR requirement to achieve a BER of 1×10^{-3} for the given dispersive-fibre length and the *M*-QAM sizes. The un-shadowed columns of the linewidth (LW) and the OSNR represent the conditions where the linewidth can still be widened than the stated range with the expense of more OSNR at the receiver. The shadowed columns represent the condition where the linewidth could not be widened since the sensitivity curve is saturated even though a high OSNR is used. These can be seen from the sensitivity graphs in Appendix 3.6 for the given fibre lengths and the QAM sizes. In this table, the linewidth has to be matched according to its respective OSNR in order to achieve the

minimum BER. For example, the linewidth from 1-to-16-MHz of 4 QAM transmitted over 500 km requires the minimum of 15.16-dB OSNR for 1 MHz linewidth and 26-dB OSNR for 16 MHz. The table also shows the increase of the required OSNR-range when a high M-size QAM is used for the transmission over the same fibre length.

6.7 Conclusions

The effects of PM-to-IM conversion noise on OFDM signal transmission have been investigated using simulations. The PM-to-IM conversion noise is imposed into the system due to the interaction between the laser's phase noise or linewidth with the chromatic dispersion in the fibre. The investigations were done by determining the effect of this interaction to a single OFDM subcarrier transmitted using a wide linewidth laser of 20 MHz and 100 MHz. The subcarrier was placed on top of the main sidelobe's peak and at the frequency null of the conversion noise's PSD. This was done to show the dominant noise of IN and the phase rotation, which has been shown using the received scatter plot. A group delay effect on the OFDM subcarrier was also investigated using wide laser linewidth to transmit the subcarrier. The subcarrier was placed at a fix frequency and the dispersive fibre length was varied. A noise pedestal around the subcarrier can be seen at the photodetector, which confirmed that the delay is induced to the subcarrier relative to the carrier. Phase rotated scatter plots were shown which determined a large phase errors experienced by the subcarrier due to the group delay effect. Another study was done by varying the subcarrier's frequency and transmitted over a fixed dispersive fibre length. The study showed that the subcarrier placed at the high frequency experiencing larger phase errors compared to the subcarrier at the low frequency or closer to the DC. This was determined by the phase rotation of the received scatter plot. This is due to the larger phase walk-off of the subcarrier away from the carrier compared to the subcarrier which is placed closer to the carrier. The interference among the noise pedestal of the adjacent subcarriers has also been investigated. This was done using several subcarriers spaced at certain frequency spacing. When a large spacing was used, the received scatter plots show a large phase rotation of the symbols, with the symbols at the outer quadrant experiencing large phase rotation compared to the inner quadrant for a 16-QAM received scatter plot. This determines that when no ISCI, the laser's phase noise gives a strong influence to the received signal scatter plot by inducing large phase errors to the received symbols.

When a small frequency spacing was used, the plotted symbols on the plane become more round, which indicates small phase rotation and intensity noise is dominant. This was when the ISCI is more dominant when the noise pedestal interfered with each other and adding up, which results in a much flat noise floor without the frequency nulls. These is also confirmed by the histogram plots which show that for a large phase errors, the plotted histogram no longer fits a Gaussian curve. The skewed histogram shows the symbols that fell close to the boundary of the other quadrant, which is far from its origin. The effects of the PM-to-IM conversion noise on the DDO-OFDM system without the influence of ASE noise was also investigated. The results show that at a long-haul transmission of 500 km using wide laser linewidths of 8 MHz and 15 MHz, the ISCI effect is dominant where round-shaped scatter plots were achieved. When an ultra-long haul transmission was performed, the received scatter plots are rotated with the linewidths of 800 kHz and 1 MHz. Even though the ISCI is dominating the signal band, a high increase of the noise floor at the high frequency subcarriers compared to the subcarriers closer to the DC can also imposed a small phase rotations on the received scatter plots. This is because the extremely high dispersion is involved, in which a large group delay is affecting the subcarriers relative to the carrier. Also plotted was the graph of BER versus linewidth for several fibre lengths. From this graph, the required linewidth can be determined a minimum BER over a certain fibre length. The interaction of the linewidth with the dispersion to a high M-QAM modulated OFDM signal was also investigated. The results show that higher M-size QAM is more susceptible to the PM-to-IM conversion noise. A wider linewidth can be used to transmit over a longer fibre length when using smaller M-size QAM. For example, with 10 MHz linewidth, 4 QAM can support the transmission over 854 km, 16 QAM over 193 km and 32 QAM over 100 km. An OSNR requirement with the PM-to-IM conversion noise was also evaluated. Sensitivity curves were plotted to determine the minimum requirement of the OSNR to achieve the minimum BER of 1×10^{-3} with varied linewidth for a certain dispersive fibre length. Results show the increase of the OSNR requirement for all M-size QAM when the linewidth is increased across a certain dispersive fibre length. A high level of OSNR is required for larger M-size QAM. For example, at 1-MHz linewidth, the 4 QAM required around 15-dB OSNR for all lengths, 16 QAM requires 7.5 dB more OSNR than the 4 QAM, and the

32 QAM requires 26 dB OSNR, which is 11-dB and 3.5-dB more OSNR than required by the 4 QAM and 16 QAM, respectively. These graphs can be used as a reference for a power sensitivity requirement to achieve a design goal that involves the use of the wide linewidth laser to reach a certain length with the available OSNR in order to transmit a certain data rate.

6.8 References

1. Hanzo, L. and T. Keller, *OFDM and MC-CDMA A Primer*. 2006: John Wiley & Sons Ltd. 411.
2. Wu, S. and B.-N. Yeheskel, *OFDM systems in the presence of phase noise: consequences and solutions*. Communications, IEEE Transactions on, 2004. **52**(11): p. 1988-1996.
3. Armada, A.G., *Understanding the effects of phase noise in orthogonal frequency division multiplexing (OFDM)*. Broadcasting, IEEE Transactions on, 2001. **47**(2): p. 153-159.
4. Armada, A.G. and M. Calvo, *Phase noise and sub-carrier spacing effects on the performance of an OFDM communication system*. Communications Letters, IEEE, 1998. **2**(1): p. 11-13.
5. Jansen, S.L., et al. *20-Gb/s OFDM Transmission over 4,160-km SSMF Enabled by RF-Pilot Tone Phase Noise Compensation*. 2007: Optical Society of America.
6. Xingwen, Y., S. William, and M. Yiran, *Phase Noise Effects on High Spectral Efficiency Coherent Optical OFDM Transmission*. Lightwave Technology, Journal of, 2008. **26**(10): p. 1309-1316.
7. Yi, X., W. Shieh, and Y. Ma. *Phase noise on coherent optical OFDM systems with 16-QAM beyond 10Gb/s*. in *33rd European Conference and Exhibition on Optical Communication 2007*. Berlin, Germany: VDE VERLAG GMBH.
8. Schmidt, B., A.J. Lowery, and L.B. Du. *Low sample rate transmitter for direct-detection optical OFDM*. in *Optical Fiber Communication - includes post deadline papers, 2009. OFC 2009. Conference on*. 2009.
9. Yamamoto, S., et al., *Analysis of laser phase noise to intensity noise conversion by chromatic dispersion in intensity modulation and direct detection optical fiber transmission*. Journal of Lightwave Technology, 1990. **8**: p. 1716-1722
10. Henry, C.H., *Theory of the linewidth of semiconductor lasers*. IEEE Journal of Quantum Electronics, 1982. **QE-18**(2): p. 259-264.
11. Lowery, A.J. *Improving Sensitivity and Spectral Efficiency in Direct-Detection Optical OFDM Systems*. in *Optical Fiber communication/National Fiber Optic Engineers Conference, 2008. OFC/NFOEC 2008. Conference on*. 2008.
12. Lowery, A.J. and J. Armstrong, *Orthogonal frequency division multiplexing for dispersion compensation of long-haul optical systems*. Optics Express, 2006. **14**: p. 2079-2084.
13. Richter, L.E., et al., *Linewidth determination from self-heterodyne measurements with subcoherence delay times*. Quantum electronics letters, 1986. **QE-22**(11): p. 2070-2074.
14. Peng, W.R., *Analysis of Laser Phase Noise Effect in Direct-Detection Optical OFDM Transmission*. Journal of Lightwave Technology, 2010. **28**(17): p. 2526-2536.

15. Lowery, A.J., L. Du, and J. Armstrong, *Performance of optical OFDM in ultra long-haul WDM lightwave systems*. Journal of Lightwave Technology, 2007. **25**: p. 131 – 138.
16. Lowery, A.J. and J. Armstrong. *Orthogonal-Frequency-Division Multiplexing for Optical Dispersion Compensation*. in *Optical Fiber Communication and the National Fiber Optic Engineers Conference*. 2007. Anahaim, USA.
17. Lowery, A.J., *Amplified-spontaneous noise limit of optical OFDM lightwave systems*. Optics Express, 2008. **16**(2): p. 860-865.
18. Lowery, A.J., L. Du, and J. Armstrong. *Orthogonal Frequency Division Multiplexing for Adaptive Dispersion Compensation in Long Haul WDM Systems*. in *Optical Fiber Communication Conference, 2006 and the 2006 National Fiber Optic Engineers Conference. OFC 2006*. 2006.
19. Schmidt, B.J.C., A.J. Lowery, and J. Armstrong. *Experimental demonstrations of 20 Gbits/s direct-detection optical OFDM and 12Gbits/s with a colorless transmitter*. in *Optical Fiber Communication Conference*. 2007. Anaheim, CA.
20. Schmidt, B.J.C., A.J. Lowery, and J. Armstrong, *Experimental demonstrations of electronic dispersion compensation for long-haul transmission using direct-detection optical OFDM*. Journal of Lightwave Technology, 2008. **26**(1): p. 196-203.
21. Shieh, W. and C. Athaudage, *Coherent optical orthogonal frequency division multiplexing*. Electronic Letters, 2006. **42**: p. 587-588.
22. Shieh, W., H. Bao, and Y. Tang, *Coherent optical OFDM: Theory and design*. Optics Express, 2008. **16**(2): p. 841-859.
23. Jansen, S.L., I. Morita, and H. Tanaka, *16x52.5-Gb/s, 50-GHz spaced, POLMUX-CO-OFDM transmission over 4,160 km of SSMF enabled by MIMO processing*. Optical Communication - Post-Deadline Papers (published 2008), 2007 33rd European Conference and Exhibition of, 2007: p. 1-2.
24. Jansen, S.L., I. Morita, and H. Tanaka, *Experimental demonstration of 23.6 Gb/s OFDM with a colorless transmitter*, in *optoelectronics and communications conference (OECC)*. 2007. p. PD1-5.
25. X. Yi, W. Shieh, and Y. Ma, "Phase noise effects on high spectral efficiency coherent optical OFDM systems," J. Lightw. Technol., vol. 26, no. 10, pp. 1309–1316, May 15, 2008
26. M. S. El-Tanany, Y. Wu, and L. Hazy, "Analytical modeling and simulation of phase noise interference in OFDM-based digital television terrestrial broadcasting systems," IEEE Trans. Broadcasting, vol. 47, no. 1, pp. 20–31, Mar. 2001
27. Qiyue, Z., A. Tarighat, and A.H. Sayed, *Compensation of Phase Noise in OFDM Wireless Systems*. Signal Processing, IEEE Transactions on, 2007. **55**(11): p. 5407-5424.

Chapter 7

EXPERIMENTAL STUDY OF LASER NOISE EFFECT ON DDO-OFDM SYSTEM

7.1 Introduction

In a transmitter system design, it is important to verify the requirements for the laser's characteristics to achieve an acceptable system performance. Many studies have shown that laser noise characteristics can increase the signal-to-noise ratio (SNR) and bit error ratio (BER) performance of a system [1-6]. In Chapters 5 and 6, the effects of the laser's PM-to-IM and group delay that imposed noise pedestals around each of the subcarriers have been presented. In this chapter, these two effects on the DDO-OFDM system will be demonstrated experimentally. In Section 7.2, a commercial distributed feedback laser (DFB) will be used in the DDO-OFDM system experimental setup. This shows that a commercial DFB laser can be used as a transmitter in the DDO-OFDM system even though it is operated at low output powers. Two types of the DDO-OFDM transmitter design will be used to investigate the effect of the DFB laser. The first setup was done using a typical transmitter design where the laser's centre frequency is unshifted. The second setup was developed using a virtual carrier, where the laser's centre frequency is shifted to an intermediate frequency by adding the I and Q data with a sinusoidal waveform. In Section 7.3, the use of laser linewidth emulator as a transmitter in the DDO-OFDM will be demonstrated. This will also show an independent linewidth effect to the DDO-OFDM system can be analysed experimentally. Finally, 7.4 presents the conclusions and Section 7.5 shows the references.

7.2 Effects of RIN and Linewidth to DDO-OFDM Transmission System

In this section, a commercial DFB laser will be used at the transmitter of a DDO-OFDM system. The characteristics of this laser have been measured and reported in Chapter 3, which includes RIN, linewidth and L-I characteristics of the laser. Two types of experimental setup will be used. The first setup is a low-rate transmitter using an unshifted laser's centre frequency. In this setup, only a quarter of the FFT-points will be

used for the OFDM subcarriers at the positive-half. The second setup will involve the use of an RF-virtual carrier transmitter design, where the laser's centre frequency is shifted to an intermediate frequency. Using this transmitter design, all of the FFT-points at both negative and positive sides can be used for the OFDM subcarriers. This increases the signal bandwidth of the system and hence increases the data rate as compared to the first setup.

7.2.1 DDO-OFDM Transmission System using a Low-Rate Un-shifted Optical Transmitter

The inter-dependent effects of a laser's RIN and linewidth on a DDO-OFDM transmission system can be shown using a low rate experimental setup as follows.

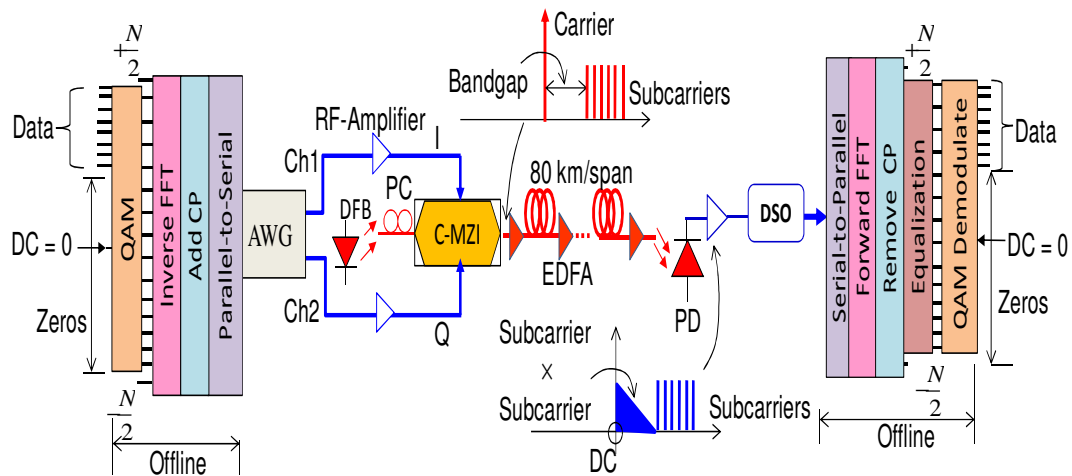


Fig. 7.2.1. Low-rate experimental setup using a commercial DFB laser with upper half-positive FFT-points are assigned as OFDM subcarriers.

Fig. 7.2.1 shows the experimental setup using a commercial DFB laser transmitting a low-rate data. The OFDM subcarriers are taken at the upper half-positive of the FFT-points and the rest are assigned with zero. This is shown at the parallel QAM-modulated data inputs. The subcarriers are assigned from $+\frac{3N}{4}$ to $+\frac{N}{2} - 1$ of inverse-FFT (iFFT) points with 100 symbols. The frequency spectrum of this subcarriers assignment on the iFFT is explained below.

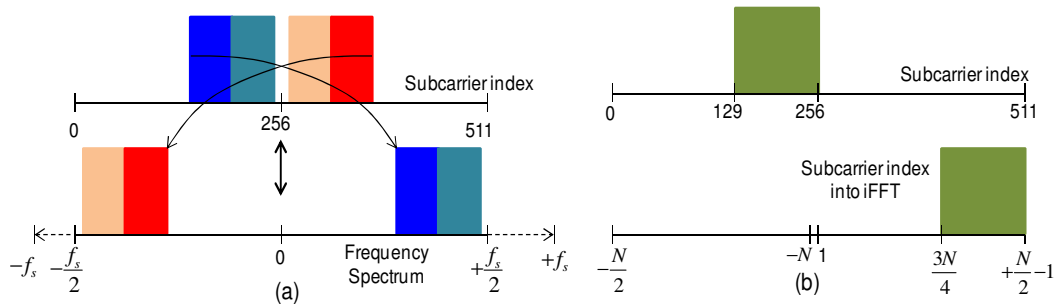


Fig. 7.2.2. OFDM subcarrier indices with its corresponded frequency spectrum showing (a) the theory and (b) data-carrying subcarriers assignment for the experiment.

Fig. 7.2.2 shows (a) the theory of a frequency spectrum representation after an FFT operation of a time domain waveform which is corresponded to the subcarrier assigned in the index from 1 to N . 1 to N index is considered since MATLAB's index starts at 1. To produce a straight forward subcarrier index with its spectrum representation, the inputs into the iFFT is made to match the resulting spectrum (after the FFT at the receiver) shown by Fig. 7.2.2 (b). This is known as a Hilbert transform in frequency domain, which produces a single sideband (SSB) frequency spectrum when the signal drives an optical complex modulator without requiring any optical filter [7].

In Fig. 7.2.1, after the iFFT converts the signal into the time domain waveforms, the parallel waveforms are transformed into a serial signal stream. Cyclic prefix (CP) is added to the front of the signal stream. Inphase (I) and quadrature (Q) components of the signal are extracted from the stream and zeros are assigned at the start of each of the signal components for a frame synchronization at the receiver. The signals are then loaded into a Tektronix arbitrary waveform generator (AWG7102), which performs a digital-to-analog conversion (DAC). The OFDM signal generations before the AWG block were made offline using MATLAB, where the code can be found in Appendix 4.1. The AWG's outputs of Ch1 and Ch2 are used which generate a 10-GSa/s of I and Q analogue baseband signals. These signals are then driven a Sumitomo complex optical Mach-Zehnder interferometer (C-MZI). The modulator is biased just away from a null power of the interferometer's transfer curve to give a suppressed optical carrier suitable for a direct-detection receiver. With a 10-GHz sampling rate, 2.5-GHz signal bandwidth can be achieved with this setup. The laser used was a fixed-wavelength 1555 nm commercial Fujitsu FLD5F6CX-E36 DFB laser with the power supply by ILX

Lightwave. A polarization controller (PC) is used at the laser's output to align its light polarization before driving the C-MZI. The light is aligned when the C-MZI's output power is at the maximum which is measured using an optical power meter without any RF signals input into the C-MZI. An optical spectrum at the output of the C-MZI can be shown by the inset of the figure, where the carrier is spaced away from the subcarrier by a frequency-bandgap with the same size of the signal band. This bandgap is used to place the unwanted subcarrier \times subcarrier mixing upon the photodetection and to avoid from interfering with the signal band [7-14]. A Lightwave2020 EDFA was used after the C-MZI to compensate its insertion loss before going into a fibre spool. Four spools of Corning single mode fibre (SMF-28e) with 80-km per span are used with the total length of 320-km. At every spool, an EDFA is used to compensate the fibre loss.

At the receiver, a DCS404A photodiode by Discovery is used to detect the signal and captured using an Agilent 81004A real-time digital storage oscilloscope (DSO). The received electrical spectrum is shown by the inset where the bandgap is filled with the unwanted subcarrier \times subcarrier mixing products. The recorded signal at the DSO is processed offline using MATLAB. The recorded signal waveform will be first plotted in order to find the start of the data frame for the frame synchronization.

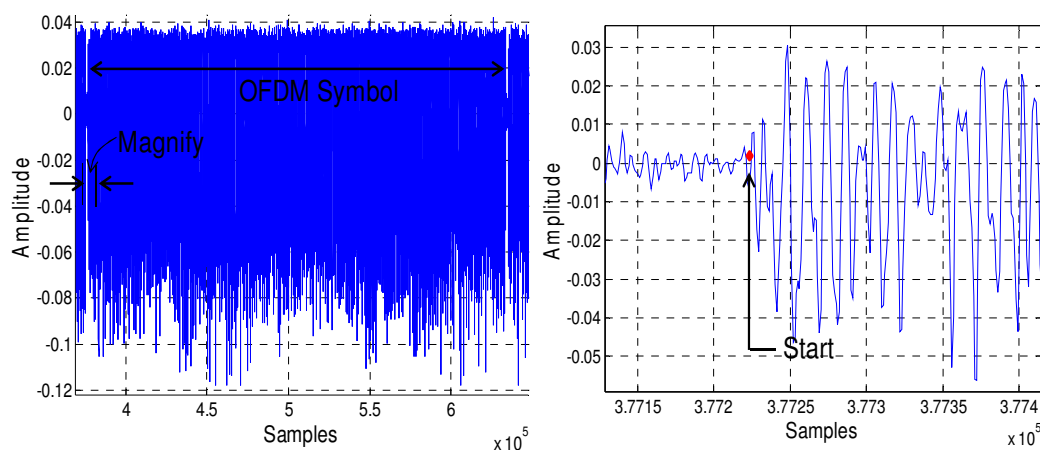


Fig. 7.2.3. Received signal waveform plotted using Matlab with one symbol frame and the magnified signal part to find the start of the frame.

Fig. 7.2.3 shows the received waveform showing an OFDM symbol frame, where the start of the symbol is identified by magnifying the plotted waveform. To obtain a precise start of the symbol, the starting time is offset over 300 points, where the highest result as a function of time offset produced is recorded. The 'silent' signal around 0 amplitude is the zeros that was assigned at the beginning of the I and Q signal

components at the transmitter. After finding the start of the frame, the signal is converted into a parallel data and demodulated using the FFT that converts the time waveform into a frequency spectrum. Channel estimation is performed and the data is equalized over the average of the channel estimation. The data is then QAM demodulated and the energy per bit, $\frac{E_b}{N_0}$ and BER performance of the signal are obtained. The MATLAB code to perform this signal processing can be found in Appendix 4.2. In this experiment, bias current, I_b supplied to the DFB laser is varied from 18- to 60-mA with the fixed dispersion of 320 km of fibre. A back-to-back transmission was also performed in order to isolate the ASE effect due to the EDFAs.

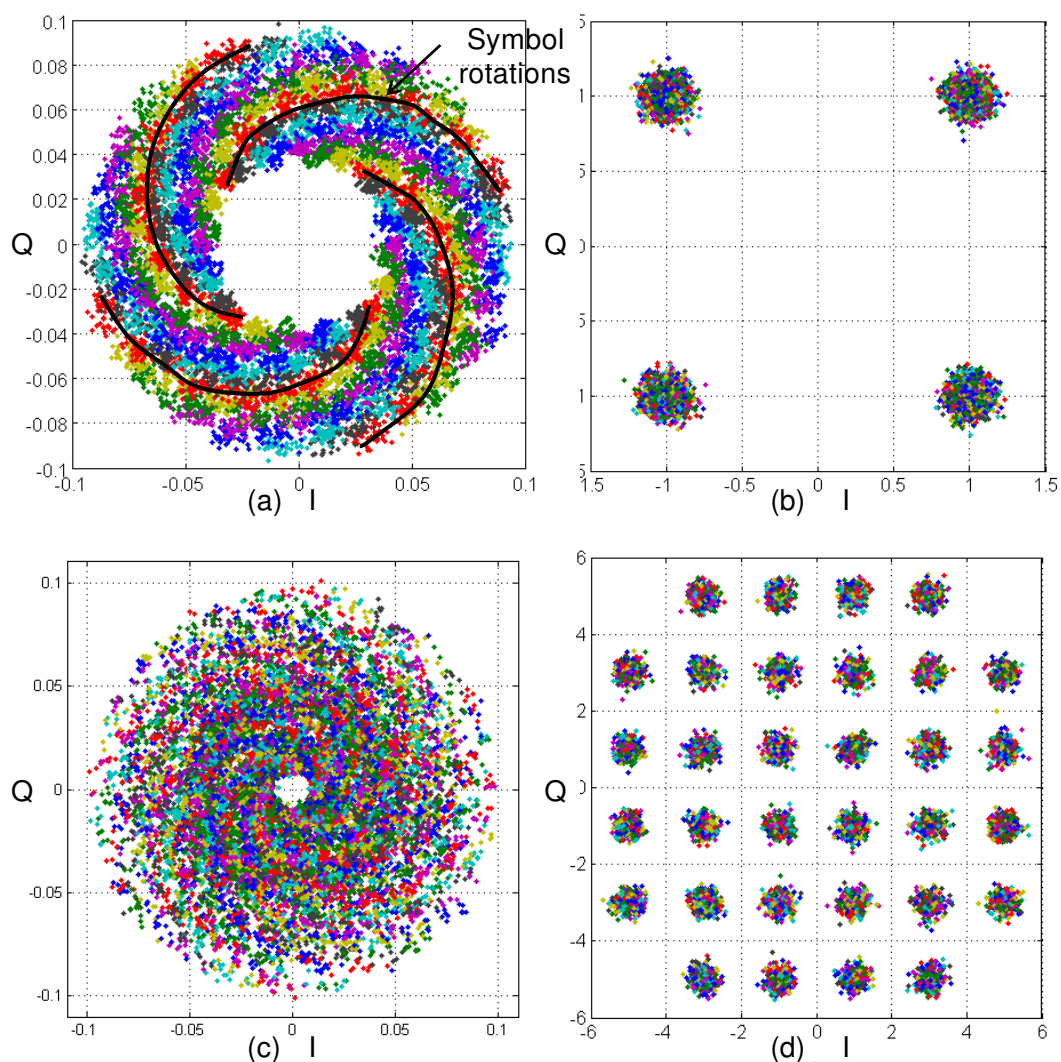


Fig. 7.2.4. Scatter plots of the OFDM symbols modulated with 4 QAM (a) before and (b) after equalization and 32 QAM (c) before and (d) after equalization.

Fig. 7.2.4. shows the scatter plots of 4 QAM and 32 QAM where (a) & (c) are the received signal plot before the equalization and (b) & (d) are the plots after the

equalization. These results were achieved using a DFB laser driven at 60 mA over a back-to-back transmission. With a 2.5 GHz signal bandwidth, the transmitted data rate for the 4 QAM and 32 QAM is 5 Gb/s and 12.5 Gb/s, respectively. With $I_b = 60$ mA, the measured linewidth and RIN is at around 7.5 MHz and -132.34 dB/Hz, respectively with the laser's output power of 5.58 dBm. The received scatter plots show phase rotations of the symbols around its origin which formed a doughnut shape. The phase rotations can be clearly seen using the line drew on top of the red symbols in Fig. 7.2.4 (a). The doughnut-shaped scatter plot is expected due the complex exponential signal of I and Q components modulation using the C-MZI. The degree of the phase rotation is due to the linewidth of the laser only. Fig. 7.2.4 (b) & (d) shows the scatter plot after the signal equalization. The equalization was performed by calculating the channel estimation using the original transmit data.

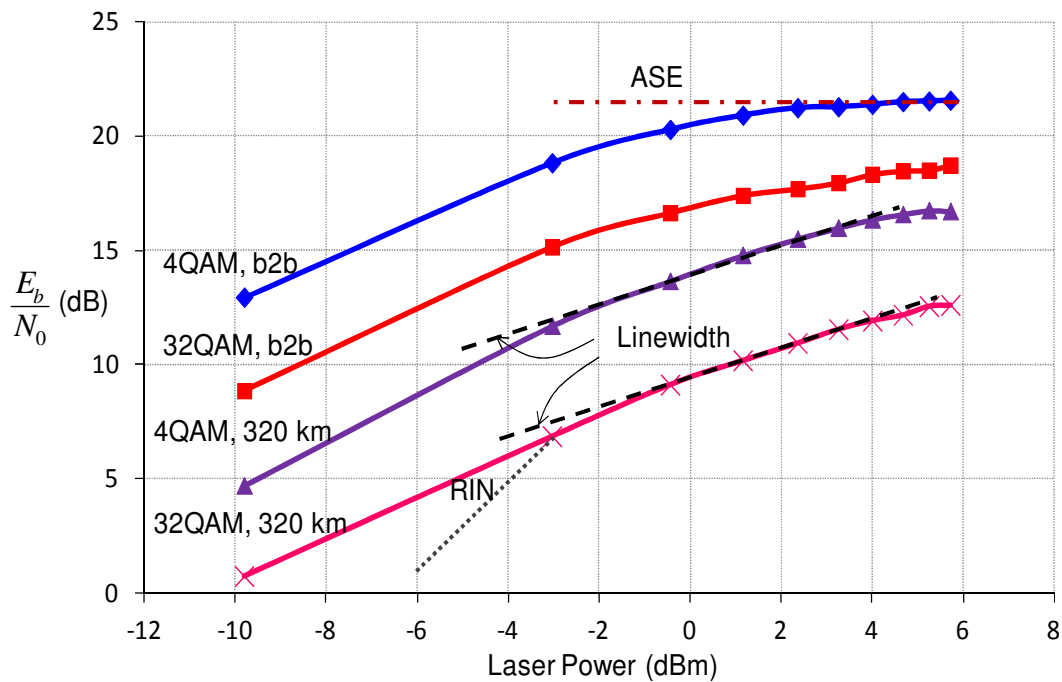


Fig. 7.2.5. Energy-per-bit over noise density versus laser's output power.

Fig. 7.2.5 shows the plots of energy-per-bit over noise density, $\frac{E_b}{N_0}$ versus DFB laser's output power for 4 QAM and 32 QAM with back-to-back (b2b) and after a transmission of 320 km of fibre. The power was varied by increasing the I_b supplied to the laser. At the low power, both b2b transmissions for the 4 QAM and 32 QAM are dominated by RIN. Using a theoretical calculation, when $\frac{E_b}{N_0}$ equal to 6.8 dB and 13.5 dB, the BER is 1×10^{-3} for 4 QAM and 32 QAM, respectively. Also plotted the

theoretical lines to indicate the gradients of the RIN and linewidth with the laser power. The lowest power was driven by a low I_b of 15-mA which produces -9 dBm. The laser power increases with the increase of I_b where this has been plotted in Fig. 3.3.2 for the laser's L-I characteristics. For the b2b system, the RIN dominates at low powers; at a high power, the system performance is limited by an ASE noise and nonlinearity in the electrical amplifiers and the optical modulator. Introducing fibre to the systems causes phase fluctuations to be converted to intensity fluctuations [18]. This lowers the signal quality at all power levels, adding to the effects of the RIN and ASE. A slope of 1-dB per dB indicates that the linewidth is dominating the signal degradation, which occurs at moderate laser powers. At very low powers (less than -9 dBm) the laser has a very high linewidth (84 MHz measured with HRS) and very high RIN (-101 dB/Hz): both these contribute to an unacceptably-low signal quality.

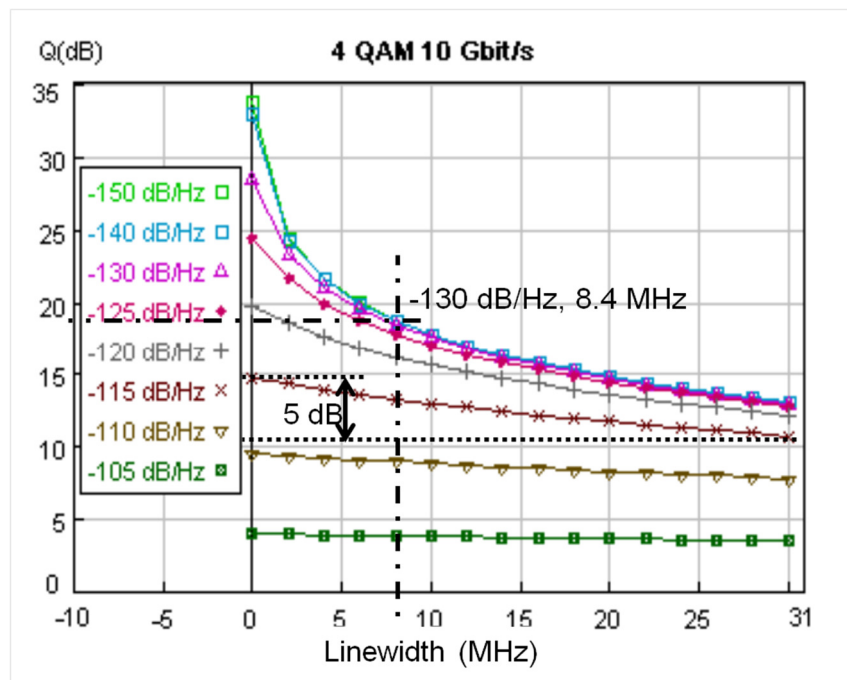


Fig. 7.2.6. Simulated signal quality, Q versus linewidth.

Fig. 7.2.6 shows the combined effects of a RIN and linewidth on a 320 km 10 Gbit/s 4 QAM system simulated with VPItransmissionMaker. Amplifier noise was excluded from the simulations to show the ultimate signal qualities available. For reference, a Q of 9.8-dB gives a BER of 1×10^{-3} for 4 QAM [12]. For a mid-range RIN values (-115 dB/Hz) suitable for 4 QAM, increasing the linewidth from zero to 30 MHz contributes to an additional 5-dB degradation, similar to the lower curves in Fig. 7.2.5. This graph can be used to specify the performance requirements of a laser. For example,

direct measurements of our laser operating at 4.67 dBm showed a RIN of -130 dB. The measured linewidth using Agilent HRS was 8.4 MHz. Reading off Figure 7.2.6 indicates a Q of 18 dB for this pair of the RIN and linewidth values, which is reasonably consistent with the E_b/N_0 of 16.5 dB, which is equal to 19.5 dB of Q (calculated from $BER = \frac{1}{2} \operatorname{erfc} \left(\frac{q}{\sqrt{2}} \right)$) for the 4 QAM experimental results in Fig. 7.2.5 when the different bit rates are accounted for.

7.2.2 DDO-OFDM Transmission System using RF-Virtual Carrier Transmitter Design

In this section, an experiment using the same DFB laser with a fixed laser power to transmit OFDM signals with 4 QAM, 16 QAM and 32 QAM as a function of fibre length is demonstrated. This is to show the effect of a PM-to-IM conversion noise due to the interaction between the laser's linewidth and dispersion. In this experimental setup, an 8-GHz OFDM signal bandwidth is used, which achieved using an RF-virtual carrier transmitter design [19].

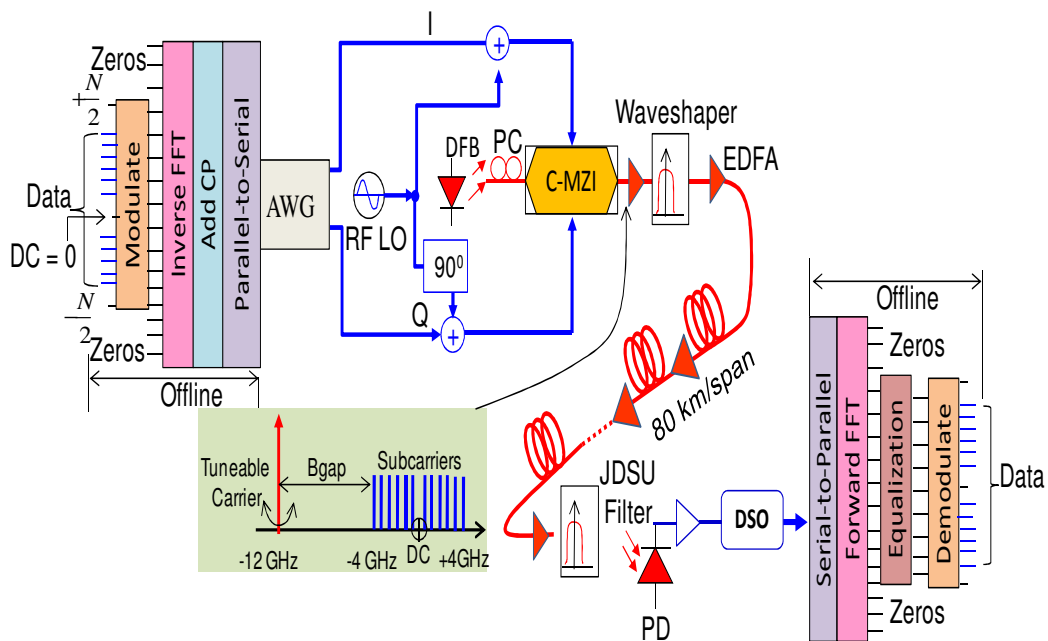


Fig. 7.2.7. Experimental setup using RF-virtual carrier transmitter design.

Fig. 7.2.7 shows the experimental setup transmitting an 8-GHz signal bandwidth over a total of 800 km of S-SMF using an RF-virtual carrier transmitter design. In this experiment, fixed I_b was used, which gives a fixed laser power, RIN and linewidth. A wider signal bandwidth compared to the setup in Section 7.2.1 was used in order to

investigate the effect of the PM-to-IM conversion noise to the subcarrier, in terms of its location relative to the carrier. The OFDM signal was generated offline using MATLAB. For this setup, the OFDM subcarriers at both positive and negative sides of the iFFT-points are used to carry the data. The data was then multiplied with a pre-emphasis data set to compensate for optical modulator's frequency response. This pre-emphasis data set consists of a linear decrease and increase amplitudes for the first and second half of the subcarriers, respectively. The details of the pre-emphasis implementation will be discussed in Chapter 9.

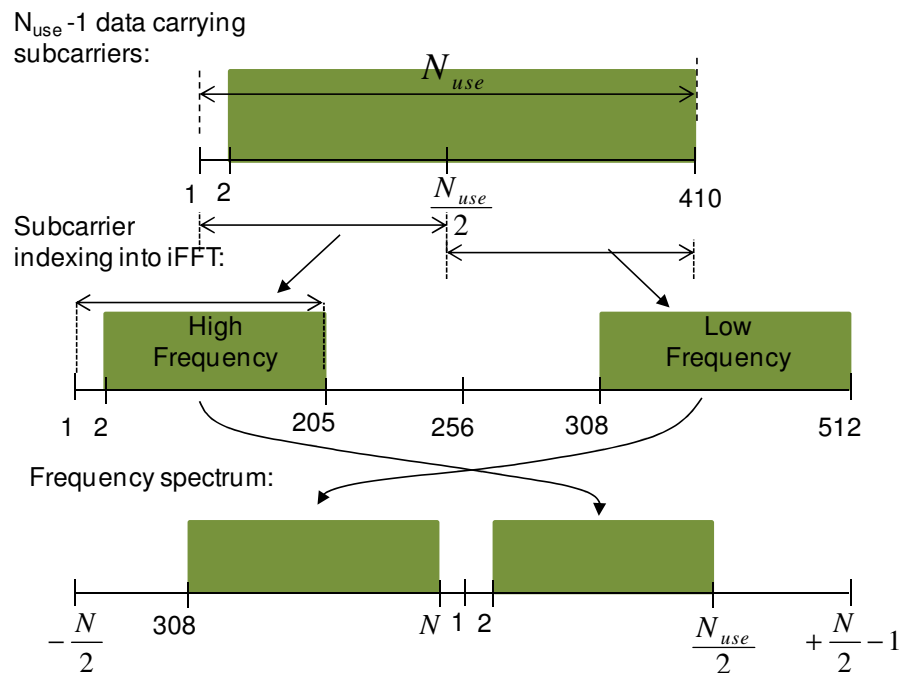


Fig. 7.2.8. Subcarrier indexing matrices of an i^{th} OFDM symbol with its corresponded frequency spectrum representation.

Fig. 7.2.8 shows the subcarrier indexing in the form of $i^{\text{th}} \times N_{use}$ matrices over a total number of iFFT points, $N = 512$, where N_{use} is the number of the subcarriers for data transmission. Also shown is the frequency spectrum representation when the signal is demodulated using an FFT. A QAM-modulated random data was generated in the form of $NSYM \times N_{use}$ matrix, where $NSYM$ is the number of OFDM symbols where $i = 1, 2, 3, \dots, NSYM$. The data was first generated for N_{use} of 410 where the first subcarrier was set to zero for the DC. This makes 409 data carrying subcarriers ($N_{use} - 1$). For the iFFT input, half of the N_{use} is assigned for the high and the other half for the low frequency. This is shown by the middle figure with subcarriers from 1 to N . The subcarrier indexing for the iFFT inputs starts at one to match the MATLAB indexing,

which starts at one. The bottom figure shows a rearrangement of the subcarrier indexing to give a correct frequency ordering of the subcarriers. After the iFFT, CP is assigned by taking a quarter end of the OFDM waveform to start of it. The parallel signal in the form of $NSYM \times \frac{5N}{4}$ matrix is then converted into serial waveforms where I and Q signal components are extracted to drive the complex modulator, C-MZI. The C-MZI was biased close to null and the optical carrier at dc is suppressed. The MATLAB code for the OFDM signal generation can be found in Appendix 4.4.

As shown in Fig. 7.2.7, the RF I and Q signals are then uploaded into a Tektronix AWG7102 to generate an 8-GHz wide baseband signal. The I and Q signals at the AWG's outputs are then added with an RF local oscillator by a Hewlett Packard 83620A synthesized sweeper to generate the virtual carrier at lower sideband with the frequency of -12 GHz. This is shown by the inset of Fig. 7.2.7. A double-sideband virtual carrier was first generated, where its upper sideband (USB) can be cancelled out using a 90° phase shift to the lower MZI. This is an efficient technique to easily sweep the carrier across the transmitted bandwidth, which also provides more signal bandwidth and gives a flexibility to increase or decrease the guardband [19].

The signal after the C-MZI is amplified and a Finisar WaveShaper 4000s optical programmable filter is used to filter out the unwanted frequency components due to devices noise, C-MZI nonlinearity and to suppress the virtual carrier USB completely. This is because some leakage of the USB virtual carrier can still be encountered due to the RF circuit imperfection such as unmatched RF cables connections for the phase shifting. The centre frequency of the bandpass filter needs to be set according to the DFB laser's centre frequency since this changes with the changes of I_b . The signal propagated along 80 km/span S-SMF with the total length of 800 km. An EDFA was used at every span to compensate for the fibre attenuation. Before a photodetection, a JDSU optical bandpass filter was used to limit the ASE noise. A PIN photodiode (PD) was used as the detector. The detected electrical signal was captured using a Tektronix 72004 20-GHz 50-GSa/s digital sampling oscilloscope (DSO). Down-conversion of the virtual carrier was done offline followed by the signal demodulation using MATLAB. The code can be viewed in Appendix 4.4. During the signal demodulation, re-ordering of the received subcarrier indexing as in Fig. 7.2.8 was done to represent the subcarriers in the right frequency-order.

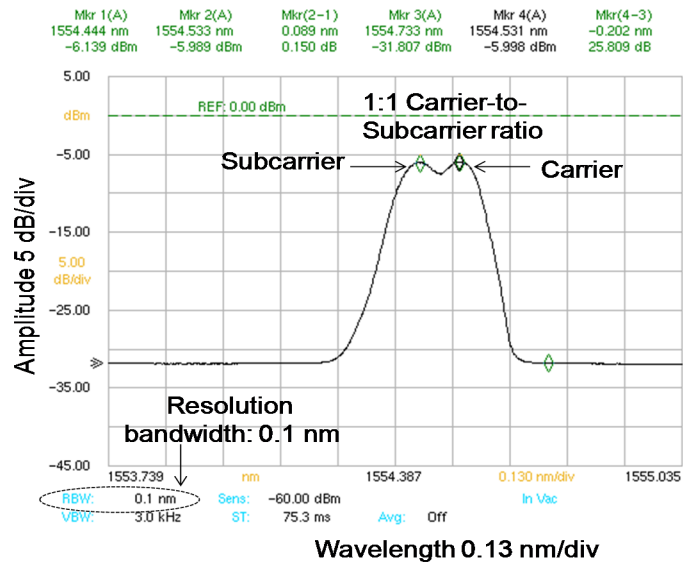


Fig. 7.2.9. Transmitted optical spectrum with 1:1 carrier-to-subcarrier ratio to achieve an optimum system performance.

Fig. 7.2.9 shows the transmitted spectrum showing 1:1 carrier-to-subcarrier ratio measured using 86142B Agilent optical spectrum analyser (OSA). The 1:1 power ratio can be easily achieved by tuning the virtual carrier power. This ratio is required to achieve an optimum system performance of the OFDM signal transmission [10-13].

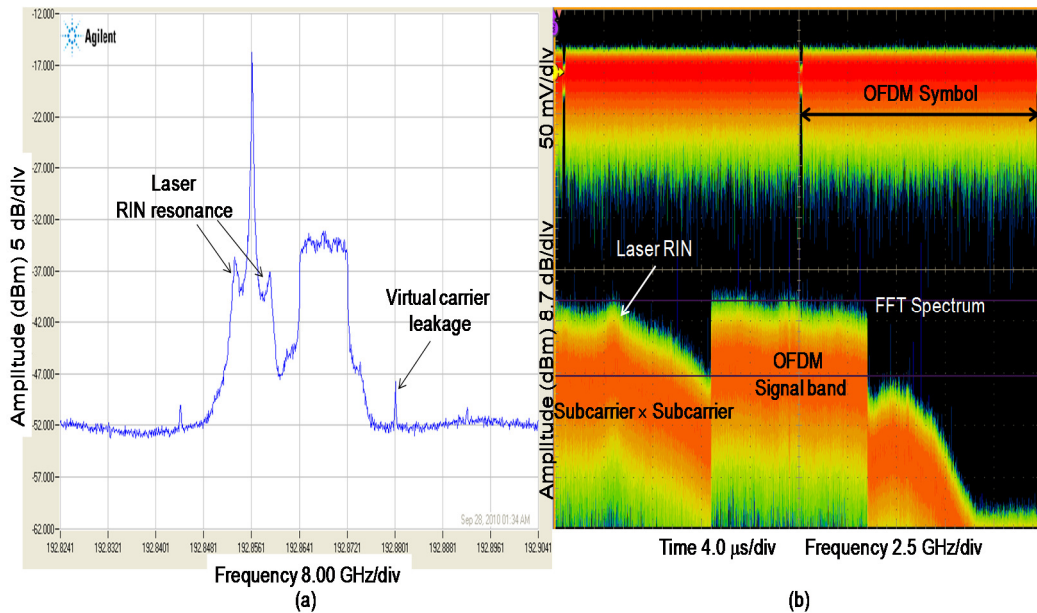


Fig. 7.2.10. OFDM spectra with a high RIN and linewidth laser driven by 10 mA; (a) optical spectrum measured with HRS and (b) received electrical spectrum after back-to-back transmission.

Fig. 7.2.10 shows the spectra using a high RIN and a wide linewidth laser achieved by driven the laser at 10 mA where (a) is the optical spectrum measured with an HRS and (b) is the received electrical spectrum after a back-to-back transmission. The laser

with the I_b of 10 mA emits a low output power of -12.3 dBm with a high RIN of -96.6 dB/Hz and linewidth of 84 MHz. By referring to the measured L-I characteristic in Fig. 3.3.2, this I_b is below the I_{Th} of the laser which is at around 13 mA. Since the laser output power is very low, the laser's output was amplified with an EDFA before driving the C-MZI. Fig. 7.2.10 (a) shows the measured optical spectrum with a DSB RIN resonance peak around the carrier and a small USB virtual carrier leakage. In (b), the RIN resonance can be seen to fall within the guardband at a peak resonance of 3 GHz, which does not interfere with the OFDM signal band. When the I_b was a little higher than the I_{Th} (14 mA to 16 mA), the RIN resonance's peak can still be seen on the HRS optical spectrum, but has no longer be seen on the received electrical spectrum on the DSO. This is because of the peak resonance power is low, in which it is 'buried' inside the subcarrier \times subcarrier inter-modulation distortion noise within the gap.

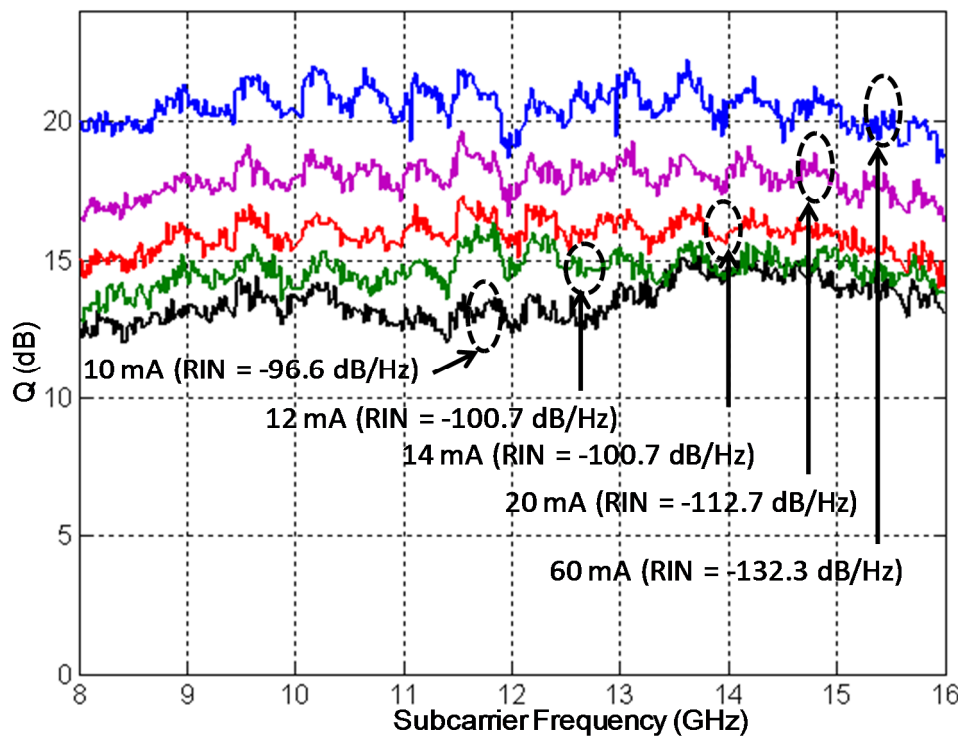


Fig. 7.2.11. Q-factor versus subcarrier frequency of back-to-back transmission using DFB laser with high RIN.

Fig. 7.2.11 shows the Q-factor versus subcarrier frequency of back-to-back transmission using high RIN DFB laser. The high RIN was achieved by driving the laser with low I_b , which produces low laser output power. This low driven DFB laser is not only produces a high RIN but also a wide linewidth. This is because, in a real system setup, the RIN and linewidth effects of a laser are inter-dependent and therefore,

the isolated effect of the RIN and linewidth to the DDO-OFDM system performance cannot be completely achieved. In order to see only the RIN effect on the Q performance across the subcarrier frequency, this back-to-back transmission with the high RIN laser was performed to exclude the effect of the PM-to-IM conversion noise. When the laser was driven by the I_b that is below than the I_{Th} of the laser, more than a half of the low frequency subcarriers experiencing low Q compared to the high frequency subcarriers. This can be seen when the I_b is at 10 mA, in which about 3-dB Q is reduced for the first 5-GHz of subcarriers as compared to the next 3 GHz of the high frequency subcarriers. Note that this I_b is around the laser I_{Th} of 13 mA where the high RIN resonance peak of the laser can be seen as in Fig. 7.2.10. The reduction at the low frequency subcarriers is due to the tail of the RIN resonance that is extended into the signal band before it dies away. The measured RIN resonance of the laser can be seen in Fig. 3.3.3. When the I_b was increased to 12 mA, the RIN resonance power is reduced and the Q across the low frequency subcarriers are increased and become reasonably flat. At the I_b of 12 mA, 14 mA and 20 mA, the RIN resonance can still be seen but with the OFDM signal band, its peak power is lower than the subcarrier \times subcarrier mixing power. The overall of the Q performance is increased with a flat Q response across the subcarriers when the I_b was increased from 12 mA to 20 mA. This shows that the RIN is added to the noise evenly across the OFDM signal band upon detection, in which each of the subcarriers owns a DSB RIN resonance which increases the noise floor as well as the ASE noise from the EDFA. At the I_b of 60 mA, the RIN is low which was measured to be -132.3 dB/Hz, with a flat PSD without any resonance peak. At this I_b , the Q performance is limited by the ASE noise.

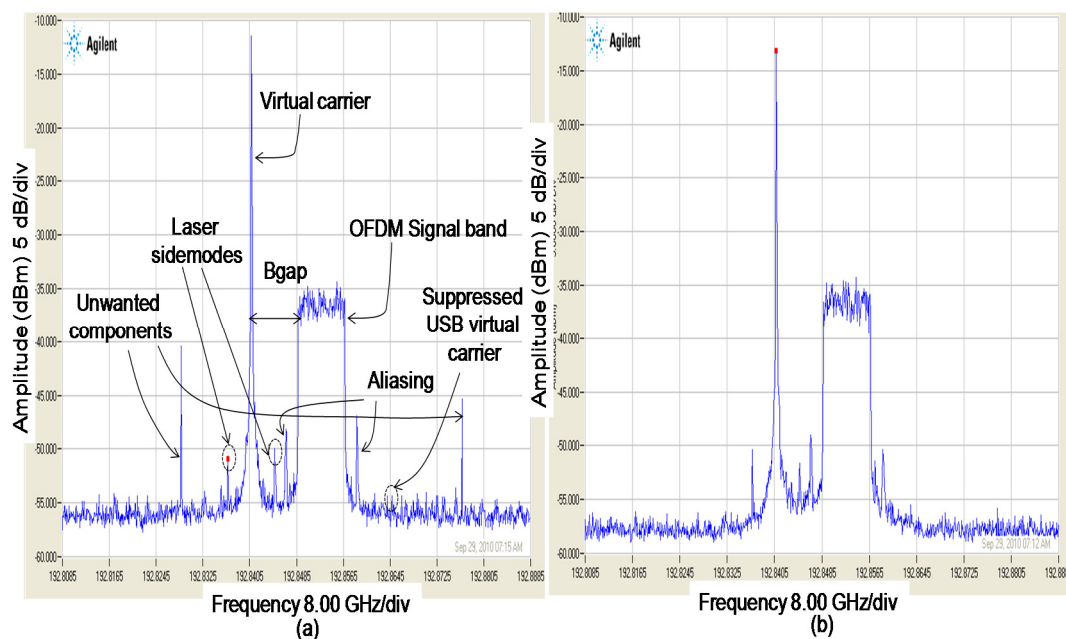


Fig. 7.2.12. Transmit optical spectra measured with HRS (a) before and (b) after WaveShaper bandpass filter using laser I_b of 40 mA.

Fig. 7.2.12 shows the transmit optical spectra at the output of the C-MZI after an optical amplification where the laser is driven by a high I_b of 40 mA measured (a) before and (b) after WaveShaper bandpass filter using the HRS. At this I_b , the laser emitted a high output power of 3.15 dBm with a low RIN of -126.2 dB/Hz and a linewidth of 11.4 MHz. The virtual carrier is spaced at 8 GHz away from the signal band by tuning the RF synthesized sweeper to 12 GHz. A guardband with the same size of the signal band is used to accommodate for the subcarrier \times subcarrier mixing products. For this spectrum, the USB virtual carrier was completely suppressed. However, some leak can be encountered from time-to-time which appeared at 8 GHz away from the signal band, which is shown by the dotted-line circle. Unwanted high-order frequency components of the DC due to the C-MZI nonlinearity were also eliminated with the programmable filter.

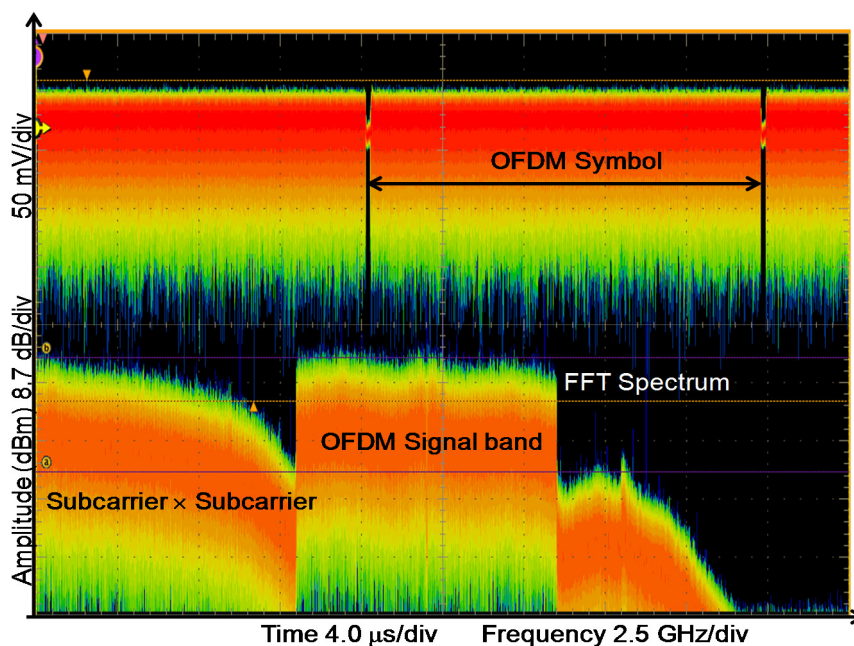


Fig. 7.2.13. Received electrical spectrum of back-to-back transmission with I_b of 40 mA.

Fig. 7.2.13 shows the received electrical spectrum of a back-to-back transmission with the laser driven by the I_b of 40 mA. The top signal shows the captured OFDM waveform which was recorded and processed offline for the OFDM signal equalization and demodulation. The bottom signal shows the OFDM frequency spectrum after the waveform is applied with an FFT function in the DSO. The spectrum shows the subcarrier \times subcarrier mixing products are placed in the guardband to avoid from the interference with the signal band. No RIN resonance peak is observed within the guardband as the RIN is relatively low at this I_b . The peak power of the mixing products is equal to the signal band peak power which was obtained by setting the 1:1 carrier-to-subcarrier power ratio of the transmit signal.

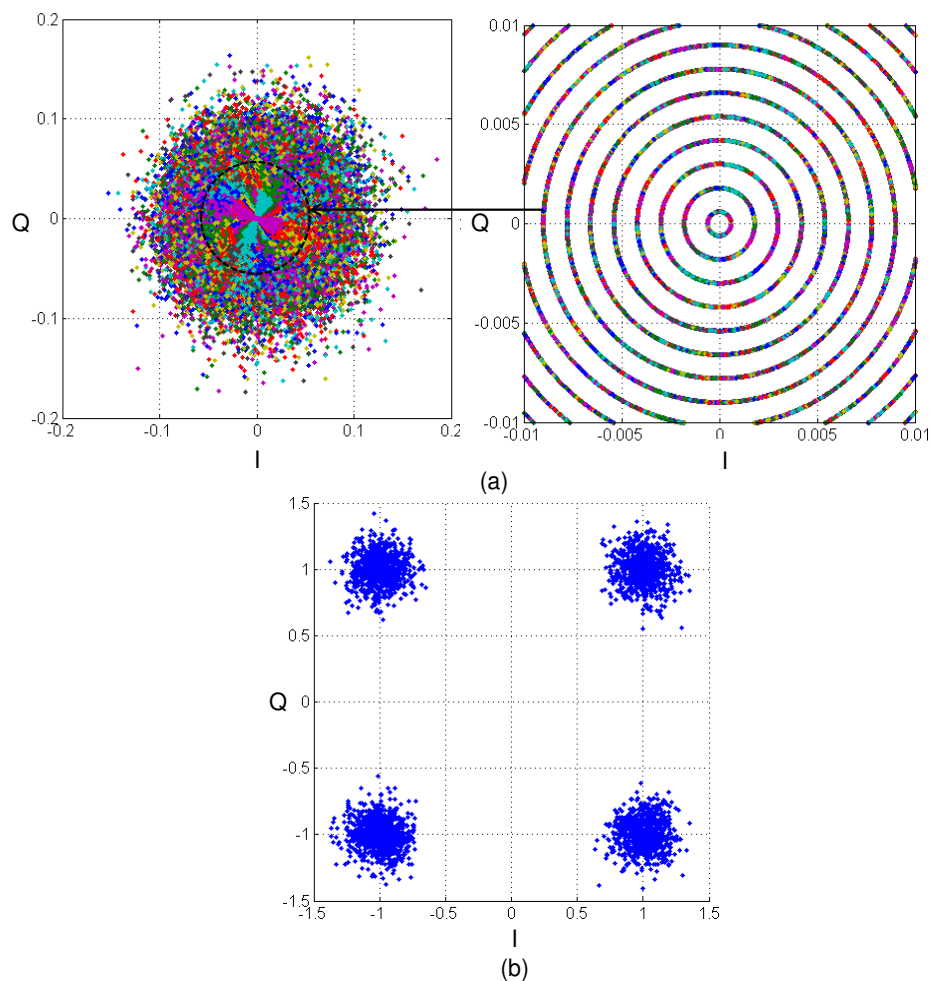


Fig. 7.2.14. Scatter plots of the received signal (a) before and (b) after signal equalization for a 4 QAM back-to-back transmission.

Fig. 7.2.14 shows the scatter plots of the received data for a back-to-back transmission where (a) is before and (b) is after signal equalization. The received scatter plot before signal equalization shows phase rotation of the symbols in the form of many circles at many magnitudes around the DC. The multiple circles are expected as the subcarriers pre-emphasized with a set of a linear magnitude response to compensate for the C-MZI frequency response. The radii of the circles are due to the pre-emphasis coefficients, which were applied to the symbols. After the signal equalization, the scatter plot of 4 QAM can be recovered as in (b).

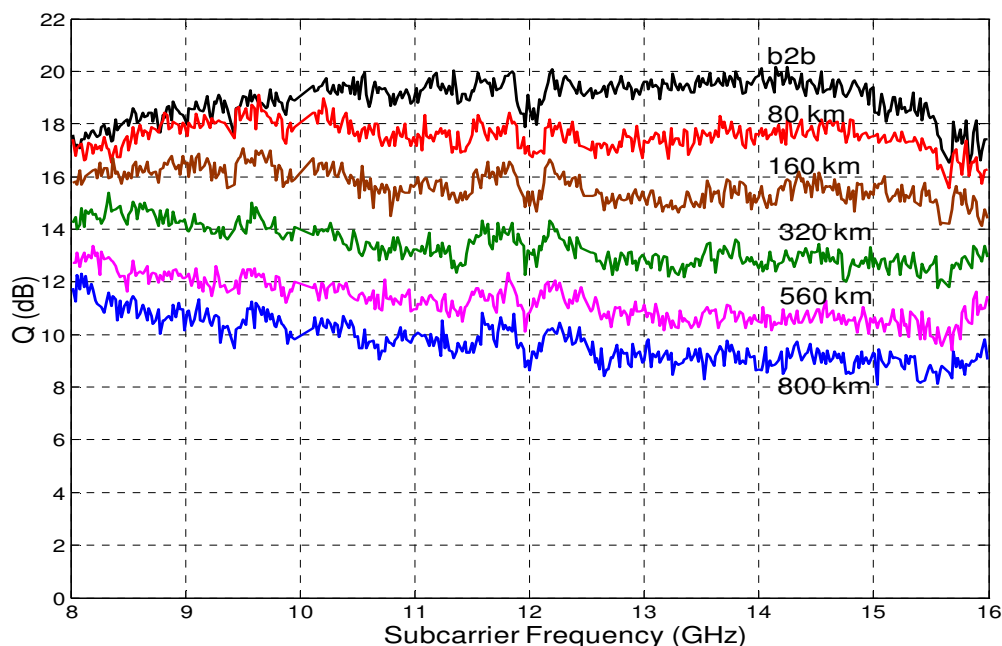


Fig. 7.2.15. Q-factor versus subcarrier frequency of 4 QAM OFDM signal transmission using laser linewidth of 11.4 MHz over back-to-back, 80-, 160- 320-, 560- and 800-km of S-SMF.

Fig. 7.2.15. shows the Q-factor versus subcarrier frequency from 8 GHz to 16 GHz for 4 QAM OFDM signal transmission, which is equivalent to 16 Gb/s transmitted using a laser linewidth of 11.4 MHz. The dispersion was varied from back-to-back (b2b) until 800 km of S-SMF with dispersion coefficient of 16.75 ps/(nm·km). For the b2b transmission, the Q across the subcarrier frequency is relatively flat, where the electrical spectrum of this was measured and shown in Fig. 7.2.13. A significant reduction of Q can be seen at the high frequency subcarriers with the presence of dispersion. At 80 km, the Q reduction at the high subcarrier frequencies is small. This reduction becomes greater when a longer fibre (more dispersion) was used. For example, at 80 km, the reduction from low to high frequency is about 1 dB, while the reduction for 800 km is 4 dB. The high Q reduction at the high frequency subcarriers is due to the group delay effect due to the dispersion imposed to the subcarriers relative to the carrier. This is because of the subcarriers are ‘walking away’ from the carrier when the signal is propagated along the dispersive fibre. The subcarriers which are far from the carrier experienced greater delay than the one closer to the carrier. Also, note that the Q is also limited by the inband ASE noise due to the EDFAs.

This shows that the phase noise due to the laser linewidth of the DDO-OFDM transmission system depends on the subcarrier frequency and the transmission length or, equivalently, the accumulated dispersion [25]. This is different in CO-OFDM transmission systems, where the phase noise is due to the lasers' linewidths at both the transmitter and receiver is common for all subcarriers. In the DDO-OFDM system, a broad noise pedestal is also induced to the higher-frequency subcarriers when it is transmitted over a long transmission length. Along with its high phase noise power (determined by the peak noise pedestal's power), this will also introduce ISCI between the adjacent subcarriers. This makes it difficult to compensate. The ISCI is different in comparison with the CO-OFDM system where the ISCI is introduced to each subcarrier by the average phase noise with a spectral shift [27]. The ISCI in the CO-OFDM system is more dominant than its CPE, when the phase noise bandwidth is similar to the subcarrier frequency spacing. In the CO-OFDM system, phase noise compensation can be designed to ignore the ISCI effect or treat it as additive noise [28], but it is impossible to do so in the DDO-OFDM system. The RF pilot tone is employed in the CO-OFDM system to compensate for both CPE and ISCI. However this requires several zeroes subcarriers in the middle of the signal bandwidth where the RF tone is placed at dc for phase estimation [29, 30]. This system is more complex to design as compared to [28] due the huge amount of calculations required at the receiver part [30]. The zeroed subcarriers and the RF tone can also reduce the spectral efficiency of the system.

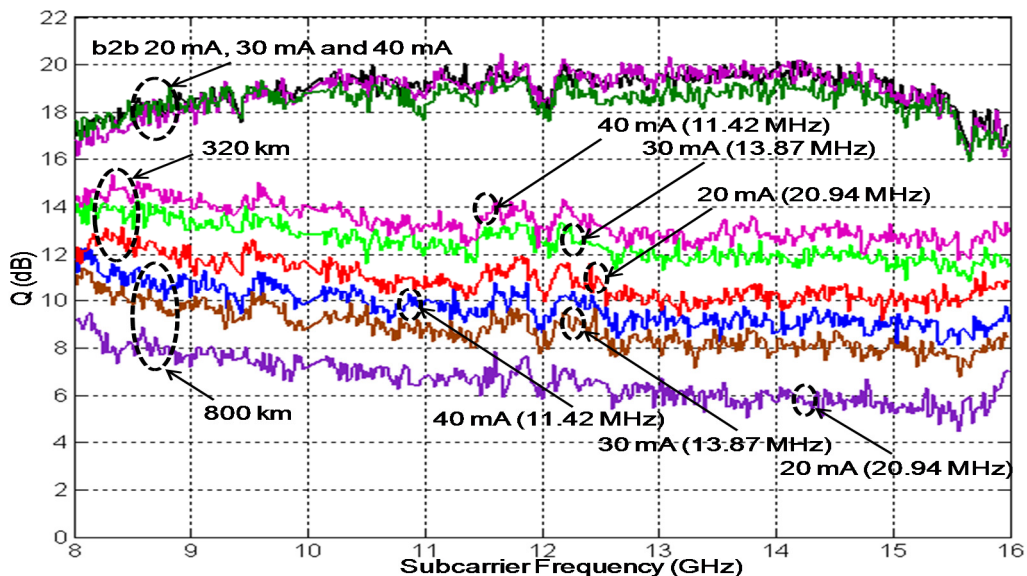


Fig. 7.2.16. Q-factor versus subcarrier frequency for laser driven by I_b of 20 mA, 30 mA and 40 mA over back-to-back, 320 km and 800 km of S-SMF.

Fig. 7.2.16. shows Q-factor performance across OFDM subcarrier frequency when the laser was driven by I_b of 20 mA, 30 mA and 40 mA over a back-to-back, 320 km and 800 km of S-SMF. The I_b of 20 mA emitted laser linewidth of 20.94 MHz, 30 mA for 13.87 MHz and 40 mA for 11.42 MHz, measured using the HRS. These I_b were chosen because they are well above the I_{Th} , with not too high RIN. The measured RIN for 20 mA I_b was -112 dB/Hz, for 30 mA was -121.27 dB/Hz and for 40 mA was -126.21 dB/Hz. The emitted laser power for 20 mA was -3.06 dBm where an EDFA was used at the output of the laser before driving the C-MZI. For 30 mA and 40 mA, the power was high enough and pre-amplifier is not required. The Q performance of the back-to-back transmission for all laser linewidths shows the same performance with reasonably flat response across the subcarrier frequency. When dispersion was applied, the overall Q performance dropped down for the high frequency subcarriers, which experienced more degradation than the low frequency subcarriers. For the 320 km, the Q degradation from the low to the high frequency is 2.3 dB for the linewidth of 11.42 MHz, 2.7 dB for 13.87 MHz and 3.1 dB for 20.94 MHz. Higher degradation between the low to high frequency subcarriers is observed for the 800 km transmission, with 4-dB for 11.42 MHz, 4.4-dB for 13.87 MHz and 5-dB Q degradation for the linewidth of 20.94 MHz. The figure also shows the wider linewidth laser degrades the overall Q across the subcarriers more than the narrow linewidth when the dispersion is applied. The average Q reduction from the transmission using laser linewidth of 11.42 MHz to 13.87 MHz for both 320 km and 800 km was 0.9 dB. When wider linewidth of 20.94 MHz was used as compared to 13.87 MHz, more average Q degradation across the subcarriers was encountered with 1.6 dB for 320 km and 2.2 dB for 800 km transmission. The overall degradation when the wide linewidth laser was used is due to the PM-to-IM conversion noise effect due to the dispersion.

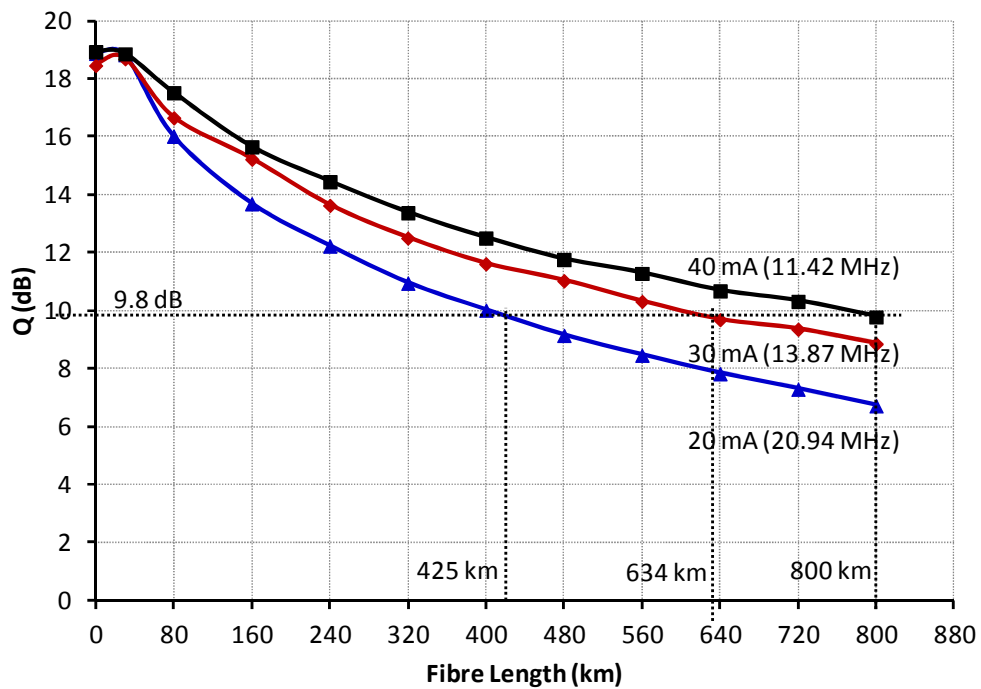


Fig. 7.2.17. Q-factor versus fibre length for 4 QAM OFDM transmission using laser linewidth of 11.42 MHz, 13.87 MHz and 20.94 MHz.

Fig. 7.2.17 shows Q versus fibre length from back-to-back until 800 km for 4 QAM OFDM signal, which is equivalent to 16 Gb/s transmission using laser linewidth of 11.42 MHz, 13.87 MHz and 20.94 MHz. These linewidths were achieved by driving the DFB laser with 40 mA, 30 mA and 20 mA of I_b . The plotted Q is the average of Q performance across the OFDM subcarriers. When no dispersion, all linewidth produced the same Q. When a short fibre length of 30 km was used, the Q is maintained with the same performance as the back-to-back transmission. The dispersion with this length is too small to reduce the Q. When 80 km fibre was used; the Q reduction of 1.4 dB for the linewidth of 11.42 MHz is shown. It becomes worst when a wider linewidth was used with 2.3-dB and 3-dB degradations for linewidths of 13.87 MHz and 20.94 MHz, respectively. A high Q reduction can be seen at a shorter fibre length from 80- to 320-km and reduces when longer fibre from 400- to 800-km was used. With this plot, a maximum distance for each laser linewidth can be determined by referring to 9.8 dB of Q to obtain 1×10^{-3} of BER. Around 800 km can be achieved using 11.42 MHz laser linewidth and 634 km using 13.87 MHz. At a wide linewidth of 20.94 MHz, the system can reach a distance of up to 425 km. This confirms that the DDO-OFDM system can be used for a long-haul transmission systems using a cheap laser such as a DFB laser

with a wide linewidth as compared to a CO-OFDM system, which requires narrow linewidth to prevent the laser's phase noise effects [20-22].

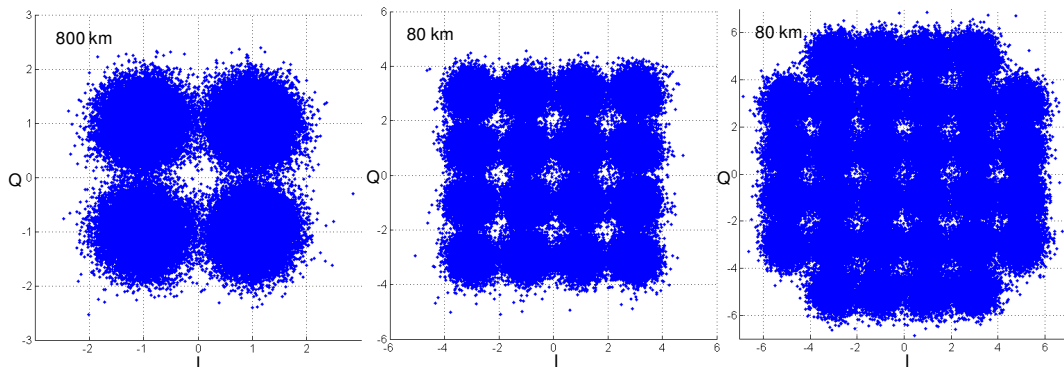


Fig. 7.2.18. Scatter plots of 4 QAM, 16 QAM and 32 QAM at BER of 10^{-3} transmitted using a laser linewidth of 11.42 MHz over 800 km for 4 QAM and 80 km for 16 QAM and 32 QAM.

Fig. 7.2.18 shows the scatter plots of 4 QAM, 16 QAM and 32 QAM OFDM signal transmitted using a laser linewidth of 11.42 MHz taken at BER of 1.55×10^{-3} (4 QAM), 2.83×10^{-3} (16 QAM) and 9.61×10^{-3} (32 QAM). These BER were achieved over the transmission of 800 km for the 4 QAM and 80 km for the 16 QAM and 32 QAM. With an 8-GHz signal bandwidth, the 4 QAM supports a raw data rate of 16 Gb/s, 16 QAM supports a 32 Gb/s and 32 QAM supports a 40 Gb/s. A higher M -size QAM data is transmitted to see the effect of the linewidth with the dispersion to the scatter plot of the received signal. The scatter plots show round and evenly scattered symbols around the origin symbol point.

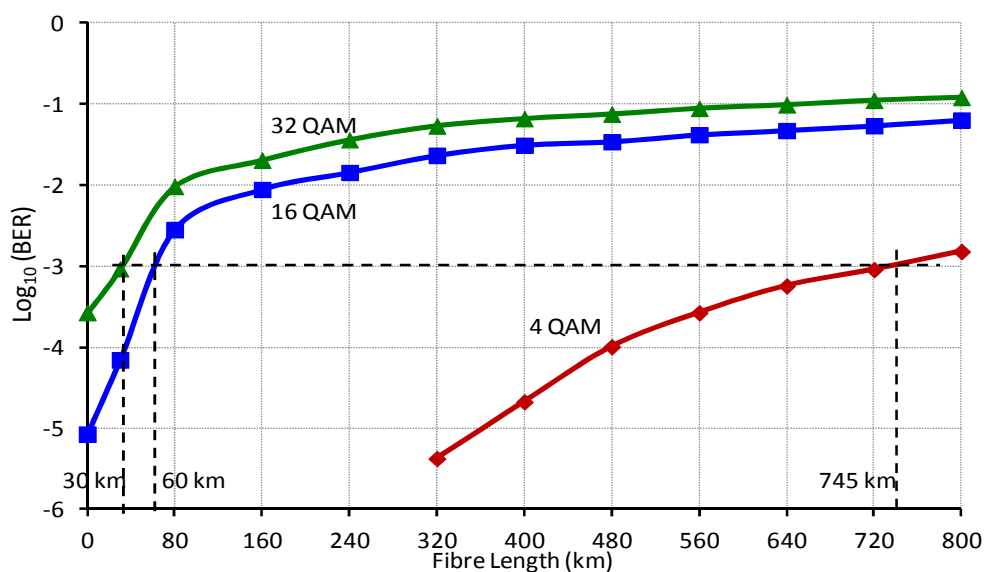


Fig. 7.2.19. BER versus fibre length for 4 QAM, 16 QAM and 32 QAM with a laser linewidth of 11.42 MHz driven by 40 mA I_b .

Fig. 7.2.19 shows BER versus fibre length for 4 QAM, 16 QAM and 32 QAM OFDM signal transmission from back-to-back until 800 km of S-SMF. The laser was driven by 40 mA of I_b which produces a 11.42 MHz linewidth. The plot shows that at a higher M -size QAM, only a short transmission length can be reached in order to achieve a minimum BER of 1×10^{-3} . For the 32 QAM, the system can only reach 30 km while the 16 QAM at 60 km. With the same laser linewidth, the transmission of 4 QAM was able to reach 745 km of fibre length. This shows that, the higher M -size QAM is more affected to the PM-to-IM conversion noise since the constellation points are closer to each other; hence they are more susceptible to the noise at the receiver.

7.3 Experimental Demonstration of DDO-OFDM Transmission System using Laser Linewidth Emulator

In this section, the laser linewidth emulator developed in Chapter 4 is used at the transmitter of a DDO-OFDM system. With this laser, the effects of the linewidth to the DDO-OFDM system with fibre dispersion can be studied without the influence of RIN.

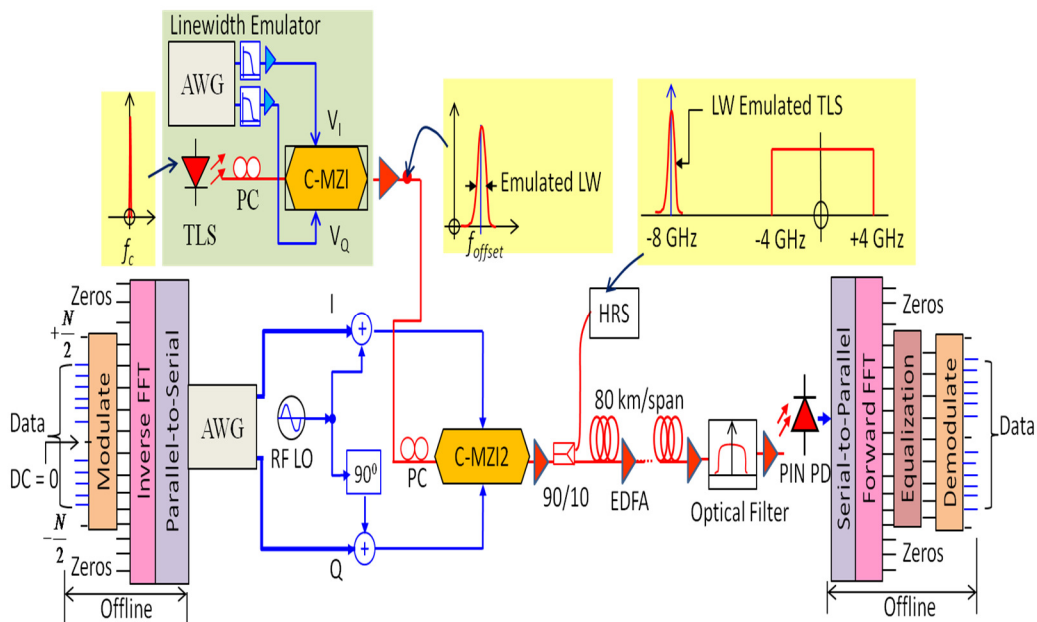


Fig. 7.3.1. Experimental setup of a DDO-OFDM transmission system using laser linewidth emulator.

Fig. 7.3.1 shows the experimental setup of a DDO-OFDM system using an RF-virtual carrier transmitter design employing a laser linewidth emulator. The emulator is shown in the green inset. In this setup, 5-GHz RF low pass filters (LPF) are used at the I and Q outputs of the AWG to filter out the image noise. Mini-Circuit ZX60-

14012L RF amplifiers are used before the signals are connected into a Sumitomo T.SBX1.5-10 20 Gb/s C-MZI. This C-MZI consists of two inner MZIs which are nested together by an outer MZI [23]. The DC biases are adjusted to ensure each of the MZIs was biased at null and the inner MZIs were biased to quadrature in the outer MZI. The original center frequency, f_c , of the emulator is provided by the Agilent 8164B tunable laser source (TLS), which is tuned to 193.1 THz. The f_c is then shifted to a 3-GHz frequency offset, f_{offset} , to overcome the DC-blocked of the microwave amplifier used at the C-MZI's RF inputs. The output of the emulator is shown as in the yellow inset. The emulated linewidth can be varied, where its linewidth can be measured using the HRS.

The emulator's output was pre-amplified using a Lightwave 2020 EDFA and connected into the second C-MZI (C-MZI2). The C-MZI2 was used to modulate the transmitted data. The transmitted data was generated offline using a pseudo-random bit sequence (PRBS) data and modulated with 4 QAM. The data is assigned onto 410 OFDM subcarriers from a total of 512 FFT-points. This was done by using an inverse-FFT. Both positive and negative sides of the FFT-points are used for the subcarriers, which produced a signal bandwidth of 8 GHz (± 4 GHz) [19]. A linear magnitude of pre-emphasis is also imposed into the OFDM data to compensate for the decreased of the high frequency response of the C-MZI2. The signals were converted onto a serial configuration and loaded into the second AWG of 2×10 GS/s. The outputs of the AWG are amplified using Marki Microwave AP-0020 5-MHz to 20-GHz amplifiers before driving a Sumitomo T-SBX1.5-20P 40 Gb/s C-MZI2. The C-MZI2 was biased at null to suppress the DC.

The optical carrier is then generated using the RF-virtual carrier technique. The virtual carrier is generated using a Hewlett Packard 83620A synthesized sweeper tuned to 12 GHz to provide an 8-GHz guardband between the carrier and the subcarriers. The lower sideband carrier was generated by adding the RF tone to the I and Q drives [19]. The upper sideband of the virtual carrier is cancelled out completely using a 90° phase shift. Apart from using the virtual carrier technique at the transmitter, a shifted optical carrier can also be generated by using a subcarrier assigned at the negative FFT-side [24]. However, this technique will provide a lower signal bandwidth compared to the

virtual carrier technique since only positive FFT-side can be used as the data subcarriers.

A 90/10 3-dB coupler is used after the output of the C-MZI2 is pre-amplified. The 90% coupler's output is connected through fibre optics cable while the 10% output is connected into the HRS. This was done to monitor the DC biasing of the C-MZI1 of the emulator setup and the C-MZI2 for the OFDM signal modulation to prevent a DC leakage. This is convenient since both of the C-MZIs' biasing can be monitored at a similar point. The output of the emulator can be measured by turning off the second AWGs' outputs that connected into the C-MZI2. The spectra of the laser linewidth emulator measured at this point are shown in Fig. 7.3.2 for dialed linewidth of 5-, 8-, 10- and 15-MHz.

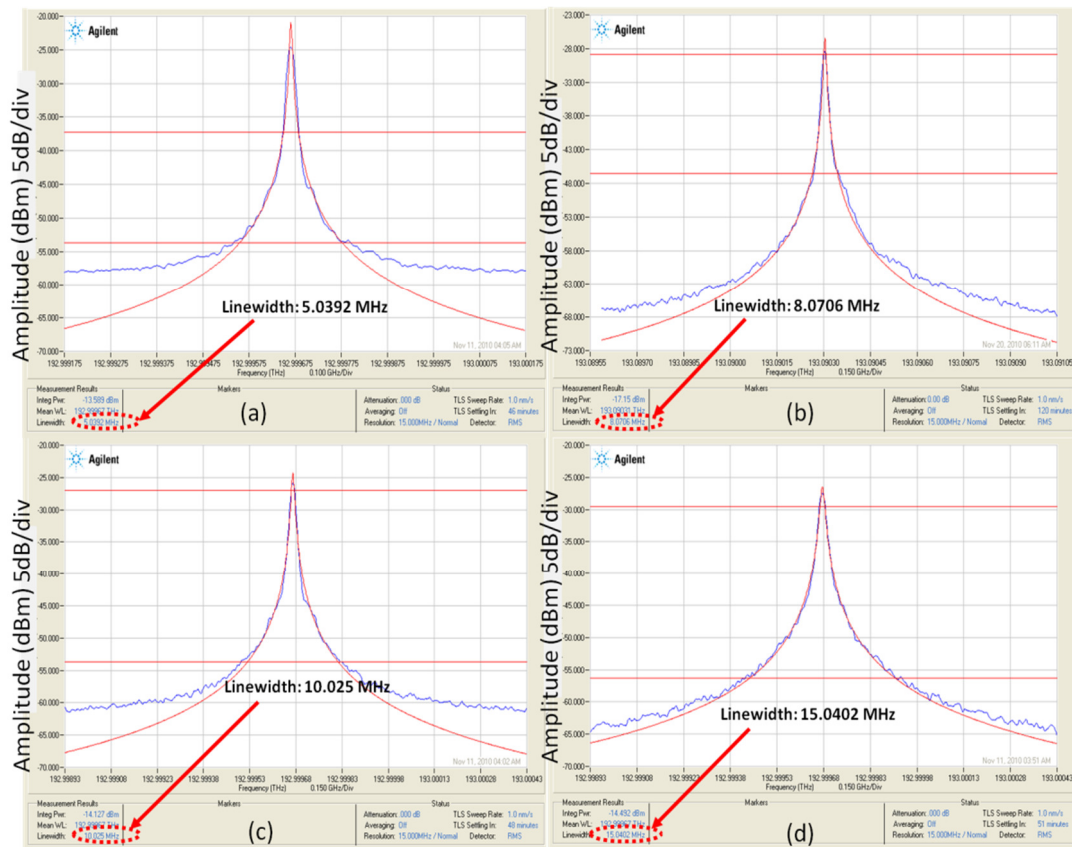


Fig. 7.3.2. HRS linewidth measurement at 10% coupler's output of dialed linewidth of (a) 5 MHz (b) 8 MHz (c) 10 MHz and (d) 15 MHz.

Fig. 7.3.2 shows the HRS linewidth measurement for the laser linewidth emulator measured at the 10% coupler's output for the dialed linewidth of (a) 5-, (b) 8-, (c) 10- and (d) 15-MHz. The measured linewidth matched well with the dialed linewidth. To transmit the OFDM signals, the second AWG's outputs connected to the C-MZI2 are

turned on with the RF-virtual carrier's sine and cosine components are added to the I and Q signals. The upper-sideband suppression of the virtual carrier is monitored using the HRS. A minimum of 20-dB suppression of the upper-sideband was required in order for the technique to work effectively.

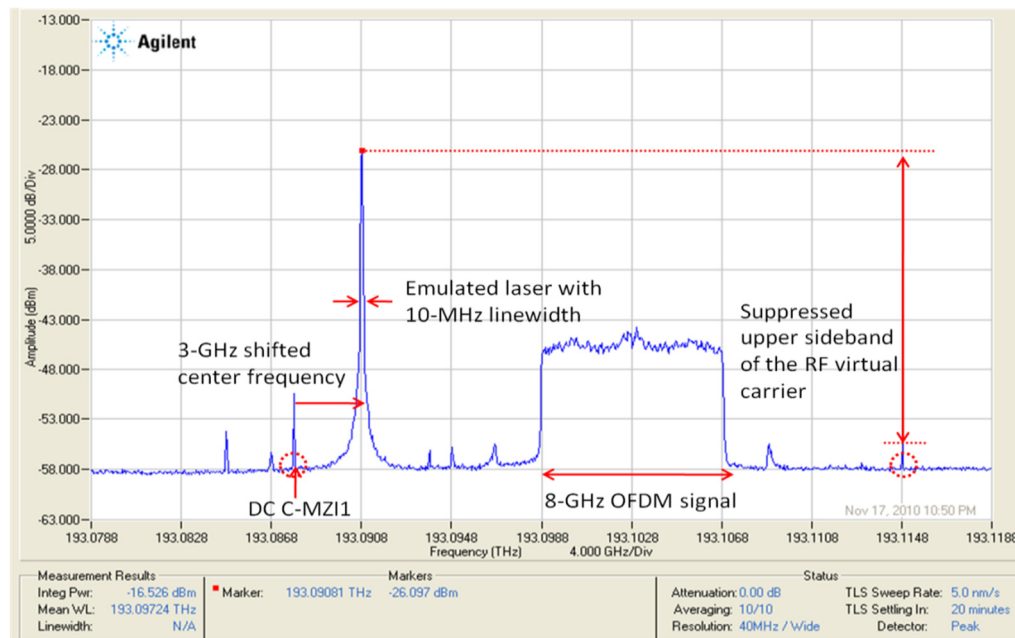


Fig. 7.3.3. HRS spectrum measurement of the OFDM signal at the transmitter's output with dialed linewidth of 10MHz.

Fig. 7.3.3 shows the measured optical spectrum of the OFDM signal at the transmitter's output with a dialed linewidth of 10 MHz. The figure shows that the optical carrier is shifted to a higher frequency by 3 GHz. This DC suppression was done at the emulator setup. The carrier is broadened from the TLS's linewidth of 256-kHz to 10-MHz dialed linewidth. The figure also shows a 28-dB suppression of the upper-sideband relative to the lower-sideband carrier. This was achieved by using the 90° phase shift of the RF tone added to the Q signal component.

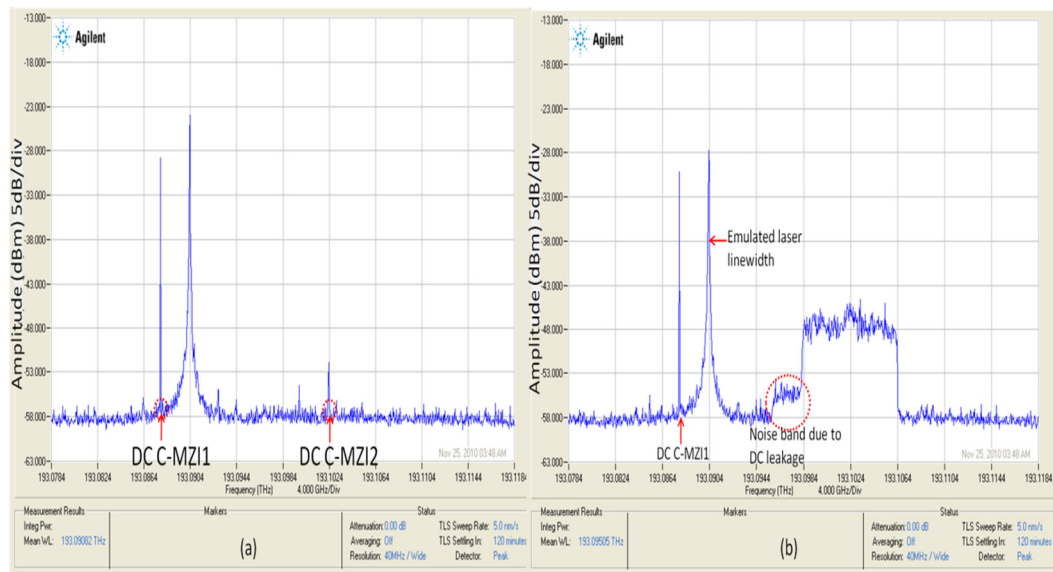


Fig. 7.3.4. C-MZI2 output signal with C-MZI1’s DC leakage when (a) the OFDM signal was off and (b) the OFDM signal was on.

Since two C-MZIs were used in this setup; the DC biasing of each C-MZI needs to be monitored to avoid DC leakage. Fig. 7.3.4 shows the spectra with the effects of the emulator’s DC leakage from the C-MZI1 when the emulator is used to drive the C-MZI2 to modulate OFDM signal. Fig. 7.3.4 (a) shows the C-MZI1 DC leakage of 28 dB. This spectrum was achieved at the C-MZI2’s output with the AWGs were turned off. When the OFDM signal was supplied (AWGs were turned on), the DC leakage is also carrying its signal bandwidth with a 3 GHz of it could be seen at the guard band while the other 5 GHz subcarrier falls within the desired signal band. This will cause interference between the unwanted DC’s signal band and the OFDM signal band, hence reduces the performance of the first 5-GHz of subcarriers. The DC leakage of the C-MZI is due to the transfer function instability over its operating time. Therefore, it is vital to monitor the DC biasing conditions of both C-MZIs during the experiment.

The signal of Fig. 7.3.3 was transmitted over 9×80 km spans of fibre and received with a DD receiver. The optical signal-to-noise ratio (OSNR) is maintained at 20 dB, which is beyond the OSNR requirement for 4 QAM in the DDO-OFDM system. The OSNR was measured using an Agilent 86142b optical spectrum analyser (OSA). A Waveshaper optical bandpass filter with 30-GHz bandwidth is used before the receiver to limit the effect of the ASE noise. The received electrical signal is captured using a Tektronix 72004 20-GHz 50-GSa/s digital sampling oscilloscope (DSO). The captured signal is then down-converted and equalized offline using MATLAB version R2007b.

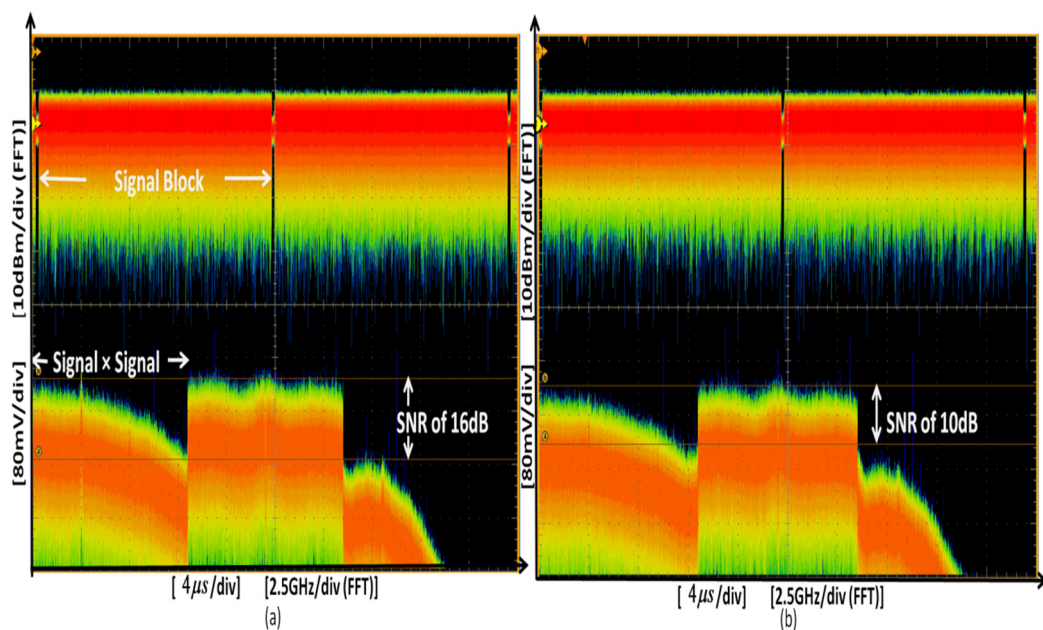


Fig. 7.3.5. Signal waveform with its FFT spectrum representation when the signal was detected after the PD for (a) back-to-back and (b) 720km transmission, with dialled linewidth of 20MHz.

Fig. 7.3.5 shows the received signal captured using the DSO. The figure shows the received waveform signal and its FFT spectrum for a back-to-back and over 720 km transmission by using a dialed linewidth of 20 MHz. The waveform shows two received signal blocks, where the second block is the repetition of the first signal block. The FFT-spectrum shows the signal \times signal beating noise falls on the bandgap. The spectra are flat across the subcarriers. The SNR of the received signal can be estimated using the top of the FFT-spectrum to the noise floor. From the spectrum, the 720 km SNR degradation can be estimated to 6 dB compared to the back-to-back transmission.

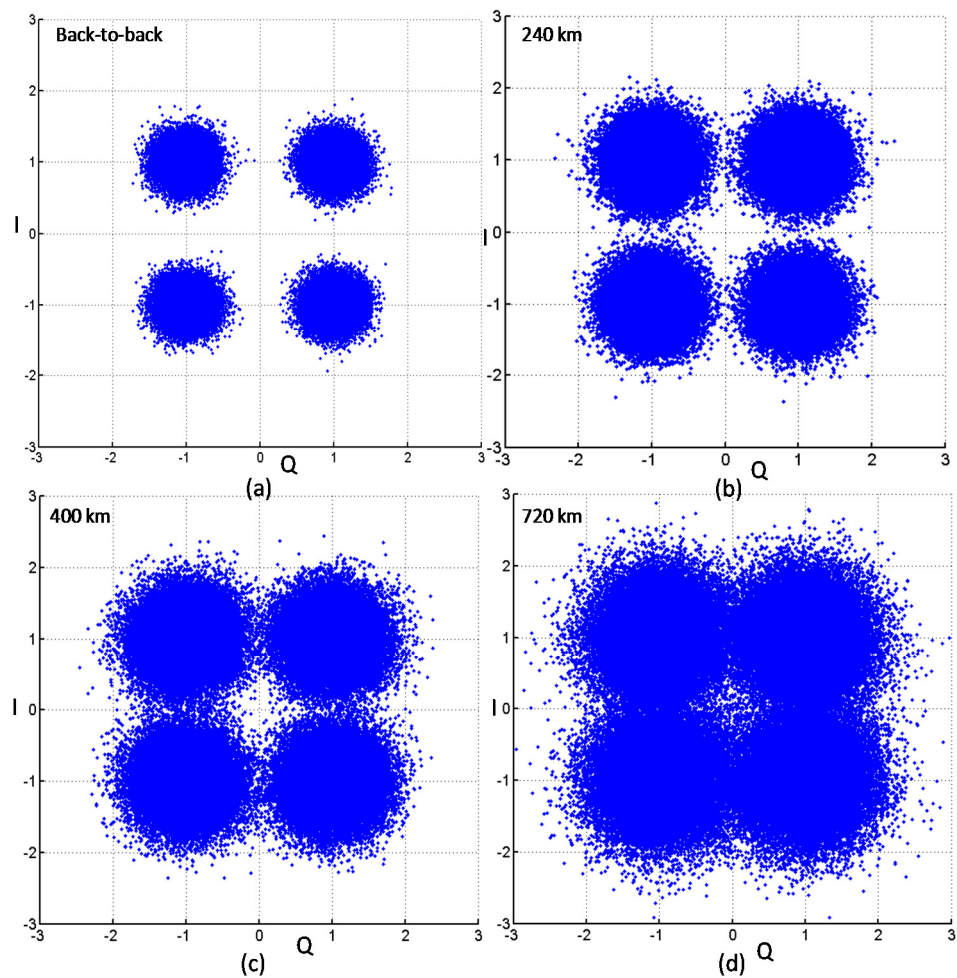


Fig. 7.3.6. Received scatter plots for a DDO-OFDM transmission over (a) back-to-back (b) 240 km (c) 400 km and (d) 720 km length of fiber with dialed linewidth of 20 MHz.

Fig. 7.3.6 shows the scatter plots after the received signals were equalized and QAM-demodulated using an offline signal processing. These plots result from the transmission over a back-to-back, 240 km, 400 km and 720 km fibre length using a dialed linewidth of 20 MHz. The symbols mapped on the scatter plots show a round shape in each quadrant without any phase rotations.

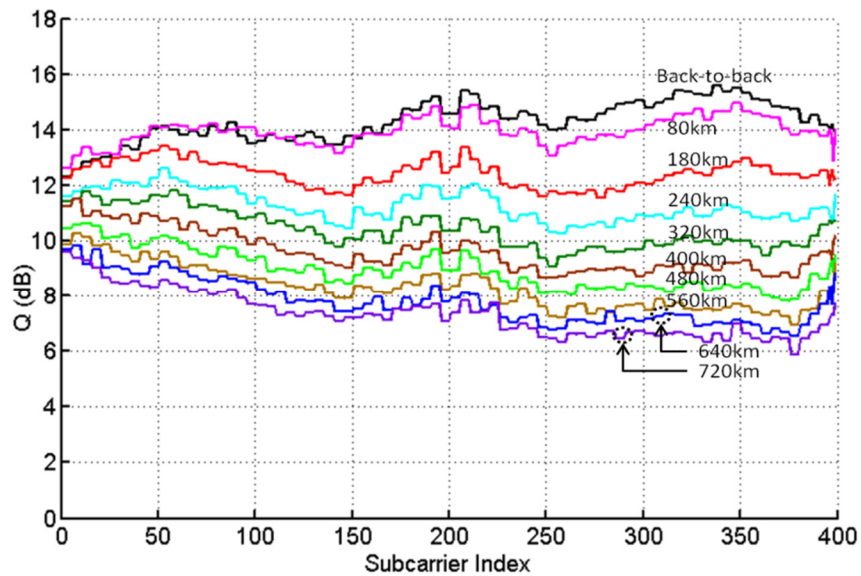


Fig. 7.3.7. Q vs. OFDM subcarrier index for every 80 km fiber length from a back-to-back to 720 km transmission using a dialed linewidth of 20 MHz.

Fig. 7.3.7 shows the Q versus subcarrier index from a low to high frequency, from 8- to 16-GHz. A 20 MHz dialed linewidth was used at the transmitter and the signal was transmitted for every 80 km of fiber span, starting from back-to-back to 720 km. The back-to-back plot shows around 1-dB higher Q at the high frequency subcarriers compared to the first 200 subcarriers. This was caused by the device limitations used in the experiment. For example, the AWG's skew and magnitude of its channel outputs can introduce a tilt in the frequency response over the time. During the experiment, these values were tuned in order to obtain a reasonably flat response across the subcarrier index during the back-to-back transmission. A drift in the C-MZI biasing can also occur over the time. This will cause the C-MZI to operate near or at the nonlinear part of its transfer function. During the measurement, to obtain the best response, the received signal is processed offline to obtain the plot of Q versus the subcarrier index. The OFDM spectrum measured with the HRS and the DSO showed a flat frequency response over the signal bandwidth as shown in Fig. 7.3.3 and 7.3.5. For the back-to-back transmission over a small dispersion of 80- and 180-km, all of the subcarrier experienced the same degradation when using a wide linewidth. This is explained by the flat response across the subcarrier index. When the dispersion was increased from 240 km to 720 km, the higher frequency subcarriers experienced more Q degradation compared to the lower frequency subcarriers. This is because the high frequency subcarriers acquired a larger time delay relative to the carrier as compared

to the low frequencies subcarriers which is closer to the carrier [25]. The delay was introduced by the group delay due to the chromatic dispersion.

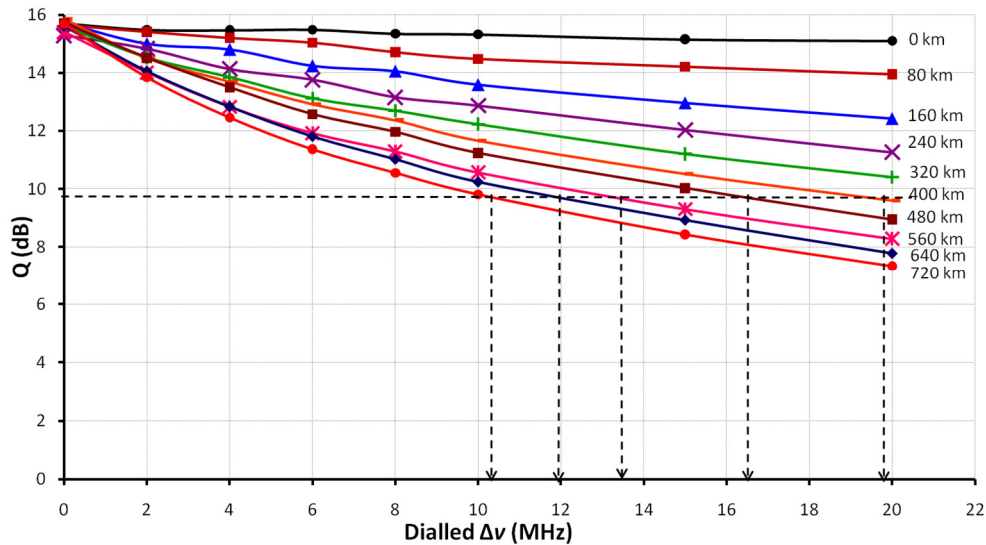


Fig. 7.3.8. Q vs. dialed linewidth of OFDM signal transmission for every 80 km of fibre span.

Fig. 7.3.8 shows the Q versus dialed linewidth when the signal is received for a back-to-back and at every additional 80 km fiber span until 720 km. The dialed linewidth was assigned from 0 to 20 MHz. Note that the 0 MHz is the narrowest linewidth of the emulator, limited by the TLS's linewidth of 256 kHz. For the back-to-back, only a small effect of linewidth is shown with a linear degradation of Q when the linewidth is increased. With a wide linewidth of 20 MHz, only 0.6-dB Q degradation is shown from 256 kHz (0-MHz) linewidth for the back-to-back transmission. This shows that the variable linewidth provided by the emulator is not affected by the IN or reduction in the laser output power. In a commercial variable linewidth DFB laser, the IN will be induced in the laser's output with a reduction in the output power when operating the laser at a wide linewidth. The back-to-back transmission also shows that the linewidth effect is not significant without the chromatic dispersion.

When a chromatic dispersion was applied to the system, the Q started to reduce for every additional 80 km of fibre span. This explains that the IN detected at the PD started to increase due to the PM-to-IM conversion noise of the linewidth with dispersion [18]. In a 4 QAM transmission, Q of 9.8 dB is required to achieve a 1×10^{-3} of BER. For 80 km to 320 km of fiber, the system's performance can tolerate the linewidth laser of more than 20 MHz. With the increase of the fiber length, the tolerable linewidth in the system is decreased. The widest linewidth that can be tolerated by 400

km is 20 MHz, 480 km with up to 16.5 MHz, 560 km with 13.6 MHz, 640 km can tolerate up to 12 MHz and the longest fiber length of 720 km can tolerate the linewidth of up to 11.2 MHz. The plot also shows a rapid Q degradation when high dispersion was induced.

7.4 Conclusions

The effects of a laser's RIN and linewidth to a DDO-OFDM system have been investigated experimentally using two types of laser: a commercial DFB laser and a laser linewidth emulator. With the commercial DFB laser, two types of transmitter design were presented. The first design was a low-rate transmitter using an un-shifted laser's center frequency to drive a C-MZI. The second design was an RF-virtual carrier transmitter design, where the laser's center frequency was shifted to an intermediate frequency using RF components to drive the C-MZI. With this transmitter, a wider signal bandwidth than the one obtained with the un-shifted laser was achieved hence; investigation on the noise effects to the low and high frequency subcarriers can be made. The wider signal bandwidth was achieved by using all of the FFT-points at both positive and negative sides as the OFDM subcarriers compared to the first design where only a quarter of the total FFT-points were used as the subcarriers. The laser's RIN and linewidth were varied by driving the laser using a low to high biasing current. This produces the laser's output power, P_o where the relation of both RIN and linewidth is known as $\text{RIN} \propto P_o^{-3}$ and $\text{linewidth} \propto P_o^{-1}$. The results using the first transmitter design show that a reasonable system performance can be obtained from a commercial fixed-wavelength DFB lasers operated at reasonably-low powers for 4 QAM, but higher powers are required for 32 QAM. The effect of the interaction of linewidth with fibre dispersion can be seen at moderate powers, but is generally masked by RIN at low laser powers. For the RF-virtual carrier transmitter design, 8-GHz OFDM signal bandwidth from 8 GHz to 16 GHz was achieved with an 8-GHz frequency guardband. Even though the RIN and linewidth are inter-dependent, the effect of RIN can still be isolated from the linewidth by a back-to-back experiment. This is because, the linewidth does not affect the system in the back-to-back case and its Q response is flat across the subcarrier band. The results show that with a high RIN, the Q of the subcarriers at low frequencies is reduced. This is due to the tail of the RIN resonance that was extended into the signal band before it dies away. The guardband not only useful to place the subcarrier \times

subcarrier mixing, but also the RIN peak power frequency also falls within this band where the RIN peak frequency is typically at several giga hertz [26]. When the RIN is decreased (-122 dB/Hz), a flat Q across the subcarrier frequency was achieved. This is because of the RIN is added to the noise floor evenly across the OFDM signal band upon detection, in which each of the subcarriers owns a DSB RIN resonance. This will also increase the system's noise floor level. At a very low RIN (-132 dB/Hz), the Q response is flat and is limited by the ASE noise.

An experiment to investigate a linewidth interaction to fibre dispersion as a function of subcarrier frequency showed that with PM-to-IM conversion noise, more Q degradation was experienced by the high frequency subcarriers. This is due to the group delay effect where the subcarriers are walking away from the carrier as they travelling along the dispersive fibre. The overall Q is also degraded when more dispersion is introduced in the system. At fixed fibre dispersion, the Q is also degraded as a function of the laser linewidth. The study also showed that the PM-to-IM conversion noise started to degrade the Q performance at a certain length. When too short an optical fibre was used, the Q performance had the same performance as the back-to-back transmission. This was shown when using 30 km dispersive fibre. The Q started to degrade at 80 km with 1.4-dB reduction when using 11.42 MHz linewidth. The Q degradations becoming worst when a wider linewidth were used. The Q reduction due to the PM-to-IM conversion noise is high when the fibre length was from 80 km to 320 km. The reduction reduces when longer fibre was used from 400 km to 800 km due to the other accumulated system noise such as the ASE noise. The plots presented in this chapter can be used to determine the maximum distance for each laser linewidth by referring to 9.8-dB of Q to obtain the minimum required BER of 1×10^{-3} . The results showed confirm that the DDO-OFDM system can be used for long-haul transmission systems using a cheap laser such as the DFB with a wide linewidth compared to a CO-ODM system which requires narrow linewidth to prevent the laser's phase noise effects [20-22]. This study also showed that the higher *M*-size QAM is more affected to the PM-to-IM conversion noise effect than the smaller size QAM. The achieved results showed that at 11.4 MHz, only 30 km can be reached by 32 QAM modulated signal and 60 km by 16 QAM. The 4 QAM can transmit the signal of up to 745 km. This is because the constellation points are closer to each other; hence the

symbols are more susceptible to the phase errors. For this experiment, the phase rotations of the symbols in the received scatter plots cannot be isolated as the dispersion is still small as well as the contribution of the other noise in the system such as the ASE noise. It has been shown using simulation in Chapter 6 that with the ASE noise, phase rotations of the symbols can be isolated when transmitting over an ultra-long haul dispersive fibre length.

The experimental study using the laser linewidth emulator design presented in Chapter 4 was implemented in the RF-virtual carrier transmitter design. With the use of the linewidth emulator, an independent linewidth effects to the DDO-OFDM system can be studied without the influence of a high RIN and low laser's output power when a wide linewidth was used. In the experimental setup, the DC carrier needs to be monitored at both C-MZIs to prevent DC-leakage and the noise band from the unshifted carrier due the leakage. The results for the Q performance over the OFDM subcarrier frequency agreed with the results obtained using the commercial DFB laser, where the Q degrades more at the high frequency subcarriers compared to the low frequency. The obtained results agreed with the experimental result using the DFB laser where 2.2-dB Q degradation was achieved when the emulator was set to 20 MHz with a fibre length of 320 km. This result is closed to the one obtained with the DFB laser where 3.1-dB Q-degradation was shown using 20.94 MHz linewidth after 320 km. The higher degradation showed by the DFB laser is due to other laser effects such as RIN. Other results showed that with the linewidth emulator at 11.2 MHz, a 720 km maximum fibre length can be achieved. This is similar to the results achieved by the transmission using the DFB laser where 11.42 MHz can reach a maximum distance of 745 km, Even though the results showed a 20-km difference in the maximum achievable distance, this 20 km is too short to be influenced by the PM-to-IM. This was shown in the experiment using the commercial DFB as in Fig. 7.2.16, where a 30-km transmission length gave the same Q as the back-to-back. The results achieved with the laser linewidth emulator agreed with the result achieved in using the commercial DFB laser. This can be seen by comparing Fig. 7.2.16 with 7.3.8. For a 4 QAM transmission using the DFB laser, the graph in Fig. 7.2.16 shows that 20.94-MHz linewidth can transmit up to 425 km. This is about similar to the result achieved with the linewidth emulator where 400 km of fibre length can tolerate up to 20-MHz linewidth using the graph in Fig. 7.3.8.

Another transmission was made with a 13.87-MHz linewidth of the DFB laser and the maximum length achieved was 643 km. Again, this is similar to the linewidth emulator setup where at 640 km, the system can tolerate up to 12-MHz linewidth.

7.5 References

1. Marshall, W.K., B. Crosignani, and A. Yariv, *Laser phase noise to intensity noise conversion by lowest-order group velocity dispersion in optical fiber: exact theory*. Optics Express, 2000. **23**(3): p. 165-167.
2. Zan, Z., A.J. Lowery, and M. Premaratne. *Laser RIN and linewidth requirements for direct detection optical OFDM*. in *Lasers and Electro-Optics CLEO 2008*. 2008. San Jose.
3. Ribeiro, R.F.S., J.R.F.d. Rocha, and A.V.T. Cartaxo, *Influence of laser phase noise on dispersive optical fiber communication systems*. photonics technology letters, 1995. **7**(12): p. 1510-1512.
4. Morgado, J.A.P. and A.V.T. Cartaxo, *Assessment of laser noise influence on direct-detection transmission system performance*. Journal of Lightwave Technology, 2003. **21**(3): p. 759-768.
5. Laurencio, P., S.O. Simoes, and M.C.R. Medeiros, *Impact of the combined effect of RIN and intermodulation distortion on OSSB/SCM systems*. Journal of Lightwave Technology, 2006. **24**(11): p. 4250-4262.
6. Ahmed, M. and M. Yamada, *Effect of intensity noise of semiconductor lasers on the digital modulation characteristics and the bit error rate of optical communication systems*. Journal of Applied Physics, 2008. **104**.
7. Schmidt, B.J.C., A.J. Lowery, and J. Armstrong, *Experimental demonstrations of electronic dispersion compensation for long-haul transmission using direct-detection optical OFDM*. Journal of Lightwave Technology, 2008. **26**(1): p. 196-203.
8. Lowery, A.J. and J. Armstrong, *10 Gbit/s multimode fiber link using power efficient orthogonal-frequency-division multiplexing*. OPTICS EXPRESS, 2005. **13**(25): p. 10003-10009.
9. Lowery, A.J. and J. Armstrong, *Orthogonal frequency division multiplexing for dispersion compensation of long-haul optical systems*. Optics Express, 2006. **14**: p. 2079-2084.
10. Lowery, A.J., L. Du, and J. Armstrong. *Orthogonal Frequency Division Multiplexing for Adaptive Dispersion Compensation in Long Haul WDM Systems*. in *Optical Fiber Communication Conference, 2006 and the 2006 National Fiber Optic Engineers Conference. OFC 2006*. 2006.
11. Schmidt, B.J.C., A.J. Lowery, and J. Armstrong. *Experimental demonstrations of 20 Gbits/s direct-detection optical OFDM and 12Gbits/s with a colorless transmitter*. in *Optical Fiber Communication Conference*. 2007. Anaheim, CA.
12. Lowery, A.J., L. Du, and J. Armstrong, *Performance of optical OFDM in ultra long-haul WDM lightwave systems*. Journal of Lightwave Technology, 2007. **25**: p. 131 – 138.
13. Lowery, A.J. and J. Armstrong. *Orthogonal-Frequency-Division Multiplexing for Optical Dispersion Compensation*. in *Optical Fiber Communication and the National Fiber Optic Engineers Conference*. 2007. Anahaim, USA.
14. Lowery, A.J., *Amplified-spontaneous noise limit of optical OFDM lightwave systems*. Optics Express, 2008. **16**(2): p. 860-865.
15. Fuqin, X., *Digital modulation techniques*. 2nd ed. 2006, Norwood, MA: Artech House. 1029.

16. Proakis, J.G. and M. Salehi, *Digital communications*. 5 ed. 2008: Mc Graw-Hill.
17. Glover, I.A. and P.M. Grant, *Digital communications*. Second ed. 2004, Dorchester: Pearson education limited.
18. Yamamoto, S., et al., *Analysis of laser phase noise to intensity noise conversion by chromatic dispersion in intensity modulation and direct detection optical fiber transmission*. *Journal of Lightwave Technology*, 1990. **8**: p. 1716-1722
19. Schmidt, B., A.J. Lowery, and L.B. Du. *Low sample rate transmitter for direct-detection optical OFDM*. in *Optical Fiber Communication - includes post deadline papers, 2009. OFC 2009. Conference on*. 2009.
20. Shieh, W. and C. Athaudage, *Coherent optical orthogonal frequency division multiplexing*. *Electronic Letters*, 2006. **42**: p. 587-588.
21. Yi, X., W. Shieh, and Y. Ma. *Phase noise on coherent optical OFDM systems with 16-QAM beyond 10Gb/s*. in *33rd European Conference and Exhibition on Optical Communication 2007*. Berlin, Germany: VDE VERLAG GMBH.
22. Jansen, S.L., et al. *20-Gb/s OFDM transmission over 4160-km SSMF enabled by RF-pilot tone phase noise compensation*. in *Optical Fiber Communication Conference*. 2007. Anaheim, CA.
23. Fonseca, D., et al. *Single sideband demonstration using a four phase-modulators structure*. in *2004 IEEE/LEOS - Workshop on Advanced Modulation Formats*. 2004.
24. Peng, W.R., et al., *Theoretical and Experimental Investigations of Direct-Detected RF-Tone-Assisted Optical OFDM Systems*. *Journal of Lightwave Technology*, 2009. **27**(10): p. 1332-1339.
25. Peng, W.-R., *Analysis of Laser Phase Noise Effect in Direct- Detection Optical OFDM Transmission*. *Lightwave Technology, Journal of*, 2010. **28**(17): p. 2526-2536.
26. Henry, C.H., *Theory of the linewidth of semiconductor lasers*. *IEEE Journal of Quantum Electronics*, 1982. **QE-18**(2): p. 259-264.
27. Armada, A.G., *Understanding the effects of phase noise in orthogonal frequency division multiplexing (OFDM)*. *Broadcasting, IEEE Transactions on*, 2001. **47**(2): p. 153-159.
28. Yi, X., W. Shieh, and Y. Ma., *Phase Noise Effects on High Spectral Efficiency Coherent Optical OFDM Transmission*. *Lightwave Technology, Journal of*, 2008. **26**(10): p. 1309-1316.
29. Jansen, S.L., et al., *Coherent optical 25.8-Gb/s OFDM transmission over 4160-km SSMF*. *Journal of Lightwave Technology*, 2008. **26**(1): p. 6-15.
30. Randel, S., S. Adhikari, and S.L. Jansen, *Analysis of RF-Pilot-Based Phase Noise Compensation for Coherent Optical OFDM Systems*. *Photonics Technology Letters, IEEE*, 2010. **22**(17): p. 1288-1290.

Chapter 8

REDUCTION OF THE IMPACT OF LASER LINEWIDTH

8.1 Introduction

Laser linewidth has been shown to be a limiting factor for a DDO-OFDM transmission system, due to the PM-to-IM conversion noise. This has been shown in Chapter 5, 6 and 7, where the subcarriers that are far from the carrier will experience higher phase walk-off than the ones closer to the carrier due to chromatic dispersion. With high accumulated dispersion, the high-frequency subcarriers also acquire high-power noise pedestals with broad bandwidths due to the laser linewidth. This will consequently introduce inter-subcarrier interference (ISCI) between the adjacent subcarriers. In this chapter, a technique to reduce the impact of a laser linewidth on a DDO-OFDM system will be presented. The technique is demonstrated experimentally using a commercial DFB laser. To demonstrate the reduction of the linewidth effects in the DDO-OFDM system, a recent variant of DDO-OFDM system; self-heterodyne O-OFDM (SHO-OFDM) system will be employed. In SHO-OFDM system, an optical filter is used to separate the carrier and subcarriers, before a coherent receiver is used to mix the carrier and the subcarriers [1, 2]. This gives a noise performance within 4 dB of a fully coherent optical OFDM. This chapter starts with the simulation works to show the reduction of the linewidth impact when a delay is used in the SHO-OFDM transmission system, presents in Section 8.2. In Section 8.3, experimental demonstrations will be presented to show the effect of the group delay on the subcarriers¹ and validate the results obtained from the simulations. The advantage of the delay assignment will be demonstrated with three experiments: transmission of a single subcarrier, multiple subcarriers and a full SHO-OFDM transmission system in order to investigate and observe a clear noise floor reduction with the assigned delay. Section 8.4 presents the conclusions for this chapter and Section 8.5 is the list of references.

¹ The experimental demonstration of this has been published in [9]: Zan Z. developed the experimental setup, performed the measurements and analysed the results. Du L. constructed the Matlab coding, Zan Z. and Lowery A.J. wrote the paper and Lowery A.J. supervised the work.

8.2 Simulation of Linewidth Impact Reduction using SHO-OFDM Transmission System

The impact of laser linewidth on DDO-OFDM systems can be explained by referring to the theory of the phase to intensity-modulation (PM-to-IM) noise conversion due to the chromatic dispersion of the fibre [3]. Another impact of linewidth combined with dispersion is the noise pedestal induced around each of the subcarriers due to group velocity dispersion (GVD). The differences in the group velocities of each of the subcarriers will impose some walk-off of the subcarriers from the carrier. In the time domain, this can be seen as a time delay on each of the subcarriers waveforms relative to the carrier. The theory of this is similar to the theory of self-heterodyne linewidth measurement, which has been presented in Chapter 5 [4]. In Chapter 5, simulation results showed that of a noise pedestal is imposed around each of the modulated RF tones. Also shown is the reduction of the noise pedestal's power when τ_D is much longer than τ_c of the received RF spectrum in Fig. 5.5.3. From this spectrum, the frequency-shifted optical beam produces an RF subcarrier separated from the optical carrier. When there is a relative delay between the subcarrier and the carrier, a noise pedestal will be induced. This simulated results also suggested that the peak of the noise pedestal is low when the delay is small but will increase when the relative delay is increased. The increase of the noise pedestal peak explains the impact of the linewidth when the CD is increased, which is also associated with the increased group delay. Also, the theory of linewidth measurement suggests that, the noise pedestal can be reduced by having a small relative delay between the subcarrier and the carrier. From Eq. (6) in Reference [4], the SNR is approximately proportional to $[1 - \exp(-\pi \Delta f \tau_g)]$, where τ_g is the differential group delay and Δv is the laser's linewidth. Thus the SNR is maximised by ensuring the phase waveforms are delay-matched.

In a CO-OFDM system, laser linewidth is known to be a limiting factor of its system performance [8, 10-13]. The CO-OFDM system requires a costly narrow linewidth external-cavity lasers (ECL) at both transmitter and receiver because the system is susceptible to phase noise, which is characterized by the laser linewidth. To deal with the phase noise effects, many compensation schemes have been developed using digital signal processing. Many of the compensation schemes can be adapted

from wireless OFDM systems [8, 10-13]. These schemes are developed to compensate for the phase distortions due to common phase error (CPE) and/or inter-subcarrier interference (ISCI). In [8, 10, 11], additional RF-pilot tones were utilized to compensate for the phase distortion due to the CPE, while in [10], the OFDM subcarriers itself have been used for the phase estimation. Besides the complexity of the digital signal processing required for the phase estimation and compensation, some of these techniques were developed only to compensate for the CPE phase distortions and ignored or taking the ISCI as an additive noise to the system. In the DDO-OFDM system, the effects of linewidth to the system are functions of subcarriers frequency and the transmission distance [14]. These are difference than the CO-OFDM system where the high-frequency subcarriers will suffer from high phase noise power and broad phase noise bandwidth. Similar compensation schemes designed for the CO-OFDM system could not benefit the DDO-OFDM system as the noise affecting the subcarriers in the CO-OFDM system is more constant and common to all subcarriers [10, 13]. In this study, simple technique to mitigate the linewidth effects using an optical delay is presented without the complexity of the digital signal processing. With this technique, no additional RF-tones are required hence the system's spectral efficiency is not affected. This technique is developed using new variant of direct detection technique known as the SHO-OFDM system. For a single photodiode receiver DDO-OFDM system, the phase noise compensation has been developed in [15] with an extension in the signal processing part upon detection, where the phase estimation were done using the central subcarriers.

In SHO-OFDM systems, a carrier is transmitted along with the subcarriers, usually with a frequency-gap, b_{gap} between the carrier and the subcarriers, similar to DDO-OFDM systems [5]. This means that the carrier and the subcarriers are derived from the same laser source, so the phase noise of the carrier and subcarriers is strongly correlated. Any delay between the carrier and subcarriers will decorrelate them. This delay is caused by the differential group delay of a chromatic dispersion in fibre. This will result in the noise pedestal around each of the subcarriers, which has been shown in Section 5.5. In [1, 2], experimental demonstrations of DD systems using an optical filter and optical hybrid to detect polarization-multiplexed signals carrying 120 Gbit/s have been shown. The optical filter was used to separate the carrier from the sideband at the receiver, so that the carrier could be amplified, then used as a local oscillator in

the receiver. The above theory suggests that the performance of such a receiver could be improved by carefully re-aligning the phase fluctuations of the carrier waveform with the sideband waveform, before photodetection. This is easily achieved by adding appropriate optical delays in the signal path or carrier path just before the optical hybrid. To examine this, simulation setup of the SHO-OFDM transmission system was developed and presented in the following figure.

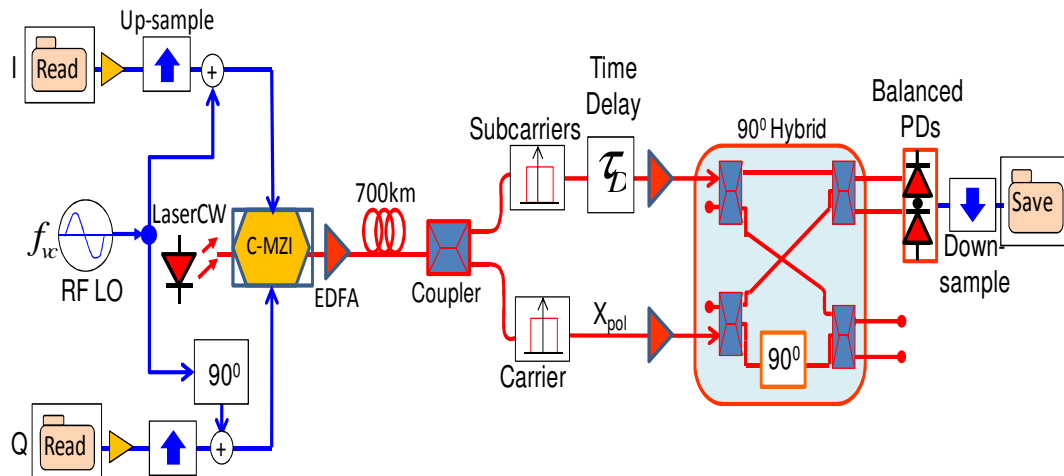


Fig. 8.2.1. Simulation setup for SHO-OFDM transmission system where the laser center frequency was shifted using the virtual carrier technique.

Fig. 8.2.1 shows the simulation setup for the SHO-OFDM system using RF-virtual carrier transmitter design. The transmitter part of the system is identical to a DDO-OFDM transmitter where the carrier is transmitted along with the subcarriers through the fibre. The I and Q signals of 4-QAM data modulated onto 1022 OFDM subcarriers that were generated using MATLAB R2008a. The transmit code is shown in Appendix 5.3. Both sides of the FFTs were used, and generated a 10-GHz signal bandwidth. The signals were read into the VPI simulation setup and amplified relative to the amplitude of the virtual carrier signal to achieve 1:1 carrier-to-subcarriers power ratio at the C-MZI's output. The RF LO is used to supply the RF subcarrier for the virtual carrier with the frequency, f_{vc} , of 15 GHz. This gives 10-GHz frequency separation, b_{gap} , between the carrier and the subcarriers. The I and Q signals are connected into the RF inputs of an IQ-modulator (C-MZI), which was driven by a `laserCW` module with the linewidth of 10 MHz.

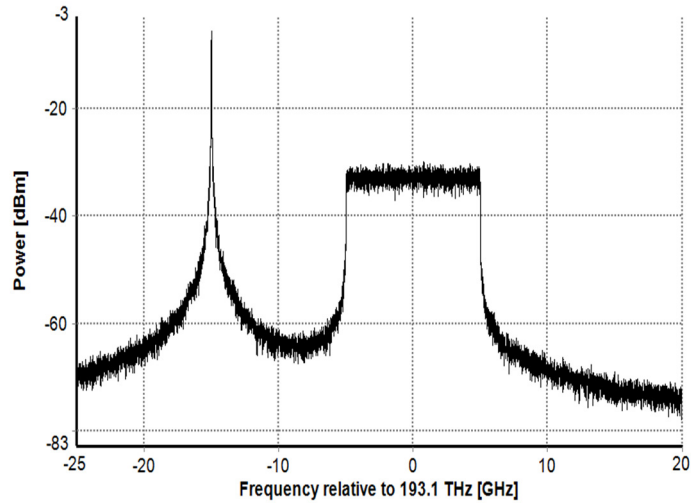


Fig. 8.2.2. Simulated optical spectrum at the C-MZI's output after a pre-amplification.

Fig. 6.2.6 shows the optical spectrum at the C-MZI's output after a pre-amplification using a noiseless amplifier. The spectrum shows 10-GHz signal bandwidth (± 5 GHz) with the optical carrier shifted to 15 GHz away from the laser's frequency, generated using the virtual carrier technique [6]. This optical signal is then transmitted over 700-km length of fibre with the CD of 16 ps/(nm·nm). In this simulation, only the laser linewidth and CD were considered. With 700 km of fibre, the transmit delay, τ_{tx} , imposed to the subcarriers can be calculated using

$$\tau_{tx} = D \cdot L \cdot \Delta\lambda \quad (8.2.1)$$

where L is the fibre length, D in s/m^2 and $\Delta\lambda$ is 0.1 nm wavelength resolution. This gives the τ_{tx} of 1.12 ns which is equivalent to a 22.4-cm length of fibre delay line with the velocity of light, c , of 3×10^8 m/s and the refractive index, n , of 1.42.

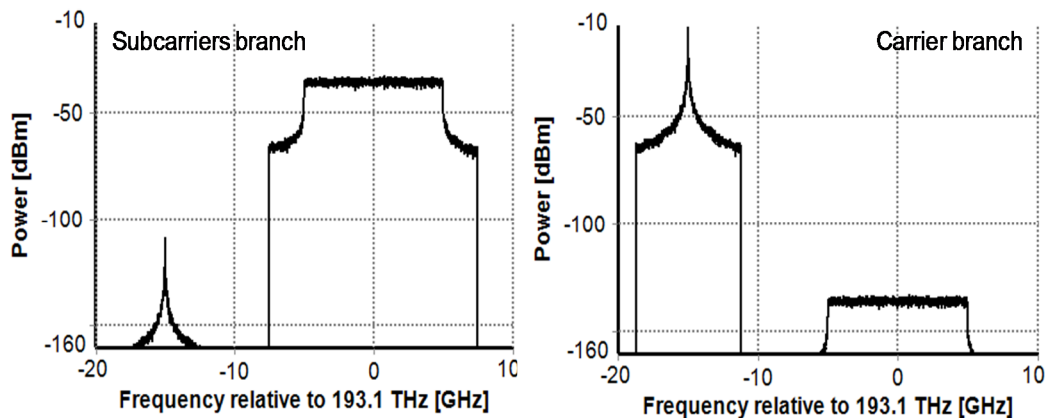


Fig. 8.2.3. Optical spectra after the subcarriers and carrier are isolated using the optical filters.

Fig. 8.2.3 shows the optical spectra at the subcarrier and carrier branches. These spectra are obtained using a rectangular bandpass filter in each branch to isolate the subcarriers and the carrier. The subcarriers branch is assigned with a time delay module to delay the subcarriers signal band relative to the carrier. A single X-polarization carrier is mixed with the delayed subcarriers by the 90° hybrid and detected using the balanced receiver, which produced a single polarization signal. The converted electrical signal is down-sampled and saved in the form of .txt file and calculated by a receiver code using MATLAB. The receiver code is shown as in Appendix 5.1. The same code used for a typical DD system with a single photodiode can be used for this system. The received signal was then equalized and demodulated to recover the transmitted data.

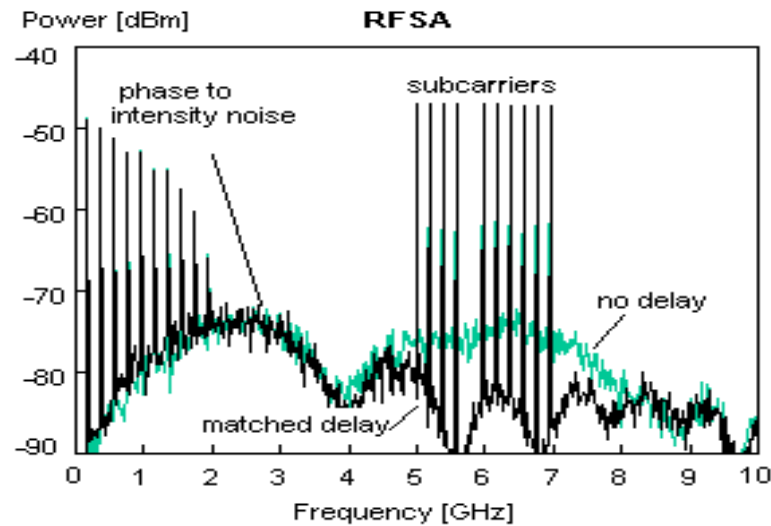


Fig. 8.2.4. Simulated results comparing the reduction of noise pedestal around several subcarriers using a matched delay to the un-delayed spectrum.

Fig. 8.2.4 shows the received spectrum with 10 subcarriers transmitted over 500-km of fibre with the linewidth of 10 MHz when the signal is not delayed relative to the carrier (except by fibre dispersion) and with an addition delay, τ_D , of 650 ps. This delay is added to the subcarriers branch to cancel the higher propagation velocity experienced by the subcarrier in the fibre. The delayed spectrum shows a dramatic decrease of the pedestal magnitude.

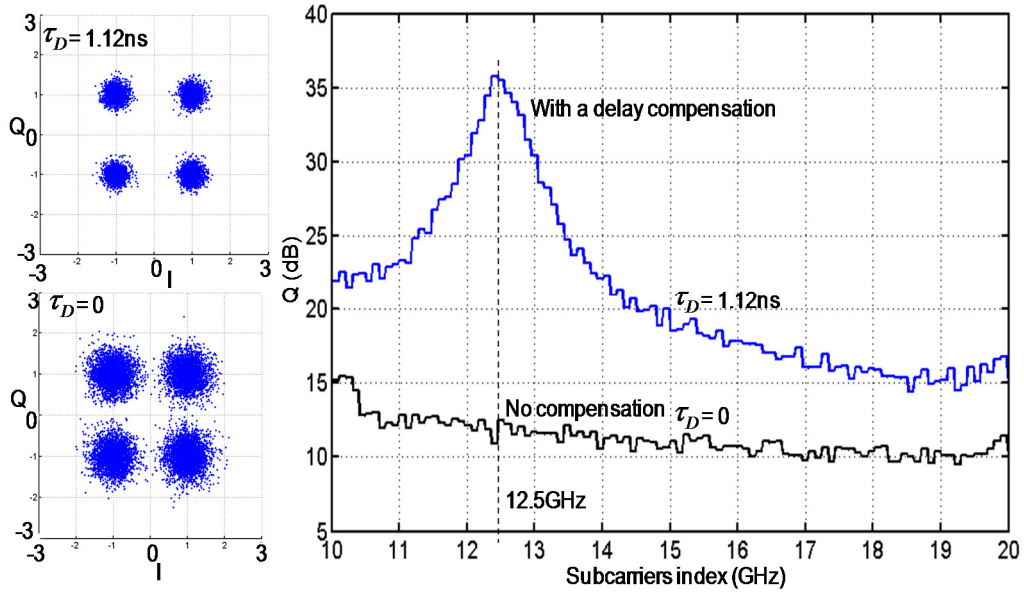


Fig. 8.2.5. Simulated signal quality, Q , vs. subcarrier frequency index with its respective scatter plots comparing the un-delayed and 1.12 ns delay of the subcarriers signal band relative to the carrier.

Fig. 8.2.5 shows the received constellation plots and Q versus subcarrier frequency index for the un-delayed subcarriers in comparison with a delay of 1.12 ns relative to the carrier. The delay of 1.12 ns gave a higher-quality scatter plot compared to the un-delayed plot. For the Q performance, the un-delayed system shows more degradation for higher frequency subcarriers. This is because the differential group delay of the subcarriers located far away is greater than for the ones closer to the carrier. When $\tau_D = 1.12$ ns, a significant increase of Q can be seen across the signal band, with a minimum increase of 5 dB. The highest increment of Q is around the subcarriers at 12.5 GHz due to the calculated τ_D at the wavelength resolution of 0.1 nm as in Eq. 8.2.1. In order to move the highest peak of Q across the signal bandwidth, the following equation can be used to calculate the required τ_D for a certain transmission length.

$$\tau_D = \frac{f_{SCx}}{12.5\text{GHz}} \times \tau_{tx} \quad (8.2.2)$$

where f_{SCx} is the frequency index of the subcarriers away from the optical carrier (GHz).

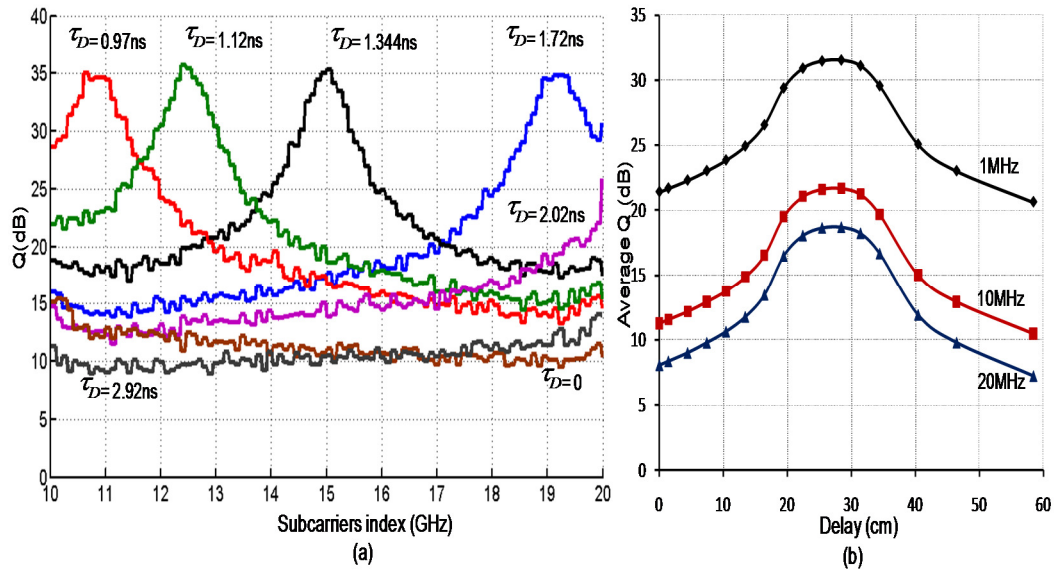


Fig. 8.2.6. Performance of 4-QAM transmission over 700-km of fibre showing (a) Q vs subcarriers frequency index comparing the response of the un-delayed with a set of τ_D and (b) the average Q vs the length of fibre delay line for linewidths of 1 MHz, 10 MHz and 20 MHz.

To show that the highest increment of Q can be initiated at a certain frequency by calculating τ_D using Eq. (8.2.2), the Q performance using several τ_D values was simulated. Fig. 8.2.6 (a) shows the Q versus subcarrier frequency. The τ_D was calculated using Eq. 8.2.2 for a fibre length of 700 km. The figure shows that when an appropriate time delay is applied to the subcarriers relative to the carrier, the overall Q of all the subcarriers is increased. With this simple delay assignment, certain subcarriers can be chosen to have higher Q values. This can also support multi-band M-QAM allocation where the subcarriers with higher Q can be allocated a higher modulation level; hence increasing the overall data capacity. However, the τ_D needs to be carefully chosen; a too long τ_D will cause phase decorrelation among the subcarriers and destroy their orthogonality. This can be shown by the plot when τ_D is equal to 2.92 ns. With this τ_D the average Q is decreased from 11.3 dB for the no delay to 10.5 dB. Fig. 8.2.6 (b) shows the plots of the average Q vs. the length of fibre delay line using the laserCW with the linewidth of 1-, 10- and 20-MHz. The length of the fibre delay line, L_D was calculated using $L_D = \tau_D \times v$, where v is the velocity of light in the fibre. This shows that a careful selection of fibre delay line is crucial in order to achieve good signal quality. More than 10-dB Q improvement can be achieved as compared with the no delay line, even with a 20-MHz linewidth laser.

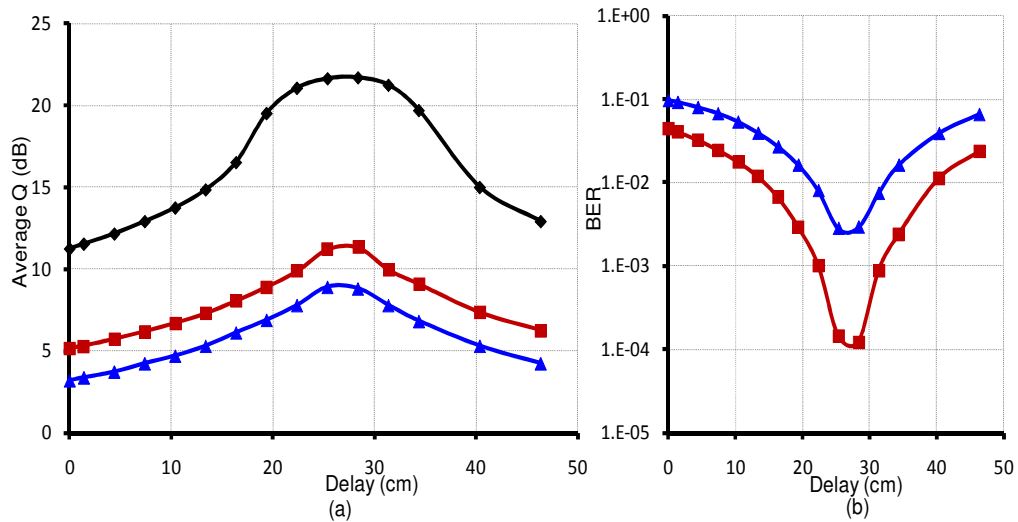


Fig. 8.2.7. Simulation result for higher M-QAM transmission with 10 MHz linewidth over 700 km (a) Q vs. the length of fibre delay line and (b) BER vs. delay for 16 QAM and 32 QAM.

To confirm that the delay is effective for higher-order QAM, 16 QAM and 32 QAM were simulated. Fig. 8.2.7 shows the simulated results for the Q (a) and BER (b) performance versus the length of fibre delay line when higher modulation level, M-QAM is used. The transmission was done with 10-MHz linewidth, adding a 10 GHz signal bandwidth over a 700-km of fibre. The Q was calculated from the BER. Fig. 8.2.7 (a) shows a large increment of 10.4 dB for 4 QAM, 6.1 dB for 16 QAM and 5.7 dB for 32 QAM when the effective delay line is assigned to the system. From the plots, the best length of the delay line that increased the total Q of the system is within the range of 25 to 28 cm for 700 km. This corresponds to when the highest peak of the Q across the subcarriers is located in the middle of the signal band. Fig. 8.2.7 (b) shows the BER versus delay line for 16 QAM and 32 QAM. 4 QAM plot is not included since the BER performance is far smaller than these two modulation formats. From this figure, the BER of 1×10^{-3} can be achieved with the delay of 22.4 cm and 32 cm. For the 32 QAM, the 1×10^{-3} could not be achieved with the delay due to the limitation of the laser linewidth for 700-km transmission length for this modulation level. However, the 5.7 dB increment of the Q provided by this technique can be used to improve the 32 QAM transmission to boost its Q and BER performance.

8.3 Experimental Demonstration of Linewidth Impact Reduction

The advantage of a delay will be demonstrated with three experiments:

- (1) Using a single subcarrier. This allows the details of the noise floor to be examined and compared with the result in Chapter 5.

- (2) With ten subcarriers which is spaced apart. This allows the effect of superimposing the noise from several subcarriers to be examined, and confirms the noise from each subcarrier adds in power. That is, the noise from a subcarrier is uncorrelated with the noise of the other subcarriers.
- (3) With a full OFDM spectrum. This shows the BER and Q factor are improved by applying the delay to the SHO-OFDM system.

8.3.1 Single Subcarrier Transmission

A single subcarrier transmission was used to show the details of the noise floor and the effect when a delay is applied to the subcarrier relative to the carrier in a self-heterodyne receiver. The developed experimental setup is shown in the following figure.

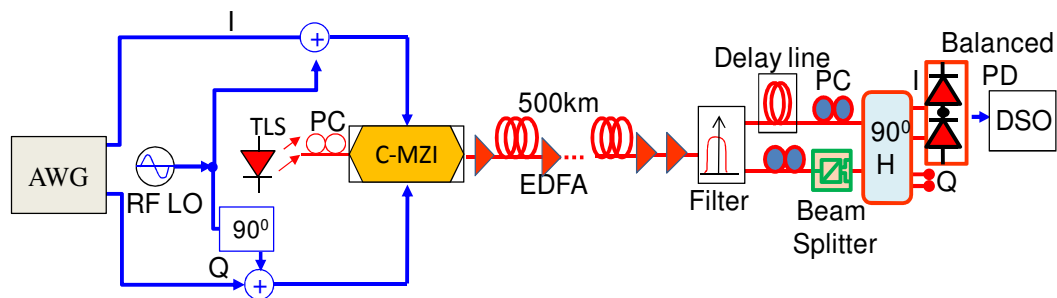


Fig. 8.3.1. Experimental setup for a single and ten RF subcarriers transmission to show the noise pedestal power reduction when a matched delay is assigned.

Fig. 8.3.1 shows the experimental setup of a self-heterodyne (SH) detection system with the transmission of a single and ten RF-subcarriers. For the single subcarrier, only the RF local oscillator (LO) at 12 GHz with a low output power was used where one input was 90° phase-shifted than the other. The signals were then used to drive the RF inputs of a Sumitomo 40-Gb/s DQPSK modulator (C-MZI). With this technique [6], the subcarrier can be easily swept across the signal bandwidth. The ten RF-subcarriers were generated using FFT in MATLAB R2008a and loaded into the Tektronix arbitrary waveform generator (AWG7102). The virtual carrier technique [6] was also employed in order to have the 12 GHz frequency separation between the middle subcarriers and the carrier. The 12 GHz frequency separation between the subcarrier and the carrier was used since the highest performance provided by the delay line used will occur in the vicinity of 12.5 GHz. The delay of 16 cm was used for the 500 km transmission length which was calculated using Eq. 8.2.1. The exact 12.5 GHz was not used in order to have a clear capture of the subcarrier on the scope.

At the fibre output, the signal was amplified using an EDFA to compensate the link loss. The output of the EDFA was connected to another EDFA to amplify the signal before the subcarriers and the carrier were filtered into two separate branches using a Finisar Waveshaper programmable optical filter. This is required to overcome the filter's insertion loss of 7 dB and prevent the tilting to the noise floor of the EDFA if the gain applied exceeded 20 dB. Also, due to the critical assignment of the delay line at the subcarriers branch, the EDFA could not be used to amplify the signal after the signals have been isolated. This is because of the unknown length of the fibre pigtailed used in the EDFA will affect the accuracy of the delay line used. Since the signal was an upper-sideband, the 16-cm delay line was assigned at the subcarriers branch. The carrier branch was fed into a polarization beam splitter to produce an X-polarization. The subcarrier and carrier were mixed using Klyia 90° hybrid (H) to produce the in-phase (I) and quadrature (Q) outputs of X-polarization. In this experiment, only the I signal was required to view the signal captures. The signal was then fed into a U²T 40-GHz balanced photodetectors. The received waveform was captured using a Tektronix 72004 20 GHz 50 Gsample/s digital sampling oscilloscope (DSO).

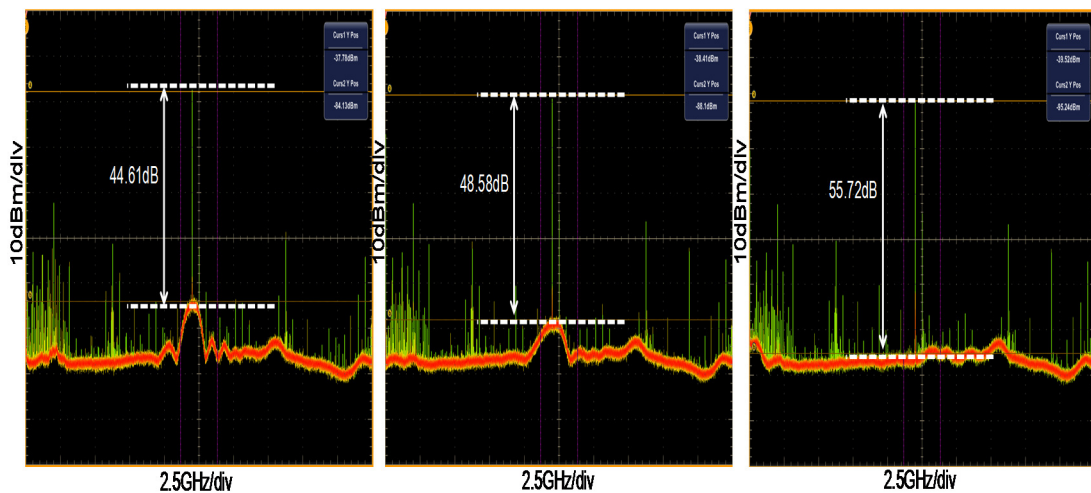


Fig. 8.3.2. Measured electrical spectrum showing the reduction of noise pedestal of a single subcarrier after 500 km with 10 MHz linewidth: (a) without a matched delay (b) 8 cm delay (c) delay matched with 16 cm.

Fig. 8.3.2 shows the electrical spectrum showing the noise reduction of a single subcarrier at 12 GHz obtained experimentally after 500 km of S-SMF with 10 MHz linewidth. To obtain this spectrum, an FFT mode of the DSO was applied to the captured waveforms. Fig. 8.3.2 (a) shows the resulting spectrum without the matched delay. The noise characteristic to 10 GHz is dominated by the laser's phase noise being

converted to intensity noise by fibre dispersion [3]. Also, owing to the CD, the carrier and subcarrier will acquire a relative delay of 800 ps which is approximately 16 cm. Fig. 8.3.2 (b) shows that the noise ‘hump’ is reduced by 4 dB with an 8-cm fibre delay and (c) is below the DSO’s noise level with a 16-cm delay. From the self-heterodyne theory, the noise could be nulled completely over a very narrow bandwidth, if phase to intensity noise conversion is ignored.

8.3.2 Multiple Subcarrier Transmission

Transmission of multiple subcarriers was done to show the impact of the superimposed noise from the adjacent subcarriers and to observe the delay effect on the noise power. This investigation was done using the same experimental setup in Fig. 8.3.1.

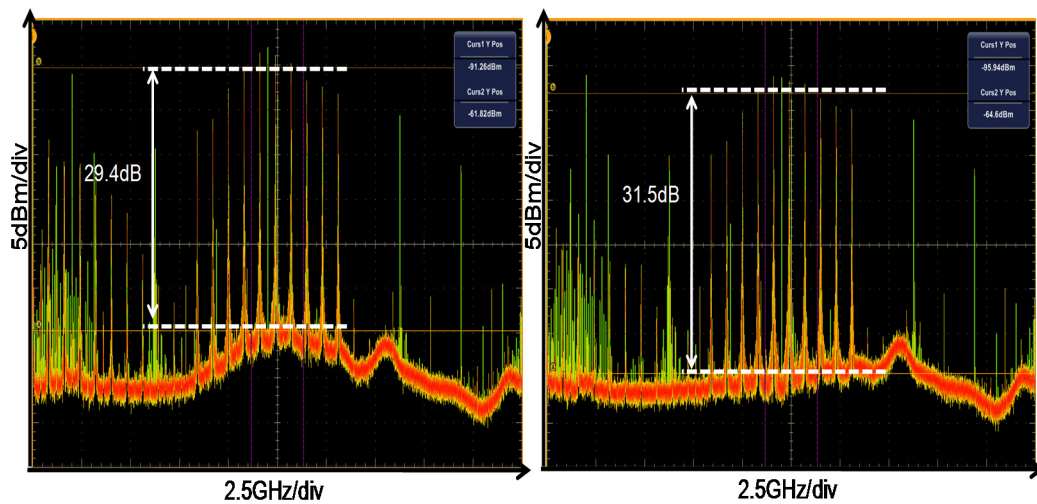


Fig. 8.3.3. The decreased of the noise pedestal power with (a) un-matched delay (b) matched delay with 16cm.

Fig. 8.3.3 shows the experimental RF spectrum for a ten subcarrier system within 8-GHz bandwidth by using a self-coherent heterodyne receiver [1]. Only ten subcarriers were used to allow the noise level in between them to be clearly seen. Fig. 8.3.3 (a) shows the RF spectrum without the matched delay and (b) with a matched delay of 16 cm. Several combinations of patch cords were used to obtain the 16 cm delay, which gave over a 1-dB loss in both signal and carrier arm into the self-heterodyne receiver. However, it is clear that the overall noise level is reduced down to the DSO’s noise floor. These measurements show that by matching the phase waveforms of the subcarrier-band and carrier reduces the noise pedestal around the subcarrier band. The noise can theoretically only be nulled for a single subcarrier, but

the result is still sufficiently useful over a wide bandwidth, particularly if the delays are matched in the centre of the band, where the noise humps of all subcarriers add.

8.3.3 SHO-OFDM Transmission System

In this section, SHO-OFDM transmission system is developed experimentally to show the benefits of a delay to the system's BER and Q performance. An experimental setup shown in the following figure was developed.

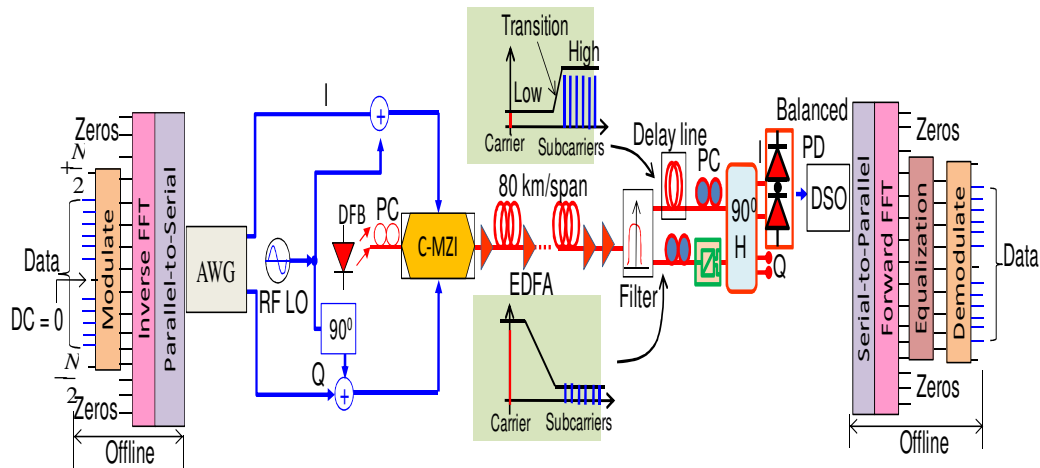


Fig. 8.3.4. Experimental setup of SHO-OFDM system showing the delay assigned to the signal branch after being filtered by a Waveshaper optical filter [1,2].

Fig. 8.3.4 shows the experimental setup of the SHO-OFDM system to reduce the impact of the linewidth to the OFDM subcarriers using a matched fibre delay line. In this setup, the OFDM subcarriers of 4 QAM are set around the DC point of the FFT. From a 512 subcarriers, 410 subcarriers are used to transmit the data. These subcarriers were generated offline using MATLAB and loaded into the AWG, to generate an 8-GHz baseband signal. An RF-virtual carrier is used to represent the optical carrier [6]. This virtual carrier is created by multiplying an RF source ($e^{j\omega t}$) to the In-phase (I) and Quadrature (Q) drives to generate a lower sideband carrier at -12.247 GHz [1, 6]. The upper sideband of the carrier was completely cancelled out with a 90° phase shift. The C-MZI was biased at null to suppress the optical carrier that falls in the middle of the signal band and leaving the -12.247 GHz subcarrier as the carrier. The biasing voltages were set to 3.81 V for DC1, 0.95 V for DC2 and 3.68 V for DC3. It is critical to tune the biasing voltages of the C-MZI since some voltage leakage can happen when the C-MZI was running over a long period of time. A commercial DFB was used which was set to 60 mA biasing current to produce 10 MHz linewidth. The linewidth measurement was done using an Agilent high-resolution spectrometer (HRS).

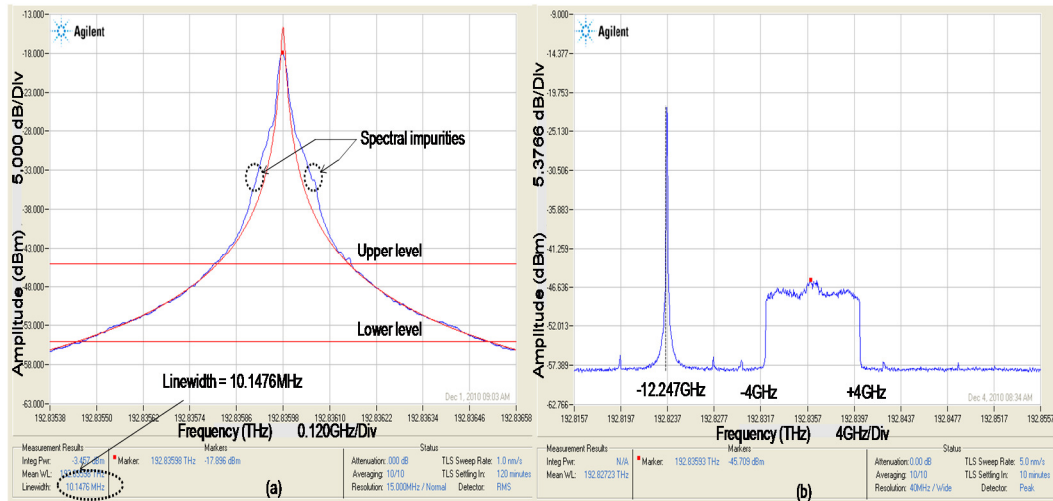


Fig. 8.3.5. Measured optical spectra using HRS: (a) Linewidth measurement (b) The C-MZI's output signal.

Fig. 8.3.5 shows the optical spectra measurements using the HRS to measure (a) the DFB's laser linewidth and (b) the C-MZI's output signal. The linewidth measurement was done by placing the upper and lower level to the spectrum that matched the Lorentzian plot in red. The un-matched part of the spectrum was excluded from the level to achieve an accurate measurement. This is because of the un-matched part is due to the spectral impurities caused by the laser side modes and harmonics. The measurement showed the linewidth to be 10 MHz at a driving current of 60 mA. Fig. 8.3.5 (b) shows the 8-GHz OFDM subcarriers band of ± 4 GHz. This is achieved by assigning the data subcarriers at both negative and positive sides of the FFT points. The virtual carrier was tuned to 12.247 GHz which gave the b_{gap} of 8 GHz. This gap is used to allocate the unwanted signal \times signal beating noise upon the photodetection [5]. A 1:1 carrier-to-sideband ratio was achieved by tuning the virtual carrier's output power and measured using the Agilent Optical Spectral Analyzer with a resolution bandwidth of 0.1 nm. The signal was then transmitted over 500 km and 720 km of fibre.

After the fibre, the signal was amplified to compensate the loss of the final fibre span. The signal was then connected to another EDFA to boost the power of the signal that goes into a Finisar Waveshaper programmable optical filter. This was done to compensate the insertion loss of the filter and to obtain a sufficient output power at the filter's outputs. The signal could not be amplified after the filter due to the unknown length of pigtails used in the EDFA. Also, the EDFA could not be amplified with a gain of more than 20 dB since it produces a tilted noise floor. The outputs of the Waveshaper

were the filtered subcarriers band and the carrier signal shown by the insets in Fig. 8.3.4.

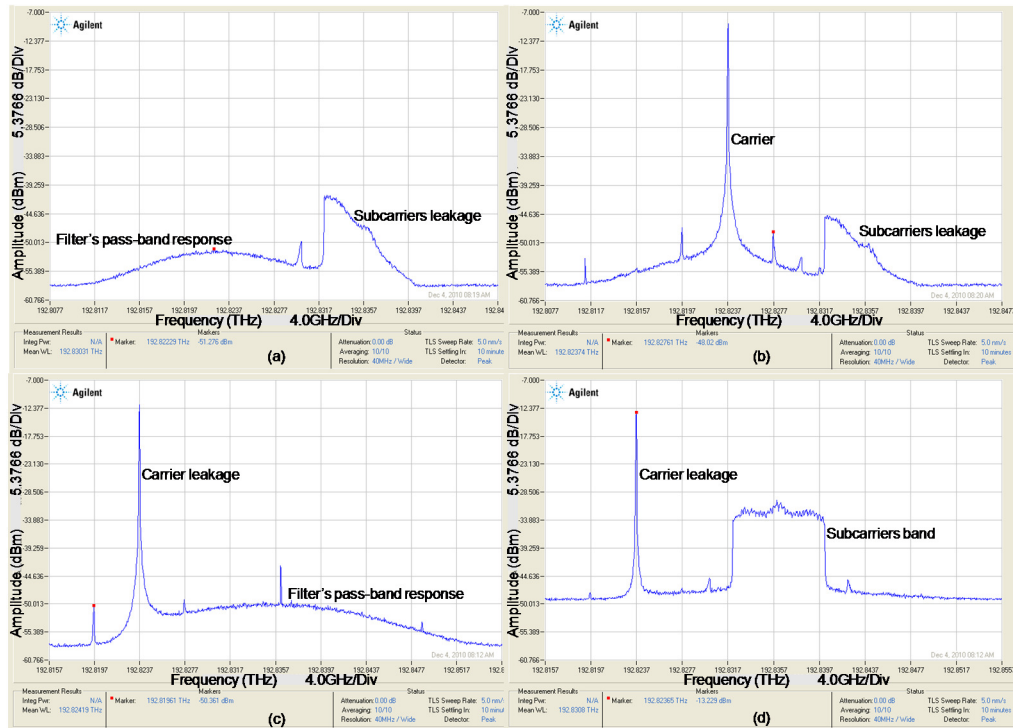


Fig. 8.3.6. HRS measurements of the carrier and subcarriers paths signals at the Waveshaper's outputs (a) carrier path filter response (b) measured signal at the carrier path (c) subcarrier path filter response and (d) measured signal at the subcarriers path.

Fig. 8.3.6 shows the measured spectra using the HRS at the Waveshaper's outputs to show the filtered subcarrier band and the carrier. The HRS was programmed to produce the best filter response for the carrier and subcarriers paths. This was done by activating (pass-band) and attenuating (stop-band) the pixel mode with the size of 0.01 THz/pixel. The Fig. 8.3.6 (a) shows the filter's pass-band response when the carrier was turned off and the subcarrier band was turned on. This was done to program the filter for the carrier path. The measured spectrum shows some subcarriers band leakages into the carrier path. Fig. 8.3.6 (b) shows the carrier path spectrum where the carrier is placed on the highest point of the filter's response. Some leakage of the subcarriers is shown since the pixel size of the filter response is larger than the b_{gap} used. Fig. 8.3.6 (c) shows the subcarriers path when the filter response was programmed to filter out or limit the power of the carrier and pass only the subcarriers band. For this measured spectrum, the carrier was turned on and the subcarrier band was off. Fig. 8.3.6 (d) shows the measured spectrum of the subcarrier path. The carrier leakage can be seen at the subcarrier path. The Waveshaper's filter response needs to

be carefully programmed in order to avoid a low signals output power since the signals could not be amplified at the filter's outputs. This is due to the unknown length of fibre pigtailed used in the EDFA that would add in the length of the delay. Therefore, small amount of signal leakage can still be tolerated at both carrier and subcarriers path. In this experiment, the signal power measured at both paths was around 2.5 dBm.

The fibre delay line was assigned at the subcarrier path since the transmitted signal is an upper-sideband (USB). The combinations of patch leads were used in order to have a set of a different length of delay. In this experiment, only the I signal was required since the carrier was offset and the hybrid became a heterodyne receiver. After the carrier and subcarriers mixing by the 90° hybrid, the I signal of the X-polarization was detected by a U²T 40 GHz balanced photodetectors. The signal was captured using the DSO and processed offline. The decoding code was done using MATLAB and is identical to Appendix 5.1 but with a transposed matrix format of the data stream.

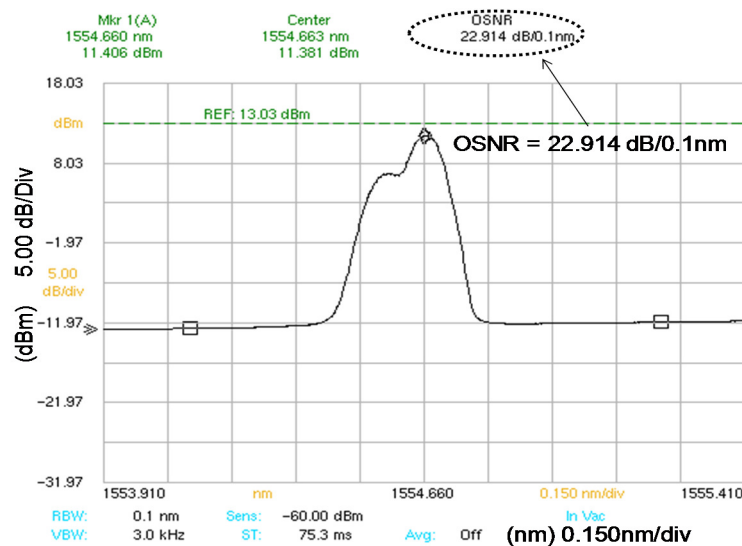


Fig. 8.3.7. OSNR measurement using an optical spectrum analyzer at the fibre's output.

Fig. 8.3.7 shows the OSNR measurement at 0.1 nm resolution using an optical spectrum analyzer at the fibre's output. The measurement of 22.9-dB OSNR was achieved and produced a good Q and BER even without the delay. However, with the delay value, the performance of Q will increase further, which shows the effectiveness of this linewidth reduction technique.

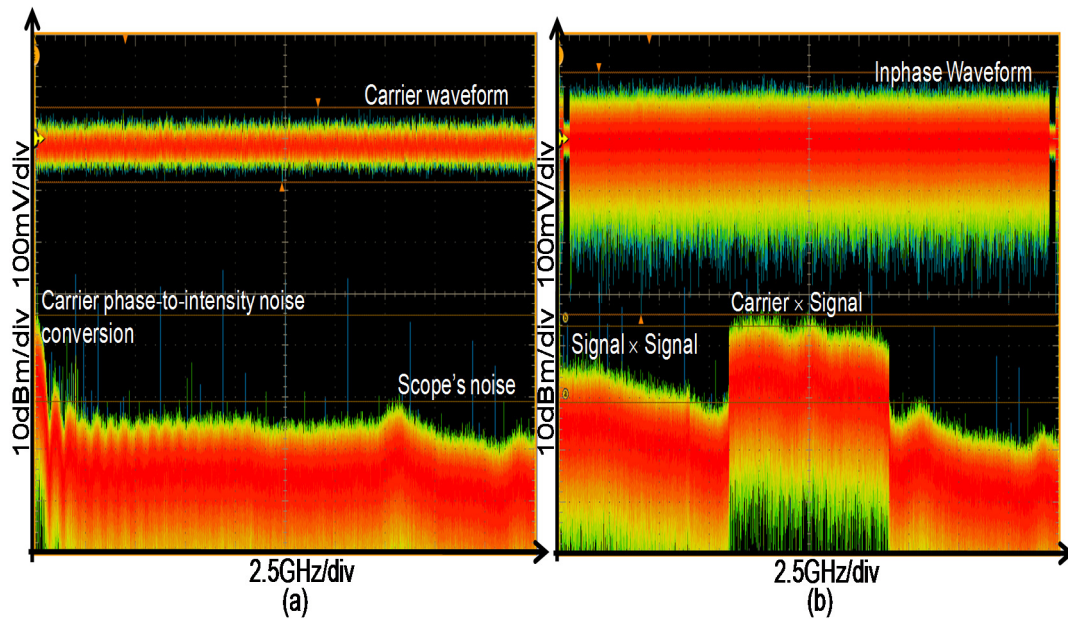


Fig. 8.3.8. Measured RF signal at the DSO after 720 km transmission with 10 MHz linewidth: (a) the carrier's phase-to-intensity noise conversion when the OFDM signal was turned off (b) the OFDM signal spectrum without any delay assignment.

Fig. 8.3.8 shows the captured RF signal at the DSO after 720 km transmission with 10-MHz linewidth when (a) the OFDM signal was turned off leaving the carrier and (b) when the signal was turned on. This spectrum was achieved by applying the FFT, to the captured carrier waveform. The DSO was running in 16-GHz bandwidth hardware mode. This gives a small peak in power of its FFT-spectrum response at 17.75 GHz of the noise floor which is due to the DSP processing to flatten the response of the DSO. In Fig. 8.3.8 (a), a noise PSD of the carrier's PM-to-IM conversion noise can be clearly seen near the DC. The spectrum shows that the intensity noise power decreased exponentially from the DC to 2.5 GHz before it completely dies out. The sidelobes of the PM-to-IM noise conversion can still be seen in the noise floor. Fig. 8.3.8 (b) shows the received I waveform and the OFDM spectrum after taking the FFT of the I waveform, when the AWG was turned on. The spectrum obtained was measured for the system without any delay assignment. The unwanted beating signal (signal \times signal) [7] fell into the b_{gap} with a less power than the signal band. The desired beating signal (carrier \times signal) [7] represented the OFDM signal bandwidth of 8 GHz.

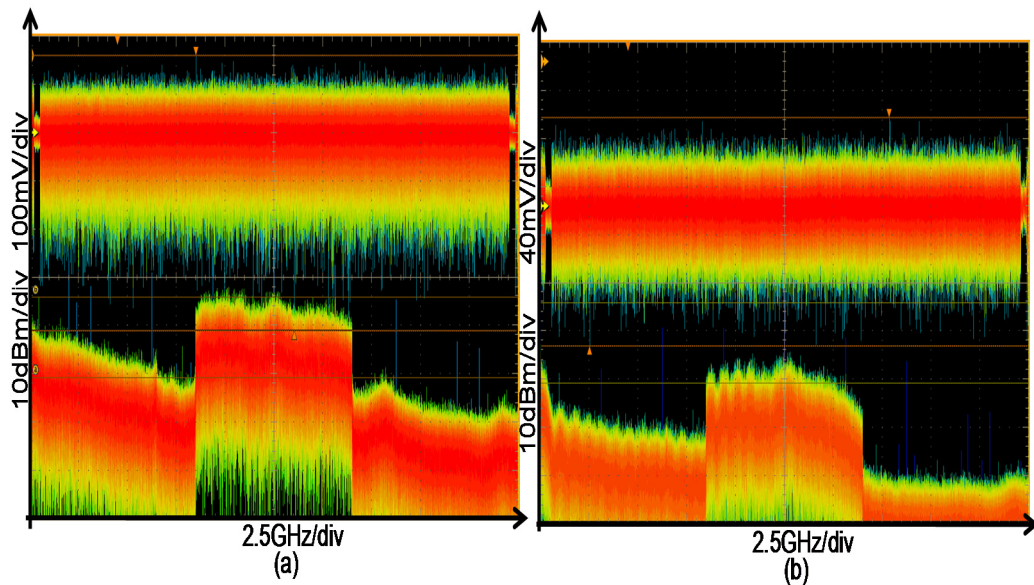


Fig. 8.3.9. The received RF spectrum after 720 km transmission when (a) similar detected power from both signal paths and (b) the power of the carrier path is higher than the subcarriers path.

To show the influence of the carrier's PM-to-IM conversion noise to the signal band, the received spectra was measured by making the carrier's power higher than the subcarrier path. Fig. 8.3.9 shows the received RF spectrum when (a) a similar power was detected from both subcarrier and carrier paths and (b) the power of the carrier path higher than the signal path. Fig. 8.3.9 (a) shows the captured spectrum obtained when the C-MZI's output signal was tuned to have a 1:1 carrier-to-subcarrier band power ratio. This was done by tuning the power of the virtual carrier. In Fig. 8.3.9 (b) the spectrum was obtained when the carrier power was higher than the subcarriers band. This was done by increasing the power of the virtual carrier at the transmitter. The spectrum shows the PM-to-IM conversion noise PSD of the carrier near the DC with the sidelobes of its tail are imposed into the subcarriers band. This shows the importance of tuning the carrier-to-subcarrier power ratio of 1:1 at the transmitter.

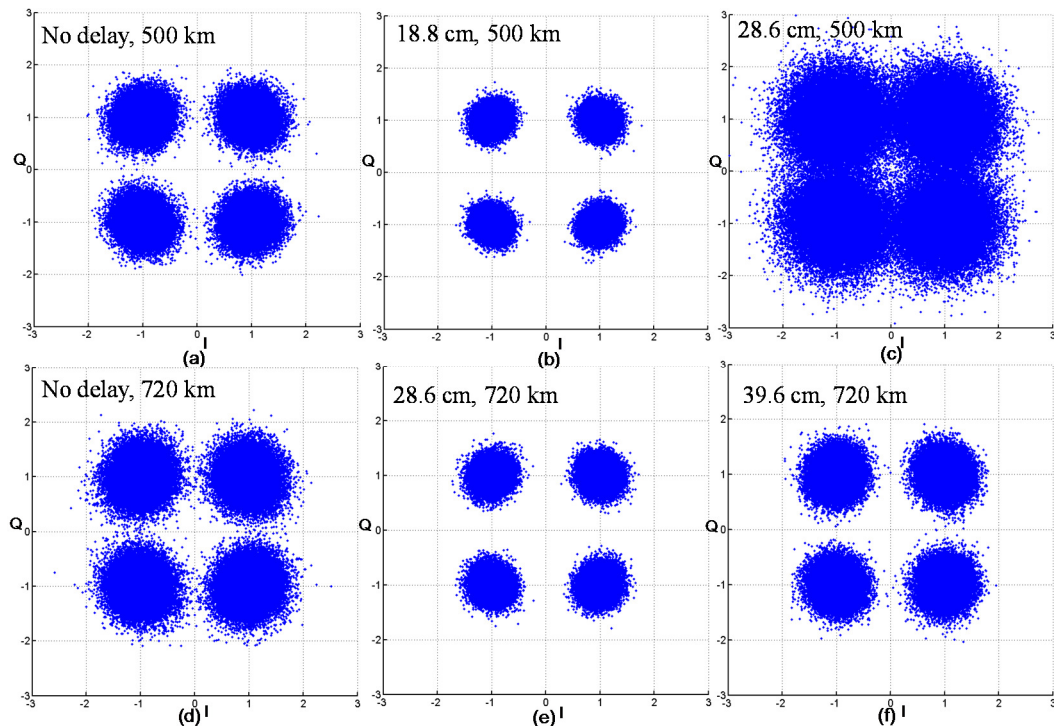


Fig. 8.3.10. Measured scatter plots comparing the length of the delay line assigned for 500 km (top) and 720 km (bottom): (a) no delay (b) 18.8 cm (c) 28.6 cm (d) no delay (e) 28.6 cm and (f) 39.6 cm.

Fig. 8.3.10 shows the scatter plots for the transmission of the OFDM signals comparing the assigned delay line of (a) no delay, (b) 18.8 cm and (c) 28.6 cm for 500 km and (d) no delay (e) 28.6 cm and (f) 39.6 cm for 720 km of fibre length. The constellation plots show the spreading of the OFDM symbols which was due to the phase noise. Fig. 8.3.10 (a) and (d) show the plots where no fibre delay was used. In Fig. 8.3.10 (b) and (d), a matched delay of 18.8 cm for 500 km and 28.6 cm for 720 km was assigned. A significant improvement of the constellation plots can be seen when a matched delay was applied for both transmission length. This shows that a delay can be used to improve the signal quality. Fig. 8.3.10 (c) shows the plot when a too long delay line was assigned to the 500 km transmission. The spreading of the symbols became worse than the plot without delay. Fig. 8.3.10 (f) shows the plot when a longer delay than the matched delay was used for 720 km. It shows a better plot than the one without any delay assignment in Fig. 8.3.10 (d).

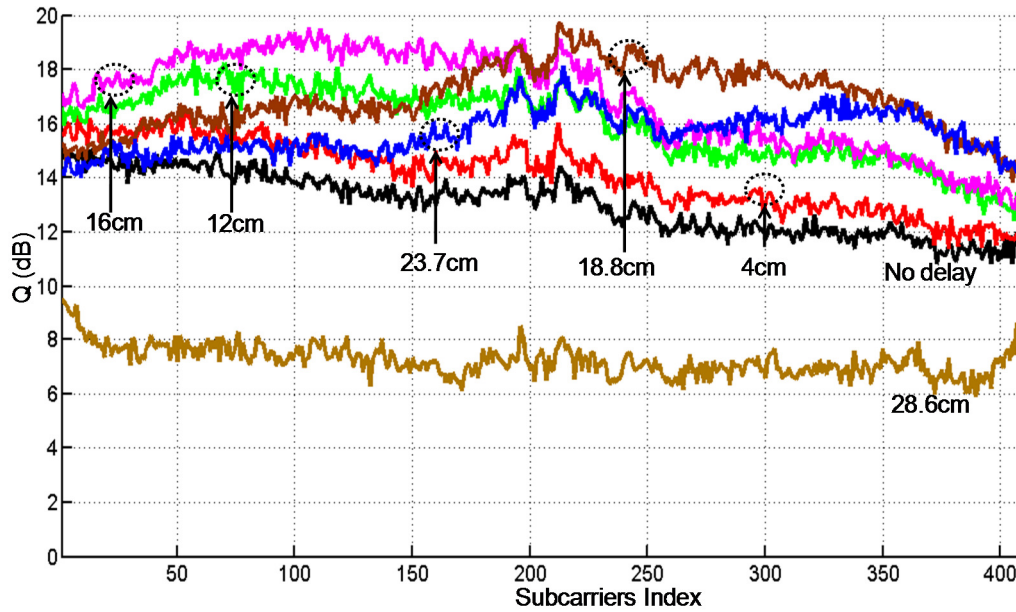


Fig. 8.3.11. Signal quality, Q , vs. subcarriers index starting from low to high frequency for 500 km transmission length.

Fig. 8.3.11 shows the Q performance versus subcarriers index starting from 8 GHz to 16 GHz frequency subcarriers for the transmission of 500 km. The Q performance for 720 km shows the same trend as the plots in this figure. The plots are presented in Appendix 5.2. When no delay was assigned, the high frequency subcarriers experienced more Q degradation than the low frequency. This is due to the differential group delay relative of the high frequency subcarrier relative to the carrier is higher than the low frequency. The variations of Q across the band can be explained by the PM-to-IM noise conversion due to fibre dispersion. The improvement of Q across the subcarriers can be seen when a delay was assigned. The plots show that the improvement in Q depending on the frequency of the subcarrier: the higher-frequency subcarriers require a longer delay than the lower-frequency subcarriers. The 16-cm (800-ps) and 18.8-cm (940-ps) delay gives the best Q located around the middle subcarriers. This is confirmed by the Eq. 8.2.1 and 8.2.2. From the calculation of the differential group delay, when the delay fibre is 23.7 cm (1185 ps), the highest Q will fall around 18.52 GHz, which is beyond the transmitted signal bandwidth. This increased the Q at the high frequency subcarriers. When a too long delay was used, the phase of the carrier and subcarriers waveforms were decorrelated and produced a worst Q degradation compared to the Q without the delay assignment. This is shown by the brown line with the delay of 28.6 cm (1430 ps).

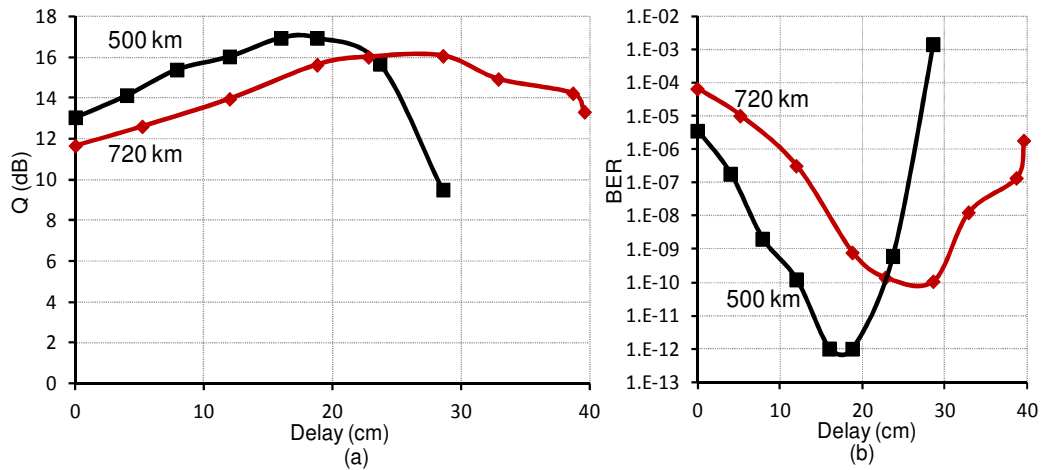


Fig. 8.3.12. Experimental results for 500 km and 720 km fibre length with combinations of delay line: (a) Q vs. delay line (b) BER vs. delay line.

Fig. 8.3.12 shows the experimental results of (a) Q and (b) BER versus the length of the delay line in centimetre for the transmission of the 4 QAM OFDM signal over 500 km and 720 km using 10-MHz linewidth. The figure shows that from 0 to 39.6 cm (720 km) and 0 to 28.6 cm (500 km), the Q is increased and the BER is reduced with the increase of the delay line length. This is when the phase waveform of the subcarriers is effectively matched to the carrier. The plots show the best delay length of 16 cm to 18.8 cm for 500 km and 22.8 cm to 28.6 cm for the 720 km of fibre length. The best matched delay was achieved when the reduction of the noise pedestal occurred at the centre of the subcarriers band, which was 12.5 GHz for this particular experiment. This is because of the peak of the noise pedestal around every subcarriers are added up to the centre of the band. The delay and its respective subcarrier frequency can be calculated using Eq. 8.2.1 and 8.2.2 for the respective fibre length. The plots show 4.4 dB for 500 km and 3.9 dB for 720 km increase of Q are achieved with the matched delay in comparison to the Q without delay. However, when the delay was increased more than the best matched delay, the Q started to reduce and BER is increased. This is confirmed by the brown plot in Fig. 8.3.8. This is because of the phase of the subcarriers and carrier became decorrelated.

8.4 Conclusions

Reduction of the linewidth impact to the transmission of the OFDM signals with fibre chromatic dispersion has been shown using simulations and experiments. The linewidth impact reduction can be achieved by matching the phase waveforms of the subcarriers signal band and the carrier, which reduces the noise pedestal around the

subcarrier band. A significant increase of Q can be seen in the results when the delay was assigned. The noise can theoretically only be nulled for a single subcarrier, but the result is still sufficiently useful over a wide bandwidth, particularly if the delays are matched in the centre of the band, where the noise humps of all subcarriers are added. The study also shows that a longer delay line is required by the higher frequency subcarriers because the high frequency experience more walk-off. The length of the delay line is crucial since a too-long delay can degrade the system performance due to the phase decorrelation of the subcarriers and carrier. For optical CO-OFDM system without a pilot-tone correction [8], this method is not useful because the phase waveforms of the transmitted waveform and local oscillator are uncorrelated, which is similar to a heterodyne linewidth measurement using two lasers.

8.5 References

1. Schmidt, B.J.C., et al., *100Gbit/s transmission using single-band direct-detection optical OFDM*, in *Optical Fibre Communication Conference (OFC/NFOEC)*. 2009, Optical Society of America (OSA): San Diego, CA. p. PDPC3.
2. Schmidt, B.J.C., et al., *120 Gbit/s over 500-km using single-band polarization-multiplexed self-coherent optical OFDM*. *Journal of Lightwave Technology*, 2010. **28**(4): p. 328-335.
3. Yamamoto, S., et al., *Analysis of laser phase noise to intensity noise conversion by chromatic dispersion in intensity modulation and direct detection optical fibre transmission*. *Journal of Lightwave Technology*, 1990. **8**: p. 1716-1722
4. Richter, L.E., et al., *Linewidth determination from self-heterodyne measurements with subcoherence delay times*. *Quantum electronics letters*, 1986. **QE-22**(11): p. 2070-2074.
5. Lowery, A.J., L. Du, and J. Armstrong, *Performance of optical OFDM in ultra long-haul WDM lightwave systems*. *Journal of Lightwave Technology*, 2007. **25**: p. 131 – 138.
6. Schmidt, B., A.J. Lowery, and L.B. Du. *Low sample rate transmitter for direct-detection optical OFDM*. in *Optical Fibre Communication - includes post deadline papers, 2009. OFC 2009. Conference on*. 2009.
7. Lowery, A.J., *Amplified-spontaneous noise limit of optical OFDM lightwave systems*. *Optics Express*, 2008. **16**(2): p. 860-865.
8. Jansen, S.L., et al. *20-Gb/s OFDM transmission over 4160-km SSMF enabled by RF-pilot tone phase noise compensation*. in *Optical Fibre Communication Conference*. 2007. Anaheim, CA.
9. Zan, Z., L.B. Du, and A.J. Lowery, *Experimental demonstration on the reduction of linewidth impact in a self-heterodyne optical OFDM system*, in *Optical Fibre Communication Conference (OFC/NFOEC)*, O.S.o.A. (OSA), Editor. 2010: San Diego Convention Center. p. JThA8.
10. Yi, X., W. Shieh, and Y. Tang, *Phase estimation for coherent optical OFDM*. *Photonics Technology Letters*, 2007. **19**(12): p. 919-921.

-
11. Yi, X., W. Shieh, and Y. Ma, *Phase Noise Effects on High Spectral Efficiency Coherent Optical OFDM Transmission*. *Lightwave Technology, Journal of*, 2008. **26**(10): p. 1309-1316.
 12. El-Tanany, M.S., W. Yiyang, and L. Hazy, *Analytical modeling and simulation of phase noise interference in OFDM-based digital television terrestrial broadcasting systems*. *Broadcasting, IEEE Transactions on*, 2001. **47**(1): p. 20-31.
 13. Qiyue, Z., A. Tarighat, and A.H. Sayed, *Compensation of Phase Noise in OFDM Wireless Systems*. *Signal Processing, IEEE Transactions on*, 2007. **55**(11): p. 5407-5424.
 14. Peng, W.-R., *Analysis of Laser Phase Noise Effect in Direct-Detection Optical OFDM Transmission*. *Lightwave Technology, Journal of*, 2010. **28**(17): p. 2526-2536.
 15. Peng, W.R., I. Morita, and H. Tanaka. *Digital phase noise estimation and mitigation approach for direct-detection optical OFDM transmissions*. in *Optical Communication (ECOC), 2010 36th European Conference and Exhibition on*. 2010.

Chapter 9

HIGH-SPEED LONG HAUL TRANSMISSION SYSTEM USING DDO-OFDM SYSTEM

9.1 Introduction

The rapidly increasing traffic demands over long-haul optical fibre communications have caused considerable interest in alternative modulation formats that can efficiently use the capacity of standard single mode fibre (SSMF) [1]. Many demonstrations have shown the potential of O-OFDM for next generation 100-Gbit/s system [high speed O-OFDM transmission]. O-OFDM using coherent reception (CO-OFDM) and PDM has been used to achieve 100 Gbit Ethernet (GbE) data rates over 1000 km [11, 13-19, 24]. In these demonstrations, the wide-band optical signal was generated by multiplexing a number of narrower signal bands (sub-bands) together. In [24], the bands were generated in the optical domain by modulating a comb of laser lines, similar to ‘Coherent WDM’ but with OFDM modulation of each line [24]. In [11], the bands were generated in the electrical domain and then up converted to selected intermediate radio frequencies (RF) before optical modulation. The use of multiple bands allows the sampling rate of the digital-to-analogue converters (DACs) to be reduced, and reduces some OFDM overheads [11]. However, these benefits come at the cost of transmitter complexity. Both systems require multiple DACs; optical multiplexing requires multiple optical modulators, and RF multiplexing requires multiple electrical mixers. There are also ‘all-optical’ versions of O-OFDM [17], using no digital processing at the transmitter. These similarly require multiple optical modulators.

In this chapter, a demonstration of a DDO-OFDM system transmitting 120 Gb/s data-rate over a long-haul fibre is presented using only one signal band per polarization¹. This is to show that the system is able to transport a 100 Gigabit

¹ In [4] and [6], Schmidt B.J.C. and Zan.Z achieved the fast DACs synchronization, designed pre-emphasis technique and built the experimental setup, Schmidt B.J.C. and Du L. developed the pol-Mux detection receive code with IQ imbalance compensation using MATLAB, Schmidt B.J.C, Zan Z. and Du L. performed the measurements and analysed the data, Schmidt B.J.C performed VPI simulation for OSNR sensitivity study, Schmidt B.J.C, Zan Z., Du L. and Lowery A.J. wrote the paper, and Lowery A.J. supervised the work.

Ethernet (GbE) in a single wavelength system. In Section 9.2, a basic transmitter design for a polarization multiplexing is presented. A technique to increase a signal bandwidth with the polarization multiplexing setup is also explained. Section 9.3 explains the design of a polarization-diversity receiver to demux a polarization multiplexed signal. The details of the experimental setup are explained in Section 9.4 including the implemented transmitter and receiver designs. A new variant of the DD receiver is also presented in this section. Section 9.5 presents the experimental results and discussions. Finally, the overall experimental demonstration is reviewed and concluded in Section 9.6. Section 9.7 presents the references.

9.2 Transmitter Design

In this system design, an optical carrier is transmitted together with the OFDM subcarriers. This carrier mixes with the optical subcarriers at the photodiode to produce a set of electrical subcarriers. Since the carrier and the subcarriers are derived from the same laser source, the phase noise of the source (due to laser linewidth) will cancel upon detection, provided there is a little differential delay between the carrier and the subcarriers.

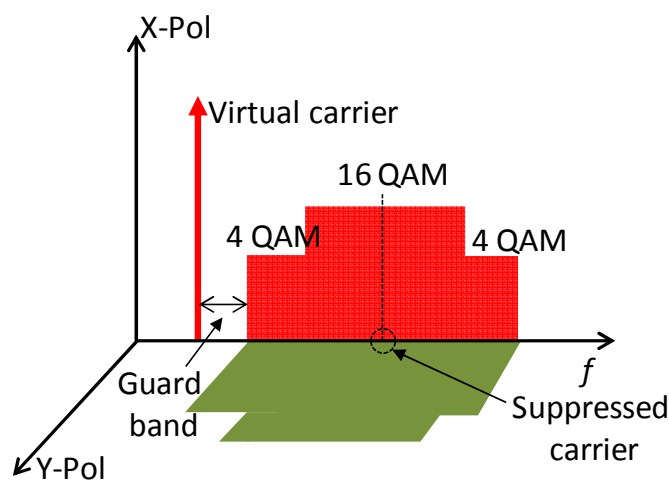


Fig. 9.2.1. Desired output spectrum of the transmitter.

Fig. 9.2.1 shows the desired output of the transmitter illustrating the signal bands, which are orthogonal in the X- and Y-polarizations. The carrier can be either at the X- or Y- polarization. The OFDM subcarriers are modulated with 16 QAM in the centre of the subcarrier band and 4 QAM at the edges of the subcarrier band. Any modulation level can be employed to the subcarriers with respect to the signal band's frequency response. The source for the carrier could be a tunable laser, to allow the

transmitter to be adjusted to any wavelength. An RF-virtual carrier design can be used. The frequency guard band was reduced to a width where it still can accommodate the laser source's phase noise. This frequency guard band will also be used to allow an optical filter to separate the carrier and subcarriers at the receiver. To generate the electrical signal bandwidth, two AWGs were used. The signal can be generated using I and Q signal components of the OFDM signal to drive a complex optical modulator (also known as a QPSK optical modulator, optical SSB modulator or cascaded triple MZI modulator) [1-5].

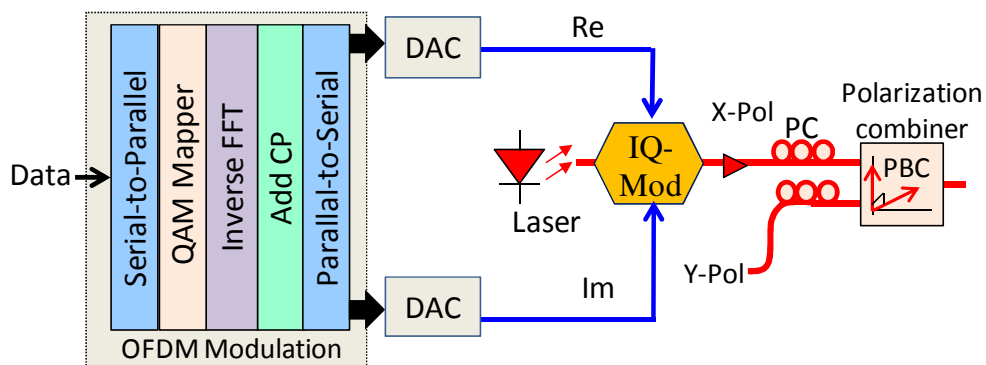


Fig. 9.2.2. Basic transmitter setup for an optical polarization multiplexed signals.

Fig. 9.2.2 shows a basic transmitter setup to combine X- and Y-polarizations using a polarization beam combiner (PBC). The electrical OFDM signal is generated by presenting parallel data to a set of QAM modulators. The QAM modulators' outputs then become the (frequency domain) inputs to an inverse fast Fourier transform (iFFT). The output of the iFFT is a superposition of subcarriers, each corresponding to a frequency of the iFFT. These are converted to a complex serial data stream and a cyclic prefix (CP) is added. This OFDM modulation can be done offline where the I and Q signal components are then uploaded into the DACs. These DACs are presented by the Tektronix arbitrary waveform generators (AWGs) 7102 in the experimental setup. The optical modulator is biased at null power so that the optical field is proportional to the electrical drive voltage [1]. This ensures a one-to-one mapping of the optical and electrical spectra, both at the transmitter and the receiver. This is necessary to enable fibre dispersion to be equalized electrically on a subcarrier-by-subcarrier basis. The signal's polarization is tuned using a polarization controller (PC). The signal is combined with the other signal of a different transmitter, tuned at a different polarization (named Y-polarization) using the PBC. For the polarization-multiplexing proof of concept, the same data signal from a single

optical OFDM transmitter can be used for the Y-polarization. This can be done in the experimental setup by separating the optical modulator's output into two paths and delayed one path for the Y-polarization data signal [6]. This is done to decorrelate the signal.

To increase the optical signal bandwidth, a virtual carrier technique presented in Fig. 2.4.4 can be used [4]. This technique makes maximum use of the AWG's bandwidth compared to the technique used in Reference [7], where an RF tone is inserted at the negative side of the FFT points leaving only positive sides to be used as the subcarriers. However, the generation of two signal polarizations with this arrangement would cause the carrier and a delayed rotated version of itself to be transmitted. This causes the carrier at the receiver to fluctuate. This is because the delayed and the straight signal paths will fluctuate in relative phase length due to vibrations. Due to this, the polarization at the receiver cannot be control manually. To overcome this problem, the carrier needs to be generated separately from the data signal using a separate modulator acting as a frequency shifter. The carrier is then added to the output of the PBC. The detail setup of this will be presented in Section 9.4.

A desirable simplification of Fig. 2.4.4 transmitter setup is to remove the carrier generation feature from one transmitter; otherwise the two carriers will have a random phase shift, and thus create a carrier with a random polarization state. One carrier is easily removed by removing one transmitter's sinusoidal generator. Another desirable simplification is to use a single tunable laser for both polarizations, as this will ensure that the bands of both polarizations have phase fluctuations correlated with the common carrier, so these phase fluctuations will cancel upon photodetection.

9.3 Receiver Design

In order to demultiplex the polmuxed signal, a polarization-diversity receiver is required in the DDO-OFDM system. The polarization-diversity receiver has been shown to compensate for the PMD effects in the DDO-OFDM system with the absence of polarization-dependent loss (PDL) [8]. This technique can be considered as a variant of the DDO-OFDM system, where the receiver mixes the carrier with the signal band and the same carrier is used at the receiver without requiring a new laser local oscillator. This receiver design is using balanced photodetectors rather than

single-ended photodetectors. With the use of the balanced photodetectors, the sensitivity limitations of conventional DD receivers [9], can be reduced. The balanced photodetection rejects unwanted spectral components, including the intermixing of subcarriers with other subcarriers. This allows a reduced frequency gap, and thus gives an increased spectral efficiency. The block diagram of the receiver design is shown in the following figure.

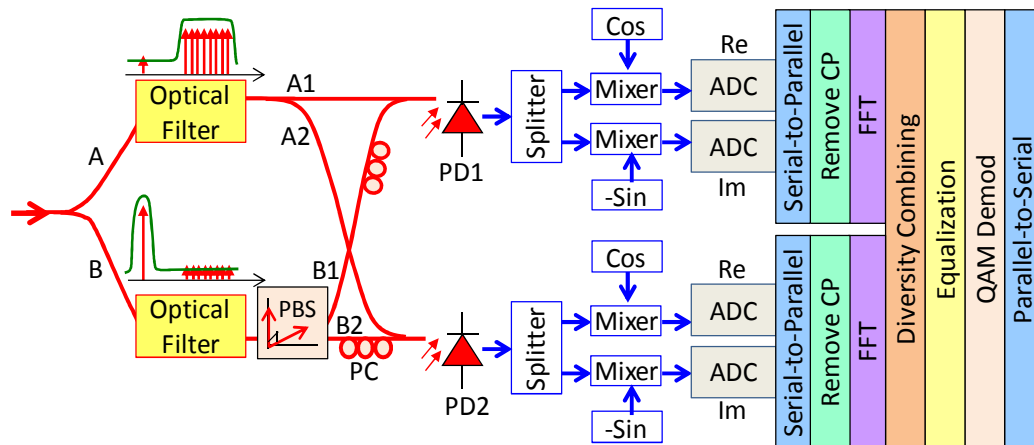


Fig. 9.3.1. Polarization-diversity receiver for a single polarization of a DDO-OFDM system.

Fig 9.3.1 shows the polarization-diversity receiver design for a single polarization transmission DDO-OFDM. The received optical signal is split into two branches: A and B. An optical filter is assigned to each branch. Branch A's optical filter rejects the carrier and passes the signal and limits the ASE noise. The optical carrier is obtained using the optical filter at Branch B. The carrier at Branch B needs to be rotated in polarization so it acts as a LO for both PD1 and PD2. This is also known as a self-coherent receiver [10]. To achieve the orthogonal SOP, a polarization beam splitter (PBS) is used with a polarization controller (PC) to control the SOP dynamically [8]. The orthogonal carriers are mixed with the signal bands at both PD1 and PD2. This receiver is a heterodyne rather than a homodyne design, so the I and Q components are recovered using RF mixers. The received signal is sampled and demodulated. The frequency domain signals after the FFT are then combined and channel estimation and equalization are performed [8, 10].

9.4 Experimental Details

This experimental demonstration presents the extended setup of the experiment presented in [3], with improved AWG analogue bandwidths to give an 18.8-GHz

optical signal bandwidth was achieved as compared with the previous experiment of 16 GHz [6]. The setup used commercially available components.

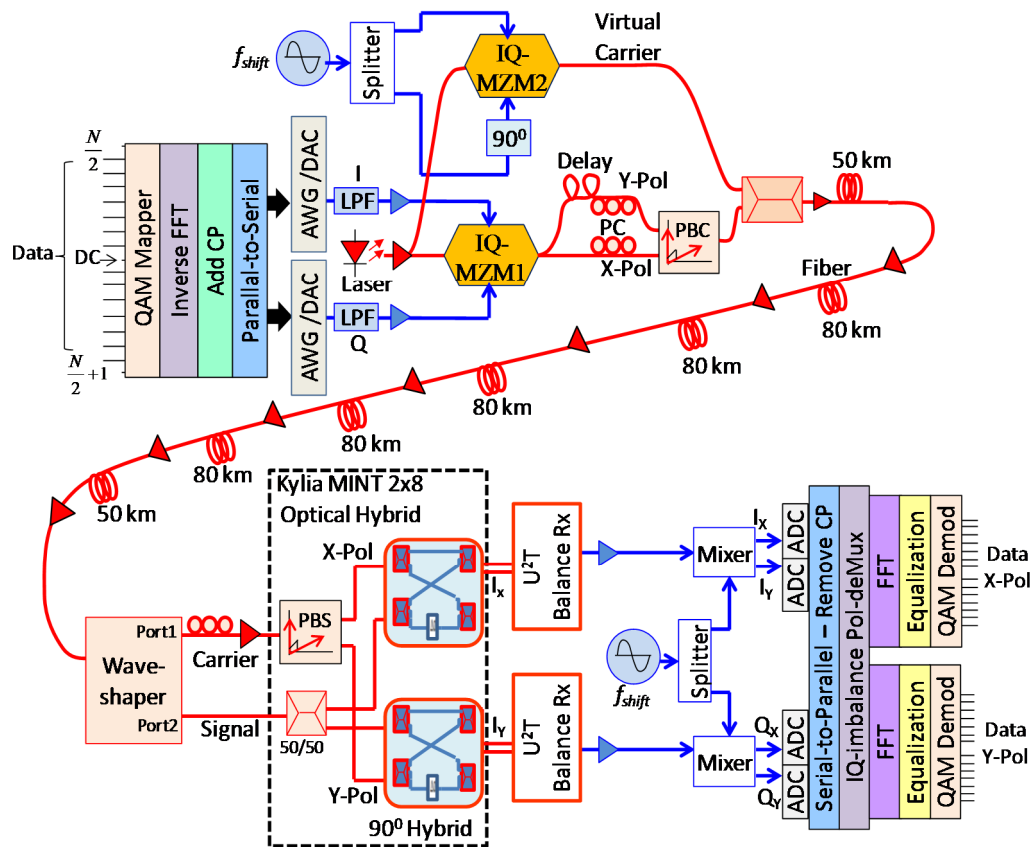


Fig. 9.4.1. Experimental setup for the demonstration of 120 Gb/s transmission with DDO-OFDM system.

Fig. 9.4.1 shows the experimental setup for the 120 Gb/s transmission demonstration using commercial off-the-shelf components and devices. Almost all of the subcarriers were used except for the DC subcarrier that is zeroed for the suppressed optical carrier and some carriers at both edges to accommodate an image-rejection filter. The signal design as presented in Fig. 9.2.1 was used with 16-QAM mapping assigned to the carrier around the DC and 4 QAM at both edges of the signal band. The 16 QAM are modulated onto 598 middle subcarriers around the suppressed optical carrier while both edges of the band (360 subcarriers in all) are modulated with 4 QAM. 64 subcarriers were allocated for the frequency guard band.

Table 9.4.1. : Transmission system experimental details.

Subcarrier Band	4 QAM	16 QAM	Unit
No. of subcarriers	360	598	-
Subcarrier BW	7	11.7	GHz
Data Rate (dual pol.)	28.1	93.4	Gbit/s
Total Subcarrier BW	18.8		GHz
Total Signal BW	29.4		GHz
Total Data Rate	121.5		Gbit/s

Table 9.4.1 shows the details of the carried data capacity of the experimental setup. The 16-QAM produced 93.4 Gb/s over a subcarrier bandwidth (BW) of 11.7 GHz and the 4-QAM produced 28.1 Gb/s over a subcarrier bandwidth of 7 GHz, giving a total of 121.5 Gb/s data rate using a dual-polarization transmission. The signal design along with the OFDM modulation was done offline using MATLAB. The generated inphase (I) and quadrature (Q) signals were uploaded into each of the DACs. The DACs used were the AWGs. In this experimental setup, the two AWGs were required to be time-synchronized.

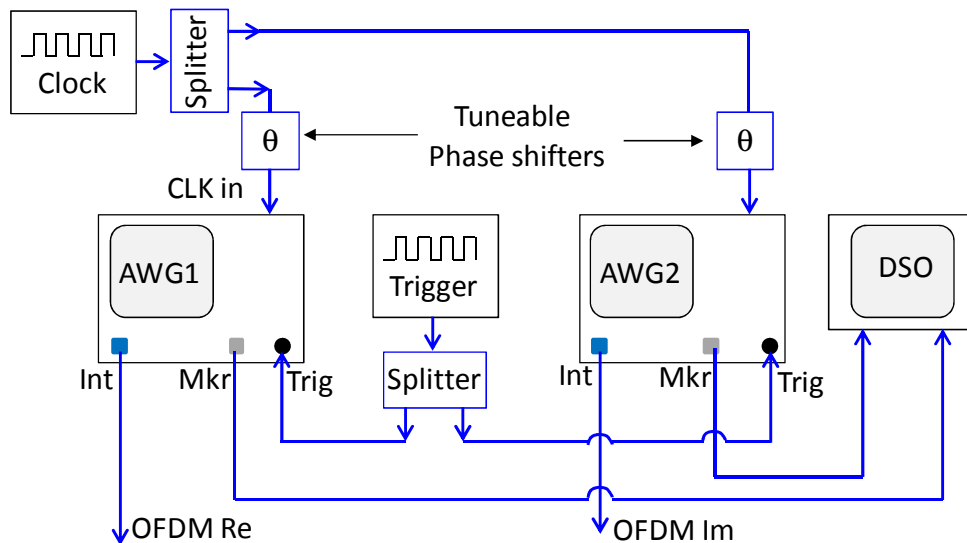


Fig. 9.4.2. AWGs synchronization setup using 20 GS/s interleave mode.

Fig. 9.4.2 shows the setup of the AWGs time-synchronization. In this setup, the AWG is set to run at 20 GS/s where the output is taken from the AWG's Interleave (Int) channel that is running in the interleaved and return-to-zero mode. A 10-MHz clock source was used to synchronize the AWGs. The clock was split into two paths by an RF splitter and supplied into both AWGs' clock inputs (CLK in). The clock source is taken from the clock output of the DSO, which provides a sharp rise-time clock signal. Pasternack tuneable phase shifters are used to compensate for the delay

caused by the mismatched in the RF paths to clock the AWGs at the same instant of time.

The two AWGs are then triggered using 10 ps pulse at 50 Hz generated from a frequency synthesizer generating a square wave. A marker signal of 0.2 V with 1024 ps pulse width was generated from each AWG is fed into a Tektronix digital sampling oscilloscope (DSO) 72004 and the timing difference of the markers of AWG1 and AWG2 are measured. The achieved mean jitter for the AWG1 and 2 was in the range of 1 ps to 4 ps. The trigger signal can be removed once the AWGs are synchronized and they remained stable over several hours. The AWG1's output represents the real signal of the OFDM signal and the AWG2 represents the imaginary part of the signal.

In order to achieve a good quality wide signal bandwidth, the AWGs were optimized so that a flat frequency response across the signal BW can be achieved with the AWGs operated at the highest sampling rate as possible. To optimize the AWGs, the frequency response relative to the intended signal band was pre-emphasized to maximise the RF signal bandwidth. This was done by applying an electronic pre-emphasis to the RF outputs of AWG1 (OFDM Re) and AWG2 (OFDM Im).

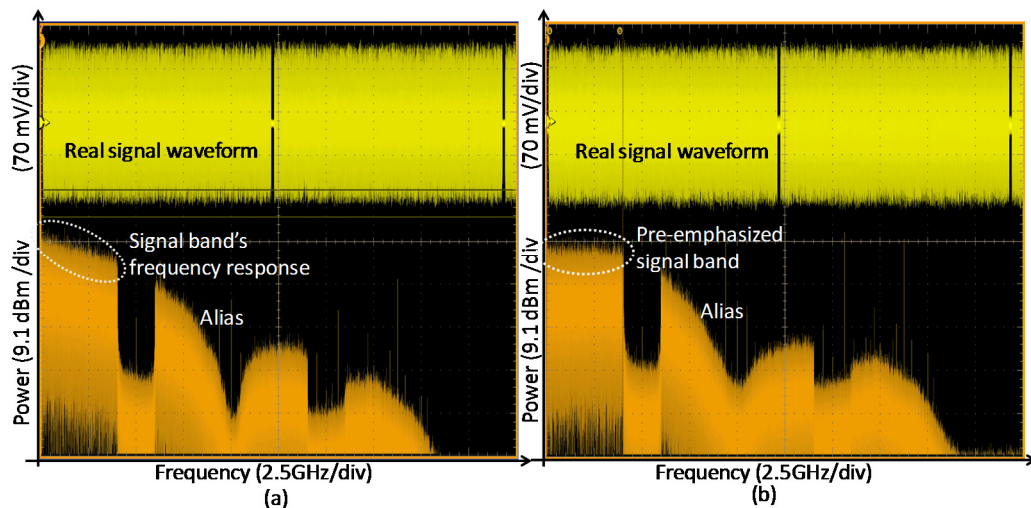


Fig. 9.4.3. OFDM signal band from an electrical back-to-back of the AWG to the DSO (a) without pre-emphasis and (b) with pre-emphasis.

Fig. 9.4.3 shows the OFDM RF waveform and signal band where the AWG's output was directly connected to the DSO. The signal band is obtained by applying the FFT of the OFDM signal waveform. The DSO was running using its 18-GHz DSP enhanced bandwidth setting. A real OFDM signal with Hermitian symmetry mapped

with 4 QAM was loaded into the AWG in order to see the AWG's frequency response. 410 subcarriers were used. The electrical spectrum shows 4 GHz of the OFDM USB, with the LSB signal mirrored onto it. Aliases are present at the higher frequencies than the signal. As shown by the spectrum in Fig. 9.4.3 (b), the amplitude of the signal band is reduced towards higher frequencies. To optimize the frequency response, the measured signal waveform was captured and demodulated using an offline signal processing with MATLAB. The signal was equalized and channel estimation was done, where the pre-emphasis file was generated by taking the inverse of the average channel estimation. The pre-emphasis contains a set of coefficients to level and smooth the response. This pre-emphasis file was multiplied with the transmit data to create the amplitude coefficients for the iFFT. The resulting flat signal band can be seen as in Fig. 9.4.3 (b).

At the AWGs outputs, sharp 10-GHz cutoff RF low-pass filters (LPFs) were used to reduce the image band caused by the sampling process. The filtered signals were then amplified with 20 GHz microwave amplifiers and connected to the input of a Sumitomo T-SBXI.5-20P 40 Gb/s DQPSK optical modulator (IQ-MZM1). The optical frequency response of the IQ-MZM1 is also pre-emphasized to achieve a maximum system performance.

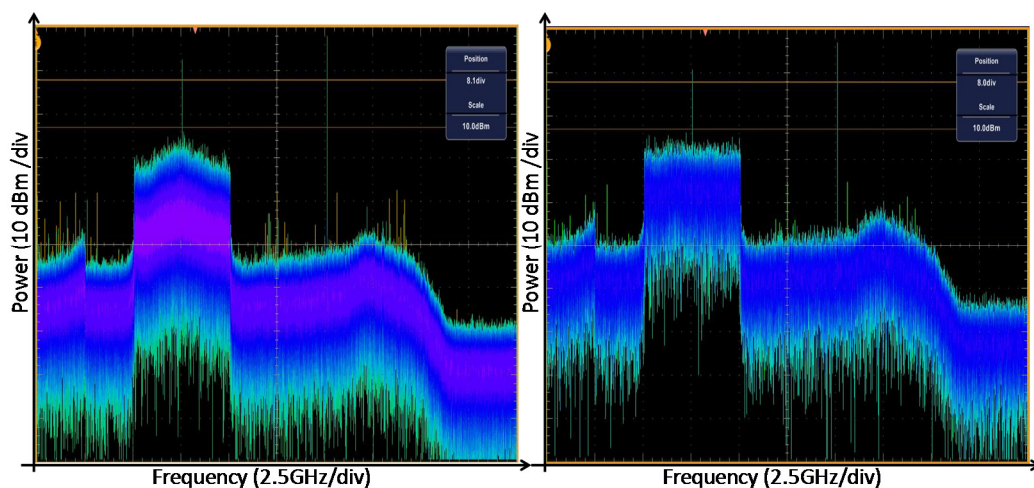


Fig. 9.4.4. Measured electrical spectrum at the output of a coherent receiver of an OFDM signal band (a) before and (b) after optical pre-emphasis.

Fig. 9.4.4 shows 8 GHz optical signal band with 4 QAM before and after the optical pre-emphasis is applied. The signal band before pre-emphasis as in Fig. 9.4.4 (a) shows a decrease in response away from the centre of the subcarrier band. The same coefficient multiplication process as in the electronic pre-emphasis was done to

obtain a flatter frequency response. After the multiplication with the pre-emphasis coefficients, the resulting OFDM signals are used to drive the IQ-MZM. The after pre-emphasis OFDM signal band is shown in Fig. 9.4.4 (b). The final OFDM signal which used in a complete transmission setup will apply both electronic pre-emphasis for the DAC's response and the pre-emphasis for the optical response. The pre-emphasized signal components are uploaded into the AWGs to drive the optical modulator.

The laser source used was a Photonetics Tunics external-cavity laser (ECL), tuned to 1550 nm. A Lightwaves2020 erbium-doped fiber amplifier (EDFA) was used before the modulator to compensate for the low output power of the laser. The output of the IQ-MZM1 was split into two where one was delayed relative to each other to decorrelate the transmitted polarizations. The delay assigned was either 54 ns or 64 ns depending on the CP length used. A polarization controller (PC) was used at each signal path to adjust the polarization before being connected into the polarization beam combiner (PBC). This produces two orthogonally polarized signals, each carrying data from a different transmitter. The carrier was generated using another IQ-MZM (IQ-MZM2) acting as a frequency shifter tuned to 20 GHz (f_{shift}) and then added to the output of the PBC. This provides a 12-GHz frequency guard band between the carrier and the subcarriers, which is less than conventional DDO-OFDM systems, which would requires a gap equal to width of the subcarriers band (16 GHz).

The transmitted signal is designed into frames of data that are continuously repeated by the AWGs' memory. 60 OFDM training symbols along with the data payload of 150 symbols (467 000 random bits) are assigned in a single frame. This frame format data is used to equalize the received signal using the training within the single frame. The allocation of the training symbols are done by placing 30 symbols interleaved with another 30 empty symbols. The delay line assigned for the polarization decorrelation causes the Y training to fill the empty symbol slots producing 60 X and Y interleaved training symbols. The training components travel directly to the X input of the PBC become the training symbols for the X polarization and the one travel to Y input will become the training symbols for the Y polarization. The training symbols are required to find the matrix coefficients for both IQ compensation and polarization demultiplexing at the receiver. However, the long

training sequence reduces the average data rate to 85 Gb/s. This overhead can be reduced by using a longer data payload and running the averaging over multiple frames to reduce the required length of each training symbol [11]. The data of the 30 training symbols is selected to give low PAPR ratios by scaling the symbol to just below the clipping level of the payload data. Since the training symbols are free from clipping noise, their increased energy can help to reduce impairments caused by the DAC noise. As shown in Fig. 9.4.1, a total of seven fiber spans of Corning SMF-28e were used, consisting of 1×50 km, 6×80 km and 1×50 km with Lightwaves2020 EDFA in between. The input power into each span was 0 dBm where the gain assigned for each EDFA was less than 20 dB to prevent a tilting noise floor. No fiber dispersion compensation was used.

The output of the final fibre span is pre-amplified and connected into a common port of a Finisar Waveshaper 4000E programmable optical filter. This filter was programmed to produce the desired pass band to separate the carrier and the signal band with carrier at Port 1 and signal band at Port 2. The separation was achieved by using 12-GHz and 20-GHz filter bandwidths for the carrier and the signal band, respectively. The carrier is then connected to a PC to maximize the output carrier level before it is boosted to 15 dBm using an EDFA to improve the receiver sensitivity [12]. The signal band is amplified to only 3 dBm to provide the equivalent of carrier boosting. The amplified carrier and signal band are fed into the input of a Klyia MINT 2×8 optical hybrids with a PBC at its LO input. This can produce I and Q outputs for both the X and Y polarizations.

Table 9.4.2. Approximate power map of the system.

Approximate Power (dBm)												
Transmitter			Fiber Spool							Receiver		
90/10 Coupler			Launch							Waveshaper		
Input1	Input2	Output (90)								Input	Output 1	Output 2
P _{vc}	P _{PBC}	Into EDFA	50 km	80 km	80 km	80 km	80 km	80 km	50 km	P _{input}	P _{carrier}	P _{signal}
-12	-19	-22	-8	0	0	0	0	0	2	12	-11.04	3.5

Approximate powers at the component level of the system are summarized in Table 9.4.2. The 90/10 coupler inputs are -15 and -19 dBm approximately, which represent the power of the virtual carrier (P_{vc}) and the output power of the PBC (P_{PBC}), respectively. These power are low due to the IQ-MZMs' insertion loss and the separation of the signal after the IQ-MZM1 for the X- and Y-polarizations. The 90

percent output port of the coupler is -22 dBm approximately, and this is amplified using the EDFA of -8 dBm into the first 50 km fibre spool. This low power launch into the first fibre spool is used to prevent power tilting due to 20-dB gain limitation of the EDFA. For the rest five fibre spools of 80 km, 0 dBm launch power is used. The last 50 km spool launch power is 2 dBm to provide sufficient power at the end of the fibre. This is because high input power is required into the waveshaper at the receiver. The Waveshaper input power is 12 dBm in order to have a reasonable power level at the Waveshaper outputs. This gives the output powers for the carrier (P_{carrier}) and the signal (P_{signal}) of -11.04 dBm and 3.5 dBm, respectively after the Waveshaper. The carrier signal at the waveshaper output is then boosted to 15 dBm.

Since the carrier is offset from the sideband, the hybrid was used as a heterodyne receiver, so only the inphase outputs for the X and Y are necessary to obtain the original data during the offline signal processing. The outputs of the hybrid are fed into two U²T 40-GHz balanced photodetectors as in Fig. 9.4.1, one for each polarization. This is used for a dual-polarization receiver design. The photodetectors' intermediate-frequency outputs are in the range 12 GHz to 28 GHz. The complex signals of I_x , Q_x , I_y and Q_y are then fed to a Tektronix 72004 4-channel 20 GHz 50-GS/s oscilloscope. The captured samples from the scope are then analysed in MATLAB, which includes algorithms for IQ imbalance correction [11], polarization demultiplexing, channel equalization and QAM decoding.

9.5 Results and Discussion

To show the 100 GbE transmission can be supported with the DDO-OFDM system, combination of 4-QAM and 16-QAM subcarrier modulation is used to demonstrate the performance of the system. A raw 120 Gb/s can be transmitted over a distance of 500 km of SSMF. The results presented here are an improved experimental version over the one reported in [3], with better DAC analogue bandwidths to achieve an 18.8-GHz optical signal bandwidth.

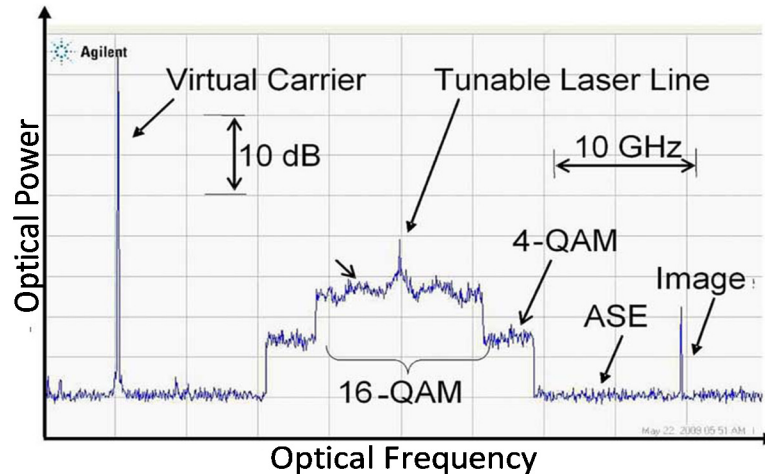


Fig. 9.5.1. Received optical spectrum measured with Agilent HRS.

Fig. 9.5.1 shows the transmitted optical spectrum measured using an Agilent High-Resolution Spectrophotometer (HRS). The signal band is stepped because of the 16-QAM modulation requires 6.7-dB higher OSNR than the 4 QAM. Careful adjustments of the modulator biasing, microwave path lengths, and attenuator pads were required to suppress the original laser line allocated at the centre of the signal band and the image of the carrier that lies above the signal band. The figure shows the virtual carrier at 20-GHz below the centre of the subcarrier band. The image of it is at +20 GHz, which is suppressed by 30 dB. The 10.6-GHz gap between the subcarrier band's lowest frequency and the virtual carrier is necessary for the optical filters to separate the carrier and signal band at the receiver, as the Waveshaper has a 7.5-GHz resolution.

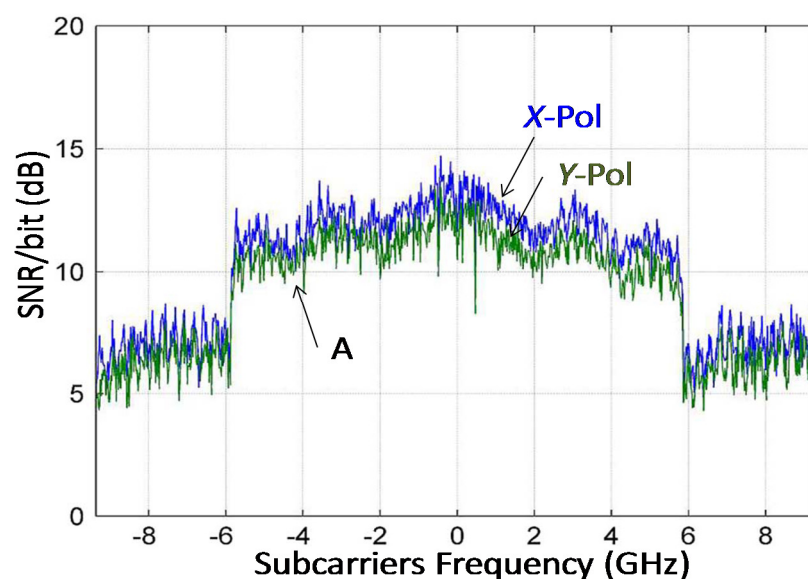


Fig. 9.5.2. Electrical SNR/bit (E_b/N_0) measured for the 120 Gb/s transmission experiment with 500 km SSMF for OSNR of 25.8 dB (0.1 nm) with BER of 8.2×10^{-4} .

Fig. 9.5.2 shows the received electrical SNR/bit (E_b/N_0) for the 120 Gb/s transmission over 500 km SMF with 25% CP. The measured OSNR was 25.8 dB (0.1 nm) and BER was 8.2×10^{-4} . The subcarrier's ordering is the same as the optical spectrum in Fig. 9.5.1. The amplitude for the optical spectrum is a useful guide for the received SNR/bit, and areas of significant difference suggested that there may be a problem with the receiver. For example, the drooping response (A) for increasing negative frequencies is caused by an overlap in the passbands of the receiver optical filters that separate the carrier and the signal band. This dip can be reduced by offsetting the frequency of the carrier filter, but this leads to less carrier power and increased noise at the input to the optical hybrid. In the experiments, a compromise between filter overlap and carrier output was used to minimize the error rate.

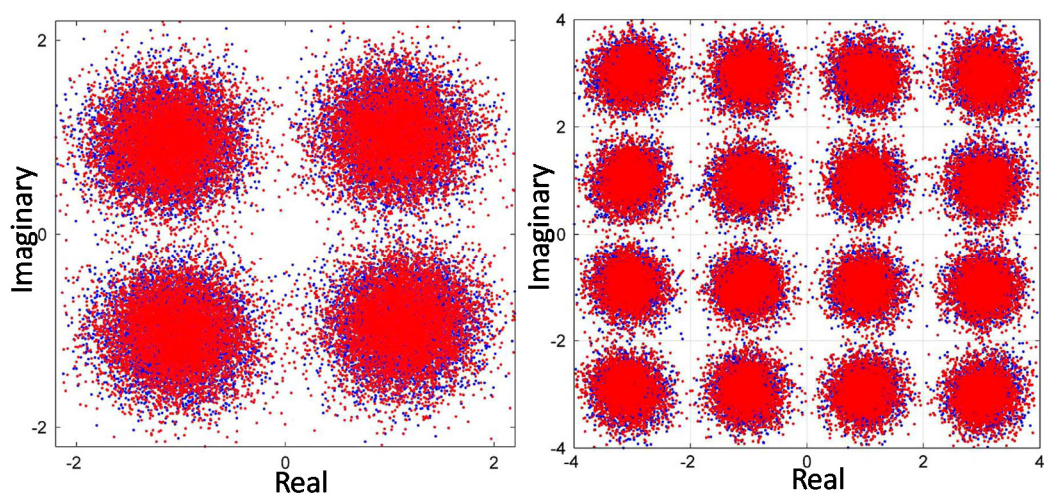


Fig. 9.5.3. Received and equalized constellations of 4-QAM and 16-QAM after 500 km.

Fig. 9.5.3 shows the equalized constellations for the 4-QAM and 16-QAM signals where red is for the X and blue is for the Y- polarization. The overall measured BER was 8.2×10^{-4} with an OSNR of 25.8 dB displayed on a 0.1 nm resolution Agilent optical spectrum analyser (OSA) after 500-km transmission. The 4-QAM and 16-QAM constellations have similar spreads compared with their separations, indicating that they will offer similar BERs.

9.6 Conclusions

The 100 GbE prototype demonstration using a variant of a DDO-OFDM system employing self-coherent receiver has been presented using commercially available devices. Several novel design features are combined to obtain the achieved performance. Two fast 20 GS/s DACs have been synchronized to achieve the

maximum electrical signal bandwidth. This permits a simple setup with reductions of the RF and optical device requirements compared to the system employing subcarrier multiplexed multi band signals and RF comb generators [11, 13-22]. In this demonstration, simple one-electrical and one-optical bands are used at the transmitter to achieve the 120 Gb/s. Pre-emphasis of both AWGs and the optical modulator frequency response relative to the intended signal band has been used to optimize the system performance. The virtual carrier technique maximizes the transmitted signal by placing the subcarrier bands at the centre of the modulator's response. The technique also provides flexibility in tuning the frequency and the amplitude of the carrier, by simply adjusting the RF frequency of the frequency synthesizer.

At the receiver, a variant of the DDO-OFDM system employing a self-coherent polarization-diversity receiver was developed providing PMD compensation and polarization demultiplexing. In this system, the carrier is transmitted along with the signal band which is common in DD systems. The LO supplied at the receiver was derived from the transmitted carrier, which was separated using a filter before the hybrid so that no free-running external laser is required. Also, the carrier is boosted which improves the OSNR performance of the system. The use of balanced photodiodes cancels a common limitation of DD systems; the subcarrier \times subcarrier beating noise. This allows a reduced width of frequency guard band. However, the guard band could not be totally omitted due to the limitation in optical filter pass band during the separation of the carrier and the signal band at the input of the optical hybrids. In the setup, the polarization of the carrier between the output of the carrier filter and the LO input of the optical hybrid was controlled manually. This is to maximize the output carrier level. For a practical implementation, this would require a closed-loop controller.

To demonstrate the high-speed signal transmission of a DDO-OFDM system, several techniques which were developed throughout the work have been employed. This includes the use of an RF virtual carrier transmitter design presented in Chapter 6, 7, and 8, in which the electrical bandwidth is increased for the data transmission. A pre-emphasis technique to improve devices' frequency response was also employed in the high-speed setup. This technique was used in Chapter 7 to show that the DDO-OFDM system can be developed using a commercial DFB laser. This similar technique was also used in Chapter 8, where a flat frequency response of a transmit

spectrum was achieved so that the effects of a linewidth and dispersion interaction to the high frequency subcarrier can be encountered. The AWGs synchronization was also used in the experiments presented in Chapter 7, where a wide transmit subcarrier band was achieved. With the wide band, the effects of the linewidth and dispersion as a function of subcarrier's frequency can be analysed. Finally, the high-speed setup also employed a variant of DDO-OFDM system where the carrier and subcarrier band were separated using an optical filter, before a coherent detection is used to mix the carrier and the subcarriers. This is known as a self-heterodyne optical OFDM, where it was also used in Chapter 8 to reduce the linewidth effect by assigning a simple delay line.

9.7 References

1. Schmidt, B.J.C., A.J. Lowery, and J. Armstrong. *Experimental demonstrations of 20 Gbits/s direct-detection optical OFDM and 12Gbits/s with a colorless transmitter.* in *Optical Fiber Communication Conference*. 2007. Anaheim, CA.
2. Schmidt, B.J.C., A.J. Lowery, and J. Armstrong, *Experimental demonstrations of electronic dispersion compensation for long-haul transmission using direct-detection optical OFDM.* *Journal of Lightwave Technology*, 2008. **26**(1): p. 196-203.
3. Schmidt, B.J.C., et al., *100Gbit/s transmission using single-band direct-detection optical OFDM,* in *Optical Fiber Communication Conference (OFC/NFOEC)*. 2009, Optical Society of America (OSA): San Diego, CA. p. PDPC3.
4. Schmidt, B., A.J. Lowery, and L.B. Du. *Low sample rate transmitter for direct-detection optical OFDM.* in *Optical Fiber Communication - includes post deadline papers, 2009. OFC 2009. Conference on.* 2009.
5. Schmidt, B., A.J. Lowery, and J. Armstrong, *Impact of PMD in Single-Receiver and Polarization-Diverse Direct-Detection Optical OFDM.* *Lightwave Technology, Journal of*, 2009. **27**(14): p. 2792-2799.
6. Schmidt, B.J.C., et al., *120 Gbit/s over 500-km using single-band polarization-multiplexed self-coherent optical OFDM.* *Journal of Lightwave Technology*, 2010. **28**(4): p. 328-335.
7. Peng, W.R., et al. *Experimental Demonstration of a Coherently Modulated and Directly Detected Optical OFDM System Using an RF-Tone Insertion.* in *Optical Fiber communication/National Fiber Optic Engineers Conference, 2008. OFC/NFOEC 2008. Conference on.* 2008.
8. Schmidt, B.J.C., A.J. Lowery, and J. Armstrong, *Impact of PMD in single-receiver and polarization-diverse direct-detection optical OFDM.* *J. Lightwave Technol.*, 2009. **27**: p. Accepted for publication.
9. Lowery, A.J., *Amplified-spontaneous noise limit of optical OFDM lightwave systems.* *Optics Express*, 2008. **16**(2): p. 860-865.
10. Mayrock, M. and H. Haunstein, *PMD Tolerant Direct-Detection Optical OFDM System.* *Optical Communication (ECOC), 2007 33rd European Conference and Exhibition of*, 2007: p. 1-2.
11. Jansen, S.L., et al., *121.9-Gb/s PDM-OFDM Transmission With 2-b/s/Hz Spectral Efficiency Over 1000 km of SSMF.* *Lightwave Technology, Journal of*, 2009. **27**(3): p. 177-188.

12. Lowery, A.J. *Improving Sensitivity and Spectral Efficiency in Direct-Detection Optical OFDM Systems*. in *Optical Fiber communication/National Fiber Optic Engineers Conference, 2008. OFC/NFOEC 2008. Conference on*. 2008.
13. Jansen, S.L., I. Morita, and H. Tanaka. *10x121.9 Gb/s PDM-OFDM Transmission with 2-b/s/Hz spectral efficiency over 1,000 km SSMF*. in *Optical Fiber Communication Conference and Exposition National Fiber Optic Engineers Conference*. 2008. San Diego
14. Sano, A., et al., *No-guard-interval coherent optical OFDM for 100-Gb/s long-haul WDM transmission*. *Journal of Lightwave Technology*, 2009. **27**(16): p. 3705-3712.
15. Kobayashi, T., et al., *Electro-optically multiplexed 110Gbit/s optical OFDM signal transmission over 80km SMF without dispersion compensation*. *Electronics Letters*, 2008. **44**(3): p. 225-226.
16. Yamada, E., et al. *Novel no-guard interval PDM CO-OFDM transmission in 4.1 Tb/s (50 x 88.8-Gb/s) DWDM link over 800 km SMF including 50-GHz spaced ROADM nodes*. in *optical fiber communication conference and exposition national fiber optic engineers conference*. 2008. San Diego.
17. Sano, A., et al. *13.4-Tb/s (134x111-Gb/s/ch) no-guard-interval coherent OFDM transmission over 3,600 km of SMF with 19-ps average PMD*. in *34th European Conference on Optical Communication (ECOC) 2008*.
18. Dong, Z., et al. *24Tb/s (24x1.3Tb/s) WDM transmission of terabit PDM-CO-OFDM superchannels over 2400km SMF-28*. in *Optoelectronics and Communications Conference (OECC), 2011 16th*. 2011.
19. Liu, X., et al. *3 x 485-Gb/s WDM transmission over 4800 km of ULAF and 12 x 100-GHz WSSs using CO-OFDM and single coherent detection with 80-GS/s ADCs*. in *Optical Fiber Communication Conference and Exposition (OFC/NFOEC), 2011 and the National Fiber Optic Engineers Conference*. 2011.
20. Liu, X., et al. *7 x 224-Gb/s WDM transmission of reduced-guard-interval CO-OFDM with 16-QAM subcarrier modulation on a 50-GHz grid over 2000 km of ULAF and five ROADM passes*. in *Optical Communication (ECOC), 2010 36th European Conference and Exhibition on*. 2010.
21. Giacomidis, E., et al., *Adaptive-Modulation-Enabled WDM Impairment Reduction in Multichannel Optical OFDM Transmission Systems for Next-Generation PONs*. *Photonics Journal, IEEE*, 2010. **2**(2): p. 130-140.
22. Dayou, Q., et al., *10Gbit/s WDM-SSB-OFDM transmission over 1000km SSMF using conventional DFB lasers and direct-detection*. *Electronics Letters*, 2008. **44**(3): p. 223-225.
23. Bülow, H. *Tutorial: Electronic Dispersion Compensation*. in *Optical Fiber Telecommunications*. 2007. Anaheim, CA.
24. Shieh, W., Q. Yang, and Y. Ma, *107 Gb/s coherent optical OFDM transmission over 1000-km SSMF fiber using orthogonal band multiplexing*. *Optics Express*, 2008. **16**(9): p. 6378-6386.
25. Ellis, A.D. and F.C.G. Gunning, *Spectral density enhancement using coherent WDM*. *Photonics Technology Letters, IEEE*, 2005. **17**(2): p. 504-506.

Chapter 10

CONCLUSIONS & FUTURE WORK

10.1 Conclusions

The aim of this thesis was to investigate the effects of laser source's noise on a long-haul DDO-OFDM transmission system. It has been shown that a system can be built using a commercially available laser source where the linewidth requirement is not as stringent as for a CO-OFDM transmission system. However, the laser also has the noise characteristics that are interdependent with each other, which was known to limit a DDO system performance [1-9]. In addition, chromatic dispersion of fibre can also introduce another noise effect due to the interaction of the laser's phase noise with the dispersion. This was also known to be a limiting factor that reduces the system's OSNR and BER.

10.2 Research findings

Based on the mentioned objectives, the research findings can be summarised as follows:

- **Laser's characteristics verification**

The relation of the measured commercial DFB laser's RIN and linewidth to the laser's output power was found to satisfy the theory of $RIN \propto P_{out}^{-3}$ and $linewidth \propto P_{out}^{-1}$ when the I_b was increased. The relation between the I_b and P_{out} can be found using the plotted L-I curve of the laser, where the P_{out} is increased with the increase of I_b . The laser's I_{Th} of 13 mA was also identified where the lasing begins around the vicinity of this current. Thus, it is important to drive the laser beyond the I_{Th} to ensure that it is operating in the linear region of the L-I curve to ensure a stable lasing operation. For the RIN measurement, high RIN resonance peak amplitudes at several giga-hertz frequency have been obtained when the laser was driven from around and beyond the I_{Th} . The resonance's peak amplitude reduces when the I_b supplied was increased until the peak was reduced down to the noise floor when the supplied I_b was at 40 mA. For the linewidth measurement, the results obtained using a delayed self-homodyne technique matched well with the HRS. Critical factors in the measurements of the RIN and linewidth have been

identified. In the RIN measurement, the RF spectrum analyser (DSO) used in the setup need to be well calibrated in order to have an accurate measurement. For the linewidth measurement using the delayed self-homodyne technique, a correct length of the delay line needs to be identified in order to produce an incoherent mixing of the light from the branches upon photodetection.

- **Dialled-up laser linewidth demonstration**

A narrow linewidth of a semiconductor laser can be broadened by phase-modulate the laser's output using digitally-generated phase modulation. The phase was then applied to the laser's output using a complex-modulator. With the modulator, the phase can be driven around the complex plane indefinitely, without the requirement for reset events.

- **RIN effects with and without externally modulated RF tones**

From the obtained simulation results, RIN resonance was not only introduced by the laser source, but also has been imposed into each of the modulated RF tone. Each tone was imposed with a double-sided RIN resonance. The RIN's peak frequency of the tone was taken from the tone to its peak frequency where the frequency difference is similar to the carrier's RIN peak frequency. This is because the RF tones were generated from the laser hence, the same RIN resonance as the carrier's RIN was imposed to each of the tone with lower RIN's peak power. This has been shown in the detected electrical spectrum. The RIN's peak power was reduced when more tones were used and when the tones power was decreased. In terms of a DDO-OFDM system, the tones can be resembled as the OFDM subcarriers. The subcarrier's RIN can be neglected since many subcarriers are used in the system and the RIN's peak power was reduced when more subcarriers (tones) were employed. The carrier's RIN can also be neglected since the resonance's peak power will fall within a frequency guardband set between the laser's centre frequency and the OFDM signal band.

- **Effects of linewidth interaction with fibre chromatic dispersion with and without externally modulated RF tones**

An analytical equation to represent a noise PSD resulting from the interaction of an unmodulated laser's linewidth or phase noise with fibre dispersion had been presented in [1]. This interaction results in a PM-to-IM conversion noise. Using a conversion noise PSD equation derived in [1], plots for the noise PSD when a wide

linewidth was used at high dispersion transmissions have been presented, where the plotted PSD matched the one presented in [1]. The noise PSD obtained from an experimental result also matched the first frequency null, which satisfied the reference. The noise floor due to this conversion noise can be determined using the upper bound of the intensity noise, which has not being presented in the reference. This upper bound equation has been derived and the plotted on the noise PSD's amplitude. This noise floor will be added into other intensity noise upon photodetection. Interaction of the wide-linewidth laser with RF tones and the fibre has been investigated using both simulation and experiments. Noise pedestal has been shown around each of the tones. The effect of a decorrelated RF tone due to the group delay has also been presented where the noise pedestal peak power around each tone is increased for the high frequency tones. Also presented was the decrease of the noise pedestal when the tones power is reduced. However, if the power of the tones is too low, the SNR will be low. Also shown is the PSD of the conversion noise and the delayed RF-tones can be added in electrical domain, which has been done using excel addition and verified using VPItransmissionMaker™ simulation.

- **Simulation of the effects of linewidth interaction with fibre chromatic dispersion to OFDM signal transmission**

Phase rotations have been shown on the received scatter plots when a single OFDM subcarrier was transmitted over a high dispersive fibre using a wide linewidth laser. This occurs when the subcarrier is placed at a high frequency away from the carrier. When the subcarrier is placed close to the carrier, a scatter plot without phase rotation has been achieved. The plotted symbols were concentrated at the origin point. This shows that the high frequency subcarrier suffers with more phase rotation than the low frequency subcarrier. From the electrical frequency spectrum, a high power noise pedestal is observed around the high frequency subcarrier compared with the low frequency subcarrier. This is due to the phase walk-off of the high frequency subcarrier is larger than the low frequency subcarrier. This is due to the group delay effect. Laser linewidth also contributed to the phase rotation of the received symbols, where more rotated symbols were achieved when a wide linewidth laser was used. For multiple subcarriers transmission, phase rotations of the received symbols occurred when wide

subcarrier spacing was used, where the symbols at the outer quadrant experienced larger phase rotation compared to the inner quadrant for a 16 QAM received scatter plot. This determines that when no ISCI, the laser's phase noise gives a strong influence to the received signal scatter plot by inducing large phase errors to the received symbols. When the ISCI is more dominant (narrow subcarrier spacing), the noise pedestal interfered with each other and adding up, which results in a much flat noise floor without the frequency nulls. Hence, the shape of the plotted symbols is more rounds without phase rotations. This was verified using histogram plots, where phase rotated symbols producing skewed histogram.

- **Experimental demonstration of laser's noise effects in DDO-OFDM transmission system**

A reasonable DDO-OFDM system performance was obtained using a commercial fixed-wavelength DFB laser. This was achieved with the laser operated at reasonably-low powers for 4 QAM, but higher powers were required for 32 QAM. The effects of the linewidth interaction with fibre dispersion has been presented at moderate powers, but generally masked by RIN at low laser powers. The effect of RIN to the OFDM subcarriers was done by driving the laser at a low output power ($RIN \propto P_{out}^{-3}$) over a back-to-back transmission. In this experiment, the effect of linewidth can be excluded even though at the same time the laser will emit a wide linewidth ($linewidth \propto P_{out}^{-1}$). This is because the linewidth does not affect the back-to-back transmission system. The RIN was shown to degrade the Q performance of the low frequency subcarriers due to the tail of the RIN resonance, which extended into the subcarriers band. The high peak power of the RIN resonance does not affect the subcarriers since it felt inside the frequency guardband at several giga hertz. This guardband is required in the system to place the subcarrier \times subcarrier mixing [10-14]. At a low RIN (high P_{out}), a flat subcarrier band's Q-response was achieved. This is because of the RIN is added to the noise floor evenly across the OFDM signal band upon the detection, in which, each of the subcarriers owns a DSB RIN resonance. This will also increases the system's noise floor level. The effect of linewidth to the OFDM subcarriers' performance was shown by varying the laser's P_{out} to vary the linewidth and transmitting the signal over a dispersive fibre. With the PM-to-IM conversion noise, more Q degradation has been shown affecting the subcarriers at a high

frequency. This is due to the group delay effect where the subcarriers are walking away from the carrier as they propagated through the dispersive fibre. The overall Q was also degraded when more dispersion is introduced in the system. When fixed fibre dispersion was used, the Q has been shown to degrade as a function of the laser's linewidth. The results showed that a cheap laser source such as the DFB with a wide linewidth can be used for DDO-OFDM long-haul transmission, compared to a CO-ODM system which requires narrow linewidth to prevent the laser's phase noise effects [15-17]. The result also showed that the higher M -size QAM is more affected to the PM-to-IM conversion noise effect than the smaller size QAM.

10.3 Research contributions

Based on the findings, the research contributions can be summarised as follows:

- **Development of laser linewidth emulator**

A laser linewidth emulator has been developed and demonstrated experimentally, where the theory and its principle has been explained using simulation. With this laser, an independent dialled-up laser with the other laser's characteristics has been achieved. A wide linewidth laser can be achieved even when the laser was operated at a high output power, which at the same time gives a low RIN. The linewidth verification has been done by measuring the emulated linewidth using HRS, where a good matched between the dialled and the measured linewidth was achieved. This emulated linewidth has been shown to be stable over several hours of operation. This laser can be used as a test and measurement device to investigate the effects of linewidth to a system without imposing the laser's other characteristics. The narrowest linewidth of the emulator is the original semiconductor laser's linewidth that was used to drive the C-MZI in the emulator's setup. Thus, using a narrow linewidth laser in the setup will provide wide dialled-up linewidth range for the emulator.

- **Development of a tool to measure complex modulator's linearity level and a phase difference between the inner MZI**

A technique to measure a complex modulator or an MZI's linearity level has also been achieved by using the emulated phase noise or linewidth of a laser source. The laser linewidth emulator setup can also be used to measure a phase difference

between the inner MZIs of a complex-modulator or nested MZIs configuration. The theory of this technique has been explained using a Lissajous curve. This has been shown using simulation results of a complex-plane with a circle, which indicated phase modulation when the MZI is driven in a linear region. When the modulator is driven into its nonlinear region, the output amplitude depends on the phase, as indicated by the square shape. This is because of the nonlinear region causes a large increase in the intensity noise of the laser linewidth emulator. An ellipse shape of I and Q plots has been achieved when the upper or lower MZI was driven with higher driving voltage. When the upper MZI's driving voltage is higher than the lower, the ellipse's largest diameter is aligned to the Q-axis and the largest diameter is aligned to the I-axis when the lower MZI's driving voltage is higher than the upper. This plot can be used to determine a power imbalance between the top and lower MZIs, or one MZI is experiencing a higher loss than the other. The phase difference between the MZIs can also be obtained in this measurement.

- **Experimental demonstration of independent linewidth effect to DDO-OFDM system using laser linewidth emulator**

An independent linewidth effect from the other's laser characteristics has been investigated experimentally using laser linewidth emulator. A critical issue in the experimental setup in order to apply the laser into the system has also been highlighted. For example, the DC carrier needs to be monitored at both C-MZIs used to prevent DC-leakage and the noise band from the original laser's centre frequency when the leakage occurred. Results of Q-factor across the subcarriers frequency index showed that the high frequency subcarriers experienced higher Q-degradation as compared to the low frequency subcarriers. This confirmed the results achieved in both simulation and experiment using a commercial DFB laser, which showed that a high group delay is imposed to the high frequency subcarriers due to fibre dispersion. The result obtained with the laser linewidth emulator can also be used to analyse the results obtained in the simulation and experiment using the DFB laser. The Q obtained when using a wide-dialled-up linewidth showed a better performance compared to the same linewidth provided by the DFB laser. This is due to the other laser characteristics that degrade the performance when operating the laser at the wide linewidth. For a narrow-dialled-up linewidth, the

results obtained agreed with the experimental results when driving the commercial DFB at a high power. This is because the RIN is very low.

- **Reduction of linewidth impact in a DDO-OFDM system**

The impact of linewidth on a DDO-OFDM system has been reduced by using a simple delay line. This has been demonstrated using simulation and experiment. The reduction was achieved by matching the phase waveforms of the subcarriers signal band and the carrier, which reduces the noise pedestal around the subcarrier band. A significant increase of Q has been seen in the results when the delay was assigned. The noise can theoretically only be nulled for a single subcarrier, but the result is still sufficiently useful over a wide bandwidth, particularly if the delays were matched in the centre of the band, where the noise pedestals of all subcarriers were added. The study also showed that a longer delay line is required by the higher subcarriers because of the high frequencies experience more walk-off than the ones closer to the carrier. The length of the delay line is crucial since a too long delay can degrade the system performance due to the phase decorrelation of the subcarriers and carrier phase fluctuations. For optical CO-OFDM system without a pilot-tone correction [17], this method is not useful because the phase waveforms of the transmitted waveform and local oscillator are uncorrelated, which is similar to a heterodyne linewidth measurement using two lasers.

- **Demonstration of a high-speed data transmission using a DDO-OFDM system**

A high-speed data transmission using a DDO-OFDM system has been shown using an experimental demonstration. A 120 Gbit/s data transmission has been built using commercially available devices. Several important device improvements was also developed and presented in order to achieve a good quality wide RF signal bandwidth. This includes the synchronization of two fast 20 GS/s DACs, signal band pre-emphasis of the DACs and a pre-emphasis employed to optimize the frequency response of the C-MZI. A virtual carrier technique was also used to increase the transmit bandwidth. This technique also provides flexibility in tuning the frequency and the amplitude of the carrier, by simply adjusting the RF frequency of the frequency synthesizer.

A variant of the DDO-OFDM system employing self-coherent polarization-diversity receiver design has been developed to provide a PMD compensation and

polarization demultiplexing. With this system, the carrier was transmitted along with the signal band, which is common in a DD system. The same carrier was used as the LO at the receiver, where the carrier was separated from the signal band using a filter before an optical hybrid. With this technique, no free-running external laser is required at the receiver. Cancellation of the subcarrier \times subcarrier mixing in a DDO-OFDM system was achieved with the use of balance photodetections. In this transmission, a frequency guardband could not be totally omitted due to the use of a wide optical filter pass band and the overlapped of passbands during the separation of the carrier and the signal band at the input of the optical hybrids.

10.4 Future works

Based on the research findings and contributions to achieve the listed research objectives, some recommendations on future works can be summarized as follows:

- **Technique to reduce PM-to-IM conversion noise effect to the DDO-OFDM system using electronic compensation**

A technique that could boost the Q performance of all subcarriers at once will be beneficial. This may be done by correcting the group delay effects digitally using electronic compensation technique, to compensate for the PM-to-IM conversion noise effects. This will also reduce the implementation cost compared with the use of an optical compensation technique. To achieve this, several challenges may need to be dealt with. For example, the technique may involve the use of a reference subcarrier in order to get the phase error information of each of the subcarriers, in order to compensate for, just like a pilot tone used in a coherent system [17]. Another issue that needs to be considered is the receiver design. Typical square-law photodetection cannot preserve the phase information of the received signal. Hence, in order to get the phase information, coherent detection needs to be employed. Also, the electronic compensation may also involve complex calculations.

The linewidth emulator could be extended to:

- **Development of a laser emulator module with dialled-up laser's characteristics for a system test and measurement**

Development of a laser emulator that provides a dialled-up function not only for the linewidth, but also for the other laser's characteristics; for example, RIN and frequency chirping effects will be an added-value and beneficial in order to perform a system test and measurement in a laboratory. A wide analysis of the requirements on a laser's performance can be performed with such laser device. This, however, comes with the challenges to produce the noise effects digitally, where one may need to consider the laser rate equations for the correlation of phase noise and intensity noise in a real laser as well as other assumptions in the design. For example, to perform a dialled-up RIN, one may need to have a predetermined set of RIN characteristics to emulate for the RIN resonance's highest peak amplitude and the RIN's peak frequency, where the peak finally reduces down to the noise floor to indicate a low RIN and the its peak frequency is varied for several gigahertz. In this work, attempts to develop a dialled-up RIN have been made. However, only a flat noise level without a RIN resonance was produced. A module that could generate the noise digitally, which can be used with any semiconductor laser source would be a good test and measurement device, including performing an optical modulator linearity test.

- **Improvement of an optical modulator's linearity test**

The experiment to demonstrate a C-MZI's linearity test can be improved by using precise lengths of RF-cables with high maximum input voltage RF devices. The limitations of the RF devices have been shown in a back-to-back electrical experiment where connection from a DAC's outputs, which supplied the digitally-generated phase noise, into a DSO. This setup involved the use of RF cables, amplifiers and attenuators to vary the RF signal power. A clipped signal was achieved for a V_p of 2.3 V where clippings becomes severe until the I-Q plot produced a square-edge plot when the V_{pp} was increased to 2.45 V and 2.7 V. This cannot be used to perform an accurate C-MZI linearity measurement as the RF voltage limitation is much smaller the V_π of the C-MZI, which is 5.6 V.

10.5 References

1. Yamamoto, S., et al., *Analysis of laser phase noise to intensity noise conversion by chromatic dispersion in intensity modulation and direct detection optical fiber transmission*. Journal of Lightwave Technology, 1990. **8**: p. 1716-1722

2. Edagawa, N., et al., *12300 ps/nm, 2.4 Gb/s nonregenerative optical fiber transmission experiment and effect of transmitter phase noise*. Photonics Technology Letters, IEEE, 1990. **2**(4): p. 274-276.
3. Lee, Y.H., J. Woo, and H.W. Tsao, *The impact of laser phase noise on the coherent subcarrier multiplexing system*. Lightwave Technology, Journal of, 1991. **9**(3): p. 347-355.
4. Lu, X., et al., *Analysis of relative intensity noise in semiconductor lasers and its effect on subcarrier multiplexed lightwave systems*. Lightwave Technology, Journal of, 1994. **12**(7): p. 1159-1166.
5. Ribeiro, R.F.S., J.R.F.d. Rocha, and A.V.T. Cartaxo, *Influence of laser phase noise on dispersive optical fiber communication systems*. photonics technology letters, 1995. **7**(12): p. 1510-1512.
6. Marshall, W.K., B. Crosignani, and A. Yariv, *Laser phase noise to intensity noise conversion by lowest-order group velocity dispersion in optical fiber: exact theory*. Optics Express, 2000. **23**(3): p. 165-167.
7. Morgado, J.A.P. and A.V.T. Cartaxo. *New semi-analytical method of estimating the influence of laser noise on direct detection system performance*. in *4th Pacific Rim Conference on Lasers and Electro-Optics (CLEO)*. 2001.
8. Morgado, J.A.P. and A.V.T. Cartaxo, *Assessment of laser noise influence on direct-detection transmission system performance*. Journal of Lightwave Technology, 2003. **21**(3): p. 759-768.
9. Ahmed, M. and M. Yamada, *Effect of intensity noise of semiconductor lasers on the digital modulation characteristics and the bit error rate of optical communication systems*. Journal of Applied Physics, 2008. **104**(1): p. 013104-7.
10. Lowery, A.J. and J. Armstrong, *Orthogonal frequency division multiplexing for dispersion compensation of long-haul optical systems*. Optics Express, 2006. **14**: p. 2079-2084.
11. Lowery, A.J., L. Du, and J. Armstrong. *Orthogonal Frequency Division Multiplexing for Adaptive Dispersion Compensation in Long Haul WDM Systems*. in *Optical Fiber Communication Conference, 2006 and the 2006 National Fiber Optic Engineers Conference. OFC 2006*. 2006.
12. Schmidt, B.J.C., A.J. Lowery, and J. Armstrong. *Experimental demonstrations of 20 Gbits/s direct-detection optical OFDM and 12Gbits/s with a colorless transmitter*. in *Optical Fiber Communication Conference*. 2007. Anaheim, CA.
13. Lowery, A.J., L. Du, and J. Armstrong, *Performance of optical OFDM in ultra long-haul WDM lightwave systems*. Journal of Lightwave Technology, 2007. **25**: p. 131 – 138.
14. Lowery, A.J., *Amplified-spontaneous noise limit of optical OFDM lightwave systems*. Optics Express, 2008. **16**(2): p. 860-865.
15. Shieh, W. and C. Athaudage, *Coherent optical orthogonal frequency division multiplexing*. Electronic Letters, 2006. **42**: p. 587-588.
16. Yi, X., W. Shieh, and Y. Ma. *Phase noise on coherent optical OFDM systems with 16-QAM beyond 10Gb/s*. in *33rd European Conference and Exhibition on Optical Communication 2007*. Berlin, Germany: VDE VERLAG GMBH.
17. Jansen, S.L., et al. *20-Gb/s OFDM transmission over 4160-km SSMF enabled by RF-pilot tone phase noise compensation*. in *Optical Fiber Communication Conference*. 2007. Anaheim, CA.


Appendices

APPENDIX 1

Appendix 1.1:

Rightslink® by Copyright Clearance Center - Google Chrome
<https://s100.copyright.com/AppDispatchServlet>

Copyright Clearance Center **RightsLink®** Home Create Account Help

 **IEEE**
 Requesting permission to reuse content from an IEEE publication

Title: Experimental Demonstrations of Electronic Dispersion Compensation for Long-Haul Transmission Using Direct-Detection Optical OFDM
Author: Schmidt, B.J.C.; Lowery, A.J.; Armstrong, J.
Publication: Lightwave Technology, IEEE/OSA Journal of
Publisher: IEEE
Date: Jan.1, 2008
 Copyright © 2008, IEEE

User ID
 Password
 Enable Auto Login
 LOGIN
[Forgot Password/User ID?](#)
 If you're a copyright.com user, you can login to RightsLink using your copyright.com credentials. Already a RightsLink user or want to learn more?

Thesis / Dissertation Reuse

The IEEE does not require individuals working on a thesis to obtain a formal reuse license, however, you may print out this statement to be used as a permission grant:

Requirements to be followed when using any portion (e.g., figure, graph, table, or textual material) of an IEEE copyrighted paper in a thesis:

- 1) In the case of textual material (e.g., using short quotes or referring to the work within these papers) users must give full credit to the original source (author, paper, publication) followed by the IEEE copyright line © 2011 IEEE.
- 2) In the case of illustrations or tabular material, we require that the copyright line © [Year of original publication] IEEE appear prominently with each reprinted figure and/or table.
- 3) If a substantial portion of the original paper is to be used, and if you are not the senior author, also obtain the senior author's approval.

Requirements to be followed when using an entire IEEE copyrighted paper in a thesis:

- 1) The following IEEE copyright/ credit notice should be placed prominently in the references: © [year of original publication] IEEE. Reprinted, with permission, from [author names, paper title, IEEE publication title, and month/year of publication]
- 2) Only the accepted version of an IEEE copyrighted paper can be used when posting the paper or your thesis on-line.
- 3) In placing the thesis on the author's university website, please display the following message in a prominent place on the website: In reference to IEEE copyrighted material which is used with permission in this thesis, the IEEE does not endorse any of [university/educational entity's name goes here]'s products or services. Internal or personal use of this material is permitted. If interested in reprinting/republishing IEEE copyrighted material for advertising or promotional purposes or for creating new collective works for resale or redistribution, please go to http://www.ieee.org/publications_standards/publications/rights/rights_link.html to learn how to obtain a License from RightsLink.

If applicable, University Microfilms and/or ProQuest Library, or the Archives of Canada may supply single copies of the dissertation.

BACK

CLOSE WINDOW

Appendix 1.2:


 Copyright Clearance Center
RightsLink[®]

[Home](#)
[Create Account](#)
[Help](#)



IEEE
 Requesting permission to reuse content from an IEEE publication

Title: Mode-partition noise in microwave subcarrier transmission systems
Author: Meslener, G.J.
Publication: Lightwave Technology, IEEE/OSA Journal of
Publisher: IEEE
Date: Jan 1994
 Copyright © 1994, IEEE

User ID

 Password

Enable Auto Login

[Forgot Password/User ID?](#)
If you're a copyright.com user, you can login to Rightslink using your copyright.com credentials. Already a **Rightslink user** or want to [learn more?](#)

Thesis / Dissertaion Reuse

The IEEE does not require individuals working on a thesis to obtain a formal reuse license, however, you may print out this statement to be used as a permission grant:

Requirements to be followed when using any portion (e.g., figure, graph, table, or textual material) of an IEEE copyrighted paper in a thesis:

- 1) In the case of textual material (e.g., using short quotes or referring to the work within these papers) users must give full credit to the original source (author, paper, publication) followed by the IEEE copyright line © 2011 IEEE.
- 2) In the case of illustrations or tabular material, we require that the copyright line © [Year of original publication] IEEE appear prominently with each reprinted figure and/or table.
- 3) If a substantial portion of the original paper is to be used, and if you are not the senior author, also obtain the senior author's approval.

Requirements to be followed when using an entire IEEE copyrighted paper in a thesis:

- 1) The following IEEE copyright/ credit notice should be placed prominently in the references: © [year of original publication] IEEE. Reprinted, with permission, from [author names, paper title, IEEE publication title, and month/year of publication]
- 2) Only the accepted version of an IEEE copyrighted paper can be used when posting the paper or your thesis on-line.
- 3) In placing the thesis on the author's university website, please display the following message in a prominent place on the website: In reference to IEEE copyrighted material which is used with permission in this thesis, the IEEE does not endorse any of [university/educational entity's name goes here]'s products or services. Internal or personal use of this material is permitted. If interested in reprinting/republishing IEEE copyrighted material for advertising or promotional purposes or for creating new collective works for resale or redistribution, please go to http://www.ieee.org/publications_standards/publications/rights/rights_link.html to learn how to obtain a License from RightsLink.

If applicable, University Microfilms and/or ProQuest Library, or the Archives of Canada may supply single copies of the dissertation.

Appendix 1.3

Rightslink® by Copyright Clearance Center - Google Chrome
<https://s100.copyright.com/AppDispatchServlet>

Copyright Clearance Center **RightsLink®** Home Create Account Help



IEEE
Requesting permission to reuse content from an IEEE publication

Title: Analysis of laser phase noise to intensity noise conversion by chromatic dispersion in intensity modulation and direct detection optical-fiber transmission

Author: Yamamoto, S.; Edagawa, N.; Taga, H.; Yoshida, Y.; Wakabayashi, H.

Publication: Lightwave Technology, IEEE/OSA Journal of

Publisher: IEEE

Date: Nov 1990

Copyright © 1990, IEEE

User ID

Password

Enable Auto Login

LOGIN

[Forgot Password/User ID?](#)

If you're a copyright.com user, you can login to Rightslink using your copyright.com credentials. Already a **Rightslink user** or want to [learn more?](#)

Thesis / Dissertaion Reuse

The IEEE does not require individuals working on a thesis to obtain a formal reuse license, however, you may print out this statement to be used as a permission grant:

Requirements to be followed when using any portion (e.g., figure, graph, table, or textual material) of an IEEE copyrighted paper in a thesis:

- 1) In the case of textual material (e.g., using short quotes or referring to the work within these papers) users must give full credit to the original source (author, paper, publication) followed by the IEEE copyright line © 2011 IEEE.
- 2) In the case of illustrations or tabular material, we require that the copyright line © [Year of original publication] IEEE appear prominently with each reprinted figure and/or table.
- 3) If a substantial portion of the original paper is to be used, and if you are not the senior author, also obtain the senior author's approval.

Requirements to be followed when using an entire IEEE copyrighted paper in a thesis:

- 1) The following IEEE copyright/ credit notice should be placed prominently in the references: © [year of original publication] IEEE. Reprinted, with permission, from [author names, paper title, IEEE publication title, and month/year of publication]
- 2) Only the accepted version of an IEEE copyrighted paper can be used when posting the paper or your thesis on-line.
- 3) In placing the thesis on the author's university website, please display the following message in a prominent place on the website: In reference to IEEE copyrighted material which is used with permission in this thesis, the IEEE does not endorse any of [university/educational entity's name goes here]'s products or services. Internal or personal use of this material is permitted. If interested in reprinting/republishing IEEE copyrighted material for advertising or promotional purposes or for creating new collective works for resale or redistribution, please go to http://www.ieee.org/publications_standards/publications/rights/rights_link.html to learn how to obtain a License from RightsLink.

If applicable, University Microfilms and/or ProQuest Library, or the Archives of Canada may supply single copies of the dissertation.


Appendix 1.4

Rightslink® by Copyright Clearance Center - Google Chrome

https://s100.copyright.com/AppDispatchServlet

Copyright Clearance Center RightsLink®

Home Create Account Help



IEEE
Requesting permission to reuse content from an IEEE publication

Title: Linewidth determination from self-heterodyne measurements with subcoherence delay times

Author: Richter, L.; Mandelberg, H.; Kruger, M.; McGrath, P.

Publication: Quantum Electronics, IEEE Journal of

Publisher: IEEE

Date: Nov 1986

Copyright © 1986, IEEE

User ID

Password

Enable Auto Login

LOGIN

[Forgot Password/User ID?](#)

If you're a **copyright.com** user, you can login to Rightslink using your copyright.com credentials. Already a **Rightslink** user or want to [learn more?](#)

Thesis / Dissertaion Reuse

The IEEE does not require individuals working on a thesis to obtain a formal reuse license, however, you may print out this statement to be used as a permission grant:

Requirements to be followed when using any portion (e.g., figure, graph, table, or textual material) of an IEEE copyrighted paper in a thesis:

- 1) In the case of textual material (e.g., using short quotes or referring to the work within these papers) users must give full credit to the original source (author, paper, publication) followed by the IEEE copyright line © 2011 IEEE.
- 2) In the case of illustrations or tabular material, we require that the copyright line © [Year of original publication] IEEE appear prominently with each reprinted figure and/or table.
- 3) If a substantial portion of the original paper is to be used, and if you are not the senior author, also obtain the senior author's approval.

Requirements to be followed when using an entire IEEE copyrighted paper in a thesis:

- 1) The following IEEE copyright/ credit notice should be placed prominently in the references: © [year of original publication] IEEE. Reprinted, with permission, from [author names, paper title, IEEE publication title, and month/year of publication]
- 2) Only the accepted version of an IEEE copyrighted paper can be used when posting the paper or your thesis on-line.
- 3) In placing the thesis on the author's university website, please display the following message in a prominent place on the website: In reference to IEEE copyrighted material which is used with permission in this thesis, the IEEE does not endorse any of [university/educational entity's name goes here]'s products or services. Internal or personal use of this material is permitted. If interested in reprinting/republishing IEEE copyrighted material for advertising or promotional purposes or for creating new collective works for resale or redistribution, please go to http://www.ieee.org/publications_standards/publications/rights/rights_link.html to learn how to obtain a License from RightsLink.

If applicable, University Microfilms and/or ProQuest Library, or the Archives of Canada may supply single copies of the dissertation.

Appendix 1.5

ELSEVIER LICENSE TERMS AND CONDITIONS

Oct 17, 2012

This is a License Agreement between zan zuraidah ("You") and Elsevier ("Elsevier") provided by Copyright Clearance Center ("CCC"). The license consists of your order details, the terms and conditions provided by Elsevier, and the payment terms and conditions.

All payments must be made in full to CCC. For payment instructions, please see information listed at the bottom of this form.

Supplier	Elsevier Limited The Boulevard, Langford Lane Kidlington, Oxford, OX5 1GB, UK
Registered Company Number	1982084
Customer name	zan zuraidah
Customer address	24 Clayton, Victoria 3168
License number	3011250724967
License date	Oct 17, 2012
Licensed content publisher	Elsevier
Licensed content publication	Optical Fiber Technology
Licensed content title	Optical orthogonal division multiplexing for long haul optical communications: A review of the first five years
Licensed content author	Arthur James Lowery, Liang B. Du
Licensed content date	October 2011
Licensed content volume number	17
Licensed content issue number	5
Number of pages	18
Start Page	421
End Page	438
Type of Use	reuse in a thesis/dissertation
Portion	figures/tables/illustrations
Number of figures/tables /illustrations	1
Format	electronic
Are you the author of this Elsevier article?	No
Will you be translating?	No
Order reference number	
Title of your thesis/dissertation	Impact of laser noise in direct detection optical orthogonal frequency division multiplexing
Expected completion date	Jan 2013
Estimated size (number of pages)	500

Elsevier VAT number	GB 494 6272 12
Permissions price	0.00 USD
VAT/Local Sales Tax	0.0 USD / 0.0 GBP
Total	0.00 USD
Terms and Conditions	

INTRODUCTION

1. The publisher for this copyrighted material is Elsevier. By clicking "accept" in connection with completing this licensing transaction, you agree that the following terms and conditions apply to this transaction (along with the Billing and Payment terms and conditions established by Copyright Clearance Center, Inc. ("CCC"), at the time that you opened your Rightslink account and that are available at any time at <http://myaccount.copyright.com>).

GENERAL TERMS

2. Elsevier hereby grants you permission to reproduce the aforementioned material subject to the terms and conditions indicated.

3. Acknowledgement: If any part of the material to be used (for example, figures) has appeared in our publication with credit or acknowledgement to another source, permission must also be sought from that source. If such permission is not obtained then that material may not be included in your publication/copies. Suitable acknowledgement to the source must be made, either as a footnote or in a reference list at the end of your publication, as follows:

"Reprinted from Publication title, Vol /edition number, Author(s), Title of article / title of chapter, Pages No., Copyright (Year), with permission from Elsevier [OR APPLICABLE SOCIETY COPYRIGHT OWNER]." Also Lancet special credit - "Reprinted from The Lancet, Vol. number, Author(s), Title of article, Pages No., Copyright (Year), with permission from Elsevier."

4. Reproduction of this material is confined to the purpose and/or media for which permission is hereby given.

5. Altering/Modifying Material: Not Permitted. However figures and illustrations may be altered/adapted minimally to serve your work. Any other abbreviations, additions, deletions and/or any other alterations shall be made only with prior written authorization of Elsevier Ltd. (Please contact Elsevier at permissions@elsevier.com)

6. If the permission fee for the requested use of our material is waived in this instance, please be advised that your future requests for Elsevier materials may attract a fee.

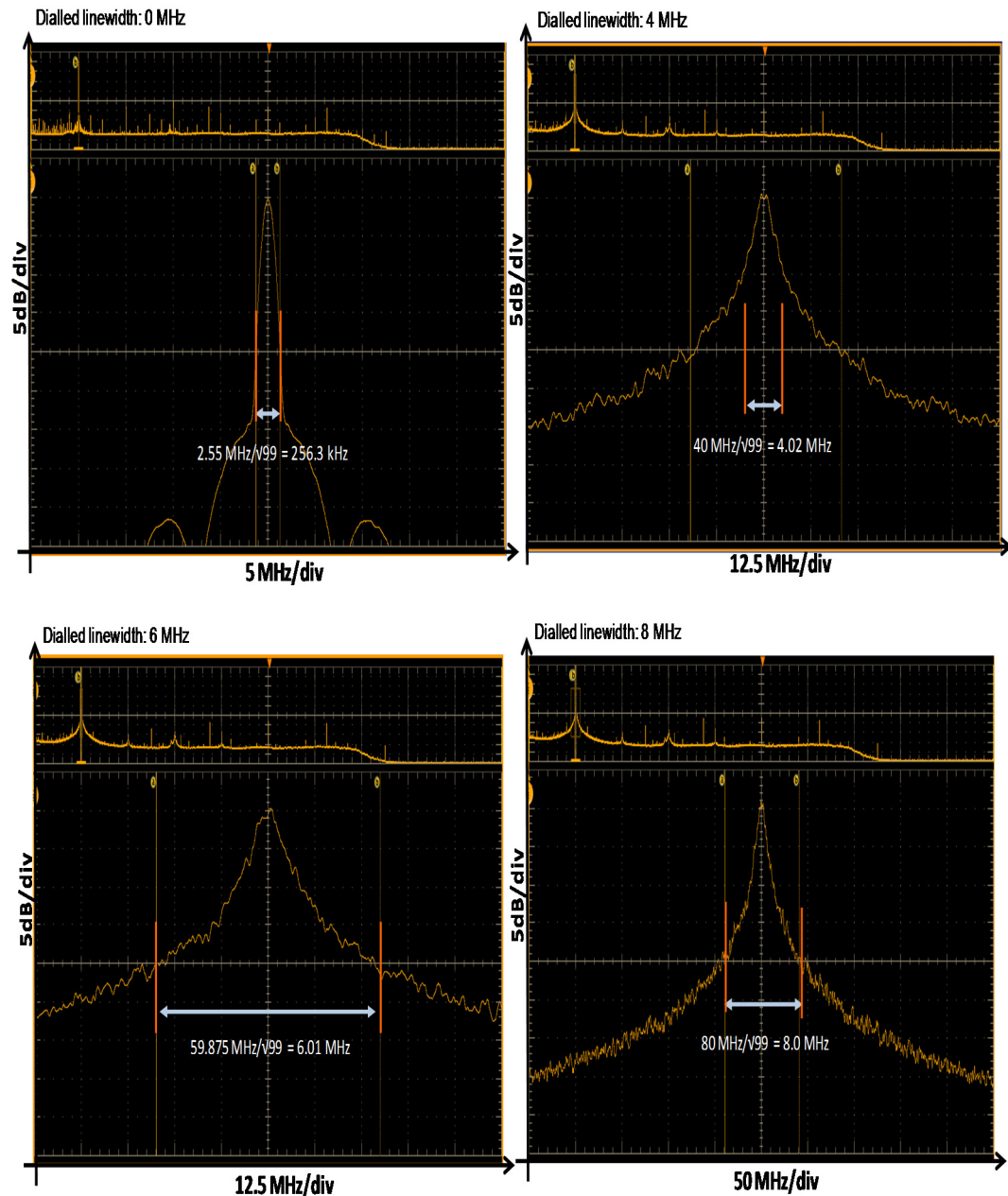
7. Reservation of Rights: Publisher reserves all rights not specifically granted in the combination of (i) the license details provided by you and accepted in the course of this licensing transaction, (ii) these terms and conditions and (iii) CCC's Billing and Payment terms and conditions.

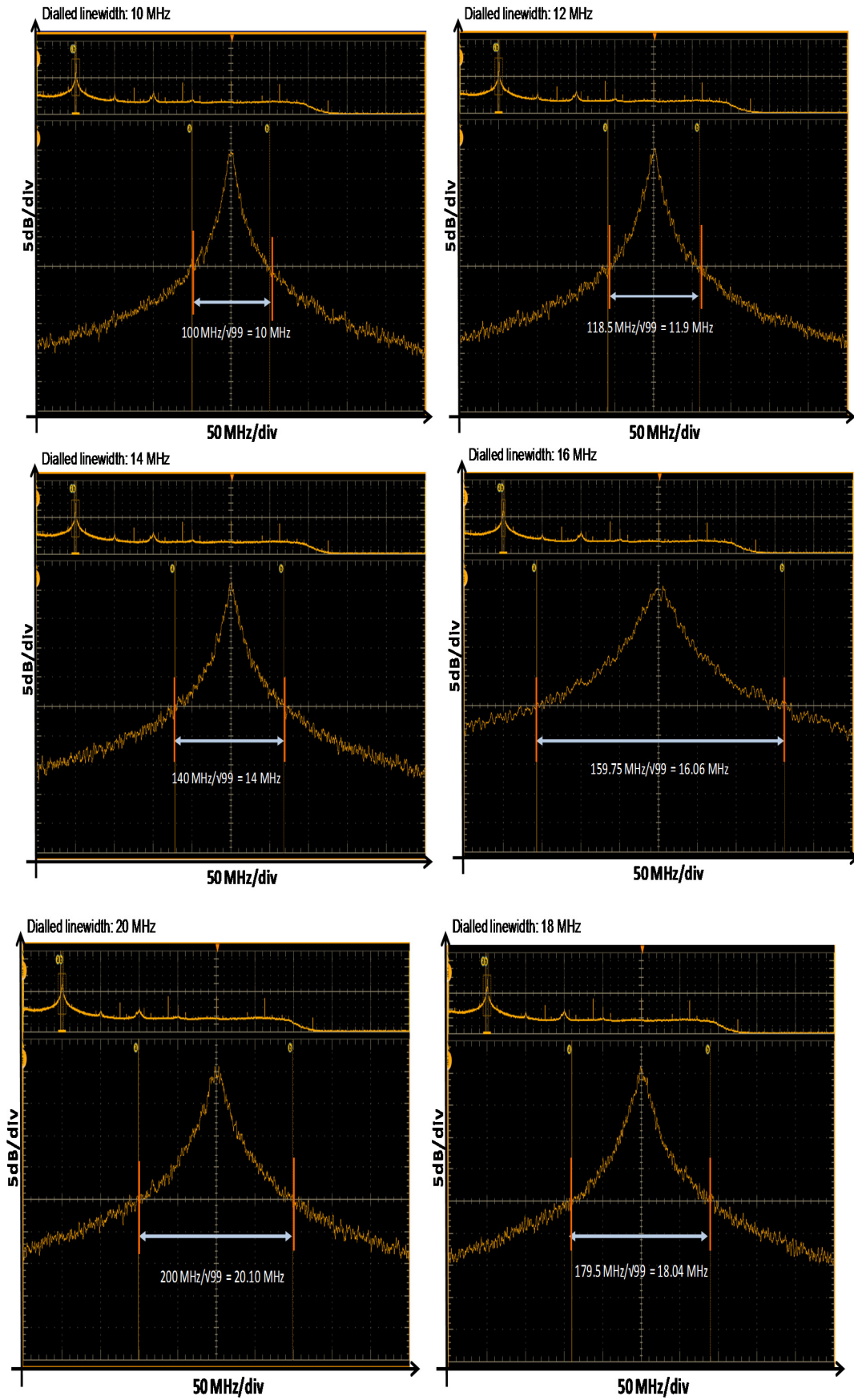
8. License Contingent Upon Payment: While you may exercise the rights licensed immediately upon issuance of the license at the end of the licensing process for the transaction, provided that you have disclosed complete and accurate details of your proposed use, no license is finally effective unless and until full payment is received from you (either by publisher or by CCC) as provided in CCC's Billing and Payment terms and conditions. If full payment is not received on a timely basis, then any license preliminarily granted shall be deemed automatically revoked and shall be void as if never granted.

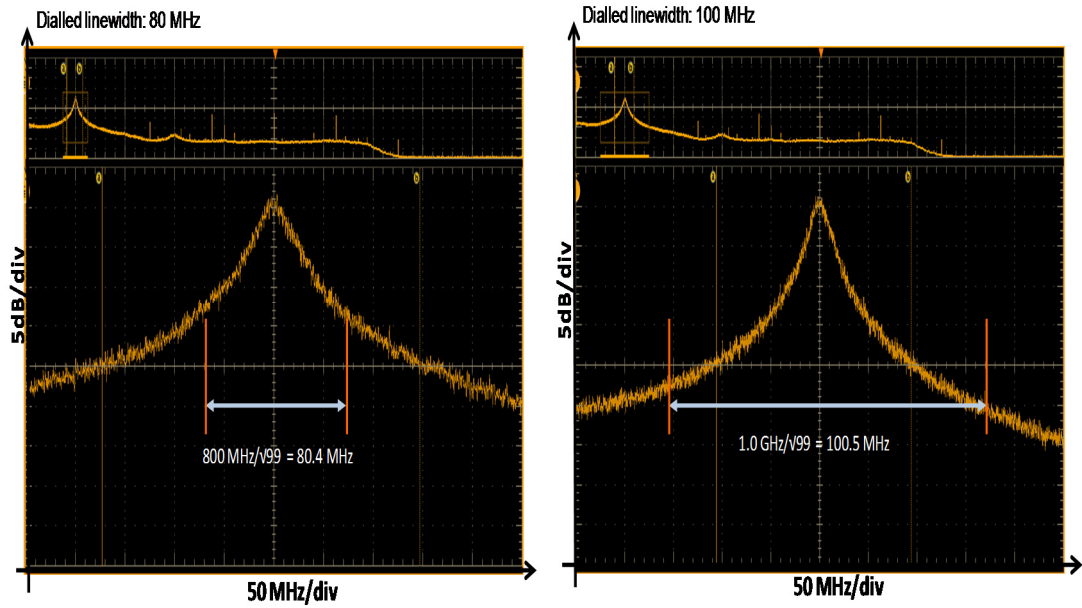
APPENDIX 2

Appendix 2.1:

Self-heterodyne linewidth measurement showing FWHM $\Delta\nu$ set for the laser linewidth emulator setup.

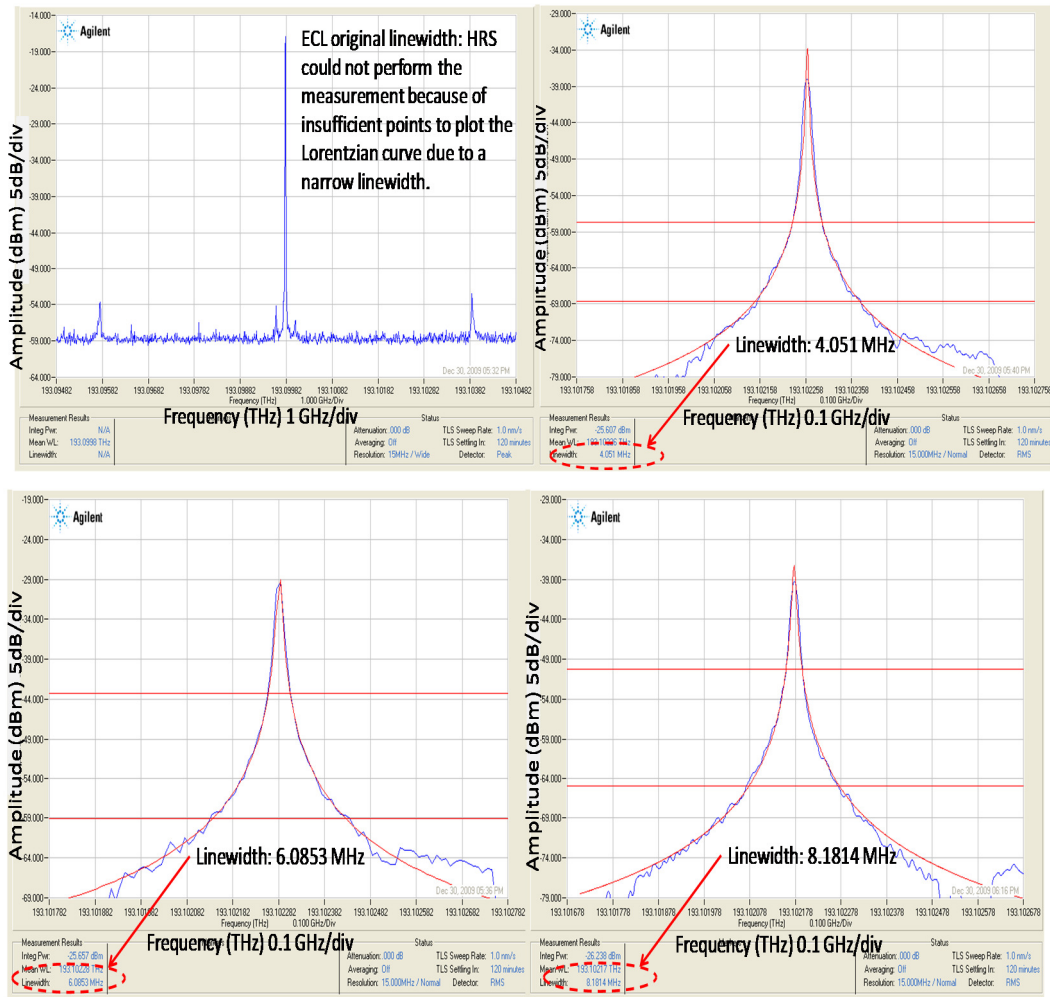


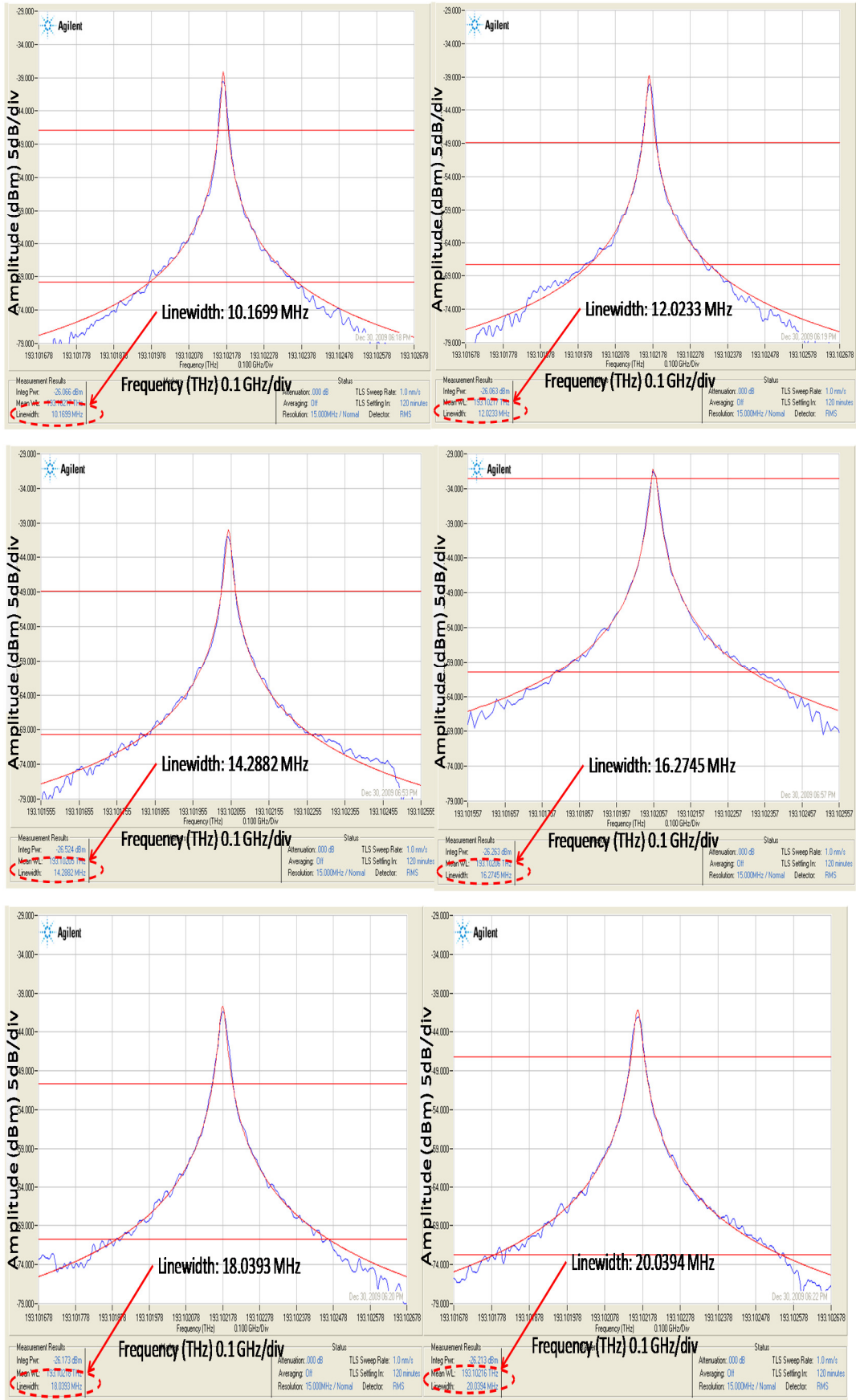


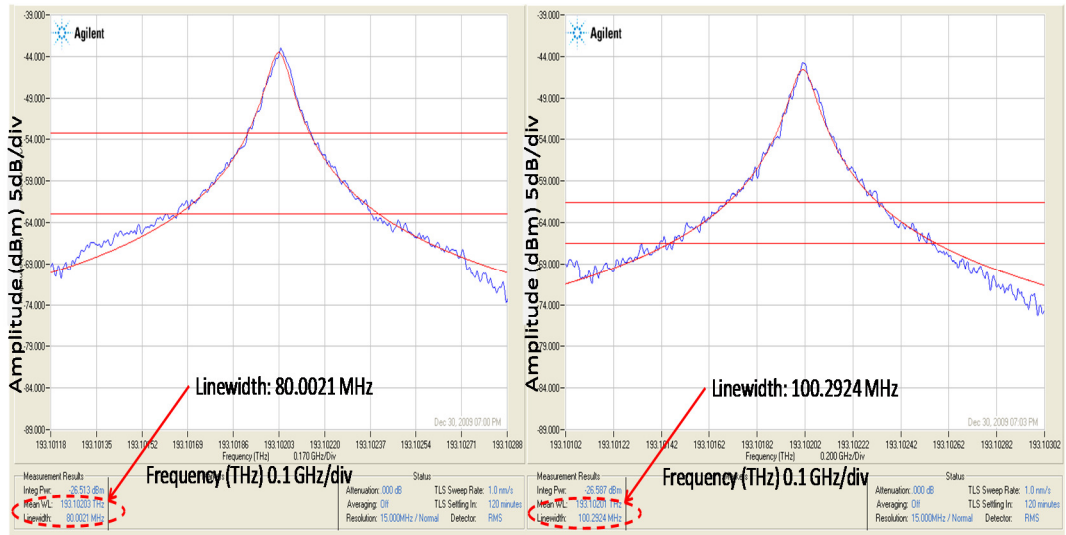


Appendix 2.2:

HRS linewidth measurement for dialled-up linewidth:







APPENDIX 3

Appendix 3.1:

Transmit code using Matlab R2008a to generate single OFDM subcarrier:

```

%% Transmit code to generate single OFDM subcarriers to study PM-
to-IM conversion noise on the subcarrier.
N           = 1024;
NSYM        = 12;
Nuse        = 1022;
Nsc         = 1;    % number of OFDM subcarrier
indxNscTx   = 745;
M           = 16;   % 16 QAM

for indxSC = indxNscTx
    indxSC = num2str(indxSC);
    runs = 100;

    for i=1:runs
        run = num2str(i);

        datai      = zeros(NSYM, N);
        datat      = zeros(NSYM, N);
        data       = zeros(NSYM, Nuse);
        datrnd     = randint(NSYM,Nsc,M); % generate random data
                % in a form of a NSYM x Nsc matrix.
        dataSC     = qammod(datrnd,M, [], 'gray');
        data(:,indxNscTx) =dataSC; % data assigned at 745
                % subcarrier index.

        for j = 1:NSYM
            datai(j,:) = [data(j,1:Nuse/2) zeros(1,N-Nuse)
                data(j,Nuse/2+1:Nuse)];
            datat(j,:) = ifft(datai(j,:));
        end

        % CP allocation %

        datat = [datat(:,(3*N/4)+1:N) datat];

        stream = reshape(datat.',1,[]);

        szstream = size(stream);
        apprxpow2 = log2(szstream(1,2));
        pow2 = ceil(apprxpow2);

        % Check Pow 2
        fprintf('\n log2 value = %d\n',apprxpow2);
        fprintf('\n pow 2 = %d\n',pow2);

        leadzeros = zeros(1,2^pow2 - szstream(1,2));

        % Clip real and imaginary streams to minimize quantising
        % errors
        CR      = 9;
    end
end

```



```

    smag = abs(stream);
    Esmag2 = mean(smag.^2);
    limit = (Esmag2*(10^(CR/10)))^0.5
    for j = 1:length(stream),
        if(smag(j)>limit) stream(j) =
(limit/smag(j))*(stream(j)); end
    end
    sR = [leadzeros real(stream)]; % lead zeros = 1024,
        % making sR size = 15360 + 1024 = 16384
    sI = [leadzeros imag(stream)];

% Check sample length
prcntLZ = length(leadzeros)/length(sR)*100;
fprintf('\n number of samples = %d\n',length(sR));
fprintf('\n number of leading zeros =
%d\n',length(leadzeros));
fprintf('\n percentage of leading zeros from no of
samples = %d\n',prcntLZ);

% Save the real and imaginary signal components and the
% transmit data.

save(['C:\Users\Zuraidah\Documents\2011Mar25 RIN & LW on
SC\Tx intoVPI4\Re_16QSC' indxSC run '.txt'],'sR','-ascii');
save(['C:\Users\Zuraidah\Documents\2011Mar25 RIN & LW on
SC\Tx intoVPI4\Im_16QSC' indxSC run '.txt'],'sI','-ascii');
save(['C:\Users\Zuraidah\Documents\2011Mar25 RIN & LW on
SC\Tx intoVPI4\sv_16QSC' indxSC run'],'data');
x=1;

end
end

```

Appendix 3.2:

Receive code for

```

%% Decoding 4QAM from VPI simulation to study the effects of Phase
and
%% Dispersion for a single OFDM subcarrier transmission. The
transmission
%% is using virtual carrier and therefore the whole FFTs (both
positive
%% and negative) are used for the subcarrier.
%% Laser Phase Noise and dispersion study for separation of SCs
over 2.5GHz signal BW, transmitted over
%% a length of fiber starting from SC at SCstart FFT point.
clear all;
delSC = 1; % This is the number of SC separation to study ICI
within a fix signal BW
for delSCf = delSC
    f = num2str(delSCf);
    LW = 4000000; % Linewidth
    for WL = LW;
        W = num2str(WL);
        Pm = 1500000;
        for h = Pm
            fnm = num2str(h);
            fnm = fnm;
            runs = 1;

```

```

for s = 1:runs

    NSYM    = 12;
    N        = 1024;
    Nuse     = 1022; % default number of subcarrier
    NfftStrt = N-128;
    PfftStrt = 2;
    indxN    = NfftStrt:delSC:(Nuse); % delSC = 1
    indxP    = PfftStrt:delSC:128;
    indxNscN = indxN;
    indxNscP = indxP;

    szNegSC  = size(indxNscN);
    szPosSC  = size(indxNscP);
    szNegSC  = szNegSC(1,2);
    szPosSC  = szPosSC(1,2);

    Nsc      = szNegSC + szPosSC; % Number of
    subcarriers used for the test.
    indxNscNrx = indxNscN - (N/2)+1;
    indxNscPrx = indxNscP + (N/2)-2;

    indxNscRx = [indxNscPrx indxNscNrx];

    M        = 16;
    OS       = 8;
    FS       = 80e9;
    FC       = 15.000000e9;
    FSIZE    = OS*N*(5/4); % 4x1024x(4/4+1/4) = 5120,
                        1/4 is CP length
    T        = NSYM*FSIZE*(1/FS);
    FCT      = (1:FS*T)*2*pi*FC/FS;

    rxR      = zeros(1,length(FCT));
    rxI      = zeros(1,length(FCT));

    run      = num2str(s)

    % Load transmitted and received data, find start
    % of frame visually
    load(['C:\Users\Zuraidah\Documents\2011Mar25 RIN &
LW on SC\Tx intoVPI2\ICI_delSC_FixSig\sv_16Q_delSC' f run]);
    txx = data(:, [Nuse/2+1:Nuse 2:Nuse/2]);
    lts = txx; %% lts = long training symbol used for
channel estimation of block type channel estimation, where
%% all subcarriers are taken as pilot symbols.
    load(['C:\Users\Zuraidah\Documents\2011Mar25 RIN &
LW on SC\Rx fromVPI 5SCs\ICI_delSC\Rx16QSC_delSC' f '_LW' W
'.0_length' fnm '.0_' run '.mat']);

    stream = stream.';

    plot(stream);

    start = 8192; % start of the frame

```



```

% Variables to modify data
for toff = -1024
    phoff = 0;
    a = 1;

% Multiply by complex exponential
for j = 1:length(FCT),
    rxR(j) = stream(j+start+toff)*cos(FCT(j));
    rxI(j) = stream(j+start+toff)*-
sin(FCT(j)+phoff);
end
cstream = a*rxR + i*rxI;

% Get index to data. With 'index', the CP is
removed
for j = 1:NSYM,
    initial(j) = (j-1)*FSIZE;
    index(j,:) =
(initial(j)+(1/4)*OS*N+1):(initial(j)+(5/4)*OS*N);
end

% Get data
for j = 1:NSYM
    rxt(j,:) = cstream(index(j,:));
end

% Demodulate, get channel response, eq the
received data, get original data

indfft = [7682:8192 2:511]; % SC index
for j = 1:NSYM,
    rxf(j,:) = fft(rxt(j,:));
    rx2(j,:) = (rxf(j,indfft));
    chest2(j,:) = rx2(j,:)./lts(j,:);
end
chest_ave(1,:) = mean(chest2,1);

% Equalized the received data
for j = 1:NSYM,
    rxx(j,:) = (chest_ave(1,:).^-
1).* (rx2(j,:));
end

% Get Eb/No per subcarrier
if(M==64) E = 42; n = 6; end
if(M==32) E = 20; n = 5; end
if(M==16) E = 10; n = 4; end
if(M==4) E = 2; n = 2; end

MSE = mean((abs(txx(:,indxNscRx) -
rxx(:,indxNscRx))).^2);
EbNo = E./(n*MSE);
EbNoA = mean(EbNo);

EbNoA_dB = 10*log10(EbNoA)
EbNo_dB = 10*log10(EbNo);
SC_use = zeros(1,Nuse-1);

```

```

        SC_use(1,indxNscRx) = EbNo_dB;
        EbNo_dB           = SC_use;

        MSE2           = mean((abs(txx(:,indxNscRx) -
rxx(:,indxNscRx))).^2);
        EbNo2          = E./(n*MSE2);
        EbNo_dB2       = 10*log10(EbNo2);

        figure(1), hold on
        subplot(2,1,1); plot(EbNo_dB,'r'); axis([1 Nuse-
1 0 50]); grid on
        title('EbN0 vs. Subcarrier'); hold on;
        subplot(2,1,2);
        plot(20*log10(abs(chest_ave(1,[1:(Nuse-1)]))), 'b*'); axis([1 Nuse-1
-30 50]);grid on
        title('Average channel estimation'); hold on;

        % Get bit error rate
        Drxx          =
gamdemod(rxx(:,indxNscRx),M,[], 'gray');
        Dtxx          =
gamdemod(txx(:,indxNscRx),M,[], 'gray');

        [number, ratio, individual] =
biterr(Drxx(:,:),Dtxx(:,:),log2(M));
        fprintf('\nBER = %d %d\n',number,ratio);
        fprintf('ntoff = %d\nphoff =
%d\n\n',toff,phoff);

        BER_SC = mean(individual(:,:));
        [number1, ratio1]=biterr(Drxx,Dtxx,log2(M));
        fprintf('\nBER = %d %d\n',number1,ratio1);
        fprintf('ntoff = %d\nphoff =
%d\n\n',toff,phoff);

        rxx_plot = rxx(:,indxNscRx);
        re_RX    = real(rxx_plot);
        im_RX    = imag(rxx_plot);
        %% Reshape to change the matrix to a single
        column matrix
        re_RX    = re_RX.';
        im_RX    = im_RX.';

        InphaseRX = reshape(re_RX,1,NSYM*(Nsc));
        QuadRX     = reshape(im_RX,1,NSYM*(Nsc));

        AbsInphaseRX = abs(InphaseRX);
        AbsQuadRX    = abs(QuadRX);

        figure(4), hold on
        plot(AbsInphaseRX,AbsQuadRX,'*r');
        title('First fold'); grid on; hold on

        AbsQuadRxN = AbsQuadRX-2;
        AbsQuadRxN(AbsQuadRxN<0) = [0];
        AbsQuadRxP = AbsQuadRX;
        AbsQuadRxP(AbsQuadRxP>2) = [0];

```

```

QuadRxFin = AbsQuadRxN + AbsQuadRxP;

AbsInphaseRxN = AbsInphaseRX-2;
AbsInphaseRxN(AbsInphaseRxN<0) = [0];
AbsInphaseRxP = AbsInphaseRX;
AbsInphaseRxP(AbsInphaseRxP>2) = [0];
InphaseRxFin = AbsInphaseRxN + AbsInphaseRxP;

% Plot the histograms
figure(2), hold on
scatterhist(InphaseRxFin,QuadRxFin); grid on;
hold on

figure(3), hold on
plot(rxx_plot, '.b'); grid on

    lngth = length(InphaseRxFin);
end
re_RXFin1(s,:) = InphaseRX;
im_RXFin1(s,:) = QuadRX;

ReFin1(s,:) = InphaseRxFin;
ImFin1(s,:) = QuadRxFin;

end
x = 1;
re_RXFin      = re_RXFin1.';
re_RXFinRun   = reshape(re_RXFin,1,lngth*s);
im_RXFin      = im_RXFin1.';
im_RXFinRun   = reshape(im_RXFin,1,lngth*s);

ReFin = ReFin1.';
ReFinRun = reshape(ReFin,1,lngth*s);
ImFin = ImFin1.';
ImFinRun = reshape(ImFin,1,lngth*s);

figure(4), hold on
scatterhist(ReFinRun,ImFinRun); grid on; hold on;

figure(5), hold on
scatterhist(re_RXFinRun,im_RXFinRun,[50 50]);
grid on; hold on;

figure(6), hold on
histfit(ReFinRun); grid on; hold on;
title('Real');

figure(7), hold on
histfit(ImFinRun); grid on; hold on;
title('Imaginary');

skewRe = skewness(ReFinRun)
skewIm = skewness(ImFinRun)

krtsRe = kurtosis(ReFinRun)
krtsIm = kurtosis(ImFinRun)

```

```

        x = 1;
    end
end
end

```

Appendix 3.3:

Transmit code using Matlab R2008a to generate 1022 OFDM subcarriers. This is used with RF virtual carrier transmitter design.

```

%% Transmit code for VPI DDO-OFDM transmission with virtual carrier
32-QAM
N      = 1024;
NSYM  = 12;
Nuse  = 1022; %% to get a signal bandwidth of -5GHz to +5GHz
M      = 32;
runs  = 25;

for i=1:runs
    run = num2str(i);

    datai      = zeros(NSYM, N);
    datat      = zeros(NSYM, N);

    datrnd     = randint(NSYM,Nuse,M);
    data       = qammod(datrnd,M, [], 'gray');

    data(:,1) = 0;

    for j = 1:NSYM
        datai(j,:) = [data(j,1:Nuse/2) zeros(1,N-Nuse)];
        data(j,Nuse/2+1:Nuse) = [data(j,1:Nuse/2) zeros(1,N-Nuse)];
        datat(j,:) = ifft(datai(j,:));
    end

    % CP allocation %

    datat = [datat(:, (3*N/4)+1:N) datat];

    stream = reshape(datat.',1, []); % 12x(1024 + 256) = 15360, where
256 is the CP

    szstream = size(stream);
    apprpow2 = log2(szstream(1,2));
    pow2 = ceil(aprpow2);

    % Check Pow 2
    fprintf('\n log2 value = %d\n', apprpow2);
    fprintf('\n pow 2 = %d\n', pow2);

    leadzeros = zeros(1, 2^pow2 - szstream(1,2));

```

```

% Clip real and imaginary streams to minimize quantising errors
CR      = 8.8;
smag    = abs(stream);
Esmag2  = mean(smag.^2);
limit   = (Esmag2*(10^(CR/10)))^0.5
for j   = 1:length(stream),
    if(smag(j)>limit) stream(j) = (limit/smag(j))*(stream(j));
end
end
sR      = [leadzeros real(stream)]; % lead zeros = 1024, making sR
size    = 15360 + 1024 = 16384
sI      = [leadzeros imag(stream)];

% Check sample length
prcntLZ = length(leadzeros)/length(sR)*100;
fprintf('\n number of samples = %d\n',length(sR));
fprintf('\n number of leading zeros = %d\n',length(leadzeros));
fprintf('\n percentage of leading zeros from no of samples =
%d\n',prcntLZ);

save(['C:\Users\Zuraidah\Documents\2010OCT VC LW MQ\Tx
intoVPI\Re_VPI4q' run '.txt'], 'sR', '-ascii');
save(['C:\Users\Zuraidah\Documents\2010OCT VC LW MQ\Tx
intoVPI\Im_VPI4q' run '.txt'], 'sI', '-ascii');
save(['C:\Users\Zuraidah\Documents\2010OCT VC LW MQ\Tx
intoVPI\sv_VPI4q' run], 'data');

end

```

Appendix 3.4:

Receive code to obtain Q-factor, $\frac{E_b}{N_0}$ and BER for 4 QAM:

```

%% Decoding x-QAM from VPI simulation.
%% Laser Phase Noise and dispersion study
%% Code to obtain scatter plot and Eb/N0 over SC for Chapter 6
thesis on
%% simulations results of Phase noise and dispersion without ASE
noise.

clear;
LW = 20000000;
for LW = LW
    LW = num2str(LW)

    Lgth = 50000;
    for L = Lgth

```

```

L = num2str(L)

runs = 25;
for s = 1:runs

    Initialize some variables
    FS = sampling rate
    T = period of five symbols = OS*N*NSYM(1/FS)
    FC = Carrier frequency

    NSYM = 12;
    N = 1024;
    Nuse = 1022;
    M = 32; %% change according to the M-size QAM; 4-,
16-, 32- etc.
    OS = 8;
    FS = 80e9;
    FC = 15.000000e9;
    FSIZE = OS*N*(5/4); % 4x1024x(4/4+1/4) = 5120, 1/4 is
CP length
    T = NSYM*FSIZE*(1/FS);
    FCT = (1:FS*T)*2*pi*FC/FS;

    rxR = zeros(1,length(FCT));
    rxI = zeros(1,length(FCT));

    run = num2str(s);

    Load transmitted and received data, find start of frame
visually
    load(['C:\Users\Zuraidah\Documents\2010OCT VC LW MQ\Tx
intoVPI 32Q\sv_32Q' run]); %% saved files for 32QAM

    txx = data(:, [Nuse/2+1:Nuse 2:Nuse/2]); %[Nuse/2+1:Nuse
2:Nuse/2]
    lts = txx; %% lts = long training symbol used for
channel estimation of block type channel estimation, where
% all subcarriers are taken as pilot symbols.

    load(['C:\Users\Zuraidah\Documents\2010OCT VC LW MQ\Rx
fromVPI\32QAM\Rx_32Q_LW' LW '.0_length' L '.0_' run '.mat']);

    stream = stream.';

    plot(stream);

    start = 8192;

    Variables to modify data
    for toff = -1024
        phoff = 0;
        a = 1;

        Multiply by complex exponential

```

```

        for j = 1:length(FCT),
            rxR(j) = stream(j+start+toff)*cos(FCT(j));
            rxI(j) = stream(j+start+toff)*-
sin(FCT(j)+phoff);
        end
        cstream = a*rxR + i*rxI;

        Get index to data. With 'index', the CP is removed
        for j = 1:NSYM,
            initial(j) = (j-1)*FSIZE;
            index(j,:) =
(initial(j)+(1/4)*OS*N+1):(initial(j)+(5/4)*OS*N);
        end

        Get data
        for j = 1:NSYM
            rxt(j,:) = cstream(index(j,:));
        end

        Demodulate, get channel response, eq the received
data, get original data

        indfft = [7682:8192 2:511]; %% [3841:4096 2:256]
        for j = 1:NSYM,
            rxf(j,:) = fft(rxt(j,:));
            rx2(j,:) = (rxf(j,indfft));
            chest2(j,:) = rx2(j,:)./lts(j,:);
        end
        chest_ave(1,:) = mean(chest2,1);

        Equalized the received data
        for j = 1:NSYM,
            rxx(j,:) = (chest_ave(1,:).^-1).*(rx2(j,:));
        end

        Get Eb/No per subcarrier
        if(M==64) E = 42; n = 6; end
        if(M==32) E = 20; n = 5; end
        if(M==16) E = 10; n = 4; end
        if(M==4) E = 2; n = 2; end

        MSE = mean((abs(txx(:, [1:(Nuse-1)]) -
rxx(:, [1:(Nuse-1)]))).^2);
        EbNo = E./(n*MSE);
        EbNoA = mean(EbNo);

        EbNoA_dB = 10*log10(EbNoA);
        EbNo_dB = 10*log10(EbNo);
        mnEbN_dB = mean(EbNo_dB);

        MSE2 = mean((abs(txx - rxx)).^2);
        EbNo2 = E./(n*MSE2);
        EbNo_dB2 = 10*log10(EbNo2);

        %% To calculate small q: Q(q) = 1/2erfc(q/sqrt(2)) q
= sqrt(2*Eb/No)%%
        q_small = sqrt(2*EbNo);
        Pb_BER = 0.5*erfc(q_small/sqrt(2));

```

```

mnPb_BER = mean(Pb_BER); %%%
Pb_BER1  = 0.5*erfc(sqrt(EbNo));

%% To calculate Q with  $Q(q) = 20\log_{10}(q)$ ;
Q_capdB  = 20*log10(q_small);
meanQ_capdB = mean(Q_capdB); %%%

%% Average channel estimation dB %%%
chest_avedB = 20*log10(abs(chest_ave(1, [1:Nuse-
1]))));

figure(2)
subplot(2,1,1); plot(EbNo_dB, 'b'); axis([1 Nuse-1 0
50]); grid on
title('EbN0 vs. Subcarrier')
subplot(2,1,2);
plot(20*log10(abs(chest_ave(1, [1:(Nuse-1)]))), 'b'); axis([1 Nuse-1 -
30 50]);grid on
title('Average channel estimation');

figure(3), hold on
plot(EbNo_dB);axis([1 Nuse-1 0 50]); grid on
title('EbN0 vs. Subcarrier');

figure(4), hold on
plot(EbNoA_dB, '*'); hold on;

Get bit error rate
Drxx = qamdemod(rxx(:, [1:(Nuse-1)]), M, [], 'gray');
Dtxx = qamdemod(txx(:, [1:(Nuse-1)]), M, [], 'gray');

[number, ratio, individual] =
biterr(Drxx(:, [1:(Nuse-1)]), Dtxx(:, [1:(Nuse-1)]), log2(M));
fprintf('\nBER = %d %d\n', number, ratio);
fprintf('ntoff = %d\nphoff = %d\n\n', toff, phoff);

meanBER = ratio;
BER_SC = mean(individual(:, 1:(Nuse-1)));

[number1, ratio1] = biterr(Drxx, Dtxx, log2(M));
fprintf('\nBER = %d %d\n', number1, ratio1);
fprintf('ntoff = %d\nphoff = %d\n\n', toff, phoff);

rxx_plot = rxx(:, [1:(Nuse-1)]);
re_RX = real(rxx_plot);
im_RX = imag(rxx_plot);
%% Reshape to change the matrix to a single column
matrix

re_RX = re_RX.';
im_RX = im_RX.';

InphaseRX = reshape(re_RX, 1, NSYM*(Nuse-1));
QuadRX = reshape(im_RX, 1, NSYM*(Nuse-1));

figure(5), hold on
plot(rxx_plot, '.b'); grid on;

```



```

end
% Save all the elements into s x Nuse matrix where s is
% the number of runs and Nuse number of data SC. This is
to get the average EbNo, Pb_BER and Biterr across the SC
Q_capdB_SCrun(s,:) = Q_capdB;
EbNo_SCrun(s,:) = EbNo_dB;
Pb_BERSCrun(s,:) = Pb_BER;
chest_avedBSCrun(s,:) = chest_avedB;
biterrSCrun(s,:) = BER_SC;

InphaseRXSCrun(s,:) = InphaseRX;
QuadRXSCrun(s,:) = QuadRX;

indvRunEbN0(s,:) = mnEbN_dB;
indvRunBiterr(s,:) = meanBER;

end
Getting mean over s runs.
mnQ_capdB_SCrun = mean(Q_capdB_SCrun);
mnEbNoRun = mean(EbNo_SCrun);
mnPb_BERSCrun = mean(Pb_BERSCrun);
mnchest_avedBSCrun = mean(chest_avedBSCrun);
mnbiterrSCrun = mean(biterrSCrun);

Mean_mnbiterrSCrun = mean(mnbiterrSCrun);

mnEbNoSC = mean(mnEbNoRun)
mnQ_dBSCrun = mean(mnQ_capdB_SCrun)

mnindvRunEbN0 = mean(indvRunEbN0);
mnindvRunBiterr = mean(indvRunBiterr)

figure(5), hold on
subplot(2,1,1); plot(mnEbNoRun); axis([1
Nuse-1 0 40]); grid on; title('Mean over runs EbNo vs SC');
subplot(2,1,2);
plot(mnchest_avedBSCrun(1,[1:1021])); axis([1 Nuse-1 -40 40]);grid
on; title('Mean over runs: Average channel estimation vs
subcarriers');

figure(6), hold on
plot(mnbiterrSCrun); hold on; grid on;
title('mean over runs: BER vs SC');

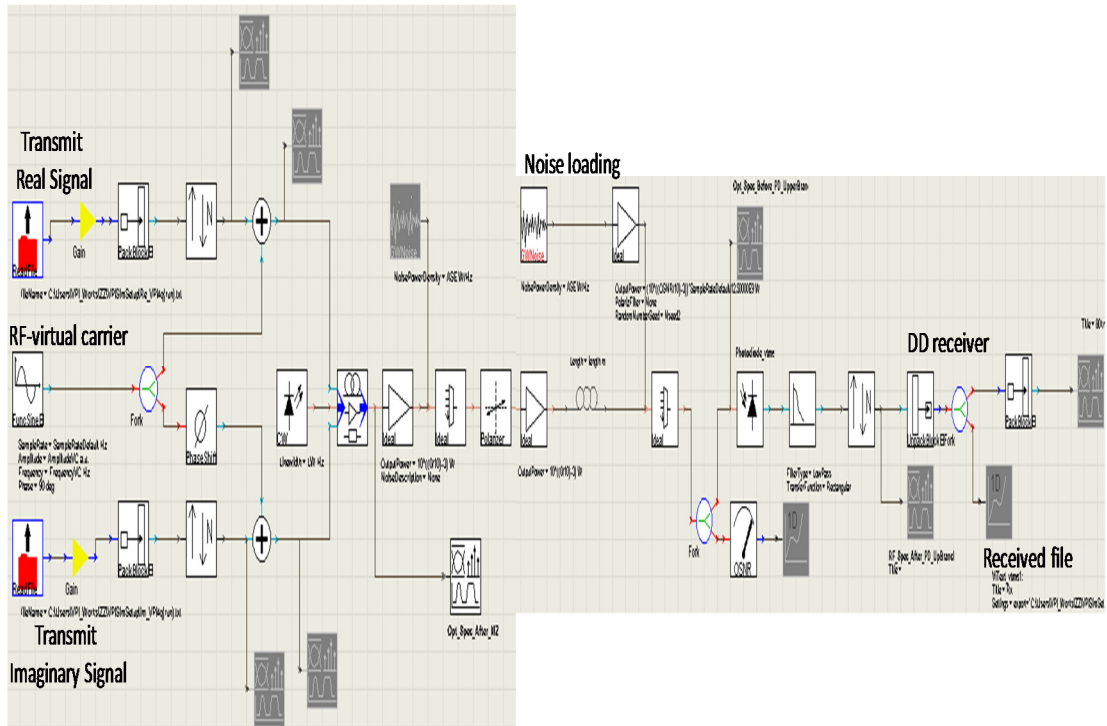
end

end

```

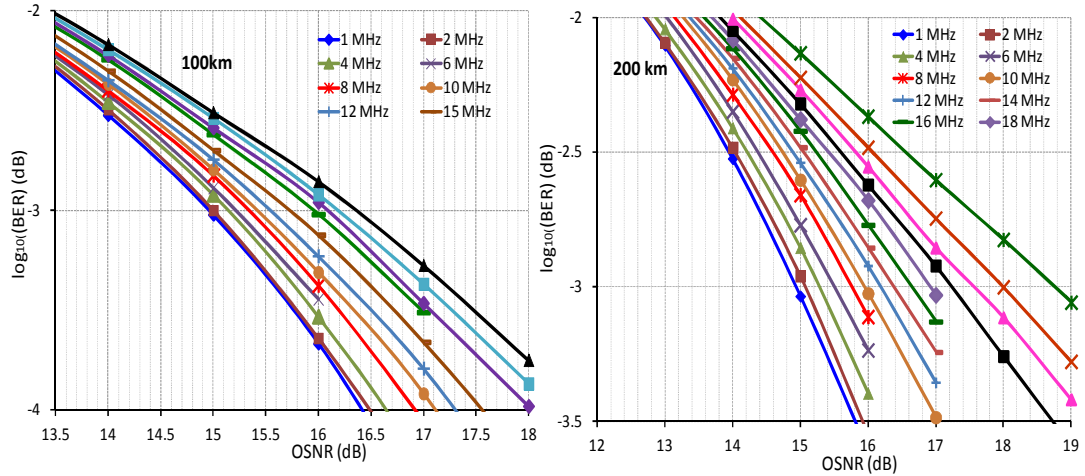
Appendix 3.5:

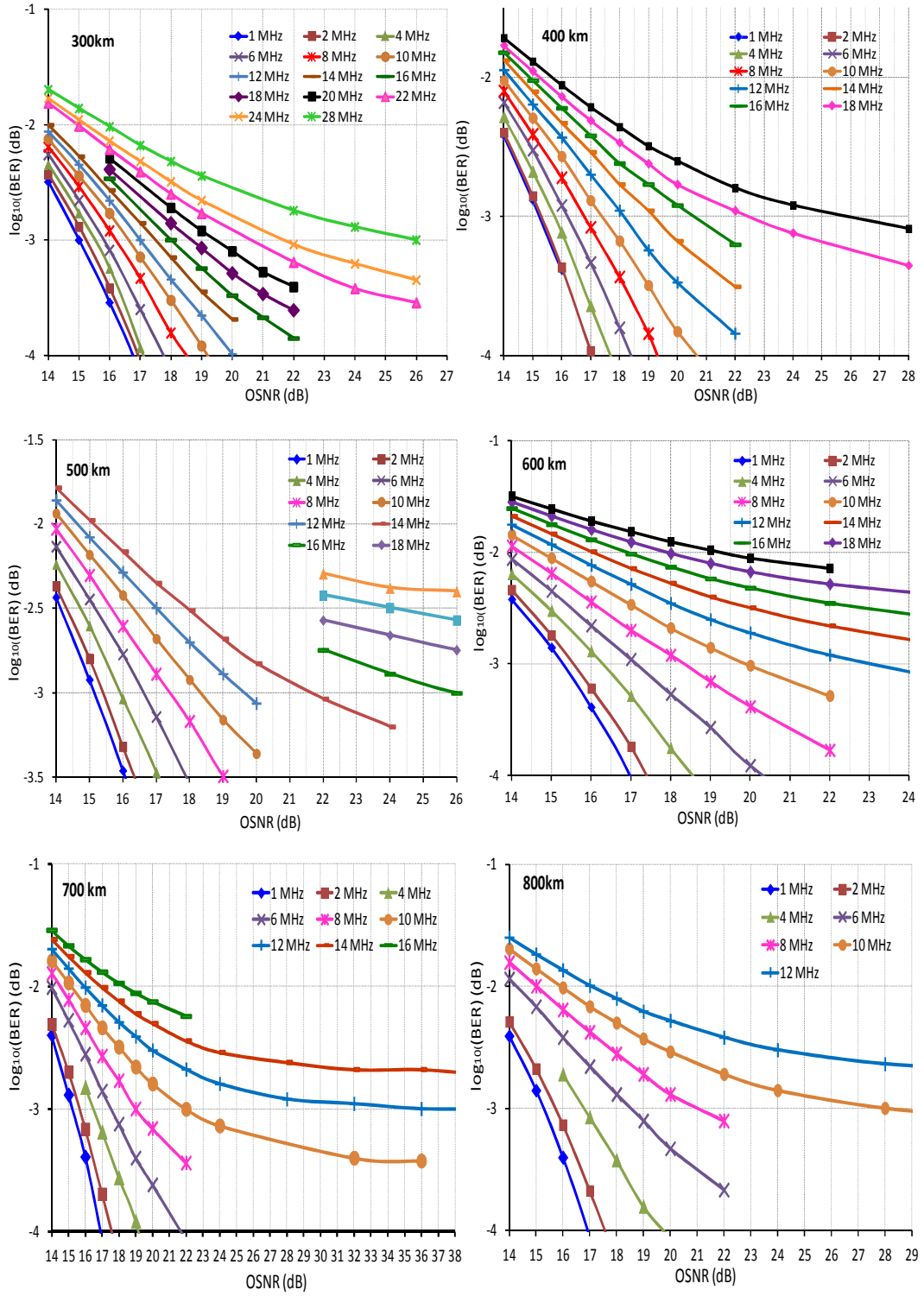
Simulation schematic using VPItransmissionMaker.

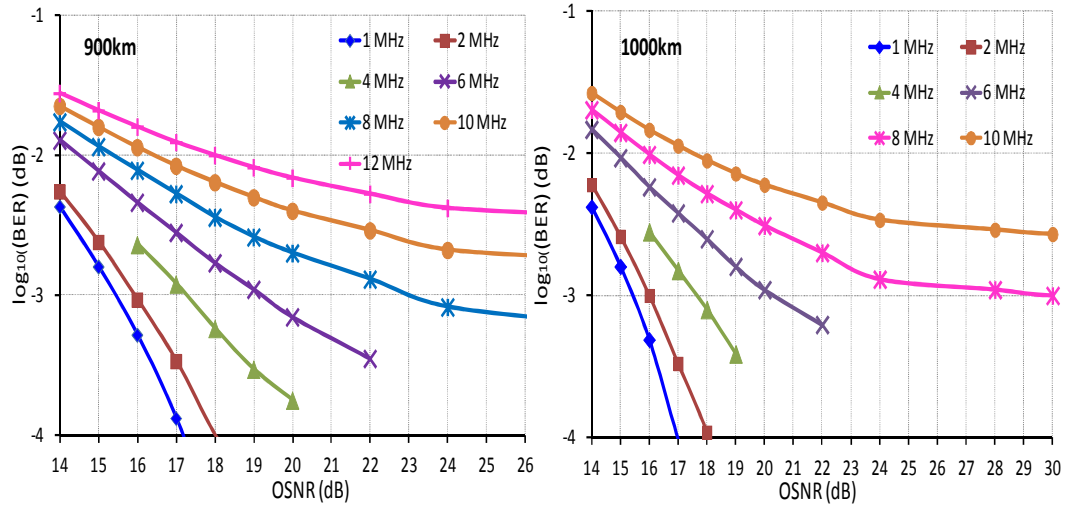


Appendix 3.6:

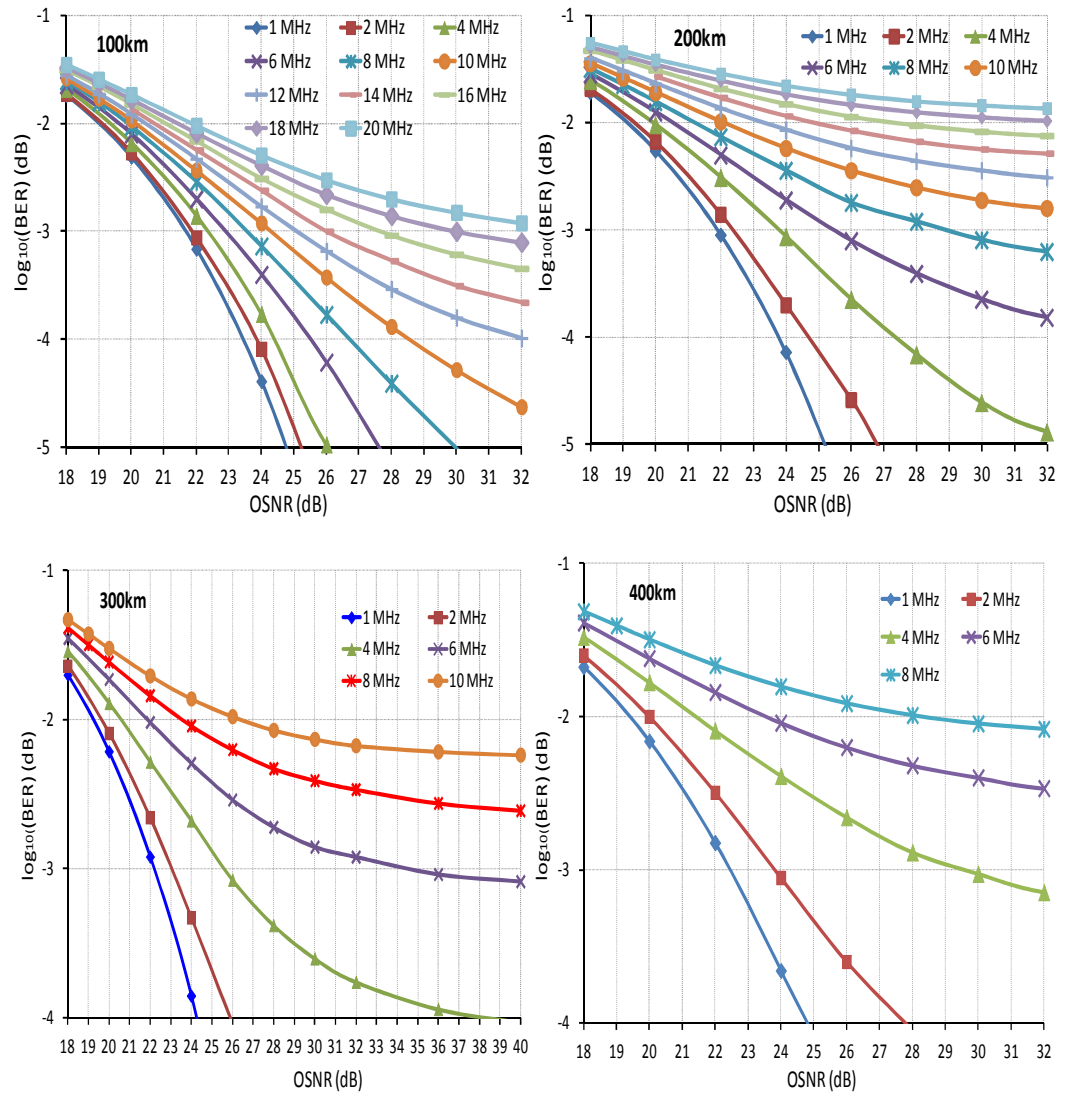
A3.3.1: Sensitivity Plots for 4 QAM Modulated OFDM Signal with 10 GHz signal bandwidth:

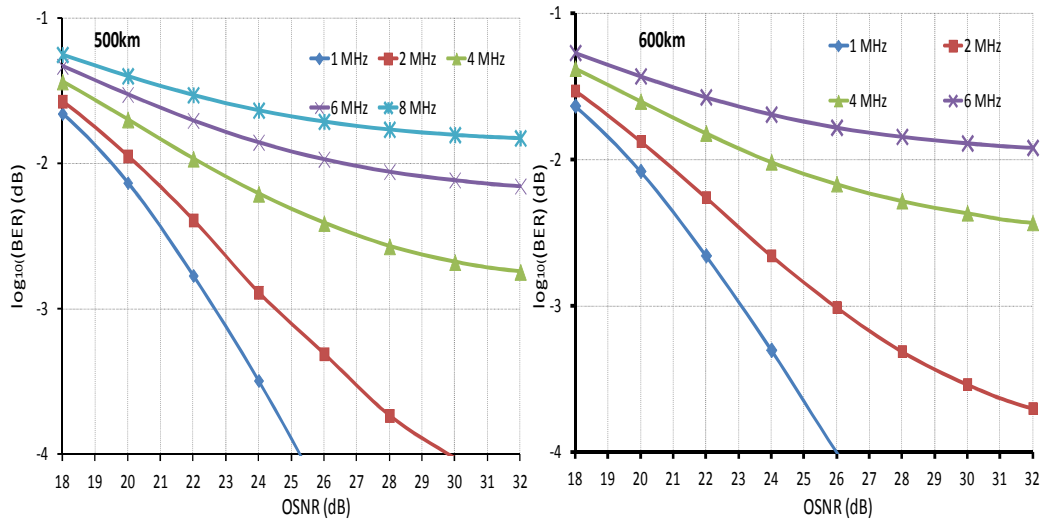




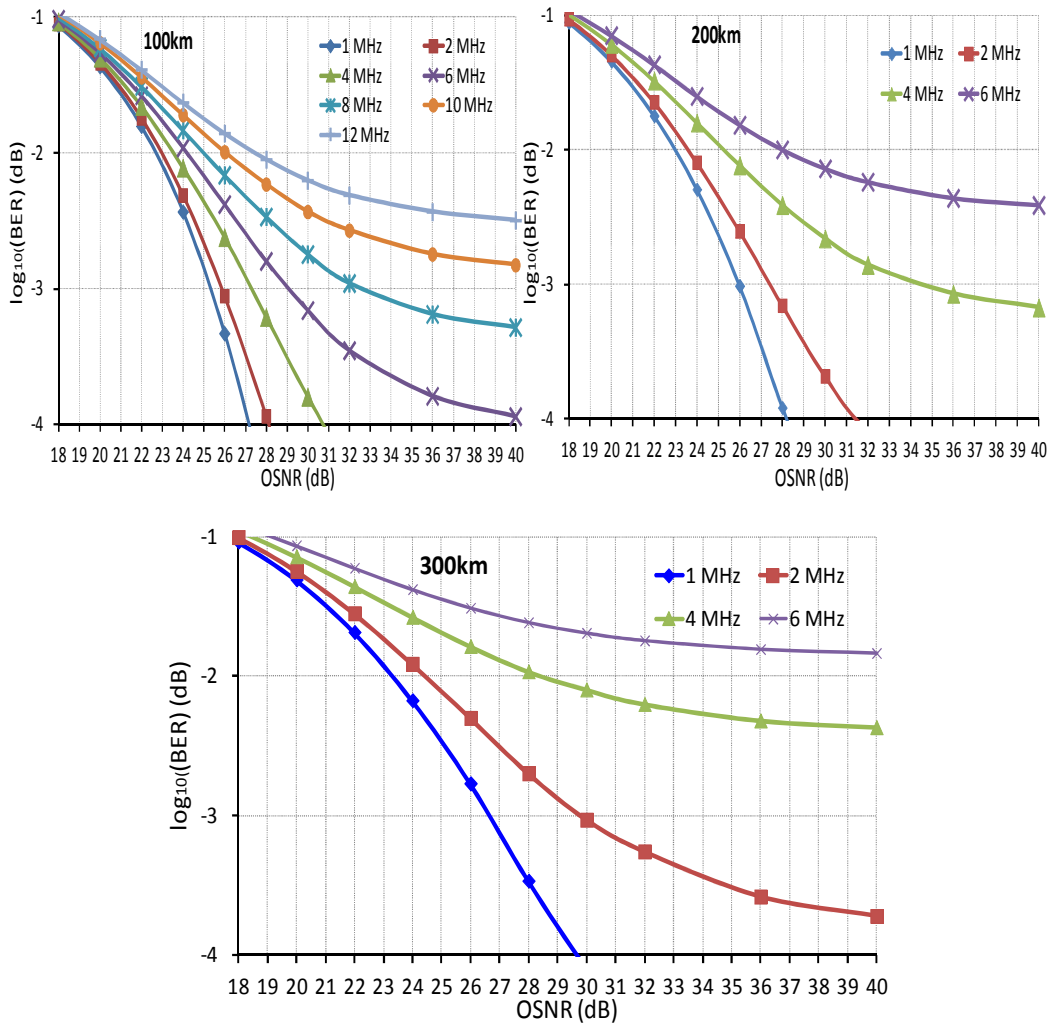


A3.3.2: Sensitivity Plots for 16 QAM Modulated OFDM Signal with 10 GHz signal bandwidth.

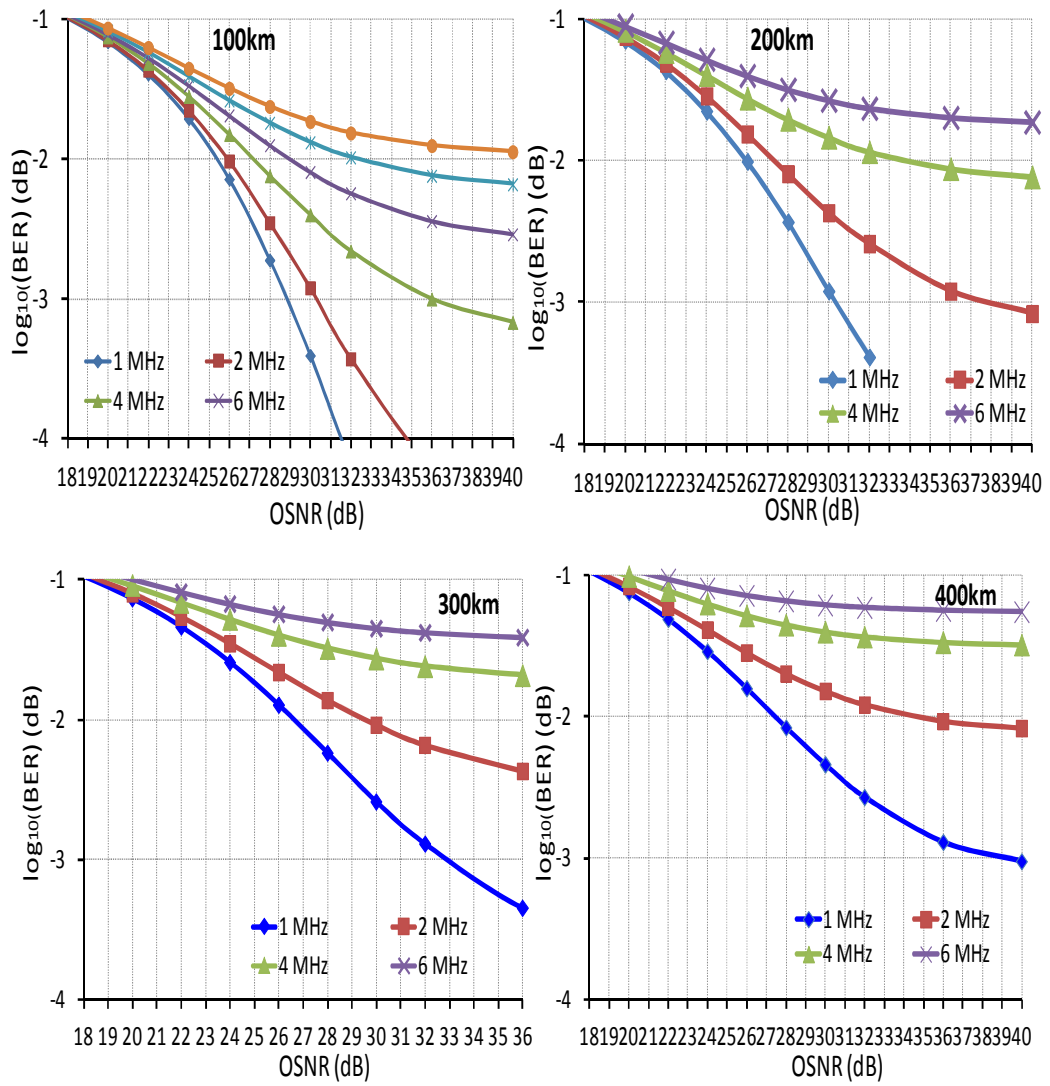




A3.3.3: Sensitivity Plots for 32-QAM Modulated OFDM Signal with 10 GHz signal bandwidth



A3.3.4: Sensitivity Plots for 64 QAM Modulated OFDM Signal with 10 GHz signal bandwidth.



APPENDIX 4

Appendix 4.1:

MATLAB transmitter code for 2.5 GHz signal bandwidth using the upper-half of the positive frequency.

```

% Use upper positive subcarriers to IFFT input and output gives I
and
% Q inputs for the dual MZI.

% Initialize some variables
NSYM = 100;
N     = 512;
M     = 4;
OS    = 1;
% Preallocate some variables
data  = zeros(NSYM,N);
ran_d = zeros(NSYM,N/4);
datai = zeros(NSYM,OS*N);
datat = zeros(NSYM,OS*N);

% Get random data, use data(:,1) to set the bias, use only highest
postive
% frequencies for SSB
ran_d = qammod(randint(NSYM,N/4,M),M);
data(:,N/4+1:N/2) = ran_d;

% Oversample, modulate and add cyclic prefix
for j = 1:NSYM,
    datai(j,:) = [data(j,1:N/2) zeros(1,(OS-1)*N) data(j,N/2+1:N)];
    datat(j,:) = (sqrt(OS*N))*(ifft(datai(j,:)));
end
datat = [datat(:,385:512) datat];

% Reshape output into single row
stream = reshape(datat.',1,[]);

% Clip real and imaginary streams to minimize quantising errors
CR = 8;
smag = abs(stream);
Esmag2 = mean(smag.^2);
limit = (Esmag2*(10^(CR/10)))^0.5
for j = 1:length(stream),
    if(smag(j)>limit) stream(j) = (limit/smag(j))*(stream(j)); end
end
sRe = [zeros(1,512) real(stream)];
sIm = [zeros(1,512) imag(stream)];

% Check sample length
fprintf('\n number of samples = %d\n',length(sR));

% Ready for Tektronix
sRe = sRe.';
sIm = sIm.';

```

```

% Check sample length
fprintf('\n number of samples = %d\n',length(stream));
% Write to files
save('TxReal.txt','sRe','-ascii');
save('TxImag.txt','sIm','-ascii');
save('savedTx','data','datai');

```

Appendix 4.2:

MATLAB receiver code for 2.5 GHz signal bandwidth using the upper-half of the positive frequency.

```

% Initialize some variables
NSYM      = 100;
N         = 512;
M         = 4;
OS        = 4;
framesize = 2560;

index_d   = zeros(NSYM,OS*N);
rec_dt    = zeros(NSYM,OS*N);
rec_d     = zeros(NSYM,OS*N);
ch_est    = zeros(NSYM,OS*N);
index_d   = zeros(NSYM,OS*N);
rec_deq   = zeros(NSYM,N/4);
rec_dsc   = zeros(NSYM,N/4);
drd       = zeros(NSYM,N/4);

% Get time domain data, load TX variables
gfstream  = load('wdm2c_ch14_300km_4q.txt');
load('SSB_RRF32');
lts = data;

plot(gfstream)
axis tight
start = 4.159e4;

% Get index to data
for toff = -300:2:0;
for j = 1:NSYM,
    initial(j) = start+toff+(j-1)*framesize;
    index_d(j,:) = (initial(j)+513):(initial(j)+2560);
end

% Get data
for j = 1:NSYM
    rec_dt(j,:) = gfstream(index_d(j,:));
end

% Demodulate, get channel response, eq the received data, get
original data
for j = 1:NSYM,
    rec_d(j,:) = ((sqrt(OS*N))^-1)*(fft(rec_dt(j,:)));
    ch_est(j,N/4+1:N/2) = rec_d(j,N/4+1:N/2)./lts(j,N/4+1:N/2);
end
ch_est_ave(1,N/4+1:N/2) = mean(ch_est(:,N/4+1:N/2));
for j = 1:NSYM,

```



```

    rec_deq(j,1:N/4)      = (ch_est_ave(1,N/4+1:N/2).^-
1).*rec_d(j,N/4+1:N/2);
    rec_dsc(j,1:N/4)     = (rec_d(j,N/4+1:N/2));
    drd(j,1:N/4)        = (data(j,N/4+1:N/2));
end

% Get Eb/No per subcarrier
if(M==64) E = 42; k = 6; end
if(M==32) E = 20; k = 5; end
if(M==16) E = 10; k = 4; end
if(M==4)  E = 2;  k = 2; end

MSE      = mean((abs(drd - rec_deq)).^2);
SNR      = E./MSE;
SNR_dB   = 10*log10(SNR);
EbNo_dB1 = SNR_dB - 10*log10(k);

EbNo     = E./(k*MSE);
EbNo_dB2 = 10*log10(EbNo);
EX_EbNo_dB = 10*log10(mean(EbNo))

figure(1)
plot(EbNo_dB1)
axis ([1 128 0 40]);
title('EbNo vrs subcarrier');
grid on;

figure(2)
plot(EbNo_dB2)
axis ([1 128 0 40]);
title('EbNo vrs subcarrier');
grid on;

% Get bit error rate
Rm = qamdemod(rec_deq,M,[],'gray');
Pm = qamdemod(drd,M,[],'gray');
[number2, ratio2, individual2] = biterr(Rm,Pm,log2(M));
fprintf('\nBER without coding = %d %d\n',number2, ratio2);
fprintf('Time offset = %d\n\n',toff);

% The "2" is to compensate for clipping
ch_mag(1,1:N/4) = abs(ch_est_ave(1,2:N/4+1));

% Fig1 displays scatterplots and channel response
figure(3)
subplot(4,4,[1:2 5:6]); plot(rec_dsc*50, '.'); title('Received
scatterplot');
axis([-7 7 -7 7]); grid on;
subplot(4,4,[3:4 7:8]); plot(rec_deq, '.'); title('Equalized
scatterplot');
axis([-7 7 -7 7]); grid on;
subplot(4,4,[9:10 13:14]); plot(10*log10(ch_mag)); title('Channel
response');
axis([1 N/4 10*log10(1e-4) 10*log10(1)]); grid on;
subplot(4,4,[11:12 15:16]); plot(sum(individual2)); title('error vrs
subcarrier before coding');
axis([1 N/4 0 50]); grid on;

```

```
drawnow
end
```

Appendix 4.3

MATLAB transmit code for 8 GHz signal bandwidth using all of the subcarriers at both negative and positive frequency:

```
%% Experiment for DFB with virtual carrier. 8 GHz signal bandwidth.
```

```
N      = 512;
NSYM   = 300;
Nuse   = 410; %% iFFT points used as subcarriers between -4GHz to
+4GHz
M      = 4;

    datai      = zeros(NSYM, N);
    datat      = zeros(NSYM, N);

    datrnd     = randint(NSYM,Nuse,M);
    data       = qammod(datrnd,M, [], 'gray');
    data(:,1)  = 0;

    pre_comp   = [linspace(1,2.1,Nuse/2) linspace(2.1,1,Nuse/2)]; %
linear increase of amplitude for C-MZI pre-emphasis
    for j = 1:NSYM,
        data_comp(j,:) = data(j,:).*pre_comp;
    end

    for j = 1:NSYM
        datai(j,:) = [data_comp(j,1:Nuse/2) zeros(1,N-Nuse)
data_comp(j,Nuse/2+1:Nuse)]; %data assigned at: 2:205 and 308:512
        datat(j,:) = ifft(datai(j,:));
    end

    % CP allocation %

    datat = [datat(:,(3*N/4)+1:N) datat];

    stream = reshape(datat.',1,[]); %

    szstream = size(stream);
    apprxpow2 = log2(szstream(1,2));
    pow2 = ceil(apprxpow2)

    % Clip real and imaginary streams to minimize quantising errors
    CR      = 8;
    smag    = abs(stream);
    Esmag2  = mean(smag.^2);
    limit   = (Esmag2*(10^(CR/10)))^0.5
    for j = 1:length(stream),
        if(smag(j)>limit) stream(j) = (limit/smag(j))*(stream(j));
    end
end
```

```

Eps      = mean((abs(stream)).^2);
s        = ((0.5/Eps).^0.5)*stream;

sR       = [zeros(1,5*N) real(stream)];
sI       = [zeros(1,5*N) imag(stream)];

sR       = sR.';
sI       = sI.';

% Check sample length

fprintf('\n number of samples = %d\n',length(sR));

save('Re_2p1a.txt','sR','-ascii');
save('Im_2p1a.txt','sI','-ascii');
save('sv_2p1a','data');

```

Appendix 4.4

MATLAB receive code for 8 GHz signal bandwidth using all of the subcarriers at both negative and positive frequency:

```

%% This Rx code is for the experiment with the DFB
% Initialize some variables
% FS = sampling rate
% T = period of five symbols = OS*N*NSYM(1/FS)
% FC = Carrier frequency

NSYM    = 300;
N       = 512;
ND      = 410;
M       = 4;
OS      = 5;
FS      = 50.0000e9;
FC      = 12.000005800e9;
FSIZE   = OS*N*(5/4); % 5x512x(4/4+1/4) = 3200, 1/4 is CP length
T       = NSYM*FSIZE*(1/FS);
FCT     = (1:FS*T)*2*pi*FC/FS;

rxR     = zeros(1,length(FCT));
rxI     = zeros(1,length(FCT));

% Load transmitted and received data, find start of frame
visually

% load('sv_2p4');
% txx = data(:, [ND/2+1:ND 2:ND/2]); %[ND/2+1:ND 2:ND/2]
% lts = txx; %% lts = long training symbol used for channel
estimation of block type channel estimation, where
% all subcarriers are taken as pilot symbols. pg
273 S.
% Bahai

```

```

    stream = load('D:\Experiment\Sem7 2010\2010Aug12 DFB LW
Experiment VC\2010Aug19_DSO\c.txt');
    save('D:\Experiment\Sem7 2010\2010Aug12 DFB LW Experiment
VC\2010Aug19_DSO\c', 'stream');
%     z = 1;

%     load('D:\Experiment\Sem7 2010\2010Aug12 DFB LW Experiment
VC\2010Aug19_DSO\g');
    rxDSO = stream;

    stream = rxDSO.';

%     plot(stream);

    start = 1.4109e4;

% Variables to modify data
for toff = -100
%     for toff = -300:10:0

        phoff = 0;
        a = 1;

        % Multiply by complex exponential
        for j = 1:length(FCT),
            rxR(j) = stream(j+start+toff)*cos(FCT(j));
            rxI(j) = stream(j+start+toff)*-sin(FCT(j)+phoff);
        end
        cstream = a*rxR + i*rxI;

        % Get index to data. With 'index', the CP is removed
        for j = 1:NSYM,
            initial(j) = (j-1)*FSIZE;
            index(j,:) =
(initial(j)+(1/4)*OS*N+1):(initial(j)+(5/4)*OS*N);
        end

        % Get data
        for j = 1:NSYM
            rxt(j,:) = cstream(index(j,:));
        end

        % Demodulate, get channel response, eq the received data,
get original data

        indfft = [2356:2560 2:205];
        for j = 1:NSYM,
            rxf(j,:) = fft(rxt(j,:));
            rx2(j,:) = (rxf(j,indfft));
            chest2(j,:) = rx2(j,:)./lts(j,:);
        end
        chest_ave(1,:) = mean(chest2,1);

        rxx = zeros(NSYM, ND-1);

        % Equalized the received data

```

```

for j = 1:NSYM,
    rxx(j,:) = (chest_ave(1,:).^-1).*(rx2(j,:));
end

% Get Eb/No per subcarrier
if(M==64) E = 42; n = 6; end
if(M==32) E = 20; n = 5; end
if(M==16) E = 10; n = 4; end
if(M==4)  E = 2;  n = 2; end

MSE      = mean((abs(txx(:, [1:ND-1]) - rxx(:, [1:ND-1]))).^2);
EbNo     = E./(n*MSE);
EbNoA    = mean(EbNo);

%      EbNoA_dB = 10*log10(EbNoA) %% EbN0 by averaging before
logarithm

EbNo_dB  = 10*log10(EbNo); %% EbN0 across SC

%%% Taking out teeth
%%%%%%%%%%%%%%%%%%%%%%%%%%%%%%%%%%%%%%%%%%%%%%%%%%%%%%%%%%%%%%%%%%%%%%%%
teethIndx = [1:103 105:390 392:ND-1]; %% teeth index when
Idfb = 40mA
teethIndx1 = [1:70 73:103 105:229 232:390 392:ND-1]; %%
teeth index when Idfb = 30.01mA
MSE2      = MSE(:,teethIndx1);
EbNo2     = E./(n*MSE2);
EbNoA2    = mean(EbNo2);

EbNoA2_dB = 10*log10(EbNoA2) %% EbN0 by averaging before
logarithm

EbNo2_dB  = 10*log10(EbNo2); %% EbN0 across SC

%%% To calculate small q: Q(q) = 1/2erfc(q/sqrt(2)) q =
sqrt(2*Eb/No)%%%
q_small   = sqrt(2*EbNo2);
Pb_BER    = 0.5*erfc(q_small/sqrt(2));
Pb_BER1   = 0.5*erfc(sqrt(EbNo2));

%%% To calculate Q with Q(q) = 20log10(q);
q_smallA  = mean(q_small); %% Average q small

Q_capdB   = 20*log10(q_small); % Q (dB) over SC

Q_dBval   = 20*log10(q_smallA)
%      BER_qsmall = mean(Pb_BER)

%%% Average channel estimation dB %%%
chest_avedB = 20*log10(abs(chest_ave(1, [1:ND-1])));

```

```

        figure(1), hold on
        subplot(2,2,1); plot(EbNo_dB, 'r'); axis([1 ND-1 0 20]);
grid on; title('EbNo vs SC');
        subplot(2,2,2); plot(EbNo2_dB,'r'); axis([1 ND-1 0 20]);
grid on; title('EbNo2 vs SC');
        subplot(2,2,3); plot(chest_avedB(1,[1:ND-1]),'r'); axis([1
ND-1 -20 30]);grid on; title('Average channel estimation vs
subcarriers');
        subplot(2,2,4); plot(Q_capdB,'r'); axis([1 ND-1 0 20]); grid
on; title('Q vs SC');

% Get bit error ratio
Drxx    = qamdemod(rxx(:, [1:ND-1]),M, [], 'gray');
Dtxx    = qamdemod(txx(:, [1:ND-1]),M, [], 'gray');

[number, ratio, individual] = biterr(Drxx(:, [1:ND-
1]),Dtxx(:, [1:ND-1]),log2(M));
fprintf('\nbiterr = %d %d\n',number,ratio);
fprintf('ntoff = %d\nphoff = %d\n\n',toff,phoff);

BER_SC = mean(individual(:, [1:ND-1]));

%%% take the teeth out from BER SC
Drxx2    = qamdemod(rxx(:,teethIndx1),M, [], 'gray');
Dtxx2    = qamdemod(txx(:,teethIndx1),M, [], 'gray');

[num, rat, ind] = biterr(Drxx2,Dtxx2,log2(M));
fprintf('\nbiterr2 = %d %d\n',num,rat);

BER_SC2 = mean(ind(:,:));

% figure(2), hold on
subplot(2,1,1); plot(BER_SC); axis([1 ND-1 0 0.01]); grid
on; title('BER vs SC');
% subplot(2,1,2); plot(BER_SC2); axis([1 ND-1 0 0.01]);
grid on; title('BER2 vs SC');

rxx_plot = rxx(:, [1:ND-1]);
re_RX = real(rxx_plot);
im_RX = imag(rxx_plot);

%%% Reshape to change the matrix to a single column matrix
re_RX = re_RX.';
im_RX = im_RX.';

InphaseRX = reshape(re_RX,1,NSYM*(ND-1));
QuadRX    = reshape(im_RX,1,NSYM*(ND-1));

figure(3), hold on
plot(rxx_plot, '.r'); grid on

% drawnow
End

```

APPENDIX 5

Appendix 5.1:

Receive code to obtain the transmitted data and examine the system performance of the SHO-OFDM transmission system.

```

NSYM = 300;
N = 512;
ND = 410;
M = 4;
OS = 5;
FS = 50.0000e9;
FC = 12.500005500e9;
FSIZE = OS*N*(5/4); % 5x512x(4/4+1/4) = 3200, 1/4 is CP length
T = NSYM*FSIZE*(1/FS);
FCT = (1:FS*T)*2*pi*FC/FS;

rxR = zeros(1,length(FCT));
rxI = zeros(1,length(FCT));

% stream = load('D:\Experiment\Sem7 2010\2010Nov30 Delay SHO
OFDM\2010DEC3DSO_720kma\a39p6_0.txt');
% save('D:\Experiment\Sem7 2010\2010Nov30 Delay SHO
OFDM\2010DEC3DSO_720kma\a39p6_0', 'stream');

% Load transmitted and received data, find start of frame
visually

load('sv_Sig');
txx = data(:, [ND/2+1:ND 2:ND/2]); %[ND/2+1:ND 2:ND/2]
lts = txx; %% lts = long training symbol used for channel
estimation of block type channel estimation, where
%% all subcarriers are taken as pilot symbols. pg
273 S.
%% Bahai
z = 1;

load('D:\Experiment\Sem7 2010\2010Nov30 Delay SHO
OFDM\2010DEC3DSO_720kma\0cm_dc3p82');

rxDSO = stream;

stream = rxDSO.';

figure(1);plot(stream);

start = 2.0095E+04 ; % for 720km

for toff = -90
% for toff = -300:10:0

phoff = 0;
a = 1;

```

```

    % Multiply by complex exponential
    for j = 1:length(FCT),
        rxR(j) = stream(j+start+toff)*cos(FCT(j));
        rxI(j) = stream(j+start+toff)*-sin(FCT(j)+phoff);
    end

    % add delay between I and Q
    delay = 0;
    rxR = rxR(1+delay:end);
    rxI = rxI(1:end-delay);
    cstream = a*rxR + i*rxI;

    % Get index to data. With 'index', the CP is removed
    for j = 1:NSYM,
        initial(j) = (j-1)*FSIZE;
        index(j,:) =
(initial(j)+(1/4)*OS*N+1):(initial(j)+(5/4)*OS*N);
    end

    % Get data
    for j = 1:NSYM
        rxt(j,:) = cstream(index(j,:));
    end

    % Demodulate, get channel response, eq the received data,
get original data
    indfft = [2356:2560 2:205];
    for j = 1:NSYM,
        rxf(j,:) = fft(rxt(j,:));
        rx2(j,:) = (rxf(j,indfft));
        chest2(j,:) = rx2(j,:)./lts(j,:);
    end
    chest_ave(1,:) = mean(chest2,1);

    rxx = zeros(NSYM, ND-1);

    % Equalized the received data
    for j = 1:NSYM,
        rxx(j,:) = (chest_ave(1,:).^-1).*(rx2(j,:));
    end

    % Get Eb/No per subcarrier
    if(M==64) E = 42; n = 6; end
    if(M==32) E = 20; n = 5; end
    if(M==16) E = 10; n = 4; end
    if(M==4) E = 2; n = 2; end

    MSE = mean((abs(tx(:, [1:ND-1]) - rxx(:, [1:ND-1]))).^2);
    EbNo = E./(n*MSE);
    EbNoA = mean(EbNo);

    EbNoA_dB = 10*log10(EbNoA) %% EbN0 by averaging before
logarithm
    EbNo_dB = 10*log10(EbNo); %% EbN0 across SC

    %% Taking out teeth

```



```

%       Indx       = [1:ND-1];
%       teethIndx2 = Indx;
teethIndx2 = [1:45 47:364 366:ND-1];

MSE2      = MSE(:,teethIndx2);
EbNo2     = E./(n*MSE2);
EbNoA2    = mean(EbNo2);

EbNoA2_dB = 10*log10(EbNoA2) %% EbN0 by averaging before
logarithm *****

EbNo2_dB  = 10*log10(EbNo2); %% EbN0 across SC

%% To calculate small q:  $Q(q) = 1/2\text{erfc}(q/\sqrt{2})$   $q = \sqrt{2*Eb/No}$ 
q_small   = sqrt(2*EbNo2);
Pb_BER    = 0.5*erfc(q_small/sqrt(2));
Pb_BER1   = 0.5*erfc(sqrt(EbNo2));

%% To calculate Q with  $Q(q) = 20\log_{10}(q)$ ;
q_smallA  = mean(q_small); %% Average q small

Q_capdB   = 20*log10(q_small); % Q (dB) over SC
mn_Q_capdB = mean(Q_capdB)

Q_dBval   = 20*log10(q_smallA); #####
%       BER_qsmall = mean(Pb_BER)

%% Average channel estimation dB
chest_avedB = 20*log10(abs(chest_ave(1,[1:ND-1])));

figure(2), hold on
subplot(2,2,1); plot(EbNo_dB, 'k'); axis([1 ND-1 0 20]);
grid on; title('EbNo vs SC'); hold on
subplot(2,2,2); plot(EbNo2_dB,'k'); axis([1 ND-1 0 20]);
grid on; title('EbNo2 vs SC'); hold on
subplot(2,2,3); plot(chest_avedB(1,[1:ND-1]),'k'); axis([1
ND-1 -25 20]);grid on; title('Average channel estimation vs
subcarriers'); hold on
subplot(2,2,4); plot(Q_capdB,'k'); axis([1 ND-1 0 20]); grid
on; title('Q vs SC'); hold on

% Get bit error ratio
Drxx      = qamdemod(rxx(:, [1:ND-1]),M, [], 'gray');
Dtxx      = qamdemod(txx(:, [1:ND-1]),M, [], 'gray');

[number, ratio, individual] = biterr(Drxx(:, [1:ND-
1]),Dtxx(:, [1:ND-1]),log2(M));
%       fprintf('\nbiterr = %d %d\n',number,ratio);
fprintf('ntoff = %d\nphoff = %d\n\n',toff,phoff);

BER_SC = mean(individual(:, [1:ND-1]));

%% take the teeth out from BER SC
Drxx2     = qamdemod(rxx(:,teethIndx2),M, [], 'gray');
Dtxx2     = qamdemod(txx(:,teethIndx2),M, [], 'gray');

```

```

[num, rat, ind] = biterr(Drxx2,Dtxx2,log2(M));
fprintf('\nbiterr2 = %d %d\n',num,rat);

BER_SC2 = mean(ind(:, :));

%       figure(15), hold on
%       subplot(2,1,1); plot(BER_SC); axis([1 ND-1 0 0.01]); grid
on; title('BER vs SC');
%       subplot(2,1,2); plot(BER_SC2); axis([1 ND-1 0 0.01]); grid
on; title('BER2 vs SC');

rxx_plot = rxx(:, [1:ND-1]);
re_RX = real(rxx_plot);
im_RX = imag(rxx_plot);

%% Reshape to change the matrix to a single column matrix
re_RX = re_RX.';
im_RX = im_RX.';

InphaseRX = reshape(re_RX,1,NSYM*(ND-1));
QuadRX    = reshape(im_RX,1,NSYM*(ND-1));

%
figure(3), hold on
plot(rxx_plot, '.g'); grid on; hold on

%
drawnow
%
figure(16), hold on
%
plot(EbNoA2_dB, '*b'); grid on; hold on

```

End

Appendix 5.2:

Signal quality, Q, versus OFDM subcarrier index which corresponds to a low to high frequency subcarriers for a 720 km transmission.

